NOVEL ANTENNAE FOR THE SENSITIZATION AND PROTECTION OF LANTHANIDE CATIONS EMITTING IN THE VISIBLE AND NEAR-INFRARED

by

Demetra Anne Chengelis Czegan

B.A., Seton Hill University, 2002

M.S., University of Pittsburgh, 2005

Submitted to the Graduate Faculty of

University of Pittsburgh in partial fulfillment

of the requirements for the degree of

Doctor of Philosophy

University of Pittsburgh

2009

UNIVERSITY OF PITTSBURGH

FACULTY OF ARTS AND SCIENCES

This dissertation was presented

by

Demetra Anne Chengelis Czegan

It was defended on

July 31, 2009

and approved by

Sunil Saxena

Adrian Michael

Alan Waggoner

Stéphane Petoud
Dissertation Director

NOVEL ANTENNAE FOR THE SENSITIZATION AND PROTECTION OF LANTHANIDE CATIONS EMITTING IN THE VISIBLE AND NEAR-INFRARED

Demetra A. Chengelis Czegan, PhD

University of Pittsburgh, 2009

Several lanthanide cations are luminescent in the visible and in the near-infrared (NIR) regions, with unique and advantageous luminescence properties compared to organic fluorophores, which make luminescent lanthanide complexes desirable for a range of applications including light amplification, optical telecommunications, biological imaging and bioanalytical techniques. To overcome the limitation of low absorptivity and weak luminescence of free lanthanide cations in solution, lanthanide complexes are formed with chromophoric groups that are capable of absorbing incident light, and transferring the resulting energy to the lanthanide cation thus sensitizing luminescence ("antenna effect"). Additionally, lanthanide cations must be protected from solvent molecules whose vibrational overtones efficiently deactivate lanthanide cation excited states through non-radiative routes. The research work presented here has focused on developing lanthanide species with improved photophysical properties, utilizing a variety of approaches to reach two main goals: providing efficient sensitization of lanthanide cations via the antennae effect and superior protection against non-radiative deactivation.

In a relatively traditional coordination chemistry approach, natural product molecules of the flavonoid family were used as antennae for NIR emitting lanthanide cations. Using a nanomaterials approach to achieve improved protection from quenching, visible emitting lanthanide cations were incorporated into CdSe semiconductor crystals, which bring their own

electronic properties, including broad absorbance bands with high epsilon values and size dependent band gaps. Thus, the nanocrystals are used to provide protection from quenching as well as sensitize lanthanide cations through the antennae effect. In an alternate nanomaterials approach NIR emitting Yb^{3+} and Nd^{3+} were incorporated into $NaYF_4$ inorganic nanoparticle matrices that were coated with organic tropolonate sensitizing groups. The nanoparticle matrix protects the lanthanide cations from non-radiative deactivation while the surface bound chromophores provide antennae effect sensitization. In addition, upconverting $NaYF_4$:Yb,Er nanocrystals were synthesized and their potential to serve as energy acceptors from a naphthalimide based antenna or energy donors to Quantum Dots were investigated. Finally, metal-organic frameworks (MOFs) were explored as method to sensitize NIR and visible emitting lanthanide cations by incorporating the lanthanide cations at metal sites in the MOF structure and/or as occupants of the pores of zinc based MOFs.

TABLE OF CONTENTS

LIST OF TABLES

LIST OF FIGURES

PREFACE

This thesis is dedicated to my family and friends who were here to see me embark on this journey, but are now only with us in spirit as it comes to end.

John Fiacco

Mary Fiacco

Chris Chengelis

Lt. Neil Sanotoriello (KIA, Operation Iraqi Freedom, August 13, 2004), whose last words to me were "P.S. Go for the PhD!"

There are many people to whom I owe credit and appreciation. Completing graduate school and finishing a thesis would not have been possible without the mountain of support I have had behind me through this process:

My exceptionally patient and supportive husband, Matthew Czegan, who tolerated all ranges of mood swings, my unpredictable work hours and stipend income with unwavering encouragement.

My son, Lukas Czegan, who we were blessed with just this past year. He has kept me solidly grounded on the realization that life is much bigger than this thesis.

My family, especially my parents Dr. Christopher and Maryanne Chengelis, who raised me to value a quality education and the opportunities it provides, and stubbornly encouraged me to stick with it despite my many moments of hating school. Also, my brothers Peter, Damon and Alexander, who were always a source of laughter and distraction when I needed it.

My dearest friend, Dr. Christin Hanigan, since our freshman year of college she has been my sounding board, my rock through all the ups and downs of life, a cheerful companion and source of illogical reason.

My graduate school sister, Dr. Valerie McCarthy. Together we not only tackled graduate school, but also the marathon: once having run 26.2 miles, anything seems possible.

The wonderful teachers and professors who inspired me to pursue an education in science and chemistry, helping me to realize my full potential while being a joy to learn from: Mr. Steve Huber, Dr. Matthew Arthur, Ms. Cora Durtschi, Sr. Susan Yochum, Dr. Frances Blanco-Yu, Dr. Paul Whitmore, and Dr. Rex Shepard.

I also must thank all those who made this research work possible:

My advisor, Professor Stéphane Petoud for his support, guidance, time, and shared knowledge.

Our collaborators who were essential to the completion of this work - Nathaniel Rosi, David Waldeck, Marcel Bruchez, Allen Waggoner, Simon Watkins, and Claudette St. Croix.

My committee – Sunil Saxena, Stephen Weber, Adrian Michael, and Alan Waggoner.

The graduate students and post-docs with whom I worked, for their moral support, insightful discussion, collaborative efforts, and enjoyable company – Matthew Lockett, Adrienne Yingling Oxley, Samuel Oxley, Chad Shade, Jian Zhang, Jason Cross, Paul Badger, Hyounso Uh, Kristy Gogick, Lijuan Su, Jihyun An, and Kiley White.

The excellent undergraduate students who I was fortunate to have working with me on portions of this research – Jeanette Cessarich and Kristen Peuschel.

The machine shop, electronics shop, and glass shop who helped make many of my visions into reality.

The staff in the chemistry department office who take care of all the important behind the scenes aspects of graduate studies.

My deepest appreciation to all you.
Thank you for helping to make graduate school and obtaining a Ph.D. possible for me.

Now, Let's Celebrate!

1. INTRODUCTION TO LUMINESCENT LANTHANIDE COMPLEXES

The series of elements whose electronic configuration is $[Xe]5s^2 5p^6 4f^n$, cerium to lutetium on the periodic table, are known as the Lanthanides (Ln). They are all naturally occurring and usually found in the tripositive oxidation state as ores, most often orthophosphate ores, with the exception of promethium which is artificially produced. They are often found as a mixture, and all have very similar chemical reactivities, which makes their separation difficult. The lanthanide cations are highly electronegative and behave as strong Lewis acids, forming mainly electrostatic bonds. The cationic radius for Ln^{3+} decreases from 1.17Å for lanthanum to 1.00Å for lutetium through the series, a phenomenon termed "the lanthanide contraction."[1] The coordination number can range from 3 to 12 for lanthanide cations, with 8 and 9 being the most common. Lanthanide cation complexes have a wide variety of possible geometries for any given coordination number, based on the contracting radii, coordinating solvent molecules, ligand geometry, steric interactions between ligands and the electrostatic nature of lanthanide cation bonds. The strongest lanthanide bonds occur with oxygen donors, since they are strong Lewis bases. In solution, monodentate oxygen ligands can dissociate; therefore bidentate chelating oxygen ligands are preferred as they form more stable bonds. Lanthanide cations can also coordinate with multidentate nitrogen and sulfur ligands, although these bonds are weaker than those formed with oxygen donors. Phosphorus and cyclopentadienyl complexes have also been reported, but these complexes display reduced stability.[2]

One of the interesting and useful properties of several lanthanide cations is their ability to absorb energy and then return to the ground state via emission of a photon. These luminescent transitions occur within the *f*-orbitals and are forbidden; meaning the probability of populating the excited state is relatively low. The forbidden nature of the lanthanide $f \rightarrow f$ electronic transitions leads to unique and beneficial luminescent properties.[3] Depending on the energy levels of a specific cation, the emitted light can be the in the ultra violet (UV), visible, or near infrared (NIR) ranges. The energy levels of several of the lanthanide cations are illustrated in Figure 1.1.[4]

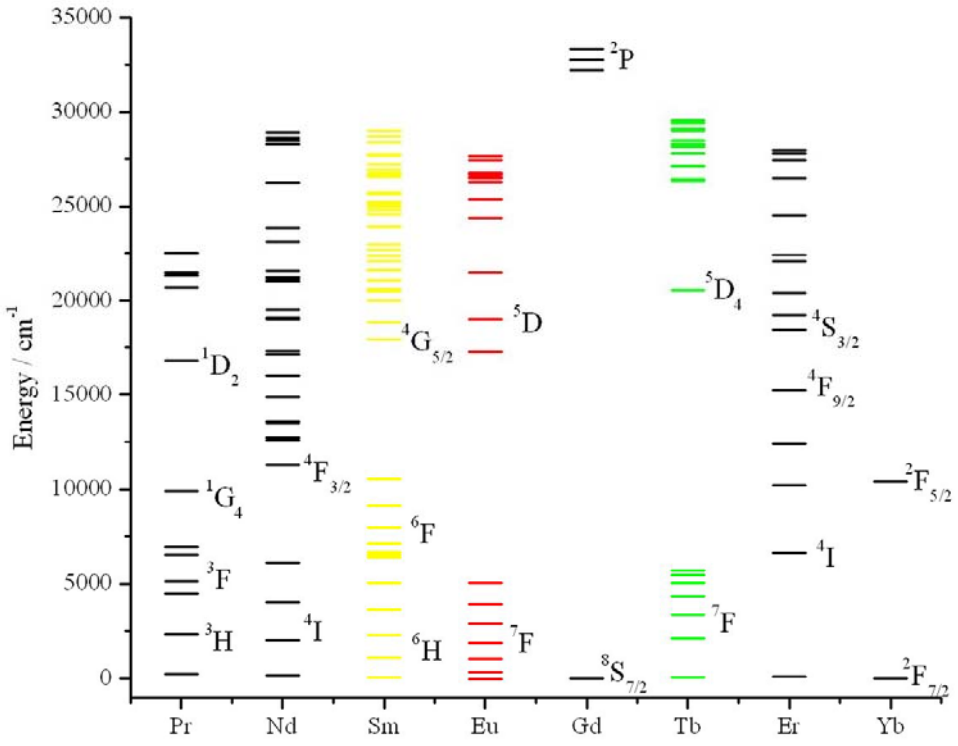

Figure 1.1. An energy level diagram depicting the energy levels within the *f*-orbitals for several lanthanide cations.[5]

Emission of UV light is less interesting than visible or NIR emission, and is therefore not discussed further. There are four lanthanide cations that emit in the visible range: Eu^{3+}, Tb^{3+}, Sm^{3+}, and Dy^{3+}, and five that emit in the NIR range: Nd^{3+}, Ho^{3+}, Er^{3+}, Tm^{3+}, and Yb^{3+}. Each has its own unique spectrum, and they are easily distinguished from one another due to their sharp (or atom-like) emission bands as shown in Figure 1.2.

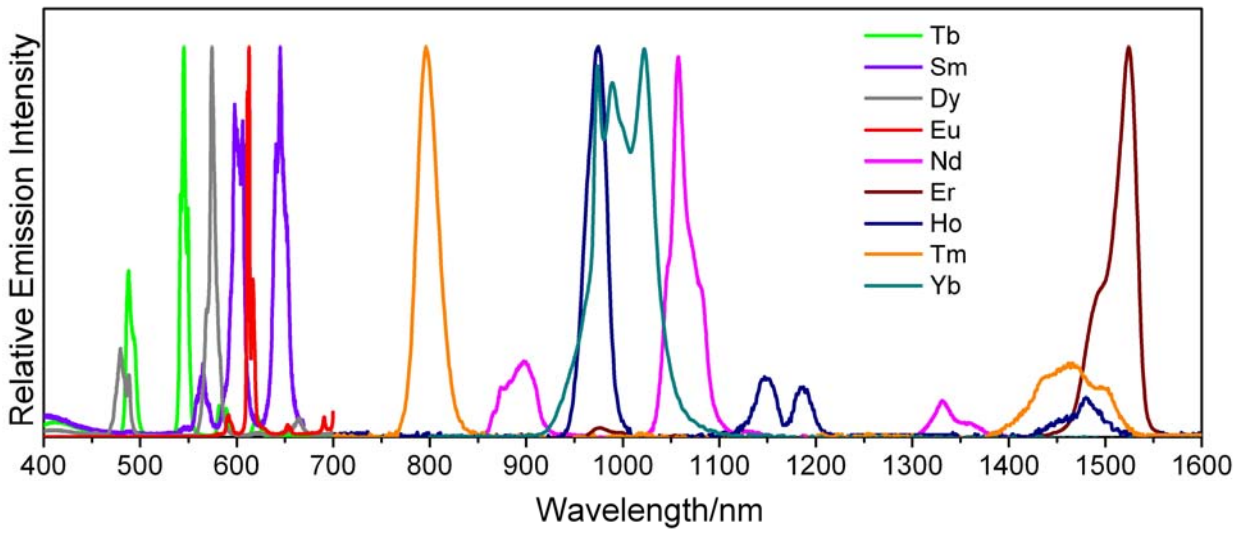

Figure 1.2. Normalized emission spectra of the luminescent lanthanide cations in complexes that emit in the visible (350-750 nm) or NIR (600-1600 nm) ranges.[6,7]

To date, most of the work done with luminescent lanthanide complexes has used Eu^{3+} and Tb^{3+}.[3] However, complexes that emit in the NIR range are of great interest as they have the potential for use in bioimaging applications.[8,9] NIR emitters have several features that give them great potential for serving as bioanalytical reporters: 1) NIR photons scatter less than visible photons, which improves image resolution and provides the opportunity for high-resolution imagery.[10] 2) Biological systems have low native autofluorescence in the NIR energy domain,[11]

resulting in higher detection sensitivity due to improved signal-to-noise ratio. 3) Biological materials have low molar absorptivity in the NIR range compared to the UV and visible ranges, thus, NIR radiation can deeply penetrate blood, skin, organs, etc., allowing for *in vivo* imaging, an extremely useful trait for imagery in medicine and biology.

Lanthanide cation luminescence differs in several advantageous ways from organic fluorophores. They have sharp, distinctive emission bands with band widths at half height of 15 nm or less, which allows for easy discrimination between the signals of different lanthanide cations. Organic molecule fluorescence bands are much broader, with band widths at half height in the range of 100 nm, so large spectral overlaps can exist between several fluorophores. Organic molecules can undergo self-quenching when the distance between the absorption band and emission band is small, or overlapping. Lanthanide complexes also have large spectral gaps between excitation and emission wavelengths, preventing self-quenching. The emission lifetimes of lanthanide cations are much longer (micro- to millisecond) compared to organic fluorophores (pico- to nanosecond), making them excellent candidates for time-resolved measurements.[12,13] This technique is especially advantageous for biological imagery applications, since it increases the signal-to-noise ratio by removing the signals arising from background autofluorescence present in biological samples. Also, lanthanide complexes rarely photobleach since the metal cations stabilize the excited states of ligand molecules, preventing irreversible photo-reactions that typically occur with organic fluorophores causing loss of signal with prolonged exposure to light.

The unique luminescent properties of lanthanide cations are based on the nature of the *f*-orbitals,[14] where the electronic transitions take place. The 4*f* orbitals are highly shielded from their environment by the 5*s* and 5*p* orbitals.[14] Theoretically, all radiative energy transfer occurs

between two quantized energy levels and should emit a photon of light at a single wavelength or specific energy. However, the energy levels of organic molecules are further split into fine vibrational levels, which broaden the emission band. This is quite limited for lanthanide cations, thus their emission bands are much sharper. The $f \rightarrow f$ transitions are parity, or Laporte forbidden, which induces their long emissive lifetimes. The Laporte selection rule forbids transitions that involve the redistribution of electrons in a single quantum shell, thus $p \rightarrow p$, $d \rightarrow d$, $f \rightarrow f$ transitions are not allowed. However, ligand field and vibrational states can interact to mix electronic states with different parity into the 4*f* functions creating admixtures which partially removes the forbidden nature of the transitions. The extent of the mixing is small though, since the 4f orbitals are well shielded, thus there is still a low probability that the excited states will be populated. This has two main impacts on the luminescence properties: they will have low molar absorptivity coefficients and long luminescence lifetimes. [3,4]

Due to the nature of their $f \rightarrow f$ transitions, free lanthanide cations in solution interact weakly with incoming light, and have exceptionally low molar absorptivities. The quantum efficiency of Ln^{3+} emission can be improved by utilizing an organic chromophore close to the lanthanide. Light is absorbed by the chromophore, and its energy is transferred to the lanthanide cation, resulting in sensitized emission. This has process was discovered in 1942 by Weissman, which he named the "Antenna Effect" (see Figure 1.3).[15]

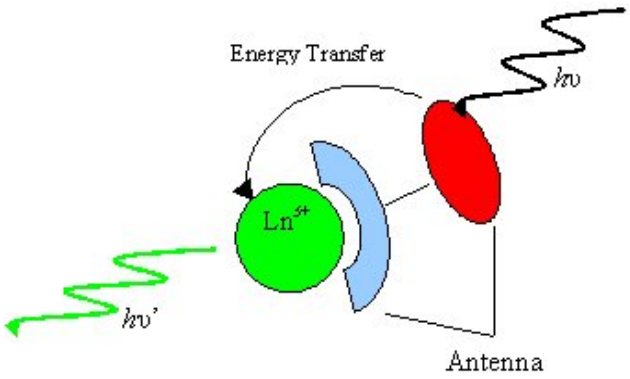

Figure 1.3. Schematic illustration of the "Antenna Effect;" the chromophore group of the antenna absorbs a photon of light, *h*ν, and transfers the resulting energy to the lanthanide cation, which emits a photon of light at a lower energy, *h*ν'.

There are two necessary parts to an antenna, a binding group to insure proximity to the lanthanide cation and a chromophore. In some cases the binding groups are part of the chromophore, and in others the chromophore is linked to a separate binding group. Criteria for an ideal chromophore group include a high yield of intersystem crossing to the triplet state, an absorbance band at 350 nm (or lower energy), and a high molar absorptivity. In order for the energy transfer and lanthanide cation luminescence to be an efficient process, the donating energy levels of the chromophore and accepting levels of the lanthanide cation must be well matched to each other. The distance between the chromophore and the metal center is another factor. The energy transfer process is more efficient when the chromophore is closer to the lanthanide cation. It is also important for the cation to be well protected from vibrational deactivations. Water, and other solvents, can be strong quenchers, since the O-H, N-H, and C-H oscillators provide a non-radiative path for returning to the ground state.[16] Thus, providing high coordination numbers (lanthanides prefer 8-12 in solution) is a criterion for the binding groups of antennae.

The energy transfer mechanism that occurs through the antenna effect involves several steps that are well illustrated through a Jablonski diagram, see Figure 1.4. First the chromophore group absorbs light, and is promoted from the ground state, S_0, to an excited singlet state, S*. From here, energy can be used for photochemical reactions, or lost through emission of a photon of light (fluorescence), non-radiative deactivation, or intersystem crossing to the triplet state, T*, of the molecule. The triplet state can relax to the ground state through emission of a photon (phosphorescence), non-radiative deactivation, or it can transfer its energy to the lanthanide cation, thus promoting the excited states in the lanthanide cation. The lanthanide excited state can return the ground state through non-radiative deactivation, or by emission of a photon (luminescence).[3,4,14] The terms donor and acceptor are often used to explain energy transfer mechanisms. In the antenna formalism, the donor is the chromophore group, which donates its excited state energy to the lanthanide cation, the acceptor.

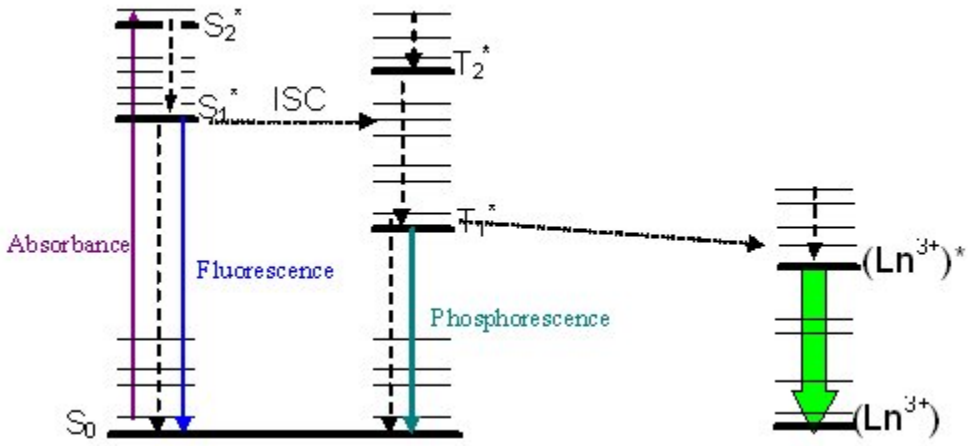

Figure 1.4. A Jablonski diagram illustrating the energy transfer mechanism involved from antenna absorption to lanthanide luminescence, along with other competing processes. The solid lines represent a radiative transition and the dashed lines represent non-radiative mechanisms.

There are three possible mechanisms for energy transfer from the excited chromorphore to the lanthanide cation, i) the Förster and ii) Dexter theories, shown in Figure 1.5, as well as iii) reduction or oxidation. According to the Förster theory,[17] energy transfer takes place through dipole-dipole resonance and requires that there be some overlap between the emission band of the donor and absorption band of the acceptor. In this case, an electron in the donor excited state returns to its ground state, while releasing energy. This energy is absorbed by an electron in the acceptor ground state, and is promoted to the excited state. There is no electron transfer in the Förster theory, only energy transfer between two different partners through dipole-dipole resonance interaction. On the other hand, the Dexter[18] theory suggests that energy transfer occurs through orbital overlap between the donor and acceptor, accompanied with electrons simultaneously exchanging from one orbital (the ligand) to the other (the lanthanide cation). The final possible mechanism is electron transfer that results in oxidation or reduction of the metal. This route is similar to Dexter in that it requires orbital overlap and an electron moving between orbitals, except it does not involve simultaneous electron exchange and is more efficient. This is the least likely route for most lanthanide complexes as the lanthanide cations have a strong preference for the three plus oxidation state; it, however, does occur, particularly with europium, samarium, and ytterbium.

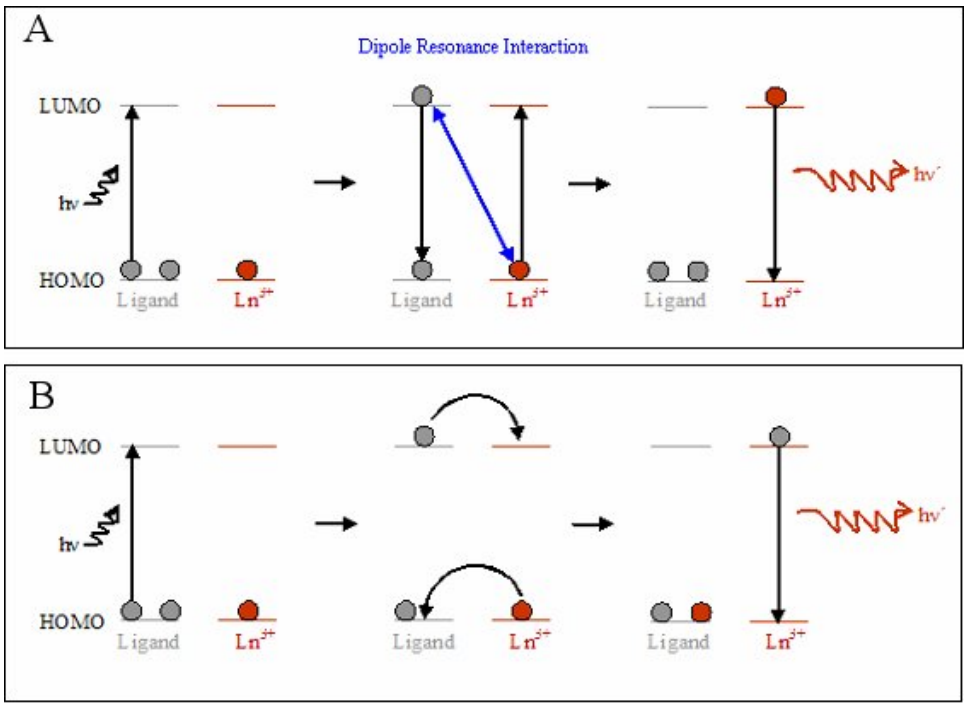

Figure 1.5. A) Förster energy transfer mechanism. B) Dexter energy transfer mechanism. Note the difference between the final locations for the two electrons of the ligand (donor) after energy transfer.

Vibrational non-radiative transitions are the main source of luminescence quenching for excited lanthanide cations. Non-radiative relaxation between J states occurs through the interaction of lanthanide electronic levels with compatible vibrational modes of the environment. The extent of this quenching is dependent on the energy gap between the lanthanide cation ground and excited states and the vibrational energy of the oscillators. Both ligand molecules and coordinated solvent molecules can be a source of quenching oscillators, which include C-H, N-H, and O-H.[16] The relative energies of these groups in comparison to the energy levels of Nd^{3+} and Yb^{3+} can be seen in Figure 1.6. Of these, the vibrational states of the O-H oscillators are the most efficient deactivators and the most important to consider. Since lanthanide cations are hard Lewis acids, they will readily coordinate to solvent molecules such as H_2O and alcohols. The result of the non-radiative deactivation is a decrease in the emission quantum yields and

luminescence lifetimes. If O-H oscillators are replaced with low-frequency O-D oscillators, the non-radiative processes become less efficient.[4]

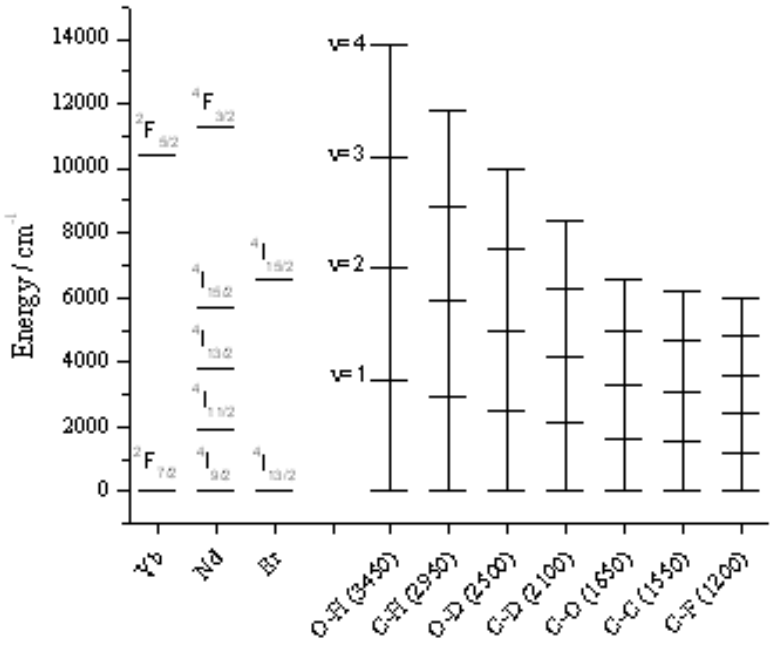

Figure 1.6. Diagram of the relative energy levels the emitting states of three NIR lanthanide cations and the first through fourth harmonics of several oscillators that are typically present in lanthanide complexes or solvent molecules. Note that the O-H oscillators are at higher energies than the O-D oscillators.

Horrocks and Sudnick[19] were able to use the decrease in luminescence lifetime and difference between O-H and O-D oscillators to determine the number of H_2O molecules coordinated to Tb^{3+} or Eu^{3+}. By carrying out experiments in H_2O and D_2O, it was possible to determine Equation 1.1, where q is 1.05 for Eu^{3+} and 4.2 for Tb^{3+}, τ is the excited state lifetime, and n is the number of coordinated water molecules.

$$n = q(1/\tau H2O - 1/\tau D2O) \quad (1.1)$$

Using the assumption that methanol behaves similarly to water as a coordinated solvent molecule, Horrocks and coworkers later determined Equation 1.2 to calculate the number of coordinated methanol molecules. This equation is similar to Equation 1.1, except *q* is replaced by *r*, which is 2.1 and 8.4 for Eu^{3+} and Tb^{3+}, respectively.

$$n = r(1/\tau_{MeOH} - 1/\tau_{MeOD}) \quad (1.2)$$

These formulas have an estimated uncertainty of 0.5 for n. In both cases, the effect of non-radiative deactivation is stronger for Eu^{3+} than Tb^{3+} because the energy gap between the ground and excited state is smaller for Eu^{3+}.[3] These equations have become quite important to lanthanide chemists, since being able to calculate the number of coordinated water or methanol solvent molecules of complexes in solution can provide valuable information on the overall coordination environment for lanthanide cation complexes in solution. Parker et al.[16] later revised these equations to account for the relative contributions of O-H, N-H, and C-H oscillators and the distance of the oscillators from the lanthanide cation, Equations 1.3 and 1.4.

$$n = q_{corr}(1/\tau_H - 1/\tau_D) \quad (1.3)$$

$$q_{corr} = A'\Delta k_{corr} \quad (1.4)$$

In Equation 1.3, τ_H is the lifetime decay of the lanthanide cation in regular solvent, and τ_D is the lifetime in deuterated solvent. In Equation 1.4, A' = 5 ms for Tb and 1.2 ms for Eu. The correction for outer sphere water molecules, Δk_{corr}, are -0.25 ms^{-1} (Tb) and -0.06 ms^{-1} (Eu), and a correction factor of -0.075 ms^{-1} is made for carbonyl-bound amide N-H oscillators with Eu. This formula has an uncertainty for n of approximately 0.1. Equations have also been reported and used to determine the number of coordinating solvent molecules for NIR emitting Yb^{3+} and Nd^{3+} in water (Equation 1.5),[4,20,21] and in methanol (Equation 1.6).[22,23]

$$q = A_{Ln}[(k_{H2O} - k_{D2O}) - B] \quad (1.5)$$

In Equation 1.5, A_{Yb} = 1.0 ms, A_{Nd} = 130 ns and B_{Yb} = 0.1 μs^{-1}, B_{Nd} = 0.003 ns^{-1}.

$$q = A_{Ln}[(k_{CH3OH} - k_{CD3OD}) - B] \quad (1.6)$$

In Equation 1.6, A_{Yb} = 2.0 μs^{-1}, A_{Nd} = 130 ns, and B = 0.1 μs^{-1} for Yb and 0.4 ns^{-1} for Nd^{3+}.

In addition to vibrational coupling, the emitting lanthanide excited states can be deactivated through thermally activated crossing to other upper-lying excited state configurations for the system. For the lanthanides that emit in the visible range, it is possible for the emitting energy levels to be sufficiently high that they are close enough to the triplet excited state energy levels of the chromophore to donate energy back to the triplet state. This process is referred to as back energy transfer and requires that a vibrational level of the emitting energy level match a vibrational level of the triplet state energy level. For lanthanide cations that emit in the NIR range, the emitting energy levels are low enough that this process is limited since most triplet

states are sufficiently high energy. For a few of the lanthanides, non-radiative deactivation of excited states can also occur through ligand-to-metal charge-transfer bands. While all lanthanide cations are most stable in the trivalent state, and most can not be oxidized or reduced easily, there are a few exceptions. Under the right conditions, Eu^{2+}, Tb^{4+}, Pr^{4+}, Ce^{2+}, Sm^{2+}, and Yb^{2+} are observed oxidation states,[2] and the resulting charge-transfer energy bands can quench luminescence.

Accounting for both radiative and non-radiative deactivation processes, it is possible to describe the overall decay rate for a luminescent level of a lanthanide cation. There are several non-radiative rates that must be considered: those that are temperature dependent, $k_{nr}(T)$, and temperature independent, k_{nr}, those that are due to O-H oscillators, $k_{nr}(OH)$, and those that are due to other vibrations, $k_{nr}(V)$. Equation 1.7 describes a general rate, and Equation 1.8 describes a system with an O-H containing solvent.

$$k = 1/\tau = k_r + k_{nr} + k_{nr}(T) \qquad (1.7)$$

$$k = 1/\tau = k_r + k_{nr}(T) + k_{nr}(OH) + k_{nr}(\text{other vibr}) \qquad (1.8)$$

The rates for these equations can be experimentally determined, making a few assumptions. It is assumed that $k_{nr}(\text{other vibr})$ is a negligible term, and that lanthanide cation excited energy level coupling with O-D oscillator energy levels is completely inefficient and can be excluded. Also, if measurements are done at 77 K, the thermally activated processes do not play a significant role. With these assumptions, k_r can be measured in deuterated solvent at 77 K, an environment where the only deactivation of the excited state available is radiation (Equation 1.9). The temperature

dependent non-radiative decay rates can be determined through comparison between lifetime in deuterated solvent at 300 K and 77 K, Equation 1.10. Finally, k_{nr}(OH) can be determined through the lifetimes at 300 K in deuterated and non-deuterated solvent, Equation 1.11.[3]

$$k_r = 1/\tau_D 77K \quad (1.9)$$

$$k_{nr}(T) = 1/\tau_D 300K - 1/\tau_D 77K \quad (1.10)$$

$$k_{nr}(OH) = 1/\tau_H 300K - 1/\tau_D 300K \quad (1.11)$$

Taking into consideration all the deactivation paths an excited lanthanide cation energy state can undergo, one can see that the environment of the cation is very important. Preventing solvent molecules, especially water and methanol, direct access to the cation can increase the luminescent efficiency. This can be achieved through choosing ligands that form strong bonds with lanthanide cations and are multidentate and/or bulky, thus preventing solvent access to the cation. In addition to preventing non-radiative deactivation paths, the luminescence intensity of lanthanide cations is related to the efficiency of light absorption.

The research work presented in this document focuses on the development and analysis of novel antennae for lanthanide sensitization and protection. Four different approaches to antennae are taken to develop novel luminescent lanthanide species. In a traditional approach using classic coordination chemistry techniques, flavonoids, a family of natural product molecules, are used to form luminescent complexes with NIR emitting lanthanide cations. Two different approaches based on nanoparticles are explored: 1) An optically inert $NaYF_4$ matrix is

doped with NIR emitting lanthanide cations, providing improved protection from non-radiative deactivation, and coated with organic chromophores to provide sensitization for the lanthanide cations.[24] This material is also used to synthesize lanthanide doped upconverting nanoparticles to investigate their potential use as both energy donors and energy acceptors in roles which open the possibility for expanding current upconversion technologies. 2) In a different nanoparticle approach, visible emitting lanthanide cations are incorporated into CdSe semiconductor nanoparticles, or "Quantum Dots," whose optical properties are used to sensitize the lanthanide cations while the inorganic matrix provides protection from non-radiative deactivation.[25] Finally, in a fourth approach, luminescent lanthanide cations are incorporated into metal-organic frameworks (MOFs) containing chromophoric organic groups to sensitize the lanthanide cations. In this approach, lanthanide cations are used as the metal sites within the MOF structures and are also impregnated into the pores of zinc based MOFs. All four complementary approaches to forming lanthanide species with antenna effect sensitization are successful, each with their own unique advantages.

2. FLAVONOIDS AS ANTENNAE FOR NEAR INFRARED LUMINESCENT LANTHANIDE CATIONS

2.1. INTRODUCTION

There is a vast demand for near infrared (NIR) luminescent probes for biological applications. Unlike visible light, near-infrared radiation can deeply penetrate blood, skin, and body tissue, resulting in the use of NIR emitting probes as non-invasive *in vivo* imaging agents.[8,9,26,27] Currently, there are only a few biological probes available that emit in the NIR,[28-30] and they are mostly organic molecules that have substantial shortcomings. Problems with light sensitivity are especially prevalent among organic dyes with NIR fluorescence due to photodecomposition, which severely limits their application. While a lot of work has been done on visible emitting lanthanides, the amount of information and literature for NIR lanthanides is much scarcer. So, there is a great deal of interest in developing new NIR luminescent lanthanide complexes, such as the ones formed with flavonoids in this project.[31]

The classical approach to forming luminescent lanthanide complexes involves using chromophoric organic molecules as ligands that coordinate directly to metal cations in solution. Here, several different flavonoids were examined as potential antennae using this approach. The goals of this work include testing the feasibility of sensitizing NIR emitting lanthanides, examining the photophysical properties of the complexes, determining the species formed in solution, and measuring their kinetics of formation and their stability in solution. Flavonoids

were chosen as potential antennae for lanthanides for several reasons. They are naturally occurring substances, commonly found in neutral products like apples, onions, tea, and wine, which are known to be biologically compatible and have been hypothesized to serve as antioxidants in the human body.[32-34] Many of them are readily available and inexpensive. They contain multiple oxygen sites and are hard Lewis bases, so they have the ability to form strong bonds with lanthanide cations, which are hard Lewis acids. Many have bidentate coordination sites where two oxygens can both bind to the lanthanide cation, thus they can act as bidentate chelating ligands. They have been shown to complex with other Lewis acid metal centers, including barium, magnesium,[35], copper,[33] zinc,[36] aluminum,[36-44] thorium,[45] niobium, and tantalum.[46] This was a strong indication that the flavonoids would bind to lanthanide cations as well. Also, they contain chromophore groups that have fairly low energy triplet states (circa 15,000 cm^{-1}), increasing the likelihood that their donating energy levels will match the accepting levels of several different lanthanide cations that emit in the NIR. Their ε values for the lowest energy absorption maxima are fairly high, in the 10^{-5} L/mol•cm range, indicating that they are efficient at harvesting incoming light. Finally, some of the flavonoids are water soluble, which is desirable for biological applications.

Woźnicka et al.[47,48] and Anasari [49] have reported that morin forms complexes with lanthanide cations, isolating and studying the solid state complexes. Morin forms ML_3 complexes with a variety of different lanthanide cations, confirmed by mass spectrometry and elemental analysis. These reports of the formation of lanthanide complexes with morin further advocate the hypothesis that flavonoids will be good sensitizing antennae for lanthanide cations. To the best of our knowledge, no studies have been presented on the photophysical properties of

these lanthanide complexes, their kinetics of formation in solution, nor their stability, which are the interests of the work presented here.

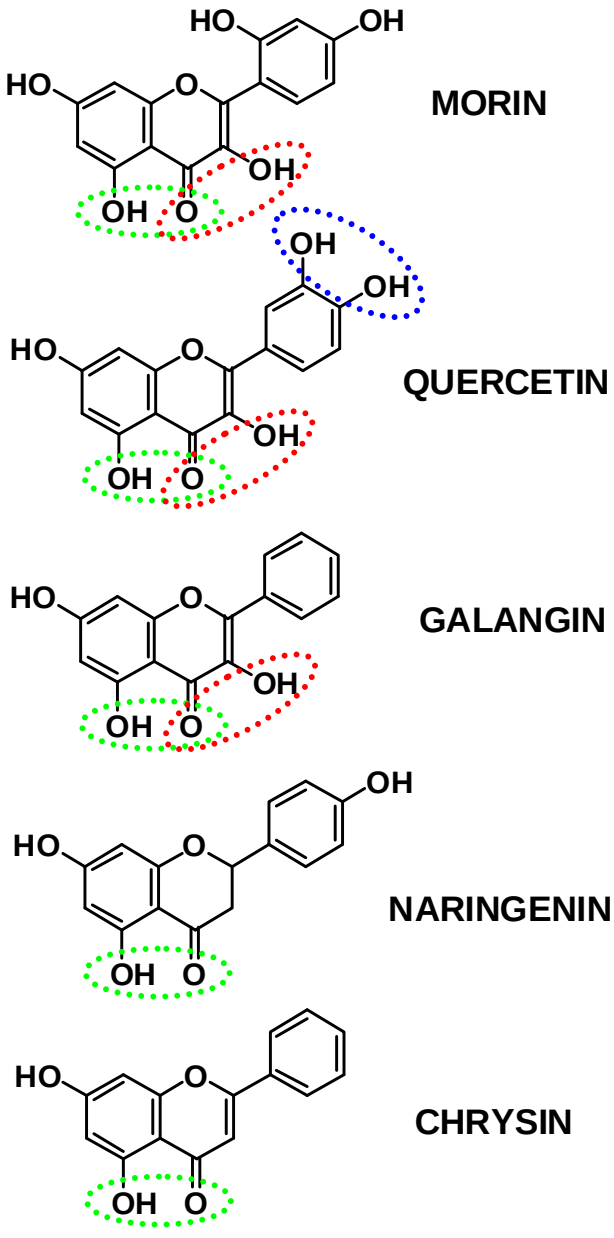

Figure 2.1. The five flavonoids studied for lanthanide sensitization with potential lanthanide binding sites indicated by colored circles.

Five different flavonoids were selected as potential antenna ligands for NIR lanthanides: morin, quercetin, galangin, chrysin, and naringenin[32] (Figure 2.1). Morin was the preferred potential antenna since it has the highest level of water solubility, and it also has a low pK_a value of 5.7 which is compatible with biological conditions. Quercetin (pK_a = 8.33) was then chosen based on the structural similarity to morin, differing only in the location of one OH group. This slight difference, however, can impact the electronic structure and energy levels resulting in different photophysical properties of the resultant lanthanide complexes. Galangin (pK_a = 8.23) was chosen for further comparison between morin and quercetin since it does not contain any OH groups on the branched phenyl ring. These three flavonoids have two potential binding sites in common, which are circled in green and red in Figure 2.1. It is predicted that the site circled in red, which will form a five member ring upon lanthanide coordination, will be the favored binding site since Al^{3+} binds at this location.[39,42,43] For comparison, two flavonoids with only one binding site were also selected for study; naringenin (pK_a = 8.23) and chrysin (pK_a = 7.98). These two flavonoids contain only the binding site which forms six member rings upon lanthanide coordination, circled in green. Quercetin also has a third binding site, shown in blue in Figure 2.1. This site has been shown to bind transition metal cations, allowing the formation of M_2L species[42,43]. Since the ultimate interest for these complexes is use in biological applications, water (buffered solution) was the first choice for solvent for these studies, followed by methanol or ethanol for flavonoids without sufficient water solubility.

The first step in studying the photophysical properties of the lanthanide - flavonoid systems was to determine if the flavonoids could sensitize lanthanide cation emission in solution. Preliminary studies showed that all five flavonoids were able to sensitize both Nd^{3+} and Yb^{3+} emission. Once lanthanide sensitization was confirmed, the next area of study was to investigate

the nature of the complexes formed in solution between these flavonoids and lanthanide cations, a feature that is important to their efficiency as antennae. While crystal structures can provide copious information, obtaining crystals can be challenging, and it is only information about the sample in the solid state. Most complexes can adopt different structures when placed in solution. Spectrophotometric titrations[50,51] are utilized here to investigate the nature of the solvated Ln-flavonoid species. Cornard et al. has used spectrophotometric techniques extensively to study the coordination of flavonoids with Al^{3+}.[39-44]

Spectrophotometric titrations involve monitoring changes in the photophysical properties of a complex with respect to varying a property such as stoichiometry or pH. UV-Vis absorbance titrations,[52,53] done with varying metal to ligand ratios, are conducted to provide information about how many ligands coordinate to a metal center, and what different M:L species are formed. Plots of absorbance versus M:L ratio at specific wavelengths can help elucidate where changes occur corresponding to specific M:L ratios (i.e., 1:1, 1:2, etc.). Solvated systems are dynamic, and as the concentration of one species increases, it will drive the equilibrium forward. For example, even if the ML_3 species forms as the species with the highest M:L ratio in solution, distinct change in absorbance or luminescence efficiency may not occur at the 1:3 solution ratio. Rather, a gradual change over increasing ratio could develop since higher flavonoid concentrations will increase the formation of this species over the ML or ML_2 species. Due to these complexities, mathematical and statistical treatment of absorbance spectra over a wide range of M:L ratios provides the most accurate results. This type of analysis requires computational programs, and SPECFIT[54] is employed in this research.

In addition to absorbance titrations, luminescence titrations based on the emission of the lanthanide cation, conducted with varying metal to ligand ratios, provide information about how

well the metal is being sensitized for each different species. As the number of chromophores around the lanthanide cation increases, so does the amount of donating energy available for metal sensitization since ε is summed over all ligands. The cation also becomes better protected from solvent quenching, thus the lanthanide emission intensity increases due to the decrease of non-radiative deactivation. However, once the coordination sphere around the lanthanide cation is saturated, the luminescence output will not further increase. Ideally, there will be a point where the lanthanide cation produces luminescence of the highest intensity for a certain number of ligands. For example, if the integrated intensity increases for metal-to-ligand ratios of 1:$^1/_4$ through 1:3, and plateau for ratios above 1:3, the formation of a ML_3 complex is indicated. For these types of spectrophotometric titrations, plots of integrated intensity values with respect to M_nL_m ratio can aid in revealing a leveling-off or breaking point; however, the same complexities can result due to the dynamics of solvated species. Luminescence titrations are also performed monitoring the emission of the ligand. When energy transfer to a lanthanide cation is efficient, a decrease in ligand emission upon lanthanide coordination will occur. The coordination of a lanthanide cation may also serve to stabilize the excited states of the ligand, resulting in increased emission intensities. In either scenario, changes of emission intensity upon lanthanide addition can provide another piece of data to provide information on the species forming in solution.

While all five flavonoids sensitized NIR emitting lanthanide cations, morin was selected for the first studies due to its water solubility and the previously published reports of complexation with lanthanide cations. Early studies with this flavonoid suggested the formation of $[ML_4]^+$ complexes in solution; however, further studies showed that these results were inconclusive. After multiple attempts to fit spectrophotometric titration data with SPECFIT

proved unsuccessful, a series of stability and kinetics of formation studies were conducted. These studies revealed several unexpected results. Both morin alone and morin – lanthanide systems proved to be unstable in buffered water solutions, prompting future investigation in methanol after a solvent stability study. In addition, it was discovered that lanthanide – morin systems in water lead to the formation of insoluble species, which were deemed to likely be polymeric matrices. Finally, kinetic studies in methanol revealed multi-step processes with unexpectedly long formation times, of up to several days. While these conditions resulted in the necessity of unpredicted studies, and complicated the interpretation of titration data, preliminary results suggest that ML_3 species form by reaction of three equivalents of morin with one equivalent of lanthanide cation in solution. Combining results from a variety of titrations performed with different experimental conditions helped provide information about the nature of the complexes that are formed. Neodymium is a larger cation than ytterbium, so they may have slightly different results with the same flavonoid. Also, even though flavonoids have the same fundamental structure and similar binding sites, they may differ in orientation around the metal center, depending on the extent of OH group substitution and how hydrogen bonding with the solvent affects the energies of all the different possible geometries. A variety of titrations were performed that supplied many sets of data, which were all merged together to provide global conclusions.

The triplet state energy levels of the several of the flavonoids were investigated to rationalize energy transfer to the lanthanide cations. In order to experimentally determine the energy level locations of the flavonoid triplet states, two steps were taken to increase their population (and measurability). First, the molecules were coordinated to Gd^{3+}, which has seven unpaired electron and is the most paramagnetic metal cation that exists. Since triplet states are

paramagnetic themselves they can interact with the paramagnetic metal, which aids in populating them. Gadolinium was used since it is a lanthanide cation and would coordinate to the flavonoids in the same manner as the NIR emitting lanthanide cations. However, the accepting and emissive energy levels of Gd^{3+} are too high in energy to accept energy from the triplet state, thus the likelihood of phosphorescence is increased.[55] Secondly, the samples were frozen at 77 K. Lowering the temperature decrease the rate of non-radiative deactivation, thus increasing phosphorescence intensity.[56]

The quantum yields of lanthanide luminescence were measured for ML_3 neodymium and ytterbium complexes formed with morin. The lanthanide centered luminescence lifetimes of these complexes were investigated in deuterated and non-deuterated solvents, allowing the number of coordinating solvent molecules to be determined. These results indicate that morin is a good antenna for the NIR lanthanide complexes. Further, the complexes in buffer solution produce sufficient signal to be detected with NIR microscopy instrumentation. While further experimentation and study will be necessary, the preliminary work presented here suggests that flavonoid – lanthanide complexes have the potential to serve in biological applications. Despite the complexity of these systems, they have beneficial properties that warrant future investigation.

2.2. EXPERIMENTAL

2.2.1. Reagents

All reagents were used as purchased, without any further purification. $LnCl_3 \bullet nH_2O$ (Ln = Nd^{3+}, Gd^{3+}, Er^{3+}, $Tm3^{+}$, and Yb^{3+}) were purchased from Sigma-Aldrich (highest purity available,

99.998%). Morin, quercetin, galangin, naringenin, chrysin, Trizma base (buffer), and KCl were purchased from Sigma-Aldrich. Methanol, ACS grade, was purchased from Fisher Scientific and ethanol, ACS grade, was purchased from Pharmco Products, Inc. Deionized water was used for all experiments with water.

2.2.2. Instrumental information

UV-Vis absorption spectra were recorded on a Perkin-Elmer Lambda 9 spectrophotometer in 1 cm quartz cells coupled with a personal computer using software supplied by Perkin-Elmer. Flavonoid and lanthanide cation luminescence emission and excitation spectra were collected with a JY Horiba Fluorolog-322 spectrofluorimeter equipped with a DSS-IGA020L, Electro-Optical Systems, Inc. NIR detector. Emission and excitation spectra were corrected for the instrumental function. Quartz cells manufactured by NSG Precision Cells, Inc. were used for all measurements.

The luminescence lifetime measurements were performed by excitation of solutions in 10 mm quartz cells using a Nd:YAG Continuum Powerlite 8010 Laser (354 nm, 3rd harmonic) as the excitation source. Emission was collected at a right angle to the excitation beam and emission wavelengths were selected using a Spectral Products CM 110 1/8 meter monochromator. The signal was monitored by a cooled photomultiplier (Hamamatsu R316-2) coupled to a 500 MHz bandpass digital oscilloscope (Tektronix TDS 754D). The signals (15,000 points each trace) from at least 500 flashes were collected and averaged. Luminescence decay curves were imported into Origin 7.0 scientific data analysis software. The decay curves were analyzed using the Advanced Fitting Tool module and fitted with mono-, bi- and tri-exponential modes. Of the three modes, the lifetime value was chosen based on the best fit of the decay curve on the criteria

of the minimum χ^2 statistical parameter. Lifetimes are averages of at least three independent determinations.

Luminescence quantum yields were measured using ytterbium tropolonate solutions as the reference.[7,24] Emission spectra were collected using a JY Horiba Fluorolog-322 Spectrofluorimeter and spectra were corrected for the instrumental function. The quantum yields were calculated using Equation 2.1:

$$\Phi_x/\Phi_r = [A_r(\lambda_r)/A_x(\lambda_x)][I(\lambda_r)/I(\lambda_x)][\eta_x^2/\eta_r^2][D_x/D_r] \quad (2.1)$$

where subscript r stands for the reference and x for the sample, A is the absorbance at the excitation wavelength, I is the intensity of the excitation light at the same wavelength, η is the refractive index and D is the measured integrated luminescence intensity.

2.2.2.1. Batch Titrations

Stock solutions were prepared at the following concentrations: 5 x 10^{-4} M flavonoid and 1 x 10^{-2} M $LnCl_3$. For titrations done in buffer, all solutions were prepared in a 1 x 10^{-3} M TRIS buffer solution adjusted to pH 7.9 with 1 x 10^{-3} M KCl added to buffer electrostatic interactions. For titrations performed in methanol, solutions were prepared with 1 x 10^{-3} M tetrabutylammonium hexafluorate salt (TBAF) to control the ionic strength to minimize the effect of electrostatic interactions between species. The stock solutions were mixed to form samples with M:L ratios ranging between 10:1 and 1:10 and diluted to the specified concentration with the appropriate solvent.

2.2.2.2. Titrations with the Auto-titrator

Automated spectrophotometric UV-visible absorbance titrations were performed with the Perkin-Elmer Lambda 19 spectrophotometer. All titrations were performed in a thermostated (25.0 ± 0.1°C) cuvette in the specified solvent (TRIS buffer and KCl aqueous solution or methanol with TBAF). In a typical experiment, 2.00 mL of morin solution with initial concentration of 5×10^{-5} M was titrated with 1 x 10^{-4} M lanthanide chloride solutions. After each addition of 20 or 40 μL of the lanthanide solution, the spectrum of the solution was measured.

2.2.2.3. Triplet state measurements

Solutions of the flavonoids with Gd^{3+} were placed in a quartz cuvette, which was then put into a quartz cryostat filled with liquid nitrogen. Once the sample was frozen at 77 K, the cryostat sample holder was placed in the instrument, and the cuvette was aligned in the excitation light beam. Measurements were conducted with a JYvon Horiba Fluorolog-322 spectrofluorimeter equipped with a phosphorimeter module and Xenon flash lamp for time-resolved detection. The emission spectra were then collected, with increasing delay times until the phosphorescence band was the main signal observed on the spectrum. Background emission spectra were then obtained of the cuvette containing the solvent only (also at 77 K). The emission spectra were corrected for the background and instrumental function. For 10^{-5} M Gd:quercetin (1:3) solution in methanol, the following parameters were used: λ_{ex} = 422 nm, λ_{em} = 435-800 nm (1.0 nm intervals). Spectra were collected at delays of 0.01, 0.02, 0.03, and 0.04 ms with collection window time 10.0 ms, 20 flashes, 40 ms per flash, and emission/excitation slits of 5/5 nm. Similar parameters were used for a 10^{-5} M solution of Gd:morin (1:2) in methanol: λ_{ex} = 415 nm, λ_{em} = 430-800 nm(1.0 nm intervals). Spectra were collected at delays of 0.01, 0.02, 0.03, and 0.04 ms with collection window time 10.0 ms, 20 flashes, 40 ms per flash,

and emission/excitation slits of 5/5 nm. The excitation and emission wavelength parameters used for a 10^{-4} M solution of Gd:galangin (1:1) in methanol were: λ_{ex} = 420 nm, λ_{em} = 435-800 nm (1.0 nm intervals), for a 10^{-4} M solution of Gd:naringenin (1:1) in methanol they were λ_{ex} = 372 nm, λ_{em} = 385-800 nm (1.0 nm intervals), and for a 10^{-4} M solution of Gd:chrysin (1:1) in methanol λ_{ex} = 390 nm, λ_{em} = 405-800 nm (1.0 nm intervals) were used. Spectra for galangin, naringenin, and chrysin solutions were all collected at delays of 0.01, 0.02, 0.03, 0.04, 0.05, 0.1, 0.2, and 0.3 ms with collection window time 20.0 ms, flash time 50.0 ms, 3 flashes, and emission/excitation slits of 7.5/7.5 nm.

2.3. RESULTS & DISCUSSION

2.3.1. Initial Studies

Morin was able to bind to and sensitize both Nd^{3+} and Yb^{3+} emission in TRIS buffer solution and methanol. The UV-Vis absorption spectrum of morin in methanol contained three maxima, located at 209 nm (ε = 32,000 L/mol•cm), 260 nm (ε = 17,000 L/mol•cm), and 359 nm (ε = 13,000 L/mol•cm). Upon addition of one equivalent of lanthanide cation, the maximum at 209 nm did not change and the other two maxima shifted to 270 nm (ε = 20,000 L/mol•cm) and 415 nm (ε = 18,000 L/mol•cm). The shift in absorbance maxima for morin provided an indication that the molecule was coordinating with the lanthanide cations. When the flavonoid binds Ln^{3+} the phenoxide forms at the binding site (Figure 2.2), and the C=O electron withdrawing is increased, which results in absorption at a lower energy and a red-shift in the spectrum.[57]

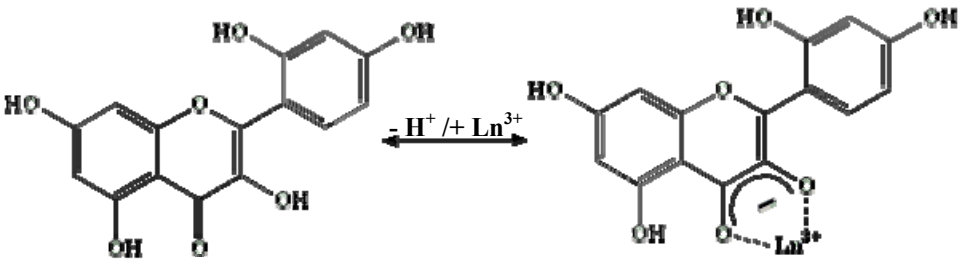

Figure 2.2: Model of morin binding with a lanthanide cation, formation of the phenoxide.

The excitation spectra collected for metal centered luminescence from both lanthanide complexes displayed maxima at 415 nm, which corresponds to the absorbance maxima at the same wavelength. This excitation wavelength is located at a fairly low energy, which is desirable for several reasons. The accepting levels of NIR emitting lanthanide cations are at lower energies compared to those of the visible emitting cations, which suggests a good energy match between donor and acceptor. Also, higher energy UV radiation is destructive to biological materials, so the lower energy excitation was a desirable aspect of biological compatibility. Metal centered luminescence for both lanthanide cations could be detected at metal ion concentrations of 10^{-5} M in TRIS buffer, with as few as 0.25 equivalents of morin for one equivalent of metal. This indicates that the energy transfer mechanism between the antenna and lanthanide cations must be efficient enough. With such a small quantity of morin to bind to the lanthanides in a water based solvent, a high number of water molecules were likely bound to the cations. Since OH vibrations are such strong quenchers, the ability to detect any lanthanide emission is remarkable and indicates an efficient energy transfer to the NIR emitting lanthanide cation. This data set provided the first indication that the flavonoid and NIR emitting lanthanide cations would be promising luminescent species.

Since the desired application for these lanthanide complexes is biological, further experiments were done in TRIS buffer. Spectrophotometric absorbance and luminescence titrations were conducted at room temperature to gather information on the coordination environment in solution. The results of these titrations with Nd^{3+} are depicted in Figure 2.3 and Figure 2.4.

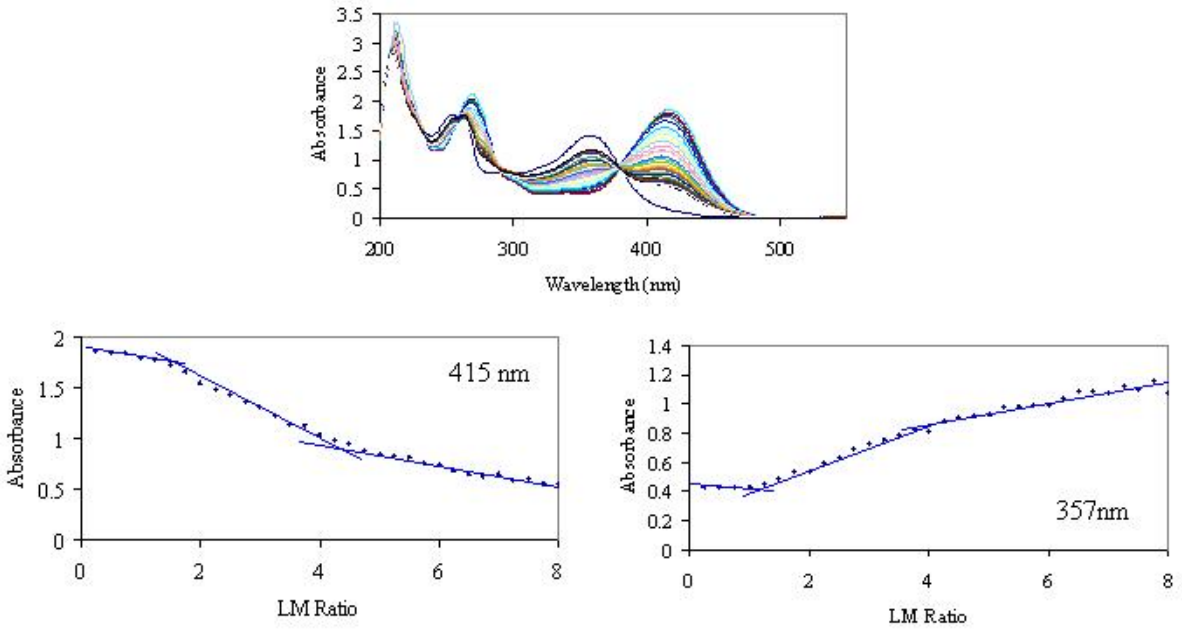

Figure 2.3: UV-Vis absorbance spectrophotometric titration results for Nd^{3+} with morin in TRIS buffer solution, morin concentration held constant at 5 x 10^{-5} M. Top: UV-visible absorbance spectra. Bottom: Plot of change in absorbance versus ligand-to-metal ratio at 415 nm (left) and 357 nm (right). Changes in the slope or leveling-off points are illustrated with blue lines.

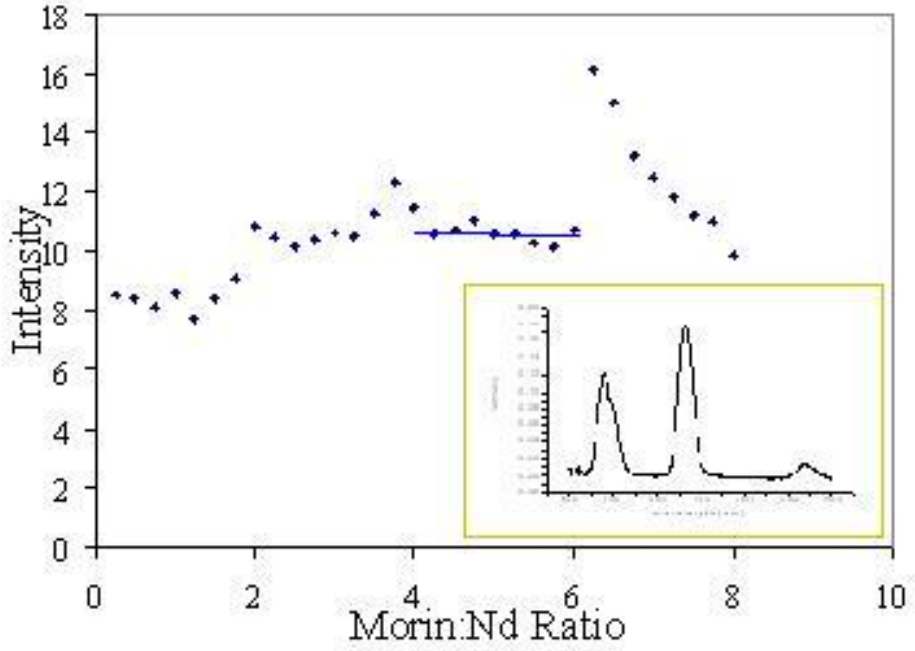

Figure 2.4: Plot of the integrated intensity of Nd^{3+} emission versus the ligand-to-metal ratio for Nd^{3+} with morin, results from a spectrophotometric luminescence titration (Nd^{3+} concentration held constant at 1 x 10^{-5} M). The leveling-off point is illustrated with a blue line. A sample Nd^{3+} emission spectrum is shown in the insert.

A plot of absorbance versus ligand-to-metal ratio was made for 357 nm and 415 nm. In both cases, the plots had two breaks for M:L stoichiometries of 1:1 and 1:4, indicating the formation of $Nd[morin]_1$ and $Nd[morin]_4$ complexes in solution. These results were further confirmed by the luminescence titration. The integrated intensity was plotted versus increasing ligand-to-metal ratio, and leveling-off point occurred after a 4 to 1 ratio. This plot also indicated that at a 6 to 1 ratio, an increase in integrated intensity was observed which may be due to the formation of a cluster.

The results obtained from titrations with Yb^{3+} were quite similar (Figure 2.5 and Figure 2.6). Plots of absorbance versus ligand-to-metal ratio were made for 425 nm and 445 nm. These plots indicated that $[Yb(morin)_4]^-$ complex was forming in solution, and the plot at 445 nm also

had a breaking point after a 1 to 1 ratio, indicating that [Yb(morin)$_1$] was forming as well. Again, the luminescence titration showed a leveling off point at a 4 to 1 ratio, further confirming the presence of the ML_4 complex. This plot also showed an increase in emission intensity at the 6 to 1 ratio.

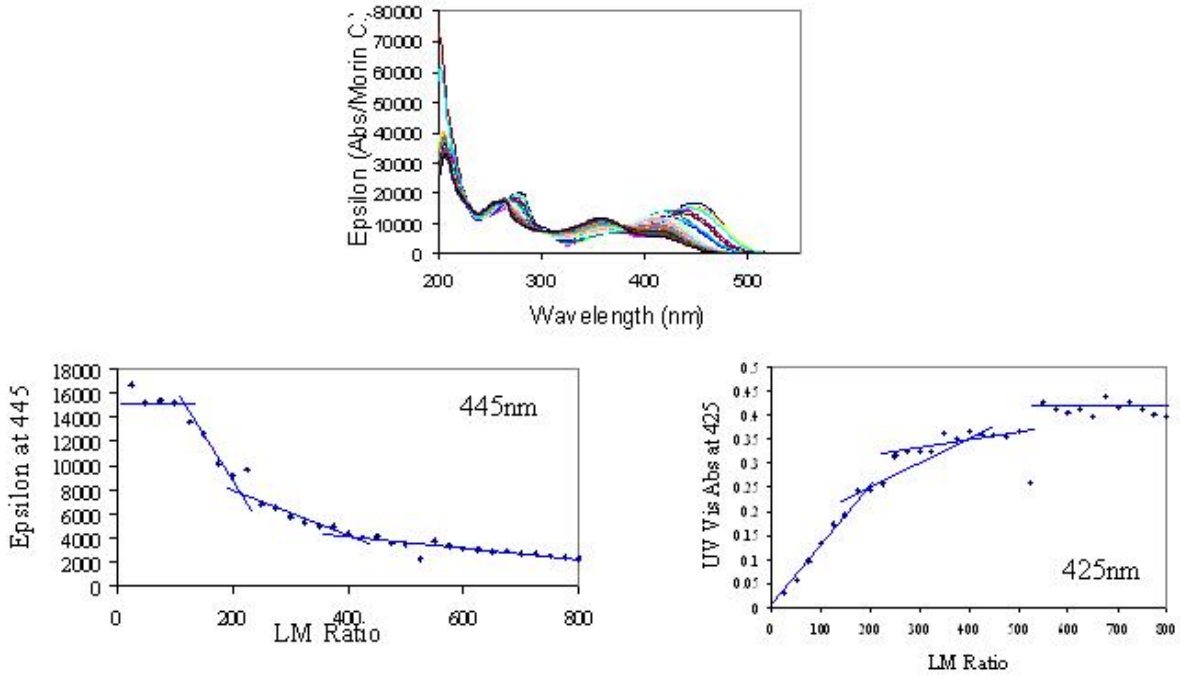

Figure 2.5: UV-Vis absorbance spectrophotometric titration results for Yb^{3+} and morin in TRIS buffer solution, morin concentration held constant at 5 x 10^{-5} M. Top: UV-visible absorbance spectra. Bottom: Plot of change in absorbance versus ligand-to-metal ratio at 445 nm (left) and 425 nm (right). Change in the slope or a leveling-off point are illustrated with blue lines.

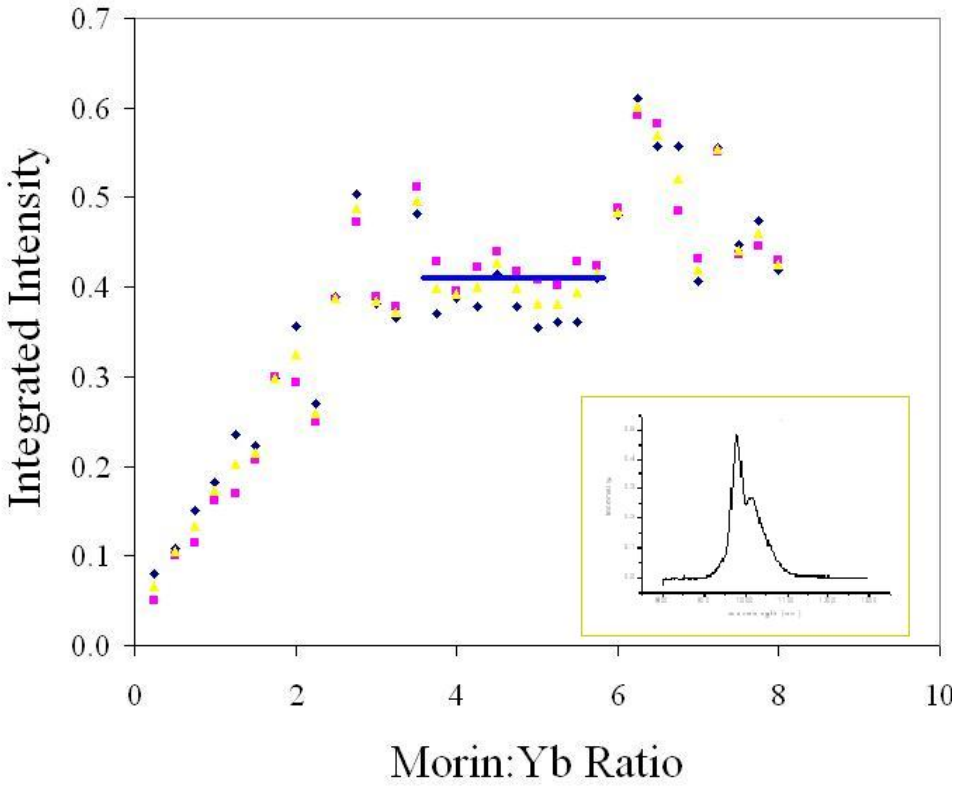

Figure 2.6: Plot of the integrated intensity of Yb^{3+} emission versus the ligand-to-metal ratio for Yb^{3+} with morin, results obtained from three spectrophotometric luminescence titrations (Yb^{3+} concentration held constant at 1 x 10^{-5} M). The leveling-off point is illustrated with a blue line. The insert contains an Yb^{3+} emission spectrum from one titration.

Based on the results of these initial titrations, it was hypothesized that morin forms mainly 4:1 complexes with lanthanide cations in solution. This would provide a coordination of eight oxygen sites around the lanthanide center, which is a reasonable coordination number for lanthanide cations.

Quercetin was able to sensitize both Nd^{3+} and Yb^{3+} emission at concentrations as low as 10^{-5} M, and with as little as 0.25 equivalents of ligand for one lanthanide cation. Quercetin had limited solubility in water, so methanol was used as the solvent for all experiments. The UV-Vis absorbance spectrum for quercetin in methanol had three maxima, located at 205 nm (ε =

34,000), 257 nm (ε = 18,000), and 370 nm (ε = 21,000). Upon addition of one equivalent of a lanthanide cation, the absorbance maximum at 205 nm was unchanged, and the maximum at 257 nm shifted to 269 nm (ε = 17,000). The absorbance band located at 370 nm decreased (ε = 8,500), while a new maximum appeared at 440 nm (ε = 14,500). These changes in the absorption spectrum indicate that bonding between the lanthanide cation and quercetin did occur. Excitation spectra collected on Nd^{3+} and Yb^{3+} emission bands displayed a main excitation band located at 432 nm, which corresponds to the transition whose absorption maximum is located at 440 nm. This excitation wavelength is slightly lower in energy than those observed for morin. This is favorable, since a low energy excitation wavelength is desirable for biological applications.

The interaction between quercetin and lanthanide cations was analyzed through a series of spectrophotometric titrations similar to those completed for morin. The results of a UV-Vis absorbance titration with Nd^{3+} are shown in Figure 2.7. Plots of absorbance versus metal-to-ligand ratio were made for 370 nm and 424 nm. These plots both showed changes in slope at 3 equivalents of quercetin to one equivalent of Nd^{3+}, indicating that $Nd[Quercetin]_3$ complex was formed in solution. This result was further confirmed through the metal centered luminescence titration, see Figure 2.8. A plot of lanthanide integrated emission intensity with respect to ligand-to-metal ratio demonstrated a change in slope at a 3 to 1 ratio. Here the slope switched from a positive to negative value, indicating that no increase in luminescence was obtained beyond 3 equivalents of quercetin for one equivalent of Nd^{3+}. UV-Vis absorbance and metal centered luminescence spectrophotometric titrations were also obtained with Yb^{3+}. Figure 2.9 and Figure 2.10 show the results from these titrations, which also indicate that a 3:1 complex was formed in solution. The absorbance values with respect to ligand to metal ratio were plotted for 370 nm 424

nm. The integrated emission intensity versus ligand-to-metal ratio has switched from positive to negative slope at 3 equivalents of quercetin.

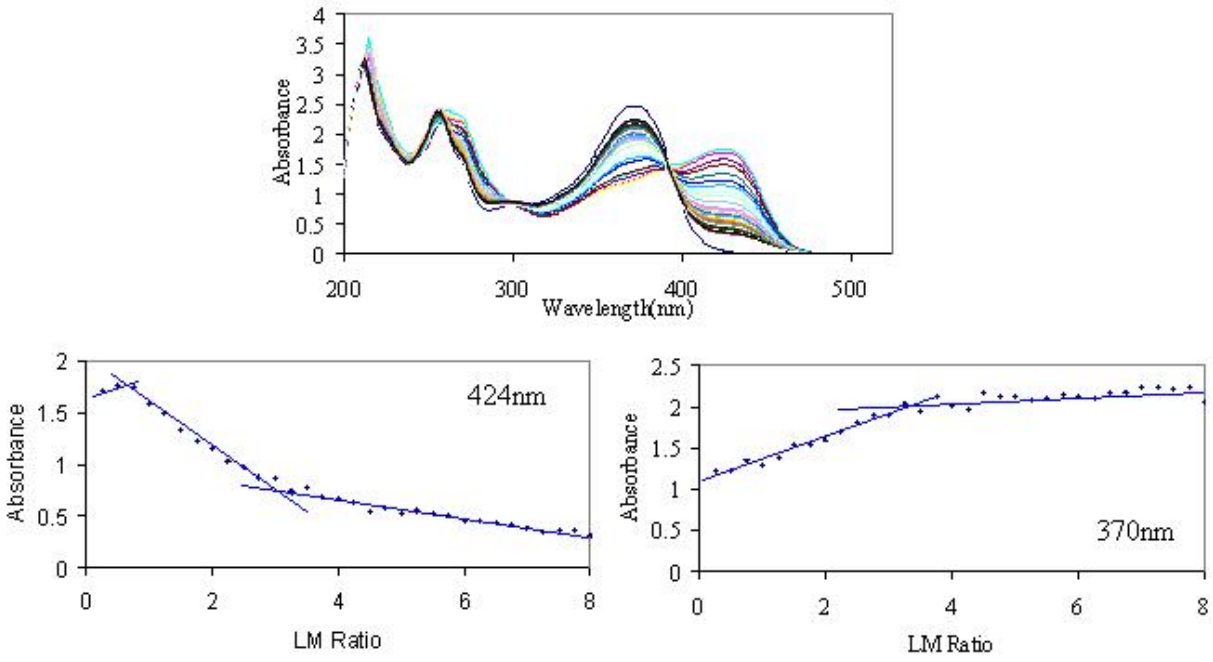

Figure 2.7: UV-Vis absorbance spectrophotometric titration results for Nd^{3+} with quercetin in TRIS buffer solution, quercetin concentration held constant at 5 x 10^{-5} M. Top: UV-visible absorption spectra. Bottom: Plot of change in absorbance versus ligand-to-metal ratio at 424 nm (left) and 370 nm (right). Changes in slope or leveling-off are illustrated with blue lines.

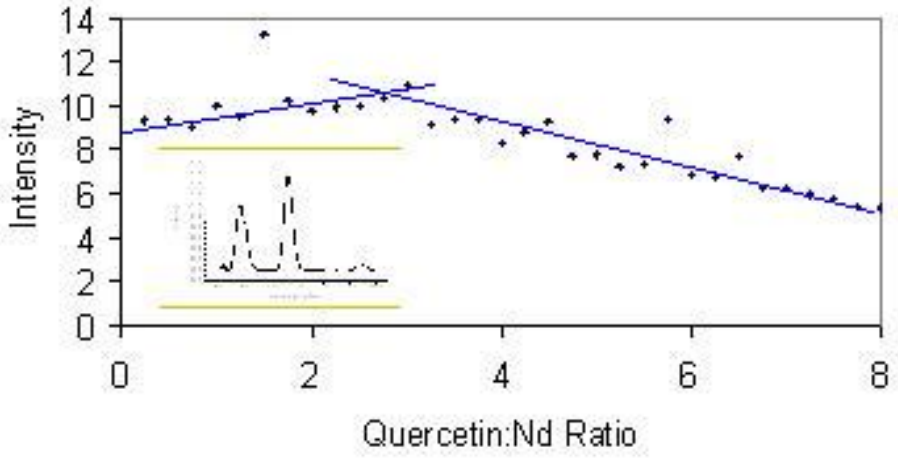

Figure 2.8: Plot of the integrated intensity of Nd^{3+} emission versus the ligand-to-metal ratio resulting from a spectrophotometric luminescence titration (Nd^{3+} concentration held constant at 1 x 10^{-5} M). The leveling-off point is illustrated with a blue line. The insert contains a Nd^{3+} spectrum from the titration.

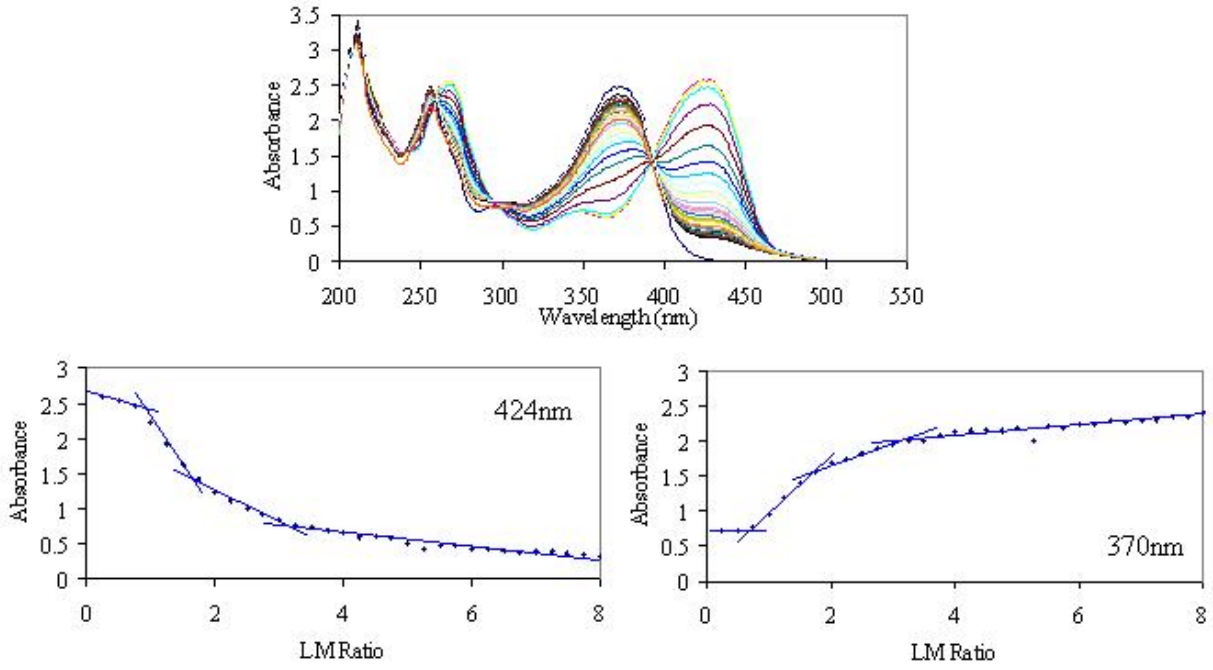

Figure 2.9: UV-Vis absorbance titration results for Yb^{3+} with quercetin in methanol, quercetin concentration held constant at 5 x 10^{-5} M. Top: UV-visible absorbance spectra. Bottom: Plot of change in absorbance versus ligand-to-metal ratio at 424 nm (left) and 370 nm (right). Changes in slope or leveling-off are illustrated with blue lines.

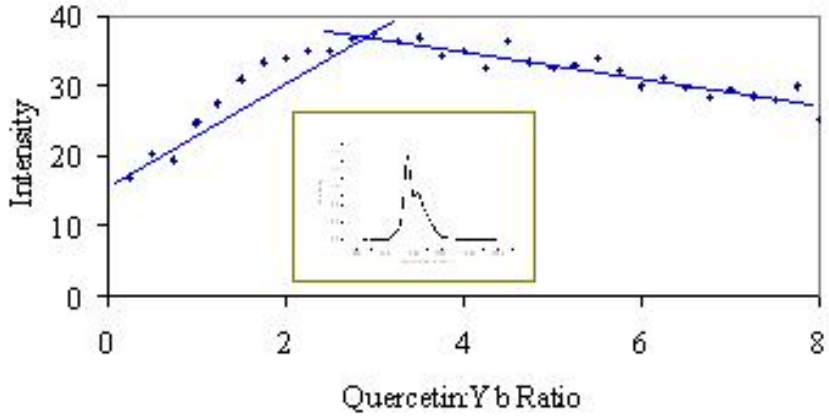

Figure 2.10: The results of a spectrophotometric luminescence titration shown as a plot of the integrated intensity of Yb^{3+} emission versus the ligand-to-metal ratio with quercetin, the change in slope is illustrated with blue lines. The insert contains one Yb^{3+} emission spectrum from the titration. Ytterbium concentration held constant at 1 x 10^{-5} M.

These initial studies indicate that quercetin forms ML_3 complexes with lanthanide cations. This result was surprising because it was anticipated that morin and quercetin would adopt similar coordination due to their structural similarity. One possible explanation for this discrepancy could be that the change in the location of one OH group also changes the way the molecules orient themselves around the metal center. Future studies (*vide infra*), however, would elucidate that morin is not stable in buffer conditions, and thus the conclusion of a ML_4 complex for morin is not valid.

Three other flavonoids were tested for their ability to sensitize Nd^{3+} and Yb^{3+} emission: galangin, chrysin, and naringenin. Here, the main interest was whether flavonoids with fewer OH groups could still bind to and sensitize the lanthanide cations. All three of these flavonoid ligands were able to bind to and sensitize Nd^{3+} and Yb^{3+}. None of these flavonoids were highly soluble in water, so experiments were carried out in either ethanol or methanol for practical reasons.

The UV-Vis absorbance spectrum of galangin in ethanol had three maxima located at 210 nm (ε = 28,800), 270 nm (ε = 26,400), and 360 nm (ε = 18,000). Upon addition of the lanthanide cation, the location of these maxima remained similar, but the absorbance band at 270 nm decreased (ε = 25,000) and two new maxima appeared at 305 nm (ε = 16,000) and 435 nm (ε = 3,000). These shifts confirmed the binding of galangin to the lanthanides. Metal centered luminescence was detected at concentrations in the range of 10^{-5} M. The main excitation band was located at 430 nm, which corresponds well with the UV-Vis absorbance maximum at 435 nm. These absorbance and excitation wavelengths are all similar to those reported for quercetin and morin, which would have been expected since they have very similar structures. Again, a desirable low energy excitation was obtained.

Chrysin was able to bind to and sensitize both Nd^{3+} and Yb^{3+} luminescence at 10^{-5} M concentrations, as determined through UV-Vis absorbance measurements and luminescence determinations. The absorbance spectrum of chrysin in methanol has three maxima, located at 213 nm (ε = 33,800), 270 nm (ε = 30,500), and 314 nm (ε = 12,700). Upon addition of the lanthanide cation, these maxima did not shift in wavelength, although the bands became slightly broader for the two lower maxima. A new maximum appeared at 380 nm (ε = 5,200). In addition to the changes in the absorbance spectra, the solution changed in color from colorless to yellow, so it was concluded that binding did occur. The excitation spectra collected on metal centered luminescence bands showed a maximum at 390 nm. This excitation energy was higher than those of the previously described flavonoids, which indicates that the absence of the OH group on the center ring does alter the energetics of the system. This wavelength is still in a biologically compatible range. Chrysin was particularly efficient at sensitizing Yb^{3+} emission, allowing detection of ytterbium emission with an instrumental band width of 2 nm, which is quite narrow

for the NIR range (the maximum slit width for the instrument is 40 nm), on a 10^{-4} M solution with ligand to metal ratio of 1:1. Chrysin was also able to sensitize Nd^{3+}; however, the lanthanide luminescence appeared less intense compared to ytterbium.

It was also possible to sensitize Nd^{3+} and Yb^{3+} emission using naringenin as an antenna in methanol. The UV-Vis spectrum of naringenin had three maxima located at 212 nm (ε = 26,300), 225 nm (ε = 24,000), and 288 nm (ε = 17,000). Upon addition of a lanthanide cation, the locations of these maxima did not change, but they did decrease slightly in intensity accompanied by the appearance of a new maximum at 368 nm (ε = 3,800). There was no visible color change in the solution. Since the pK_a value for naringenin is in the same range as chrysin, galangin, and quercetin, which were all compatible for the coordination of lanthanide cations, it was unlikely that the molecule did not deprotonate and coordinate to the lanthanide cation. Instead, the naringenin energy levels that are responsible for light absorption were probably only weakly affected by lanthanide binding in comparison to the other flavonoids. Out of all the flavonoids tested, lanthanide cations bound to naringenin demonstrated the least intense luminescence. This result suggests that the energy levels are not as well matched to the accepting levels of the considered lanthanide cations.

Phosphorescence band energy locations were measured for three of the five flavanoids. The phosphorescence band of quercetin was centered on the maximum at 578 nm, which corresponds to 17,300 cm^{-1}. For morin, the phosphorescence band was centered at 667 nm (14,990 cm^{-1}). The phosphorescence band of galangin was centered at 620 nm or 16,130 cm^{-1} (Figure 2.11).

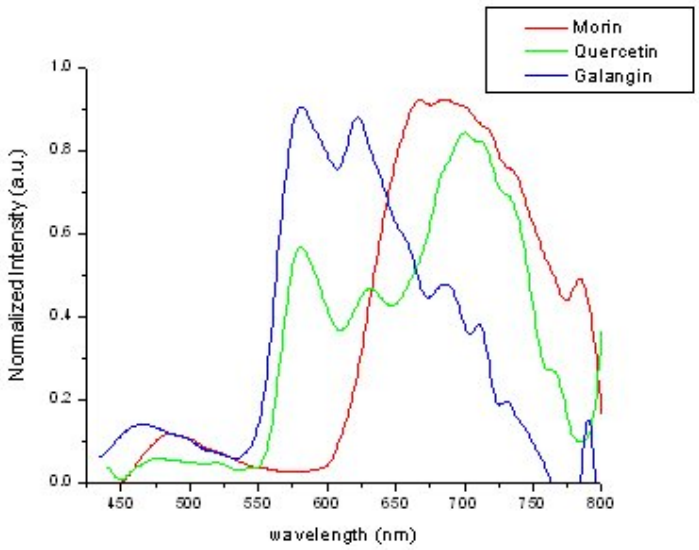

Figure 2.11: Normalized phosphorescent emission spectra of morin (red), quercetin (green), and galangin (blue), monitored for flavonoid complexes with gadolinium (see Section 2.2.2.3 for full experimental details).

There was no observable phosphorescent emission band for naringenin or chrysin. Only fluorescence bands centered at 494 nm for naringenin and 515 nm for chrysin were detected, which decreased in intensity as delay time increased. The accepting levels for Nd^{3+} and Yb^{3+} are located between 11,000 cm^{-1} and 15,000 cm^{-1}, so the all the measured triplet states fall in an a good range for energy transfer, as illustrated in Figure 2.12.

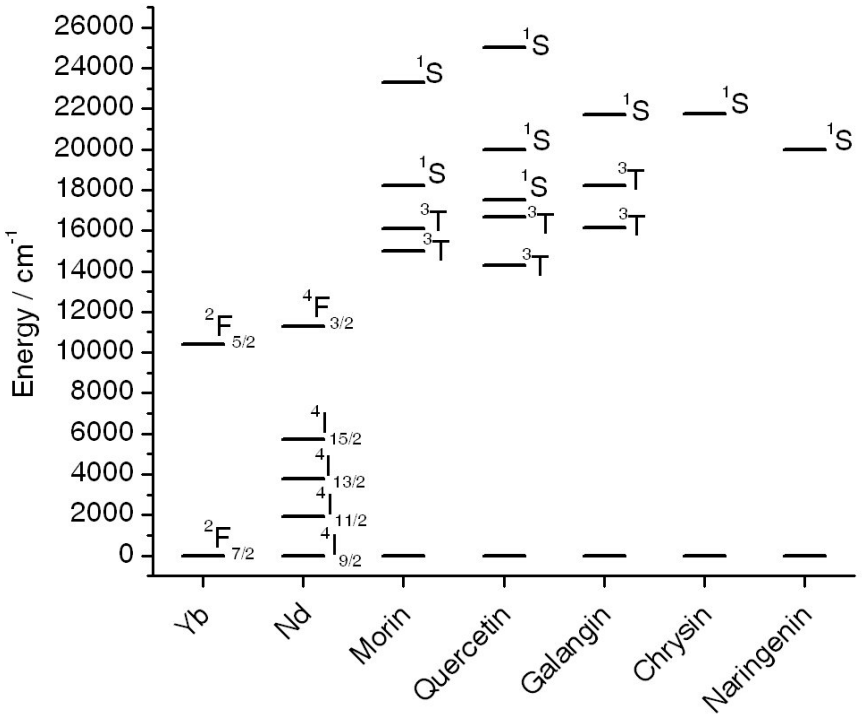

Figure 2.12: Energy level diagrams of Nd^{3+} and Yb^{3+} and measured flavonoid triplet and singlet states. The energy values used for triplet states correspond to the onset and maxima of the phosphorescence bands; and those for singlet states correspond to the maxima in the fluorescence spectra.

2.3.2. Further Studies of Ln^{3+} – Morin Systems

Since the NIR emitting lanthanide flavonoid systems were studied with the intent of potential biological applications, work was focused mainly on morin whose water solubility is desirable for such applications. To determine the ability of morin to sensitize NIR emitting lanthanide cations, solutions were prepared in 1:1 M:L ratio with the following lanthanide cations in dimethyl sulfoxide (DMSO): Nd^{3+}, Er^{3+}, Ho^{3+}, Tm^{3+}, Yb^{3+}. For these sensitization tests, DMSO is used since it is a less quenching solvent than water or methanol due to the absence of –OH vibration. The emission and excitation spectra of these lanthanide solutions showed that morin was able to sensitize four cations emitting in the NIR range; Nd^{3+}, Er^{3+}, Tm^{3+},

and Yb^{3+}. The normalized lanthanide emission spectra are shown in Figure 2.13. These results are exciting as few chromophores are able to sensitize four different lanthanide cations. Only ytterbium and neodymium signals could be detected in aqueous or methanolic solutions, which is not surprising given that the low lying energy levels of erbium and thulium are more susceptible to non-radiative deactivation through overtones of solvent vibrational modes.

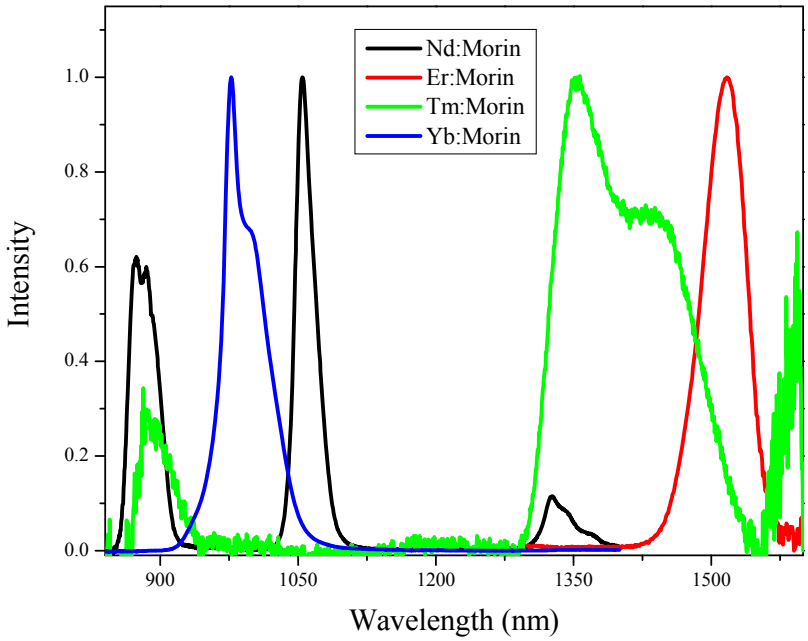

Figure 2.13. Normalized lanthanide luminescence spectra of lanthanide-morin complexes in DMSO monitored in the NIR range collected upon excitation through morin at 420 nm (1 mm cuvettes, 1 x 10^{-3} M)

Initially, spectrophotometric titration studies with morin were done as batch titrations (see Section 2.3.1). Both UV-visible absorbance spectra and lanthanide luminescence spectra were monitored. This data indicated the possible formation of a ML_4 species in solution. To determine the stability constant of this species, as well as the ML – ML_3 species, the UV-vis

absorbance data was treated with SPECFIT. The results produced by this analysis, however, were not coherent and no good fit of the titrations was possible. Since batch titrations involve the manual preparation of a series of samples, there is an increased chance for human error and slight variations from the desired concentrations may occur. It was hypothesized that this was leading to titration absorbance spectra which SPECFIT could not accurately analyze. To improve the accuracy of the titration, a high precision mechanical titration system was employed.

In this auto-titration system, a mechanical buret capable of accurately delivering microliter quantities is used to add a lanthanide solution to a solution of morin directly into the cuvette located in the spectrometer. In order for auto-titrations to work, there must be a reasonably rapid kinetic of formation of the different complexes. To test the kinetic of formation, a lanthanide-morin (M1:L4) solution in buffer was prepared in the cuvette in the instrument, and its absorbance spectrum monitored over several minutes to determine if the solution's absorbance spectrum showed slow changes, indicative of a slow kinetic. These spectra, shown in Figure 2.14, did not show any signs of major change, and the system was deemed appropriate for analysis via auto-titration.

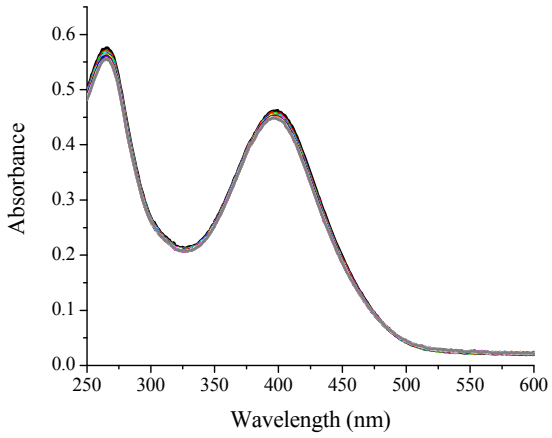

Figure 2.14. Absorbance spectra of solution of 5 x 10^{-5} M morin and 1.25 x 10^{-5} M $NdCl_3$ in HEPES/KCl buffer solution (pH = 7.9); collected at 75 s intervals over 1500 s.

Several auto-titrations were performed with lanthanide cations across the series in buffer solution. Spectra collected for neodymium and ytterbium are shown in Figure 2.15. As seen, the spectra show consistent changes over lanthanide addition. Again, despite the apparent consistency of these data, SPECFIT was unable to produce a reasonable interpretation of the experimental spectra.

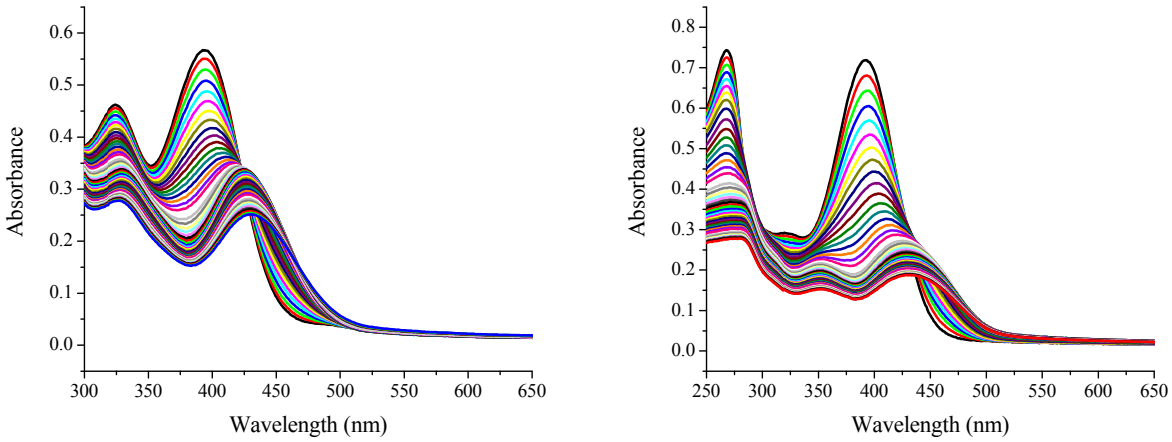

Figure 2.15. UV-visible absorbance spectra of Nd:Morin (left) and Yb:Morin (right) collected throughout auto-titration in TRIS buffer (pH 7.9); initial morin concentration of 5 x 10^{-5} M and final M:L ratio of 1:1.

The inability to fit the auto-titration data with SPECFIT prompted an investigation into the stability of the system in aqueous conditions. This stability study, see Section 2.3.2.1 for details, revealed that morin was not stable in aqueous conditions for an extended period of time. A solvent study was performed which indicated that methanol would be a better solvent for morin, with proven stabilities for up to 48 hours, even when deprotonated. With this knowledge, a new set of auto-titrations were formed in methanol; resulting spectra with neodymium and ytterbium are shown in Figure 2.16.

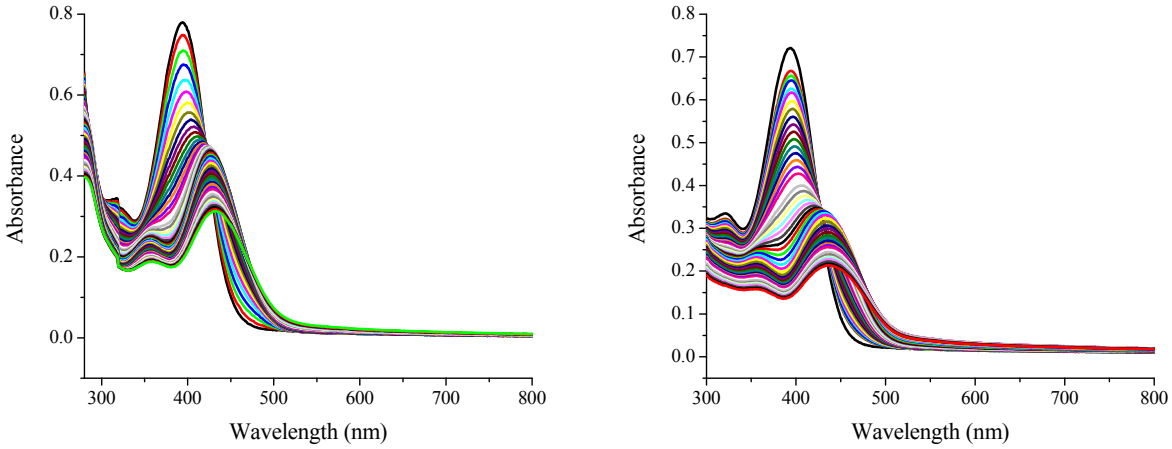

Figure 2.16. UV-visible absorbance spectra of Nd:Morin (left) and Yb:Morin (right) collected throughout auto-titration in methanol; initial morin concentration of 5 x 10^{-5} M and final M:L ratio of 1:1.

Again, the absorbance spectra throughout the auto titration showed consistent changes; however, SPECFIT could not produce any reasonable fittings for these data. This prompted a more in depth study of the kinetics of formation, which are described in Section 2.3.2.2. The kinetic study indicated that changes in the morin absorbance spectrum continued to occur for approximately 45 min after lanthanide addition, which was much slower than originally thought based on the 1500 s trial experiment. Given that a 45 min time for formation of the complex is too long for auto-titration analysis, another set of batch titrations were performed, this set being in methanolic conditions. Lanthanide and morin solutions were prepared in methanol with one equivalent of KOH added in order to deprotonate morin, and TBAF was added to maintain ionic strength. Solutions were prepared 2 to 24 h prior to the collection of the UV-visible absorbance spectra. Sample absorbance spectra are shown in Figure 2.17 for titrations with ytterbium and neodymium in these experimental conditions.

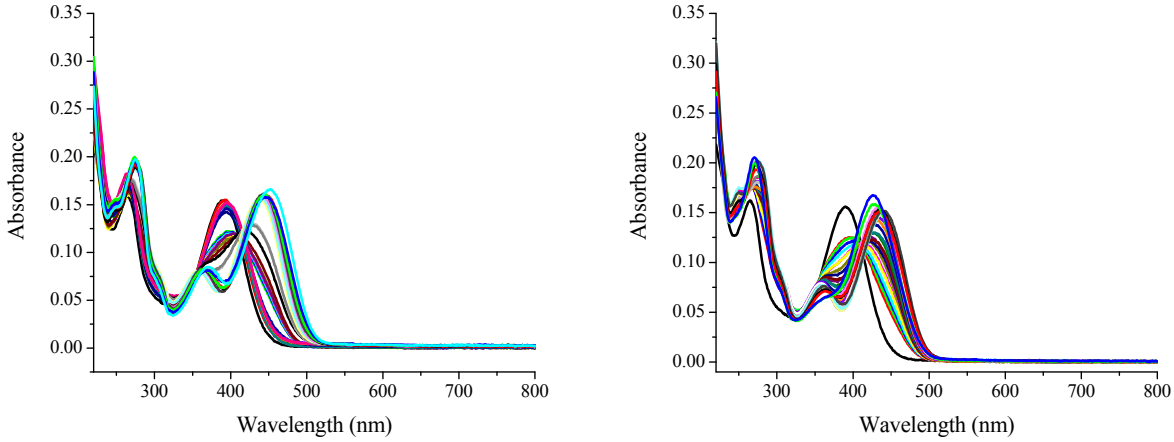

Figure 2.17. Absorbance spectra collected as batch titrations of morin with ytterbium (left) and neodymium (right) in methanolic solution; morin concentration held constant at 1 x 10^{-5} M, inonic strength was maintained using TBAF (5 x 10^{-4} M).

These absorbance spectra showed consistent changes with increasing lanthanide concentration; however, once again, SPECFIT could not produce reasonable fittings for these spectra. After further kinetic studies, see Section 2.3.2.2, it was determined that formation times were even longer, up to several days for ytterbium, which explains the difficulty to gain kinetic information from these titrations.

In addition to monitoring the absorbance spectra for the methanolic solutions prepared for batch titrations, luminescence spectra were also monitored. Since the ytterbium complex has a longer formation time, the results with this cation were difficult to interpret. Neodymium, however, forms faster and the luminescent data could be interpreted. The emission spectra of morin fluorescence in the visible range and neodymium luminescence in the NIR range were both monitored. A graph of the intensity of morin emission corrected for absorbance at the 420 nm excitation wavelength shows that intensity of morin emission increases with M:L ratio, until a 1:3 ratio is reached, after which no further changes occur (Figure 2.18), indicating the

formation of ML_3 species. The profile of the fluorescence spectrum also changes upon lanthanide addition, the fluorescence band increased to higher wavelengths, which suggests that the cation binding induces the lowering of the emitting level of the morin singlet state.

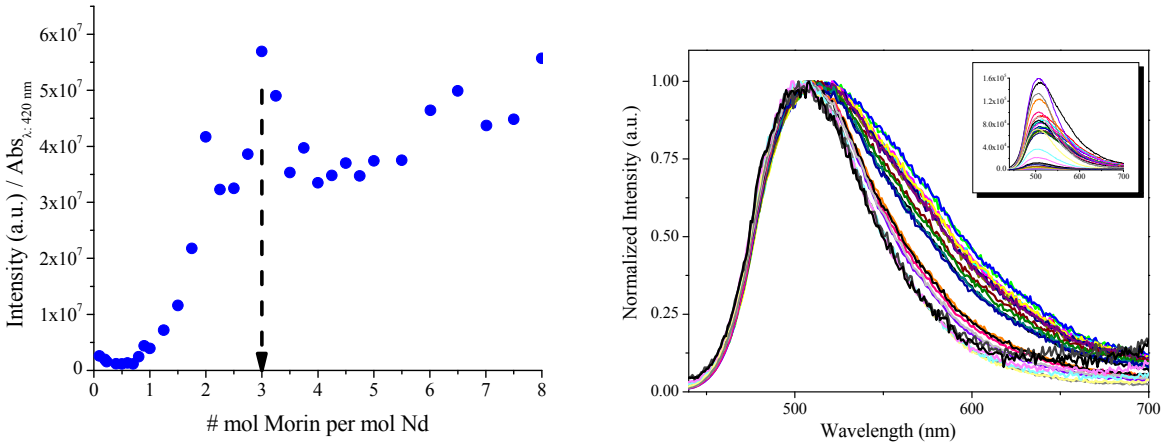

Figure 2.18. Luminescence titration of morin emission upon addition of Nd^{3+}; morin concentration held constant at 2 x 10^{-5} M (methanol, TBAF (5 x 10^{-4} M)). Left: Plot of the integrated intensity of morin emission upon excitation at 420 nm divided by solution absorbance at 420 nm vs. the morin to neodymium ratio. The arrow illustrates the ML_3 point where the intensity appears to stop increasing. Right: Normalized morin emission spectra, inset shows spectra before intensity normalization.

The luminescence intensity of neodymium emission corrected for absorbance at the 420 nm excitation wavelength and the concentration of neodymium was plotted versus M:L ratio, as shown in Figure 2.19. This plot showed an increase in neodymium emission as morin concentration increases, until it levels off after a ratio of 1:3. This provides further indication of the formation of the ML_3 species. These results are consistent with the published reports of $Ln(morin)_3$ complexes.

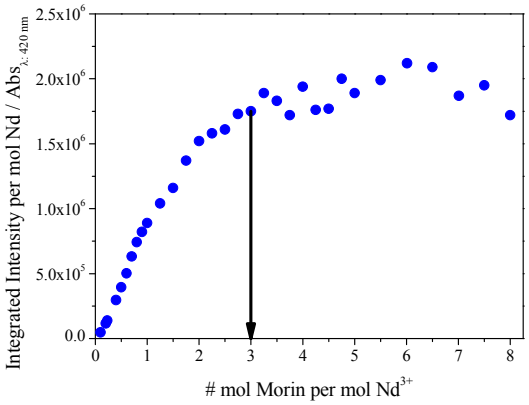

Figure 2.19. Luminescence titration of neodymium centered emission in the NIR range upon excitation at 420 nm over increasing morin ratios; morin concentration held constant at 2 x 10^{-5} M (methanol, TBAF (5 x 10^{-4} M)). Plot of the integrated intensity of neodymium emission, divided by the concentration of neodymium, divided by the absorbance value of the solution at 420 nm vs. the morin to neodymium ratio. The arrow illustrates the ML_3 point where the intensity appears to stop increasing.

2.3.2.1. Stability Studies

For many of the titration experiments, stock solutions of morin in aqueous buffer were prepared. It was noticed that these solutions were changing color after several days on the lab bench and some precipitate was formed. A precipitate was also observed after several days on the lab bench in mixed lanthanide – morin solutions in aqueous conditions prepared for batch titrations. Given these observations combined with the inability to fit auto-titrations performed in aqueous buffer conditions, the stability of morin in the buffer solution was investigated. These studies were performed by monitoring the absorbance spectra over time. First, the stability of morin in aqueous buffer (TRIS buffer, pH 7.9) was monitored. The absorbance spectrum was collected immediately after preparation of a 5 x 10^{-5} M solution, and then at 60 and 140 hours after preparation. Between absorbance spectra, the solution was left on the lab bench in a clear glass vial, exposed to ambient light and air conditions. The spectra, shown in Figure 2.20, clearly indicate that morin is undergoing change, with the band at 400 nm decreasing, and a band at 325

nm increasing. Given that flavonoids are known to be anti-oxidants, it is hypothesized that these changes are due to reactions with oxygen.[33,34]

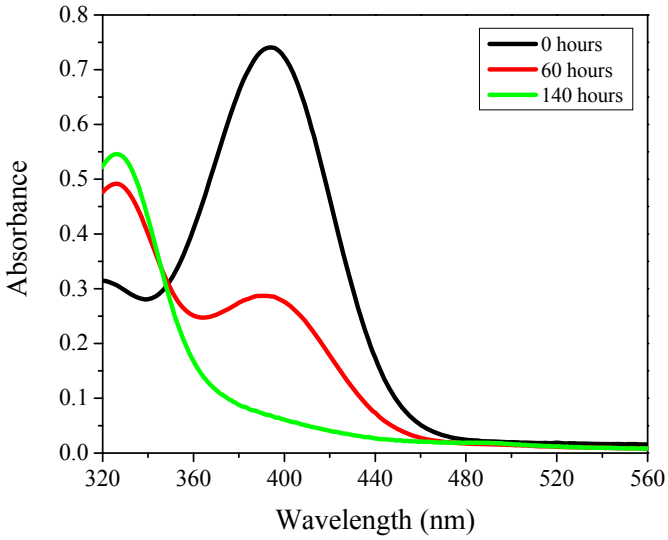

Figure 2.20. Absorbance spectrum of morin in TRIS buffer solution (5 x 10^{-5} M) monitored after exposure to ambient conditions (light, air) over 140 h.

Since lanthanide cations are known to stabilize the electronic structure of organic chromophore ligands and prevent their photobleaching, the effect of binding lanthanide cations on the stability of the solution was monitored via absorbance spectra over 24 h for both morin alone and morin with ¼ equivalent of neodymium, Figure 2.21. In both cases, the absorbance spectrum continuously changed indicating that the presence of the metal was not sufficient to prevent change in the morin electronic structure.

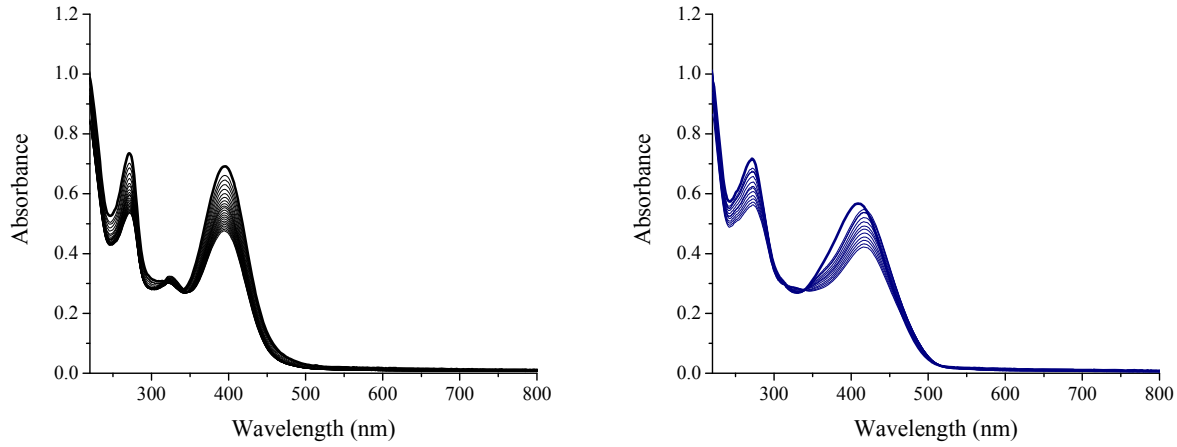

Figure 2.21. Absorbance spectra of 2 x 10^{-5} M morin (left, black) and 2 x 10^{-5} M morin with ¼ equivalents of Nd^{3+} (right, blue) in TRIS buffer solution (5 x 10^{-4} M) monitored over 24 h.

To determine the impact of environmental conditions on the rate of change in morin structure, two sets of solutions were prepared and exposed to various conditions and their absorbance spectra monitored over five days. Both solutions of morin and morin with one equivalent of neodymium (5 x 10^{-5} M in 5 x 10^{-4} M TRIS buffer, pH 7.9) were made. The solutions were exposed to one of the following conditions: presence of ambient light and air, absence of ambient light and air, presence of ambient light and nitrogen purging, absence of ambient light and nitrogen purging, presence of ambient light in a nitrogen glove box, and absence of ambient light in a nitrogen glove box. The absorbance spectra from all sets of solutions and the various conditions are shown in Figure 2.22. As seen, even for solutions that were kept in absence of ambient light in a nitrogen glove box, significant changes to the absorbance spectra still occurred, indicating that it is not possible to stabilize morin or lanthanide-morin species in water for a sufficient length of time to perform titrations.

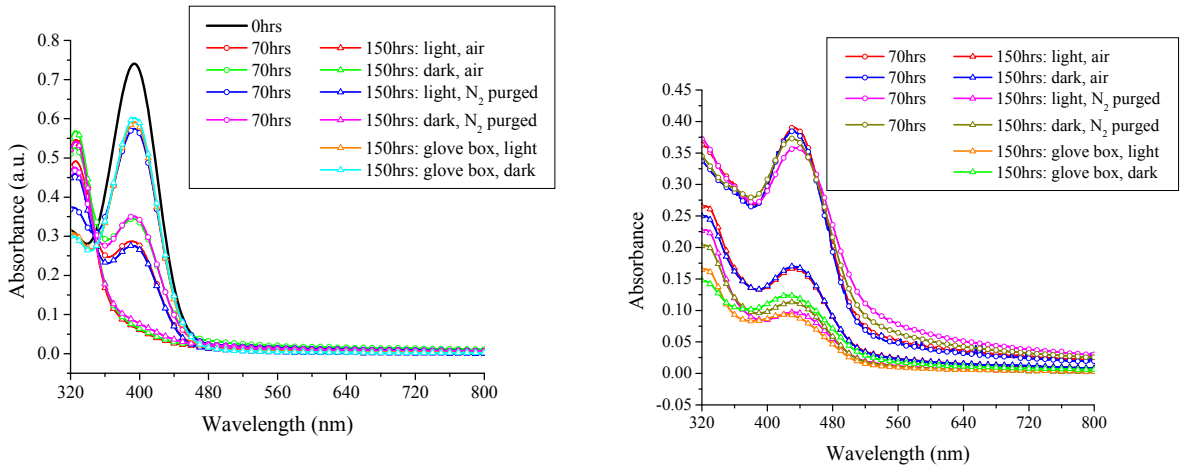

Figure 2.22. Absorbance spectra of 2 x 10^{-5} M morin (left) and 2 x 10^{-5} M morin with 1 equivalent of Nd^{3+} (right) in 5 x 10^{-4} M TRIS buffer solution (pH 7.9) over approximately one week under various conditions.

During these experiments, it was observed that significantly more precipitate forms in solutions of lanthanide and morin mixed together than for morin alone. This suggested that one or more lanthanide-morin complexes species may be insoluble in water. The solutions were centrifuged to isolate the precipitate which was redispersed in DMSO, and the emission spectra were monitored for lanthanide luminescence. The precipitates in DMSO for ytterbium, erbium, and neodymium all displayed lanthanide luminescence spectra with excitation profiles indicative of morin sensitization. These results confirmed that some of the lanthanide-morin complexes have limited water solubility. However, further attempts to isolate and purify the precipitate for identification resulted in redissolution of the precipitate in water. This suggests that the precipitate may be an insoluble polymeric complex of some sort, rather than a discrete species. Therefore, it is likely that lanthanide-morin species are soluble in water at lower concentrations, which is beneficial for any potential biological applications; however, studying these systems with titrations is not possible in aqueous conditions.

Since lanthanide-morin species have limited water solubility and morin is unstable in water, it was necessary to identify another potential solvent to use for titration studies. Methanol, ethanol and DMSO were selected as potential solvents based on the solubility of morin in these solvents. Morin solutions were prepared in each of these solvents at 5 x 10^{-5} M concentration both with and without deprotonation with one equivalent of KOH. The absorbance spectra were monitored immediately after preparation of the solutions and after 48 hours, Figure 2.23. Deprotonated morin remained stable over 48 h in methanol, with no change to its absorbance spectrum, so future titrations and studies were performed in this solvent. It is hypothesized that morin is less stable in water than methanol because the product of reaction with oxygen is not soluble in water. Morin reacts with oxygen and the product precipitates out of solution, driving the reaction to the right. On the other hand, in methanol the product remains in solution and the reaction proceeds at a slower rate allowing morin to remain stable for a longer duration.

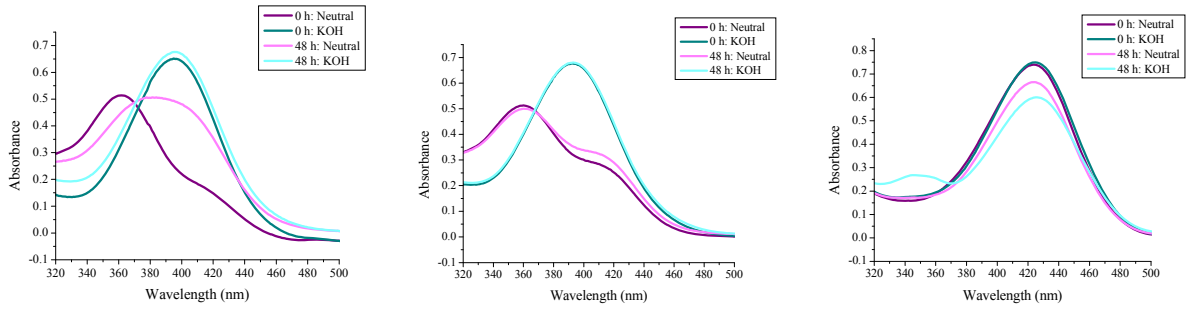

Figure 2.23. Absorbance spectra of morin and deprotonated morin in ethanol (left), methanol (center), and DMSO (right) after 0 and 48 h exposure to ambient conditions (light, air); 2 x 10^{-5} M morin concentration.

2.3.2.2. Kinetic Studies

The inability to fit auto-titration results from methanolic solutions of morin and lanthanide prompted a study of the length of time to formation of lanthanide-morin species in solution.

Since early titration studies in buffer solution gave some indication of the formation of a $[ML_4]^+$ complex, a lanthanide-morin solution was prepared in 1:4 ratio in methanol, and the absorbance spectra were monitored over 180 minutes. As shown in Figure 2.24, a plot of the absorbance at 415 nm shows that no changes occur after approximately 45 minutes. This result indicates a longer kinetic formation of the complex than originally anticipated. A similar experiment was performed with ytterbium, using an M:L ratio of 1:3 based on some batch titration results with neodymium. These results, shown in Figure 2.25, indicated that no changes occurred after approximately 30 minutes.

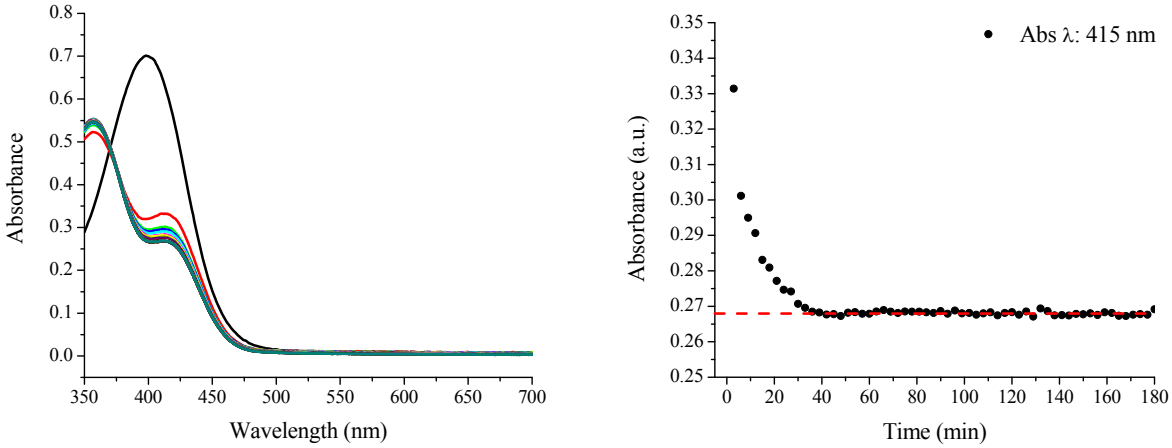

Figure 2.24. Left: Absorbance spectra over 180 min for a solution of 5 x 10^{-5} M morin, 5 x 10^{-5} M KOH, and 1.25 x 10^{-5} M $NdCl_3$ in methanol, black line depicts deprotonated morin prior to lanthanide addition. Right: Plot of the absorbance at 415 nm vs. time for the spectra on the left.

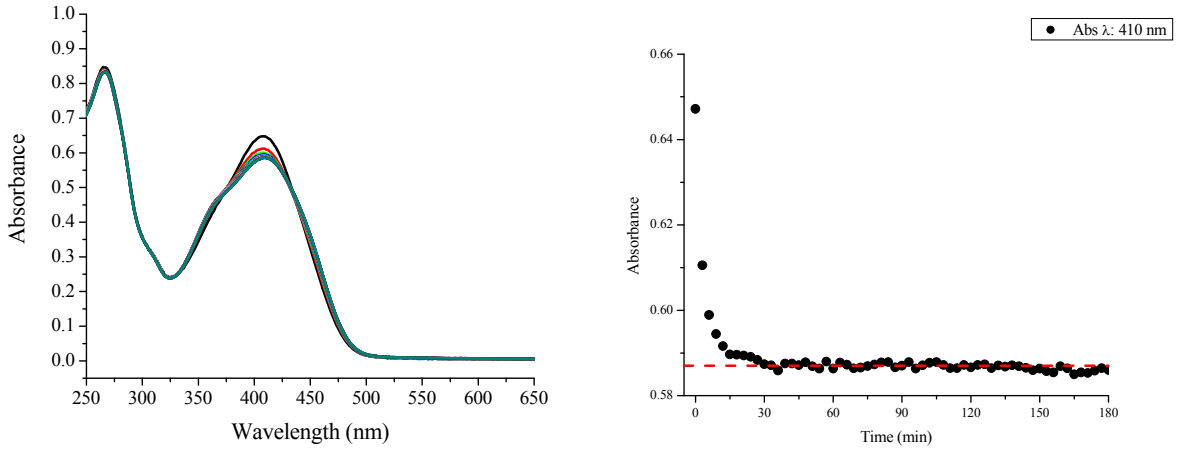

Figure 2.25. Left: Absorbance spectra over 180 min for a solution of 5 x 10^{-5} M morin, 5 x 10^{-5} M KOH, and 1.7 x 10^{-5} M $YbCl_3$ in methanol, black line depicts deprotonated morin prior to lanthanide addition. Right: Plot of the absorbance at 410 nm vs. time for the spectra on the left.

In an attempt to isolate the rate of formation for the ML and ML_2 species, ytterbium–morin solutions were prepared at these ratios, and the absorbance spectra were monitored over 17 h (Figure 2.26 and Figure 2.27).

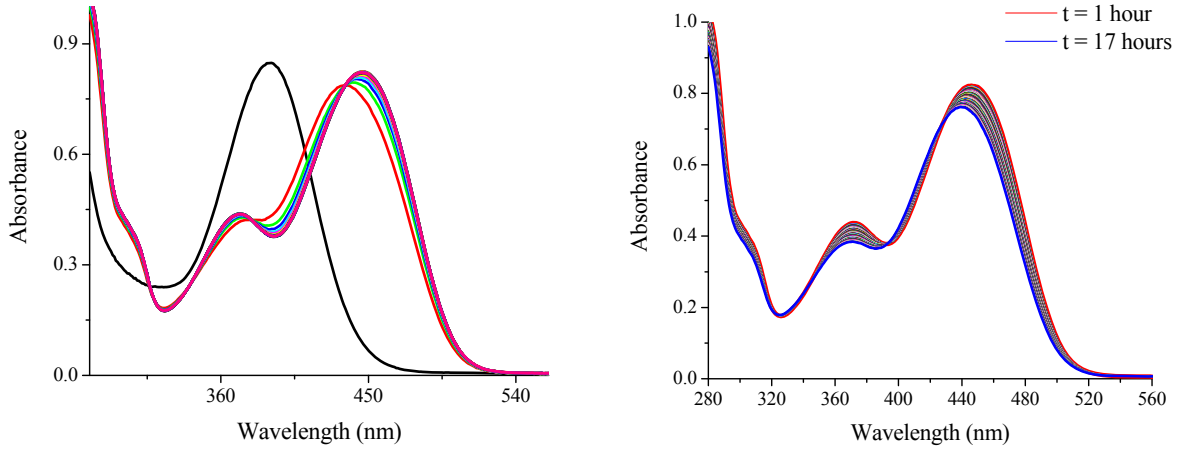

Figure 2.26. Absorbance spectra of a solution of 5 x 10^{-5} M morin, 5 x 10^{-5} M $YbCl_3$, 5 x 10^{-5} M KOH, and 1 x 10^{-3} M TBAF in methanol (M:L ratio of 1:1). Left: Spectra at 90 s intervals for 1 h, black line represents deprotonated morin prior to lanthanide addition. Right: Spectra at 10 min intervals for 17 h.

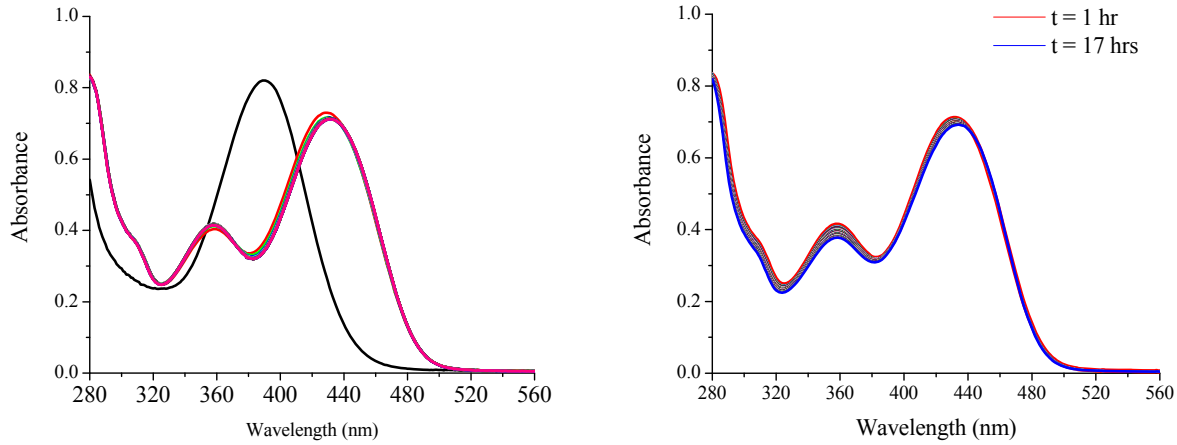

Figure 2.27. Absorbance spectra of a solution of 5 x 10^{-5} M morin, 2.5 x 10^{-5} M $YbCl_3$, 5 x 10^{-5} M KOH, and 1 x 10^{-3} M TBAF in methanol (M:L ratio of 1:2). Left: Spectra at 90 s intervals for 1 h, black line represents deprotonated morin prior to lanthanide addition. Right: Spectra at 10 min intervals for 17 h.

Plots of the absorbance at 410 nm for these solutions versus time, Figure 2.28, both indicated that changes stopped occurring at around 1000 s or 17 minutes. However, upon examination of the whole absorbance spectra, it appeared that changes were still occurring after 17 hours.

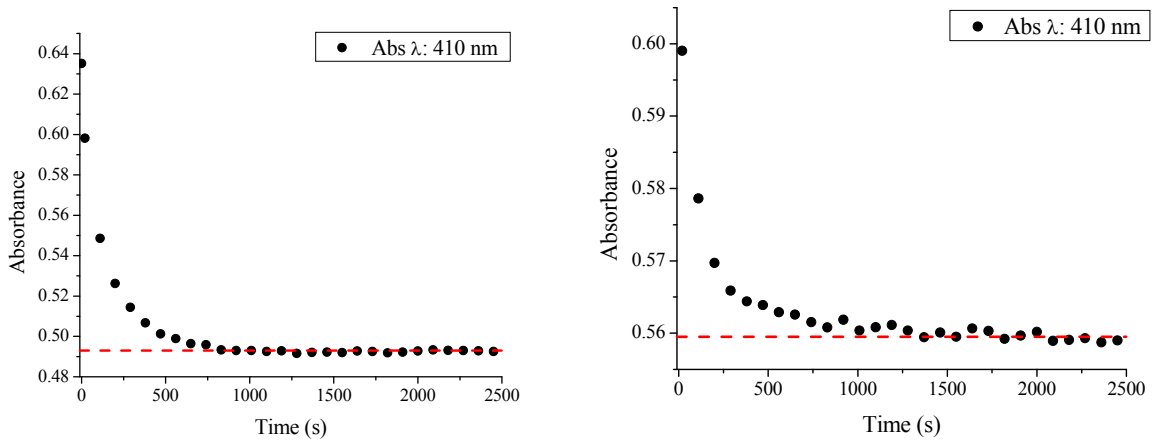

Figure 2.28. Plot of the absorbance at 410 nm vs time for the Yb:morin spectra at a 1:1 M:L ratio in Figure 2.26 (left) and at a 1:2 M:L ratio in Figure 2.27 (right).

Since the absorbance spectra appeared to show changes after 17 hours for ytterbium and morin mixtures in methanol, combined with the continued difficulty to fit batch titration data with SPECFIT, more extensive kinetic studies were preformed. A ytterbium:morin (1:3) solution was prepared in methanol with TBAF to maintain constant ionic strength, and the absorbance was monitored at several wavelengths over two days. The absorbance was also monitored for a solution of morin without lanthanide to serve as a control for the study. The results at 358 nm and 410 nm from this study are shown in Figure 2.29 and Figure 2.30 respectively.

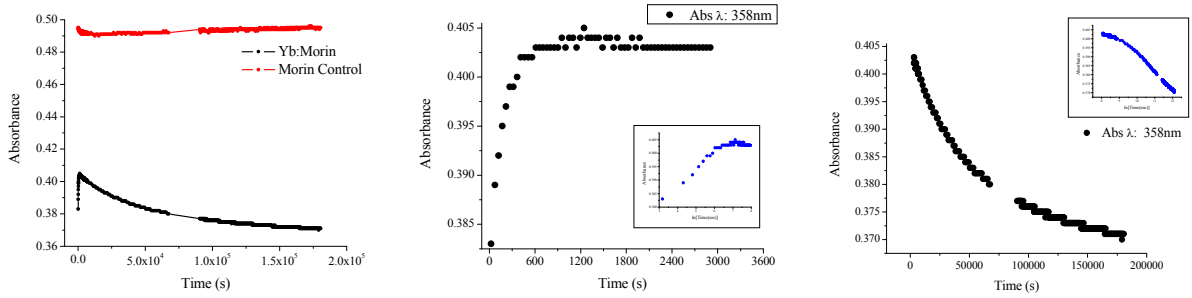

Figure 2.29. Absorbance at 358 nm of a solution of 5 x 10^{-5} M morin, 1.7 x 10^{-5} M $YbCl_3$, 5 x 10^{-5} M KOH, and 1 x 10^{-3} M TBAF in methanol (M:L ratio of 1:3) monitored over 2 days. Left: Black line represents Yb:morin and red line represents a morin control solution. Center: Zoom view of changes in first 1 h of measurements, inset is plot of ln[Time(s)]. Right: Zoom view of changes after 1 h through day 2, inset is plot of ln[Time(s)].

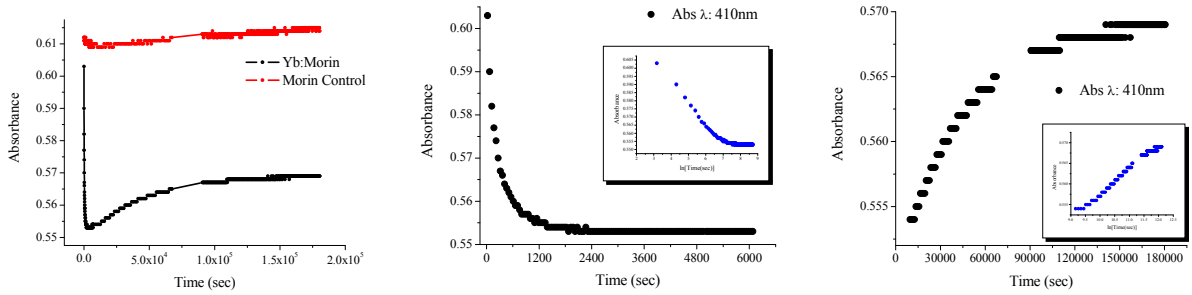

Figure 2.30. Absorbance at 410 nm of a solution of 5 x 10^{-5} M morin, 1.7 x 10^{-5} M $YbCl_3$, 5 x 10^{-5} M KOH, and 1 x 10^{-3} M TBAF in methanol (M:L ratio of 1:3) monitored over 2 days. Left: Black line represents Yb:morin and red line represents a morin control solution. Center: Zoom view of changes in first 2 h of measurements, inset is plot of ln[Time(s)]. Right: Zoom view of changes after 1 h through day 2, inset is plot of ln[Time(s)].

Interestingly, there are two distinct rates of change. Initially, upon the first several hours of monitoring the absorbance, changes appear to stop occurring (center graphs in Figure 2.29 and Figure 2.30). However, when a much longer time scale is plotted, a second slower change is revealed (right-hand graphs in Figure 2.29 and Figure 2.30). For both wavelengths, changes in the morin absorbance are negligible compared to the solutions with lanthanide added. These results suggest that an initial formation of some M:L species is relatively quick, and followed by a slow formation of another species. The first species may be the $[ML_2]^-$ which forms quickly, and the second change may correspond to the slower formation of the ML_3 species. Alternatively, both changes could correspond to an ML_3 species of two different conformations.

To learn more about this unexpected and interesting dual kinetics of formation, a similar study was performed for a longer time of 5 days. In this case both ytterbium and neodymium solutions were prepared with morin at 1:3 ratios in methanol with TBAF. The absorbance was monitored at five different wavelengths for each metal. These results are shown in Figure 2.31. For 430 nm (Figure 2.32), 410 nm (Figure 2.33) and 358 nm (Figure 2.34), these results are shown in greater detail. On the left is plotted the absorbance over the first couple hours, and on the right the absorbance over the entire duration of the study is plotted. These plots reveal that ytterbium and neodymium have different behavior. Neodymium complexation with morin has one rate of change which is slower than the first but faster than the second rate of change for the ytterbium system. It is hypothesized that since neodymium is a larger cation than ytterbium, the formation of the ML_3 species is faster since there is less steric hindrance around the metal center to accept the third ligand.

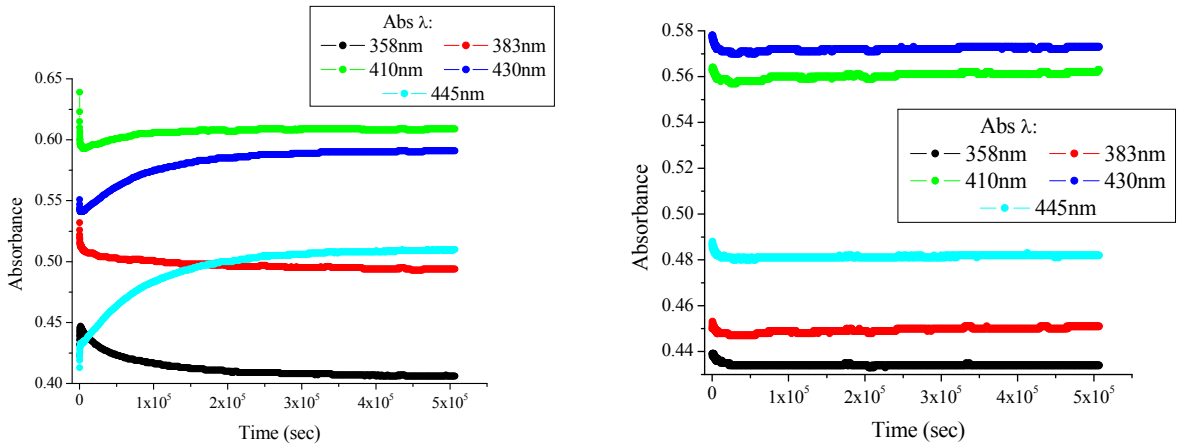

Figure 2.31. Absorbance at various wavelengths of a solution of 5 x 10^{-5} M morin, 1.7 x 10^{-5} M $YbCl_3$ (left) or $NdCl_3$ (right), 5 x 10^{-5} M KOH, and 1 x 10^{-3} M TBAF in methanol (M:L ratio of 1:3) monitored over 6 days.

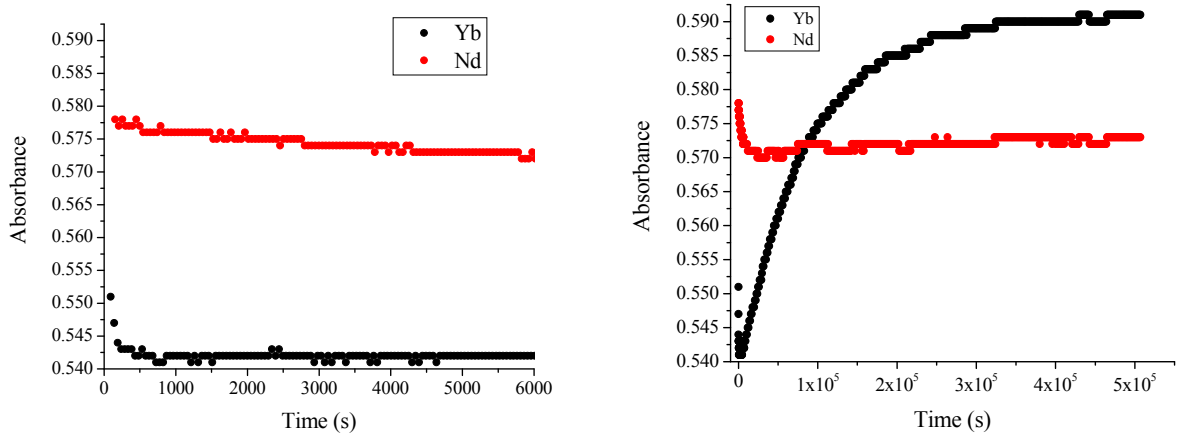

Figure 2.32. Absorbance at 430 nm of a solution of 5 x 10^{-5} M morin, 1.7 x 10^{-5} M $LnCl_3$ (Yb: black, Nd: red), 5 x 10^{-5} M KOH, and 1 x 10^{-3} M TBAF in methanol (M:L ratio of 1:3) monitored over 6 days. Left: Zoom view of changes in first 2 h of measurements.

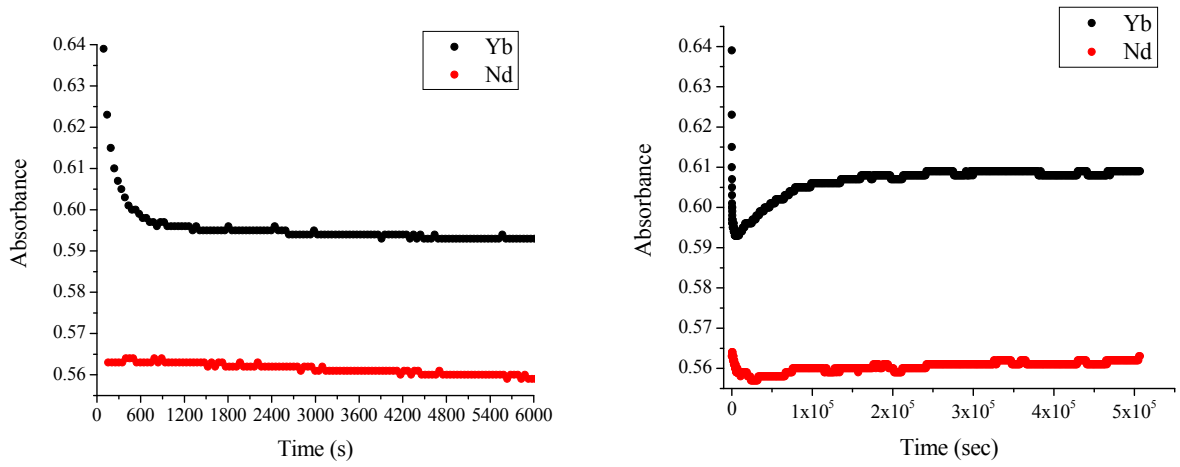

Figure 2.33. Absorbance at 410 nm of a solution of 5 x 10^{-5} M morin, 1.7 x 10^{-5} M $LnCl_3$ (Yb: black, Nd: red), 5 x 10^{-5} M KOH, and 1 x 10^{-3} M TBAF in methanol (M:L ratio of 1:3) monitored over 6 days. Left: Zoom view of changes in first 2 h of measurements.

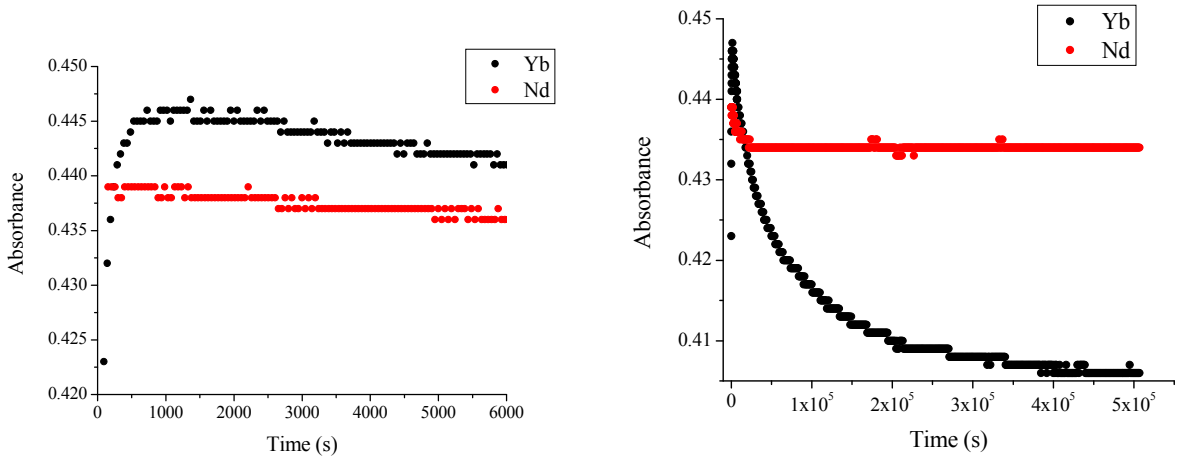

Figure 2.34. Absorbance at 358 nm of a solution of 5 x 10^{-5} M morin, 1.7 x 10^{-5} M $LnCl_3$ (Yb: black, Nd: red), 5 x 10^{-5} M KOH, and 1 x 10^{-3} M TBAF in methanol (M:L ratio of 1:3) monitored over 6 days. Left: Zoom view of changes in first 2 h of measurements.

These kinetic studies have shown that a much longer rate of formation exists for the lanthanide-morin complexes than originally demonstrated by short initial studies. While these results are interesting, they also prove that more extensive stability studies of morin in methanol

will be necessary to determine if morin remains stable in this solvent for a long enough period of time to do batch titrations on this system. Also, these results show that batch titrations will have to be done on solutions that have been prepared at least 5 days prior to analysis in order to obtain results that are reliable.

2.3.2.3. Characterization of the ML_3 complexes

Based on the luminescence titration results, as well as on published accounts of the ML_3 species for lanthanide-morin systems, it is hypothesized that this is the most likely complex forming in solution. To further characterize the photophysical properties of $Yb(morin)_3$ and $Nd(morin)_3$, the quantum yields and luminescent lifetimes were measured. For these studies, measurements were performed on two sets of solutions. First the isolated solid materials were prepared according to published procedures[47,49], and were dispersed in methanol for analysis. Also, lanthanide–morin solutions in methanol were prepared at 1:3 ratios from stock morin and lanthanide solutions. The luminescent lanthanide quantum yields are listed in Table 2.1. As seen, the quantum yields are similar for both sets of sample preparation, further verifying the formation of a well-defined 1:3 species.

Table 2.1. Luminescence quantum yields of lanthanide centered luminescence from 10^{-5} M $Ln(morin)_3$ complexes in methanol formed in solution and from precipitate, excited via the antenna effect through morin at 420 nm.

	In Situ	From PPT
$Yb(morin)_3$	$5.3 \pm 0.4 \times 10^{-4}$	$5.7 \pm 0.4 \times 10^{-4}$
$Nd(morin)_3$	$1.2 \pm 0.1 \times 10^{-4}$	$1.9 \pm 0.1 \times 10^{-4}$

For both systems, the quantum yields are slightly higher for the solutions prepared from precipitate. This is likely due to solution preparation factors. When the precipitate is dissolved, the exact ratio of metal and ligand remains intact. However, when samples are prepared in solution, the ratio depends on the accuracy of the concentration of the stock solutions. Since lanthanide salts are highly hydroscopic, it is possible that their molecular weight is slightly higher than calculated due to the presence of additional water molecules. Thus, the concentration of the lanthanide stock solution may be slightly lower than its calculated value. In the mixed solutions, this leads to a slightly lower lanthanide concentration and consequently higher morin concentration. In this case, there is morin in the solution that is not bound to lanthanide that can absorb light but not transfer the energy to the lanthanide, causing a slight depreciation in the quantum yield values. Regardless of this, the quantum yield values are reasonably close to one another.

The quantum yield values are modest compared to values reported for other ytterbium and neodymium complexes with quantum yields up to the 10^{-2} range; [58-61] however, NIR microscopy images indicate there is still sufficient luminescence for good detection under conditions suitable for application as a biological imaging agent. These images (Figure 2.35) were collected at the University of Pittsburgh Center for Biological Imaging in collaboration with Profs. Claudette St. Croix and Simon Watkins. $Ln(morin)_3$ solutions were prepared in aqueous buffer, which would be even more quenching than methanol, and $Ln(quercetin)_3$ solutions were prepared in methanol.

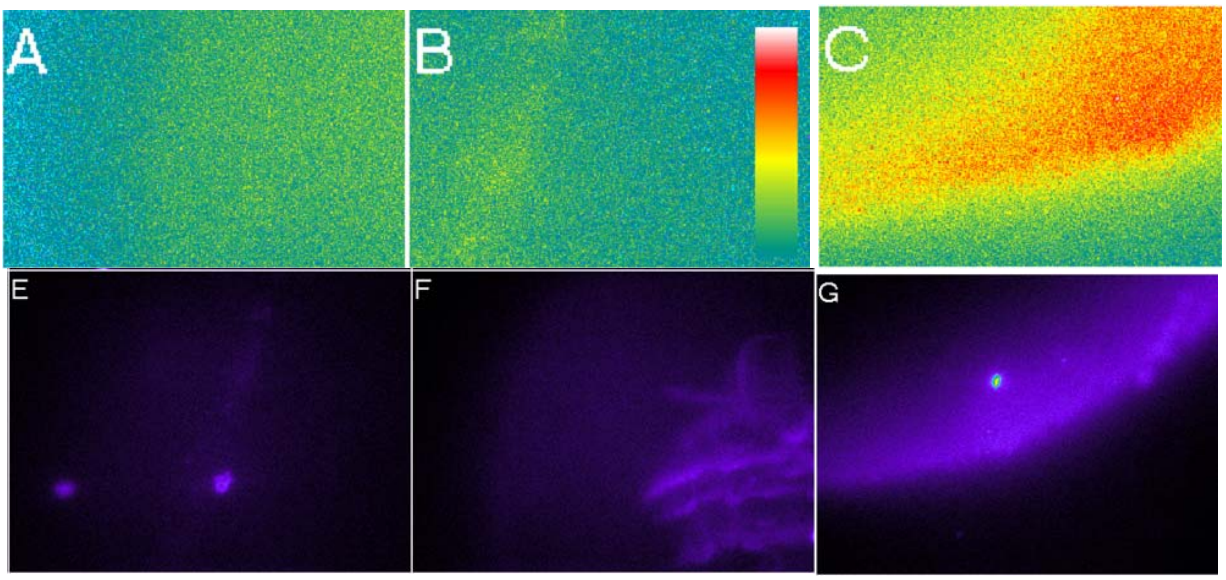

Figure 2.35. Images collected of lanthanide-flavonoid solutions with a NIR fluorescence microscope (200 nL spotted on nitrocellulose membranes, imaged with 10x objective, 50 ms, 20 MHz). A) Yb: morin, B) Nd: quercetin, C) Nd: morin, E) Nd: quercetin, F) Yb: morin, G) Nd: morin; collected in collaboration with Claudette St. Croix and Simon Watkins and the University of Pittsburgh Center for Biological Imaging.

The lanthanide centered luminescent lifetimes were measured for ytterbium and neodymium ML_3 complexes with morin, both on solution prepared mixtures and from dissolved precipitate, reported in Table 2.2.

Table 2.2. Luminescent lifetimes of lanthanide centered luminescence monitored at 980 nm for Yb^{3+} and 890 nm and 1050 nm for Nd^{3+} at room temperature. The q values, number of coordinating solvent molecules, were calculated according to equations in Section 1.

	τ_{MeOH}	τ_{MeOD}	q
$Yb(morin)_3$	0.77 ± 0.05 μs	25.3 ± 0.9 μs	2
$Nd(morin)_3$	84 ± 2 ns	750 ± 20 ns	3

The same lifetime values were obtained from both sets of solutions, indicating further that the same species forms in solution and it is likely the ML_3 complex. For both lanthanide cations, the decay profiles were best fit with mono-exponential decays, indicative of a single environment for

the lanthanide cations. Luminescence lifetimes were also measured in deuterated solvent so that the number of coordinating solvent molecules (q value) could be calculated. These results indicate that ytterbium has 2 coordinating molecules of the methanol while neodymium has 3 coordinating solvent molecules, with a M:L ratio of 1:3, this gives coordination numbers of 8 and 9 for ytterbium and neodymium respectively. Since neodymium is a larger cation than ytterbium, these slightly different results are reasonable. They also corroborate the modest quantum yield values, suggesting that these low values are likely due to solvent quenching rather than inefficient energy transfer from morin to the lanthanide cations.

2.4. CONCLUSIONS

Preliminary studies have demonstrated that five different flavonoids are capable of sensitizing two NIR emitting lanthanide cations. Morin, quercetin, galangin, chrysin, and naringenin all demonstrated the ability to bind to and sensitize NIR emission from Nd^{3+} and Yb^{3+}. The flavonoids demonstrate several beneficial features for sensitization, confirming that they are a good choice for antennae of NIR emitting lanthanide cations. The binding groups are located on the chromophore, keeping the chromophore close to the lanthanide cations which is necessary for efficient energy transfer. The triplet states measured for morin, quercetin, and galangin are in an appropriate range for energy transfer to the lanthanide accepting levels. They also have absorbances that are sufficiently low in energy to have biologically compatible excitation bands in 400 – 430 nm range.

Changes in the UV-Vis absorbance spectra upon addition of a lanthanide cation to a flavonoid solution confirmed that the flavonoids coordinate to the metal centers in solution. All of the flavonoids were soluble in methanol, which contains OH oscillators and is thus a highly quenching solvent. Despite this, lanthanide sensitization still occurred, which confirms that flavonoids were a good choice for lanthanide antennae. Morin was the only water soluble flavonoid used here and was able to sensitize lanthanide cation emission in this highly quenching solvent, even at low ligand to metal ratios such as 0.5:1. In this situation, protection from water quenching would be minimal, so the efficiency of energy transfer between the chromophore and lanthanide cation must be high for the lanthanide luminescence to be detected.

Since morin was the only flavonoid to demonstrate water solubility, extensive studies focused on lanthanide systems with this ligand. Initial experiments suggested the formation of ML_4 complexes in buffer, however, stability studies later revealed that morin is not stable in aqueous conditions and these results were inconclusive. Several sets of spectrophotometric titrations were performed including batch titrations in buffer and methanol and automated titrations in buffer and methanol. In all cases UV-visible absorbance spectra were analyzed with the SPECFIT program, which was unable to fit the data to reasonable stability constants. This prompted several series of stability and kinetic studies, ultimately revealing several interesting findings. Morin is not stable in aqueous conditions and furthermore lanthanide-morin systems produce insoluble polymeric species in water, thus titration studies in this solvent were not possible. Stability studies demonstrated that morin remains stable in methanol for reasonable lengths of time, and is a better solvent for titration study. Extensive kinetic studies revealed an unexpectedly long formation time for Nd:morin complexes and a dual step formation for Yb:morin complexes with an exceptionally long second step of up to 5+ days. Luminescence

batch titrations performed on Nd:morin systems provided evidence for the formation of ML_3 complexes in solution. The luminescent quantum yields for ytterbium and neodymium complexes in methanol were modest, and luminescent lifetime studies revealed 2 to 3 coordinating solvent molecules suggesting that solvent quenching occurs. Nevertheless, the Yb:morin and Nd:morin systems were soluble in water at lower concentrations, and the lanthanide luminescence could be detected with excitation profiles indicative of morin sensitization, demonstrating that these complexes still have potential to serve in biological application. To further advocate the potential for these systems to serve as biological imaging reagents, NIR microscopy images were successfully collected under standard experimental conditions.

Some preliminary results with quercetin indicate that this ligand also forms ML_3 complexes with the lanthanide cation. Further study of this flavonoid will be necessary to determine stability and formation kinetics to determine ideal conditions for spectrophotometric titrations that have conclusive results. Future titrations with morin, applying the time conditions determined through the kinetic studies, should produce results that could be interpreted with the help of SPECFIT software. Since the flavonoids have several beneficial features for NIR lanthanide sensitization, future study of the other three flavonoids and their complexes with lanthanide cations is of interest.

3. CdSe SEMICONDUCTOR NANOCRYSTALS AS NOVEL ANTENNAE FOR LANTHANIDE CATIONS

Parts of the work presented here have been completed in collaboration with Adrienne Yingling and Chad Shade (Stéphane Petoud Research Group, Department of Chemistry, University of Pittsburgh). A portion of the results presented here have been published in *The Journal of the American Chemical Society*, Vol. 127, No. 48, p 16752, 2005: "Incorporating Lanthanide Cations with Cadmium Selenide Nanocrystals: A Strategy to Sensitize and Protect Tb(III)."[25]

3.1. INTRODUCTION

Taking an alternate approach to organic chromophore lanthanide antennae, luminescent cadmium selenide (CdSe) nanocrystals are used to sensitize lanthanide cations emitting in the visible range. Using nanocrystals as an antenna involves incorporating luminescent lanthanide cations in nanocrystals and allowing the excited electronic states of the nanocrystal to sensitize the lanthanide cation emission. In comparison to organic antennae types, semiconductor nanocrystals (also known as Quantum Dots) offer the ability to protect lanthanide cations from quenching solvent molecules without supplying any high energy vibrations of their own, thus preventing non-radiative deactivation of the lanthanide cation excited states. Nanocrystals such

as CdSe have several advantages as species that absorb and emit photons. They have broad absorbance bands with high epsilon values, and their emission wavelengths can be easily tuned through their size, which is controlled through synthesis conditions.[62,63] As illustrated in Figure 3.1, using CdSe semiconductor nanocrystals as an antenna for lanthanide cations results in a product that combines the best of two worlds: a new luminescent species with sharp emission bands, long luminescence lifetimes, strong absorbance (high epsilon values), and tunable excitation, all without any efficient deactivations through vibrational states. In addition, including lanthanide cations in CdSe nanocrystals allows the formation of polymetallic lanthanide compounds, which is a strategy to maximize the number of lanthanide cations per unit of volume, and thus the number of photons emitted and the corresponding detection sensitivity.

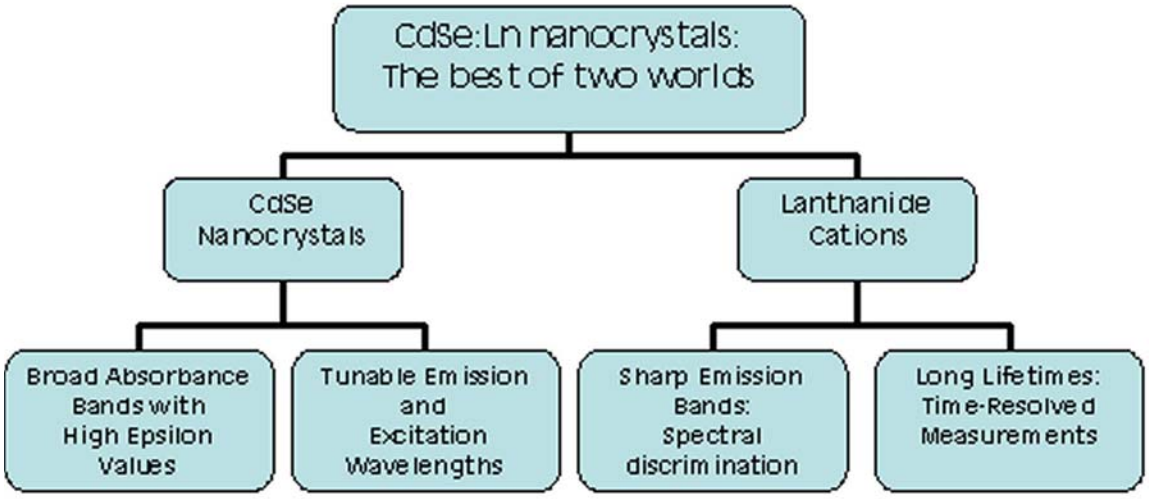

Figure 3.1: A flow chart illustrating the advantages of using nanocrystals as antennae for lanthanide cations and creating a new luminescent species that combines the best of two fluorophores.

Nanometer-sized semiconductor particles are nanomaterials, a category of matter that lies at the interface between molecules and solids. They have many size dependent physical and chemical properties that make them very interesting for scientific investigation. The most commonly known of these properties is the established relationship between their size and their optical properties.[63] Known as the size quantization effect, the smaller the particle, the higher the energy of absorption and emission.[64] In a bulk semiconductor material the electronic carriers are free in all directions, thus electrons can move freely throughout the material. When this same material is spatially confined, interesting changes occur in the allowed carrier energies. In the bulk, the carriers exist in nearly continuous bands. However, when confined in all three directions, which is the case for nanocrystals, carriers become restricted to a specific set of completely quantized energy states. By solving for the Eigen-energies of the Schrödinger wave equation for the carriers in a confined space, the effect of this quantum confinement can be obtained. This leads to a calculated relationship between the size of the confined energy system and the resulting change in energy levels. Equation 3.1 is the simplified expression for the energy of a confined system

$$E = [\hbar^2 \alpha_n^2 n^2] / [2mL^2] \qquad (3.1)$$

where $\hbar$ is Plank's constant divided by 2π, m is some carrier effective mass that depends of the degree of confinement, α_n is the n zeroes of the spherical Bessel function of order 1, and L is the confinement dimension. This equation shows that the resulting energy state is inversely proportional to the square of L, which means the band gap can be shifted to higher energies by spatially confining the electronic carriers.[65]

The minimum energy required to form free carriers in a bulk semiconductor material is known as the band gap energy. Any value below this cannot excite free carriers; however, it is possible to promote an exciton at energy lower than the band gap at low temperatures. An exciton is an electron and hole that are bound to each other. Since the electron is bound to the hole, a lower energy is required to achieve this type of excitation. When a system is spatially confined, as it is in a nanocrystal, the resulting quantized energy states are formed by excitons. An exciton is similar in behavior to the hydrogen atom; as the electron orbits the hole, a set of hydrogen-like energy states are created. An electron orbiting a nucleus has a characteristic dimension, the Bohr radius. Similarly, when an electron orbits a hole in a nanocrystal exciton, it also has a characteristic dimension that is called the exciton Bohr diameter, a_x, which is basically a measure of the diameter of the exciton. This is a material-dependent property that varies in a similar way to the band gap and is therefore a critical parameter which provides a basis on which to judge the criteria for size confinement in different materials.[65]

As materials approach the size of the exciton Bohr radius, confinement effects must be taken into account. There are both strong and weak confinement effects which are determined by the degree of coupling between the electron and the hole. While these give different resulting energy state equations, they both lead to the same trend in the relationship between energy and crystal size: a blue-shift in energy results as the size of the crystal decreases. When nanocrystals absorb light of the appropriate wavelength and enter an excited state, excitons are created within and then recombine radiatively to create photons. Photoluminescence spectra taken of nanocrystals yield a plot of the intensity of the signal measured from the radiative recombination as a function of the wavelength being detected. This allows for directly measuring the different energy states present in a nanocrystal. As the nanocrystals increase in size, the energy from the

radiative recombination of the excitons decreases. This causes emission of the photon to shift to higher wavelengths (red-shift), as predicted by quantum confinement theory.[65] This quantum confinement effect, illustrated in Figure 3.2, is one of the most desirable characteristics of nanocrystals.

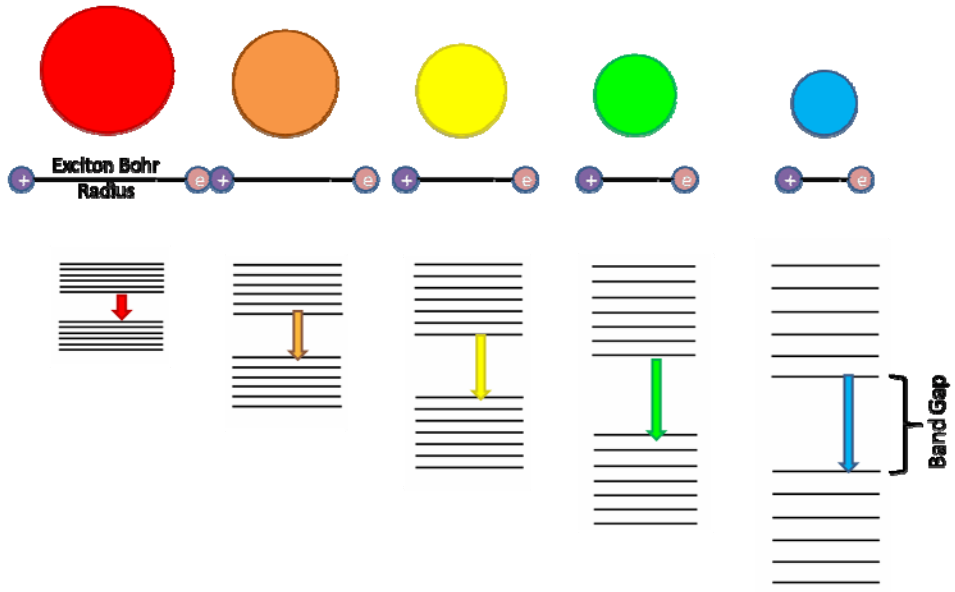

Figure 3.2. Illustration of the quantum confinement effect that leads to the tunable band gap emission color of CdSe semiconductor nanocrystals based on the particle diameter.

While emission color is dependent on size, the color purity of semiconductor nanocrystal emission is dependent on the size and shape distribution of a nanocrystal sample. There are two other properties that are important to the overall efficiency of nanocrystal emission: brightness and stability. These later properties all depend on a well-controlled synthesis method.[66] In addition to the size quantization effect, nanocrystals have other properties of interest, such as nonlinear optical properties, unusual fluorescence behavior such as blinking, catalytic properties,

structure and phase transitions, transport properties, surface chemistry, and use as precursors for nano-structured materials processing.[63,64]

Nanocrystals have vast potential as a new class of fluorescent species for many biological and biomedical applications, mostly due to their advantages over currently employed organic dyes.[62,63] Since the emission spectra are narrower, symmetrical, and tunable according to size and material composition, nanocrystals allow closer spacing of different probes without substantial spectral overlap. Also, their absorption spectra are very broad, with high ε values, so it is possible to excite different sizes (and colors) of nanocrystals simultaneously with a single light source. If the appropriate wavelength is chosen, it is even possible to minimize sample autofluorescence by simply avoiding its excitation. Another advantage is increased stability. Nanocrystals exhibit much better photostability than organic dyes as they do not photo-bleach over reasonable lengths of exposure time (180 s).[67] They also do not dissociate in solution, which allows them to be used at very high dilutions. Additionally, recent advances in nanocrystal research indicate that near infrared range (NIR) emission can be achieved,[62] which is extremely useful for bioimagery applications as NIR radiation can penetrate skin, blood and other organs.[65] For many of the same reasons, semiconductor nanocrystals are also being explored for electronic applications such as light emitting diodes (LED).[68]

Despite claims that doping of CdSe and other nanomaterials of wurtzite or rock salt structure is unlikely and even impossible,[69-72] many groups have made attempts at incorporating dopant ions within CdSe host lattices. These approaches are often aimed at using dopant ions to tune or enhance the attractive photophysical properties possessed by CdSe nanocrystals. CdSe typically forms with a wurtzite crystal structure, which the literature strongly suggests is not conducive to doping based on the surface energy ratios within these materials, and that doping

within these materials is only possible through the use of polychalcogenide precursors.[70] However, it has also been shown that CdSe can be forced into a zinc blende crystal structure, which can incorporate dopant ions more readily within the typical high temperature injection syntheses.[70,73] Overall, it is suggested that doping concentration within host lattices is strongly dependent on a number of factors including surface morphology, nanocrystal shape, and most importantly, the crystal structure.[70,72]

A great deal of literature can be found regarding the doping of CdSe nanocrystals with transition metal ions. There are currently two separate approaches to achieving this goal: (1) the formation of zinc blende crystal structures to incorporate dopant ions based on surface energies[70,72] and (2) the use of single source or polychalcogenide precursors to form wurtzite structures with dopant ions.[74-76] Wurtzite structures have been reported containing either cobalt or manganese, while zinc blende structures have been observed for magnesium and manganese.[70,72,74-76] Forcing the CdSe nanocrystals to adopt a zinc blende structure has the advantage of slightly lower temperature synthetic conditions, with the formation of the zinc blende structures resulting from temperatures at approximately 220°C. To date, successful doping with cobalt and manganese has been reported.[70,72,74-76] While most of the work with transition metal dopants in CdSe nanocrystals focuses on magnetic properties, more recent studies have shown that the incorporation of dopants may lead to better tunability of band gap energies and, as a result, improved control of emission properties. The tuning of the band gap through dopants has only been studied using zinc blende crystal structures and has just recently been established.

Transition metal dopants are attractive for the resulting magnetic properties that arise from doped CdSe nanocrystals, however, doping with rare earth metals has become increasingly

attractive to obtain nanomaterials with novel and/or improved photophysical properties. A number of studies have reported fluorescence enhancement through the use of trivalent lanthanide dopant ions.[77-79] Additional studies have been conducted on doping of CdS with lanthanide cations.[80-83] Some studies involve doping a matrix containing nanocrystals, while others describe the doping of the nanocrystal material itself. Additional studies illustrate advantages of surface bound lanthanide cations. In all cases, characteristic lanthanide emission resulting from forbidden f → f transitions has been observed. Europium (III) and terbium (III) are most widely studied in these systems due to their visible emission. In the case of silica matrices containing CdSe nanocrystals alongside Eu^{3+}, the antennae effect was not observed, however, enhanced emission intensities of Eu^{3+} were found in the presence of CdSe.[77] This enhancement is the result of non-radiative energy transfer to the Eu^{3+} from the CdSe electron-hole recombination.[77] While many studies exist on doping of CdS nanocrystals with lanthanides, the only known attempt of doping CdSe was by Strouse et al. This work focused on structural characterization of CdSe:Eu nanocrystals, where it was found Eu^{3+} are incorporated/associated with CdSe nanocrystals, however, the antennae effect was not studied nor was it observed.[79]

Here, CdSe nanocrystals are synthesized with lanthanide dopants. In this system the lanthanide is incorporated within (surface and/or internal sites) the nanocrystals and not incorporated into a matrix surrounding the nanocrystals. Luminescent studies show that antenna effect sensitization of the lanthanide cations is possible. Also, luminescent lifetime studies produced long lifetime values for the lanthanide cations, indicating dopant locations that are likely within the CdSe structures with efficient protection against non-radiative deactivations. The studies presented herein demonstrate that small nanocrystal sizes are optimal for terbium and europium sensitization. Methods to etch larger nanocrystals to smaller sizes have been

investigated as a potential route to obtain higher energy nanocrystals which may have improved lanthanide sensitization.

Characterizing lanthanide cation doped CdSe semiconductor nanocrystals has been done through a variety of analytical techniques. Photophysical analyses, including UV-Vis absorbance and luminescence spectroscopy, provides information about the size and electronic structures of the nanocrystals.[62] Lanthanide cation luminescence lifetime decay measurements are performed to gain information on the degree of protection of lanthanide cations from non-radiative deactivations and on whether the Ln^{3+} cations in the crystal have different environments. The luminescence lifetimes of a lanthanide cation vary with different environments; therefore, different lifetimes are expected for cations located on the surface of the nanocrystal versus inside the nanocrystal structure. Quantum yield measurements provide insight into the efficiency of lanthanide sensitization through the antenna affect. Transmission electron microscopy (TEM) imaging of the nanocrystals can provide direct evidence that the nanocrystals actually exist and confirm their crystallinity. Additionally, TEM images can provide information on what size they are, how mono-disperse they are, and what shape they are.[84,85] Energy dispersive X-ray fluorescence spectroscopy (EDXRF) is employed to determine the content of the nanocrystals. EDXRF is a simple yet powerful semi-quantitative analysis tool, which provides data on the types of atoms present in a sample.[86] This method is used to confirm the presence of Tb^{3+} and Eu^{3+} dopants, as well as the relative atomic composition of the materials.

3.2. EXPERIMENTAL

3.2.1. Reagents

Trioctylphosphine [TOP] (90%), trioctylphosphine oxide [TOPO] (99%), cadmium oxide (99.99% puratrem), n-tetradecylphosphonic acid [TDPA] (98%), 1-hexadecylamine [HDA] (98%), butylamine, and lanthanide (Ln^{3+} = Tb^{3+} Eu^{3+} Sm^{3+}) nitrate (99.998%) were purchased from Sigma-Aldrich-Fluka. Selenium powder (99.99%) and dysprosium nitrate (99.998%) were purchased from Strem Chemicals. Methanol, ethyl acetate, carbon tetrachloride, toluene, and hexane were purchased from Fischer Scientific, and chloroform was purchased from EMD. Gadolinium nitrate (99.998%) was purchased from Alfa Aesar. 1-octanol (98%) was purchased from Acros Organics and 1-butanol and potassium hydroxide were purchased from J.T. Baker. Argon and nitrogen gas were purchased from Valley National, Pittsburgh. All chemicals were used as purchased without purification, except toluene which was distilled before use.

3.2.2. Synthesis methods

CdSe nanocrystals with lanthanide cations incorporated within the crystal structure (occupying surface and/or core sites) have been synthesized using procedures adapted from the works from Peng et al.[73,87,88] and Strouse et al.[79] These syntheses involve the use of the less toxic CdO precursor compared to the previously used $Cd(CH_3)_2$ at high temperatures (~300°C) in TOPO/TOP solvent systems. From the original procedures, the cation concentrations were adjusted to account for lanthanide cations, however the total cation concentrations remain constant with Se being in excess.

3.2.2.1. Early synthetic methods

Selenium stock solutions were prepared as follows: 1 mmol of selenium powder was dissolved in 4 mL of TOP and 0.1 mL of toluene through vigorous stirring in a schlenk tube. Excess air was removed through Schlenk techniques under a nitrogen atmosphere. The solution was stored under nitrogen until used.

To synthesize the nanocrystals, the following procedures were followed; the same basic procedure was used in all cases with some different variations. Many batches were made and analyzed, all resulting in a product with consistent properties. For batches where TDPA was used as the ligand, 10.0 mmol of TOPO, 0.33 mmol of CdO, 0.07 mmol of $Tb(NO_2)_3 \cdot 6H_2O$, and 0.80 mmol of TDPA were used, corresponding to 12% doping with terbium. Batches were also made using HDA as the ligand, and there were two different terbium doping levels. For doping at 12%, 0.80 mmol of HDA was used with the same amounts of all other reagents with TDPA as the ligand. For 10% doping, 10.0 mmol of TOPO, 0.36 mmol of CdO, 0.04 mmol of $Tb(NO_2)_3 \cdot 6H_2O$, and 0.80 mmol of HDA were used. All starting reagents were placed together in the reaction vessel, a three-neck 50 mL round bottom flask. The flask necks were fitted with water condensers. Contents were placed under argon and heated to 300ºC, using a heating mantle connected to a variable autotransformer (Staco Energy Products, Inc., Dayton, OH) for temperature control. Selenium stock solution was injected at 300ºC, and the temperature was reduced to 250ºC for the duration of nanocrystal growth. In some cases, the synthesis was carried out at slightly lower temperatures of injection at 250ºC followed by growth at 230ºC. Aliquots were removed at a variety of times ranging from seconds to hours after injection using a syringe. For purification, samples were dissolved in chloroform then purified through centrifugation and precipitation in methanol. It was possible to transfer purified nanocrystals into hexane, toluene

and a variety of other organic solvents, as well as chloroform; most analytical studies of the nanocrystals were completed using chloroform.

3.2.2.2. Improved synthesis methods

In the initial synthetic procedures, the lanthanide salt, $Ln(NO_3)_3$, was placed in the reaction flask with CdO, HDA, and TOPO. In this procedure, the reaction mixture was never able to completely dissolve because of the presence of the dopant material. In order to allow for complete dissolution of CdO procedures were modified, including subsequent injection of a lanthanide stock solution. The adapted procedures are as follows: the following reagents were placed in a three neck 50 mL round bottom flask, the necks of which had been fitted with water condensers (Figure 3): 10 mmol TOPO, 0.33 - 0.36 mmol CdO, and 0.80 mmol HDA or TDPA. Contents were placed under argon and heated to 300˚C. A terbium stock solution (0.04 - 0.07 mmol $Ln(NO_3)_3$) was injected once the reaction mixture reached 300˚C and the solution became clear (approximately 3 h). The reaction was left to stir for 1 h before a second stock solution containing selenium was added and the temperature was reduced to approximately 250˚C for the duration of growth (since the stock solution was at room temperature the reaction temperature immediately dropped and then stabilized over a period of minutes). Alternatively, for slower growth, the selenium stock solution was injected at 250˚C and nanocrystals were grown at 230˚C. Aliquots were removed at different synthetic times ranging from seconds to hours after injection using a glass syringe. For injection and growth at higher temperatures, growth times of 15 to 30 s were optimal, while at the lower temperatures, growth times of 30 s to 1 min were best to maximize terbium sensitization. Resulting products were stored as a raw solid until

photophysical analysis was performed, at which point they were purified and suspended in chloroform.

The CdSe:Ln samples have been primarily purified by precipitation with methanol and centrifugation followed by re-dissolution of the nanocrystals. However, this method leaves a large amount of unreacted starting material (HDA and TOPO) on the surface of the nanocrystals, which interferes with TEM imaging. Thus a more efficient and sophisticated purification procedure was used prior to TEM analysis. The nanocrystals were suspended in butanol and precipitated with methanol twice. To the precipitated nanocrystals a small amount of octanol was added; the nanocrystals remain soluble in the octanol, however, the excess of HDA precipitates out. The octanol solution is then transferred into a new vial, leaving behind the precipitate, and 1 - 2 mL of ethyl acetate (which allows the octanol and methanol to be miscible) are added followed by the addition of an excess of methanol. The solution was centrifuged and the decant was poured off. The precipitated nanocrystals were redissolved in chloroform.

3.2.3. Instrumental

Absorption spectra were recorded on a Perkin-Elmer Lambda 9 BX Spectrometer coupled with a personal computer using software supplied by Perkin-Elmer. Time-resolved and steady state luminescence spectra and excitation spectra were recorded with a Cary Eclipse coupled to a personal computer using software supplied by Varian or a modified Jobin-Yvon Spex Fluorolog-322 spectrofluorimeter. Chloroform-resistant well plates were machined out of high-density black polyethylene, which allowed for a quick analysis of the different samples of batches of nanocrystals with the well-plate adapter on the Cary Eclipse. This insured consistent

instrumental settings while studying the changes in photophysical properties with size (growth time) of a batch of nanocrystals.

Steady state luminescence quantum yields were measured using quinine sulfate (Φ = 0.546) solutions as the reference.[89] Emission spectra were collected using a JY Horiba Fluorolog-322 Spectrofluorimeter and spectra were corrected for the instrumental function. The quantum yields were calculated using Equation 3.2:

$$\Phi_x/\Phi_r = [A_r(\lambda_r)/A_x(\lambda_x)][I(\lambda_r)/I(\lambda_x)][\eta_x^2/\eta_r^2][D_x/D_r] \quad (3.2)$$

where subscript r stands for the reference and x for the sample; A is the absorbance at the excitation wavelength, I is the intensity of the excitation light at the same wavelength, η is the refractive index and D is the measured integrated luminescence intensity.

Time-resolved luminescence quantum yields were measured using Tb(H22IAM) reference solutions in methanol, which has a known quantum yield of 0.59.[6] Luminescence lifetime decays were collected for both the nanocrystals and the reference solutions with an excitation wavelength of 350 nm, along with time-resolved emission spectra. The time-resolved emission spectra were collected with a delay time of 0.1 ms using the SPEX phosphorimeter module of the Jobin-Yvon Spex Fluorolog-322. Exponential decays were integrated from 0 to 25 ms and from the delay time to 25 ms. The 25 ms value was chosen because it is a point long past any remaining luminescence for either Tb^{3+} complex. The differences in these two integrated values were used to determine the amount of luminescence intensity lost to the time-delayed measurement, using Equation 3.3:

$$I_0 = [I^* \times A_0] / A^* \quad (3.3)$$

where A^* is the area under the lifetime curve from the delay time to 25 ms, A_0 is the area from time zero, I^* is the integrated intensity measured after the delay, and I_0 is the calculated total intensity. Once the intensities have been calculated, the quantum yield of the sample can be calculated through Equation 3.4:[90]

$$\varphi_S = \varphi_{ref} [I_s/I_{ref}][A_s/A_{ref}][\eta_S/\eta_{ref}] \quad (3.4)$$

where φ_S and φ_{ref} are the quantum yields of the sample and reference respectively, I is the calculated intensity, A is the absorbance value, and η is the refractive index of the solvent.

Lanthanide luminescence lifetimes were measured using a Nd:YAG Continuum Powerlite 8010 laser (354 nm, third harmonic) as the excitation source. Emission was collected at a right angle to the excitation beam, and wavelengths were selected by a Spectral Products CM 110 1/8 meter monochromator. The signal was monitored by a Hamamatsu R316-02 photomultiplier tube for the NIR range, and was collected on a 500 MHz band pass digital oscilloscope (Tektronix TDS 754D). Alternatively, luminescence lifetimes in the visible range were measured using an Oriel 79110 Nitrogen laser (λ_{ex}: 337 nm) or the flash lamp of the JY Horiba, as the excitation source, and the emission signal was collected at a 90 degree angle with the JY Horiba Fluorolog detector. The signal was monitored with the same oscilloscope. Signals from >1000 flashes were collected and averaged. Luminescence decay curves were treated with Origin 7.0 software using exponential fitting models. Decay curves were fit with exponential models with increasing numbers of components, and the reduced chi-squared values were

monitored to determine the quality of the fit. The exponential model which produced the lowest chi-squared value was chosen as the best fit. Three decay curves were collected on each sample, and reported lifetimes are an average of at least two independent measurements. Luminescent lifetimes in the nanosecond regime were collected by Hongjun Yue in collaboration with the research group of Dr. Waldeck at the University of Pittsburgh using time correlated single photon counting (TCSPC) methods.

3.2.4. Transmission electron microscopy

Transmission electron microscopy (TEM) images were obtained using Ted Pella 300 mesh copper grids with 50 angstrom carbon coating as a solid support for low resolution measurements while measurements using high resolution transmission electron microscopy (HRTEM) were obtained on samples placed on Ted Pella 400 mesh Ultrathin Carbon coated copper grids. Purified nanocrystal solutions were either aerated or dropped onto the copper grids and the solvent was removed. Prepared grids were then washed with water and allowed to dry prior to analysis to further remove impurities that might be present.

Low resolution imaging was performed on a variety of instruments at different locations. Initial imaging was performed on an FEI Morgagni 268 TEM located in the University of Pittsburgh Biology Department Microscopy Center, Figure 3.3. This instrument operates at 80 kV and does not have sufficient resolution to record clear images of nanocrystals in the 2 – 10 nm diameter range, in which the CdSe:Ln fell. A JEOL 1210 TEM operating at 120 kV located in the University of Pittsburgh Center for Biological Imaging was also used, Figure 3.4; however the resolution was not sufficient to allow an assessment of the level of crystallinity of our samples. Additional low resolution TEM imaging was obtained at Carnegie Mellon University

using a Hitachi H-7100 TEM operating at 75 kV coupled to an AMT Advantage 10 CCD Camera System for capturing digital images, Figure 3.5. Finally, low resolution imaging was also performed through collaboration with the University of Pittsburgh, Department of Materials Science and Engineering, Figure 3.6. The instrument used was a JEOL 2000-FX Scanning Transmission Electron Microscope operated at a maximum of 200 kV, used to obtain initial images of particles to verify sample thickness. Sample TEM images collected with these four different instruments are shown below.

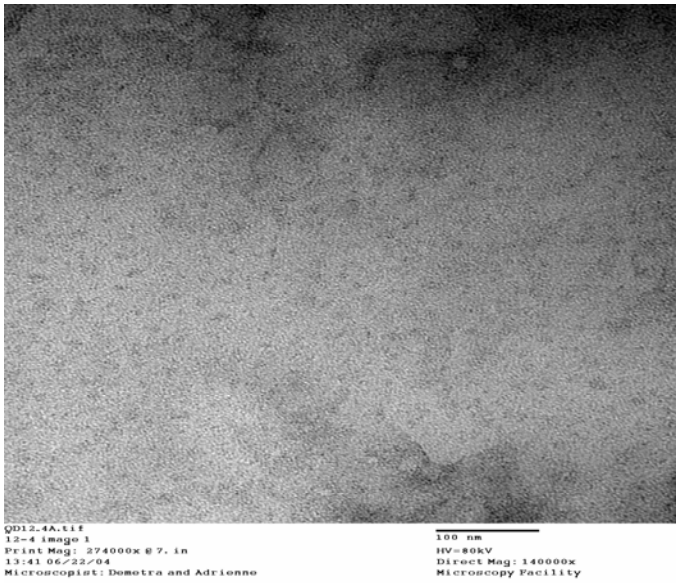

Figure 3.3. CdSe:Tb TEM image collected with the FEI Morgagni 268 TEM located in the University of Pittsburgh Biology Department Microscopy Center, scale bar represents 100 nm.

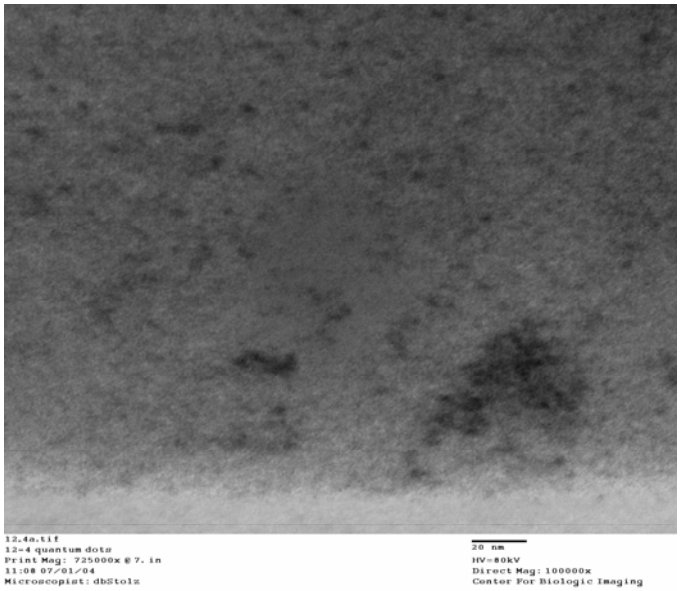

Figure 3.4. CdSe:Tb TEM image collected using the JEOL 1210 TEM operating at 120 kV located at the University of Pittsburgh Center for Biological Imaging, scale bar represents 20 nm.

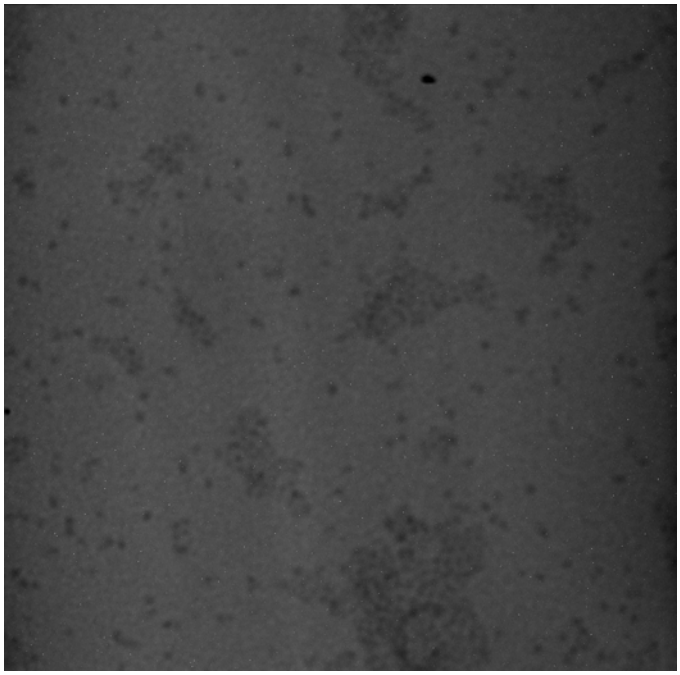

Figure 3.5. CdSe:TbEu TEM image obtained at Carnegie Mellon University using a Hitachi H-7100 TEM operating at 75 kV coupled to an AMT Advantage 10 CCD Camera System for capturing digital images.

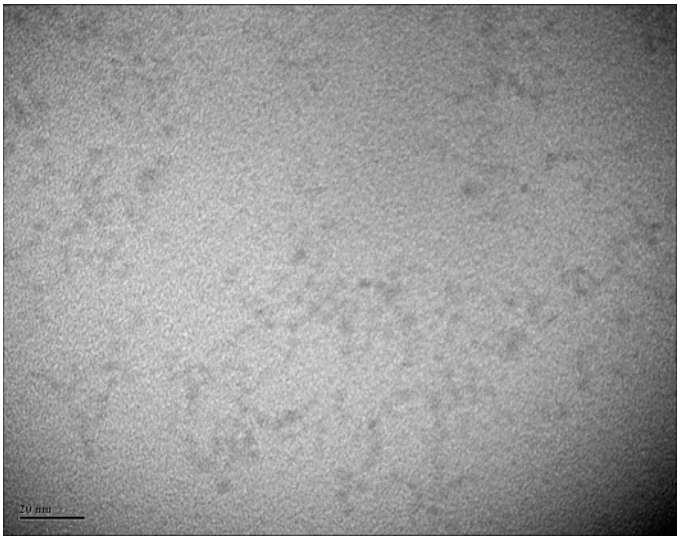

Figure 3.6. CdSe:Tb TEM image collected with the JEOL 2000-FX Scanning Transmission Electron Microscope operated at a maximum of 200 kV located at the University of Pittsburgh Department of Materials Science and Engineering, scale bar represents 20 nm.

High resolution TEM imaging was performed through collaboration with Dr. James McBride from Vanderbilt University. The measurements were performed at Oak Ridge National Laboratory using a VG Microscopes model HB603U STEM. The instrument operates at 300 kV and is fitted with a C_s corrector from Nion. Data collection occurs through a digital micrograph coupled to a personal computer.

3.2.5. Energy dispersive X-ray fluorescence spectroscopy

Energy dispersive X-ray fluorescence spectroscopy (EDXRF) was performed using three different instruments housed in the Engineering Department at the University of Pittsburgh. The first instrument was coupled to a Philips XL-30 field emission scanning electron microscope. Compositional information was obtained through attached energy dispersive X-ray spectroscopy detectors. This particular instrument set-up allowed for analysis of a larger spot size of a nanocrystal sample. The second instrument was coupled to the JEOL-2100 CF HRTEM, located

within the University of Pittsburgh Peterson Institute of NanoScience and Engineering (PINSE). This allowed for analysis of a more focused spot size to gain better information of the composition of individual nanocrystals rather than the overall sample. Energy dispersive X-ray spectroscopy measurements were obtained through the use of an Inca platform attachment from Oxford instruments. The third and final instrument was a Genesis 2000 from EDAX, Inc. The instrument was coupled to a Philips XL30 FEG SEM. This instrument was used for all reported CdSe:Ln compositional analysis.

3.2.6. Etching Experiments

3.2.6.1. Butylamine

Toluene and buytlamine were purchased from EMD and Spectrum Chemicals, respectively, and used without further purification. Lanthanide doped nanocrystals were synthesized following the improved synthesis method. The nanocrystals were purified in methanol and dispersed in toluene. A solution of 50% butylamine was prepared by mixing 10 mL of toluene with 10 mL of butylamine. Then 0.75 mL of each of the following nanocrystal samples were dispersed in pure toluene and in the 50:50 toluene:butylamine mix: CdSe:Sm, CdSe:Gd, and CdSe:Tb. UV-visible absorption spectra were recorded on a Perkin-Elmer Lamda 9 spectrometer, with 1 cm matched quartz cuvettes manufactured by NSG Precision Cells, Inc. The instrument was zeroed with two cells of toluene. Absorbance spectra of the nanocrystals dispersed in toluene and the 50:50 toluene:butylamine mix were collected after 30 min, 1 day, and 5 days. The initial and final sizes of the nanocrystals were determined based on the wavelength of the low energy peak in the absorbance spectra (see Section 3.3.1.2).[3,4]

3.2.6.2. Carbon Tetrachlroide

CdSe:Tb nanocrystals were synthesized according to improved synthetic methods. The nanocrystals were purified through precipitation in methanol and dispersed in carbon tetrachloride. The nanocrystal centered emission spectra were monitored in 1 cm quartz cuvettes over a period of two weeks with a Cary Eclipse fluorimeter.

3.3. RESULTS & DISCUSSION

CdSe:Ln nanocrystals have been synthesized with visible emitting Tb^{3+}, Eu^{3+}, Sm^{3+}, and Dy^{3+}, as well as Gd^{3+}, which is spectroscopically silent in the visible range, to serve as a control. The nanocrystals have been characterized physically and photophysically.

3.3.1. Physical Characterization

3.3.1.1. Nanocrystals from early synthetic procedures

The first attempt at obtaining TEM images was done with the raw samples dissolved in chloroform. Samples were prepared by placing a drop of solution on the grid and allowing the solvent to evaporate. The TEM in the University of Pittsburgh Biology Department Microscopy Center was used. The grids appeared highly disarrayed, which indicated that the nanocrystal solutions contained a lot of impurities. The nanocrystals were purified through centrifugation with methanol, dissolved in chloroform, and new samples were prepared. Upon examination under the microscope, these samples appeared to have lost most of the carbon coating off the grids, although in a few areas some blurry images were obtained. The loss of the carbon coating

may have been due to chloroform dissolving the surface, so the nanocrystals were transferred into hexane. There was less carbon degradation, but clear images were still not obtained. This TEM instrument was operated at 80 kV, which is a low resolving power compared those reported with most published TEM images of nanocrystals for which 200 or 300 kV voltage was typical.

Another attempt at obtaining TEM images of the CdSe:Tb nanocrystals was made using a JEOL 1210 TEM, which can operate at 120 kV, located in the Center for Biological Imaging at the University of Pittsburgh. The nanocrystals were used in their purified form, dissolved in chloroform. For sample preparation, the grids were dipped into a solution of the nanocrystals and allowed to dry. This time, it was possible to get images of the nanocrystals, although they were fairly blurry due to the limited resolution of the instrument. They did, however, give an indication of the size of the nanocrystals; samples collected at growth times of 15 and 120 s were both approximately of 2 nm in size. The monodispersity of the samples at this range was difficult to assess due to cloudiness of the image. While it was possible to see the nanocrystals, the edges were poorly defined, so it was difficult to determine exact sizes.

The third and most successful attempt at TEM was obtained in collaboration with Cole Van Ormer in the Materials Science and Engineering Department at the University of Pittsburgh. TEM images were obtained with a JEOL 2000-FX Scanning Transmission Electron Microscope. The TEM there operates at up to 200 kV, providing a much brighter and clearer image. The sample grids were prepared with purified nanocrystals dissolved in hexane. The nanocrystal solution was aspirated onto the grids with an atomizer, as follows: The grid was held by a pair of jewelers tweezers and then secured to a ring stand in the hood, with the darker side of the grid facing out to insure the solutions are put on the side with the carbon coating. The nanocrystal solution was put in a capillary tube, which was put into a holder at the top of an air canister, and

then sprayed onto the grid. This type of sample preparation was recommended by Van Ormer and tends to provide even distribution of the nanocrystals on the grid surface. The samples were allowed to dry for a few minutes and then examined under the microscope.

The nanocrystal sample collected after 120 s was the first to be examined and several difficulties were noted. First, severe darkening of the sample was occurring where the electron beam was hitting the sample, which was likely due to the migration of hydrocarbons present from the hexane solvent. In the direct path of the electron beam, the hydrocarbons will heat up, and start moving. Once they hit the edge of the beam the temperature decreases, thus causing them to cease migration. This led to dark circles that made it almost impossible to look for images of the nanocrystals. To address this problem, future samples were prepared several hours ahead and exposed to a halogen light to help evaporate off all the hexane. An additional problem was that microscope needed to be calibrated in order to achieve the desired magnification. With all of this considered, another grid was prepared with the nanocrystal sample collected at 15 s, and the microscope was calibrated. The acceleration voltage was 200 kV and the magnifications were up to 850,000X. Photographed images were obtained in TEM mode using a Gatan CCD camera and Gatan software. These results proved to be much more promising. The dark circles were still observed, but it was possible to work around them as they appeared more slowly in this case. The calibration allowed for going to higher magnifications, and it was possible to detect smaller dots on the surface. A TEM of an empty background section was taken for comparison. There was a definite difference between the blank area and the area containing the nanocrystal sample. While the nanocrystals did not produce extremely dark images, they were still clearly visible. They appeared to be comprised in a range of 2 - 4 nm in size, based on a size bar.

Unfortunately the imaging software used with this instrument did not have a point to point measurement tool, so precise measurements were not possible.

A TEM image of CdSe:Tb with 60 s growth times, also collected with Van Ormer, is shown in Figure 3.7.

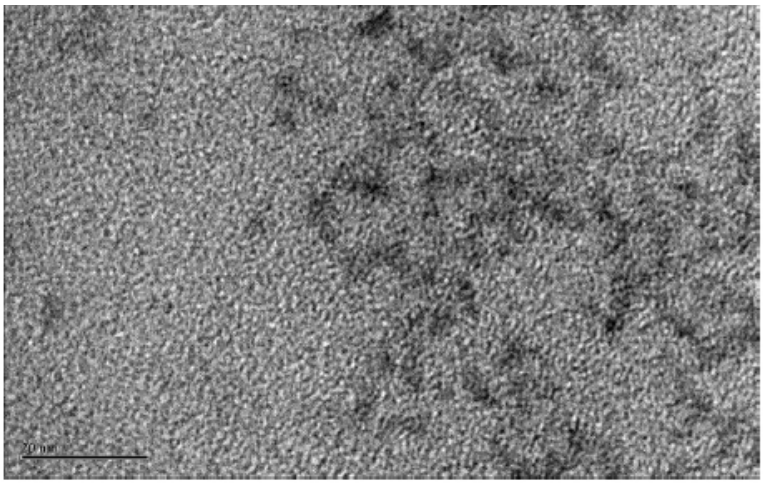

Figure 3.7. TEM image of CdSe:Tb nanocrystals (60 s growth time), taken at a magnification of 850X. The size bar represents 20 nm. Individual nanocrystals are approximately 2 - 3 nm in size.

An analysis of the size distribution revealed the nanocrystals range between 2 - 3 nm. The image does appear to be slightly blurry, which makes an exact determination of the size difficult. Most TEM images of CdSe nanocrystals appear slightly blurry, due to the large lattice structure (long spacings) and the small size of the nanocrystals. At this size range the orientation of the crystals in the electron beam becomes very important. If the Bragg angle is optimal, a clearer image, even one with visible crystalline structure, is possible. However, whenever the angle diverges, a much dimmer image results. In fact, it could be possible for the electron beam to pass through without resulting in an image. This phenomenon results from the proportionality of elastic versus

inelastic scattering that occurs when the electron beam passes through the sample. If the beam bounces off the sides of the nanocrystal or passes through the crystal spacing unperturbed, a much weaker signal results compared to when the electrons are absorbed by the nanocrystals.[84] Therefore, despite the fact that this TEM image may seem a little blurry it is actually quality data and provides substantial information.

The nanocrystal sample that is shown in Figure 3.7 was also analyzed with energy dispersive spectroscopy (EDXRF). The results from this analysis are shown in Figure 3.8, and provide proof that the nanocrystal samples contain Cd, Se, and Tb. The results shown here are qualitative due to the absence of calibration, and cannot be used to accurately determine the relative amounts of the three metals. Nonetheless, the presence of Tb in the nanocrystals confirms that the synthesis method used here successfully incorporated the lanthanide cations at either core or surface sites. Further experiments would be necessary to determine the actual location of the lanthanide cation within the CdSe:Tb crystal.

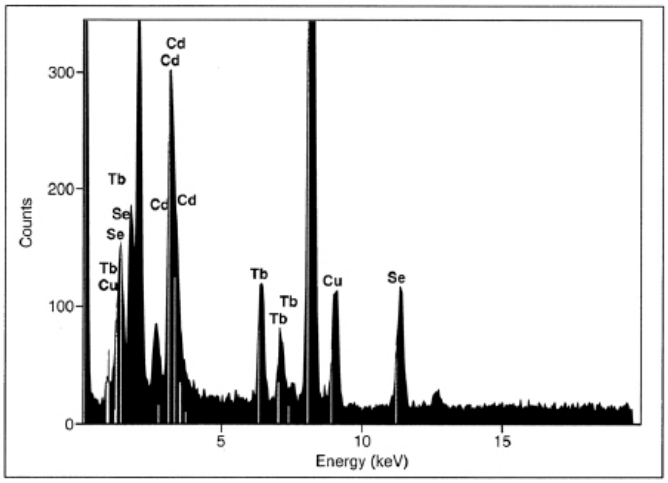

Figure 3.8. Results from a qualitative EDXRF experiment performed on the CdSe:Tb nanocrystal sample that was imaged in Figure 3.7.

3.3.1.2. Nanocrystals from improved synthetic route

Low resolution TEM imaging was used to confirm the synthesis of nanocrystals under the improved methods. A sample TEM image is shown in Figure 3.9; this image is of CdSe:Eu nanocrystals synthesized with 60 min growth time. These particles are approximately 5 nm in diameter. The larger size, which is expected for the longer growth time, enabled easier imaging of the nanocrystals. The aggregation seen here may be the result of drying effects upon grid preparation and is not representative of nanoparticle behavior in solution.

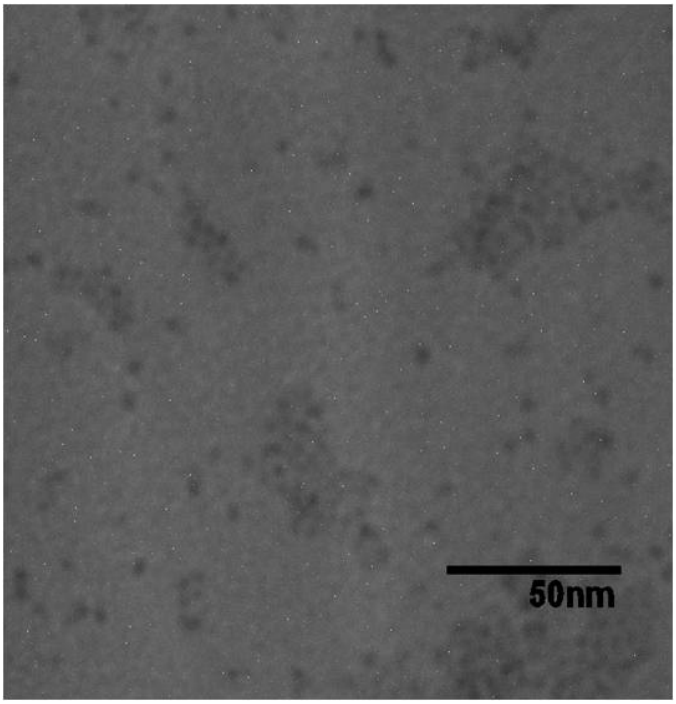

Figure 3.9. CdSe:Eu nanocrystals with 60 min growth time, obtained at Carnegie Mellon University using a Hitachi H-7100 TEM operating at 75 kV coupled to an AMT Advantage 10 CCD Camera System.

While low-resolution TEM imaging was able to confirm the synthesis of nanocrystals, high-resolution imaging enabled the crystallinity of the CdSe:Ln to be investigated. The high-resolution image of a CdSe:Tb nanocrystal is shown in Figure 3.10. This TEM imaging was

possible through collaboration with Dr. James McBride of the Rosenthal group at Vanderbilt University and Oak Ridge National Laboratory. This image was obtained only after extensive purification of the nanocrystals involving dissolution of particles in butanol, precipitation in methanol, dissolution in octanol, and further precipitation in methanol followed by dissolution in hexane for analysis. This high resolution TEM image clearly illustrates the crystallinity of the CdSe:Ln nanocrystals and also demonstrates that the nanocrystals are not present as aggregates in solution, but are rather individual discrete nanocrystals.

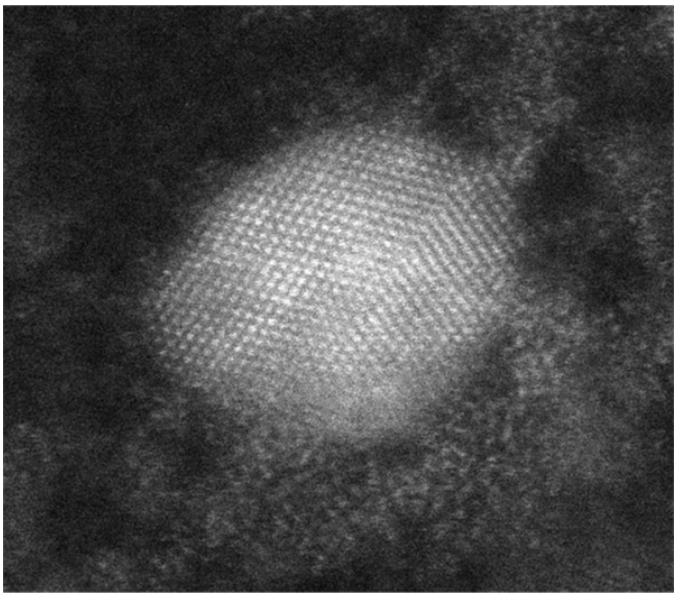

Figure 3.10. High resolution TEM image of a CdSe:Tb nanocrystal, obtained at facilities at Oak Ridge National Laboratory, through collaboration with Dr. McBride and Dr. Rosenthal at Vanderbilt University.

For CdSe:Ln synthesized under the improved procedure, a 15% lanthanide dopant concentration (relative to Cd content) was standard, and selenium was always used in ten-fold excess to the cation content. While these are ratios used during synthesis, the actual atomic composition of the nanocrystals is expected to vary from this. It is hypothesized that only a small

portion of the dopant lanthanide cations would be incorporated into the nanocrystal. Determining the actual composition of the nanocrystal samples is important for interpreting the results of photophysical analyses. CdSe:Tb, CdSe:Eu, and CdSe:TbEu were analyzed with EDXRF to determine their composition. The nanocrystal samples were purified with precipitation in methanol prior to analysis, in the same manner as prior to photophysical analyses. The same purification methods were used so that results of atomic composition would correlate with the photophysical studies.

The atomic composition of CdSe:Tb and CdSe:Eu nanocrystals have been investigated with energy dispersive X-ray fluorescence spectroscopy (EDXRF) measurements. Following purification via precipitation in methanol and redispersion in chloroform, samples were put on copper TEM grids for analysis; these results are listed in Table 3.1.

Table 3.1. Atomic composition of CdSe:Ln samples determined by EDXRF analysis.

	% Cd	% Se	% Ln
Tb-2-2	62 ± 4	26 ± 4	11 ± 5
Tb-12-2	45 ± 9	23 ± 7	32 ± 11
Tb-12-4	40 ± 6	19 ± 9	41 ± 11
Tb-12-6	59 ± 3	25 ± 5	16 ± 4
Eu-3-2	56 ± 5	30 ± 3	14 ± 3
Eu-6-2	45 ± 7	25 ± 7	30 ± 9
Eu-6-4	58 ± 5	31 ± 5	10 ± 2
TbEu-6-2	60 ± 2	21 ±1	19 ± 2

The results from both analyses differ significantly from what was expected. Since the syntheses are performed with an excess of Se, it was expected that the nanocrystals would contain slightly more than 50% Se, as the extra Se should form the final nanocrystal layer. Also, with 15% lanthanide content added during synthesis, the maximum lanthanide content was expected to be

7%, and cadmium content should be around 40 – 45%. In contrast, these results show about 20 – 30% selenium content. In addition, the lanthanide and cadmium content were higher than expected, and the relative amounts of each cation varied significantly between samples. The consistent large excess of cation content throughout multiple samples suggests that cadmium and lanthanide complexes (likely formed with TOPO or HDA) are coordinating to the nanocrystal surfaces. Given that TEM imaging experiments were complicated by excess organic layers, and required extra purification steps, it is not unreasonable to conclude that excess cations could also be coordinating to the nanocrystals. It is worth noting, however, that there does not appear to be any preferential binding between terbium or europium, indicating that both lanthanide cations are incorporated into the nanocrystal samples in the same manner. Unfortunately, these results are inconclusive for providing information on how much lanthanide cation is actually incorporated into the nanocrystals. It does, however, tend to indicate that there are significant amounts of lanthanide cations coordinating to the surfaces of the nanocrystals. These results illustrate that more extensive purification methods will be necessary to isolate the nanocrystals from excess reactants and resulting impurities, which could then be analyzed for atomic composition more accurately.

3.3.2. Photophysical Characterization

3.3.2.1. Nanocrystals from early synthetic procedures

Cadmium selenide nanocrystals incorporated with terbium have been synthesized, and energy transfer to terbium through the nanocrystal electronic structure has been demonstrated through emission and excitation spectra of these novel types of nanocrystals. When measurements were collected in steady state mode, only the overall broad emission arising from

the nanocrystal electronic structure was detected. When a time-resolved excitation spectrum was collected on the emission at 545 nm, the main band for Tb^{3+}, two maxima were detected. The first was located at 220 nm, which corresponds to an allowed d→f transition.[91] The second maxima at 284 nm correlated perfectly in shape and location to the excitation spectra for nanocrystal emission. Time-resolved emission spectra using both these wavelengths for excitation produced a characteristic terbium emission spectrum. The results of this luminescence analysis are illustrated in Figure 3.11. The ability to sensitize terbium emission through the nanocrystal electronic structure was crucial, as it provided proof of the concept that nanocrystals could serve as antennae for lanthanide cations and lays the foundation for future work in this area. As further indication that sensitization occurs through the lanthanide, the excitation spectrum of terbium in CdSe:Tb is compared to the excitation spectrum of terbium nitrate in Figure 3.12.

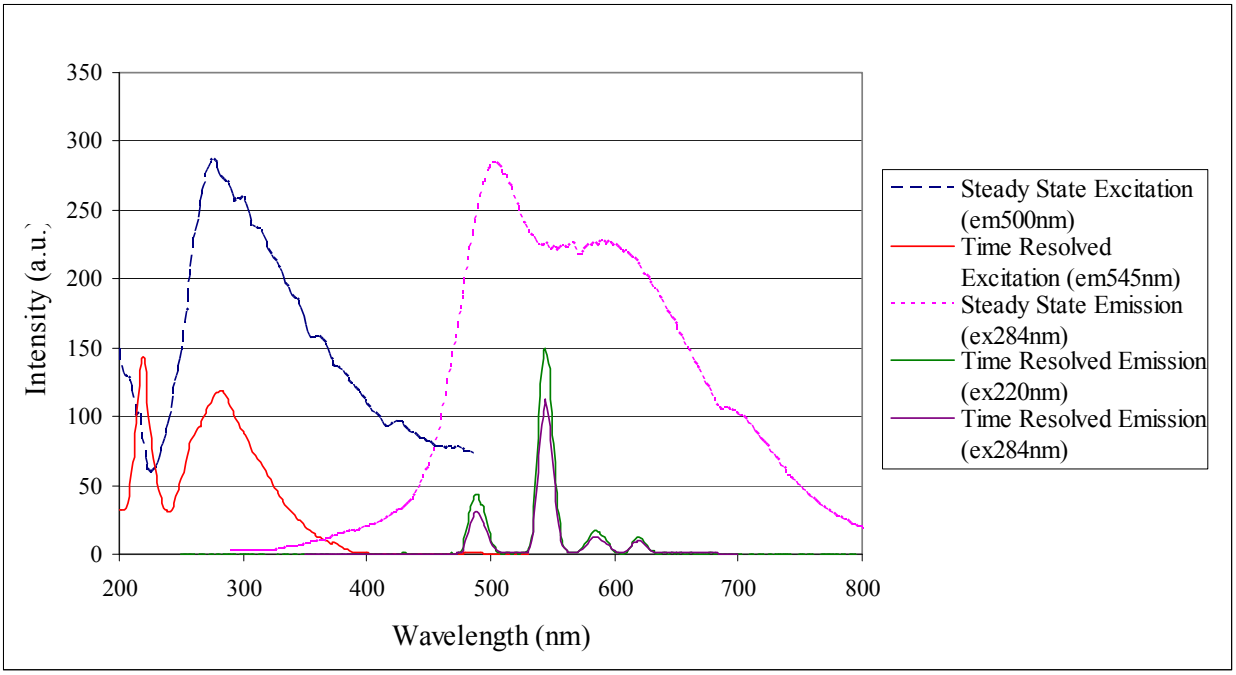

Figure 3.11. Steady state and time-resolved emission and excitation spectra for a sample of purified CdSe:Tb nanocrystals collected 15 s after injection, in chloroform. Terbium emission is discriminated from nanocrystal emission through time-resolved measurements.

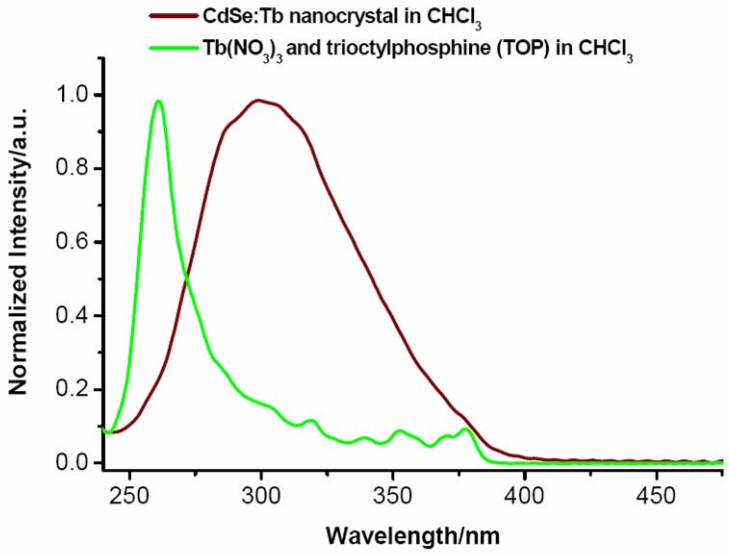

Figure 3.12. Excitation spectra of terbium centered emission at 545 nm for CdSe:Tb nanocrystals (brown) and terbium nitrate (green).

The size of the CdSe:Tb nanocrystals was controlled through the length of growth time during synthesis. The red-shift in absorption and emission energies of the nanocrystals with increasing size could be observed by the human eye, as shown in the photograph of a batch of nanocrystals taken under ambient and UV radiation, Figure 3.13.

Figure 3.13. Photographs taken of a series of aliquots from a batch of CdSe:Tb nanocrystals; samples are displayed left to right from shortest (15 s) to longest (3600 s) growth times. The top image is taken under visible light and shows the shift in absorbance, while the bottom image is illuminated with UV light, allowing the nanocrystal emission to be seen.

Collecting emission and excitation spectra of the different samples for a batch of nanocrystals allowed a relative comparison of emission wavelength versus growth time to be determined. The Cary Eclipse fluorimeter equipped with a plate-reader was helpful for this type of analysis, as it enabled a systematic comparison and rapid evaluation. It has been possible to monitor the respective position of the fluorescence maximum of the nanocrystals in relation to growth time through their emission spectra. In Figure 3.14 the steady state emission spectra for the different samples of a batch of CdSe:Tb nanocystals are shown, illustrating the shift to lower energies as

size increases for longer growth times. A graph of the wavelength of maximum emission versus the growth time is shown in Figure 3.15. The steady rate at which the emission maxima shift to lower energies with increased growth time confirms that the synthetic route provided control over the emission energy of the nanocrystals.

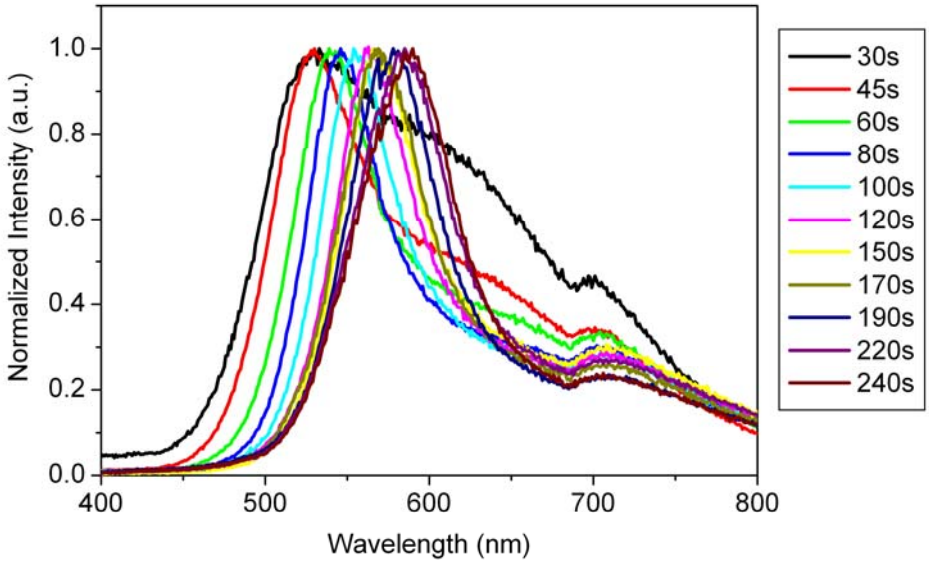

Figure 3.14. Normalized emission spectra of a batch of CdSe:Tb nanocrystals in chloroform; growth times indicated in the legend (λ_{ex}: 300 nm).

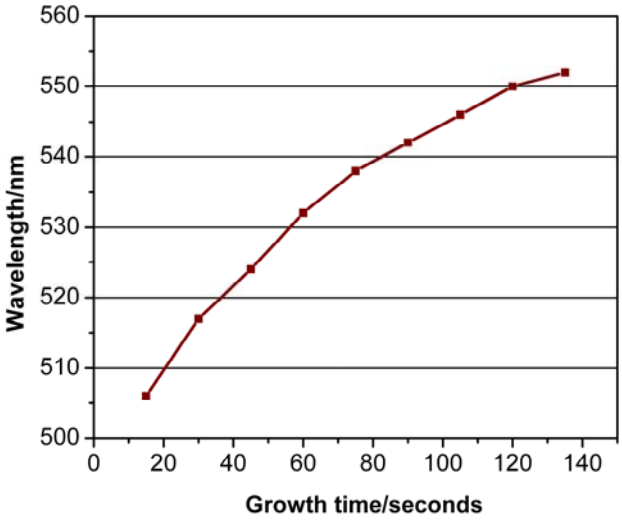

Figure 3.15. Emission wavelength maximum versus growth time for a batch of CdSe:Tb nanocrystals, demonstrating the control of size and emission color by synthesis.

Time-resolved emission spectra were also monitored, which allowed terbium emission to be discriminated from the nanocrystal emission. Therefore, with the same instrument and sample set up, it was possible to determine the relative extent of lanthanide sensitization for each different growth time / nanocrystal size. Using this screening method, the ideal growth times for producing the most intense terbium emission per a standard amount of sample were determined to be comprised between 15 and 60 s, with a maximum around 30 s, see Figure 3.16. Based on results from TEM measurements and absorbance spectra, this growth time correlates with nanocrystals that are about 2 nm in diameter and have emission energy maxima around 20,000 cm^{-1}. The lowest excited state of Tb^{3+}, the $^5D_4$ transition, is located at 20,545 cm^{-1}. The energies of the donating levels of the nanocrystal and the accepting level of Tb^{3+} are close in value. The nanocrystal sample contains a distribution of nanocrystal sizes, so it is possible that only the smaller nanocrystals in the sample, those possessing higher emissive energies (400-475 nm), are

actually sensitizing terbium. To obtain solutions of doped nanocrystals with ideal levels of Tb^{3+} sensitization, more narrow size distribution would be ideal.

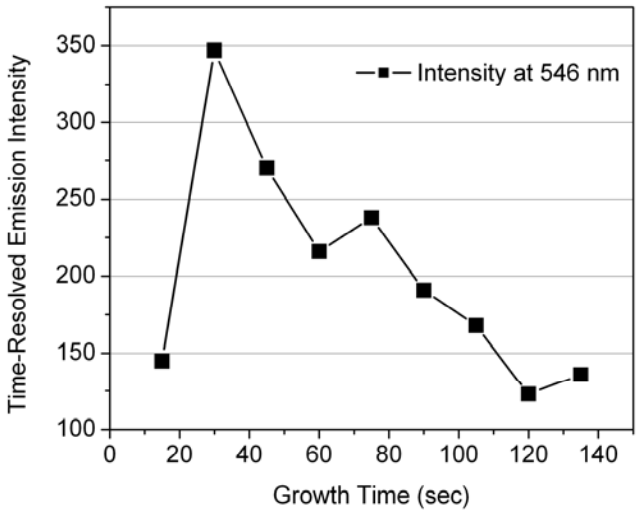

Figure 3.16. Intensity of terbium emission at 545 nm in time-resolved emission spectra collected on a batch of CdSe:Tb nanocrystals (chloroform, λ_{ex}: 285 nm) versus the growth time.

For a batch of CdSe:Tb nanocrystals that were prepared with 10% doping, HDA as the ligand, and synthesis temperatures of 250ºC and 230ºC, an interesting emission profile was observed. The steady state emission spectra of the samples with different growth times all displayed two maxima. There was a higher broader energy band located at 400 nm that was present for all samples. In addition, there was a lower energy band that shifted to higher wavelengths (450-600 nm) as growth time increased. As an example, the spectrum of nanocrystals with 300 s growth time is shown in Figure 3.17. The appearance of these two bands may be tentatively explained by the existence of two types of emissive energy states in the nanocrystals. The emission at 400 nm, which did not shift in energy with growth time, could be

due to surface trap energy states, which are independent of nanocrystal size. The maximum that shifts to lower energies is due to the quantum confined exciton energy states, which depend on the size of the nanocrystal.

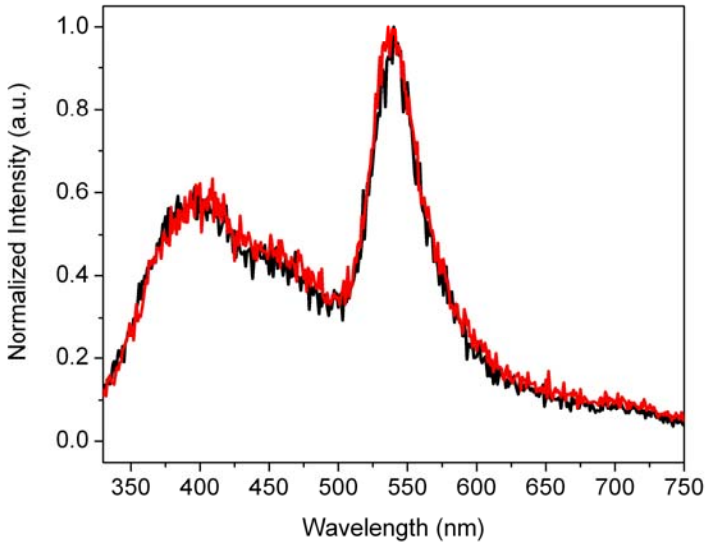

Figure 3.17. Steady state emission spectra of CdSe:Tb with 300 s growth time (chloroform, λ_{ex}: 300 nm), an example of the two emission bands produced by this batch of nanocrystals. (Spectra were collected with the plate reader adapter of the Cary Eclipse; spectra of the same sample were collected in two different cells to account for possible error with in this method).

For a more quantitative analysis of the nanocrystals the JY Horiba Fluorolog-322 spectrofluorimeter, which has a photon-counting detection unit, was used. It is equipped for both room temperature and low temperature measurements. Quantum yield measurements were performed with this instrument, which had also been fitted with a homemade quantum yield automatic sample holder and corresponding software to facilitate the ease and accuracy of these measurements. The quantum yield apparatus allowed for simple data collection, despite the different excitation wavelengths for the samples and the reference. The quantum yield measured

for the total nanocrystal emission of a sample of CdSe:Tb nanocrystals in chloroform (10% doping, HDA ligand, 250°C/230°C, 15 s growth time) at room temperature was 2.90% (+/- 0.25%). The measured quantum yield for the terbium emission of the same sample was roughly 0.02%. Low quantum yields are typical for uncoated nanocrystals, coating the CdSe nanocrystals with a thin layer of another semiconductor, such as ZnS, has been shown to increase quantum yields.[62]

The luminescence lifetimes of terbium were also measured, and are reported in Table 3.2. These lifetimes were collected using a xenon flash lamp excitation source, which has a 40 μs decay time, thus only the long lived terbium decay profiles, and not the shorter nanocrystal centered emission bands, could be discriminated from the lamp flash. Measured luminescence lifetimes of the terbium emission were in the range of 2-3 ms. The values monitored with direct excitation and excitation through the nanocrystal are within error of each other, indicating that the same cations are excited in both routes (as opposed to lanthanide cations at two different locations). The values are lower, however, for the purified sample than for the unpurified. This may indicate that the removal of some excess reactants from the surfaces of the nanocrystals allows closer contact of the lanthanide cations with solvent molecules, which would suggest the lanthanide cations are at or near the nanocrystal surface. Both sets of lifetime values are relatively long with respect to those reported in literature for terbium complexes formed with organic ligands, which indicates that good protection of the lanthanide cation. Luminescence lifetime values are often short due to deactivation through non-radiative transitions from OH, NH, and CH oscillators.[92,93] Since these types of oscillators are not present in the CdSe nanocrystals, longer lifetimes are possible.

Table 3.2. Luminescent lifetimes of terbium centered emission in CdSe:Tb nanocrystals with 15 – 30 s growth times; with and without purification, measured with both direct excitation (220 nm) of terbium and through the nanocrystal (285 nm).

	λ_{ex}: 220 nm	λ_{ex}: 285 nm
CdSe:Tb (purified)	2.4 ± 0.2 ms	2.3 ± 0.2 ms
CdSe:Tb (unpurified)	2.9 ± 0.2 ms	2.8 ± 0.2 ms

A month-long stability study was performed on the CdSe:Tb nanocrystals. A sample of nanocrystals was collected after 15 s of growth time, and half the sample was kept in its raw form and the other half of the sample was purified. Both the purified and raw samples were studied so that a comparison could be made between the two. In order to account for instrumental variations, standards were tested alongside the nanocrystals. A 10^{-5} M Tb(H22IAM)[6] solution in methanol was used as the standard for comparison for Tb^{3+} luminescence lifetime measurements and time-resolved excitation and emission measurements. A quinine sulfate solution was used for comparison with steady state emission measurements. For the study, measurements were taken every day for the first two weeks, then every other day for the remaining days of the month.

The stability study conducted on samples of both raw and pure nanocrystals did not provide consistent data, so results from this study are limited. However, the data collected throughout the study demonstrated qualitatively that the photophysical properties of the CdSe:Tb nanocrystals remained relatively unchanged over the course of one month. In this study, the nanocrystal samples were removed from their container, placed in a cuvette for measurements and then returned to their containers every day that measurements were made. During this process, solvent was lost to evaporation, which constantly modified the concentration of the samples. These factors led to variations in the emission intensities that rendered the data of measurements done over time to difficult to interpret. Emission intensities appeared to increase,

but this was likely due an increase in concentration rather than any stability effects. Over the course of the month-long study, there was never a loss of general nanocrystal or terbium emission, which does confirm the stability, although it cannot be quantified. Luminescence lifetime values are independent of concentration, so these measurements have been unaffected by the loss of solvent. However, the results for this study were also inconclusive, as the data collected for the reference produced sporadic values, see Figure 3.18 for a graphical representation of the results.

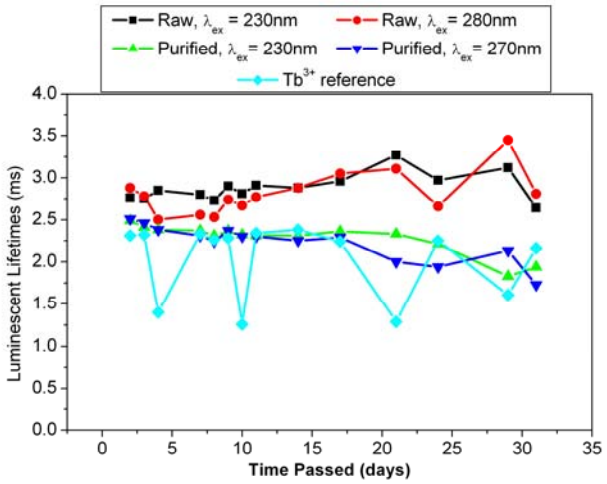

Figure 3.18. Terbium luminescence lifetimes measured through out the stability study, results from raw and pure samples excited directly, through the allowed d-f transition at 230 nm and through the electronic states of the nanocrystals at 270/280 nm; compared to the those for the Tb^{3+} reference.

The luminescence lifetimes for the nanocrystals did appear to remain fairly constant, but the reference values did not, jumping between values of ~2.2 and ~1.4 ms, so any drawn conclusions cannot be verified at this time. Disregarding the inconsistency in the reference measurements, the results verify the raw nanocrystals have longer lifetimes than the purified ones, and indicate that

the raw CdSe:Tb samples maintain the same terbium luminescent lifetimes for a longer time. The protective coating provided by TOPO on the nanocrystals may have been partially removed during purification, which possibly led to a slightly lowering of the stability over time.

3.3.2.2. Nanocrystals synthesized with improved procedures

As demonstrated by the nanocrystal spectra shown in Figure 3.11, Figure 3.14, and Figure 3.17 the nanocrystal centered emission bands from CdSe:Tb made with the early synthetic procedures were not narrow and contained significant amounts of signals from impurities such as surface trap states. In addition, the differences in lifetimes between raw and purified samples suggested lanthanide cations were located at the nanocrystal surfaces rather than totally encapsulated within the nanocrystal. Finally, syntheses according to the methods described in Section 3.2.2.1 frequently produced undesired black side products rather than luminescent nanocrystals. For these reasons, the synthetic method was altered as described in Section 3.2.2.2. This synthetic procedure produced nanocrystals with narrow band gap emission bands and longer terbium centered lifetimes. Using the same method, a total of six different CdSe:Ln systems were synthesized and studied, with the goal of using the CdSe band gap as an antenna for the four visible emitting trivalent lanthanide: Eu, Tb, Sm and Dy. The materials include: CdSe:Tb, CdSe:Eu, CdSe:Dy, CdSe:Sm, CdSe:Gd, and doubly doped CdSe:Tb,Eu. CdSe:Gd nanocrystals serve as a control for the study of the photophysical properties of these doped systems because Gd^{3+} is a spectroscopically silent species. The photophysical data obtained for Gd^{3+} doped materials resemble undoped CdSe nanocrystals.

For all the CdSe:Ln nanocrystals, the absorption bands consistently exhibit red shifts with increasing growth time, regardless of the lanthanide dopant added, corresponding to increase in

nanocrystal size. Absorbance spectra representative of the overall CdSe:Ln samples are shown in Figure 3.19. The UV-Vis absorption spectra exhibit the characteristic shift in wavelength as the nanocrystal growth time and size increase. As the particle size increases, the absorbance shifts to lower energy and corresponds to quantum confinement effects within CdSe particles.[73,87,94-96] The broad absorption of these particles is an attractive feature because it allows for excitation at a broad range of wavelengths.

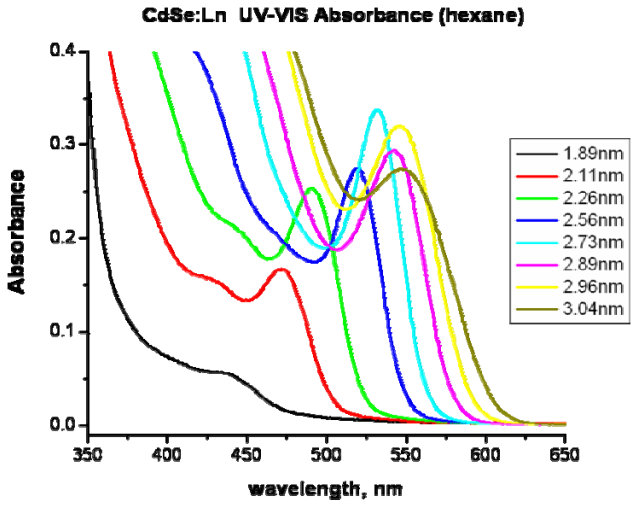

Figure 3.19. UV-visible absorption spectra of CdSe:Eu nanocrystals of the same batch with different growth times, illustrating the shift in band position with nanocrystal size.

The size of the nanocrystals can be determined based on the position of the lower energy absorbance band, using calculations based on the work of Peng et al. and Alivisatos et al.[97,98]. The nanocrystal diameter (D) can be determined using the wavelength of the first absorption peak and Equation 3.5.[99]

$$D(nm) = (1.6122 \times 10^{-9})\lambda^4 - (2.6575 \times 10^{-6})\lambda^3 + (1.6242 \times 10^{-3})\lambda^2 - (0.4277)\lambda + (41.57) \quad (3.5)$$

The extinction coefficient (ε) can be determined using the absorbance of this band with Equation 3.6 or the empirical formula in Equation 3.7.[99]

$$\varepsilon = 1600\ \Delta E\ D^3 \quad (3.6)$$

$$\varepsilon = 5857\ D^{2.65} \quad (3.7)$$

Once ε and D are known, the molecular weight (M_n) can be determined with the formula in Equation 3.8.[100]

$$M_n = \pi/6\ NA\ \delta\ \sigma^3 \quad (3.8)$$

Using these formulas and the absorbance spectra, the diameters were calculated for CdSe:Ln nanocrystals. Data for two batches of nanocrystals grown at 250°C and 230°C are shown in Table 3.3 and Table 3.4, respectively. In both cases these data show how the nanocrystals rapidly increase in size in the first minute of growth time, and then grow more slowly. Also, it can be seen that nanocrystals grown at 250 °C grow faster than at 230°C.

Table 3.3. Growth time and calculated size for a batch of CdSe:Tb nanocrystals grown at 250°C.

Growth Time (s)	Diameter (nm)
10	1.97
20	2.35
30	2.55
45	2.71
210	3.75
300	4.17
600	4.41

Table 3.4. Growth time and calculated size for a batch of CdSe:Eu nanocrystals grown at 230°C.

Growth Time (s)	Diameter (nm)
15	2.15
30	2.39
45	2.55
60	2.67
120	2.89
240	3.26
360	3.46
600	3.60
1200	3.66
3600	3.89

Nanocrystals produced through the early synthetic methods have broad emission bands, indicative of polydisperse nanocrystal samples, and multiple bands resulting from impurities and trap states. Through the optimization of the synthetic procedures, the broad nanocrystal emission bands have been replaced by more narrow bands with less background signal, indicating improved dispersity and better quality nanocrystals. The emission spectra for a batch of CdSe:Eu nanocrystals are shown in Figure 3.20 as an example. These steady state emission spectra are specific to CdSe nanocrystals and show that the introduction of lanthanide dopant ions does not affect the general luminescence properties of the semiconductor nanocrystals.

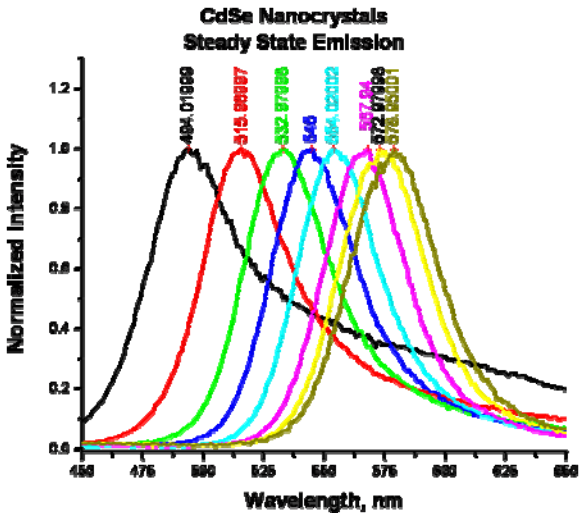

Figure 3.20. Fluorescence spectra of a batch of CdSe:Eu nanocrystals illustrating the red shift in emission maxima with nanoparticle size.

A plot of the nanocrystal size verses the wavelength of maximum emission intensity (Figure 3.21) reveals a linear relationship between size and emission energy, consistent with quantum confinement effects.

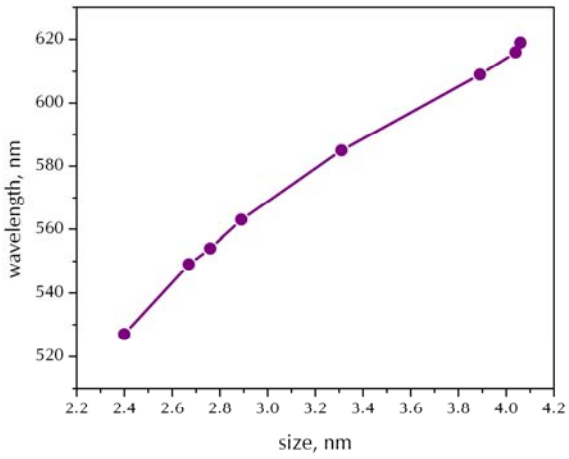

Figure 3.21. Graph of wavelength of maximum emission intensity versus nanocrystal diameter for CdSe:Eu.

Under the improved synthetic conditions, the ideal growth time for CdSe:Tb was short, around 15 s. The steady state and time-resolved emission and excitation spectra for CdSe:Tb are shown in Figure 3.22. The nanocrystal emission is centered around 500 nm, and the excitation profile of the nanocrystal has a maximum around 280 nm. The typical terbium emission spectrum is revealed upon time-resolved measurement, and the time-resolved excitation spectrum shows a maximum at 280 nm also, confirming sensitization through the antenna effect. It can be seen that the terbium excitation profile is narrower than the nanocrystal profile. This suggests that only the smallest nanoparticles in the sample are sensitizing terbium, and that terbium can only be sensitized in the range where it has direct excitation bands. Since the direct excitation bands correspond to accepting energy levels, it is logical that terbium can not be efficiently excited at higher wavelengths.

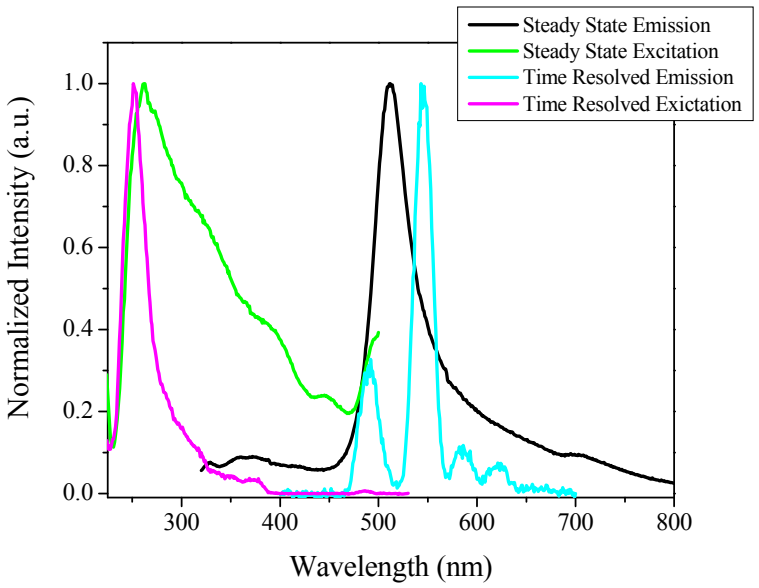

Figure 3.22. Steady state and time-resolved emission and excitation profiles for CdSe:Tb nanocrystals made with optimized synthetic procedures, growth time: 15 s.

As observed for CdSe:Tb nanocrystals, the steady-state emission spectrum of CdSe:Eu nanocrystals upon excitation at 300 nm indicates mainly the presence of an emission band with an apparent maximum located at 500 nm that can be attributed to the band gap transition of CdSe. In order to observe the Eu^{3+} luminescence, time-resolved measurements were employed. The steady state and time-resolved measurements are shown in Figure 3.23. The comparison of the steady state and time-resolved excitation spectra of the CdSe:Eu nanocrystals indicates that the electronic structure of CdSe can provide an antenna effect to sensitize Eu^{3+}. Lanthanide emission is obtained through energy transfer from the nanocrystal band gap, which is evident based on the overall shape and position of the steady state and time-resolved excitation spectra. For comparison, the direct excitation spectrum of europium nitrate is included in the inset, which is notably different from the europium excitation spectrum in CdSe:Eu.

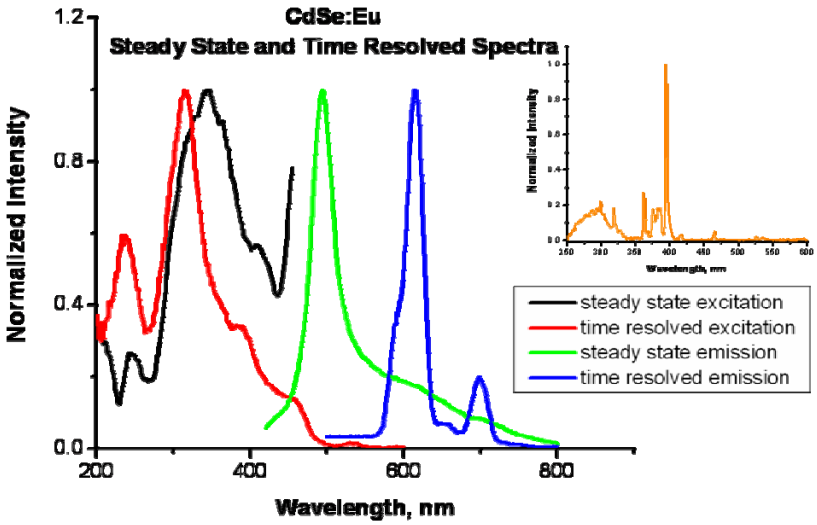

Figure 3.23. Steady state emission and excitation spectra (green, λ_{ex}: 330 nm and black, λ_{em}: 500 nm, respectively) and time-resolved emission and excitation spectra (blue, λ_{ex}: 330 nm and red, λ_{em}: 614 nm, respectively) for CdSe:Eu in chloroform. The inset shows the direct excitation spectrum of europium emission at 614 nm for europium nitrate solution in chloroform.

Compared to CdSe:Tb, there is more overlap between the nanocrystal and lanthanide excitation profiles. The accepting levels of the Eu^{3+} are lower in energy than Tb^{3+} and are better matched with the band gap emission, thus resulting in improved sensitization.

Doping procedures were carried out in the same fashion for Dy^{3+} and Sm^{3+} as for Tb^{3+} and Eu^{3+}, and nanocrystals of corresponding growth times were analyzed and found to yield similar trends in emission spectra with an observed bathochromic shift in emission with increased particle size. Spectra were collected for CdSe:Dy nanocrystals and are shown in Figure 3.24. The dysprosium emission signal was not detected in steady state measurements, as was the case for CdSe:Tb and CdSe:Eu. Even under time-resolved mode, the dysprosium signal was difficult to detect. Only under certain instrumental conditions was the signal arising from dysprosium detected. Unlike what was observed for the Eu^{3+} and Tb^{3+} nanocrystals, the corresponding emission bands did not appear as well defined narrow bands, but instead appear as shoulders in these spectra, the other component arising from the band gap emission of the nanocrystal. As discussed in detail later in this section, there is a relatively long lived component in the nanocrystal emission decay profile. For terbium and europium, the lanthanide lifetimes are still much longer than the nanocrystal, and this allows them to be easily separated with time gated techniques. On the other hand, the dysprosium lifetime is shorter, and falls into a similar range as the nanocrystal long lived component. Since these two emitters have similar luminescent lifetimes, it is not possible to fully isolate the emission profile of Dy^{3+} from the nanocrystal.

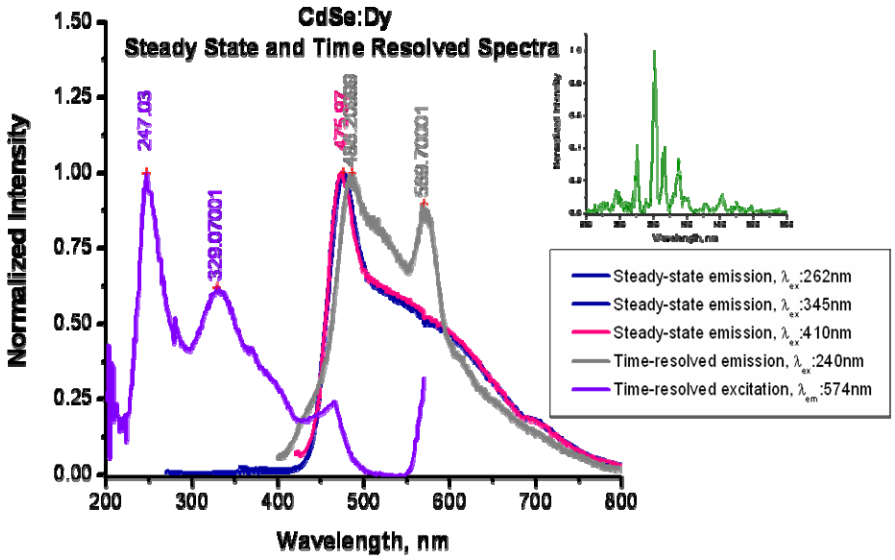

Figure 3.24. Normalized luminescence spectra of CdSe:Dy nanocrystals in hexane. Measurements were collected with a Varian Cary Eclipse using 1 mm cuvettes. Maximum slit widths (20 nm) were used to obtain the lanthanide signal. Delay time: 0.20 ms, decay time: 0.020 s, scan rate: slow (0.25 nm intervals with an averaging time of 0.5 s), PMT voltage: High (800 V), flashes: 1. The inset shows the direct excitation spectrum of dysprosium emission at 570 nm for dysprosium nitrate solution in chloroform.

The results for CdSe:Sm are similar to CdSe:Dy, as seen in Figure 3.25. While Sm^{3+} and Dy^{3+} are sensitized to some extent as supported by these experimental data, the signal is difficult to discriminate from nanocrystal signal. Due to this, it is not possible to isolate an excitation profile for Sm^{3+} or Dy^{3+}, which would be necessary to interpret whether or not antenna effect sensitization is possible.

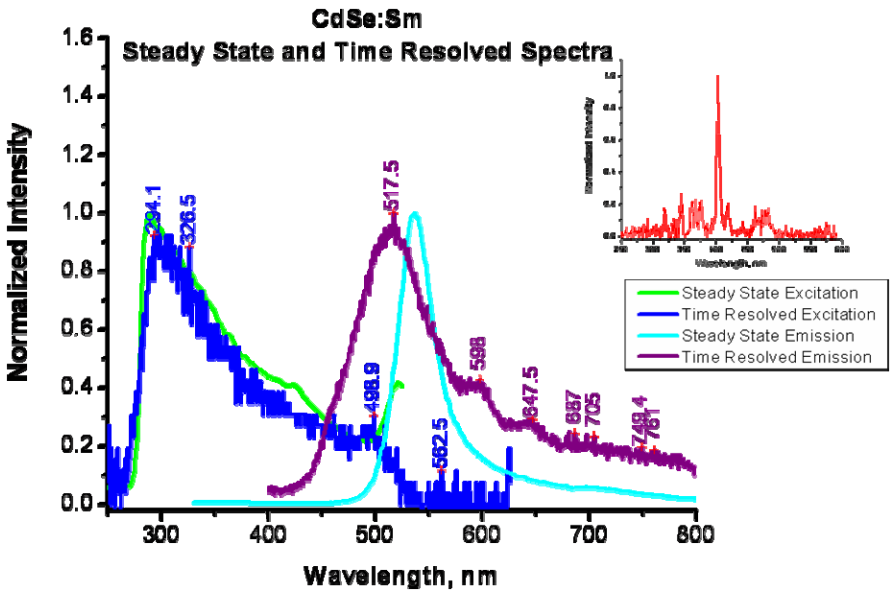

Figure 3.25. Normalized luminescence spectra of CdSe:Sm nanocrystals in hexane. Measurements were collected using a Varian Cary Eclipse in time-resolved mode, with 1 mm cuvettes. Maximum slit widths (20 nm) were used to obtain the lanthanide signal. Delay time: 0.10 ms, decay time: 0.020 s, scan rate: slow (0.5 nm intervals with an averaging time of 0.2 s), PMT voltage: High (800 V), flashes: 5. The inset shows the direct excitation spectrum of samarium emission at 645 nm for samarium nitrate solution in chloroform.

CdSe:Gd nanocrystals were synthesized for comparison with the visible emitting lanthanide doped CdSe nanocrystals. The steady-state emission and excitation spectra of the nanocrystals were collected using the Cary Eclipse Flourimeter with the well-plate adapter and custom made black high molecular weight polyethylene well plates. The steady state emission spectra of the samples with an excitation wavelength of 300 nm are shown in Figure 3.26.

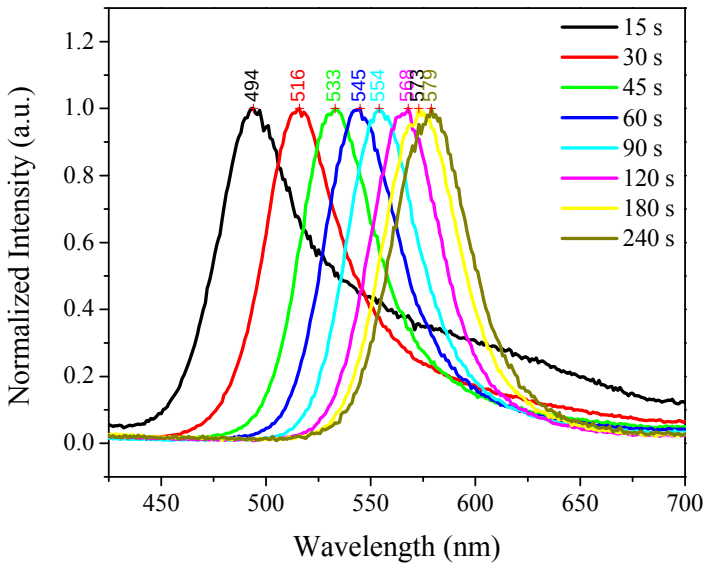

Figure 3.26. Emission spectra of a batch of CdSe:Gd nanocrystals, λ_{ex}: 300 nm.

The nanocrystals showed the expected color shift, from yellow to orange to red with increasing growth time. The emission bands are narrow, with half-height band widths of approximately 50 nm, as expected for the improved synthetic conditions. However, the first sample, with a 15 second growth time, displayed a wider emission band, with a long tail. This is a result which has been observed in other batches of nanocrystals as well. It is likely that as the nanocrystals first begin to grow there are more defect sites. As nanocrystals grow, they also anneal which causes these trap sites to contribute less to the emission spectra.

In addition to CdSe doped with one lanthanide cation, CdSe nanocrystals with both terbium and europium dopants were synthesized. In this synthesis, each lanthanide cation was included at 8% doping, for a total lanthanide content of 16% relative to cadmium. The emission spectra for a CdSe:TbEu sample with 15 s growth time are shown in Figure 3.27.

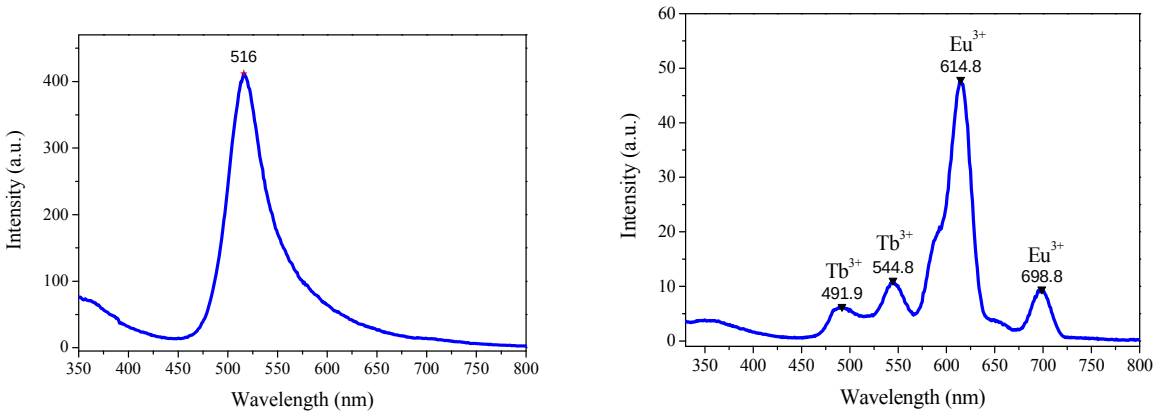

Figure 3.27. Left: Steady state spectrum of CdSe:TbEu nanocrystal showing the nanocrystal centered emission. Right: Time-resolved spectrum of the same sample, showing the terbium and europium emission profiles.

In steady state mode, the nanocrystal centered emission is detected, centered at 516 nm. In time-resolved mode, the emission profiles of terbium and europium are seen. The europium signal is more intense than the terbium signal. Since the EDXRF data indicated there was no preference for one lanthanide over the other, these results suggest that europium is sensitized better. In addition, it is also possible to have terbium to europium energy transfer in solid state materials, since europium has a lower energy accepting level than terbium's emitting level. This could also cause a decrease in the terbium emission intensity relative to europium. The excitation spectra in steady state and time-resolved mode are shown in Figure 3.28. The spectra for terbium centered excitation are shown on the left. The direct excitation spectrum of terbium, collected on terbium nitrate is included for comparison. As seen, the terbium excitation profile in CdSe:Tb resembles the steady state excitation profile of nanocrystal band gap centered emission rather than the direct excitation profile, indicating successful antenna effect sensitization. A similar trend is seen for europium on the right. In both cases, the lanthanide excitation spectrum shows that the best

excitation ranges are where overlap between the lanthanide accepting states and nanocrystal excitation bands occur. These results confirm that multiple lanthanide cations can be incorporated into CdSe nanocrystals and sensitized via the antenna effect at the same wavelength. Such materials could be of interest for the future development of barcoded tags.

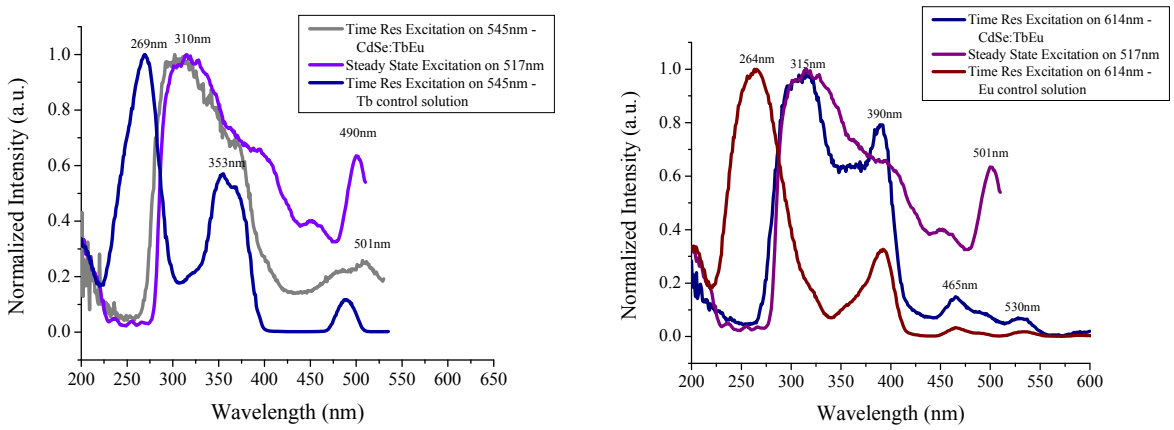

Figure 3.28. Steady state excitation profile of nanocrystal centered emission and time-resolved excitation profiles of lanthanide centered emission for CdSe:TbEu and lanthanide nitrate controls (toluene); Left: terbium centered excitation, Right: europium centered excitation.

To elucidate how the donating nanocrystal emission bands overlap with the lanthanide accepting levels, a series of energy level diagrams overlaid with matrices representing emission maxima of the nanocrystals were made. This series of analysis was performed to support the results with terbium and europium dopants, as well as provide a basis to predict the sensitization of future lanthanide dopants. As the nanocrystals grow in size, their emission is shifted to lower energies. This shift in energy allows for potential tuning of the band gap emission to match the accepting levels of various lanthanide cations. In the case of smaller nanocrystals emitting around 500 nm, which was determined to be ideal for terbium sensitization, Figure 3.29, the

band gap emission is located at suitable energy to transfer to Tb^{3+} and Eu^{3+}, as well as Sm^{3+} and potentially Er^{3+}, Ho^{3+}, Nd^{3+}, and Pr^{3+}. Energy transfer to Tb^{3+}, Eu^{3+} and Sm^{3+} were observed to varying degrees, and studies on CdSe:Tb confirmed maximum terbium emission intensities from smaller CdSe nanocrystals.

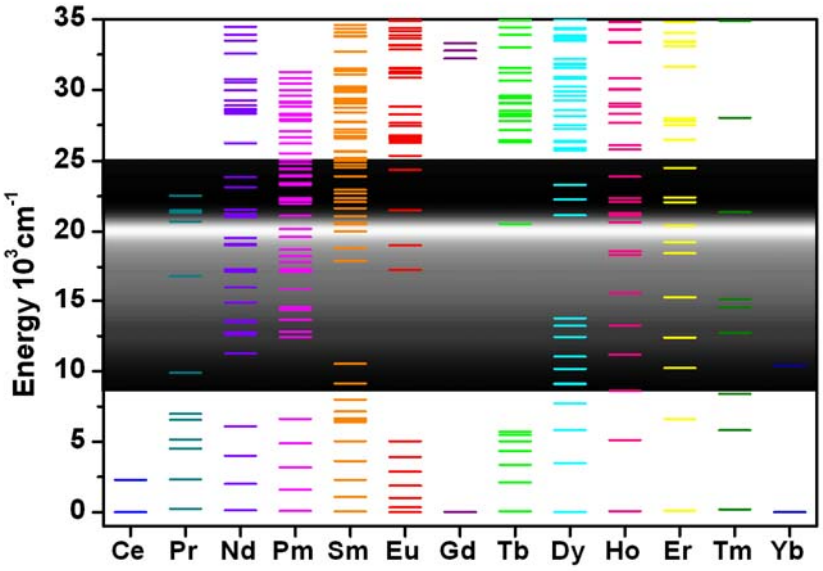

Figure 3.29. Energy level diagram for Ln^{3+} overlaid with the nanocrystal centered emission band; the dark region is a matrix representing the fluorescence obtained upon excitation of the nanocrystal band gap (λ_{ex} = 350 nm) and the white region represents the emission maximum of 500 nm.

As the nanocrystal band gap emission is shifted further, it is expected that Tb^{3+} will no longer be sensitized by the band gap of the material. This is evident for the energy diagrams representing emission at 515 nm and longer, Figure 3.30. The emission band is now below the accepting levels of the Tb^{3+}. The experimental results agree with this model; time-resolved excitation spectra of terbium centered emission from larger nanocrystals (with emission maxima above 515 nm) display direct excitation bands rather than excitation bands which overlap with nanocrystal

band gap excitation profiles. Nanocrystals with sizes corresponding to approximately 540 nm emission and longer wavelengths are no longer efficient for Eu^{3+} sensitization. Experimental results also confirm this, larger nanocrystals with longer growth times exhibit excitation profiles with more direct excitation character than smaller nanocrystals.

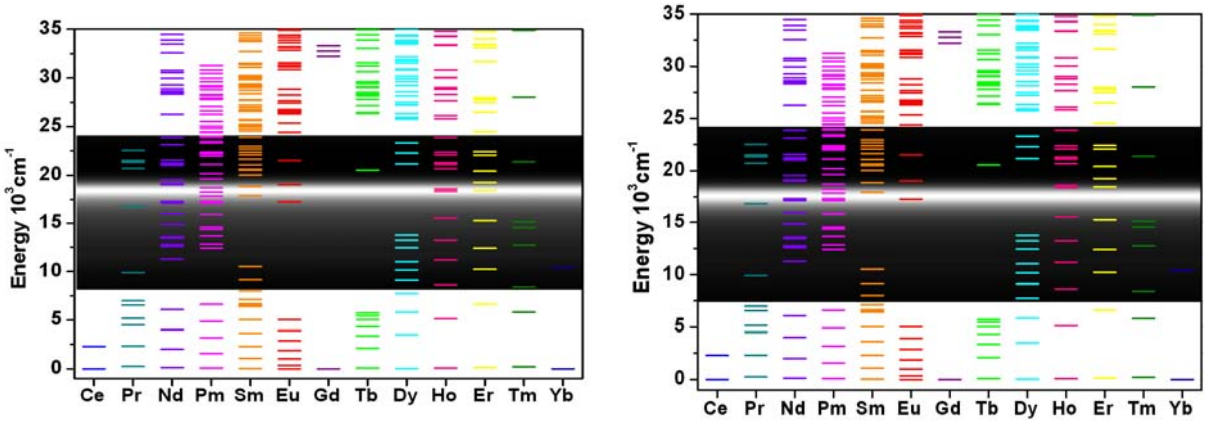

Figure 3.30. Energy level diagram for Ln^{3+} overlaid with the nanocrystal centered emission band; the dark region is a matrix representing the fluorescence obtained upon excitation of the nanocrystal band gap (λ_{ex} = 350 nm) and the white region represents the emission maximum of 515 nm (left) or 540 nm (right).

While Sm^{3+} and Dy^{3+} are sensitized to some extent, as supported by the data presented for small CdSe nanocrystals, the lanthanide signals can not be fully discriminated from the nanocrystal signals due to their similar luminescence lifetime components. Predictions using this hypothesis should lead to sensitization of several other lanthanides based on band gap emission wavelengths. In theory, it should be possible to sensitize Er^{3+}, Ho^{3+}, Nd^{3+}, and Pr^{3+}. Initial studies on some of the NIR emitting lanthanides yielded no detectable lanthanide emission signals, however, time-resolved measurements are not possible in the NIR range. Thus, the lack

of lanthanide signal may be the result of inability to distinguish it from the nanocrystal emission signals, which have tails into the NIR range.

The luminescence lifetimes of CdSe:Tb, CdSe:Eu, CdSe:TbEu CdSe:Gd, CdSe:Dy, and CdSe:Sm were measured and analyzed. Decay profiles of both lanthanide centered and nanocrystal band gap centered emission were collected and analyzed. For these decay curves, two to three component exponential models were used to fit best the experimental data (depending on the time window analyzed). Overall lifetime values were determined through the comparison of chi squared values for multiple exponential decay fittings, lower chi squared values indicating a better fit of the experimental data. The CdSe:Gd nanocrystal lifetimes were used as the control for the other nanocrystals; CdSe:Gd lifetimes are attributed to the nanocrystals themselves, as Gd is spectroscopically silent and therefore does not emit. The longest lifetimes measured for CdSe:Gd nanocrystals were approximately 50 μs; thus lifetimes above this range could be conclusively assigned as originating from lanthanides. For terbium and europium centered decay profiles, two components were found to be longer than CdSe:Gd lifetimes, and these were assigned to the lanthanide cations. CdSe:Dy and CdSe:Sm were more difficult in their analysis because their decay profiles has components similar to the nanocrystal centered bands in CdSe:Gd. The luminescence lifetimes attributed to the lanthanide cations are illustrated and described in detail below.

Luminescent lifetimes measured on nanocrystal centered emission bands for a variety of different samples are shown in Table 3.5. This is a small sample of the many lifetimes that were measured. As can be seen, the lifetime components varied extensively between samples, and ranged from the nanosecond to microsecond time scale. No errors are included because it was not possible to calculate average lifetimes given the range of different lifetime values detected.

Table 3.5. Luminescent lifetimes of nanocrystal centered bands on a variety of CdSe:Ln samples, λ_{ex}: 354 nm or 330 nm, chloroform solutions.

Sample ID	t_1	t_2	t_3
Tb-1-1	8.28 μs	40.8 μs	-
Tb-1-1	0.084 ns	1.73 ns	12.8 ns
Tb-12-1	4.7 μs	16.2 μs	-
Tb-1-2	0.103 ns	1.71 ns	13.4 ns
Tb-12-2	5.2 μs	23.9 μs	-
Tb-12-3	4.3 μs	12.6 μs	-
Tb-12-5	5.0 μs	24.2 μs	-
Eu-16-1	5.3 μs	23 μs	-
Eu-4-2	6.34 ns	50.3 ns	204 ns
Eu-4-3	6.25 ns	46.5 ns	169 ns
Eu-15-6	0.627 ns	10.1 ns	61.5 ns
Eu-16-2	4.7 μs	16.2 μs	-
Eu-15-9	2.18 ns	15.4 ns	69.9 ns
Eu-16-3	5.3 μs	24.1 μs	-
Dy-1-1	8.46 μs	55.4 μs	-
Dy-1-2	7.47 μs	36.5 μs	-
Dy-1-3	7.40 μs	36.2 μs	-
Dy-1-7	6.93 μs	33.4 μs	-
Sm-1-2	7.67 μs	38.7 μs	-
Gd-1-1	8.51 μs	46.7 μs	-
Gd-1-2	8.33 μs	46.7 μs	-
Gd-1-3	2.49 ns	17.8 ns	76.9 ns
Gd-1-4	7.58 μs	40 μs	-
Gd-1-6	7.74 μs	40 μs	-
Gd-1-7	7.53 μs	36.7 μs	-

The multiple lifetime components are attributed to the nature of ensemble measurements. Bawendi et al. studied the luminescent lifetimes of single Quantum Dots, and found that the lifetime of a single Quantum Dot fluctuates with time, and this fluctuation correlated with the blinking nature of Quantum Dot emission.[101] Since our instrumental set up only allows for ensemble measurements, which will be a mixture of all the different emitting states of the nanocrystals, it is not possible to accurately determine the lifetimes of the Quantum Dot emission bands. Rather, these data can only provide a basis to discriminate the lanthanide signals from the

nanocrystal signals. If the instrumentation to perform single nanocrystal lifetime analysis becomes available in the future, these experiments may provide a route to study which nanocrystal states donate energy to sensitize the lanthanide cations.

The lanthanide centered luminescent lifetimes of CdSe:Ln are reported in Table 3.6. Fittings of the lanthanide decay profiles produced two components that could be assigned to lanthanide luminescence, indicating the presence of two lanthanide environments within these systems. It is hypothesized that the longest lifetime components results from lanthanide cations residing at internal sites within the crystal structure protected from solvent vibrations, while the shorter component results from surface bound lanthanide cations. In all cases, the longer lifetime contributed less to the overall decay profile than the shorter components. These results correlate with the elemental analysis data that suggested that a large amount of lanthanide cations were coordinating to the surface of the nanocrystals, embedded in TOPO and HDA coatings.

Table 3.6. Luminescent lifetimes of lanthanide centered emission in CdSe:Ln in chloroform or hexane, λ_{ex}: 354 nm.

	$\lambda_{emission}$	t_1	t_2
CdSe:Tb	545 nm	2.3 ± 0.2 ms	5.0 ± 0.4 ms
CdSe:Eu	614 nm	0.66 ± 0.02 ms	2.4 ± 0.2 ms
CdSe:TbEu	545 nm	1.07 ± 0.04 ms	2.99 ± 0.04 ms
CdSe:TbEu	614 nm	0.81 ± 0.05 ms	2.60 ± 0.01 ms
CdSe:Dy	574 nm	100 ± 12 μs	-
CdSe:Sm	644 nm	60 ± 3 μs	-

CdSe:Tb nanocrystals exhibited two lifetime components which could be assigned to terbium centered luminescence. The longest component was 5.0 ms, which is significantly longer for terbium, and likely correlates to cations that are in the nanocrystal matrix and well protected from solvent vibrations. A lifetime component of 2.3 ms for terbium was also measured. This is

the same lifetime that was measured for CdSe:Tb synthesized under early synthetic procedures. This lifetime probablly correlates with terbium ions on the surface of the nanocrystal. The presence of a second, longer luminescence lifetime component for terbium synthesized under the new methods suggests that this synthetic procedure incorporates the terbium cations better than the early procedure. Well protected lanthanide complexes in solution found in the literature have reported lifetime values of 1.3 ms,[102] significantly shorter than reported here, further illustrating the superior protection of lanthanide cations within the nanocrystal structure. Even the shorter lifetime reported here is relatively long in comparison to terbium lifetimes reported for molecular complexes.[6] Since terbium cations on the surface of the nanocrystals are likely in a TOPO/HDA matrix, and measurements were performed in chloroform which is not a highly quenching solvent, this relatively long lifetime is reasonable.

CdSe:Eu also exhibits a biexponential decay with a longer component of 2.4 ms, most likely resulting from lanthanide cations embedded in the core of the nanocrystal structure and a slightly shorter component of 0.66 ms corresponding to surface bound lanthanide cations. These values are shorter than the lifetimes measured for terbium because europium has a shorter natural radiative lifetime. However, the lifetimes are significantly longer (more than twice the value) than other europium lifetimes reported in the literature for lanthanide complexes in solution.[102] The level of protection of the lanthanides and subsequent assignment of location within the nanocrystal is based on comparison of lifetime values to values typically observed for Eu^{3+} (2 to 3 ms)[16].

For CdSe:Tb,Eu nanocrystals, both terbium and europium centered lifetimes were measured. For these nanocrystals, the lifetimes were measured as a potential method to determine if terbium to europium energy transfer was occurring. Since europium has a shorter

lifetime than terbium, if europium lifetimes were measured that were on the range of terbium lifetimes, this would indicate the presence of energy transfer. Also, if terbium donates energy to europium, it may display shorter luminescent lifetimes. As seen by the results in Table 3.6, the europium lifetimes are within in the same time scale as CdSe:Eu nanocrystals. On the other hand, the terbium lifetimes are both quenched, which indicates that terbium is donating energy to some accepting level, which is most likely europium since this cation has accepting levels at the appropriate energy. While these lifetime results are not completely conclusive because europium lifetimes do not appear to be increased, this is strongly indicative of energy transfer from terbium to europium.

In addition to CdSe:Tb and CdSe:Eu, CdSe:Dy and CdSe:Sm lifetimes were collected. For both of these nanocrystals, only one lifetime component over 50 μs was detected. Lifetimes of 100 μs for dysprosium and 60 μs for samarium are assigned to lanthanide cations within the nanocrystals, as these lifetimes are relatively long for these lanthanide cations. It is likely that a second lifetime component is present in the nanocrystals corresponding to lanthanide cations on the surface; however, since these lifetimes fall into the same range as lifetimes measured for nanocrystal centered emission, it is not possible to determine these. These findings correlated with the difficulty to spectroscopically separate the lanthanide and nanocrystal emission bands through time resolution for these nanocrystals due to the long lived electronic states of semiconductor nanocrystals.

Quantum yield values were measured for Tb^{3+} and Eu^{3+} doped CdSe nanocrystals in toluene, the values are reported in Table 3.7.

Table 3.7. Lanthanide centered luminescence quantum yields (Φ_{Ln}) for CdSe:Ln nanocrystals, purified and dispersed in toluene; λ_{ex}: 330 nm.

	Φ_{Ln}
CdSe:Tb	1.5 (±0.1) x 10^{-5}
CdSe:Eu	4 (± 2) x 10^{-5}
CdSe:TbEu	2.8 (±0.5) x 10^{-5}

While the quantum yields observed for CdSe:Tb, CdSe:Eu, and CdSe:Tb nanocrystals are significantly lower than values obtained for lanthanide complexes in solution (63% for Tb^{3+} and 2.3 % for Eu^{3+}),[102] these values are compensated by the formation of polymetallic species. Multiple lanthanide cations incorporated within the crystal structure result in enhanced emission intensity despite low quantum yield values. The quantum yield for europium luminescence is larger than for terbium, which is consistent with improved sensitization for this lanthanide.

Lanthanide centered quantum yield data could not be obtained for Dy^{3+} or Sm^{3+} due to instrumental limitations (see above). While emission has been observed for both systems, the methods used to obtain emission does not allow for quantification of the efficiency of these two lanthanide systems. Spectra for both Dy^{3+} and Sm^{3+} could only be observed using the Varian Cary Eclipse fluorimeter, which has higher sensitivity for time-resolved measurements than the JY Horiba Fluorolog. Correction functions for detector sensitivity have not been established for this instrument, thus quantitative meausrements were not possible.

3.3.3. Etching Experiments

It has been determined that small nanocrystals with higher energy emission bands are optimal for sensitization of terbium and europium cations. Since the nanocrystals grow rapidly in the first few s of synthesis, it is difficult to isolate nanocrystals smaller than approximately 2 nm. However, nanocrystals that are smaller than 2 nm with higher energy emission states may lead to

improved lanthanide sensitization. Therefore, etching has been explored as a potential method to obtain smaller nanocrystals post-synthetically.

El-Sayed et. al[103] reported the use of butylamine in high concentrations (0.1-0.25 M) to etch small CdSe nanocrystals. They report that the addition of butylamine to small CdSe nanocrystals (under 1.6 nm) led to a distinct shift in the low energy absorbance band to 414 nm; however no change was observed for larger nanocrystals. Temperature studies indicated the interaction between butylamine and the nanocrystals was exothermic. The authors suggest that the small CdSe nanocrystals may be undergoing a transformation to zinc blende structure, or, alternatively, are etched until a "magic size" with a thermodynamically stable structure is reached. No TEM measurements were done to elucidate these results. This method was adapted to the CdSe:Ln nanocrystals and studied as a route to obtain both smaller and more monodisperse nanocrystals, with potentially improved lanthanide sensitization. Several lanthanide doped CdSe nanocrystals with short growth times were treated with butylamine and size changes were monitored through UV-visible absorption spectroscopy.

As can be seen in the spectra shown in Figure 3.31, all samples displayed a slow blue shift upon exposure to butylamine over 5 days. For the CdSe:Gd and CdSe:Tb nanocrystals, the low energy absorbance band remained visible over the entire experiment length; however, for CdSe:Sm, the band was no longer visible after days. Also, by the fifth day the low energy band was much less defined than in the original absorbance spectrum for CdSe:Tb. The loss of this defined low energy maximum in the absorbance spectra suggest that the nanocrystals may have begun to dissociate or lose crystallinity.

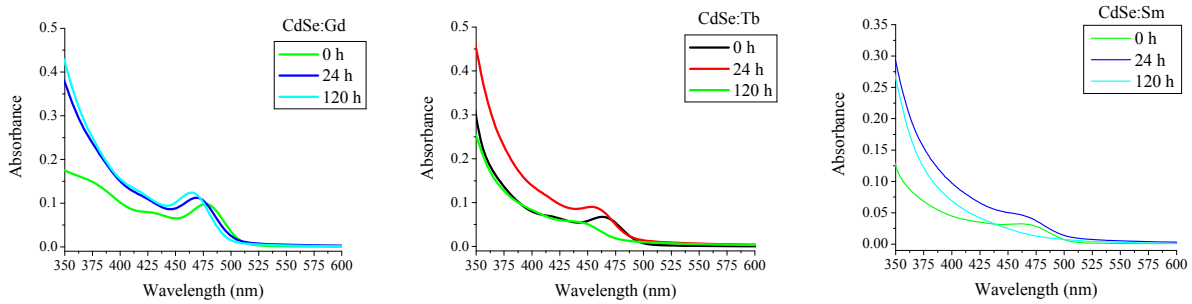

Figure 3.31. UV-visible absorbance spectra of CdSe:Gd (left), CdSe:Tb (center), and CdSe:Sm (right) monitored during butylamine etching experiments.

Table 3.8. Results of butylamine etching on CdSe:Ln nanocrystals after exposure for 24 and 120 h.

Sample	Absorbance (nm)			Diameter (nm)		
	0 h	24 h	120 h	0 h	24 h	120 h
CdSe:Gd	477	469	464	2.15	2.09	2.05
CdSe:Tb	462	454	439	2.04	1.98	1.87
CdSe:Sm	465	462	gone	2.06	2.04	n/a

Using the previously described methods, the diameters of the nanocrystals were calculated using the low energy absorbance maxima, these results are tabulated in Table 3.8. Based on these calculations, the nanocrystals have undergone some etching of approximately 0.1 – 0.2 nm, or 5 – 8% diameter loss. Under these experimental conditions, CdSe:Ln exposure to butylamine led to slight etching; however, there was no development of a "magic" size nanocrystal with thermodynamically favorable structure, nor a peak at 414 nm. It is possible that the nanocrystals were too large at the onset of etching for the necessary chemical effects to occur. It could also be possible that the lanthanide cations disrupt the crystal structure enough that the "magic" size (and corresponding 414 nm absorbance) is no longer stable, limiting the potential for butylamine to etch in this case. Since the changes in size were relatively minor, and did not result in

nanocrystals that were any smaller than could be obtained synthetically, no further studies were performed.

Exposure to carbon tetrachloride was studies as an alternative route to etch CdSe:Ln nanocrystals. The ability of carbon tetrachloride (CCl_4) to etch the nanocrystals was discovered when CdSe:Tb nanocrystals were dispersed in this solvent for lifetime measurements. It was of interest to determine if removing the C-H vibrational mode of the solvent affected the shorter lanthanide lifetime component. It was observed that the nanocrystal solution went from yellow to colorless over the course of a few days. Photoluminescence studies on this sample confirmed the disappearance of the nanocrystal centered luminescence. To further understand the interaction between the nanocrystals and CCl_4, a sample of CdSe:Tb was purified and dispersed in this solvent, and the luminescence was monitored over two weeks. The nanocrystal band gap emission band was monitored to determine if the carbon tetrachloride slowly etched the nanocrystal, which would cause a blue shift in the emission maximum, or if the solvent caused a rapid decomposition of the nanocrystals, which would cause a steady decrease in emission intensity. The emission spectra are shown in Figure 3.32.

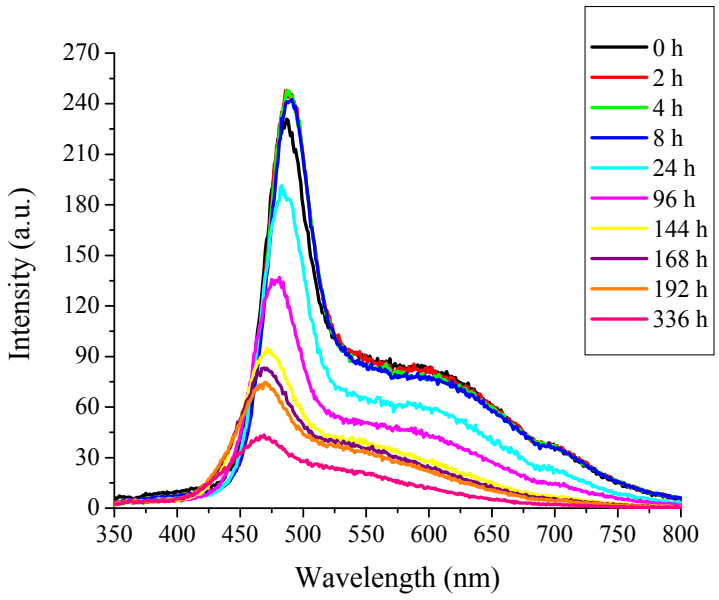

Figure 3.32. Fluorescence spectra (steady-state mode, λ_{ex}: 330 nm) of nanocrystal band gap emission from CdSe:Tb in carbon tetrachloride collected over the course of two weeks to monitor etching.

Initially, for the first several hours, exposure to CCl_4 caused no change in the wavelength or intensity of the emission maximum. However, after 24 h, a steady decrease and red shift in the emission maximum was detected. These results suggest that the carbon tetrachloride first dissolves the organic coating on the nanocrystals, and during this process the band gap emission is unaffected. Once the organic coating of the nanocrystal is gone, the nanocrystal begins to slowly dissociate, accompanied by both a red shift and loss in emission intensity. Since the precipitation methods normally used to isolate CdSe nanocrystals (i.e., addition of methanol) are based on the solubility of the organic coating, it was not possible to isolate the nanocrystals once etching took place. Thus, etching continued until the nanocrystals were dissolved, and studying the effect of size on lanthanide sensitization was not possible. Given that carbon tetrachloride is

an environmental hazard, combined with the difficulty to control the extent of etching, other methods should be explored in the future to obtain smaller nanocrystals.

3.4. CONCLUSIONS

CdSe:Ln nanocrystals have been synthesized with terbium, europium, samarium, dysprosium, and gadolinium dopants, as well as with terbium and europium co-dopants. The synthetic conditions have been improved to yield nanocrystals with narrower size distribution, increased crystallinity, and improved lanthanide incorporation. The photophysical investigation of these nanocrystals demonstrates antenna effect sensitization of both terbium and europium. Long lanthanide centered luminescence lifetimes indicated doping within the nanocrystal as well as surface incorporation [statistical distribution over a sphere]. These results confirm the hypothesis that lanthanide incorporation within the nanocrystal will provide effective shielding from non-radiative deactivation through solvent vibrational modes, while also providing sensitization via the antenna effect. The nanocrystals have been characterized physically, including high resolution TEM which demonstrated crystallinity. The atomic composition of the CdSe:Ln showed higher than expected levels of cadmium and lanthanide, suggesting the presence of coordination complexes of these cations in the TOPO/HDA organic surface matrix. Small nanocrystal sizes (< 2 nm) have been determined to be optimal for terbium and europium sensitization..

The CdSe:Ln nanocrystal systems synthesized and studied here offer several advantages over luminescent semiconductor nanocrystals or molecular lanthanide complexes for

applications in solution. These include the formation of polymetallic species to overcome limitations of lower quantum yields of molecular lanthanide complexes. Despite the low efficiency of energy transfer in these systems, the emission intensity is enhanced by the incorporation of a large number of lanthanide cations within the nanocrystal and the high absorptivities. These materials exhibit emission spanning the visible spectrum as well as broad absorbance bands allowing for excitation in suitable ranges for bioanalytical applications. In addition, by tuning the band gap energy within the nanocrystals, we can hope to better match the energy with the excited states of the Ln^{3+} for more efficient energy transfer.

While a number of different lanthanide doped CdSe nanocrystals systems have been synthesized and characterized for their photophysical properties, we have yet to determine the exact location of the lanthanides within the crystal structure (surface sites vs. internal sites, interstitial doping vs. substitution), which would increase our level of understanding of these compounds based on their structures. Electron energy loss spectroscopy (EELS) and superconducting quantum interference devices (SQUID) could both provide information regarding the lanthanide locations in these systems. Also, further studies should be conducted on nanocrystals which have been more extensively purified to remove the excess organic coating and coordinating cadmium and lanthanide complexes. This will allow better quantification of dopant concentrations, and more precise photophysical studies on incorporated lanthanide cations. In addition, alternative routes to control nanocrystal size so that smaller nanocrystals can be obtained should be targeted.

4. INCORPORATING LANTHANIDE CATIONS INTO $NaYF_4$ NANOPARTICLES

Part of the work presented here has been completed in collaboration with Jian Zhang, Chad Shade, and Hyounso Uh (Stéphane Petoud Research Group, Department of Chemistry, University of Pittsburgh). A portion of the results presented here have been published in *The Journal of the American Chemical Society*, Vol. 129, No. 48, p 14834, 2007: "A Strategy to Protect and Sensitize Near-Infrared Luminescent Nd^{3+} and Yb^{3+}: Organic Tropolonate Ligands for the Sensitization of Ln^{3+}-Doped NaYF4 Nanocrystals."[24]

4.1. INTRODUCTION

4.1.1. $NaYF_4$:Yb,Er Upconverting Nanocrystals as Energy Acceptors & Donors

Luminescence resulting from upconversion, when a species absorbs photons of energy then emits them at a higher energy wavelength, is an unusual and valuable property that can be obtained with some lanthanide cation combinations when incorporated into certain inorganic materials. Both Yb:Er and Yb:Tm are lanthanide cation combinations known to produce upconversion via Yb^{3+} NIR absorption followed by energy transfer to Er^{3+} or Tm^{3+}, which then emit in the visible range. Upconverting materials are of particular interest for harvesting sunlight for solar energy use, as well as for use in spectroscopic methods. For spectroscopic methods,

upconverting materials are useful because they offer high signal to noise ratios and, therefore, good sensitivity detection. Materials must be specifically designed to be capable of energy upconversion, so there is very small likelihood of detecting a signal from anything except the sample, avoiding risks of false positives and decreasing fluorescence background. This feature would be especially beneficial for biological detection methods, where autofluorescence often limits detection sensitivity. Also, UV light, which is commonly used to excite current biological fluorescence labels, can damage or destroy DNA, cells, proteins, and other biological samples; thus the use of NIR light for excitation would be highly advantageous.

As a tool for the harvesting of solar energy, upconverting materials are highly useful because they offer a route to absorb low energy NIR photons hitting the earth's atmosphere and convert them into useful energy corresponding to visible range photons. The earth's atmosphere acts as a filter, altering the solar spectrum of sunlight, which results in significant reductions in both the UV and IR ranges. Nevertheless, as illustrated in Figure 4.1, a large quantity of NIR irradiance hits the earth's surface and is a vast potential source of energy that is not currently utilized.[104]

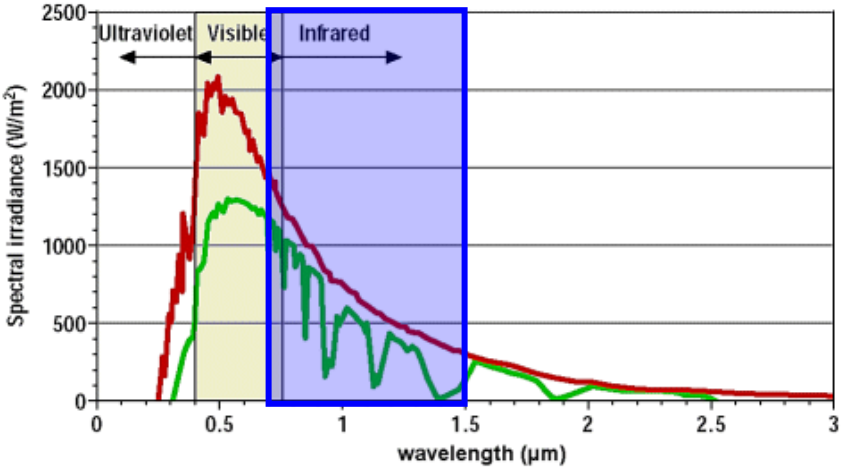

Figure 4.1 Solar spectrum of sunlight (red), solar spectrum of sunlight after passing through earth's atmosphere (green).[104] The NIR region is highlighted in blue.

Recently, there has been an interest in developing nano-sized upconverting materials, whose small sizes facilitate their use for biological imaging, amongst other applications. Based on current literature, $NaYF_4$:Yb,Er appears to be among the most efficient upconverting nanomaterials.[105-109] The upconversion process (illustrated in Figure 4.2) in this material begins with Yb^{3+} absorbing a photon of light at 980nm, then the corresponding energy is transferred to the $^4I_{11/2}$ Er^{3+} accepting energy level. Yb^{3+} then absorbs a second 980nm photon and again transfers the energy to Er^{3+}, populating the $^4F_{7/2}$ level, followed by non-radiative relaxation to erbium's $^2H_{11/2}$ and $^4S_{3/2}$ energy levels, which produce green emission when energy is released during relaxation to the $^4I_{15/2}$ ground state. Nonradiative relaxation to the Er^{3+} $^4F_{9/2}$ level can also occur, followed by red emission upon relaxation to the $^4I_{15/2}$ ground state. While in the $^4I_{13/2}$ exited state, Er^{3+} can also absorb a 980nm photon of light, or accept energy from Yb^{3+} and fill the $^4F_{9/2}$ energy level, followed by red emission upon relaxation to the $^4I_{15/2}$ ground state, as shown in Figure 4.3.[110]

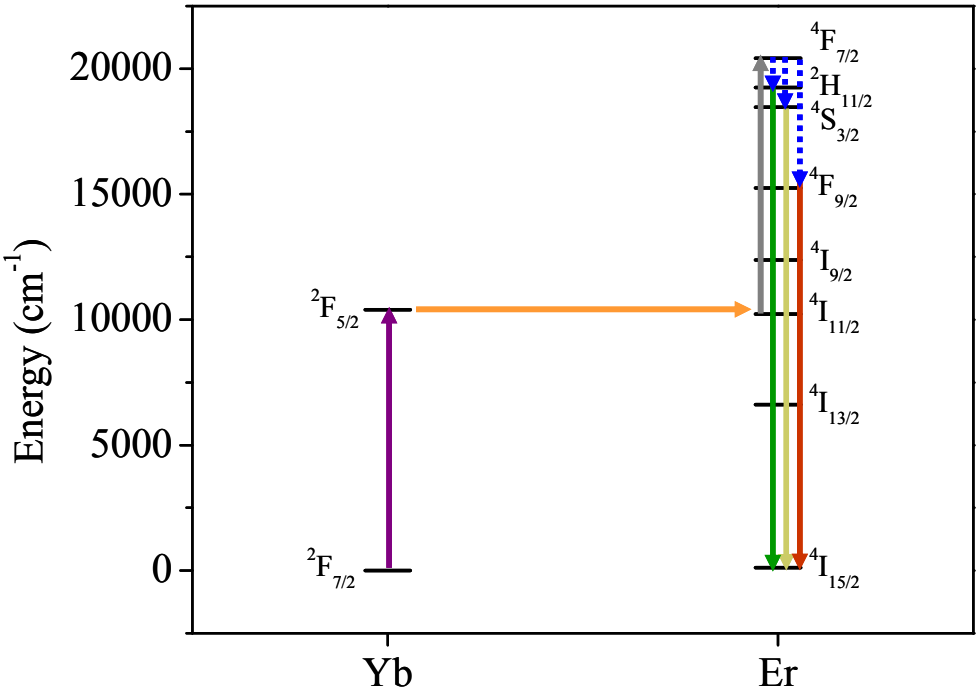

Figure 4.2 Scheme of the upconversion process from Yb^{3+} to Er^{3+}. Yb^{3+} absorbs a photon of light at 980nm (purple arrow), then transfers energy to the $^4I_{11/2}$ Er^{3+} energy level (orange arrow). Yb^{3+} then absorbs a second 980nm photon and again transfers the energy to Er^{3+}, populating the $^4F_{7/2}$ level (gray arrow); followed by non-radiative relaxation to erbium's $^2H_{11/2}$ and $^4S_{3/2}$ energy levels (blue arrows), which produce green emission when photons are released during relaxation to the $^4I_{15/2}$ ground state (light and dark green arrows). Nonradiative relaxation to the Er^{3+} $^4F_{9/2}$ level can also occur (blue arrow), followed by red emission upon relaxation to the $^4I_{15/2}$ ground state (red arrow).[110]

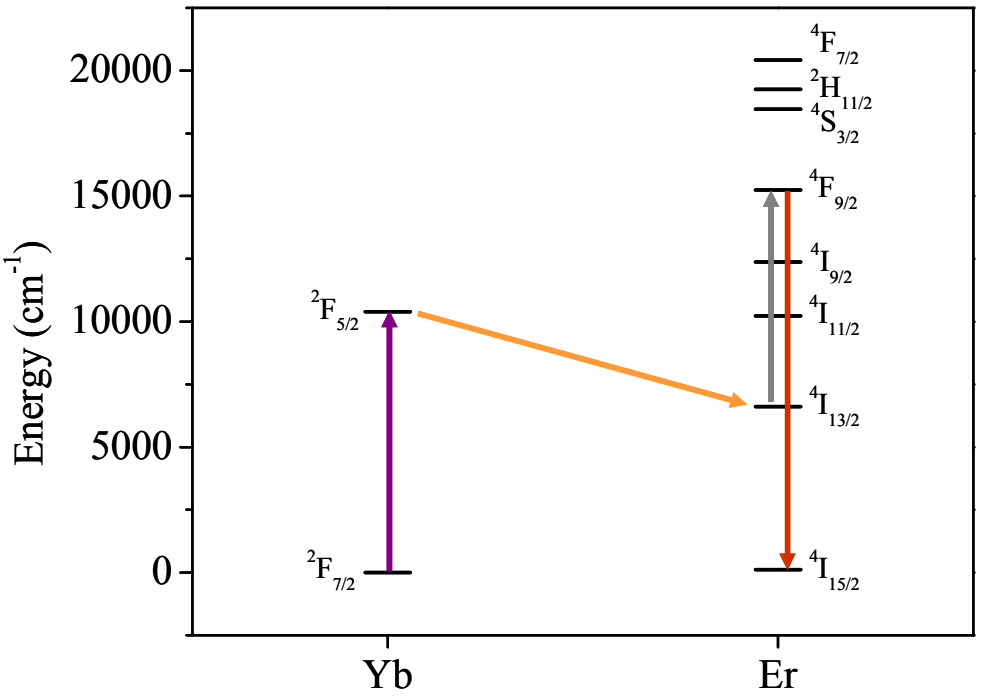

Figure 4.3 Scheme of alternative upconversion process from Yb^{3+} to Er^{3+}. While in the $^4I_{13/2}$ exited state, Er^{3+} can also absorb a 980nm photon of light (gray arrow), or accept energy from Yb^{3+} (purple and orange arrows) and fill the $^4F_{9/2}$ energy level, followed by red emission upon relaxation to the $^4I_{15/2}$ ground state (red arrow).[110]

4.1.1.1. $NaYF_4$:Yb,Er Upconverting Nanocrystals as Energy Donors to Quantum Dots

Currently, one of the major limitations of upconverting lanthanide materials is the scarce number of emission wavelengths possible. Lanthanide luminescence bands are very narrow, and are not affected by their environment; therefore, only specific and nonadjustable wavelengths of emission are produced by Yb:Er or Yb:Tm mixtures. If the energy from excited Er^{3+} or Tm^{3+} could be transferred to excite another chromophore, which would in turn emit at a different wavelength, many more emission colors become possible. Quantum Dots, or semiconductor nanocrystals, have several advantages that make them good candidates to serve as energy

acceptors for this purpose.[99,111-116] The wavelength of their emission bands are dependent on size, and thus are easily tuned, allowing many emission colors to be possible through a single material. Since Quantum Dots of various sizes all have broad absorbance (and excitation) bands, it is possible to excite Quantum Dots with several different emission wavelengths through the energy transfer from Er^{3+} or Tm^{3+}. Compared to organic chromophores, which might also be considered as energy acceptors for this application, Quantum Dots offer the benefit of having greater photostability. By combining $NaYF_4$:Yb,Er upconverting lanthanide nanocrystals with Quantum Dots it would be possible to envision a species that excites at 980 nm and emits at a variety of wavelengths between 525 and 850 nm with high photostability. A material with these properties has many potential applications, including multiplex biological assays, electronic displays, and hidden tags for security purposes.

Among the first steps to developing a Quantum Dot – upconverting nanocrystal species is to determine the feasibility of energy transfer between the two nanomaterials. There are several published methods for synthesizing $NaYF_4$:Yb,Er nanocrystals,[105,106,117,118] so different ones were followed to make this material to determine which synthesis produces the best nanocrystals for our purpose. After tests, an aqueous room temperature synthesis with high temperature annealing,[118] and a high temperature organic solvent based method[106,117] were used in parallel to synthesize NaYF4:Yb,Er upconverting nanocrystals. CdSe semiconductor nanocrystal Quantum Dots were synthesized as described in Chapter 3, and CdSe:CdTe core:shell nanocrystal Quantum Dots were obtained from Quantum Dot, Corp. Once synthesized, the two materials were combined in both solution and solid state mixtures and were spectroscopically investigated to test for energy transfer to the Quantum Dots.

4.1.1.2. Antennae for Sensitizing $NaYF_4$:Yb,Er Upconverting Nanocrystals

An additional limitation of current upconversion technologies is their constricted efficiency, which affects their ability to serve in harvesting solar light energy. The upconversion process requires two photons of light to be absorbed for one photon to be emitted, so the inherent maximum quantum efficiency of the system is 50%. Additionally, the $NaYF_4$:Yb,Er nanocrystals are excited through directly populating the Yb^{3+} $^2F_{5/2}$ level. Since lanthanide cations have low molar absorptivity, this limits the efficiency of obtaining upconverting emission signals and requires laser excitation sources to produce upconversion emission that can be easily detected. Also, like their emission bands, lanthanide direct excitation bands are narrow, thus only a small window around 980 nm of the solar spectrum can be utilized by $NaYF_4$:Yb,Er upconverting materials. By attaching an organic chromophore on the surface of $NaYF_4$:Yb,Er nanocrystals that can sensitize Yb^{3+} through the antennae effect, it may be possible to improve the number of photons generated through the upconversion process. Since organic chromophores have much broader absorption spectra and larger extinction coefficients than lanthanide cations, it will also allow a greater portion of the solar spectrum to be utilized.

As we have demonstrated through the coordination of tropolonate to the surface of ytterbium doped $NaYF_4$ nanoparticles, it is possible to sensitize lanthanide cations within the nanoparticle through antennae at the surface (see sections 4.1.2, 4.2.2.3, 4.3.2, and 4.4.1 for details).[24] However, in order to maintain the upconversion property, an antenna for the ytterbium cations in $NaYF_4$:Yb,Er nanocrystals must also adhere to certain criteria. The erbium emission bands in $NaYF_4$:Yb,Er are centered at 523 nm, 545 nm, and 650 nm, thus a potential antenna must have absorbance above at least 550 nm. An absorbance of above 650 nm would be ideal, as that would allow all three erbium bands to be detected. Here, a group of naphthalimide molecules are tested for their potential to sensitize Yb^{3+} at the necessary wavelengths and to

serve as antennae for upconverting $NaYF_4$:Yb,Er nanocrystals. The naphthalimide molecules, shown in Figure 4.4, were chosen as potential antennae for several reasons. They have low energy absorption bands, are known to have high rates of intersystem crossing to the triplet state[119] (a highly populated triplet state increases likelihood of energy transfer to lanthanide cations), and contain carboxylic acid groups for binding to lanthanide cations and Quantum Dot nanocrystals. To determine the feasibility of these four naphthalimide molecules to serve as antennae for $NaYF_4$:Yb,Er nanocrystals, their complexes with Yb^{3+} were formed and studied spectroscopically. The nitro substituted molecule (**Naphth-NO_2**) displays the ability to sensitize Yb^{3+} at sufficiently low energy, and was tested as an antenna for upconversion.

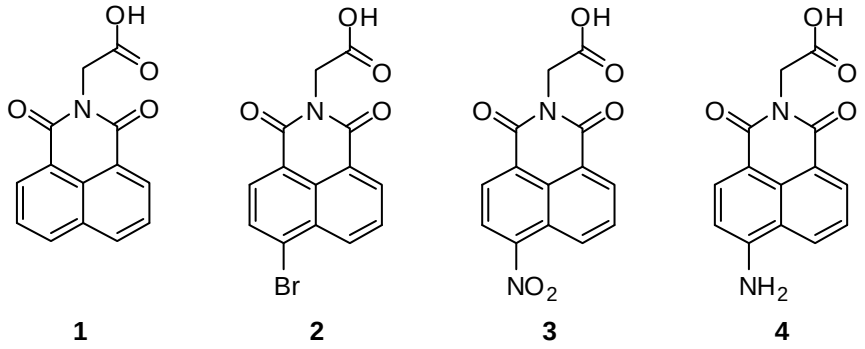

Figure 4.4 Family of naphthalimide molecules chosen as potential antennae for $NaYF_4$:Yb,Er nanoparticles; 1) *N*-Glycine-1,8-naphthalimide (Naphth-H), 2) *N*-Glycine-4-bromo-1,8-naphthalimide (Naphth-Br), 3) *N*-Glycine-4-nitro-1,8-naphthalimide (Naphth-NO_2), and 4) *N*-Glycine-4-amino-1,8-naphthalimide (Naphth-NH_2).

4.1.2. Tropolonate capped $NaY_{(1-x)}Ln_xF_4$ Nanocrystals

Lanthanide based NIR emitters have a great potential to serve as bioanalytical reporters; however, the "antenna effect" approach to sensitizing lanthanide cations with organic chromophores has intrinsic limitations. The lanthanide luminescence is easily quenched through

non-radiative routes when the cations are in close proximity to the vibrational overtones of -OH, -NH and -CH groups present in the sensitizing ligand and/or solvent.[16] This effect is particularly dramatic for NIR emitting Ln^{3+} due to relatively small energy gaps between ground and excited electronic states.[16] To alleviate this limitation, Ln^{3+} have been incorporated into inorganic matrices, such as LnF_3,[120] Ln_2O_3,[121] $LnPO_4$,[122] $LnVO_4$,[123] TiO_2,[124] and Zeolites.[125] These materials protect lanthanide cations from nonradiative quenching, however, they have either limited (e.g. $LnVO_4$) or no absorbance in the UV range. Thus, they can not efficiently sensitize lanthanide luminescence in the manner that organic sensitizers can, decreasing the number of emitted photons and detection sensitivity.

To overcome the limited lanthanide sensitization a new strategy is employed, where organic tropolonate chromophoric groups are bound to the surface of $NaYF_4$ nanocrystals doped with NIR emitting Nd^{3+} or Yb^{3+}, shown in Figure 4.6. This novel approach uses the $NaYF_4$ matrix to protect Ln^{3+} from non-radiative deactivations, while a chromophoric coating sensitizes their luminescence.[24] Tropolonate was chosen as a capping ligand since it has been previously demonstrated to be a suitable sensitizer for several lanthanide cations emitting in the NIR range when coordinated in $KLn(Trop)_4$ molecular complexes.[7,126]

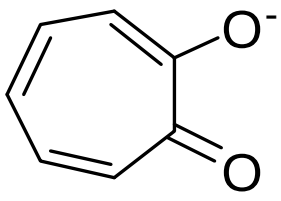

Figure 4.5 Molecular structure of the tropolonate capping ligand.

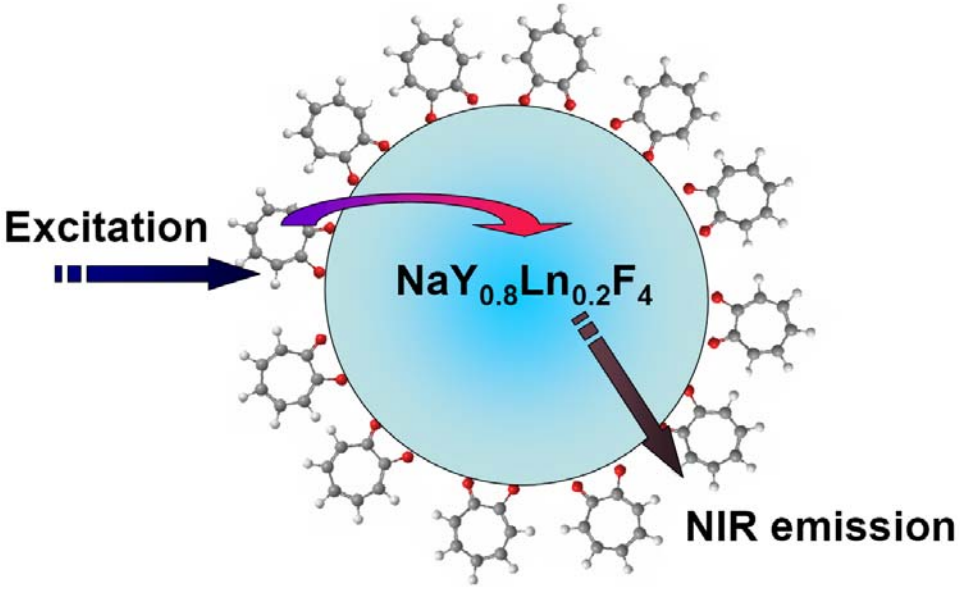

Figure 4.6 Schematic illustration of tropolonate capped Nd^{3+} or Yb^{3+} doped $NaYF_4$ nanocrystals and the energy transfer process.

4.2. EXPERIMENTAL

4.2.1. Reagents

Tropolone, Y_2O_3, Nd_2O_3, Yb_2O_3, Er_2O_3, oleic acid (90%), oleylamine (>80%), 1-octadecene (>90%), trifluoroacetic acid (99%), $NaCF_3COO$ (>97%), $ErCl_3{\cdot}xH_2O$, $YbCl_3{\cdot}xH_2O$, EDTA, KOH standard solution in methanol (0.100 N), NaOH standard in water, 1,8-naphthalic anhydride, 4-bromo-1,8-naphthalic anhydride, 4-nitro-1,8-naphthalic anhydride, and 4-amino-1,8-naphthalic anhydride were purchased from Aldrich. NaF was purchased from Spectrum. Glycine was purchased from Avacado. Concentrated HCl was purchased from EMD and diluted with deionized water. Absolute ethanol was purchased from Pharmco-AAPER. Rhodamine590, rhodamine610, rhodamine640, LDS698, and LDS750 were purchased from Exciton. All reagents were used as received. All the solvents, absolute ethanol and chloroform, were used as received.

$Y(CF_3COO)_3$, $Nd(CF_3COO)_3$, $Er(CF_3COO)_3$, and $Yb(CF_3COO)_3$ were prepared according to literature method.[127]

4.2.2. Synthesis of Ln^{3+} doped $NaYF_4$ particles

4.2.2.1. Organic solvent method

Based on methods published by Boyer et al.[117] and Mai et al.[106], lanthanide doped $NaYF_4$ nanocrystals were synthesized using organic solvents and high temperatures; size and crystallinity were controlled through a combination of temperature and growth time. Nanocrystals were doped with Yb^{3+} and Er^{3+} to create an upconverting system, as well as with either Yb^{3+} or Nd^{3+} to investigate sensitization through binding surface antennae.

The synthesis was carried out using standard oxygen-free procedures. Sodium trifluoroacetate (0.136g, 1.0mmol), $Y(CF_3COO)_3$ (0.386g, 0.8 mmol) and $Ln(CF_3COO)_3$ (0.2 mmol) were added to the reaction vessel with octadecene (5.05 g, 20 mmol), oleic acid (2.82g, 10 mmol) and oleylamine (2.68 g, 10 mmol). The mixture was heated to 100°C under vacuum and stirred for 30 min to remove the residual water and oxygen. The solution was then heated to 325°C under argon and maintained at this temperature for 40 min. Subsequently, the mixture was allowed to cool down to room temperature, and the resulting nanocrystals were precipitated by addition of ethanol and isolated via centrifugation. The resulting solid was then washed twice with ethanol and dried under vacuum for 24 h.

4.2.2.2. Aqueous method

$NaYF_4$ nanoparticles doped with Yb^{3+} and Er^{3+} to produce an upconverting material were synthesized following a water based method published by Guangshun Yi et al.[118] The

$NaYF_4$:Yb,Er nanoparticles were formed through a co-precipitation method in the presence of EDTA, and the size of the nanoparticles (40 – 160 nm diameter) was controlled through the molar ratio of EDTA to lanthanide cations, with ratios ranging between 0:1 to 2:1, and higher EDTA yielding smaller nanoparticles.

All solutions were prepared in deionized water unless stated otherwise. An EDTA:Ln solution was prepared by mixing the following: 20 mL 0.2 M EDTA (deprotonated with NaOH), 16 mL of 0.2 M YCl_3 (pH=2), 3.4 mL of 0.2 M $YbCl_3$ (pH=2), and 0.6 mL of 0.2 M $ErCl_3$ (pH=2). In a separate flask, 0.05 moles (2.1g) of NaF was dissolved in 60 mL of water. While stirring, the EDTA:Ln mixture was quickly injected into the NaF solution. After stirring for 1 h, 12mL of 1M HCl was added to the reaction mixture, producing a white precipitate. After 1 h of stirring, the precipitate was isolated with centrifugation, and washed three times with deionized water and once with absolute ethanol. The precipitate was dried under vacuum for 24 h. To obtain nanoparticles with improved crystallinity and upconverting properties, the particles were annealed in MgO trays manufactured by Accumet Materials, Co. at temperatures ranging from 400 to 700°C under an H_2:Ar (5:95) environment.

4.2.2.3. Solid State Mixing of $NaY_{(0.78)}Yb_{(0.20)}Er_{(0.02)}F_4$ Nanocrystals with Quantum Dots

The following procedure was used to mix the $NaY_{(0.78)}Yb_{(0.20)}Er_{(0.02)}F_4$ nanocrystals and Quantum Dots (CdSe or CdSe:CdTe nanocrystals). Approximately 5 mg of $NaY_{(0.78)}Yb_{(0.20)}Er_{(0.02)}F_4$ nanocrystals (annealed at 400^{o}C) in powder form was placed on a glass microscope slide. A drop of concentrated solution of Quantum Dots in chloroform was placed on top of the $NaY_{(0.78)}Yb_{(0.20)}Er_{(0.02)}F_4$ nanocrystals and allowed to adsorb onto it while the chloroform evaporated. This step was repeated three to five times to insure adequate Quantum

Dot coverage on the upconverting material. The mixture was then sandwiched between a second microscope slide to hold it in place for spectroscopic analysis.

4.2.2.4. Syntheses of the Glycine-Attached Naphthalimides

N-Glycine-1,8-naphthalimide (**Naphth-H**), Figure 4.4 (**1**), was synthesized as follows: 0.628 g (3.17 mmol) of 1,8-naphthalic anhydride and 0.237 g (3.16 mmol) of glycine were suspended in 10 mL of DMSO. The reaction mixture was heated to reflux for 1 hour. After cooling to room temperature, the reaction mixture was poured into 100 mL of water. The precipitate was filtered, washed with water and dried in a vacuum oven. The compound was obtained as white solid (0.732 g, 91%). ^{1}H-NMR (300 MHz, DMSO-d_6, δ): 13.2 (s, 1H, -COOH), 8.52 (m, 4H, Ar H), 7.91 (t, J=7.5 Hz, 2H, Ar H), 4.73 (s, 1H, -CH_2-).

N-Glycine-4-bromo-1,8-naphthalimide (**Naphth-Br**), Figure 4.4 (**2**), was synthesized as follows: 0.516 g (1.86 mmol) of 4-bromo-1,8-naphthalic anhydride and 0.140 g (1.86 mmol) of glycine were suspended in 7 mL of DMSO. The reaction mixture was heated to reflux for 1 hour. After cooling to room temperature, the reaction mixture was poured into 50 mL of water. The precipitate was filtered, washed with water and dried in a vacuum oven. The compound was obtained as buff colored solid (0.604 g, 97%). ^{1}H-NMR (300 MHz, DMSO-d_6, δ): 8.63-8.60 (m, 2H, Ar H), 8.38 (d, J=7.8 Hz, 1H, Ar H), 8.27 (d, J=7.8 Hz, 1H, Ar H), 8.40 (t, J=8.0 Hz, 1H, Ar H), 4.72 (s, 1H, -CH_2-).

N-Glycine-4-nitro-1,8-naphthalimide (**Naphth-NO_2**), Figure 4.4 (**3**), was synthesized as follows: 0.0960 g (0.395 mmol) of 4-nitro-1,8-naphthalic anhydride and 0.0300 g (0.400 mmol) of glycine were suspended in 3 mL of DMSO. The reaction mixture was heated to reflux for 1 hour. After cooling to room temperature, the reaction mixture was poured into 10 mL of water.

The precipitate was filtered, washed with water and dried in a vacuum oven. The compound was obtained as yellow solid (0.0901 g, 76%). ^{1}H-NMR (300 MHz, DMSO-d_6, δ): 13.2 (s, 1H, -COOH), 8.76 (d, *J*=8.7 Hz, 1H, Ar H), 8.69-8.65 (m, 2H, Ar H), 8.58 (d, *J*=8.1 Hz, 1H, Ar H), 8.13 (t, *J*=8.0 Hz, 1H, Ar H), 4.75 (s, 1H, -CH_2-).

N-Glycine-4-amino-1,8-naphthalimide (**Naphth-NH$_2$**), Figure 4.4 (**4**), was synthesized as follows: 0.310 g (1.45 mmol) of 4-amino-1,8-naphthalic anhydride and 0.110 g (1.47 mmol) of glycine were suspended in 30 mL of DMSO. The reaction mixture was heated to reflux for 1.5 hours. After cooling to room temperature, the solvent was removed in a vacuum oven. The mixture was purified by column chromatography (silica gel) using a 4:1 (v:v) methanol:dichloromethane mixture as the eluent. The compound was obtained as an orange colored solid (0.0943 g, 24%). ^{1}H-NMR (300 MHz, DMSO-d_6, δ): 8.58 (d, *J*=8.1 Hz, 1H, Ar H), 8.37 (d, *J*=6.9 Hz, 1H, Ar H), 8.14 (d, *J*=8.1 Hz, 1H, Ar H), 7.62 (t, *J*=7.8 Hz, 1H, Ar H), 7.32 (s, 2H, -NH_2), 6.82 (d, *J*=8.4 Hz, 1H, Ar H), 4.27 (s, 1H, -CH_2-).

4.2.2.5. Naphth-NO$_2$ capped nanocrystals

The **Naphth-NO$_2$** capped nanocrystals were synthesized using the following procedure: **Naphth-NO$_2$** was dissolved in ethanol, then deprotonated with an equimolar amount of triethylamine in ethanol. Chloroform was added to obtain a 1:1 (v:v) EtOH:$CHCl_3$ solvent mixture. This solution was added to a purified solution of $NaY_{(0.78)}Yb_{(0.20)}Er_{(0.02)}F_4$ nanocrystals (synthesized following Section 4.2.2.1) dispersed in chloroform (approximately 1 mg/mL). The resulting mixture was sonicated for 2 hours, and the solvent was removed through centrifugation and decanting. The resulting solid was washed with ethanol and dispersed in DMSO for analysis.

4.2.2.6. Tropolonate capped nanocrystals

The Tropolonate capped nanocrystals were synthesized using the following procedure: potassium tropolonate was dissolved in methanol, then deprotonated with an equimolar amount of KOH in methanol. Chloroform was added to obtain a 1:1 (v:v) MeOH:$CHCl_3$ solvent mixture. This solution was added to a purified solution of nanocrystals dispersed in chloroform. The resulting mixture was sonicated for 2 hours and the solvent was removed under vacuum. The resulting solid was washed with ethanol and DMSO and dried under vacuum for 24 h.

4.2.3. Instrumental Methods

4.2.3.1. UV-visible Absorption Spectroscopy

UV-vis absorption spectra were recorded on a Perkin-Elmer Lambda 19 spectrophotometer. Samples were analyzed in 10 mm matched quartz cuvettes purchased from NSG Precision Cells, Inc. Spectral analysis was performed following instrumental zeroing with cuvettes containing solvent only.

4.2.3.2. FT-IR Spectroscopy

FT-IR spectra were recorded on a Perkin-Elmer Spectrum BX FT-IR instrument on samples incorporated into KBr and pressed into pellets.

4.2.3.3. Luminescence Spectroscopy

Lanthanide luminescence emission and excitation spectra were measured using a Jobin Yvon-Horiba Fluorolog-322 spectrofluorimeter equipped with a detector for the NIR domain (DSS-IGA020L, Electro-Optical Systems, Inc.). Excitation was achieved with the spectrofluorimeter 450W Xenon lamp, as well as with diode laser sources at 635 nm and 980 nm

[S2011 (635 nm, 4.5 mW) and L980P030 (980 nm, 30 mW) from ThorLabs, Inc.). Cut-on filters were used to remove second order signals from the samples and excitation sources. Samples were analyzed in 1 or 10 mm quartz cuvettes (NSG Precision Cells, Inc.)

For analysis of solid state upconverting materials, samples were prepared by placing a small amount of the solid state product between two glass microscope slides. The two slides were taped together with strips of NUNC-Nalgene well-plate cover sheets, used in lieu of traditional tapes to avoid autofluorescence or absorbance interference during measurements. Emission and excitation spectra were collected using a JY Horiba Fluorolog3 fitted with excitation monochromators tailored to allow high intensity around 700 nm. A solid state sample holder was used to position the sample at a -45 degree angle to the incident light and +45 degree angle to the detector. Three cut-on filters were placed between the lamp and the sample in order to remove any second or third order (490 nm or 653 nm) light coming through the gratings from the lamp. Alternatively, the samples were excited with diode lasers (emitting at 630 nm or 980 nm) and 500 nm cut-on filter was positioned between the sample and the detector to prevent half-order bands from interfering with the spectra. These set-ups are illustrated in Figure 4.7.

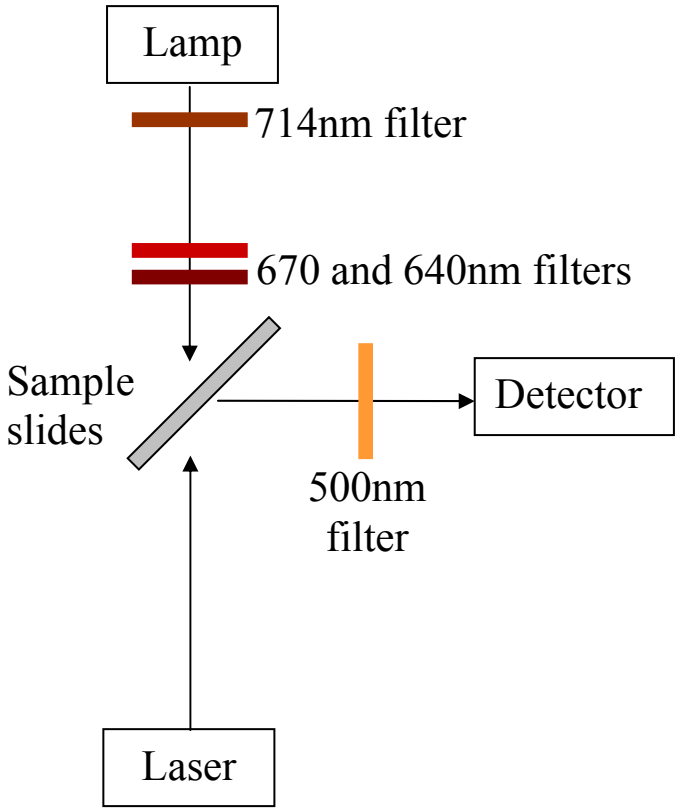

Figure 4.7 Illustration of instrumental set up for analysis of upconverting samples in solid state with either xenon arc lamp or diode laser excitation (635 nm or 980 nm), with samples aligned at 45 degrees from the excitation source, as illustrated here for laser excitation.

The luminescence lifetime measurements were performed by excitation of solutions in 10 mm quartz cells using a Nd:YAG Continuum Powerlite 8010 Laser (354 nm, 3rd harmonic) as the excitation source. Emission was collected at a right angle to the excitation beam and emission wavelengths were selected using a Spectral Products CM 110 1/8 meter monochromator. The signal was monitored by a cooled photomultiplier (Hamamatsu R316-2) coupled to a 500 MHz bandpass digital oscilloscope (Tektronix TDS 754D). The signals (15,000 points each trace) from at least 500 flashes were collected and averaged. Luminescence decay curves were imported into Origin 7.0 scientific data analysis software. The decay curves were analyzed using the Advanced Fitting Tool module and fitted with mono-, bi- and tri-exponential modes. Of the

three modes, the lifetime value was chosen based on the best fit of the decay curve on the criteria of the minimum χ^2 statistical parameter. Lifetimes are averages of at least three independent determinations.

4.2.3.4. X-Ray Diffraction

Powder X-ray diffraction (XRD) patterns of dried nanoparticle powders were recorded on a Philips X'pert diffractometer (PW3710) with a slit of 1/2° at a scanning rate of 3° min^{-1}, using Cu Kα radiation, λ=1.5406 Å). Samples were evaporated or pressed onto glass microscope slides.

4.2.3.5. Transmission Electron Microscopy

A small drop of solution containing the sample was placed on a carbon coated copper grid. After several seconds, the drop was removed by blotting with filter paper. The sample that remained on the grid was allowed to dry before inserting the grid into the microscope. The grids were viewed on a transmission electron microscope (Hitachi H-7100 TEM, Hitachi High Technologies America, 5100 Franklin Drive, Pleasanton, CA, 94588) operating at 75 kV. Digital images were obtained using an AMT Advantage 10 CCD Camera System (Advanced Microscopy Techniques Corporation, 3 Electronics Ave., Danvers, MA, 01923) and NIH Image software. Particle diameter was measured using a negatively stained catalase crystal as a calibration standard.

4.3. RESULTS & DISCUSSION

4.3.1. $NaYF_4$:Yb,Er Upconverting Nanocrystals as Energy Donors & Acceptors

4.3.1.1. $NaYF_4$:Yb,Er upconverting nanocrystal syntheses

$NaY_{(0.78)}Yb_{(0.20)}Er_{(0.02)}F_4$ upconverting nanocrystals (**UCNCs**) were synthesized following both a room-temperature aqueous method and an organic solvent high-temperature method. In both cases, the Yb^{3+} and Er^{3+} doping levels were the same, and were based on doping ratios demonstrated to be ideal for upconversion.[105,106,108,109,117] To confirm successful syntheses of the desired product, the nanoparticles were analyzed with powder XRD, TEM, and fluorescence spectroscopy.

The successful synthesis of **UCNCs** with a decomposition reaction at high temperatures in organic solvents was confirmed through TEM and fluorescence spectroscopy. The synthetic procedure resulted in reasonably monodisperse nanocrystals of approximately 20 nm in diameter, as shown by the TEM image in Figure 4.8. The relatively small size of these nanocrystals, combined with their monodispersity, provide beneficial attributes for potential biological applications. The fluorescence spectrum monitored in the visible range upon excitation through Yb^{3+} at 980 nm (with the xenon arc instrument lamp) displays the two visible Er^{3+} red and green emission bands, shown in Figure 4.9, confirming that these nanocrystals have the expected upconversion properties. The noise on the spectrum indicates that the upconversion emission signal is relatively weak, however, and a laser excitation source is necessary to maximize the upconversion emission signal.

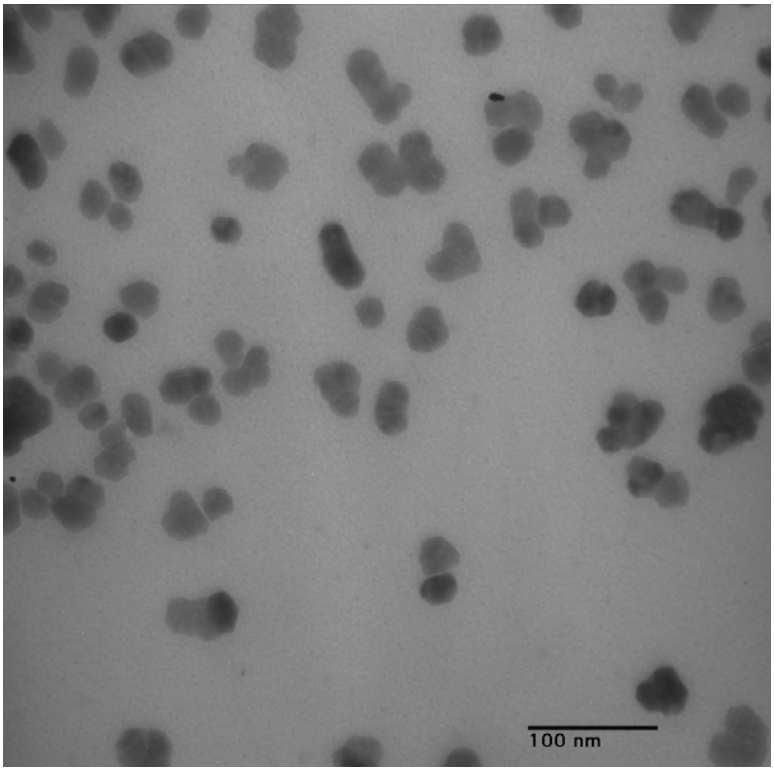

Figure 4.8 TEM image of UCNCs synthesized through the high-temperature, organic solvent method.

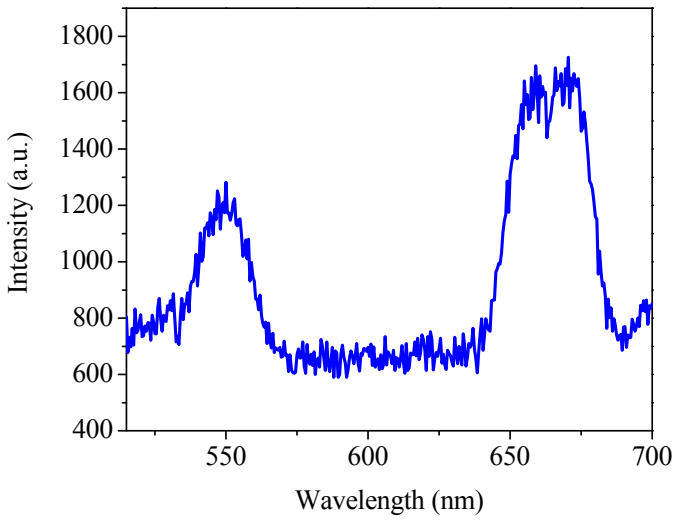

Figure 4.9 Emission spectrum in the visible range upon excitation at 980 nm with a 450 W xenon lamp of UCNCs synthesized through the high-temperature, organic solvent methodology. The presence of two Er^{3+} emission bands in the visible range confirms upconversion properties of these nanomaterials.

The **UCNCs** synthesized in aqueous conditions were analyzed before annealing at high temperatures. The powder XRD pattern, Figure 4.10, reveals the formation of cubic $NaYF_4$ (ICDD, No. 77-2042), with diffraction peak positions at 27, 32, 46 and 55, correlating with published values.[118] The XRD pattern collected provides only qualitative data, as the collection time was short (30 min), and can not be used to obtain size information on the nanoparticles. Transmission electron microscopy (TEM) images were also collected of the **UCNCs** prior to annealing at high temperatures. As shown in Figure 4.11, the TEM image confirms the synthesis of nanocrystals. Although the nanocrystals are aggregating, making it difficult to determine size of individual nanocrystals, the image provides some indication of the size, which ranges between 5 and 75 nm in diameter. This is a wide size distribution, which is a detrimental property for some potential practical applications.

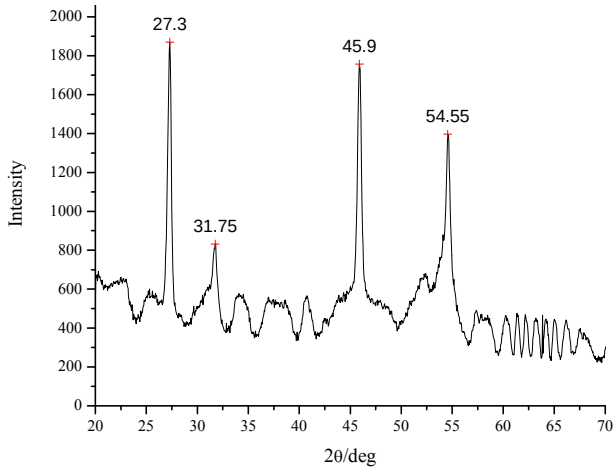

Figure 4.10 Powder X-ray diffraction pattern of UCNCs synthesized in aqueous conditions, prior to annealing at high temperatures.

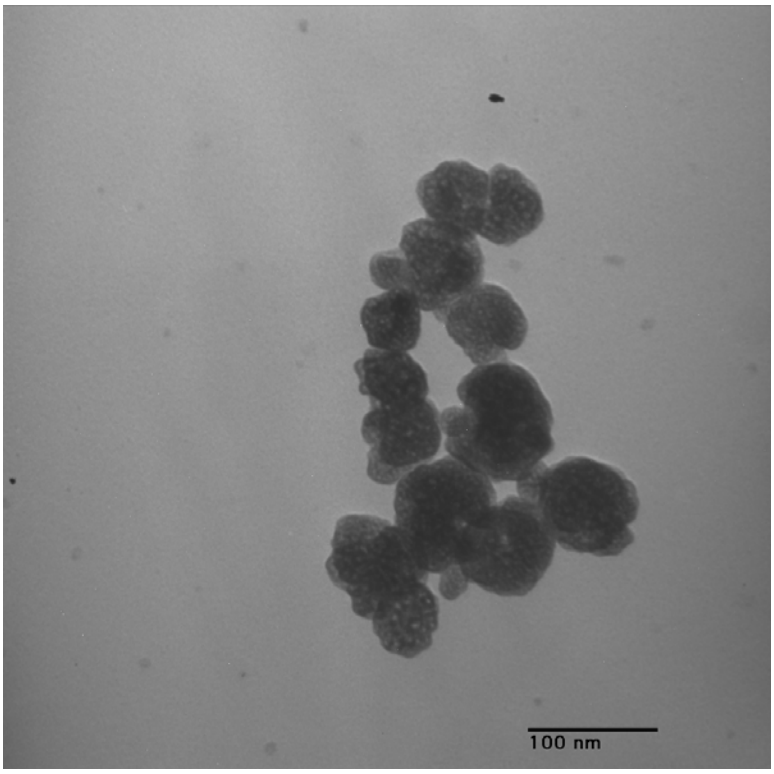

Figure 4.11 TEM image of UCNCs synthesized in aqueous conditions, prior to annealing at high temperatures.

To confirm that the **UCNCs** had upconverting properties, the luminescence spectrum of the sample was collected, exciting through ytterbium at 980 nm with the diode laser. As seen in the emission spectrum, Figure 4.12, the Er^{3+} emission band centered at 545 nm is distinguishable; however, the signal is weak and the other bands are not identifiable. Despite the weak signal, these results confirm the nanocrystals do have upconverting properties. The weak signal is expected of nanocrystals that have not been annealed, as the annealing process is important to achieve better crystallinity and upconversion efficiency.[118]

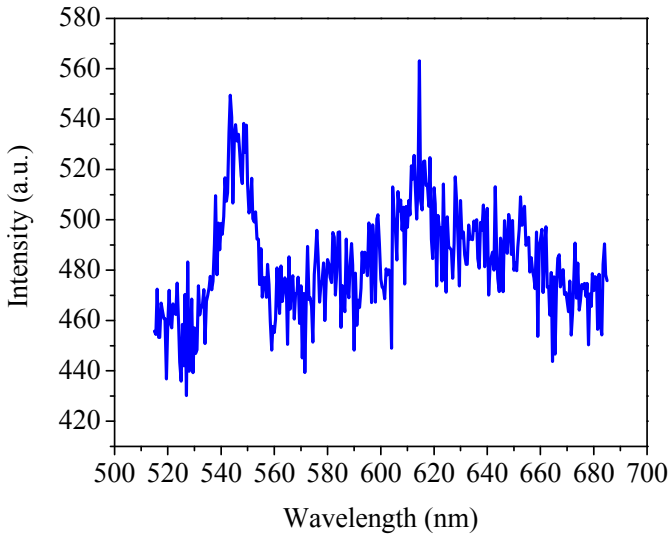

Figure 4.12 Luminescence spectrum of UCNCs before annealing, λ_{ex}: 980 nm (diode laser). A weak Er^{3+} signal is seen at 545 nm, confirming the presence of upconversion.

The **UCNCs** were annealed in an H_2:Ar (5:95, v/v) environment at 400°C and 600°C. After annealing, TEM analysis was performed to determine the effects of the annealing process on the size and shape of the nanocrystals. The TEM results, shown in Figure 4.13, show that annealing at 400°C did not affect particle size, but 600°C resulted in particle growth and shape change. Thus, nanocrystals annealed at 400°C were chosen for future work. The upconversion luminescent properties of these nanocrystals were monitored, and they displayed improved upconversion efficiency over the unannealed nanocrystals, as well as the nanocrystals synthesized under high-temperature, organic solvent methods (see Figure 4.9). The emission spectrum collected in the visible range upon excitation through ytterbium at 980 nm with the diode laser displayed characteristic Er^{3+} emission bands centered at 523, 545, and 650 nm, as shown in Figure 4.14. The excitation spectrum collected on Er^{3+} emission at 545 nm, Figure

4.15, confirms that the emission is a result of upconversion energy transfer from Yb^{3+} to Er^{3+} as it is comprised of sharp emission band at 980 nm, which matches the excited energy level of ytterbium. It also demonstrates the narrow window of the light spectrum that upconverting materials are able to utilize. These fluorescence results confirm the successful synthesis of upconverting $NaYF_4$:Yb,Er material.

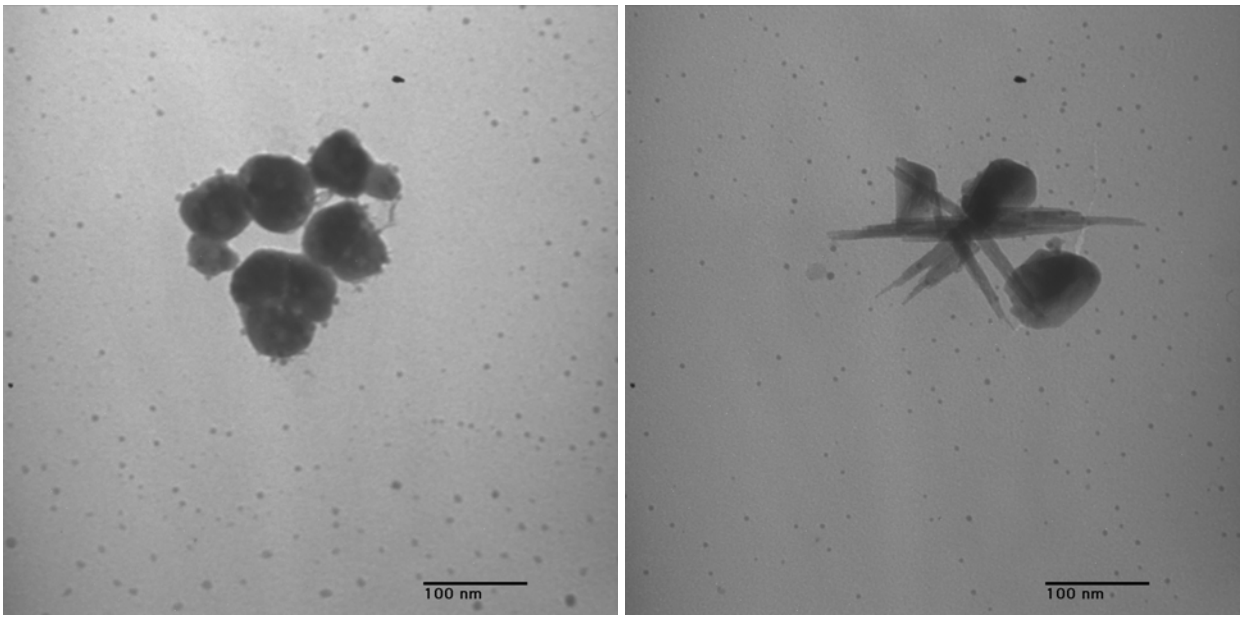

Figure 4.13 TEM images of UCNCs after annealing at 400°C (left) and 600°C (right), which causes the nanocrystals to change in shape and size.

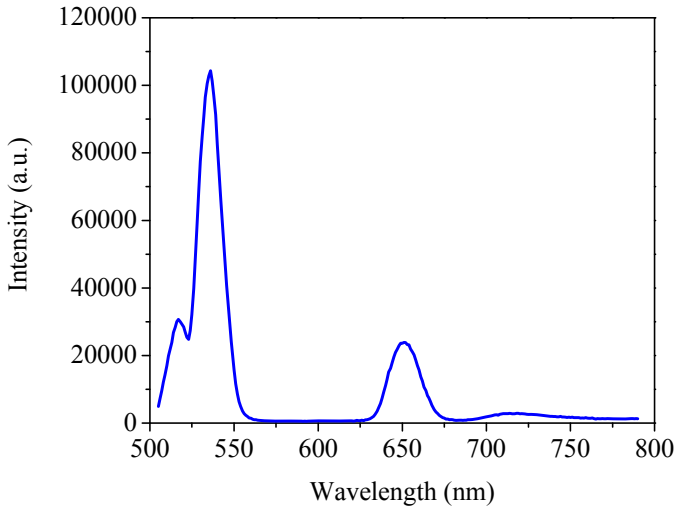

Figure 4.14 Emission spectrum of UCNCs after annealing at 400°C, λ_{ex}: 980 nm; the characteristic Er^{3+} emission bands centered at 523, 545, and 650 nm confirm upconversion properties.

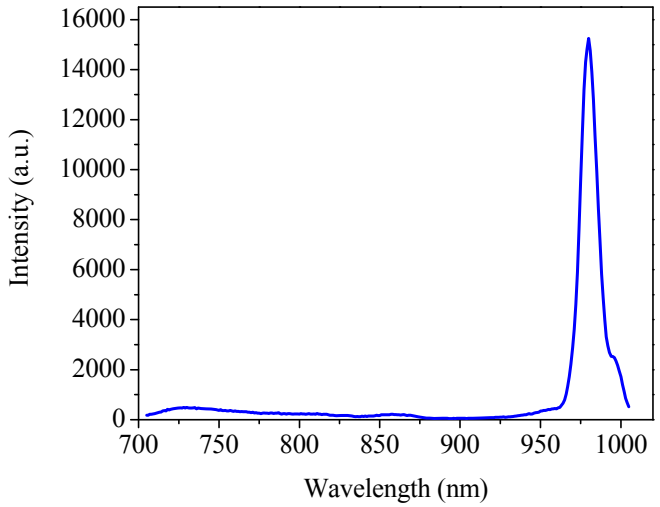

Figure 4.15 Excitation spectrum of UCNCs after annealing at 400°C, monitoring Er^{3+} emission at 545 nm.

4.3.1.2. $NaY_{(0.78)}Yb_{(0.20)}Er_{(0.02)}F_4$ Nanocrystals as Energy Donors to Quantum Dots

The $NaY_{(0.78)}Yb_{(0.20)}Er_{(0.02)}F_4$ upconverting nanocrystals (**UCNCs**) were combined with CdSe Quantum Dots (**QDs**) in the solid state to eliminate the potential for deactivation of excited states through solvent vibrations. It also provided direct contact between the two materials. **UCNCs** synthesized following the aqueous method were used here, as their powdery properties allowed easier manipulation in the solid state and they displayed more intense upconversion bands. Two CdSe nanocrystals synthesized as described in Section 3.2 with emission bands centered around 600 nm were used. **QDs** with emission at 600 nm (**QD600**) were chosen because this wavelength range falls between the two bands of erbium emission, allowing detection of any **QD** emission resulting from energy transfer from the first erbium band. To make sure the emission bands of the CdSe **QDs** could be detected in the experimental set up, microscope slides were prepared by dropping three to five drops of concentrated CdSe **QD** sample in chloroform on the slide and allowing the solvent to evaporate. As shown in Figure 4.16, these **QDs** have emission bands around 600 nm. These spectra also confirm that the CdSe **QD** emission can be detected in the solid state with the experimental setup that we have developed.

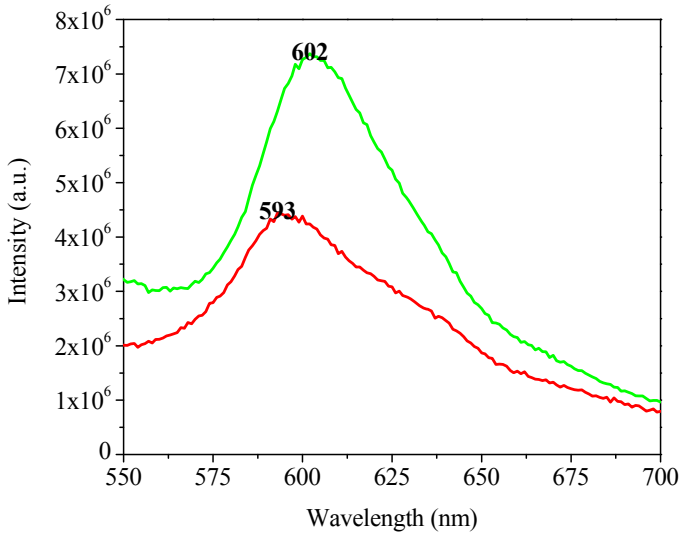

Figure 4.16 Emission spectra of two CdSe QD emitting around 600 nm.

Emission spectra were measured for the **UCNCs** and **UCNC/QD** samples, using a 980 nm diode laser for excitation of the sample through ytterbium. The resulting spectra, Figure 4.17, both show the characteristic Er^{3+} bands, but there is no detectable emission arising from the **QDs** at 600 nm. There is, however, a decrease in the intensity of the 523 and 545 nm erbium bands in the mixed sample. This decrease in erbium signal could indicate that some energy is transferred to the **QDs**, however, the resulting **QD** emission is too weak to be detected with our set-up. Alternatively, the **QDs** may be acting as filters, absorbing part of the erbium emission.

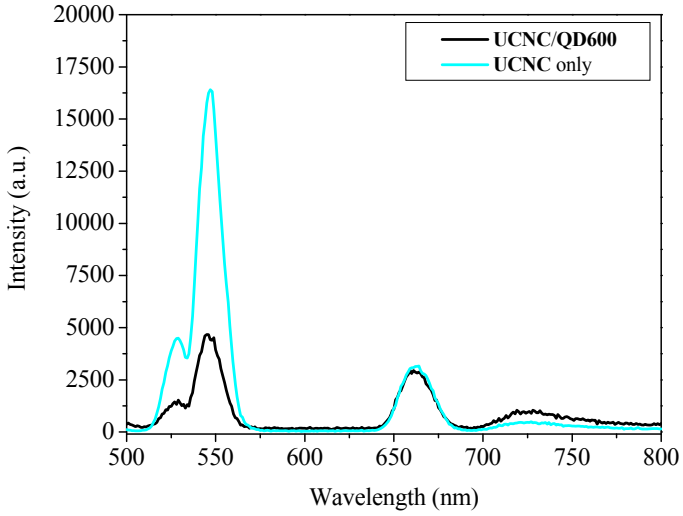

Figure 4.17 Emission spectra in the visible range upon excitation at 980 nm of UCNCs and UCNCs/QD600.

CdSe **QDs** have relatively low quantum yields in comparison to core-shell nanocrystals such as CdSe:CdTe **QDs**. This is due to the large surface area relative to total crystal size, which allows for extensive surface deactivation processes of the excited states through non-radiative routes such as surface trap states.[113,128-131] Since the experiments with **QD600** indicated the decrease in erbium signal, but no resultant **QD600** emission bands, it is possible that the **QD600** emission is quenched due to excited state relaxation through non-radiative routes rather than emission. Therefore, the experiment was repeated using 705 nm emitting CdSe:CdTe core-shell **QDs** (**QD705**). The results of this combination are shown in Figure 4.18. When excited at 545 nm, the sample displays **QD705** emission, indicating that the **QD** sample can be excited at the appropriate wavelength to accept erbium energy transfer and produce detectable emission in the solid state. When excited at 980 nm with the diode laser, a weak erbium signal is detected in the visible range; however, no detectable **QD705** emission is seen. Since the **QD705** absorbance

band extends over both the erbium bands, it is not possible to determine if **QD705** is absorbing the erbium energy by comparing the relative intensities of the two erbium bands. However, the erbium signal is much weaker for this system than observed without **QDs,** so it is likely that the **QD** is absorbing energy from erbium. Similar to the **QD600** system, no Quantum Dot emission is observed upon excitation through ytterbium, which may again be due to QD relaxation through non-radiative routes rather than emission.

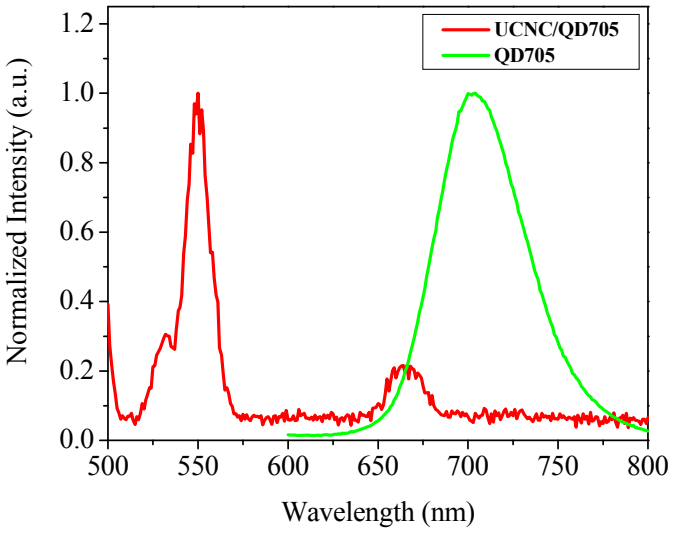

Figure 4.18 Emission spectra in the visible range of QD705 in the solid state excited at 450 nm and an UCNC/QD705 sample excited at 980 nm.

Evidence of absorption of erbium energy by the **QDs** has been demonstrated, however, it has not resulted in detectable sensitized **QD** emission. Thus the actual results of these experiments are not conclusive. There may be energy transfer, but not sufficient levels of **QD** emission to detect. Or, the decreased erbium emission intensities may be due to a non-radiative

quenching by the QD or the broad absorbance bands of the **QDs** acting as filters, absorbing the erbium emission prior to reaching the detector. To further investigate the possibility of energy transfer from upconverting nanocrystals to another chromophore with broader emission bands, the **UCNCs** were mixed with a variety of organic dyes. The organic dyes were chosen because of their high quantum yields, which increases the likelihood of detecting any emission due to energy transfer from the erbium band of upconverting materials. Five organic dyes with appropriate absorbance and emission wavelengths were chosen to test: rhodamine590 (Figure 4.19), rhodamine610 (Figure 4.20), rhodamine640 (Figure 4.21), LDS698 (Figure 4.22), and LDS750 (Figure 4.23).

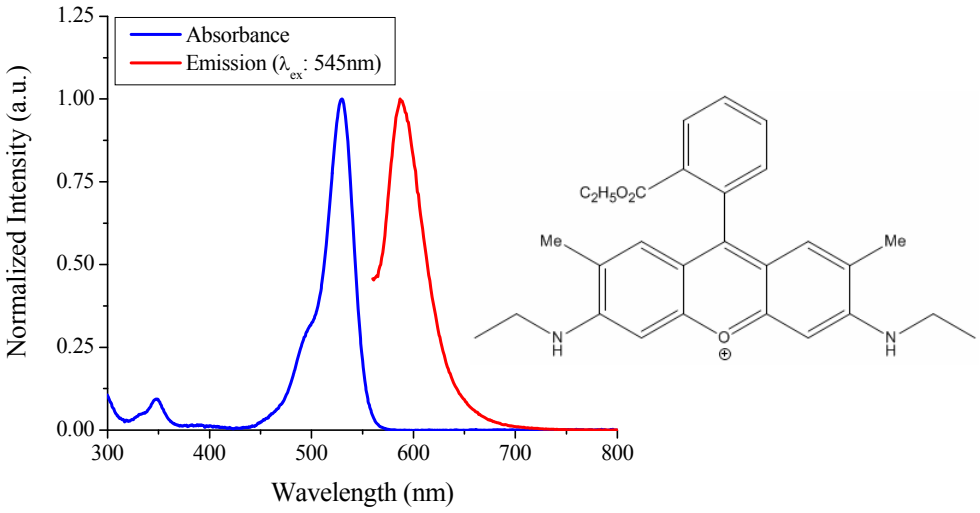

Figure 4.19 Rhodamine 590 structure (right) and absorbance and emission spectra (left).

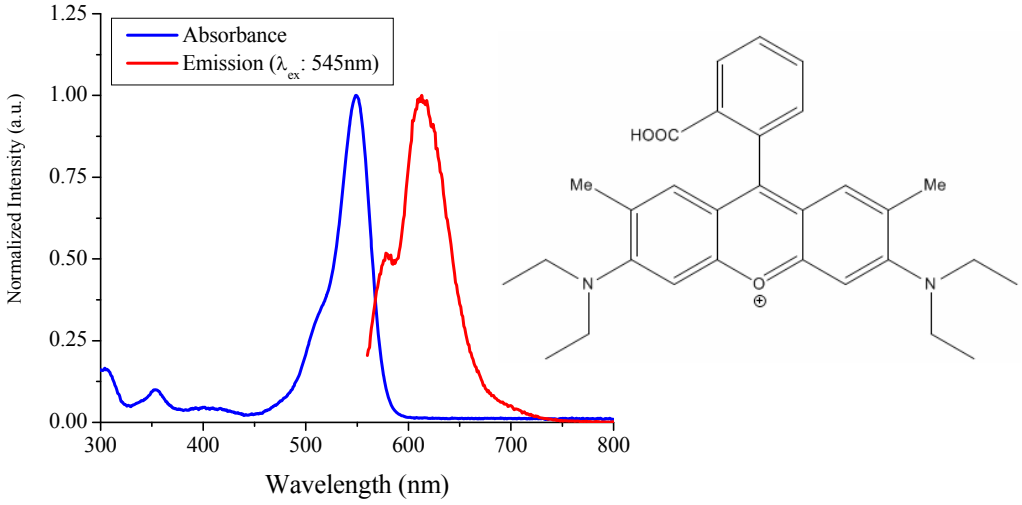

Figure 4.20 Rhodamine 610 structure (right) and absorbance and emission spectra (left).

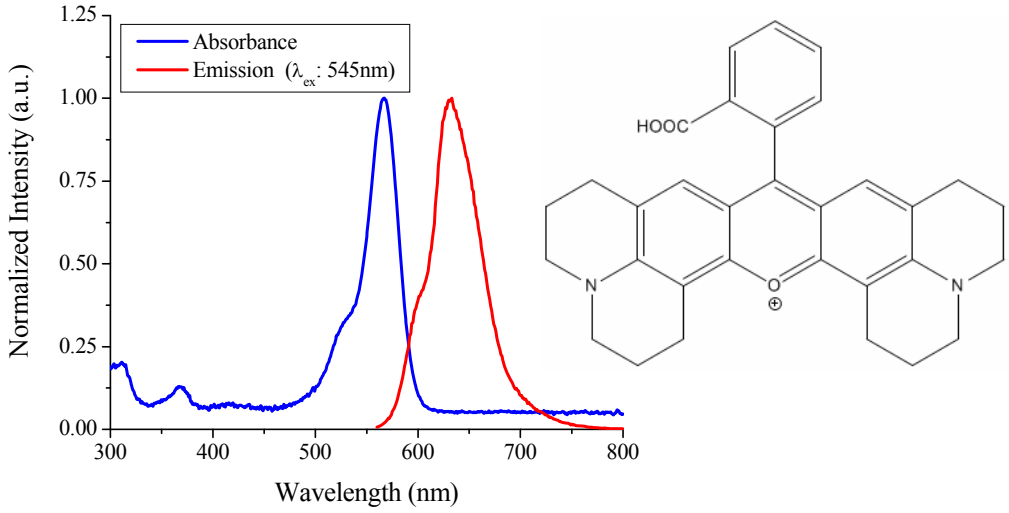

Figure 4.21 Rhodamine 640 structure (right) and absorbance and emission spectra (left).

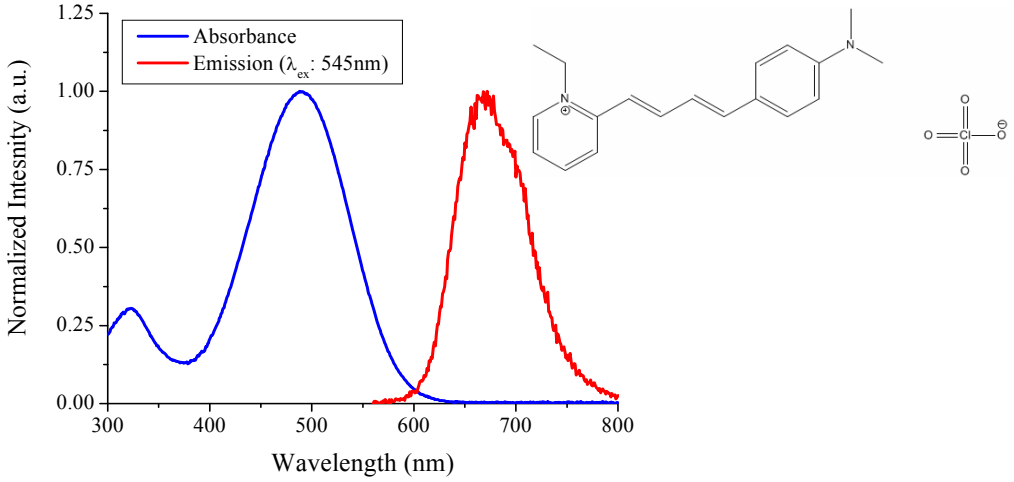

Figure 4.22 LDS698 structure (right) and absorbance and emission spectra (left).

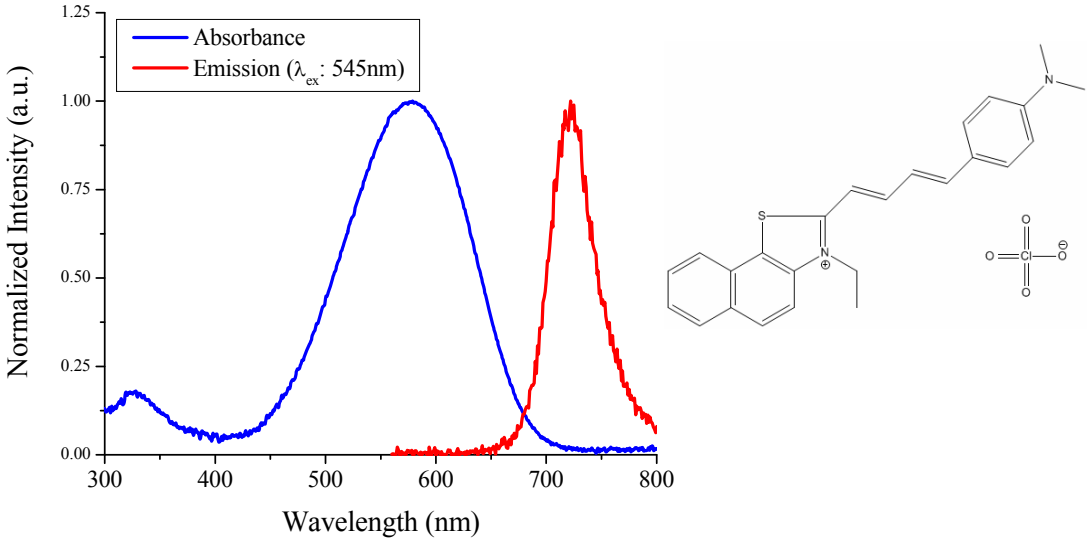

Figure 4.23 LDS750 structure (right) and absorbance and emission spectra (left).

The **UCNCs** were dispersed in water with sonication and mixed with concentrated (approximately 1 mg/mL) solutions of organic dyes in ethanol to make 50:50 ethanol:water solutions of dye and nanocrystals. The solutions were prepared such that there was a large excess

of dye to **UCNCs** in order to maximize the amount of energy transfer acceptors and the corresponding potential emission signal. Emission spectra were collected in the visible range upon excitation at 980 nm with the diode laser for the solutions, shown in Figure 4.24. Similar to the results with **QD** mixes, the solutions with the LDS dyes displayed a change in the relative intensity of the two erbium bands indicating some absorption of the erbium signal, but no dye emission was detected. However, with the rhodamine dye mixtures the green emission bands of erbium are quenched, and some dye emission is detected. These spectra indicate that sensitized emission of a chromophore as a result of energy transfer (i.e. FRET) from upconverting nanocrystals may be possible.

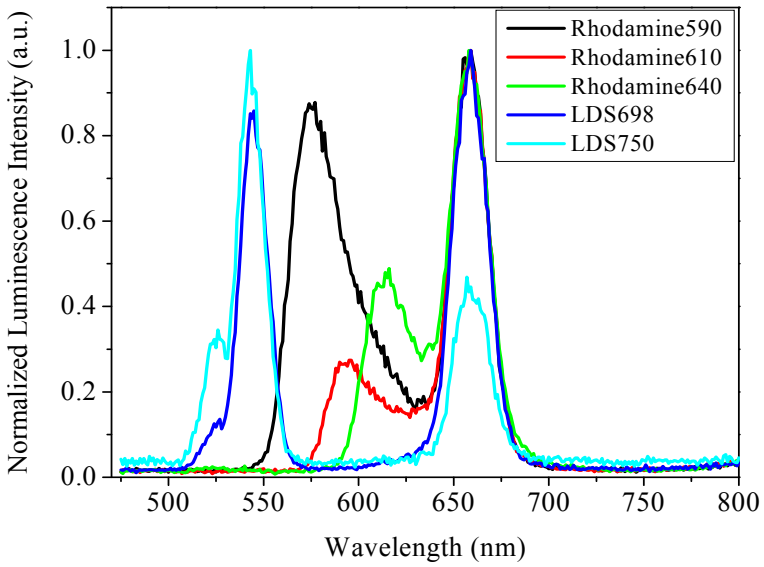

Figure 4.24 Emission spectra of the upconverting nanocrystal and organic dye solutions collected upon excitation at 980 nm with a diode laser.

These results are exciting; however, they are not conclusive. The ratio of the intensity of the dye emission bands to the erbium emission bands is within the quantum yield efficiency of the rhodamine dyes, which have exceptionally high quantum yields of nearly 100% at room temperature.[132,133] The detected emission may be due to the dye absorbing the emitted erbium photons resulting in excited rhodamine molecules which relax via emission; thus a non-radiative energy transfer operating through a fluorescence resonance energy transfer (FRET) mechanism can not be assumed. In other words, the erbium photons may be acting as a lamp to excite the dyes, with no actual energy transfer taking place.

To further clarify our interpretation of these results, there are two different paths for energy transfer to occur between the upconverting nanoparticles and organic dyes. 1) FRET, which involves a dipole/dipole resonance between the donor and acceptor, which can occur when there is an overlap between the emission band of the donor and the absorbance band of the acceptor. This is an efficient mechanism of energy transfer. 2) Reabsorption, where energy transfer occurs when photons emitted by the donor are absorbed by the acceptor, which is much less efficient. Due to the high quantum yields of organic chromophores in these experiments, the possibility of detecting emission resulting from energy transfer through the latter route is reasonable. Based on the current results, it can not be determined which energy transfer mechanism takes place between the upconverting nanoparticles and the organic dyes. One method to distinguish between the two energy transfer processes would involve monitoring the radiative lifetimes of the visible range erbium emissive states with and without the presence of the organic dyes. For a FRET mechanism, a decrease in the erbium radiative lifetimes would be observed, whereas no change in donor lifetime should occur for energy transfer through

reabsorption. Unfortunately these experiments would require a pulsed 980 nm laser excitation source which is not currently available.

4.3.1.3. $NaY_{(0.78)}Yb_{(0.20)}Er_{(0.02)}F_4$ Nanocrystals as Energy Acceptors from Naphthalimides

The first step to determine if any of the four naphthalimide molecules (see 4.1.1.2) are appropriate antennae for sensitizing Yb^{3+} to Er^{3+} upconversion luminescence involved analyzing the properties of their complexes with Yb^{3+}. It was necessary to determine if they sensitize Yb^{3+} luminescence with the appropriate wavelengths for upconversion, above at least approximately 550 nm, preferably above 650 nm. The Yb^{3+} naphthalimide complexes were formed in DMSO or DMF by first dissolving the naphthalimide molecule, deprotonating with 1 equivalent of tetraethylamine hydroxide, and finally adding 1/3 of an equivalent of Yb^{3+} for an M:L ratio of 1:3. Successful formation of complexes with Yb^{3+} were confirmed by the sensitized luminescence of Yb^{3+} detected spectroscopically (see Figure 4.28, Figure 4.29, Figure 4.30, and Figure 4.31). The 1 to 3 ratio was chosen based on balancing the charge, the actual ratio of the complexes in solution may vary from this. However, the goal of these experiments was only to establish if the naphthalimide molecules could bind to and sensitize ytterbium, thus determining the exact nature of the complexes formed in solution is beyond the scope of this research.

The absorbance spectra of the four Yb^{3+} - naphthalimide complexes are shown in Figure 4.25. As seen, Yb:**Naphth-NH_2** has the lowest energy absorbance bands, followed by Yb:**Naphth-NO_2**. However, the absorbance spectra of Yb:**Naphth-H**, Yb:**Naphth-Br**, and Yb:**Naphth-NO_2** taken at higher concentration, shown in Figure 4.26, show that all have absorbance shoulders in the 550 nm wavelength region. Interestingly, the absorbance spectra of the naphthalimide molecules do not change upon deprotonation or addition of the lanthanide

cation, as demonstrated by the Yb^{3+}:**Naphth-NO_2** spectra shown in Figure 4.27. This indicates that the electronic structures of the chromophoric groups are not influenced by changes to the carboxylic acid binding site. This is beneficial for the proposed application as antennae for ytterbium in upconverting nanocrystals, since they will be bound at the surface of the nanoparticle, and not necessarily bound to only lanthanide cations. If binding to the lanthanide cation was necessary to obtain the appropriate donating energy levels for the antenna, then when bound to the nanoparticle surface at both lanthanide and non-lanthanide coordinating sites, only a portion of the ligands could excite the lanthanide cations, reducing the potential efficiency of this method.

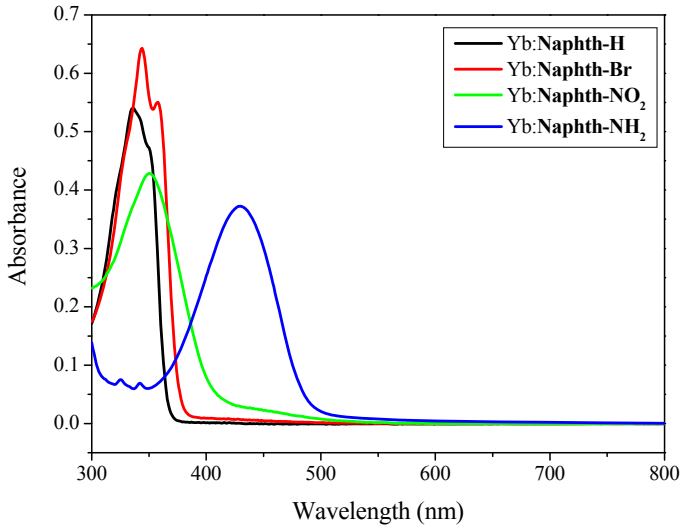

Figure 4.25 Absorbance spectra of the Yb^{3+} - naphthalimide complexes in DMSO (5 x 10^{-5} M naphthalimide concentration).

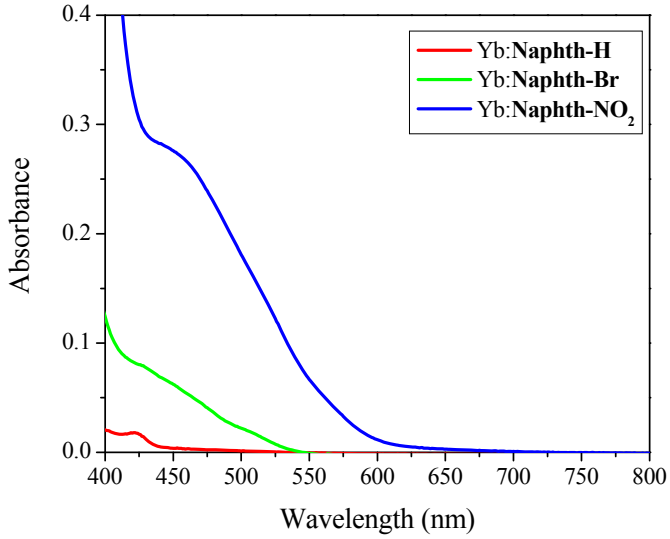

Figure 4.26 Absorbance spectra of the Yb^{3+} - naphthalimide complexes in DMSO (5 x 10^{-4} M naphthalimide concentration).

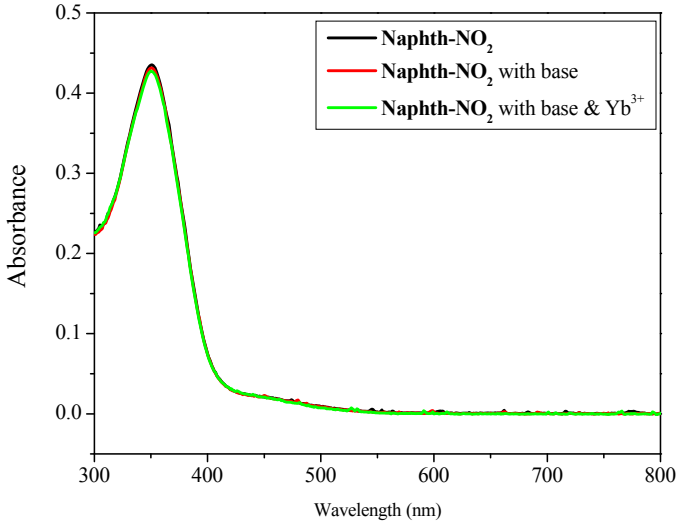

Figure 4.27 Absorbance spectra of Naphth-NO_2 in DMSO, deprotonated with tetraethylamine hydroxide in DMSO, and with Yb^{3+} in DMSO.

The emission and excitation spectra of the Yb^{3+} - naphthalimide complexes were monitored to determine the wavelength ranges in which the naphthalimide molecules could sensitize ytterbium emission. As seen in Figure 4.28, Figure 4.29, and Figure 4.30, **Naphth-H**, **Naphth-Br**, and **Naphth-NO_2** follow similar trends to their absorption spectra. The most efficient excitation wavelengths for ytterbium are above 500 nm; however, the lower energy shoulder wavelengths are also able to sensitize the NIR emission. For all three complexes, excitation wavelengths out to 650 nm are possible, with Yb:**Naphth-NO_2** also exciting up to 700 nm. The Yb:**Naphth-NH_2** complex had different properties, however, as seen in Figure 4.31. While this complex had the lowest energy absorbance bands of the four naphthalimides, it does not have a lower energy shoulder. The low energy band is efficient at sensitizing ytterbium, and the excitation spectrum profile mirrors the absorbance spectrum. In addition to ytterbium emission in the NIR, **Naphth-NH_2** has a large triplet state band which makes the ytterbium band difficult to detect; it can be seen as a small bump on the triplet state band. Since the two signals can not be separated, it is not possible to determine an excitation spectrum for the ytterbium band alone. To determine if **Naphth-NH_2** would be a possible antenna for the **UCNCs**, the Yb: **Naphth-NH_2** complex was excited at 630 nm with a diode laser, and the NIR emission spectrum was monitored for Yb^{3+} luminescence. As seen in Figure 4.32, there is no detectable ytterbium emission; thus **Naphth-NH_2** is not a suitable antennae for the **UCNCs**. Based on these results, **Naphth-NO_2** was chosen as the best potential antennae and was used for future experiments.

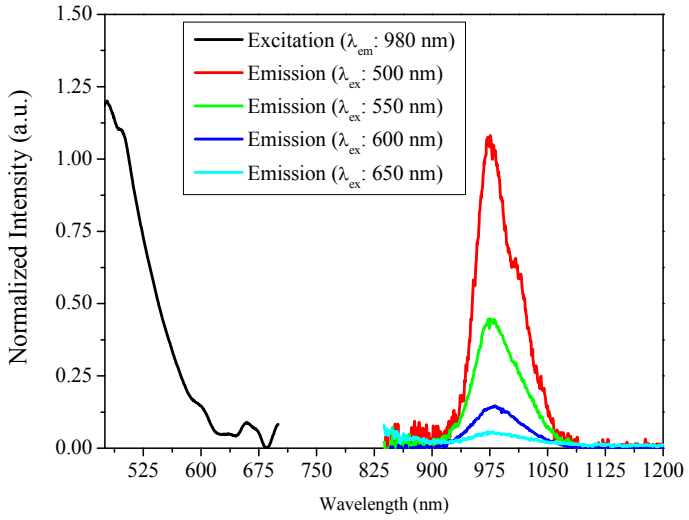

Figure 4.28 Excitation and emission spectra of ytterbium luminescence for Yb:Naphth-H in DMSO.

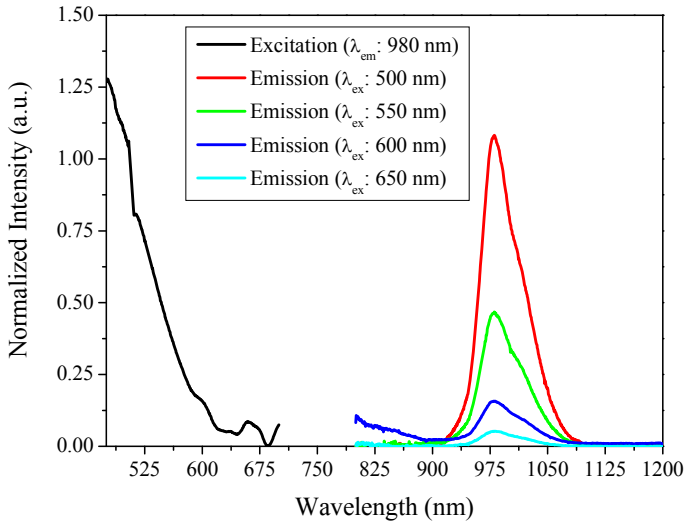

Figure 4.29 Excitation and emission spectra of ytterbium luminescence for Yb:Naphth-Br in DMSO.

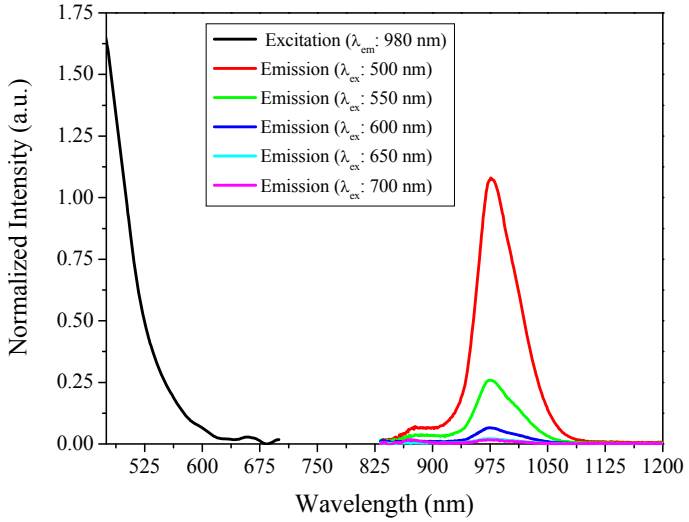

Figure 4.30 Excitation and emission spectra of ytterbium luminescence for Yb:Naphth-NO_2 in DMSO.

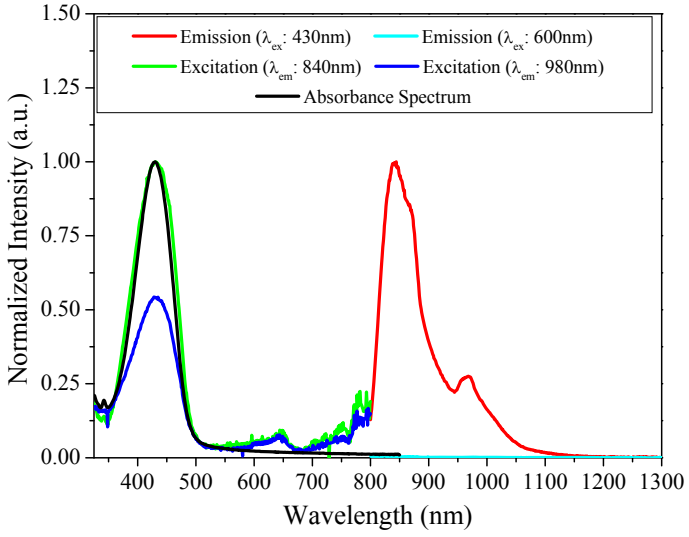

Figure 4.31 Absorbance spectrum and excitation and emission spectra of NIR luminescence for Yb:Naphth-NH_2 in DMF; the NIR emission spectrum shows a large triplet state emission band as well as a less intense ytterbium signal at 980 nm. The profile of the triplet state emission band is distorted by the effect of the 780 nm cut-on filter.

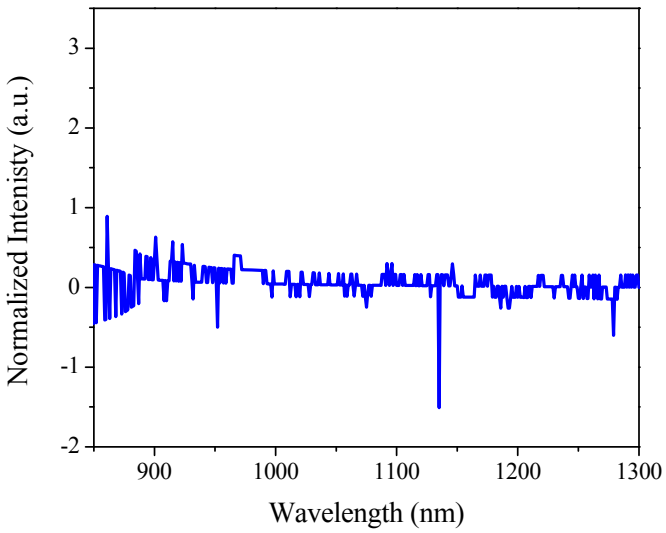

Figure 4.32 Emission spectrum in the NIR of Yb:Naphth-NH_2 in DMF with 630 nm diode laser excitation.

To determine if **Naphth-NO_2** could act as an antenna for ytterbium in **UCNCs**, **Naphth-NO_2** capped **UCNCs** (**UCNC-NAP**) were prepared and analyzed. For this work, **UCNCs** prepared with the high temperature organic solvent method were used. They were chosen because the organic groups coating the surface of the nanocrystals after synthesis provide improved solubility in organic solvents, which facilitates the surface exchange reactions to coat the nanocrystals with **Naphth-NO_2**. While these **UCNCs** display weaker upconversion erbium spectra than the annealed aqueous samples, when a 980 nm diode laser excitation is used instead of the SPEX Fluorolog xenon arc lamp, the erbium emission is sufficiently intense to be clearly detected (demonstrated in Figure 4.37). Absorbance and emission spectra of the **UCNC-NAP** confirm the presence of **Naphth-NO_2** on the nanocrystal surface, as shown in Figure 4.33.

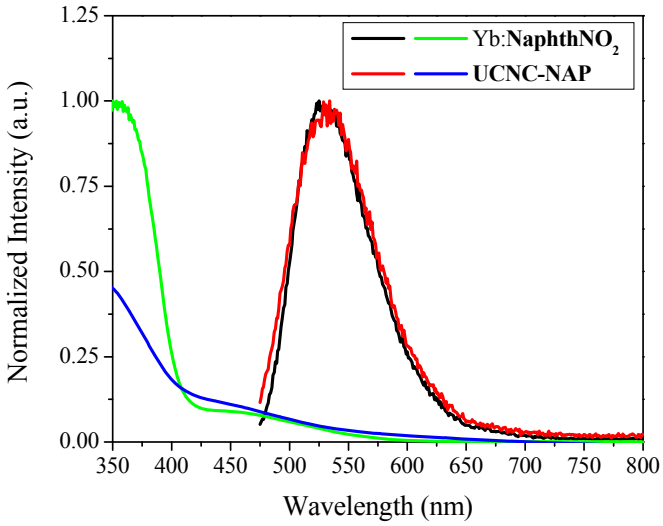

Figure 4.33 Absorbance (green & blue) and emission spectra (red & black) with λ_{ex}: 435 nm of Yb:NaphthNO$_2$ and UCNC-NAP. The good overlap of the spectra between the two samples demonstrates successful surface exchange with Naphth-NO$_2$.

The **UCNC-NAP** were analyzed spectroscopically for evidence of antenna sensitized erbium upconversion luminescence. The emission spectra monitored in the NIR range upon exciting through **Naphth-NO$_2$** at 435 nm with the JY Horiba Fluorolog xenon arc lamp and at 630 nm with a diode laser both display ytterbium emission at 980 nm (Figure 4.34). When compared to the NIR spectra of the Yb:**Naphth-NO$_2$** collected under the same conditions, one can see that the **UCNC-NAP** also contain an erbium emission band around 900 nm. These spectra provide evidence that **Naphth-NO$_2$** is able to sensitize ytterbium within the nanocrystals, which is a necessary feature for serving as an antenna for the system. In addition, the spectra demonstrate that the **Naphth-NO$_2$** can also sensitize detectable levels of erbium within the nanocrystal. This was an unexpected result as erbium is only present in a small amount (2% of total lanthanide concentration) in the **UCNC-NAP**. The excitation spectrum corresponding to

UCNC-NAP emission at 980 nm is dominated by the absorbance bands of Er^{3+}, shown in Figure 4.35. Large band pass slit widths (14 nm for the excitation source and 40 nm for the emission detector) are necessary for the sample to produce sufficient signal for our instrument to detect. At these large slit widths, much resolution is lost and the erbium emission band at 900 nm is also detected, causing this effect. Interestingly, the excitation band begins to get intense after 400 nm, where the absorbance of the **Naphth-NO_2** decreases significantly. This is likely due to the inner-filter effect, where the high absorbance in this range prevents excitation light from passing all the way through to the center of the cuvette so no excited luminescence can be detected.

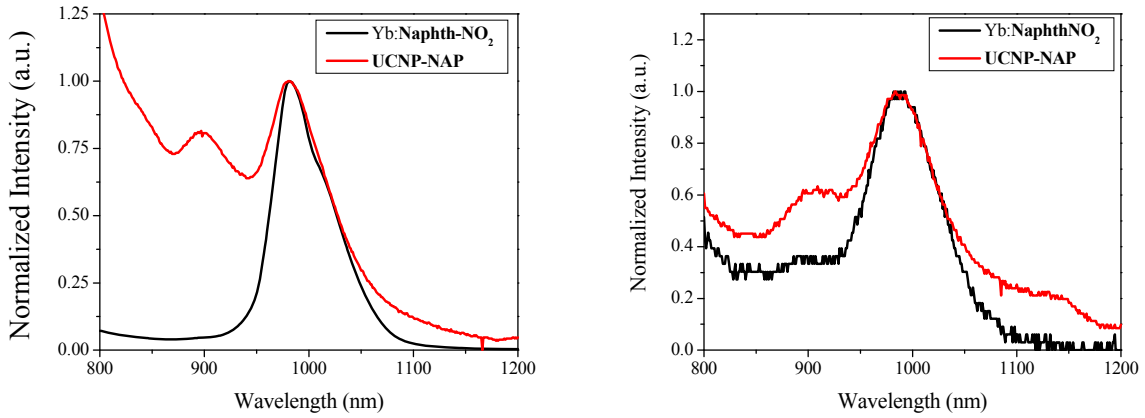

Figure 4.34 NIR emission spectra of Yb:Naphth-NO_2 and UCNC-NAP with Xenon λ_{ex}: 435 nm (left) and diode laser excitation at 630 nm (right) .

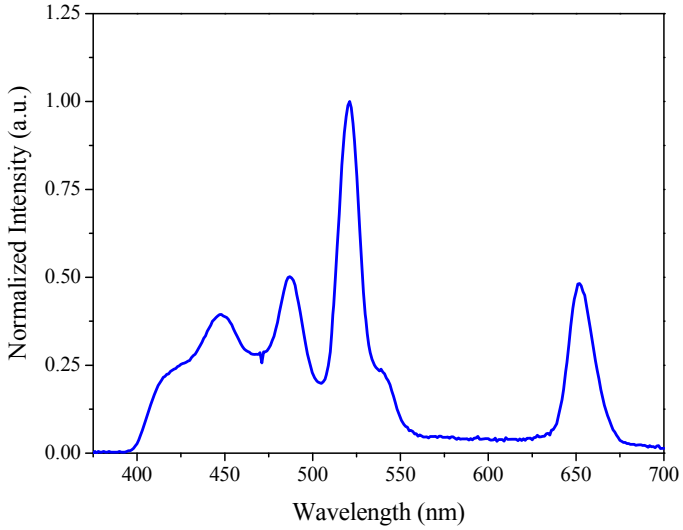

Figure 4.35 Excitation spectrum upon monitoring the UCNC-NAP emission at 980 nm.

The **UCNC-NAP** were excited at 630 nm with a diode laser, and their emission spectrum in the visible range was monitored for evidence of erbium emission bands located between 500 and 550 nm. With emission slits corresponding to band widths up to 5 nm, no erbium emission was detected, as seen in Figure 4.36 left. However, the diode laser produced emission with a shoulder out to approximately 580 nm, as seen in the emission spectrum of the diode laser, Figure 4.36 right. As the emission slits of the instrument are widened to increase the likelihood of detecting any sensitized erbium upconversion luminescence, this shoulder becomes increasingly problematic and interferes with the desired detection regions. Thus, while no sensitized erbium upconversion luminescence was seen, it may be present but not sufficiently intense to be evidenced (separated spectroscopically) within the constraints of the instrumentation.

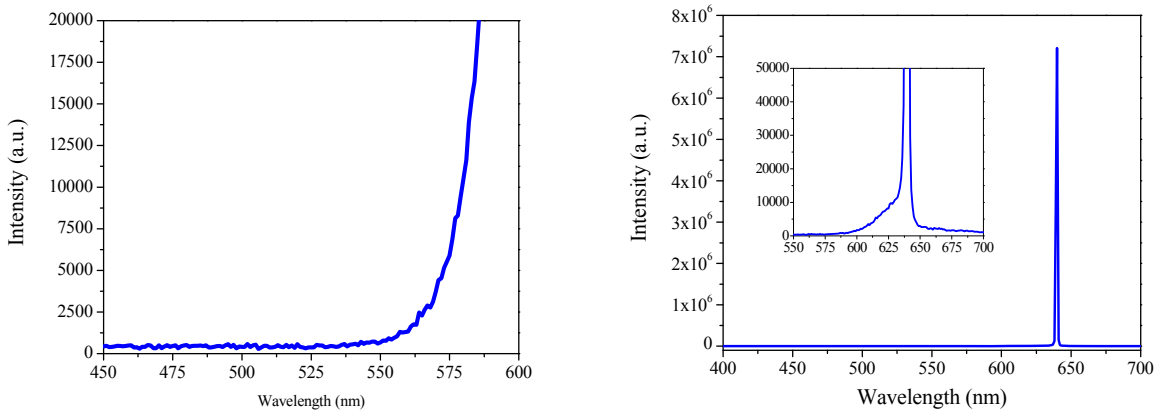

Figure 4.36 Left) Emission spectrum of UCNC-NAP in DMSO with 630 nm diode laser excitation and 5 nm emission slits. Right) Emission spectrum of the 630 nm diode laser with 1 nm emission slits; inset is the magnified view of the 550 – 700 nm region.

Since **Naphth-NO_2** has absorbance up to around 550 nm, covering the 500 to 550 nm region where erbium upconversion bands should appear, quenching of the erbium bands by the **Naphth-NO_2** may be a problem. The **UCNC-NAP** were excited with a diode laser at 980 nm, and their emission spectrum in the visible was monitored. As seen in the spectrum in Figure 4.37, the erbium bands are clearly detected, thus indicating that the **Naphth-NO_2** absorbance does not fully quench the erbium emission and this can not explain the lack of erbium signal when exciting the system through **Naphth-NO_2** bands at 630 nm.

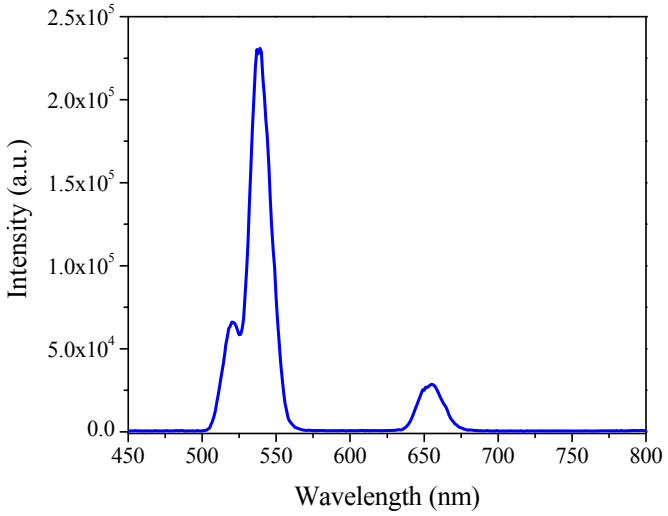

Figure 4.37 Emission spectrum in the visible range for UCNC-NAP in DMSO upon excitation at 980 nm.

Since the results described here give evidence that suggests upconversion through ytterbium sensitized by the Napth-NO_2 would be possible, future experiments with a more intense and narrow excitation laser could be conducted.

4.3.2. Tropolonate capped $NaY_{(1-x)}Ln_xF_4$ Nanocrystals

The results presented here have been published in the Journal of the American Chemical Society, Vol. 129, No. 48, p 14834 (2007).[24]

The binding of the tropolonate groups to the surface of nanocrystals was monitored through FT-IR spectroscopy, as illustrated in Figure 4.38. Upon reaction, the absorption bands assigned to the original capping ligands of the nanocrystals (oleic acid, oleylamine, and octadecene) present at 2,924 and 2,854 cm^{-1} disappear, and are replaced by the characteristic absorption bands of tropolonate at 1,595 and 1,510 cm^{-1}.

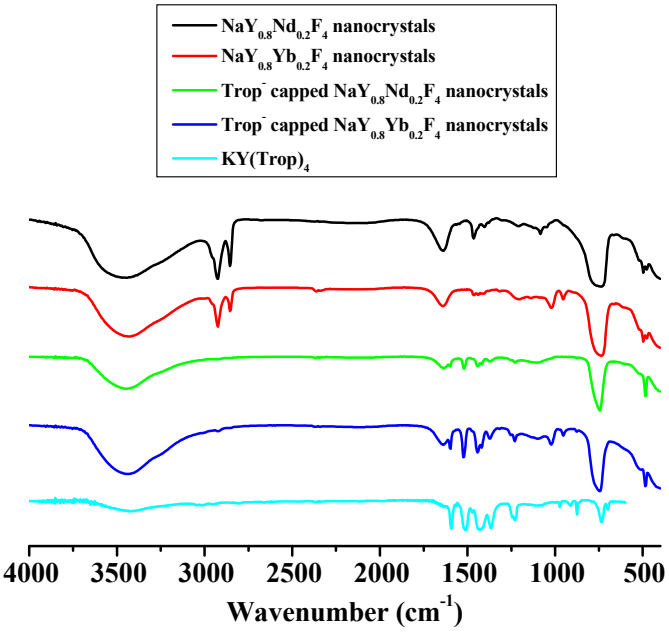

Figure 4.38. **FT-IR spectra of $NaY_{0.8}Nd_{0.2}F_4$ and $NaY_{0.8}Yb_{0.2}F_4$ nanocrystals, tropolonate capped $NaY_{0.8}Nd_{0.2}F_4$ and $NaY_{0.8}Yb_{0.2}F_4$ nanocrystals. For comparison, the FT-IR spectra of $KY(Trop)_4$ is also depicted.**

The XRD patterns (Figure 4.39) of the uncapped and capped $NaY_{0.8}Ln_{0.2}F_4$ nanocrystals (Ln: Nd or Yb) reveal the formation of cubic α-$NaYF_4$ (space group: $Fm\bar{3}m$). All diffraction peak positions and intensities agree well with calculated values.[134]

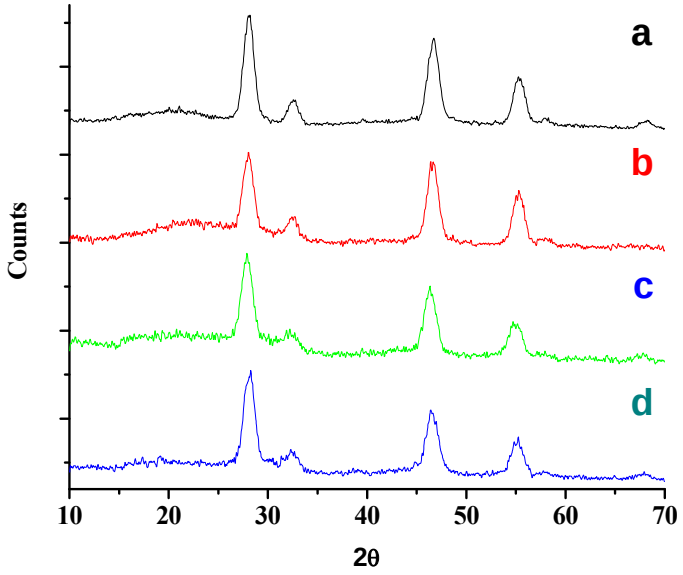

Figure 4.39 X-ray diffraction patterns of uncapped and capped nanocrystals. a: **$NaY_{0.8}Yb_{0.2}F_4$ nanocrystals,** b: **Tropolonate capped $NaY_{0.8}Yb_{0.2}F_4$ nanocrystals,** c: **$NaY_{0.8}Nd_{0.2}F_4$ nanocrystals,** d: **Tropolonate capped $NaY_{0.8}Nd_{0.2}F_4$ nanocrystals.**

Transmission electron microscopy (TEM) images (Figure 4.40) of both uncapped and capped nanocrystal samples also indicate that the obtained nanocrystals are of single-crystalline nature with high crystalline size uniformity. They are relatively monodisperse with roughly spherical shape. The average sizes are 6.1±0.6 nm, 6.0±0.6 nm, 5.3±0.7 nm and 5.3±0.6 nm for $NaY_{0.8}Yb_{0.2}F_4$ nanocrystals, tropolonate capped $NaY_{0.8}Yb_{0.2}F_4$ nanocrystals, $NaY_{0.8}Nd_{0.2}F_4$ nanocrystals and tropolonate $NaY_{0.8}Ln_{0.2}F_4$ nanocrystals, respectively (Figure 4.41). Such relatively small sizes are compatible for use in many bioanalytical applications.

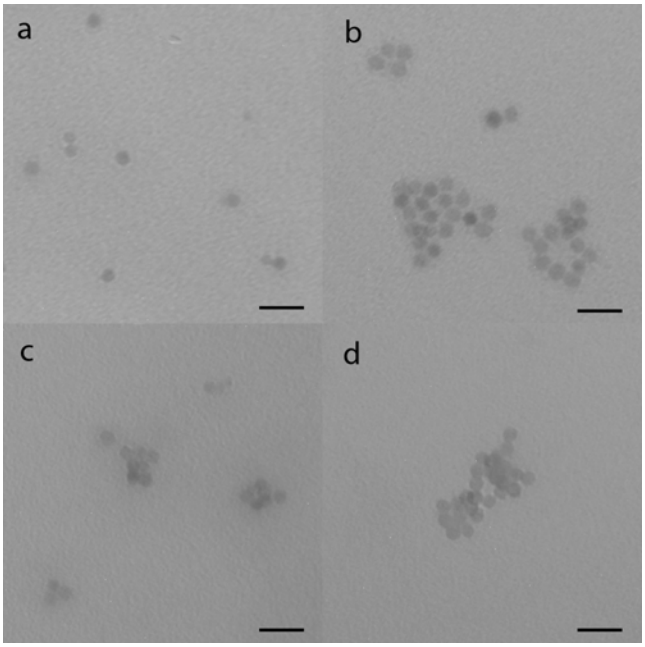

Figure 4.40 Transmission electron microscopy images (scale bar: 20 nm) of uncapped and capped nanocrystals. a: **$NaY_{0.8}Yb_{0.2}F_4$ nanocrystals,** b: **Tropolonate capped $NaY_{0.8}Yb_{0.2}F_4$ nanocrystals,** c: **$NaY_{0.8}Nd_{0.2}F_4$ nanocrystals,** d: **Tropolonate capped $NaY_{0.8}Nd_{0.2}F_4$ nanocrystals.**

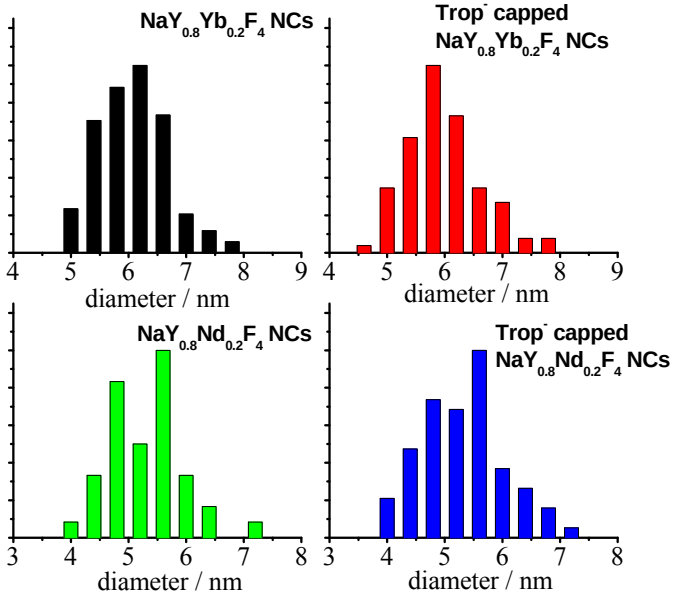

Figure 4.41 Histogram of the nanocrystal size distribution derived from the TEM images.

The UV-vis absorption spectra (Figure 4.42) of tropolonate capped nanocrystals in DMSO reveal the presence of two bands with apparent maxima centered around 323 nm and 384 nm, similar to those observed for $[Ln(Trop)_4]^-$, further confirming the presence of tropolonate on the surface of nanocrystals. Upon excitation at 340 nm, the characteristic sharp NIR emission bands arising from Nd^{3+} or Yb^{3+} were observed (Figure 4.42). Both Nd^{3+} and Yb^{3+} luminescence have similar excitation profiles (Figure 4.43), and neither of the free lanthanide cations has absorbance at these wavelengths; thus this demonstrates that the lanthanide cations are sensitized through the electronic structure of the tropolonate ligand. There is a significant energy gap between the energy donating levels of tropolonate and accepting levels of the Yb^{3+}. Energy transfer over this large gap could be explained by phonon assisted or electron-transfer mechanisms.[19,135]

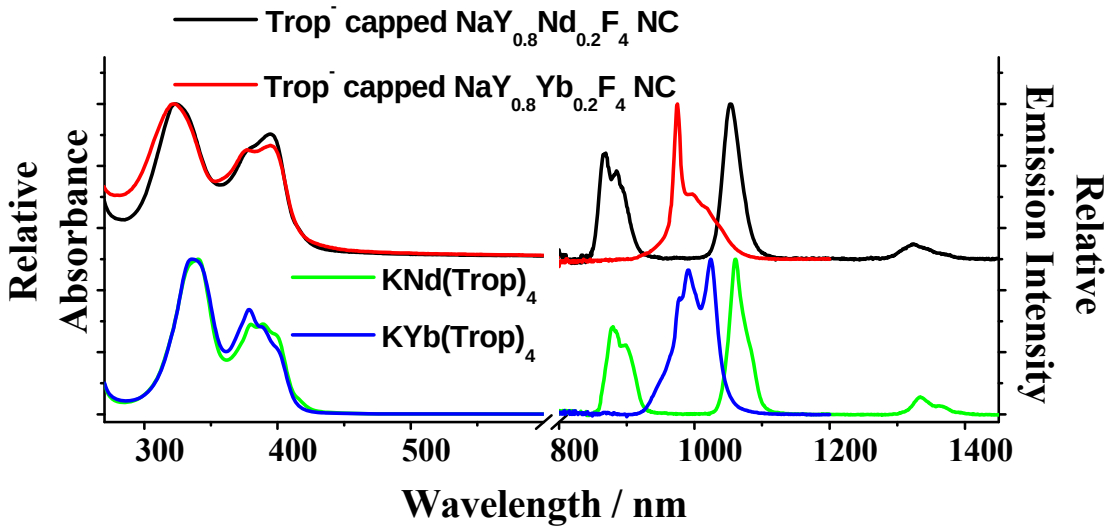

Figure 4.42 Normalized UV-visible absorption (left) and NIR luminescence emission spectra (right) of the $[Ln(Trop)_4]^-$ complexes (bottom) (λ_{ex} = 340 nm, 10^{-4} M) and tropolonate capped nanocrystals (c.a. 1 gL^{-1}) in DMSO (top).

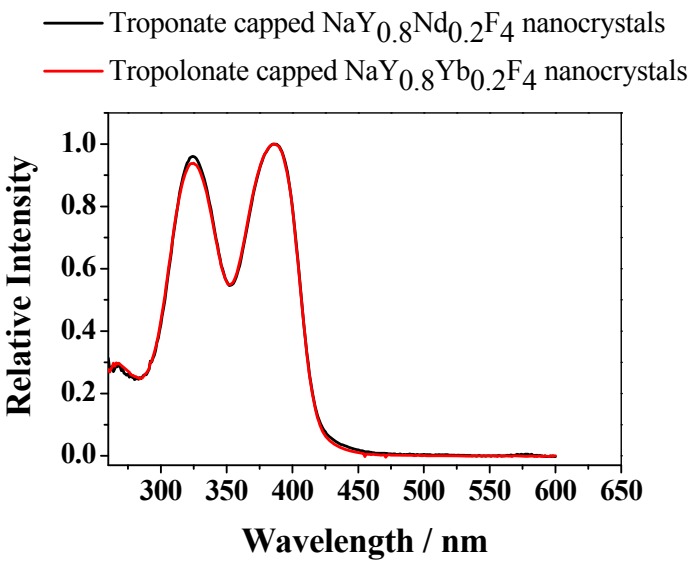

Figure 4.43 Normalized NIR luminescence excitation spectra of the complex tropolonate capped nanocrystals (c.a. 1 gL^{-1}) in DMSO. Emission wavelengths were set as 1055 nm for neodymium and 975 nm for ytterbium.

The lifetimes of the luminescence arising from Nd^{3+} and Yb^{3+} in tropolonate capped nanocrystals and in $[Ln(Trop)_4]^-$ complexes in DMSO are reported in Table 4.1.[24] It is important to note that the Nd^{3+} and Yb^{3+} luminescence decays in $[Ln(Trop)_4]^-$ complexes are best fit as mono-exponential decays, indicating a unique coordination environment around the central Ln^{3+}.[7] Since there should be more than one coordination environment for Ln^{3+} in the nanocrystals (*ie.* core and surface), multi-exponential decay profiles are expected. The experimental results reflect this hypothesis. For Yb^{3+} in the nanocrystals, the experimental decay was best fitted as a bi-exponential function. The longest component is attributed to the luminescence decay from cations in the nanocrystal core and is the major contribution to the overall intensity. The second component is significantly shorter and can be attributed to Yb^{3+} with a lower level of protection from non-radiative deactivation, likely located at the surface of the nanocrystals. The experimental decay recorded for Nd^{3+} in the nanocrystals is best fit with a

triple exponential decay. Similar to Yb^{3+}, there is a long component which corresponds to luminescence decay from Nd^{3+} in the nanocrystal matrix. The two shorter components are assigned to Nd^{3+} at or near the nanocrystals surface in different coordination environments. Since Nd^{3+}, unlike Yb^{3+}, has a large number of excited states, and thus additional routes for non-radiative deactivations, it may be more sensitive to coordinating ligands than Yb^{3+} resulting in additional lifetime components.

Table 4.1 Luminescence lifetimes (microseconds) of the lanthanide tropolonate complexes and tropolonate capped nanocrystals; contribution to luminescence intensity in brackets.[24]

	$NaY_{0.8}Ln_{0.2}F_4$ nanocrystal	$KLn(Trop)_4$
Yb	68(3), [80(2)%]	12.43(9)
	4.1(4), [20(2)%]	
Nd	12.6(9), [22(1)%]	1.10(4)
	3.7(2), [63(6)%]	
	1.1(2), [15(6)%]	

Globally, significantly longer luminescence lifetimes were observed for the tropolonate capped Yb^{3+}/Nd^{3+} doped nanocrystals than for the corresponding molecular complexes. The longest components among the luminescence lifetimes were more than 5 times longer for Yb^{3+} and more than 11 times longer for Nd^{3+}. These values prove that the strategy to increase protection around the lanthanide cations through their incorporation in nanocrystals is successful.

4.4. CONCLUSIONS

4.4.1. $NaY_{(0.78)}Yb_{(0.20)}Er_{(0.02)}F_4$ Nanocrystals as Energy Donors to Quantum Dots

$NaY_{(0.78)}Yb_{(0.20)}Er_{(0.02)}F_4$ nanocrystals were combined with Quantum Dots to investigate the potential of **UCNCs** to serve as donors to other chromophores and thus provide the potential for a wider range of upconversion emission bands. Mixing the two materials in the solid state did demonstrate that there may be energy transfer to **QDs**, however, no detectable **QD** emission was seen. Combining the **UCNCs** with organic rhodamine dyes did result in quenching of the donor emission bands along with the appearance of rhodamine emission bands, providing further indication that energy transfer to the **QDs** is occurring, but they are not producing sufficient levels of emission intensity to be detected.

Since energy transfer processes are distance dependent, chemically linking the two nanocrystals together may increase the efficiency of any energy transfer taking place and improve the likelihood of detecting it. The **UCNCs** can be made much larger than the **QDs**, whose size dictate the emission wavelength and are not variable, so designing a linker to allow multiple Quantum Dots to adhere to the surface of a single **UCNC**, as demonstrated below in Figure 4.44 would be the most feasible first step. Such linking could be achieved through DNA chains,[136,137] or bioconjugation using interacting protein pairs such as biotin and streptavidin[138]. If these nanomaterials demonstrate successful Quantum Dot upconversion emission via energy transfer from **UCNC** erbium emission bands, they could be encapsulated within a silica matrix for a biologically compatible final product.[139]

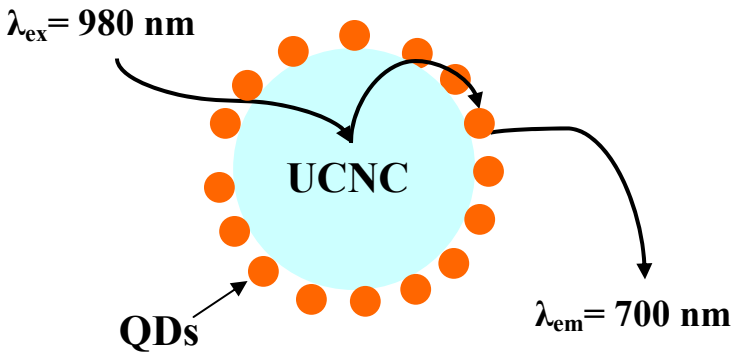

Figure 4.44 Scheme of UPNC-QD700 combined upconverting nanomaterial.

4.4.2. $NaY_{(0.78)}Yb_{(0.20)}Er_{(0.02)}F_4$ Nanocrystals as Energy Acceptors from Naphthalimides

A series of naphthalimide molecules were investigated for their potential to serve as antennae for upconverting $NaY_{(0.78)}Yb_{(0.20)}Er_{(0.02)}F_4$ nanocrystals. **Naphth-NO_2** demonstrated the necessary traits for an organic chromophore antenna for this purpose, including low energy absorbance that does not fully quench the erbium upconversion emission bands in the 500 to 550 nm range and the capacity to sensitize ytterbium emission at 630 nm. However, despite these positive attributes, when bound to the surface of the **UCNCs**, exciting through **Naphth-NO_2** failed to produce any detectable levels of erbium upconversion luminescence. It may be that the process occurs, however, it is beyond the detection limits of the instrumentation. Alternatively, since the **Naphth-NO_2** is able to sensitize erbium emission in the NIR, the excited erbium may interfere with the upconversion process. Future experiments could be conducted with a laser that produces a more intense and narrow excitation band centered at a slightly higher energy (circa 600 nm) to elucidate what is happening within the **UCNC-NAP** system.

4.4.3. Tropolonate capped $NaY_{(1-x)}Ln_xF_4$ Nanocrystals

The innovative strategy to protect and sensitize NIR emitting Nd^{3+} and Yb^{3+} cations via doping in $NaYF_4$ nanocrystals coated with sensitizing tropolonate chromophores has demonstrated success. The nanocrystal matrix protects the Ln^{3+} from non-radiative deactivation via high energy vibrations of solvent molecules and/or of organic ligands, as proven by the longer luminescence lifetimes. This work has established proof of principle that it is possible to combine the antenna effect provided by organic chromophores with the protection from an inorganic matrix, thereby reducing the usual limitations of NIR lanthanide luminescence in coordination complexes.[24] This is a general strategy that can be expanded for application to different combinations of organic chromophores, lanthanide cations, and inorganic matrices. The nanocrystals have a relatively small size, and combined with the proper choice of ligand system(s) to give the capped nanocrystals water solubility, it could be possible to extend this methodology to bioanalytical applications.

5. METAL-ORGANIC FRAMEWORKS AS ANTENNAE FOR LANTHANIDE CATIONS

The work presented here has been completed in collaboration with Kiley White, Jihyun An and George Norton (Nathaniel L. Rosi Research Group, Department of Chemistry, University of Pittsburgh). A portion of the results presented here have been published in *Chemical Communications*, Vol. 30, p 4506, 2009: "Near-infrared Emitting Ytterbium Metal-Organic Frameworks with Tunable Excitation Properties."[140]

5.1. INTRODUCTION

In this approach to luminescent lanthanide complexes, the use of metal-organic framework (MOF) materials as a means to sensitize lanthanides and optimize their excitation and emission properties is explored. Metal-organic frameworks (MOFs) are a relatively new class of porous materials that consist of metal ions or clusters linked together into periodic two- or three-dimensional lattices via multitopic organic ligands.[141-145] The metal ions and ligands can be chosen to impart specific function to the MOF. To date, MOFs have been designed for many applications including gas storage and sequestration,[146-158] catalysis,[159-162] and separations.[163-166]. Several lanthanide-containing MOFs have been prepared, and sensing applications based on their

visible emission properties were explored.[167-175] However, MOFs have not yet been specifically designed to sensitize NIR emitting lanthanides.

The vast majority of MOFs have been synthesized with *d*-block metals; however, interest in using lanthanide cations has recently developed.[169,170,174,176-180] The hard lanthanide metal cations have a strong affinity for bonding with oxygen atoms, making carboxylate linkers ideal candidates for MOF reactions with lanthanides. The higher coordination numbers of lanthanide cations over *d*-block metals, along with the dependence of their coordination geometry on the sterics of the coordinated ligands rather than the coordination sphere of the metal, result in the formation of new topologies with potentially interesting properties.[181] For example, a recently synthesized MOF containing Eu^{3+} in an unprecedented icosahedra environment with a coordination number of 12 has demonstrated both the first example of an icosohedron geometry and the highest coordination number in a MOF.[180]

Solvent molecules typically coordinate to fill empty coordination sites of lanthanide cations. In lanthanide based MOFs, the solvent molecules can be removed upon heating, leaving empty Lewis-metal acid sites for the potential application in sensing or catalysis.[171,174] For example, upon solvent exchange (DMF to acetone) of a Eu MOF with coordinated water molecules, the luminescence did not change. However, after heating the MOF and removing the coordinated waters to free Lewis-acid metal sites, the luminescence output decreased with increasing acetone concentration and increased with increasing DMF concentration.[171] Importantly, this and other lanthanide containing frameworks remain intact after water or solvent removal.[173,178,182,183] The high coordination number of lanthanides combined with the porous nature of MOFs allows for interesting sensing capabilities.

Lanthanides are also being utilized in a novel area of metal-organic framework research: nanoscale MOFs (**NMOFs**). Only a few **NMOFs** have been synthesized to date, and to this point a synthetic strategy involving reverse microemulsions has been employed.[179,184] The particles or rods that form can be coated easily with silica to improve their biocompatibility and allow for post-synthetic functionalization for biological applications. The silica shells allows for enhanced water dispersibility and the controlled release of metal components. Wenbin Lin's group has already synthesized Gd MOFs doped with Eu^{3+} or Tb^{3+} that show potential to serve as contrast agents for multimodal imaging.[179] **NMOFs** also show great promise for biological sensing.[172] For example, a silica coated Eu^{3+}-doped Gd **NMOF** has been functionalized with a Tb-EDTA derivative, which is used as a luminescence probe for DPA, a molecular marker in spore producing material. Tb^{3+} luminescence was only visible upon addition of the DPA, indicating formation of a Tb-EDTA-DPA complex.[172] These few examples demonstrate the vast potential for combining the beneficial attributes of metal-organic frameworks with the unique luminescent properties of lanthanide cations.

The first goal of this work is to identify organic chromophores that can sensitize lanthanide cations via the antenna effect, which are suitable for the formation of MOFs. Then these organic chromophores will be utilized to develop lanthanide based metal-organic frameworks following two strategies: 1) Lanthanides will be incorporated as the metal component in the frameworks. 2) Lanthanide cations will be impregnated into the pores or cavities of rigid frameworks made with *d*-block metals.

Incorporating lanthanide cations as part of the MOFs offers several attractive features for lanthanide sensitization. Metal-organic frameworks are well-organized, rigid materials that allow for good control over the coordination environment around the lanthanide. They are constrained

in space, which can provide effective shielding of lanthanides from solvent vibrations even while in solution. MOFs can adopt a variety of topologies, which can be designed in an *a priori* fashion. MOFs allow for the careful control over the distance and angles between the sensitizers with respect to each other within the structure, which could lead to lower excitation energies. Topologies will be targeted to achieve π–π interactions between the organic groups, which provides the potential for tuning the electronic properties of the materials. Additionally, similar to lanthanide doped nanoparticles, the MOFs are polymetallic species with a high density of lanthanide cations, and thus photon emitters, per unit of volume. These structures can incorporate a large number of metal cations per unit volume, and the metal ion coordination spheres are often completely saturated by the ligands. In the context of lanthanide sensitization and luminescence, these features are important because increasing the density of lanthanide cations within a material will improve emission intensities.[185] The high number of chromophoric groups (ligands) surrounding each lanthanide will help maximize the absorption of excitation light, leading to more intense lanthanide luminescence. This has been demonstrated to be an effective approach for improved emission intensities.[185] Finally, multiple metal MOFs can be targeted, allowing for incorporation of different luminescent lanthanides (i.e., Nd^{3+} & Yb^{3+}) into a single material, thus allowing for the development of multimode sensors.

Sensitizing lanthanides by placing the ions in the pore of previously synthesized MOFs offers several specific advantages, as well. First, the Cambridge database already has thousands of 3-D MOF crystal structures, so frameworks that contain suitable antennae can be easily identified and synthesized. The addition of lanthanides into the cavity of these frameworks allows for a facile, thorough study of topology-photophysical relationships. Also, the building block approach has been studied more thoroughly with *d*-block metals than lanthanides. So even

when utilizing a new ligand for the assembly of the frameworks, targeted topologies could be more easily synthesized. Moreover, one topology can be used to study the sensitization of many lanthanides. Multiple lanthanides can also be incorporated into one framework cavity. Like synthesizing MOFs containing multiple lanthanides, adding different lanthanides inside the cavity has the potential for a multimode sensor or multiplex assay. Finally, it allows a greater range of potential antennae in MOFs to be explored, as the organic group does not need to bind directly to the lanthanide cation, thus oxygen binding groups are not necessary.

This work began by identifying ligands that could both sensitize lanthanide cations and direct their assembly into an extended porous network. Two organic components were selected to test for the ability to sensitize lanthanide cations. Terpyridyl benzoic acid (TPBA), Figure 5.1, was chosen as a potential antennae for lanthanide cations based on its high conjugation and two potential binding sites for lanthanide cations, a chelating oxygen site at the carboxylic acid as well as a multidentate nitrogen site.

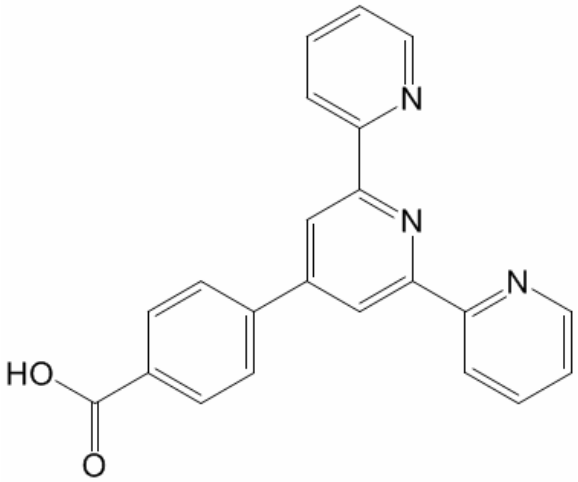

Figure 5.1. Terpyridyl benzoic acid (TPBA) ligand for visible emitting lanthanide cations.

A second organic component, 4,4'-[(2,5-dimethoxy-1,4-phenylene)di-2,1-ethenediyl]bis-benzoic acid (H_2-PVDC), Figure 5.2, was chosen because it has strong absorptivity in the visible range, and its length could promote the formation of large, accessible pores within the MOF structure. H_2-PVDC was designed with specific attributes: 1) After deprotonation, the carboxylate binding groups can bond strongly to lanthanide cations resulting in a multitude of topologies. 2) The trans olefin bonds promote planarity and complete conjugation throughout the molecule, leading to enhanced electronic and fluorescent properties. 3) The methoxy groups allow for the OPV to be dissolved in common organic solvents.

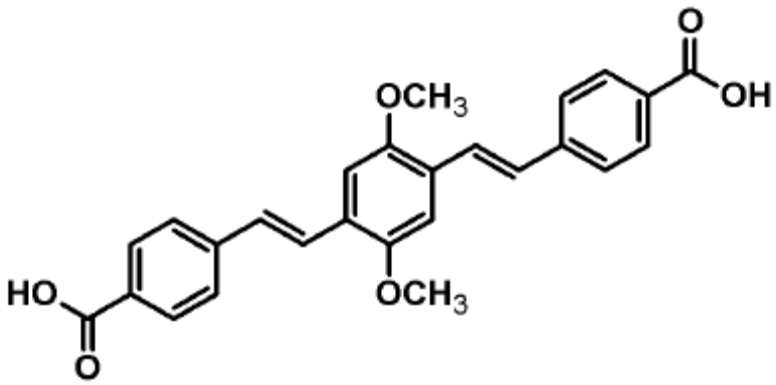

Figure 5.2. H_2-PVDC ligand for the sensitization of NIR lanthanide in MOFs.

The preliminary studies, see sections 5.3.1 and 5.3.2 for details, indicated that both of these organic components are capable of sensitizing several lanthanide cations in solution. TPBA sensitized four visible emitting lanthanide cations (Tb^{3+}, Eu^{3+}, Sm^{3+}, Dy^{3+}) and PVDC sensitized the NIR emission of four lanthanide cations (Yb^{3+}, Er^{3+}, Nd^{3+}, Ho^{3+}) in DMSO.

Working with H_2-PVDC and the NIR emitting lanthanide cations, MOFs with infinite Ln-carboxylate chains, or infinite secondary building units (SBUs) were targeted.[186] Infinite SBUs force the ligands into parallel packing arrangements, which was hypothesized to possibly lead to meaningful ligand-ligand (inter-antennae) interactions. Also, a few lanthanide-based MOFs exhibiting infinite SBUs have previously been reported.[187] In this research, several NIR emitting MOFs formed with H_2-PVDC and lanthanide cations at the metal sites are developed and investigated. These Ln-PVDC MOFs provide evidence that increasing the density of lanthanide cations and chromophore groups within a material improves emission intensities. Two different Yb-PVDC MOFs are formed and analyzed, and they demonstrate how by inducing subtle modifications to the MOF architecture, favorable changes in photophysical properties were obtained. Both an Er-PVDC and Nd-PVDC MOF with the same structure as one of the Yb-PVDC MOFs are formed and analyzed as well. Finally, MOFs are formed with varying combinations of erbium and ytterbium cations, introducing the ability to produce multiple emission signals from one MOF and the potential to create controlled bar code emission patterns. These **Er_xYb_{1-x}-PVDC-1** MOFs also display properties suggestive of inter-lanthanide energy transfer, which opens the possibility for other applications including upconverting materials and using the rigid, well-defined structure of the MOF for more thorough studies of the lanthanide energy transfer mechanisms.

Using H_2-PVDC, a zinc based MOF was synthesized (**Zn-PVDC-1**) which has pores that lanthanide cations can occupy. This allows another method for the sensitization of lanthanide cations by MOFs. Single crystal X-ray diffraction studies showed that **Zn-PVDC-1** has four interpenetrating cages composed of octahedral Zn-O-C secondary building units connected by

PVDC linkers. **Zn-PVDC-1** is able to sensitize several NIR emitting lanthanide cations, as expected based on results obtained for the molecular complexes (see 5.3.2 for details).

Incorporating lanthanide cations within the MOF pores could be a versatile and facile way of forming luminescent lanthanide materials. For this system, sensitization of the lanthanide cations would have to occur through a Förster mechanism[17], since the accepting metal cations will not be bound directly to the donors, which would be required for a Dexter mechanism.[18] Although this process is dependent on the distance between the antennae and lanthanide, the interpenetrating framework would allow for lanthanide metals to occupy the pores while remaining suitably positioned from the antennae to allow for sensitization. Since **Zn-PVDC-1** is a neutral framework, the anions of the lanthanide salt must reside in the pore to balance the cationic lanthanides; thus, $LnCl_3$ salts were chosen for these experiments because of the small diameter of chloride ions compared to other lanthanide salts.

This approach is further extended to a second Zn based MOF, **BioMOF-1**, which is a water soluble and stable MOF.[188,189] It is a three-dimensional porous framework in which zinc-adenine (Figure 5.3) clusters are linked by 4, 4'-biphenyldicarboxylic acids (Figure 5.3).

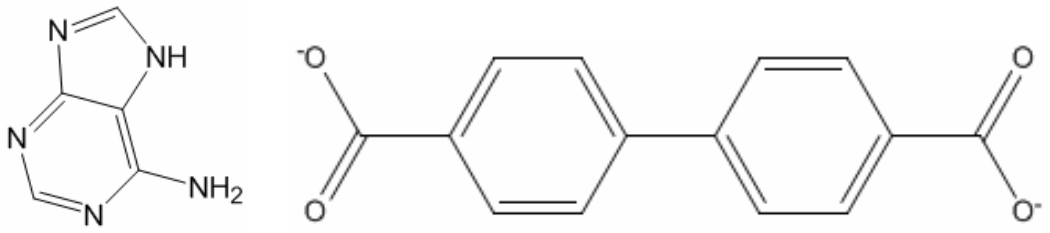

Figure 5.3. Adenine (left) and 4,4'-biphenyldicarboxylic acid, BPDC (right); the two organic components of BioMOF-1.

Since this MOF has two chromophore groups, one of which (adenine) can not form strong bonds with lanthanide cations, no preliminary studies were performed on this system to determine if lanthanide sensitization was possible. The cavities of this MOF are anionic and have an overall charge of -0.5, which is hypothesized to attract and hold lanthanide cations. Several different lanthanide cations were loaded into the MOF pores, and photophysical studies were conducted to determine successful lanthanide sensitization. The results show that lanthanide cations are easily incorporated into **BioMOF-1**, and lanthanides emitting in the visible and NIR are successfully sensitized in water.

5.2. EXPERIMENTAL

Syntheses of the ligands and MOFs, and their structural characterization were performed by Kiley White, George Norton, and Jihyun An, in collaboration with the research group of Dr. Nat Rosi.

5.2.1. Reagents

Dimethoxybenzene, paraformaldehyde, triphenylphosphine, methanol, NaOMe, THF, DMF, $TbCl_3{\cdot}xH_2O$, $EuCl_3{\cdot}xH_2O$, $SmCl_3{\cdot}xH_2O$, $DyCl_3{\cdot}xH_2O$, $NdCl_3{\cdot}xH_2O$, $YbCl_3{\cdot}xH_2O$, $ErCl_3{\cdot}xH_2O$, $HoCl_3{\cdot}xH_2O$, $Tb(NO_3)_3{\cdot}xH_2O$, $Eu(NO_3)_3{\cdot}xH_2O$, $Sm(NO_3)_3{\cdot}xH_2O$, $Dy(NO_3)_3{\cdot}xH_2O$, $Nd(NO_3)_3{\cdot}xH_2O$, $Yb(NO_3)_3{\cdot}xH_2O$, $Er(NO_3)_3{\cdot}xH_2O$, $Ho(NO_3)_3{\cdot}xH_2O$, 0.1 N KOH in methanolic solution, and tetrabutylammonium hydroxide were purchased from Aldrich. Glacial acetic acid, hydrochloric acid, was purchased from Fisher. Hyrdobromic acid (33% in AcOH) was purchased

from Fluka. Anhydrous toluene (99.8%) was purchased from Acros. Argon gas was purchased from Valley National. Methyl 4-formylbenzoate was purchased from TCI. Ethanol was purchased from Pharmco. KOH was purchased from Alfa Aesar. All reagents were used as received without further purification.

5.2.2. Synthetic Procedures

5.2.2.1. Synthesis of Ln - TPBA complexes

TPBA was synthesized by George Norton and was used as received without further purification.

Terbium and europium complexes with TPBA prepared as follows: 1.0 mL of $1x10^{-4}$ M TPBA was deprotonated with 1 equivalent of tetraethylamine hydroxide (0.1 M solution in DMSO). One-half equivalent of lanthanide cation (from chloride salt in DMSO solution) was added to this solution to yield a final stoichiometric ratio of 1:2, metal to ligand. The solution was then diluted with DMSO to bring the final concentration to $2.5x10^{-5}$ M TPBA and $1.25x10^{-5}$ M lanthanide chloride. Alternatively, dysprosium and samarium complexes with TPBA were prepared as follows: 6.0 mL of 1×10^{-4} M H_2-PVDC was deprotonated with 1 equivalent of tetraethylamine hydroxide (0.1 M solution in DMSO). One equivalent of lanthanide cation from chloride salt in DMSO solution (0.01 M) was added to this solution to yield a final stoichiometric ratio of 1:1, metal to ligand. The solutions were allowed to stand overnight to allow complete complexation prior to analysis.

5.2.2.2. Synthesis of H_2-PVDC and its lanthanide complexes

1,4-Bis(bromomethyl)-2,5-dimethoxybenzene (**1**) was an intermediate and was prepared following an established procedure,[190] which is detailed below. To a stirred solution of 1,4-dimethoxybenzene (10.00 g, 72.37 mmol) in glacial acetic acid (50 mL), paraformaldehyde (4.27 g, 144.75 mmol) and HBr/AcOH (33%, 30 mL) were added slowly. The mixture was stirred at 50ºC for one hour and hydrolyzed in water (200 mL) after cooling to room temperature. The white solid was collected by filtration, suspended in $CHCl_3$ (50 mL), and refluxed for 10 min. After cooling to room temperature, the white solid was again collected by filtration and washed with water (15.75 g, 67%). ^{1}H NMR (300 MHz, $CDCl_3$, δ): 6.88 (s, 2H), 4.54 (s, 4H), 3.87 (s, 6H); ^{13}C NMR (75 MHz, CDCl3, δ): 151.9, 128.0, 114.5, 56.9, 29.1; FTIR (KBr pellet, cm-1): 2962 (w), 2934 (w), 2834 (w), 1509 (vs), 1461 (s), 1428 (w), 1404 (vs), 1319 (m), 1228 (vs), 1205 (s), 1179 (w), 1103 (w), 890 (w), 874 (w), 718 (w).

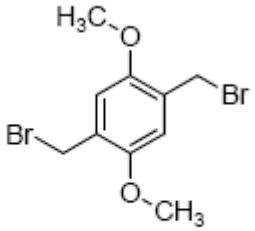

(1)

(2,5-Dimethoxy-1,4-phenylene)bis(methylene)bis(triphenylphosphonium bromide **(2)** was synthesized as follows. A mixture of 1,4-bis(bromomethyl)-2,5-dimethoxybenzene (9.59 g, 29.60 mmol) and triphenylphosphine (18.63 g, 71.04 mmol) was refluxed in anhydrous toluene

(80 mL) under argon for 6 hours. The crude white powder was obtained by filtration and used for subsequent reaction without further purification.

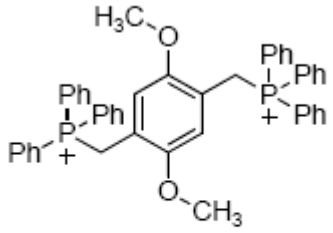

(2)

Dimethyl 4,4'-(1*E*,1'*E*)-2,2'-(2,5-dimethoxy-1,4-phenylene)bis(ethane-2,1-diyl)dibenzoate (**3**) was synthesized following a procedure adapted from a previously reported synthesis.[191] A mixture of (2,5-Dimethoxy-1,4-phenylene)bis(methylene)bis(triphenylphosphonium bromide) (25.68g, 30.26 mmol) and methyl 4-formylbenzoate (12.42 g, 75.66 mmol) were dissolved in dry methanol (120 mL) under argon. NaOMe (0.5 M in methanol, 160 mL) was added via a cannula. A yellow precipitate formed immediately. The reaction was stirred under argon for 4 h. After addition of water (140 mL), the yellow powder was filtered and washed with aqueous ethanol (60%, 3 x 75 mL). Pure trans product was isolated via crystallization from toluene in the presence of few crystals of iodine (11.95 g, 86%). ^{1}H NMR (300 MHz, $CHCl_3$, δ): 8.02 (d, J=8.7, 4H), 7.59 (m, 6H), 7.16 (m, 4H), 3.95 (s, 6H), 3.93 (s, 6H); ^{13}C NMR (75 MHz, $CHCl_3$, δ): 167.5, 152.4, 142.9, 130.6, 129.4, 128.8, 127.2, 127.0, 126.3, 109.9, 56.9, 52.66; FTIR (KBr pellet, cm^{-1}): 3007 (w), 2943 (w), 2835 (w), 1714 (vs), 1604 (m),

1493 (w), 1464 (w), 1437 (sh), 1410 (m), 1277 (vs), 1209 (s), 1183 (m), 1111 (s), 1041 (m), 1014 (w), 971 (trans =C-H, w), 875 (sh), 849 (w), 766 (m), 702 (w).

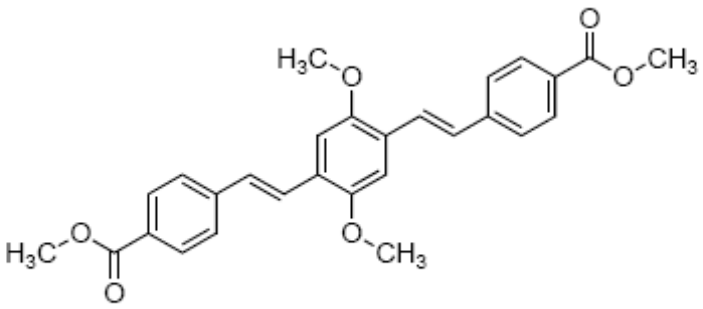

(3)

4,4'-(1*E*, 1'*E*)-2,2'-(2,5-dimethoxy-1,4-phenylene)bis(ethene-2,1-diyl)dibenzoic acid (**4**) was synthesized as follows. To dimethyl 4,4'-(1*E*,1'*E*)-2,2'-(2,5-dimethoxy-1,4-phenylene) bis(ethane-2,1diyl) dibenzoate (5.46 g, 11.9 mmol) was added KOH (6.2 g, 121 mmol), methanol (60 mL), THF (60 mL), and H_2O (30 mL). The mixture was refluxed overnight, cooled, and H_2O (60 mL) was added, resulting in a clear yellow solution. The solution was acidified with 2N HCl, and the resulting yellow solid was collected by filtration and was then recrystallized from DMF to yield a bright yellow powder (4.24 g, 83%). ^{1}H NMR (300 MHz, DMSO-d_6, δ): 12.87 (s, 2H), 7.95 (d, J=7.5, 4H), 7.70 (d, J=8.4, 4H), 7.51 (d, J=21.9, 2H), 7.45 (d, J=15.9, 2H), 7.39 (s, 2H), 3.93 (s, 6H); ^{13}C NMR (75 MHz, DMSO-d_6, δ): 168.14, 152.30, 142.64, 130.94, 130.43, 129.33, 127.45, 126.94, 126.01, 110.59, 57.27; FTIR (KBr pellet, cm^{-1}): 2938 (b), 2831 (b), 2543 (m), 2361 (w), 1680 (C=O, s), 1600 (s), 1536 (w), 1491 (w), 1462 (m), 1315 (m), 1290 (s), 1209 (m), 1045 (m), 959 (trans =C-H, w), 859 (w), 771 (w).

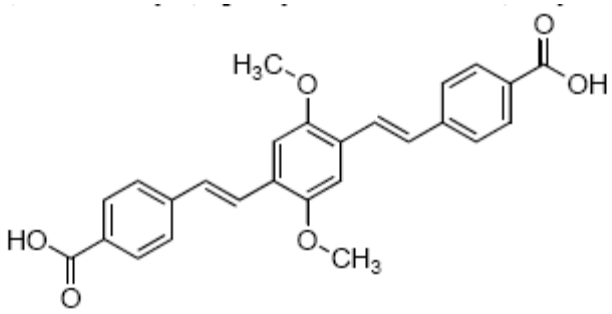

(4)

Lanthanide cation complexes with H_2-PVDC were prepared as follows: 0.60 mL of 5 x 10^{-4} M H_2-PVDC was deprotonated with 1 equivalent of tetraethylamine hydroxide (0.1 M solution in DMSO). One equivalent of lanthanide cation (from chloride salt in DMSO solution) was added to this solution to yield a final stoichiometric ratio of 1:1, metal to ligand. The solution was then diluted with DMSO to bring the total volume to 3.0 mL and the final concentration to 1.0 x 10^{-4} M for each reagent. The solution was allowed to stand overnight to allow complete complexation prior to analysis. If two equivalents of base were used to fully deprotonate H_2-PVDC, or if any ratios other than 1:1 were used, the mixture produced insoluble polymeric complexes.

5.2.2.3. Synthesis of Ln-PVDC MOFs

Yb-PVDC-1 ($Yb_2(C_{26}H_{20}O_6)_3(H_2O)_2$•$(DMF)_6(H_2O)_{8.5}$) was synthesized as follows: In a glass vial (4 mL), a solution of H_2-PVDC (8.60 mg, 0.020 mmol) in DMF (0.4 mL) was added to a solution of $Yb(NO_3)_3$•$5H_2O$ (6.75 mg, 0.015 mmol) and 1M HNO_3(aq) (20.0 μL) in DMF (0.3

mL) to produce a neon green solution. The vial was capped and placed in an isotemp oven at 85ºC for 48 hours to produce yellow crystalline needles of the product. The crystals were collected, washed with DMF (4 x 3 mL), and air dried (8.6 mg, 42.4%). EA Calcd. (%) for $Yb_2(C_{26}H_{20}O_6)_3(H_2O)_2\bullet(DMF)_6(H_2O)_{8.5}$: C, 51.04; H, 5.49; N, 3.72. Found: C, 50.97; H, 4.57; N, 3.91. EA. Calcd. (%) for the chloroform exchanged product, $Yb_2(C_{26}H_{20}O_6)_3(H_2O)_2\bullet(CHCl_3)_{2.75}(DMF)_{0.3}$: C, 48.61; H, 3.44; N, 0.21. Found: C, 48.79; H, 3.10; N, 0.21. FT-IR (KBr pellet, cm^{-1}): 3432 (br), 2933 (w), 1665 (DMF C=O, m), 1600 (m), 1538 (s), 1414 (COO-, vs), 1256 (w), 1209 (s), 1180 (w), 1106 (w), 1042 (s), 962 (m), 861 (w), 780 (trans C=C-H, s), 709 (w).

Yb-PVDC-2 ($Yb_2(C_{26}H_{20}O_6)_3\bullet(DMF)_{12}(H_2O)_{10}$) was synthesized as follows: In a glass vial (20 mL), a solution of 4,4'-(1*E*, 1'*E*)-2,2'-(2,5-dimethoxy-1,4-phenylene)bis(ethene-2,1-diyl)dibenzoic acid (H_2-PVDC) (86.0 mg, 0.20 mmol) in DMF (4 mL) was added to a solution of $Yb(NO_3)_3\bullet5H_2O$ (22.5 mg, 0.05 mmol) and 1M HNO_3(aq) (10 μL) in DMF (1 mL) to yield a neon green solution. The vial was capped and placed in an isotemp oven at 105ºC for 36 hours to produce orange block-like crystals of the product. The crystals were collected, washed with DMF (4 x 5 mL) and air dried (48 mg, 51.9%). EA Calcd. (%) for $Yb_2(C_{26}H_{20}O_6)_3\bullet(DMF)_{12}(H_2O)_{10}$: C, 50.93; H, 6.15; N, 6.25. Found: C, 50.95; H, 5.40; N, 6.47. EA. Calcd. (%) for the chloroform exchange product, $Yb_2(C_{26}H_{20}O_6)_3\bullet(CHCl_3)_{7.5}(H_2O)_{.5}(DMF)_{.5}$: C, 40.62; H, 2.82; N, 0.27. Found: C, 40.66; H, 2.75; N, 0.23. FT-IR (KBr pellet, cm^{-1}): 3433 (br), 2930 (w), 1655 (DMF C=O, m), 1602 (s), 1536 (m), 1418 (COO- sym st, vs), 1208 (C-O-C as st, s), 1180 (w), 1103 (w), 1041 (C-O-C sym st, w), 960 (trans =C-H, w), 862 (w), 780 cm^{-1} (m).

Er-PVDC-1, **Nd-PVDC-1**, **Er_xYb_{1-x}-PVDC-1**, and **$Nd_yEr_xYb_{1-(x+y)}$-PVDC-1** were all made following the synthetic procedure for **Yb-PVDC-1**, and the MOFs have the same structure.

Solvent exchange of the DMF and H_2O guest molecules in was performed using anhydrous solvents as follows: 30 min soak in exchange solvent followed by solvent removal (repeated 3x); overnight soak in exchange solvent and then solvent removal; 24 h soak in exchange solvent and solvent removal; and final addition of fresh solvent.

5.2.2.4. Syntheses of the Zn-PVDC-1 MOFs

Yellow block **Zn-PVDC-1** crystals ($Zn_4O(C_{26}H_{20}O_6)_3$•$(DMF)_{18}(H_2O)_5$) were synthesized in a vial from $Zn(NO_3)_2$·$4H_2O$ and excess H_2-PVDC in DMF and isopropanol in an 85ºC isotemp oven for 48 hrs, as detailed here. In a glass vial (20 mL), a solution of 4,4'-(1*E*, 1'*E*)-2,2'-(2,5-dimethoxy-1,4-phenylene)bis(ethene-2,1-diyl)dibenzoic acid (H_2-PVDC) (86.0 mg, 0.20 mmol) in DMF (4.0 mL) was added to a solution of $Zn(NO_3)_2$•$4H_2O$ (39.2 mg, 0.15 mmol) in DMF (3.0 mL) and isopropyl alcohol (5.0 mL) to yield a neon green solution. The vial was capped and placed in an 85ºC isotemp oven for 48 hours to produce golden brown block-like crystals of the product. The crystals were collected, washed with a DMF:iPrOH solution (7:5) (4 x 5 mL) and air dried. EA Calcd. (%) for $Zn_4O(C_{26}H_{20}O_6)_3$•$(DMF)_{18}(H_2O)_5$: C, 53.41; H, 6.65; N, 8.49. Found: C, 53.33; H, 6.41; N, 8.47. FT-IR (KBr pellet, cm^{-1}): 3429 (br), 2931 (w), 1670 (DMF C=O, vs), 1600 (s), 1551 (m), 1497 (w), 1400 (COO-, vs), 1257 (w), 1211 (m), 1180 (w), 1095 (w), 1041 (m), 972 (trans =C-H, w), 864 (w), 817 (w), 780 (m).

To exchange the pores of **Zn-PVDC-1** with lanthanide cations, a solution of lanthanide chloride salt in DMF at the chosen concentration was made. The MOFs were soaked in the lanthanide solution for 5 min, followed by solvent removal, a 30 min soak in the lanthanide

solution, then solvent removal (repeat 4x); a 24 h soak in the lanthanide solution and solvent removal; a 5 min soak in DMF followed by solvent removal (repeat 5x); 24 h soak in DMF followed by solvent removal; and a final addition of fresh solvent.

5.2.2.5. Synthesis of BioMOF-1 with lanthanide exchanged cavities

The exact details of the synthetic conditions for **BioMOF-1** can be found in published documents.[188,189] Briefly, a zinc acetate dihydrate stock solution (DMF), a 4, 4'-biphenyl dicarboxylic acid stock solution (DMF), and an adenine stock solution (DMF) are mixed and heated with nitric acid to produce colorless, rod-shaped crystals which were washed with DMF (3 x 3 mL) and dried under argon gas (30 min). EA Calcd. (%) for $C_{33}H_{39.5}N_{7.5}O_{11}Zn_2$ = $Zn_2(Ad)(BPDC)_{1.5}O_{0.25}\cdot 0.5(NH_2(CH_3)_2)^+$, 2DMF, 2.75$H_2O$: C, 46.74; H, 4.70; N, 12.39; Found: C, 46.58; H, 4.55; N, 12.49. FT-IR (KBr pellet, cm^{-1}): 3341.39 (br), 3188.47 (br), 2930.38 (w), 1663.76 (s), 1606.79 (s), 1544.77 (m), 1472.12 (m), 1382.97 (s), 1280.50 (w), 1213.98 (m), 1176.56 (m), 1153.11 (m), 1100.61 (m), 845.33 (m), 772.43 (s), 702.00 (m).

To exchange the dimethyl ammonium cations for lanthanide cations, the following procedure is used: the as-synthesized materials were rinsed with DMF 3x in a 20.0 mL vial. A 0.1 M $Yb(NO_3)_3$ solution in DMF was added to the vial and the material was soaked in the solution for 10 min, and the solution was removed; fresh solution was added; repeated twice. New fresh lanthanide solution was added, and the material was soaked in the solution for 24 hours and removed; repeated every 24 to 48 hours for 3 weeks.

To switch from DMF to water, the lanthanide cation exchanged material was rinsed with DMF 5x, and Nanopure (NP) water was added to the vial. The Ln:**BioMOF-1** soaked in NP water for 10 min; the water was removed. Fresh water was added to the vial, and the material

soaked for 10 min; followed by solvent removal. Fresh water was added to the vial and the material was soaked in NP water for 24 hours. To exchange water for D_2O, solvent exchange was performed once daily for 5 days.

5.2.3. Analytical Methods

^{1}H NMR (300 MHz) and ^{13}C NMR (75 MHz) were recorded on a Bruker Avance 300.

Fourier transform infrared (FT-IR) spectra were measured on a Nicolet Avatar 360 FT-IR spectrometer, using KBr pellet samples. Absorptions are described as very strong (vs), strong (s), medium (m), weak (w), shoulder (sh), and broad (br) and stretches (st) are labeled symmetric (sym) or asymmetric (as). Data was analyzed using the Omnic Software Package.

Thermogravimetric analysis (TGA) was performed using a TA Q500 thermal analysis system. All TGA experiments were run under a nitrogen atmosphere from 20-600 ºC at a rate of 1 ºC/min. Data were analyzed using the TA Universal Analysis software package.

X-ray powder diffraction patterns were taken using a Bruker AXS D8 Discover powder diffractometer at 40 kV, 40 mA for Cu Kα, (λ = 1.5406 Å) with a scan speed of 0.20 sec/step and a step size of .02018º. The data were analyzed for d-spacing measurements using the EVA program from the Bruker Powder Analysis Software package. The simulated powder patterns were calculated using PowderCell 2.4. The purity and homogeneity of the bulk products were determined by comparison of the simulated and experimental X-ray powder diffraction patterns.

The elemental microanalysis was performed by the University of Illinois, Department of Chemistry, Mircroanalytical Laboratory using an Exeter Analytical CE440.

Energy-dispersive X-ray analysis (EDX) measurements were performed on a Philips XL 30 SEM 50 equipped with an EDAX CDU leap detector.

Single crystal XRD data was collected on a Bruker SMART APEX II CCD-based X-ray diffractometer equipped with a normal focus Mo-target X-ray tube (λ = 0.71073 Å) operated at 2000 W power (45 kV and 35 mA). The detector was placed at a distance of 6.002 cm from the crystal. 1800 frames were collected with a scan width of 0.3° in omega and phi with an exposure time of 10 s/frame. Crystals were mounted in glass capillaries, and the X-ray intensities were measured at 253 K for **Yb-PVDC-1** and **Zn-PVDC-1**, and at 298 K for **Yb-PVDC-2** and **BioMOF-1**, respectively. Crystal data and details of data collection are found in Appendix A.

Absorption spectra were recorded on a Perkin-Elmer Lambda 9 Spectrometer coupled with a personal computer using software supplied by Perkin-Elmer. Spectra were collected after instrumental zeroing with two quartz cuvettes of solvent.

Emission and excitation spectra in the visible range were measured using a Varian Cary Eclipse Fluorescence Spectrophotometer equipped with a well-plate reader coupled to a personal computer with software provided by Varian. For samples consisting of solvated species in solution, 1 or 10 mm quartz cuvettes were used. For samples consisting of solid state MOF materials under solvent, sample holders were made by using paraffin to create circular boundaries on glass microscope slides. The MOFs were loaded into these sample holders and solvent was periodically added throughout the analysis to prevent the samples from drying due to solvent evaporation. The glass slides were then placed on top of a well plate, and the MOFs were aligned with one of the wells, loaded into the instrument and analyzed.

Alternatively, solid state samples were analyzed using a Jobin Yvon–Horiba Fluorolog-322 spectrofluorimeter fitted with an integrating sphere developed by Frédéric Gumy and Jean-Claude G. Bünzli (Laboratory of Lanthanide Supramolecular Chemistry, École Polytechnique Féderale de Lausanne (EPFL), BCH 1402, CH- 1015 Lausanne, Switzerland) as an accessory to

the Fluorolog FL3-22 spectrometer (Patent pending) using quartz tube sample holders.[192] Spectra in the visible and near infrared range were measured using a Jobin Yvon–Horiba Fluorolog-322 spectrofluorimeter equipped with an Electro-Optical Systems, Inc. DSS-IGA020L detector for the NIR domain. Emission and excitation spectra of the solid state materials were collected with the integrating sphere.

Quantum yield measurements of the solid state samples were measured using the integration sphere. For measurements in the visible region, the procedure is described as follows, using the same instrumental parameters for all measurements.

1) To determine the amount of light absorbed by the sample, an emission spectrum is collected of an empty cuvette (Ex_B) and the of the sample (Ex_S) of the excitation light. For example, if 340 nm is used as the excitation wavelength, spectra are collected from 320 – 360 nm. The spectra are integrated, and Ex_S is subtracted from Ex_B. Due to the high intensity of the lamp, neutral density filters are employed and the integrated values are corrected accordingly.

2) The emission of the sample (I_S) and an empty cuvette (I_B) in the visible region are measured. The spectra are corrected for variations in lamp output and the response of the detector. The emission bands are integrated, and the total sample emission is given by $I_S - I_B$.

3) The quantum yield (Φ) is calculated using Equation 5.1:

$$\Phi = (I_S - I_B) / (Ex_S - Ex_B) \qquad (5.1)$$

For quantum yield measurements in the NIR range with the integration sphere, the analysis is more complex as two different detectors are used, a visible detector to determine the absorbance of light and a NIR detector to monitor the sample emission. It is necessary to measure a relative quantum yield using a sample with a known value. The procedure is described below, using ytterbium or erbium tropolonate, $[Ln(trop)_4]^-$ in DMSO ($\Phi_{Yb} = 1.9x10^{-2}$, $\Phi_{Er} = 1.7x10^{-4}$)[7] as the reference.

1) To determine the amount of light absorbed by the sample and the reference, emission spectra are collected of the excitation light from the lamp for the sample (ExS) and the reference (ExR), as well as an empty cuvette (ExB). Due to the high intensity of the lamp, neutral density filters are employed and the integrated values are corrected accordingly. The light absorbed is given by: $Ex_B - Ex_S$ and $Ex_B - Ex_R$.

2) Emission spectra are collected in the NIR range of the sample (I_S) and the reference (I_R), as well as of an empty cuvette (I_B). If the sample and reference emission spectra are collected with different excitation or emission wavelengths, two corresponding emission spectra of the empty cuvette will be necessary. To eliminate second order bands, glass cut on filters are placed before the detector. The spectra are corrected for lamp variation, detector response and signal attenuation from the cut on filters. The emission bands for the sample, reference, and blank(s) are integrated, and total emission is given by: $I_S - I_B$ and $I_R - I_B$.

3) Using the known quantum yield of the reference, a scalar ($X_{NIR\text{-}VIS}$) is created to offset the NIR emission spectra to the same scale as the visible spectra of the excitation, as shown in Equation 5.2.

$$X_{\text{NIR-VIS}} = [\Phi(Ex_{\text{B}} - Ex_{\text{R}})] / (I_{\text{R}} - I_{\text{B}}) \qquad (5.2)$$

4) The quantum yield (Φ) is calculated using Equation 5.3.

$$\Phi = [X_{\text{NIR-VIS}}(I_{\text{S}} - I_{\text{B}})] / (Ex_{\text{B}} - Ex_{\text{S}}) \qquad (5.3)$$

Alternatively, quantum yields in the visible range were also measured with this method, using TbH_2IAM as a reference,[6] removing the necessity to correct for neutral density filters.

Lanthanide luminescence lifetimes were measured using a Nd:YAG Continuum Powerlite 8010 laser (354 nm, 3rd harmonic) as the excitation source. Emission was collected at a right angle to the excitation beam, and wavelengths were selected by a Spectral Products CM 110 1/8 meter monochromator. The signal was monitored by a Hamamatsu R316-02 photomultiplier tube for the NIR range, and was collected on a 500 MHz band pass digital oscilloscope (Tektronix TDS 754D). Alternatively, luminescence lifetimes in the visible range were measured using an Oriel 79110 Nitrogen laser (λ_{ex}: 337 nm) or the flash lamp of the JY Horriba fluorimeter as the excitation source, and the emission signal was collected at a 90 degree angle with the SPEX Fluorolog detector. The signal was monitored with the same oscilloscope. Signals from >1000 flashes were collected and averaged. Luminescence decay curves were treated with Origin 7.0 software using exponential fitting models. Three decay curves were collected on each sample, and reported lifetimes are an average of at least two independent measurements.

5.3. RESULTS & DISCUSSION

5.3.1. Visible emitting lanthanide complexes with TPBA

The photophysical properties of TPBA were investigated to determine which lanthanide cations it would likely be able to sensitize. The absorbance spectrum was monitored for TBPA, deprotonated TPBA, and for the deprotonated TPBA mixed with one-half equivalent of europium chloride, shown in Figure 5.4. As seen, there is a strong absorbance band around 275 nm, with a shoulder around 325 nm. There are very minor changes between the three absorbance spectra, which indicate that changes at the carboxylic acid site do not influence the electronic structure of the TPBA. This is not surprising as this site is fairly removed from the conjugated portions of the molecule.

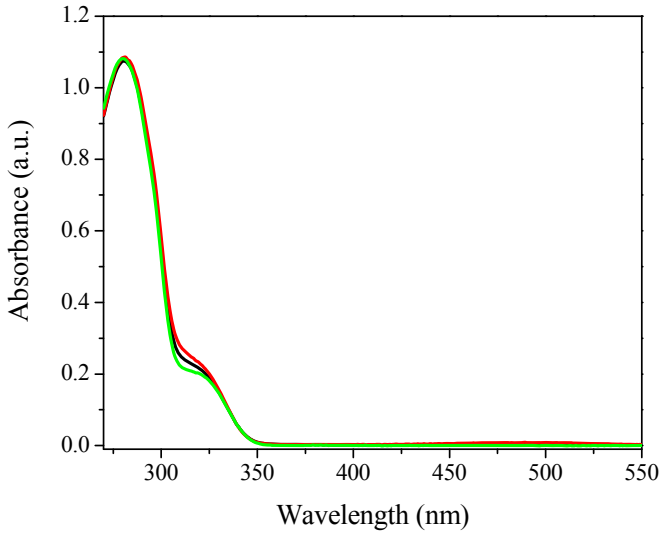

Figure 5.4. Absorbance spectra of 2.5 x 10^{-5} M TPBA in DMSO (black), 2.5 x 10^{-5} M deprotonated TPBA in DMSO (red), and 2.5 x 10^{-5} M deprotonated TPBA with 1.25 x 10^{-5} M $EuCl_3$ in DMSO (green).

The fluorescence spectrum resulting from exciting TPBA at either absorbance maxima contained one strong emission band at 365 nm, as well as a weaker band at 515 nm, Figure 5.5. The excitation spectrum of TPBA emission at 365 nm corresponds well with the absorbance spectrum. With its relatively high energy absorption and emission bands, it is hypothesized that TPBA will be a suitable antenna for visible emitting lanthanide cations.

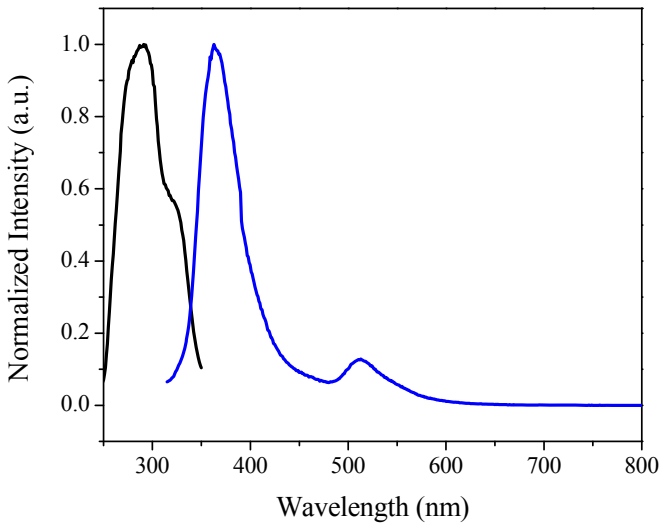

Figure 5.5. Emission spectrum, λ_{ex}: 320 nm (blue) and excitation spectrum, λ_{em}: 365 nm (black) of TPBA (2.5 x 10^{-5} M, DMSO).

To test the ability of TPBA to bind to and sensitize lanthanide cations, complexes in solution were prepared and their photophysical properties were investigated. As shown in Figure 5.6, TPBA was able to sensitize Eu^{3+}, Tb^{3+}, Sm^{3+}, and Dy^{3+}. The europium and terbium emission spectra were collected in a time-gated manner, which allowed for the removal of TPBA fluorescence from the spectra; however, samarium and dysprosium spectra were collected in

steady-state mode so there is some TPBA signal in their spectra. This is an exciting result as few ligands are able to sensitize four lanthanide cations.

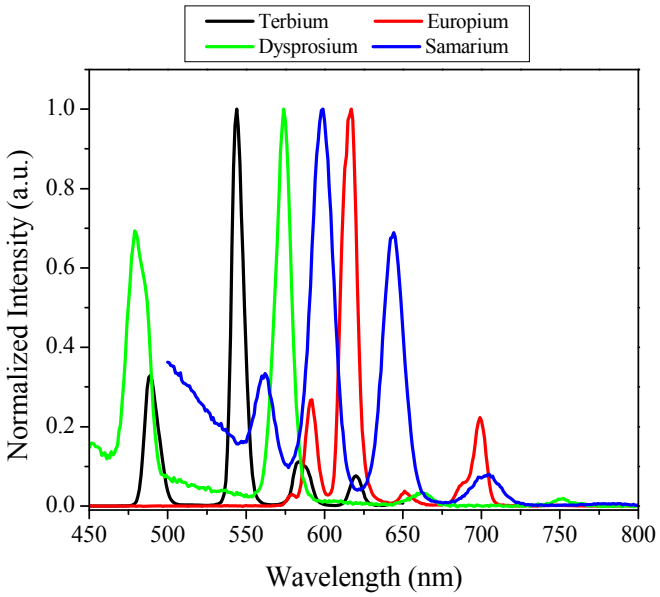

Figure 5.6. Emission spectra (λ_{ex}: 320 nm) of Ln:TPBA complexes in DMSO. Terbium (black) and europium (red) spectra were collected in time-resolved mode while dysprosium (green) and samarium (blue) were collected in steady state mode, thus some emission of the TPBA is also detected, which results in the angled baseline at higher energy for these two spectra.

The excitation spectrum of europium in the complex formed with TPBA, shown in Figure 5.7, contains a band at 320 nm with a shoulder out to about 350 nm. Excitation at 320 nm produces a characteristic europium spectrum in the visible range (Figure 5.7). The excitation spectrum is the same for complexes with all four lanthanides and, as demonstrated by the europium complex, is similar to the excitation spectrum of TPBA fluorescence, Figure 5.8. This result provides evidence that the lanthanide cations are sensitized via the antennae effect by TPBA.

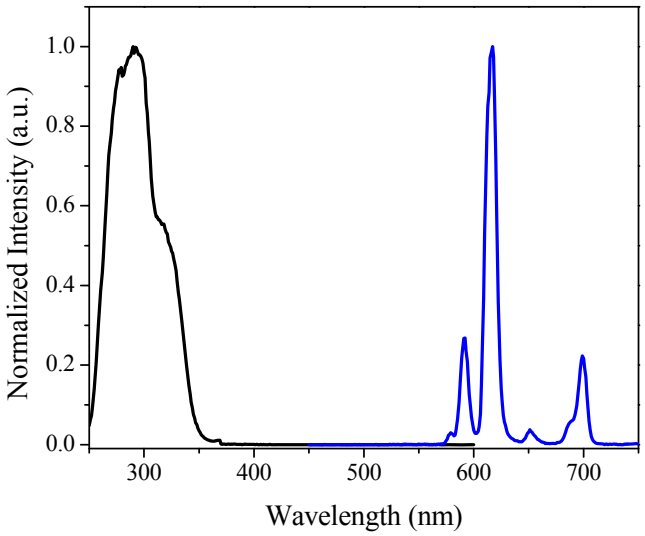

Figure 5.7. Europium emission spectrum, λ_{ex}: 320 nm (blue) and corresponding excitation spectrum (black) of 1:2 Eu:TPBA (1.25×10^{-5} M, DMSO), collected in a time-gated mode to isolate the lanthanide emission from other fluorescence.

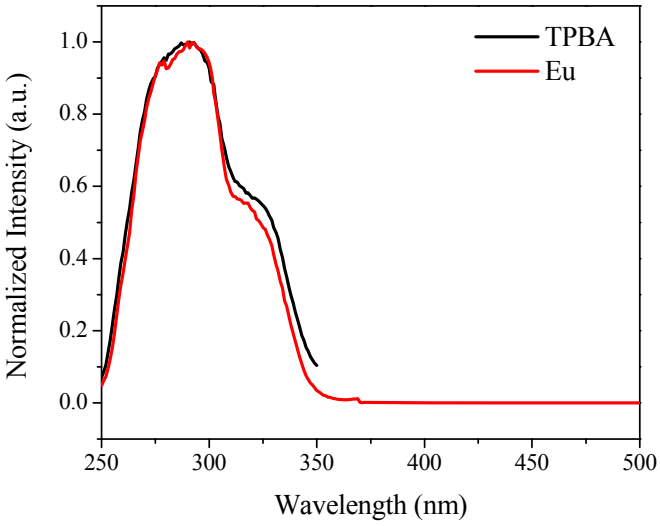

Figure 5.8. Excitation spectra of TBPA emission monitored at 365 nm (black) and europium emission monitored at 614 nm (red).

Unfortunately, all attempts to form lanthanide based MOFs with TPBA resulted in the formation of discrete lanthanide complexes, with all binding occurring at the carboxylic acid site. This is not surprising given lanthanide cations preference for oxygen binding sites. While these lanthanide complexes may have interesting properties worth further investigation, this is beyond the scope of this present research, which is focused at the development and analysis of lanthanide incorporating MOFs.

5.3.2. NIR emitting lanthanide complexes with H_2-PVDC

The photophysical properties of H_2-PVDC were investigated to determine which lanthanide cations it would likely be able to sensitize. As seen in Figure 5.9, H_2-PVDC has fluorescence excitation band at 485 nm, to which correspond two excitation maxima centered at 340 nm and 420 nm. The excitation spectrum of H_2-PVDC corresponds well with the absorbance spectrum, as shown in Figure 5.10. With emissive energy levels well into the visible region, and relatively low energy absorbance bands, it is hypothesized that this will be a suitable antenna for NIR emitting lanthanide cations.

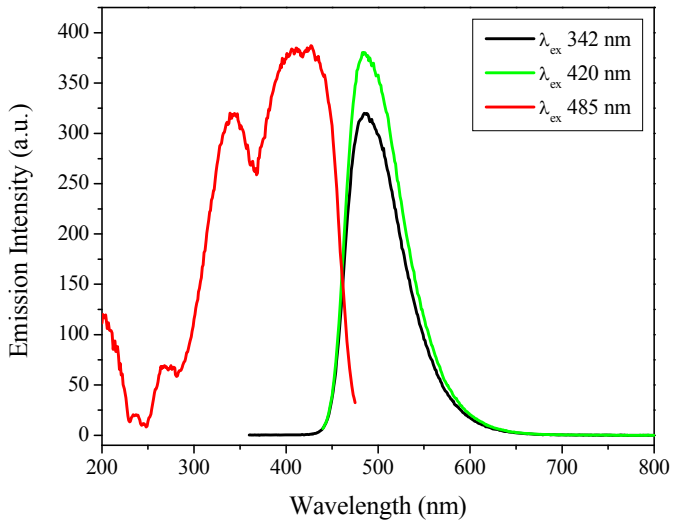

Figure 5.9. Emission and excitation spectra of H_2PVDC in DMSO.

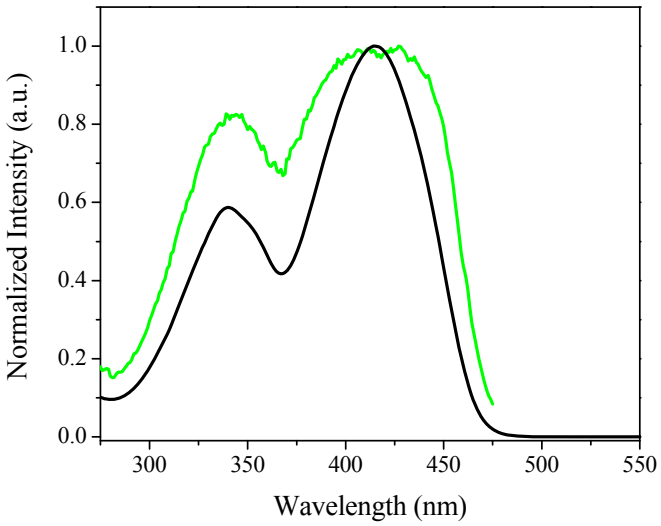

Figure 5.10. Absorbance (black) and excitation (green) spectra of H_2PVDC in DMSO.

To test the ability of H_2-PVDC to bind to and sensitize the NIR lanthanide cations, complexes in solution were prepared and their photophysical properties were investigated. H_2-PVDC was able to sensitize Yb^{3+}, Nd^{3+}, and Er^{3+} as seen in Figure 5.11, Figure 5.12, and Figure 5.13 respectively. The excitation spectra of the complexes in solution corresponding to all three lanthanide cations are similar, and resemble the absorbance spectrum of H_2-PVDC, as shown in Figure 5.14. This indicates that the lanthanide emission is operating through the electronic levels of the chromophore as a result of sensitization by H_2-PVDC through the antenna effect. H_2-PVDC was also able to sensitize Ho^{3+} in solution, although obtaining a good excitation spectrum was difficult due to the very weak emission intensity. Nevertheless, this is an exciting result because there are few reports of sensitized holmium emission in solution. The normalized emission spectra (λ_{ex}: 410 nm) of the four NIR emitting lanthanide cations in complex with H_2-PVDC are shown in Figure 5.15.

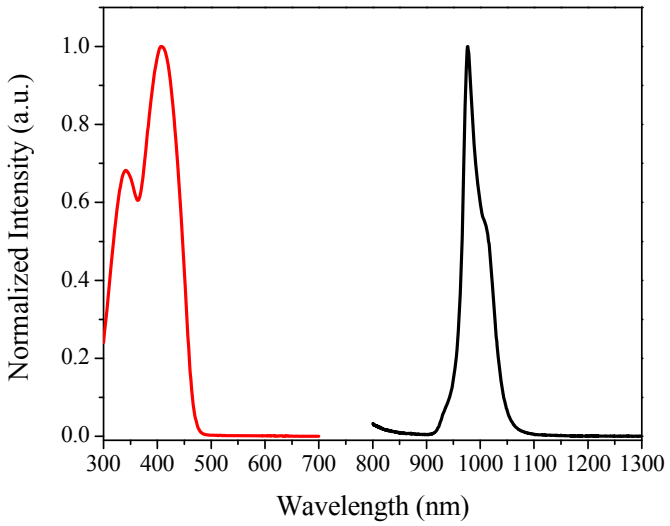

Figure 5.11. Excitation spectrum (red) of ytterbium centered emission at 980 nm and emission spectrum (black) in the NIR upon excitation at 420 nm for the Yb:PVDC complex in DMSO.

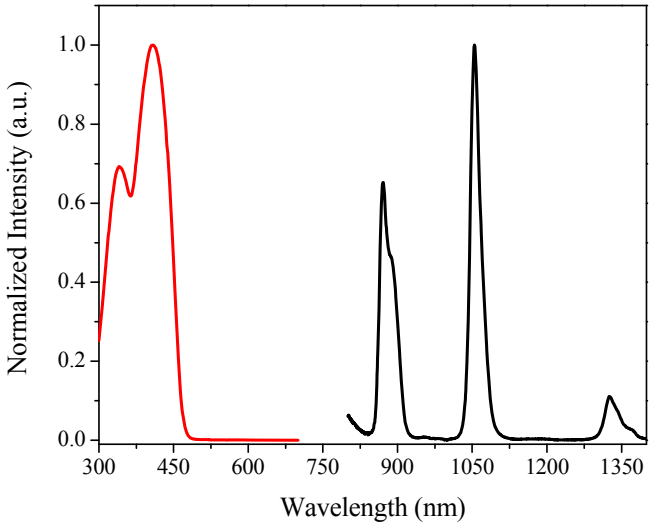

Figure 5.12. Excitation spectrum (red) of neodymium centered emission at 1054 nm and emission spectrum (black) in the NIR upon excitation at 420 nm for the Nd:PVDC complex in DMSO.

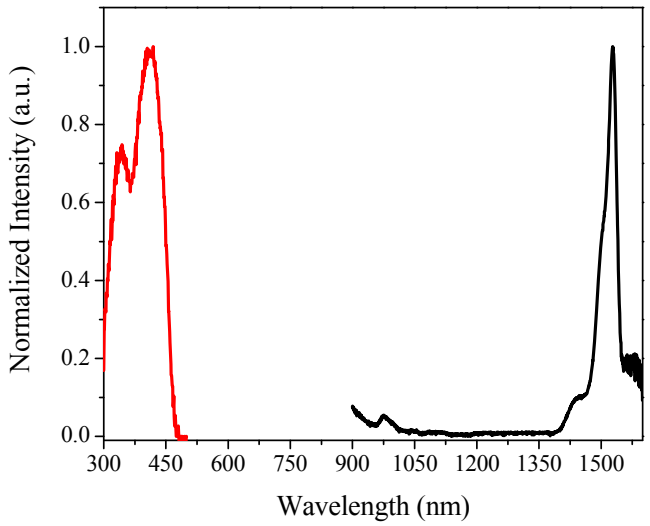

Figure 5.13. Excitation spectrum (red) of erbium centered emission at 1054 nm and emission spectrum (black) in the NIR upon excitation at 420 nm for the Er:PVDC complex in DMSO.

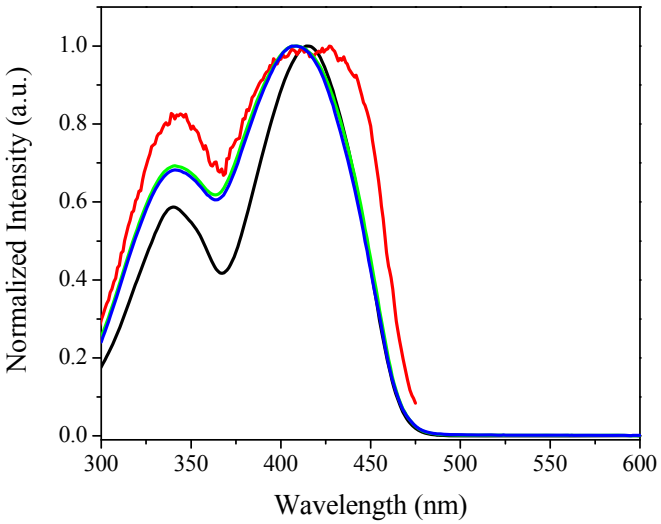

Figure 5.14. Absorbance spectrum (black) and excitation spectrum of visible emission at 485 nm (red) of H_2PVDC and the excitation spectra of ytterbium (blue) and neodymium (green) Ln:PVDC complexes in DMSO.

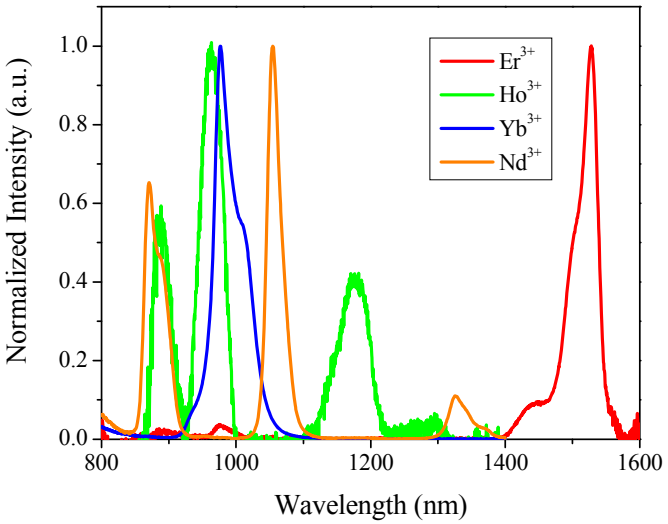

Figure 5.15. Normalized emission spectra for the four NIR emitting Ln:PVDC complexes in DMSO.

5.3.3. Ln-PVDC MOFs: Incorporation of lanthanide cations within MOFs via occupation of metal sites

Reacting $Yb(NO_3)_3 \bullet 5H_2O$ with H_2-PVDC yielded yellow needle-shaped crystals of **Yb-PVDC-1**, formulated as $[Yb_2(C_{26}H_{20}O_6)_3(H_2O)_2] \bullet (DMF)_6(H_2O)_{8.5}$, shown in Figure 5.16. The materials maintain their crystallinity in a variety of solvents, including chloroform and dimethylformamide, as confirmed by complete solvent exchange experiments and powder X-ray diffraction studies.

Figure 5.16. Photograph of Yb-PVDC-1, showing its yellow crystalline nature.

Single crystal X-ray diffraction analysis revealed that **Yb-PVDC-1** crystallizes in the high symmetry *F*ddd space group and is composed of infinite Yb-carboxylate chains that run along the *a* crystallographic direction. These chains are connected along the [110] via the phenylene vinylene portion of the ligand resulting in the formation of large rhombus-shaped channels

measuring approximately 24 x 40 Å (Figure 5.17). The chains consist of alternating octa- and hexa-coordinated Yb^{3+}, which are bridged together in a di-monodentate fashion via the carboxylates of three different PVDC linkers (Figure 5.16 and Figure 5.17). Two water molecules are terminally coordinated to the eight-coordinate Yb^{3+}.

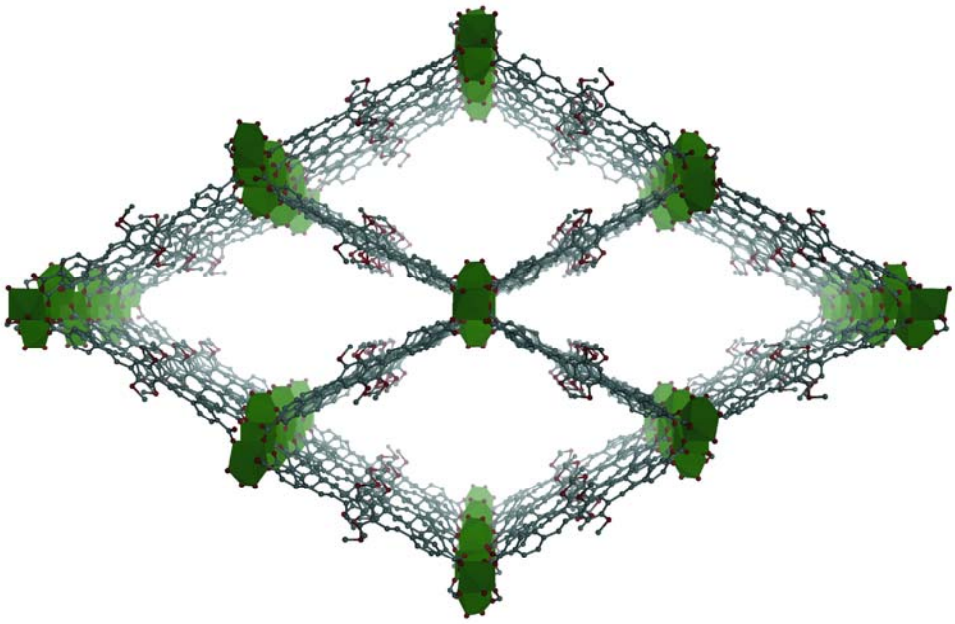

Figure 5.17. Projection view of Yb-PVDC-1 framework viewed along the *a* crystallographic direction.

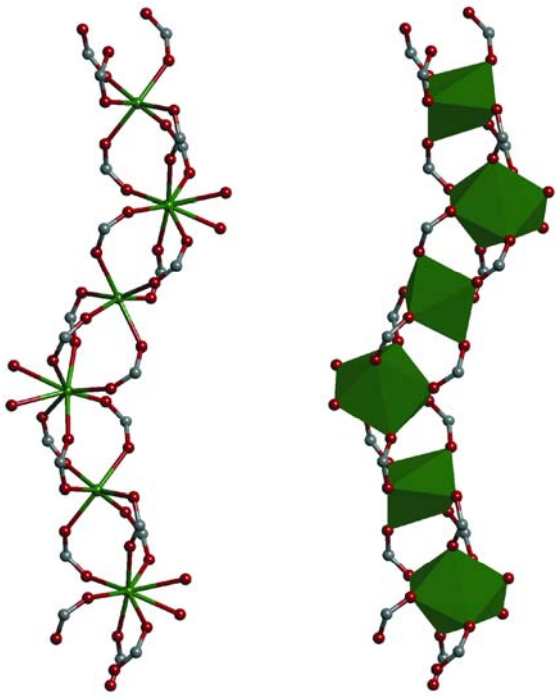

Figure 5.18. Ball and stick depiction, C: grey; O: red; Yb: green (left), and with Yb^{3+} polyhedra represented in green (right) of infinite SBU for Yb-PVDC-1.

The emission and excitation spectra were measured for **Yb-PVDC-1** and compared to corresponding spectra for H_2-PVDC and a Yb-PVDC molecular complex to determine how the MOF structure impacts the luminescence properties of the system (Figure 5.19). Luminescence analysis of crystalline **Yb-PVDC-1** in chloroform displays Yb^{3+} luminescence in the NIR. Interestingly, the MOF excitation spectrum is notably red-shifted, displaying bands with maxima at 370 nm and 470 nm. The apparent maximum of the excitation band shifts from 415 nm for the Yb-PVDC complex to 470 nm for **Yb-PVDC-1**, which is a significant change.

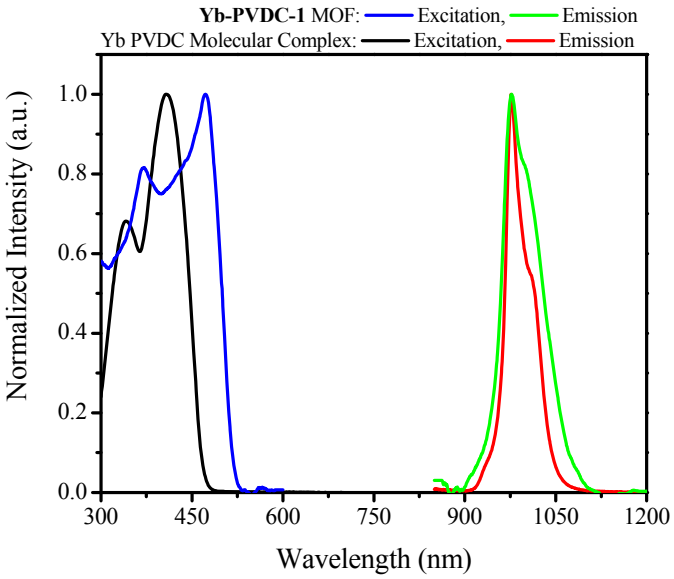

Figure 5.19. Luminescence spectra for the MOF Yb-PVDC-1($CHCl_3$) and corresponding molecular complex in solution (DMSO). The excitation spectra (blue and black, respectively) show the shift towards lower energy induced by the MOF structure, while emission spectra (green and red, respectively) both display characteristic Yb^{3+} emission bands centered at 980 nm.

Although the Yb-PVDC complex experiments were performed in DMSO due to solubility constraints, this shift of over 50 nm can not solely be attributed to solvatochromic effects between DMSO and chloroform. Rather, a significant component of this shift is attributed to organizational constraints the MOF architecture imparts on the phenylene vinylene linkers. Within the structure of **Yb-PVDC-1**, the ligands are arranged in parallel along the [110] plane, which may allow for weak interactions between neighboring ligands (Figure 5.20). These interactions are hypothesized to affect the electronic structure of the chromophore, resulting in the lowering of the excitation energy of the antennae. This result is important because it indicates that the structural rigidity of the MOF architecture can impact the photophysical properties of the Ln-antennae couple and thus produce low energy excitation pathways.

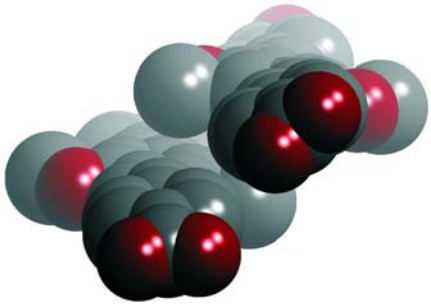

Figure 5.20. Image of the ligand stacking motif within Yb-PVDC-1 along [110], illustrating the proximity of the ligands to each other, which may be allowing for weak π-π interactions.

To further evaluate whether ligand-ligand interactions play a role in the excitation and emission properties of Yb-PVDC systems, a second MOF was prepared, **Yb-PVDC-2**, formulated as $[Yb_2(C_{26}H_{20}O_6)_3]\bullet(DMF)_{12}(H_2O)_{10}$. A lower amount of water was added during the synthesis of **Yb-PVDC-2** in comparison to **Yb-PVDC-1** in an attempt to eliminate the coordinated water molecules and free sites on the Yb^{3+} for ligand coordination. **Yb-PVDC-2** is a more orange color than **Yb-PVDC-1**, with block-like crystalline nature (Figure 5.21).

Figure 5.21. Photograph of Yb-PVDC-2, showing its yellow-orange crystalline nature.

Yb-PVDC-2 crystallizes in the orthorhombic *Pnna* space group and also exhibits infinite Yb-carboxylate SBUs (Figure 5.22). However, the connectivity within the SBU differs from that of **Yb-PVDC-1**. The SBU is composed of alternating octa- and hexa-coordinated Yb^{3+}. The Yb^{3+} are bridged by two carboxylates in a di-mondodentate fashion and by a third carboxylate that chelates the octa-coordinate Yb^{3+} and coordinates in a monodentate fashion to the hexa-coordinate Yb^{3+} (Figure 5.23). These coordination modes result in a chain of corner-sharing polyhedral Yb^{3+}. Each chain is linked to six other chains via the phenylene vinylene portion of the PVDC linkers.

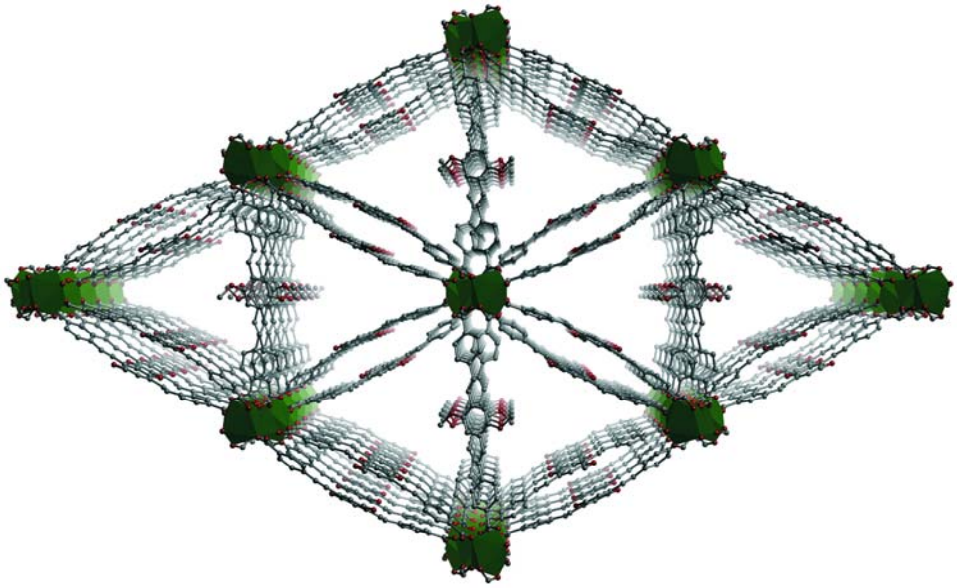

Figure 5.22. Projection view of Yb-PVDC-2 framework viewed along the *a* crystallographic direction.

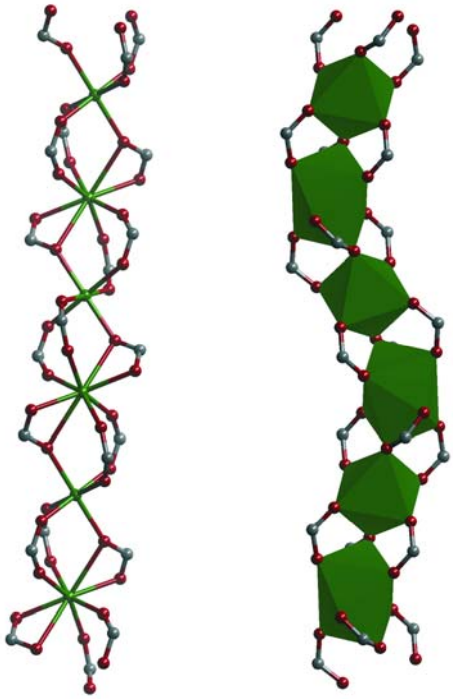

Figure 5.23. Ball and stick depiction, C: grey; O: red; Yb: green (left), and with Yb^{3+} polyhedra represented in green (right) of infinite SBU for Yb-PVDC-2.

The linkers that connect the chains along the [001] stack in parallel with one another, while those that connect the chains in the [011] form pairs that criss-cross with one another, resulting in close π-π interactions (3-3.5 Å) between the central phenyl rings of the PVDC linkers (Figure 5.24). Because each infinite SBU is connected to six other SBUs, the resulting triangular channels are necessarily smaller than those observed for **Yb-PVDC-1**, measuring approximately 13-14 Å from corner to edge (Figure 5.22).

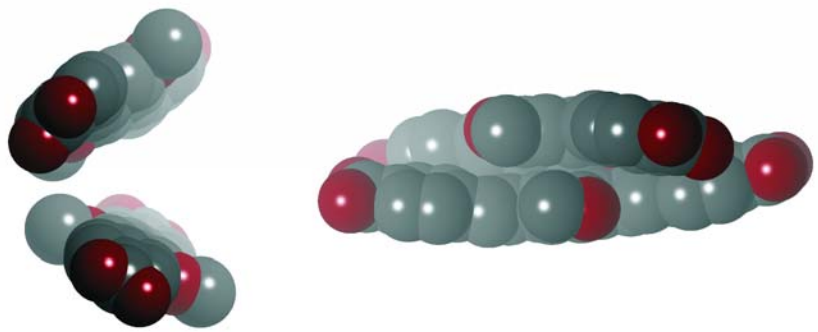

Figure 5.24. Ligand stacking motifs within Yb-PVDC-2, illustrating the proximity of the ligands to each other, which may be allow for π-π interactions.

The luminescence properties of **Yb-PVDC-2** were investigated to determine the impact of these close ligand-ligand π-π interactions on the system.[193,194] The excitation spectrum collected upon monitoring the emission intensity of Yb^{3+} luminescence at 980 nm displayed apparent band maxima at 370 nm and 500 nm (Figure 5.25). The emission spectra collected in the near-infrared range upon excitation at wavelengths corresponding to these maxima produce characteristic Yb^{3+} emission. Interestingly, the lowest energy excitation band of **Yb-PVDC-2** is further red-shifted from 470 nm in **Yb-PVDC-1** to 500 nm. It is rationalized that the close π-π

interactions between the PVDC linkers decreases the $\pi \rightarrow \pi^*$ transition, thus resulting in a decrease in the excitation energy.

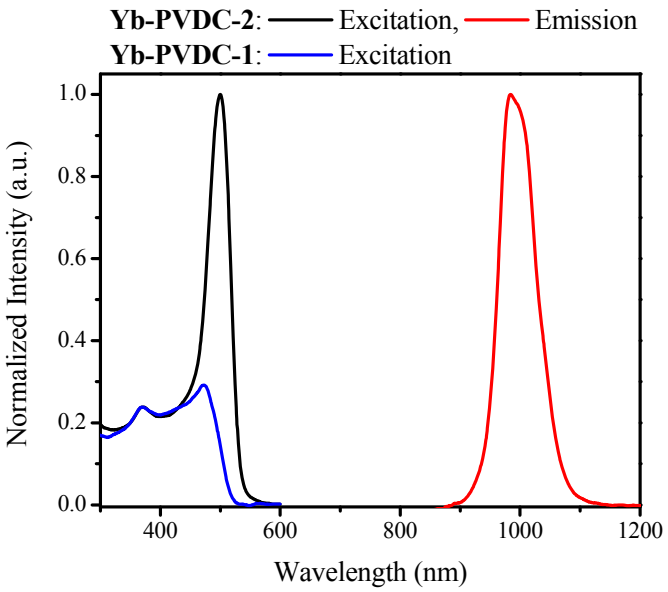

Figure 5.25. Emission spectrum (red) monitored in the NIR upon excitation at 500 nm and excitation spectrum of Yb^{3+} emission at 980 nm (black) of Yb-PVDC-2. The excitation spectrum for Yb-PVDC-1 (blue) is included for comparison.

To determine whether the MOF architecture provides efficient protection for the lanthanide cations from solvent quenching and to quantify the intramolecular energy transfer of the systems, quantum yield values were measured and the results are reported in Table 5.1. The quantum yield of **Yb-PVDC-2** is five times higher than **Yb-PVDC-1** when excited through the lower energy band (490 nm), indicating the improved efficiency of the $\pi \rightarrow \pi^*$ transition for intramolecular energy transfer. The quantum yield of **Yb-PVDC-2** is among the highest values reported so far for ytterbium systems under solvent.[58-61] It is important to note that these quantum

yields are global: the excitation is performed through the sensitizer and the emission is observed through the Yb^{3+} cations that have two different coordination environments and levels of protection in both MOFs. In **Yb-PVDC-1**, the octa-coordinate Yb^{3+} are coordinated by two water molecules which quench ytterbium emission and lower the global quantum yield.

Table 5.1. Absolute emission quantum yields (Φ) for Yb^{3+} luminescence in Yb-PVDC MOFs as crystalline solids under chloroform. λ_{ex} = 490 nm was used for quantum yield determinations, error included in parentheses.

Sample	Φ_{Yb}
Yb-PVDC-1	3.3 (±0.5) x 10^{-3}
Yb-PVDC-2	1.8 (±0.2) x 10^{-2}

The ytterbium centered luminescence lifetimes were monitored in order to further determine the effectiveness of the MOFs in protecting the lanthanide cations from nonradiative deactivation. Both MOFs displayed multi-exponential decay patterns and were best fit with four components, listed in Table 5.2.

Table 5.2. Luminescent lifetimes of Yb^{3+} centered emission at 980 nm of MOFs as crystalline solids under chloroform, λ_{ex}= 354 nm, error included in parentheses.

Sample	τ_1 (μs)	τ2 (μs)	τ_3 (μs)	τ_4 (μs)
Yb-PVDC-1	29 (±2)	10 (±1)	1.5 (±0.5)	0.34 (±0.06)
Yb-PVDC-2	22 (±4)	5.6 (±1.5)	1.7 (±0.3)	0.61 (±0.17)

These four components are tentatively attributed to four different lanthanide environments: the hexa-coordinate and octa-coordinate Yb^{3+} sites within the core of the MOF structures and those along the terminating edges of the crystals, where the lanthanide cations are more exposed to

sources of non-radiative deactivating species present in the environment. Since luminescence lifetimes of lanthanide cations are strongly influenced by the cation coordination environment as well as the extent of quenching, the two MOFs are expected to have different lifetime profiles. However, both MOFs display comparable luminescence lifetime values for the longest component, despite the presence of the water molecules coordinated to one of the Yb^{3+} within **Yb-PVDC-1**, which quench luminescence and shorten the lifetime. The long component values are two times longer than the longest lifetimes reported for Yb^{3+} molecular species in solution.[7,195,196] These luminescence lifetimes demonstrate that MOFs can provide coordination environments with better protection from quenching than molecular complexes.

Luminescence spectra and quantum yields for **Yb-PVDC-2** were both measured in a variety of solvents to investigate any solvent effects. **Yb-PVDC-2** sensitizes ytterbium under chloroform, toluene, benzene, and DMF. The excitation spectra of ytterbium emission at 980 nm in these different solvents are shown in Figure 5.26.

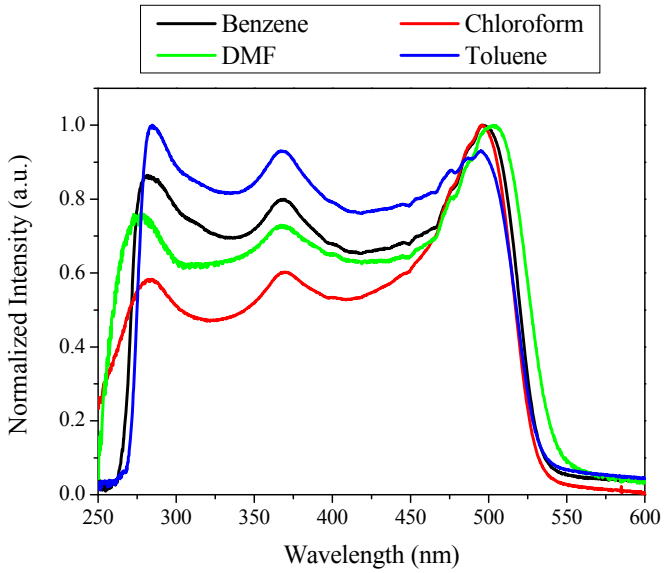

Figure 5.26. Ytterbium excitation spectra (λ_{em}: 980 nm) for Yb-PVDC-2 under different solvents.

All excitation spectra have similar profiles, with maxima at centered at the same wavelengths. There are some variations in the intensities at higher energy, which is likely due to differences in the solvent absorption. It is important to note there are no major shifts in the locations of the excitation maxima between solvents, which confirms that the dramatic differences in excitation wavelengths for the MOFs versus the molecular complex can not be due to solvatochromic effects. The quantum yields are reported in Table 5.3.

Table 5.3. Absolute emission quantum yields (Φ) for Yb^{3+} luminescence in Yb-PVDC-2 under different solvents. λ_{ex} = 490 nm was used for quantum yield determinations, error included in parentheses.

Solvent	Φ_{Yb}
Benzene	1.5 (+/- 0.1) %
Toluene	1.6 (+/- 0.1) %
Chloroform	1.8 (+/- 0.2) %
DMF	0.4 (+/- 0.2) %

The values among benzene, toluene, and chloroform are within error of each other, which is rational since none of these solvents contain highly quenching modes. In contrast, the quantum yield under DMF is much lower; however, this is likely due to instability of this compound in this solvent rather than quenching effects. Alternatively, DMF is a highly hygroscopic solvent so the water content may be much larger which could also lead to decreased quantum yields. It was noted that after a few days under DMF, the solvent became yellow, indicating breakdown of the crystal structure.

For practical applications, especially biological applications, water solubility is a highly desirable property, thus water was tested as a solvent for the two ytterbium MOFs. **Yb-PVDC-1** displayed stability under water, however, it was limited to 1 – 2 days. The quantum yield of **Yb-PVDC-1** in water is 8.1 (± 0.6) x 10^{-5}, which is a value that reflects some quenching from its value of 3.3 (±0.5) x 10^{-3} in chloroform. Since water is an efficient quencher for NIR emitting lanthanide cations, and this MOF has limited stability in water, these results are not surprising. The luminescence lifetimes of ytterbium were also measured, and three components were obtained: 0.266 ± 0.002 μs, 0.70 ± 0.01 μs, and 4.3 ± 0.7 μs. These values are much shorter than the long values measured for **Yb-PVDC-1** under chloroform, indicating that water can penetrate the pores to be in close proximity to the ytterbium cations. Also, only three components were measured for in water compared to four in chloroform, which may be due to some ytterbium cations being highly coordinated with water, decreasing the luminescence intensity below the instrumental detection limits. Despite the limited stability, these results in water are exciting. If nano-MOFs were targeted with this material, they may have sufficient water stability to allow encapsulation in a micelle or some other method of protection which would render them useful for applications such as biological imaging.

A MOF was also successfully synthesized with PVDC and NIR emitting erbium, **Er-PVDC-1**. This MOF is synthesized under the same conditions, and adopts the same topology and structure as **Yb-PVDC-1**. Photophysical analyses reveal that erbium emission is also sensitized via the antenna effect by PVDC, and its excitation spectrum is similar to that of **Yb-PVDC-1**. The emission and excitation spectra for **Er-PVDC-1** in DMF are shown in Figure 5.27.

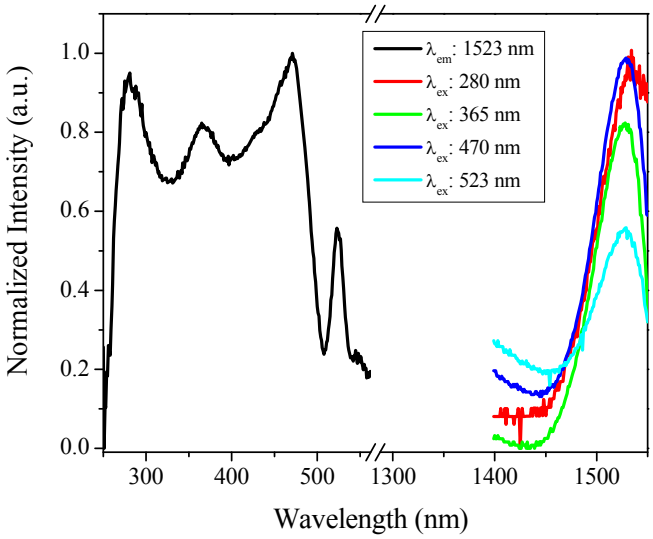

Figure 5.27. Excitation spectrum of NIR erbium luminescence at 1523 nm and corresponding emission spectra of Er-PVDC-1 under DMF.

As seen in the excitation spectrum, there are bands located at 280 nm, 370 nm, and 470 nm, similar to the spectrum for **Yb-PVDC-1**. There is also a narrow band at approximately 520 nm, which corresponds to an erbium absorbance band and is a result of direct excitation of the metal. Since solvents can have high absorptivity above 300 nm, the band at 280 nm may be a distorted shoulder of a higher energy transition and is therefore not considered further. Excitation in the

visible range is of more interest for practical applications and is also easier to study as the instrument lamp output is much greater in this range (compared to the UV range); thus the bands at 370 nm and 470 nm are considered the dominant two excitation bands. Excitation at both of these wavelengths, in addition to direct band at 523 nm, lead to luminescence in the NIR at around 1525 nm, characteristic of erbium.

Er-PVDC-1 was also stable under chloroform, and to allow for an easier comparison with **Yb-PVDC-1**, the photophysical properties were also investigated in this solvent. As seen in Figure 5.28, the excitation spectrum collected upon monitoring erbium emission at 1525 nm displays bands at 370 nm, 470 nm, 520 nm (appears as a shoulder) and 650 nm; the latter two are due to direct excitation of the metal.

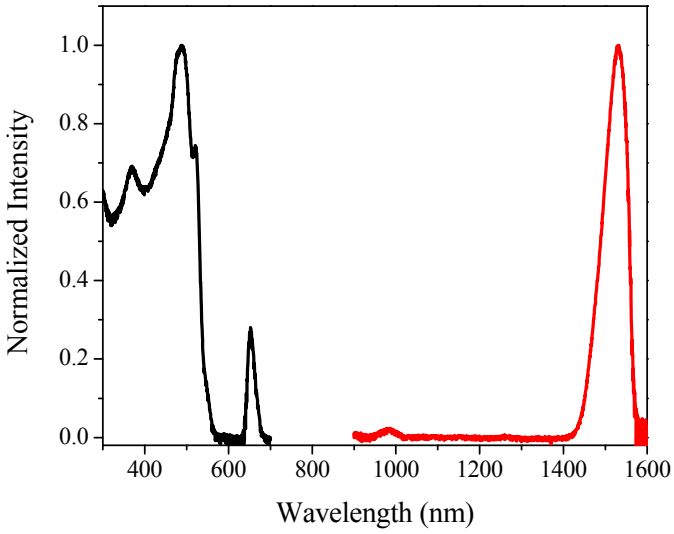

Figure 5.28. Excitation spectrum (black) of erbium emission at 1525 nm and NIR emission spectrum (red) resulting from excitation at 490 nm for Er-PVDC-1 in chloroform.

In this spectrum the bands at 470 nm and 520 nm are broadened and overlap, causing the lower energy band to appear as more intense. The presence of the relatively strong direct excitation bands in the spectrum indicate that the energy transfer between PVDC and erbium may be weak, and that the MOF can provide adequate protection for the erbium to allow for detectable levels of erbium emission resulting from direct lanthanide excitation. Frequently, in molecular complexes in solution, only excitation bands through the antennae effect are detected because there is too much quenching for the direct excitation bands to be efficiently detected. Excitation at 490 nm produces a characteristic erbium emission spectrum in the NIR range with a dominant band at 1525 nm and a minor band at 975 nm. This higher energy emission band at 975 nm is quite weak and difficult to detect and to discriminate from background signal, thus, the band at 1525 nm is used for characterizing the material.

The quantum yield of erbium luminescence for **Er-PVDC-1** upon excitation through the low energy band 490 nm is 8.5 (± 0.4) x 10^{-5}. (490 nm is used as the excitation wavelength rather than 470 nm to allow for comparison with **Yb-PVDC-1**, whose quantum yields were measured at 490 nm. Since these wavelengths fall in the same band and therefore the same electronic transitions, the quantum efficiency should be the same for both wavelengths.) This quantum yield is in the same range as the highest values reported for erbium complexes in solution,[7,197] which indicates that the MOF provides good protection of the lanthanide cations. Due to instrumental constraints, it is not possible to monitor the luminescence lifetimes of erbium emission at 1525 nm, and the higher energy band at 975 nm does not produce sufficient intensity to measure a luminescence lifetime. Thus, it is not possible to study the luminescence lifetimes of erbium in **Er-PVDC-1** to further determine the level of protection the MOF provides.

In addition to **Yb-PVDC-1** and **Er-PVDC-1** a neodymium MOF was also synthesized with PVDC. This MOF, **Nd-PVDC-1** resembles the other PVDC-1 MOFs, however, it displays poor crystallinity and thus the exact structure of the material could not be determined. The much larger size of neodymium compared to the other two lanthanide cations is likely to be the cause of this difference from the other MOFs. The photophysical properties of **Nd-PVDC-1** were investigated nevertheless. The excitation and emission spectra of the MOF under DMF can be seen in Figure 5.29.

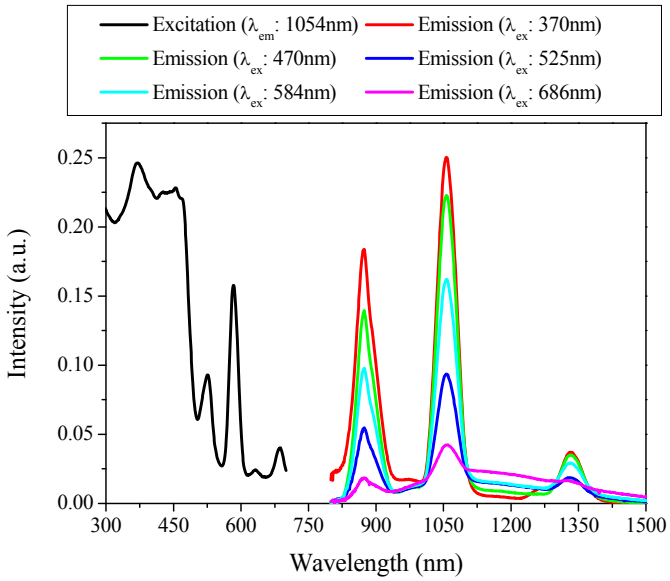

Figure 5.29. Excitation and emission spectra of neodymium luminescence in the NIR for Nd-PVDC-1 in DMF.

The excitation spectrum of Nd^{3+} emission centered at 1054 nm revealed a combination of direct excitation bands and antennae effect excitation bands. Bands located at 280 nm, 370 nm, and 470 nm are similar to the excitation profile for **Er-PVDC-1** and **Yb-PVDC-1**, and are evidence of

antennae effect sensitization of Nd^{3+} in this MOF. It is noteworthy, however, that the band at 470 nm is weaker for **Nd-PVDC-1**, which may be due to this MOFs poor crystallinity effecting the strength of the PVDC interchain electronic dynamics. Emission spectra collected with excitation through all six bands (280 nm, 370 nm, 470 nm, 525 nm, 585 nm, and 685nm) results in Nd^{3+} emission bands. The emission spectrum collected at 685 nm also produces a broad band centered around 1120 nm, which is a background signal arising from the quartz cuvette and integration sphere set-up; corrections can be done to remove this and isolate the sample signal. **Nd-PVDC-1** does show PVDC sensitized luminescence in the NIR, however, due to its limited crystallinity, no further analysis has been conducted.

After demonstrating that several individual lanthanide **PVDC-1** systems could be synthesized and result in sensitized NIR emitting products, multiple lanthanide MOFs were targeted. Since **Yb-PVDC-1** and **Er-PVDC-1** were the most stable MOFs, a variety of $\mathbf{Er_xYb_{1-x}}$-**PVDC-1** MOFs were synthesized, with the goal of obtaining a bar-coded material. A material that can excite at one wavelength and produce two luminescence bands whose respective intensities could be controlled by the composition of the material would be desirable for a wide range of applications such as sensors, hidden tags, or security purposes. MOFs with erbium contents ranging from 30 – 80% were synthesized following the same procedure for **Er-PVDC-1** or **Yb-PVDC-1**, and their photophysical properties were investigated. The relative concentrations of the two lanthanide cations during synthesis are shown in Table 5.4, along with the actual percentages of erbium in the MOFs as determined by EDX analyses. These results show that the **PVDC-1** MOF show no preference toward one lanthanide cation, and the relative ratios of the two lanthanides can be easily controlled through the synthetic conditions of the material.

Table 5.4. Relative erbium and ytterbium content for Er_xYb_{1-x}-PVDC-1 MOFs during synthesis and as determined by EDX in the final product.

	PVDC (mmol)	$Er(NO_3)_3$ (mmol)	$Yb(NO_3)_3$ (mmol)	Theoretical Er^{3+} (%)	Actual Er^{3+} (%)
$Er_{0.3}Yb_{0.7}$-PVDC-1	0.02	0.00125	0.0025	33	32 (± 2)
$Er_{0.6}Yb_{0.4}$-PVDC-1	0.02	0.00375	0.0025	60	58 (± 2)
$Er_{0.7}Yb_{0.3}$-PVDC-1	0.02	0.00625	0.0025	71	70 (± 2)
$Er_{0.8}Yb_{0.2}$-PVDC-1	0.02	0.00625	0.00125	83	81 (± 3)

Powder XRD patterns of the **Er_xYb_{1-x}-PVDC-1** MOFs were taken to insure that the structures were the same as previously observed for **Yb-PVDC-1**. As seen in by the results in Figure 5.30, the XRD pattern remains the same regardless of the amount of erbium added to the system indicating that no changes to the MOF structure are induced by the introduction of a second metal.

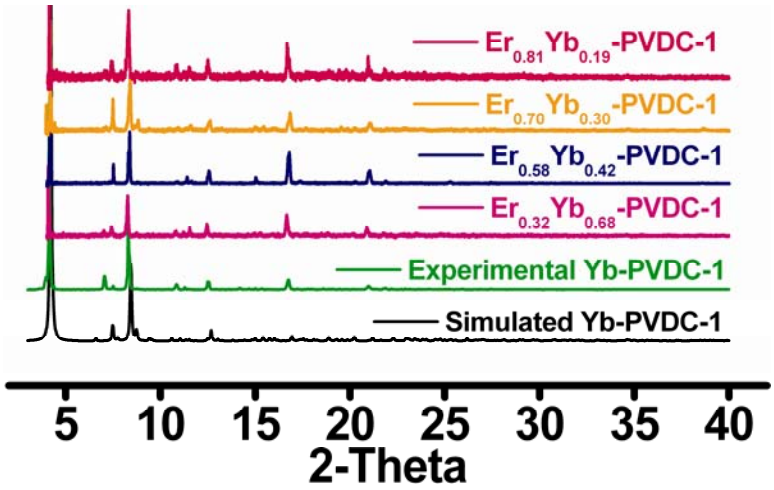

Figure 5.30. Powder XRD patterns for Er_xYb_{1-x}-PVDC-1, compared to Yb-PVDC-1 showing that the MOF structure remains the same for all these systems.

The photophysical studies of these **Er_xYb_{1-x}-PVDC-1** MOFs presented some interesting findings. As expected, these materials display both erbium and ytterbium emission bands in the

NIR when excited at both 370 nm and 490 nm, whose relative intensities vary with their relative atomic composition. Based on the quantum yields of **Yb-PVDC-1** and **Er-PVDC-1**, it was expected that ytterbium should be much more intense than erbium, however, the reverse was observed. Surprisingly, erbium emission is more intense than ytterbium emission in the **Er_xYb_{1-x}-PVDC-1** MOFs. This can be seen the spectra shown in Figure 5.31 and Figure 5.32, which are the luminescence spectra of four different erbium:ytterbium contents normalized to the erbium and ytterbium bands, respectively. Even with only 30% erbium added, **$Er_{0.3}Yb_{0.7}$-PVDC-1** produces a more intense erbium band in comparison to the ytterbium band.

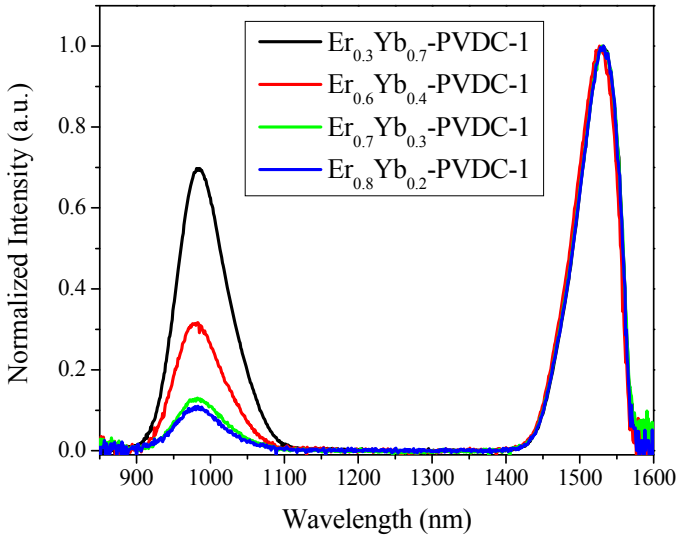

Figure 5.31. NIR emission spectra (λ_{ex}: 490 nm) of Er_xYb_{1-x}-PVDC-1 in chloroform, normalized to erbium emission band.

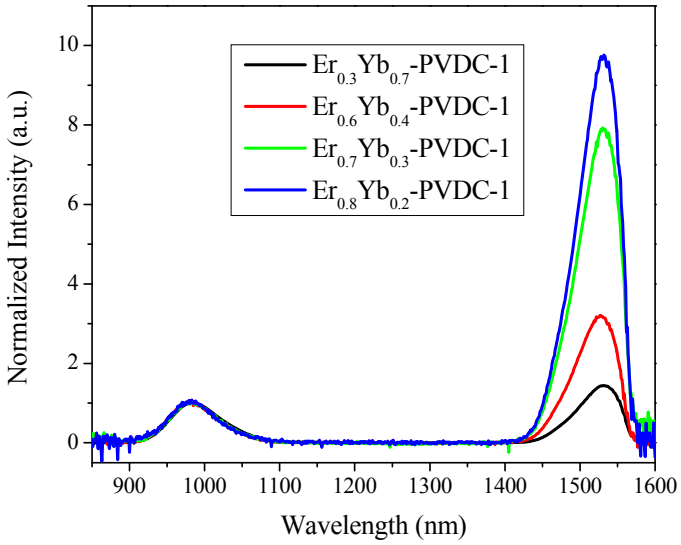

Figure 5.32. NIR emission spectra (λ_{ex}: 490 nm) of Er_xYb_{1-x}-PVDC-1 in chloroform, normalized to ytterbium emission band.

Despite the unexpected intensity of erbium compared to ytterbium in the **Er_xYb_{1-x}-PVDC-1**, the MOFs still displayed a linear relationship between the ratio of the atomic composition of the MOF and the ratio of the intensities of emission of the two lanthanide cations. This trend was seen for excitation at both 370 nm and 490 nm, and the results are plotted in Figure 5.33. These measurements were conducted on **Er_xYb_{1-x}-PVDC-1** in chloroform, and the reported values for each ratio are averages of three independently synthesized MOFs; absolute variance is indicated by the error bars. For both excitation wavelengths, a linear relationship (red trend line) is seen in these plots. This is an exciting result from the perspective of generating a bar-coded material, as it demonstrates that the NIR emission signal can be generated in a predicted and controlled manner through the synthetic conditions of the material.

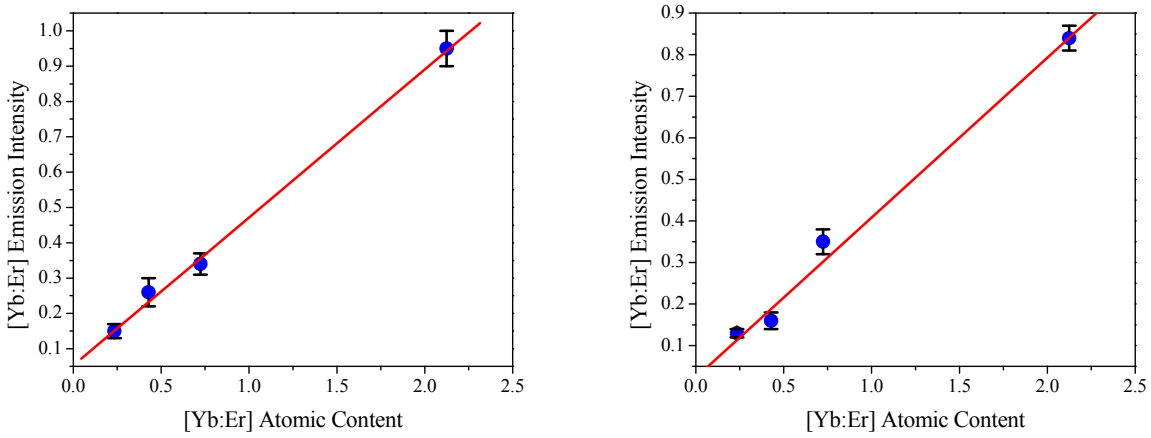

Figure 5.33. Plots depicting the linear relationship between the ytterbium:erbium atomic content and the ytterbium:erbium emission intensities in the Er_xYb_{1-x}-PVDC-1 MOFs under chloroform, when excited at 370 nm (left) and 490 nm (right).

Since most practical applications of a bar-coded luminescent material would require removing the MOFs from solvent, the photophysical properties were also investigated on a few of the MOFs after allowing the chloroform to evaporate, leaving the MOFs dry, under ambient atmosphere. These MOFs produce overall weaker emission spectra than the MOFs under chloroform, resulting in lower signal to noise ratios and larger margins of error. This might be explained by dry material compacting more in the cuvette, allowing less of the MOF to be excited and its luminescence detected. Nevertheless, as shown in the plots in Figure 5.34, the linear relationship between atomic composition and relative emission intensity remains.

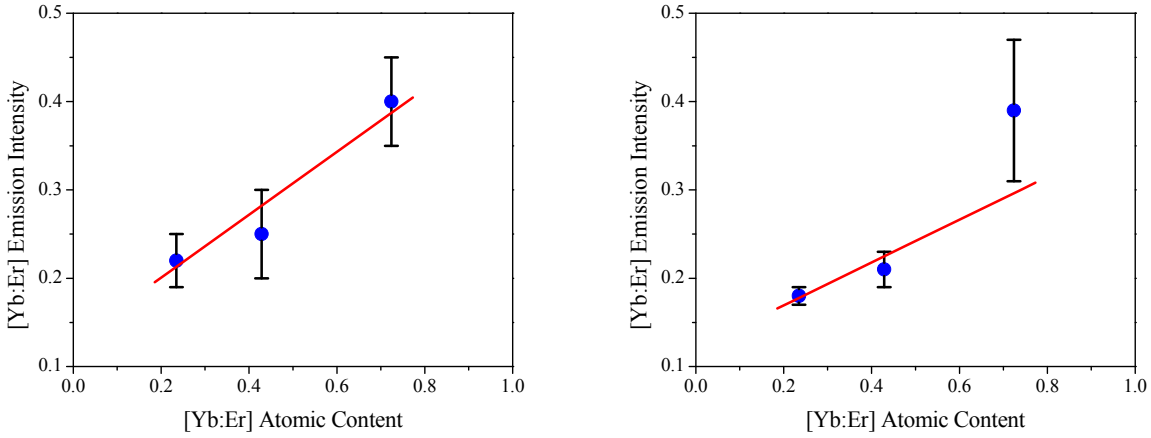

Figure 5.34. Plots depicting the relative linear relationship between the ytterbium:erbium atomic content and the ytterbium:erbium emission intensities in the Er_xYb_{1-x}-PVDC-1 MOFs dry (in air), when excited at 370 nm (left) and 490 nm (right).

Even more importantly, when a small sample is glued to the surface of a microscope slide (shown in Figure 5.35), a sufficiently bright emission for facile detection is produced upon excitation at 490 nm. **Er_xYb_{1-x}-PVDC-1** has the necessary properties to serve as a bar-coded luminescent material, and pursuing future practical applications with this material will be exciting.

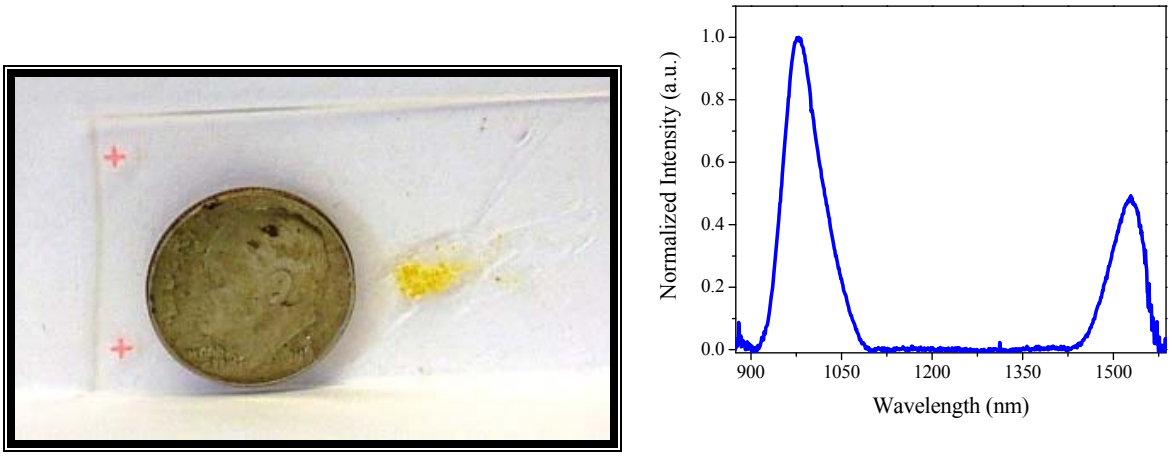

Figure 5.35. Left: $Er_{0.6}Yb_{0.4}$-PVDC-1 sample, dried and glued to a microscope slide (dime is shown for size perspective). Right: The NIR emission spectrum (λ_{ex}: 490 nm) of this sample.

The unexpected relative intensity of erbium in the **Er_xYb_{1-x}-PVDC-1** MOFs prompted further study of its photophysical properties. The intense erbium emission could be due to either quenched ytterbium emission or enhanced erbium emission, or a combination of these two. Quantum yields of both erbium and ytterbium emission were measured for two ratios, the results are tabulated in Table 5.5.

Table 5.5. Absolute emission quantum yields (Φ) for Ln^{3+} luminescence in Er_xYb_{1-x}-PVDC-1 MOFs as crystalline solids under chloroform. λ_{ex} = 490 nm was used for quantum yield determinations, error are included in parentheses.

	Φ_{Yb}	Φ_{Er}
Yb-PVDC-1	3.3 (±0.5) x 10^{-3}	-
Er-PVDC-1	-	8.5 (± 0.4) x 10^{-5}
$Er_{0.3}Yb_{0.7}$-PVDC-1	9.7 (±0.2) x 10^{-5}	1.1 (±0.1) x 10^{-4}
$Er_{0.8}Yb_{0.2}$-PVDC-1	7.8 (±0.3) x 10^{-6}	6.0 (±1.0) x 10^{-5}

As the amount of ytterbium decreases, so does its quantum yield. In fact, the quantum yield decreases by over an order magnitude upon the addition of only 30% erbium. It decreases by another order of magnitude when the erbium content increases to 80%. These extreme changes in quantum yield indicate that the ytterbium emission is being quenched. On the other hand, the erbium quantum yield is actually slightly higher for the 30% erbium MOF than it is for the 100% erbium MOF. This can not be over-interpreted, as all the erbium quantum yields fall within a similar range to each other. If the PVDC groups in the MOF absorb an excess of photons, then the quantum yield should not change as the amount of erbium decreases. However, it could also be possible that PVDC does not absorb an excess of photons, and that the erbium quantum yield is enhanced due to energy transfer from the ytterbium; a hypothesis which the decrease in ytterbium quantum yield supports. Since the only difference between **Yb-PVDC-1** and **Er_xYb_{1-x}-PVDC-1** is the addition of the erbium cations, energy transfer from ytterbium to the erbium is the single most likely explanation for the quenched ytterbium luminescence and enhanced erbium intensity.

To further explore the quenched nature of ytterbium in **Er_xYb_{1-x}-PVDC-1** luminescent lifetimes of ytterbium in **$Er_{0.3}Yb_{0.7}$-PVDC-1** were measured, and displayed biexponetial behavior with values of 0.27 (±0.03) μs and 0.77 (±0.09) μs. Luminescence lifetime measurements for ytterbium were also conducted on **$Er_{0.8}Yb_{0.2}$-PVDC-1**, however, the signal was too weak to be discriminated from the background. These values reflect a significant quenching from the longed lived values reported for **Yb-PVDC-1** in Table 5.2. Moreover, there are only two values detected for this MOF compared to four components in the ytterbium only system. These shortened lifetimes provide further indication of energy transfer from ytterbium to erbium in the **PVDC-1** MOF. It would be interesting to monitor the erbium luminescence

lifetimes to determine if they display longer values; however, we do not currently have a detector capable of measuring lifetimes above 1450 nm.

In addition to the **Er_xYb_{1-x}-PVDC-1**, a MOF containing three NIR emitting lanthanide cations was synthesized. As seen in Figure 5.36, an emission spectrum comprised of bands from all three lanthanide cations is produced upon excitation at 490 nm. The individual lanthanide excitation spectra all show **PVDC-1** profiles, indicating antenna effect sensitization. The neodymium excitation spectrum also contains significant direct excitation bands, similar the **Nd-PVDC-1** results. These preliminary results are exciting as they demonstrate the potential for future development of more sophisticated bar-coded materials.

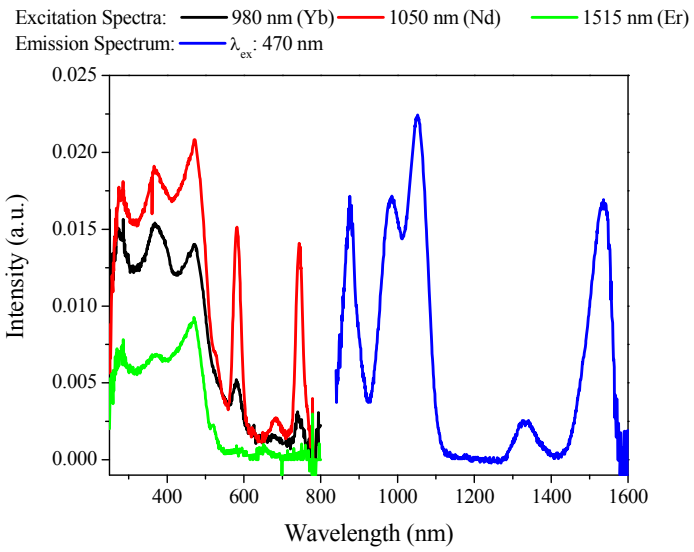

Figure 5.36. Emission spectrum (blue) in the NIR range upon excitation at 470 nm for $Nd_{0.1}Er_{0.5}Yb_{0.4}$-PVDC-1 under chloroform, and the corresponding excitation spectra of each lanthanide: neodymium emission at 1050 nm (red), erbium emission at 1515 nm (green) and ytterbium emission at 980 nm (black).

5.3.4. Zn-PVDC MOFs as host networks for NIR emitting lanthanide cations

Yellow block **Zn-PVDC-1** crystals were synthesized in a vial from $Zn(NO_3)_2 \cdot 4H_2O$ and excess H_2-PVDC in DMF and isopropanol in an 85ºC isotemp oven for 48 hrs. X-ray diffraction revealed that **Zn-PVDC-1** crystallized in the monoclinic space group P2/c with a = 25.954(8), b = 36.012(11), c = 44.264(13); $\alpha = \gamma = 90.00º$, $\beta = 123.747(3)º$. Upon deprotonation of the carboxylic acid groups, the carboxylates bonded to the Zn^{2+} atoms to form a $Zn_4O(COO)_6$ octahedral secondary building unit, *in situ*, shown in Figure 5.37. PVDC connects the octahedral Zn-O-C clusters into a primitive cubic system, as shown in Figure 5.38. Four interlocking cubic frameworks make up the final structure of **Zn-PVDC-1**, shown in Figure 5.39. This interpenetration was expected considering the length of the PVDC linker. Despite **Zn-PVDC-1** having four interpenetrating units, it contains 70% free volume, which is an extremely high value.[176,198] Elemental analysis data determined that 18 DMF molecules and 5 H_2O molecules occupy the pore, giving a general formula of $Zn_4O(C_{26}H_{20}O_6)_3 \cdot (DMF)_{18}(H_2O)_5$.

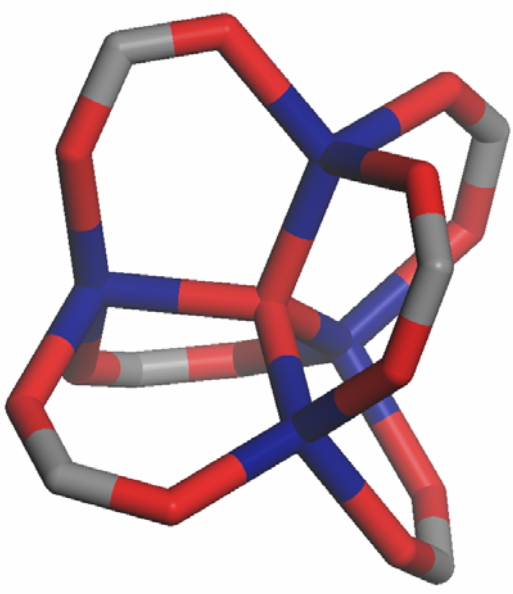

Figure 5.37. $Zn_4O(COO)_6$ octahedral secondary building unit that connects PVDC chains in Zn-PVDC-1.

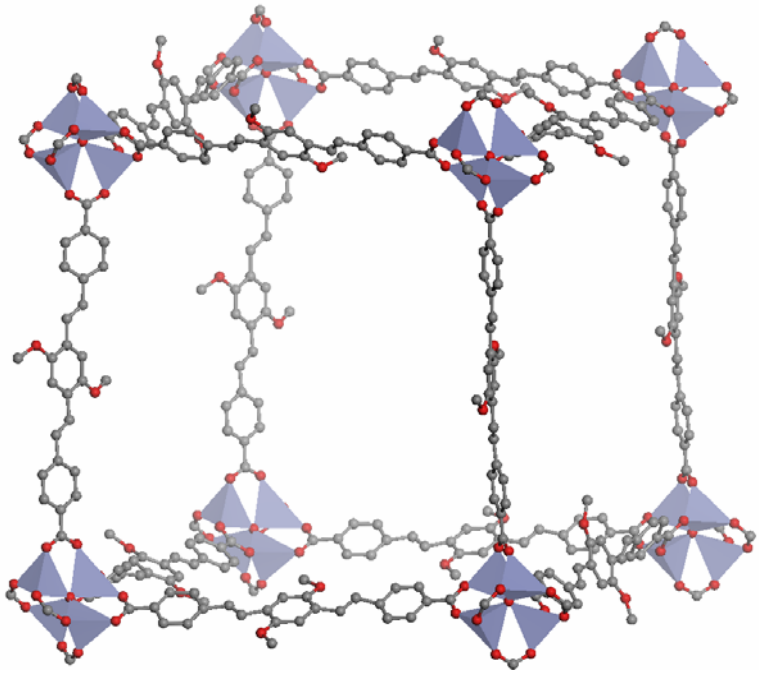

Figure 5.38. One cubic unit of Zn-PVDC-1, Zn: blue, O: red, C: grey.

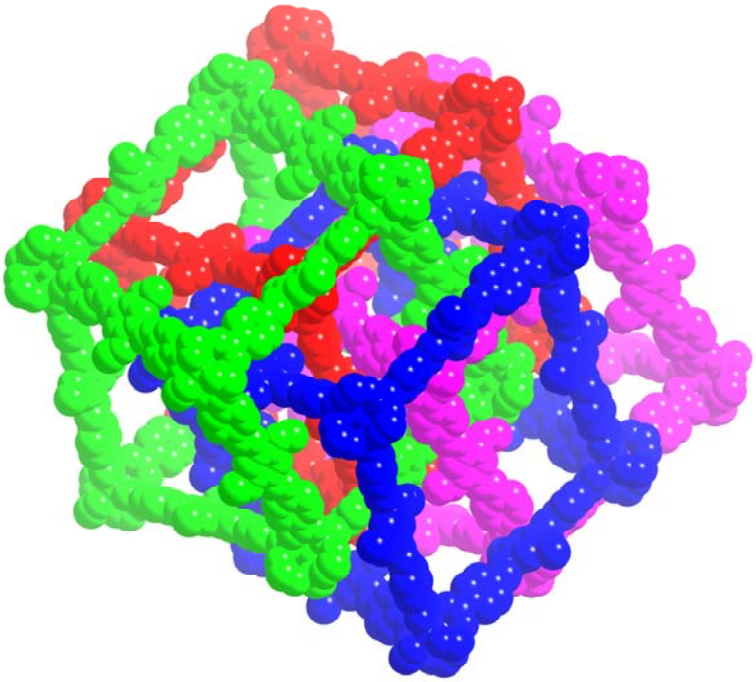

Figure 5.39. van der Waals radii depiction of the 4-fold interpenetrating Zn-PVDC-1.

Powder X-ray diffraction patterns were collected and analyzed to determine the purity of the bulk synthesized material, shown in Figure 5.40.

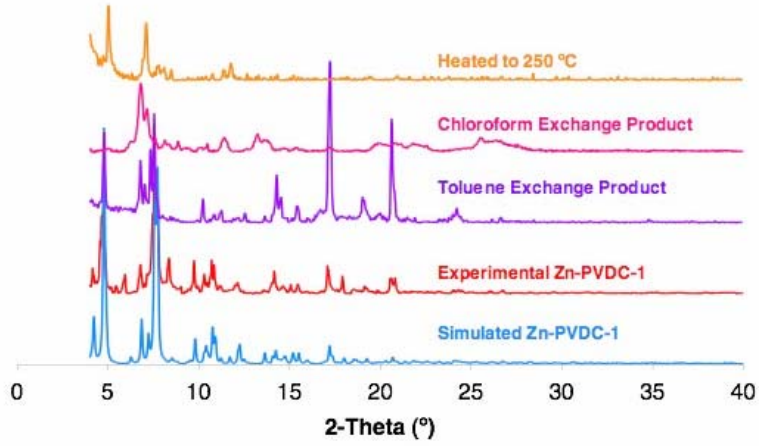

Figure 5.40. PXRD patterns of Zn-PVDC-1 in various solvents.

The d-spacings of the experimental PXRD pattern correspond well with the pattern simulated from the X-ray crystal structure, indicating phase purity. PXRD patterns confirm the stability of **Zn-PVDC-1** after solvent exchange (from DMF to toluene or chloroform), as well as after heating to 250ºC for complete solvent removal. The toluene exchange product gives a PXRD pattern that matches well with the simulated and experimental patterns. The presence of the most intense peaks in the PXRD pattern shows that **Zn-PVDC-1** is also stable in chloroform.

Preliminary studies of **Zn-PVDC-1** were conducted to determine the effect of guest molecules on the framework's fluorescence. A similar MOF composed of Zn_4O clusters connected by stilbene dicarboxylate (PVDC's precursor) demonstrated fluorescence that was dependent upon solvent guest molecules and the possibility for sensing applications[199]. The increase in benzene rings from stilbene to H_2-PVDC could make the fluorescence of **Zn-PVDC-1** more apt to have a dependence on guest molecules. Emission spectra were collected of the MOF in DMF:isopropanol (5:7), chloroform, and toluene (Figure 5.41). The fluorescence of the three crystals varied only slightly, with about a 10 nm difference in the emission spectra, which may be due to solvachromatic effects.

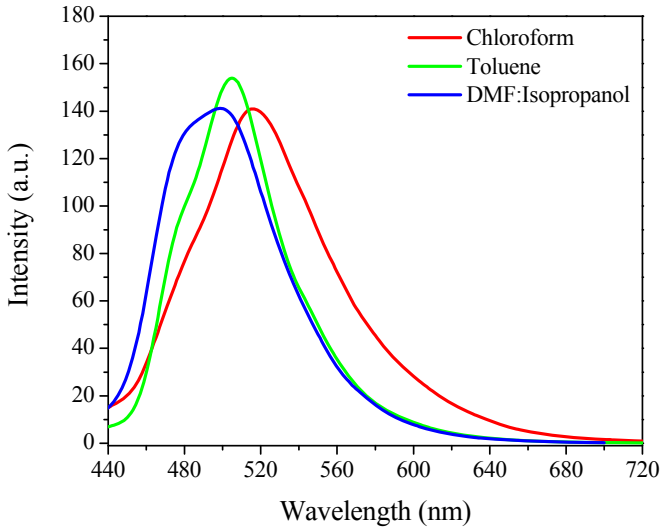

Figure 5.41. Fluorescence of Zn-PVDC-1 in different solvents; λ_{ex}: 400 nm.

Although **Zn-PVDC-1**'s fluorescence may be more sensitive to other guest molecules, such as gasses, at this time the focus was redirected to incorporating lanthanide cations as guest molecules inside the cavities of **Zn-PVDC-1**. These experiments were performed by dissolving $LnCl_3$ in DMF to a desired concentration, and then rinsing the **Zn-PVDC-1** with solvent multiple times to remove any lanthanide cations in solution which were not incorporated into the MOF pores. Photoluminescence experiments were done to determine if lanthanide sensitization was occurring and how its emission intensity related to the concentration during the exchange process. Also, energy-dispersive X-ray spectroscopy (EDX) was performed to correlate the number of lanthanide cations to the lanthanide concentration giving the brightest emission. The zinc to lanthanide ratios also provide information on the amount of lanthanide in the system and their locations. If the lanthanide metals were residing in the pores and not on the surface, there would be a large excess of lanthanide cations in comparison to zinc cations in the framework. In

addition, for systems where a mixture of lanthanide cations were put in the MOF pores, EDS can determine if one metal preferentially occupies the pores over other metals, which may occur due to size differences (i.e., neodymium is larger than ytterbium).

Ytterbium chloride was the first lanthanide cation to be incorporated into **Zn-PVDC-1**, since it the least easily quenched of the four lanthanide cations that PVDC could sensitize. This provided the greatest opportunity for determining the success of this method. The first set of experiments done were to determine if lanthanide sensitization could be achieved via this method, and to optimize the concentration of lanthanide guest molecules for the brightest emission while avoiding self-quenching. $YbCl_3$ was dissolved in DMF to a concentration of 0.05 M, 0.01 M, and 0.005 M, and the crystals were washed with the lanthanide solution, followed by rinsing with DMF to remove any extraneous cations. Photoluminescence analysis revealed effective sensitized Yb^{3+} emission, as shown in Figure 5.42. The excitation profile of ytterbium in **Zn-PVDC-1** contains three bands with maxima at 280 nm, 370 nm, and 470 nm. These wavelengths are similar to those obtained for **Yb-PVDC-1** and are red-shifted in comparison to those observed for the Yb-PVDC complex, whose maxima is at 415 nm. Excitation at all three wavelengths gave Yb^{3+} emission in the NIR range centered at 980 nm.

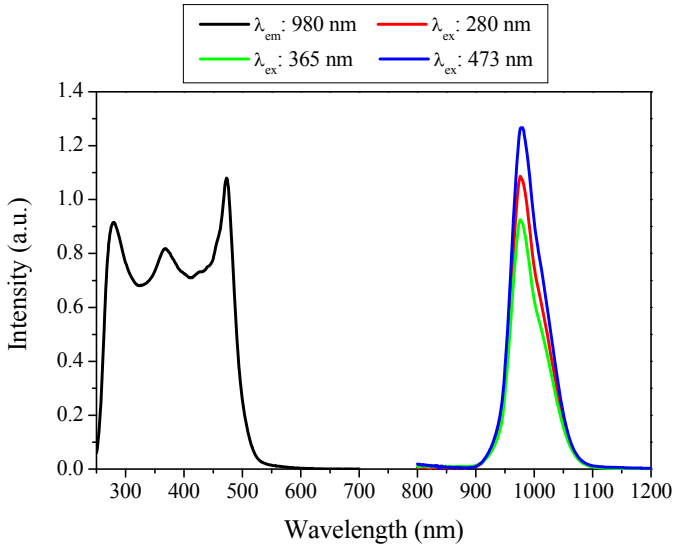

Figure 5.42. Excitation spectrum of ytterbium emission at 980 nm (black) and NIR emission spectra (red, green, and blue) for Zn-PVDC-1 washed with 0.005 M $YbCl_3$.

The emission spectra of the samples with different concentrations were normalized for the sample volume by dividing the emission spectra by their relative absorbance at 370 nm (found by subtracting the Rayleigh band of the sample from that of an empty cuvette). Interestingly, the concentration dependence study revealed that the 0.005 M $YbCl_3$ solution gave the brightest emission, followed by 0.01 M, and then 0.05 M, the most concentrated solution giving the weakest emission, as shown in Figure 5.43. Since the ytterbium solutions are made with $YbCl_3 \cdot 6H_2O$, which can release water upon dissolution, and **Zn-PVDC-1** loses crystallinity in water, a loss of structure may have occurred. To determine if any breakdown in structure took place, the PXRD pattern of **Zn-PVDC-1** with 0.01 M $YbCl_3$ was collected, and indicated that most structural integrity was maintained (Figure 5.44). Energy dispersive x-ray fluorescence (EDS) was used to determine the relative amounts of the two metal cations, shown in Table 5.6. Interestingly, the EDS data suggest that the ytterbium concentrations in the MOF did not

correlate directly with the concentration of the wash solutions. Also, while the 0.005 M $YbCl_3$ had the highest concentration of ytterbium relative to zinc and the highest ytterbium signal, the 0.01 M $YbCl_3$ contained less ytterbium but produced a more intense emission than the 0.05 M $YbCl_3$ sample. Since EDS is sensitive to matrix effects, ytterbium ions on the surface of the MOFs may contribute more to the relative %'s than the zinc and ytterbium cations with in the MOF structures, which may explain some of this discrepancy. It is also likely that some self-quenching between ytterbium cations may have occurred for the more concentrated samples, leading to less intense emission for higher ytterbium washing concentrations, which is the most probable reason.

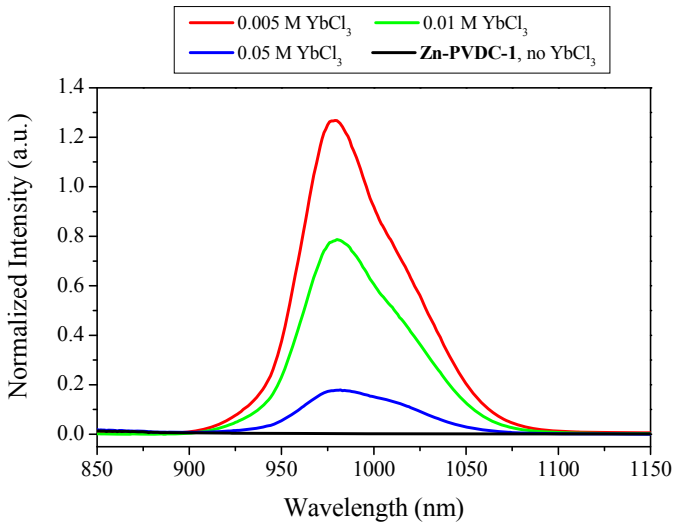

Figure 5.43. NIR luminescence spectra (λ_{ex}: 470 nm) of Zn-PVDC-1 with $YbCl_3$, incorporated at 0.005 M (red), 0.01 M (green), and 0.05 M (blue). The spectrum of Zn-PVDC-1 without ytterbium is shown in black as a control.

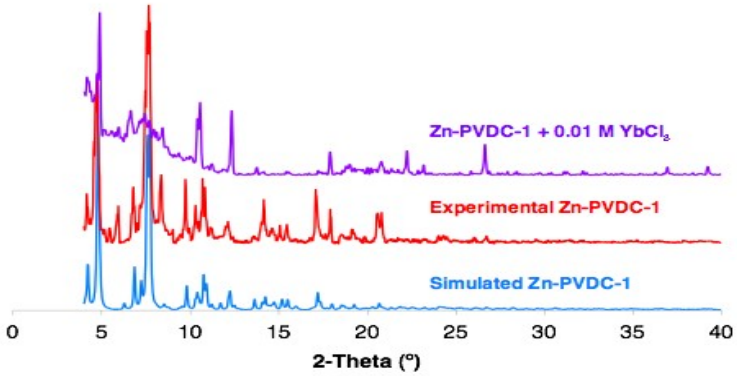

Figure 5.44. Powder XRD patterns of Zn-PVDC-1 with and without ytterbium chloride (0.01 M in DMF).

Table 5.6. EDS data for Zn-PVDC-1 washed with ytterbium chloride solutions, showing the relative amounts of ytterbium and zinc in the systems.

[$YbCl_3$] (M)	Zn^{2+} (%)	Yb^{3+} (%)
0.005	6	94
0.01	24	76
0.05	11	89

$YbCl_3$ was further diluted to determine if even lower concentrations could increase emission intensity; and in fact, 0.0025 M produced the most intense ytterbium emission as seen in Figure 5.45. Again, the EDS data (Table 5.7) does not correspond well with the emission intensity results; however, it does correlate with the concentration of the $YbCl_3$ solutions for this series.

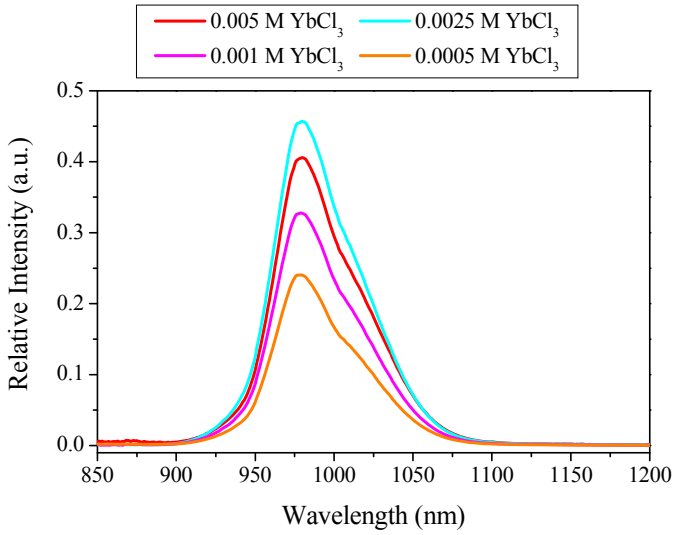

Figure 5.45. NIR luminescence spectra (λ_{ex}: 470 nm) of Zn-PVDC-1 with $YbCl_3$, incorporated at 0.005 M (red), 0.0025 M (cyan), 0.001 M (magenta), and 0.0005 M (orange).

Table 5.7. EDS data for Zn-PVDC-1 washed with ytterbium chloride solutions, showing the relative amounts of ytterbium and zinc in the systems.

[$YbCl_3$] (M)	Zn^{2+} (%)	Yb^{3+} (%)
0.005	6	94
0.0025	18	82
0.001	11	89
0.0005	77	23

As the ytterbium concentration decreases, the relative percentages of ytterbium decreases. There is a marked decrease of ytterbium from 0.001 to 0.0005 M, which suggests there may be a concentration threshold necessary to encourage lanthanide occupation of the pores. The emission intensity is stronger for 0.0025 M than for 0.005 M, which further suggests there may be quenching of the ytterbium cations. Despite the dramatic decrease in the ytterbium percentage from 0.001 to 0.0005 M solutions, the relative ytterbium emissions for these are not that different. Perhaps the ytterbium cations can be located at different locations within the MOF

pores (i.e., close to and further away from the PVDC units or near coordinating solvent molecules) and be sensitized with different efficiencies. Thus, while a greater ytterbium concentration within the pores of the MOF may result in higher concentrations in the wash solutions, not all these lanthanide cations may be in the ideal locale(s) for efficient sensitization. If the ideal sensitization occurs at the locale with the strongest attraction to the ytterbium cations, this would explain how a low percentage of ytterbium cations can still result in a MOF producing a reasonable emission intensity. Elemental analysis via a procedure such as ICP-AES or ICP-MS may clarify how accurate the EDS experiment were to determine Zn:Yb ratios and whether matrix effects are skewing the results. Despite the variance of EDS data, the results of this concentration study suggest that higher washing concentrations lead to higher ytterbium occupation of the pores, and that self-quenching begins to limit ytterbium luminescence output. The ideal washing concentration is determined to be 0.0025 M $LnCl_3$.

Once the method of sensitizing lanthanide cations by incorporating them within the pores of **Zn-PVDC-1** was determined to be successful through experiments with ytterbium chloride, the method was expanded and applied to other NIR emitting lanthanides. Since H_2-PVDC was able to sensitize neodymium, holmium, and erbium, these lanthanide cations were incorporated into **Zn-PVDC-1** in varying ratios, at total lanthanide concentrations of 0.005 M. These studies were conducted immediately following the first results with ytterbium, thus 0.005 M was used instead of 0.0025 M for the lanthanide washes.

Zn-PVDC-1 was able to sensitize neodymium (Figure 5.46) and erbium (Figure 5.47) in the MOF pores, however, no holmium emission was detected. Since holmium emission is often easily quenched, and there are few reports of holmium emission in solution, this is not surprising. Both neodymium and erbium excitation spectra show significant levels of direct excitation in

addition to the PVDC bands, which was not seen for ytterbium because there is only one energy level for this lanthanide so it does not have any direct excitation bands in the visible region. This high level of direct excitation in comparison to the PVDC complexes in solution suggest that the sensitization is not as efficient, perhaps due to the distance between donor and acceptor for this system.

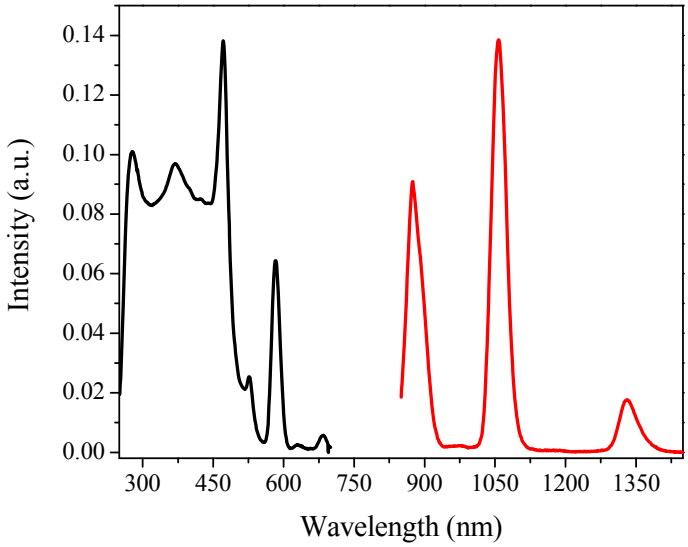

Figure 5.46. NIR luminescence spectrum, λ_{ex}: 470 nm (red) and neodymium excitation spectrum (black) for Zn-PVDC-1 washed with 0.005 M $NdCl_3$ in DMF.

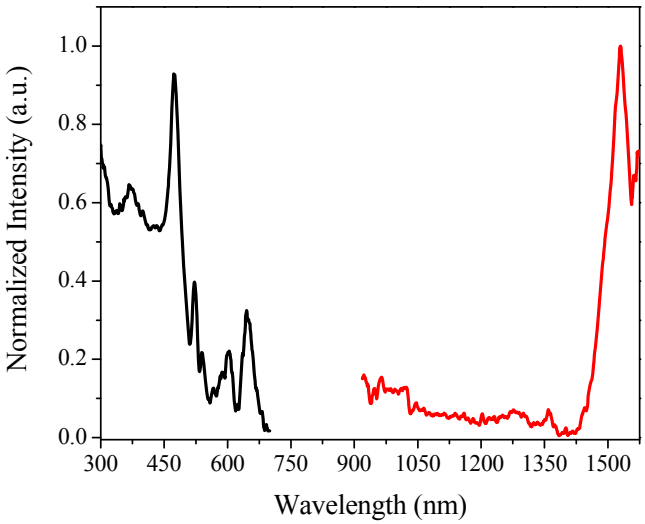

Figure 5.47. NIR luminescence spectrum, λ_{ex}: 470 nm (red) and erbium excitation spectrum (black) for Zn-PVDC-1 washed with 0.005 M $ErCl_3$ in DMF.

The Nd^{3+} exchanged MOF displayed the second highest intensity of lanthanide emission (after ytterbium) for the **Zn-PVDC-1** systems, as evident in Figure 5.48. **Zn-PVDC-1** was exchanged with equimolar quantities of Yb^{3+} and Nd^{3+}, and displayed both luminescence from both lanthanide cations upon excitation at 490 nm through PVDC, demonstrating effective simultaneous sensitization for one compound with one excitation wavelength (Figure 5.49). EDS data showed that equal amounts of each lanthanide were incorporated into the MOF, however, the ytterbium emission remained much brighter. Also, it should be noted that the ytterbium emission of the combined system is brighter than the system with only ytterbium. This is not surprising since it was determined that 0.0025 M exchange conditions produce improved intensity over 0.005 M conditions.

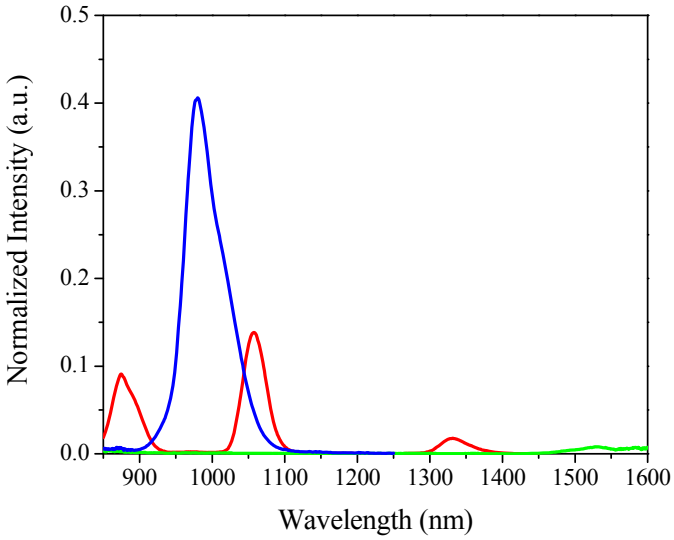

Figure 5.48. NIR luminescence spectra, λ_{ex}: 470 nm, for Zn-PVDC-1 with $NdCl_3$ (red), $ErCl_3$ (green), and $YbCl_3$ (blue) in the pores, made with 0.005 M wash solutions in DMF.

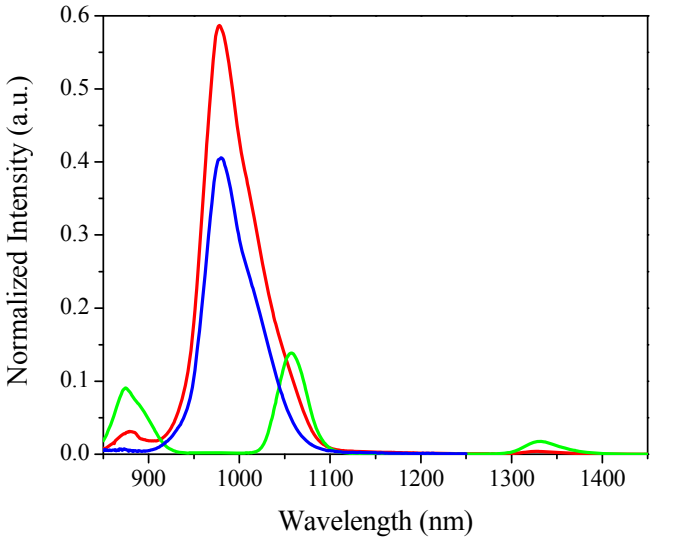

Figure 5.49. NIR luminescence spectra, λ_{ex}: 470 nm, for Zn-PVDC-1 with lanthanide chlorides in the pores, 0.005 M $NdCl_3$ (green), 0.005 M $YbCl_3$ (blue), and 0.0025 M $NdCl_3$ + $YbCl_3$ (red).

Table 5.8. EDS data for Zn-PVDC-1 washed with lanthanide chloride solutions, showing the relative amounts of lanthanide and zinc cations in the systems.

[$LnCl_3$] (M)	Zn^{2+} (%)	Yb^{3+} (%)	Nd^{3+} (%)	Er^{3+} (%)
0.005 Yb^{3+}	6	94		
0.005 Nd^{3+}	18		82	
0.005 Er^{3+}	4			96
0.0025 Yb^{3+}, 0.0025 Nd^{3+}	19	41	40	

The EDS data (Table 5.8) for the lanthanide exchanged systems all showed a much larger number of lanthanide cations compared to zinc cations, which indicates the lanthanide cations are likely residing in the pores. It is possible, however, that they are also occupying some surface sites on the MOF. Also, the EDS data of the single exchanged lanthanide systems show that more erbium and ytterbium are incorporated than neodymium. Since neodymium is larger than the other two cations, this result is not surprising. However, when both ytterbium and neodymium are exchanged, there is only a slight preference for ytterbium. Thus, it can not be conclusively stated that the size of the lanthanide cation influences the level of incorporation within the MOF cavities. The difference between emission intensities of the three lanthanide cations is most likely due to variance in how well each lanthanide is sensitized by PVDC as well as the extent of its quenching. Since erbium has the lowest energy levels, it is most easily quenched by solvent vibrations, followed by neodymium and ytterbium cations.

5.3.4.1. BioMOF-1 as host networks for visible and NIR emitting lanthanide cations

BioMOF-1[188,189] has a unique and interesting structure. First of all, there are adenine-zinc motifs which have an octahedron shape as shown in Figure 5.50. N1 and N2 of the adenine bridge the Zn^{2+} metal ions and N7 and N9 also connects other Zn^{2+} metal ions together. The zinc cations adopt a tetrahedral geometry by coordinating to two adenines and two oxygen atoms

from the dicarboxylate linker. Four adenines are connecting eight zinc metal ions together in this fashion. As seen in Figure 5.51, the zinc cations located in the middle of the octahedra are coordinated by two dicarboxylic acids, expanding the structure by connecting zinc-adenine octahedra together. Two zinc cations on the top and bottom of the octahedra are bridged by sharing an oxo anion. This oxo anion is also shared by two otehr zinc cations from another zinc/adenine octahedra, thus fusing the two octahedra together. The zinc-adeninate octahedra are connected in this manner and form a one-dimensional chain of fused zinc-adeninate octahedra. It should be noted that the zinc/adeninate octahedral each have a small space inside as represented with an orange ball in Figure 5.51. However, the NH_2 group of the adenine effectively obstructs the entrance to these small cavities, rendering the space inaccessible.

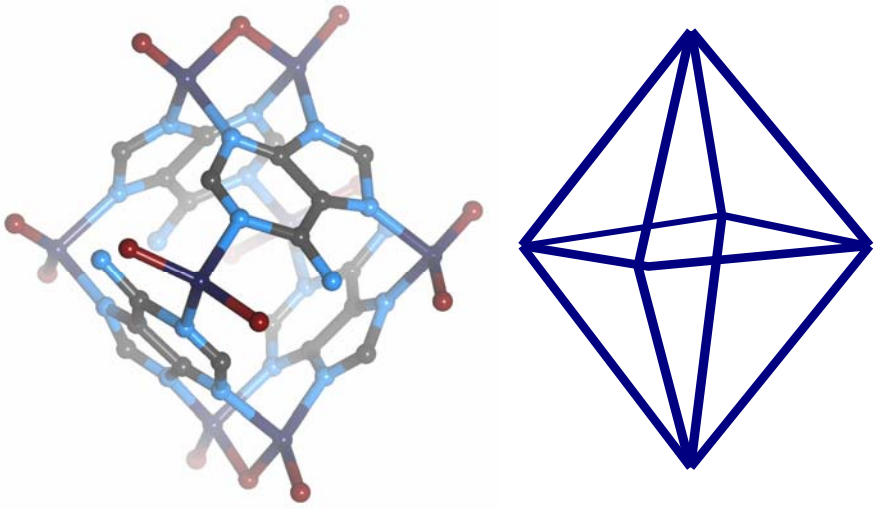

Figure 5.50. Zinc-adenine cluster (right) and octahedron shape of the cluster, left.[188]

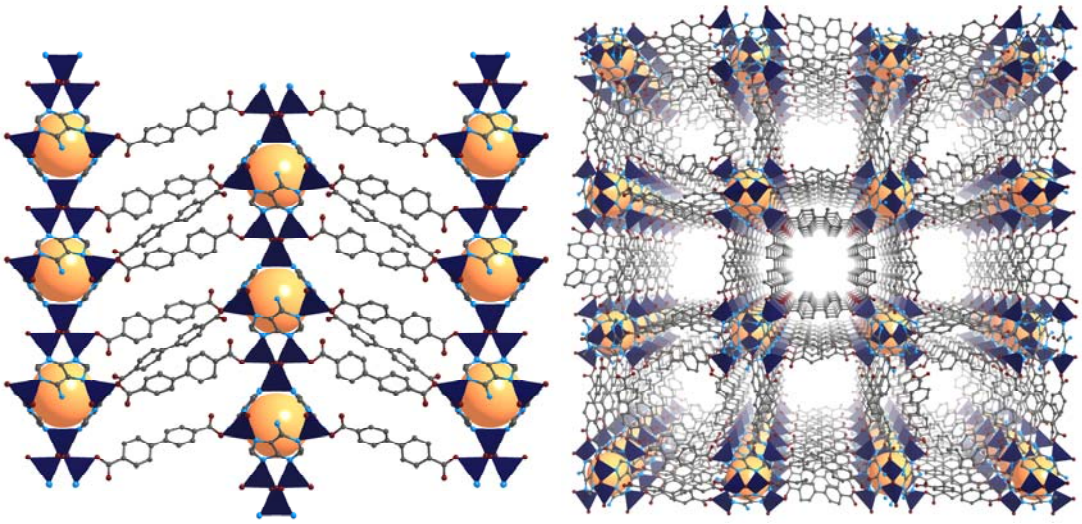

Figure 5.51. Zinc-adenine cluster lined by BPDC (left) and perspective view along the C- crystallographic axis (right). (O: red, N: blue, C: gray, Zn polyhedra: purple, space in the Zn/adenine cluster: orange ball)[188]

4,4-Biphenyldicarboxylates connect the chains of zinc-adeninate octahedra, resulting in the formation of one-dimensional channels as seen in Figure 5.52. The resulting channels have two different sizes and they are approximately 7.6 Å and 9.4 Å.

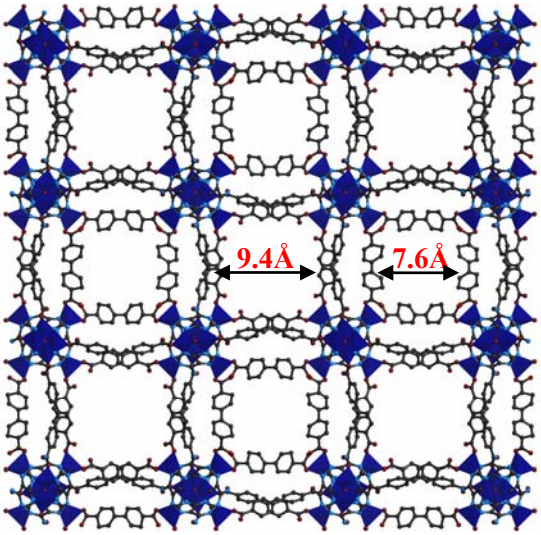

Figure 5.52. The two different pore sizes in BIO-MOF-1.[188]

Elemental analysis data is used to estimate the number of molecules inside of pores of the framework. As synthesized, the crystals are estimated to contain 2.75 water molecules, 2 DMF molecules and 0.5 dimethyl ammonium cations within the channels per formula unit. Since the framework has a net anionic charge (-0.5 per formula unit), the overall framework is neutralized with 0.5 dimethyl ammonium cations. These cation molecules are not part of the framework structure, thus the dimethylammonium cations can be easily exchanged with other cationic molecules, such as lanthanide cations.[188,189]

BioMOF-1 is stable in water and biological buffers at different pHs.[188,189] Incorporating luminescent lanthanide cations into this framework may allow for the development of a novel highly luminescent bioimaging agent with robust properties due to the high density of lanthanide cations per unit of volume.

The photophysical properties of **BioMOF-1** were analyzed to determine where its energy levels are located and which lanthanide cations it may be able to sensitize. The crystals were analyzed in the solid state under DMF using an integration sphere. As seen in Figure 5.53, there are two fluorescence bands. A strong band centered at 415 nm, as well as a weaker emitting band centered around 340 nm. Each fluorescence band corresponds to a unique excitation spectrum, with maxima at 385 nm and 280 nm, respectively. The excitation spectrum corresponding to emission at 415 nm also displays a shoulder around 350 nm.

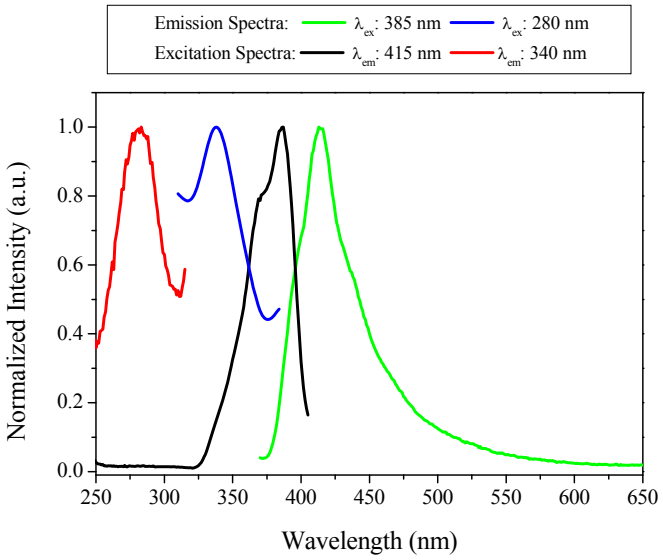

Figure 5.53. Fluorescence spectra, λ_{ex}: 280 nm (blue) and λ_{ex}: 385 nm (green) of BIO-MOF-1 in DMF and corresponding excitation spectra, λ_{em}: 340 nm (red) and λ_{em}: 415 nm (black) of the band maxima.

In order to understand what these two bands correspond to, the absorbance spectra of the two MOF components were measured, Figure 5.54. Adenine was dissolved in water, however, BPDC is not water soluble and was dissolved in DMSO for analysis. BPDC displays an absorbance band centered at 285 nm. Adenine has two absorbance bands with maxima at 205 nm and 260 nm.

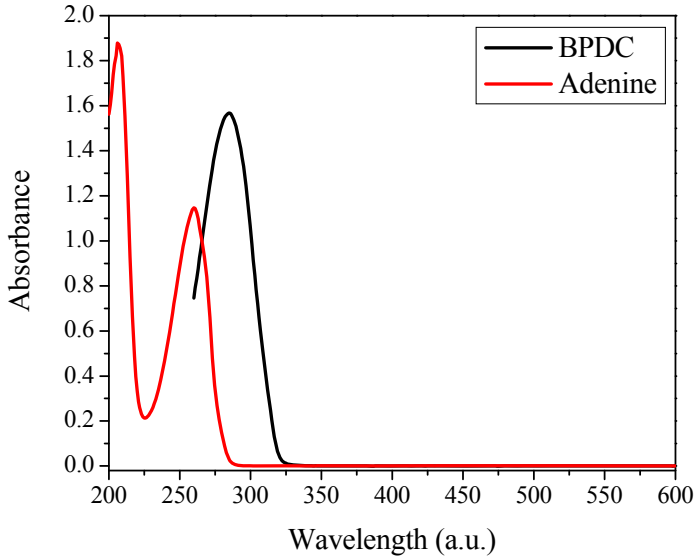

Figure 5.54. Absorbance spectra of BPDC in DMSO (black) and adenine in water (red).

Since the BPDC band at 285 nm and the adenine band at 260 nm are overlapping, it is difficult to specifically assign the **BioMOF-1** excitation band at 280 nm to either component. Surprisingly, neither component has absorbance bands at 385 nm, where the main excitation band of **BioMOF-1** fluorescence lies. Based on the difference between the absorbance spectra of the two components and the photophysical properties of **BioMOF-1**, it can be deduced that the MOF structure imparts new electronic states on the system, similar to the results found for the PVDC MOFs. The two excitation bands at 280 nm and 385 nm provide a wide range of potential donating energy levels, and thus both visible and NIR emitting lanthanide cations were tested with this system. Exchanges were performed with terbium, europium, dysprosium, samarium, and ytterbium. All of these lanthanide cations, except dysprosium, were successfully sensitized in water solution.

It is hypothesized that the lanthanide cations will exchange with the dimethyl ammonium cations to balance the charge of the MOFs. Based on this, there should be 0.16667 Ln^{3+} for each 2 Zn^{2+}, for an overall ratio of approximately 92% zinc and 8% lanthanide. The amount of lanthanide in the Ln:**BioMOF-1** systems were determined by EDX after exchange, and the results are shown in Table 5.9.

Table 5.9. Lanthanide content in the Ln:BioMOF-1 relative to Zinc, as measured with EDX, error included in parentheses.

	Yb:BioMOF-1	**Eu:BioMOF-1**	**Tb-BioMOF-1**	**Sm-BioMOF-1**
Ln^{3+} %	10.2 (± 0.2) %	7 (± 1) %	5.1 (± 0.7) %	7 (± 1) %
Zn^{2+} %	98.2 (± 0.2) %	93 (± 1) %	94.9 (± 0.7) %	93 (± 1) %

The results range between 5 and 10% lanthanide content, which is consistent with the expected content. Without use of control materials of precise known composition (which are currently not existing for these measurements) to account for matrix effects, EDX as a tool for elemental composition is semi-quantitative within 25%. Therefore, these results fall within range of each other and the expected values. Residual sodium or potassium cations may occupy some of the pore sites, which could explain slightly lower values than expected for europium, terbium and samarium. Also, ytterbium is the smallest of the four lanthanide cations, which could allow a higher amount to fit in the MOF pores. However, given the limited accuracy of EDX, these variances and the possible reasons for them are speculative and discussed further.

Initial experiments were conducted with **BioMOF-1** exchanged with ytterbium in DMF, shown in Figure 5.55. Shown in green is the excitation spectrum of ytterbium emission at 980 nm. It displays maxima at 315 nm and 360 nm, which are relatively high in energy, and different from the two excitation bands of **BioMOF-1** fluorescence; although the band at 360 nm does

correspond to the shoulder of the 415 nm **BioMOF-1** excitation spectrum. The higher energy excitation results in more intense emission from the compound, suggesting one component more efficiently sensitizes ytterbium than the other.

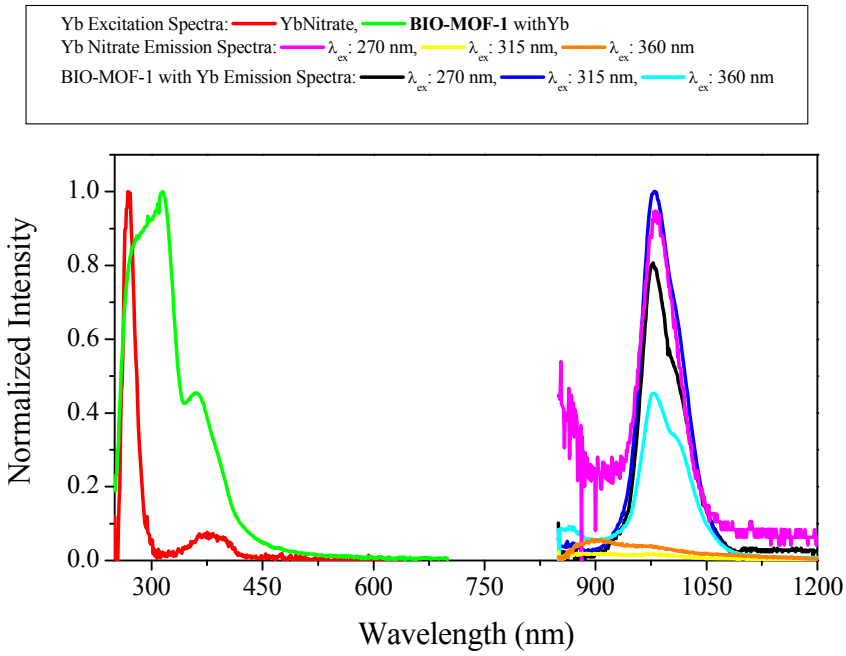

Figure 5.55. Emission and excitation spectra for BIO-MOF-1 with ytterbium in DMF and ytterbium nitrate in DMF, for control purposes.

The overall excitation profiles suggest that the electronic states that are most effective for ytterbium sensitization differ from those that efficiently sensitize MOF emission. Excitation through both these bands produces characteristic ytterbium emission centered at 980 nm (blue and cyan). For control purposes, ytterbium nitrate in DMF was also analyzed, as shown in red. It displays a narrow band at high energy, 270 nm, as well as a weak broad band at lower energy. The emission spectra (yellow and orange) resulting from exciting at these lower energies do not

contain any ytterbium signal, and are due to background noise from the cuvette and integration sphere. The excitation spectrum of ytterbium in Yb:**BioMOF-1** is quite different from ytterbium nitrate, confirming sensitization through the antennae effect. Also, it should be noted that these are normalized spectra so the ytterbium emission intensities appear the same, however, the ytterbium nitrate signal is in fact much weaker, further confirming the presence of the antennae effect.

Since ytterbium was successfully sensitized and detected in Yb:**BioMOF-1** in DMF, the solvent was exchanged for water. Shown in Figure 5.56 are the luminescence emission and excitation spectra in water.

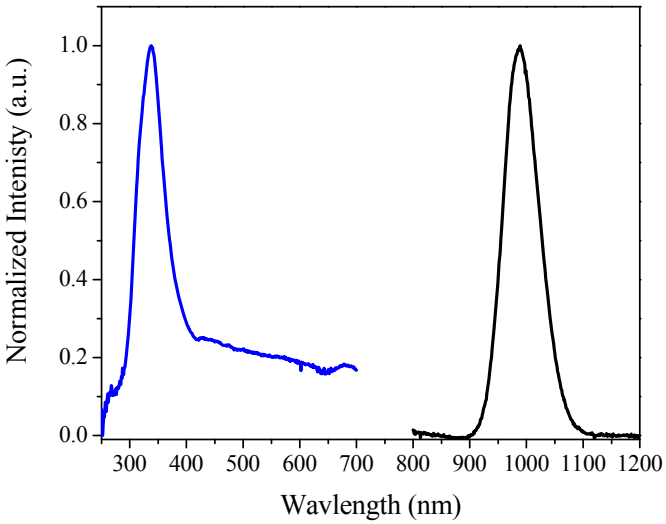

Figure 5.56. Excitation spectrum (blue) of ytterbium luminescence at 980 nm and the NIR emission spectrum (black) with λ_{ex}: 340 nm.

Despite the strong ability of water to quench NIR emitting lanthanides, the ytterbium signal is still easily detected in the NIR with a main excitation band at 340 nm (due to background signals, the excitation spectrum does not baseline to zero). The higher energy excitation band is not present in water. This can be potentially explained by the high absorbance of water at this range preventing access of these photons to sensitize ytterbium. For biological applications, as well as green chemistry reasons, water is a desirable solvent and thus all further characterization of the system is performed in water.

The emission and excitation spectra for Tb:**BioMOF-1** in water were monitored in steady-state and time-resolved modes, and are shown in Figure 5.57.

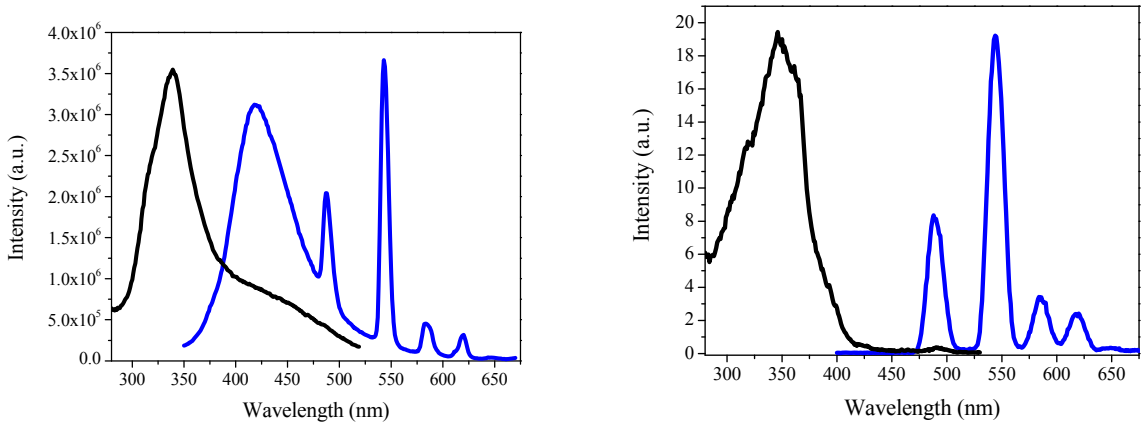

Figure 5.57. Steady-state (left) and time-gated (right) excitation, λ_{em}: 545 nm, (black) and emission, λ_{ex}: 340 nm, (blue) spectra for Tb:BioMOF-1 in water.

In steady-state mode, the emission spectrum contains bands from both **BioMOF-1** and terbium, and the excitation spectrum of emission at 545 nm produces a band with maximum at 340 nm. Since there is both terbium and **BioMOF-1** emission at 545 nm, this excitation spectrum is a

combination of these. To fully resolve the terbium, measurements were made in a time-gated mode, and reveal a similar excitation band with maximum at 340 nm. The excitation profile for Tb:**BioMOF-1** is similar to Yb:**BioMOF-1** in water, and again corresponds to the shoulder of the **BioMOF-1** excitation spectrum. This shows that both lanthanide cations are excited through the same pathway within the MOF, and that excitation at this wavelength does also produce **BioMOF-1** emission.

Shown in Figure 5.58 are the steady-state and time-resolved emission and excitation spectra for Sm:**BioMOF-1**.

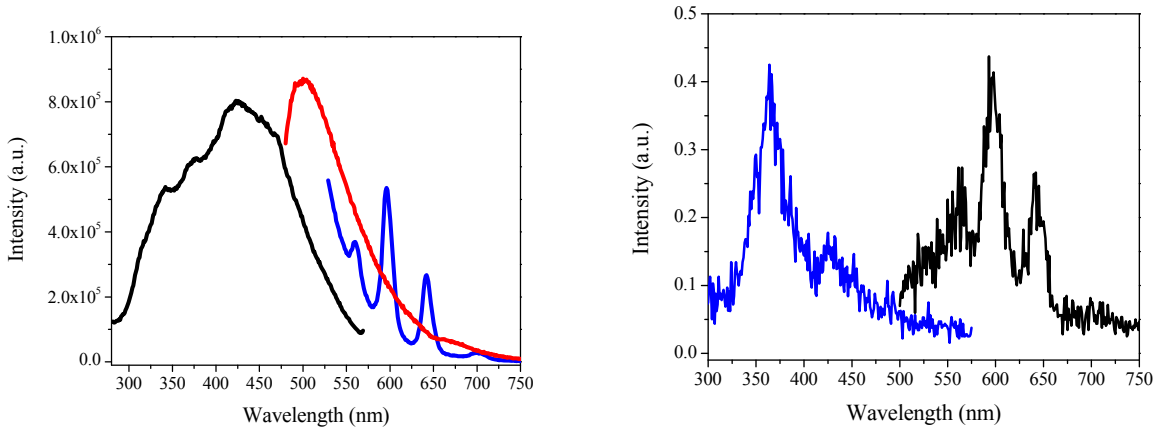

Figure 5.58. Steady-state (left) and time-gated (right) excitation, λ_{em}: 596 nm, (black) and emission, λ_{ex}: 340 nm (blue), λ_{ex}: 425 nm (red), spectra for Sm:BIO-MOF-1 under water.

The emission spectra both show characteristic samarium emission bands, indicating successful sensitization of this lanthanide cation. Similar to Tb:**BioMOF-1**, the steady state emission spectra contains both lanthanide and **BioMOF-1** signals, and the excitation spectrum is combination of bands that excite these two emission signals. The excitation spectrum

corresponding to the emission at 596 nm produces a broad band, with excitation out to over 450 nm. However, excitation through the lower energy band at 425 nm produces only **BioMOF-1** emission, suggesting that this electronic state can not effectively sensitize samarium cations. To resolve samarium from the **BioMOF-1**, time-gated spectra were collected which confirm a 340 nm centered excitation band, similar to ytterbium and terbium. Due to the short lifetimes of samarium, the time-resolved spectra are weakly intense and therefore noisy.

Eu:**BioMOF-1** was also analyzed in water, and the steady-state spectra are shown in Figure 5.59. The characteristic europium emission bands are seen upon excitation at 340 nm. The excitation spectrum of europium emission at 615 nm produces a band with maximum around 340 nm, similar to all other Ln:**BioMOF-1** systems. The europium emission in steady state mode was much more intense than the lanthanide signals for Tb^{3+} or Sm^{3+}, however, and since the main europium emission band is at lower energy (614 nm), time-resolved analysis was not necessary to discriminate from **BioMOF-1** emission bands. The excitation profile also shows two weak direct excitation bands at 390 nm and 475 nm. The relative strength of the band at 340 nm compared to these bands indicates an efficient antenna effect sensitization of europium by the MOF.

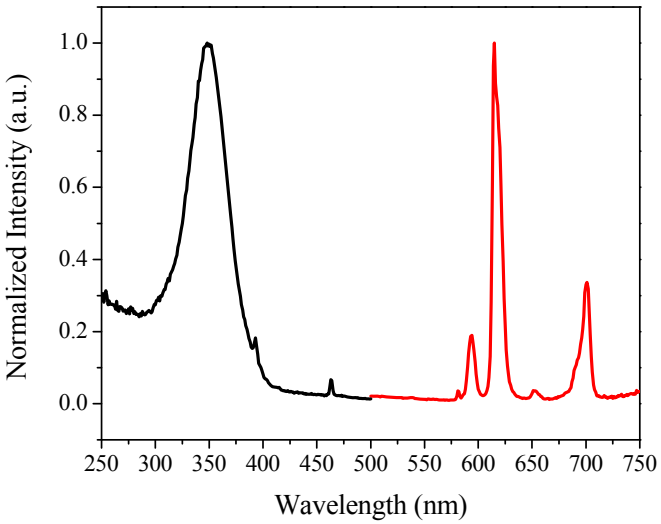

Figure 5.59. Steady-state excitation spectrum (black) of europium emission at 615 nm and the emission spectrum (red) monitored upon excitation at 340 nm for Eu:BioMOF-1 under water.

The quantum yield of the Ln:**BioMOF-1** under water are reported in Table 5.10. The quantum yields are all reasonably high considering the water environment, providing an indication that the lanthanide cations are protected to some extent within the pores, and the energy transfer to the lanthanide from the MOF chromophores has a good efficiency. The quantum yield value provides information on the protection of the lanthanide cations and the efficiency of their sensitization, however, it is not a direct measure of the luminescence intensity of the material. Since the MOF approach allows a large number of lanthanide cations to be encapsulated in a small volume, the luminescence intensity of the Ln:**BioMOF-1** can be quite high. In fact, the red europium, green terbium, and violet samarium emission are easily seen with the naked eye when excited with a standard laboratory UV lamp, as shown in the photograph in Figure 5.60.

Table 5.10. Absolute quantum yields of lanthanide luminescence for Ln:BioMOF-1 under water.

	Yb	Eu	Tb	Sm
Φ_{Ln}	2.5 (± 0.2) x 10^{-4}	8.4 (± 0.1) x 10^{-2}	1.7 (± 0.1) x 10^{-2}	2.8 (± 0.2) x 10^{-3}

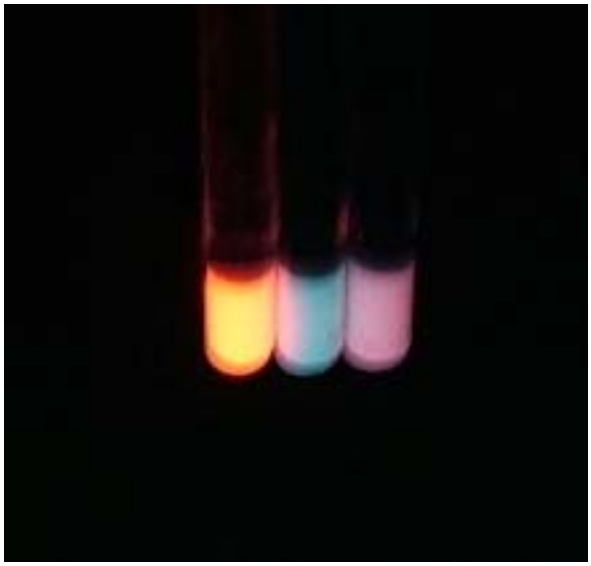

Figure 5.60. Photograph of Eu:BioMOF-1, Tb:BioMOF-1, and Sm:BioMOF-1 (from left to right) under D_2O, illuminated by an Entela Mineralight lamp (model UVGL-55) with 365 nm excitation (115 V, 0.16 amp); a 450 nm glass cut-on filter was placed in front of the camera lens to remove the UV light.

An emission spectrum of each of the Ln:**BioMOF-1** systems emitting in the visible range collected during the quantum yield measurements are shown in Figure 5.61. These spectra illustrate how the relative quantum yields of the three lanthanide cations correlate with their relative luminescence intensities, as expected.

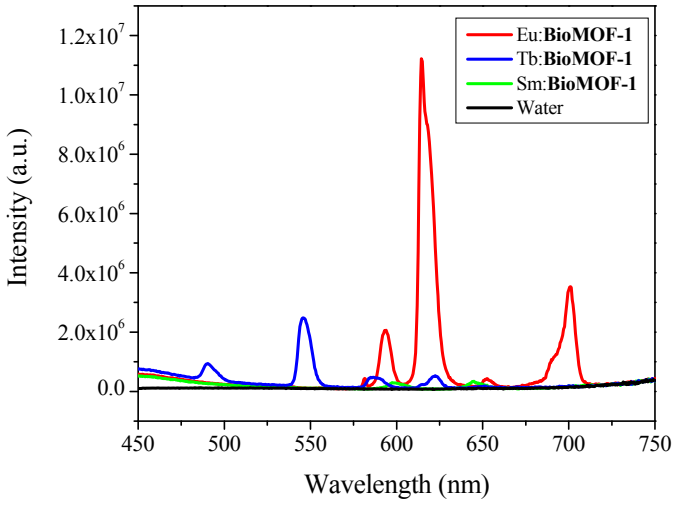

Figure 5.61. Emission spectra (λ_{ex}: 340 nm) of the three visible emitting Ln:Bio-MOF1 under water, collected for quantum yield determinations, showing the relative intensities of the three different lanthanides.

The luminescence lifetimes of the some of the lanthanide cations in Ln:**BioMOF-1** have been determined in water, as well as deuterated water, to gain information on the environment of the lanthanide cations in the MOFs. The results, presented in Table 5.11, have several interesting features.

Table 5.11. Luminescence lifetimes for Ln:BioMOF-1 in H_2O (τ_{H2O}) and D_2O (τ_{D2O}), and the calculated number of coordinating water molecules (q).

	τ_{H2O}	τ_{D2O}	q
Yb	0.58 ± 0.02 µs	11.6 ± 0.1 µs	1
Eu	0.299 ± 0.001 ms	1.6 ± 0.1 ms	3
Sm	†	0.58 ± 0.02 µs	n/a

† Samarium lifetimes in water could not be measured due to sample and instrumental limitations.

Eu:**BioMOF-1** displays the longest lifetimes correlating with its high quantum yield; however it also has a calculated q value of 3, which suggests that the MOF provides only minimal protection from water. For the samarium system, only lifetimes in D_2O could be measured and distinguished from the background, suggesting that water is binding to and quenching the samarium cations. The ytterbium lifetime values are in comparable ranges to other ytterbium complexes in water reported in the literature and also show quenching from bound water molecules. However, the q value for ytterbium is only 1, compared to 3 for europium. This discrepancy may be partially explained by the size difference between the two lanthanide cations (ytterbium is smaller than europium and may not be able to bind as many water molecules), as well as the limited accuracy of the empirical formulas to determine q, which have errors of ± 0.5. It should also be noted that measuring the lifetimes of the MOF samples is complicated by their solid state nature, which causes scattering and inner-filter effects and amplifies the effects of background signals and noise on the detected decay curves. It was often necessary to fit decay curves with multi-exponential fittings, however, values that comprised less than 10% of the total signal were disregarded. For all samples, one dominant value (80 – 95%) was found, and these are the reported values. Luminescent lifetimes for terbium centered emission were not possible to measure to due interference of the MOF emission bands combined with instrumental constraints.

Thermogravimetric analysis of the Ln:**BioMOF-1**'s after lanthanide exchanges were performed. These results (Figure 5.62) show two different losses corresponding to water for all the lanthanides.

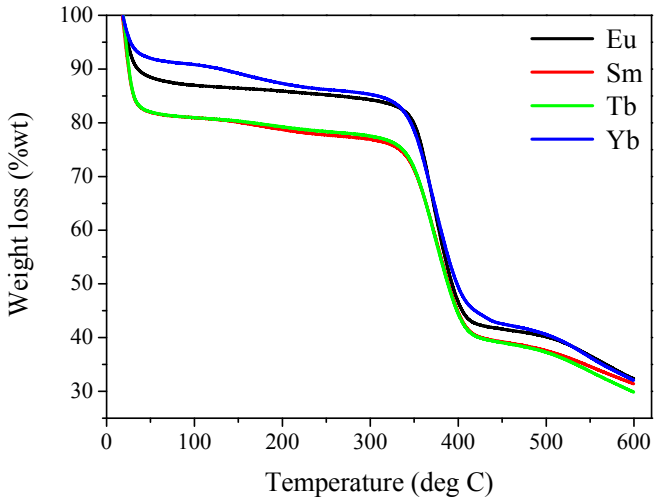

Figure 5.62. TGA results for the Ln:BioMOF-1 samples.

There is first a sharp loss of weight around 25°C, followed by a more gradual change in weight around 145°C, and a large weight change at 375°C corresponding to decomposition of the MOF. These two different temperatures for water loss likely correspond to water that is residing in the pores of the MOF in two states. Free water molecules in the pores that are not bound to either the MOF or a lanthanide cation will be removed more easily and correspond to the first loss. The second water loss correlates to water molecules which are coordinating to a moiety located in the MOF; it is highly likely that they are coordinated to the lanthanide cations since the pores are hydrophobic. The q values calculated from lifetimes also confirm that water is binding to the lanthanide cations in the MOF pores.

5.4. CONCLUSIONS

An organic chromophore, TPBA, was demonstrated to successfully sensitize four visible emitting lanthanide cations; however, no lanthanide based MOFs were obtained with this material. Future work might be targeted at the development of a multi-metal MOF, where a transition metal which binds well to nitrogen sites is used along with lanthanide cations that bind to the oxygen sites. Ruthenium cations could be a good choice for the second metal, and may introduce new photophysical properties to the material; ruthenium complexes have been used to sensitize lanthanide cations through the antenna effect.[200-205] As a discrete molecular complex, the Ln-TPBA system would be interesting to study, also, and could have some sensing capabilities utilizing the terpyridyl portion.

Another organic chromophore, H_2-PVDC, was demonstrated to successfully sensitize four NIR emitting lanthanide cations. This organic chromophore was also able to direct the assembly of lanthanide based MOFs, leading to the development of two ytterbium based MOFs and an Er based MOF. These systems have illustrated that a MOF-based approach to sensitize NIR emitting lanthanides results in materials with enhanced luminescence properties. Specifically, we have shown that chromophoric antennae molecules and NIR emitting lanthanides can be assembled into rigid MOF structures that effectively control the coordination environments around the lanthanide cations and the arrangement of chromophoric antennae. Using this strategy, it was possible to obtain a lower energy excitation wavelength by modifying the 3-D MOF structure to allow for close π-π interactions between the chromophores. The intrinsic structures of the MOFs also provide protection of the lanthanide cations from solvent vibrations. Finally, MOFs constitute rigid and organized polymetallic systems with high

densities of sensitizing groups and lanthanide cations per unit of volume for enhanced emission intensity.

In addition to the single lanthanide MOFs, multiple metal MOFs were also developed and display promising properties. MOFs formed with Er and Yb demonstrate the principle of bar-coded luminescent materials. By varying the amounts of each metal in the material, the luminescent intensities of each metal can be linearly controlled during the synthesis. A Nd, Er, Yb MOF was also synthesized and displayed luminescence bands of all three metal cations in the NIR, acting as a proof of concept for the development of more complex bar-coded materials. The **ErYb-PVDC-1** displayed interesting Yb to Er energy transfer abilities. While inter-lanthanide energy transfer is reported in the literature, its properties are not well understood, mostly due to the lack of well-defined systems with which to study the phenomenon, especially rigid systems that induce a well defined and constant distance between the two metal ions. In many cases, inter-lanthanide energy transfer is studied in doped solid state materials, where the exact distance between lanthanide cations is not known. Alternatively, it could be studied with molecular complexes. However, in solution their structures are dynamic and again the exact three-dimensional relationship between lanthanide cations is not known. MOFs offer an exciting alternative to this and may be beneficial for fundamental studies of these energy transfer mechanisms and what properties beneficially or negatively affect their efficiencies. Another exciting possibility for the Er,Yb-PVDC MOF is investigating upconversion properties (see Section 4.1.1.1 for details).

As described in Section 4.1.1.1, ytterbium to erbium energy transfer which results in upconverted luminescence is possible within materials. Exciting the **Er_xYb_{1-x}-PVDC-1** MOFs at 980 nm, however, did not result in any detected upconversion luminescence in the visible range.

While the material does not currently display upconverting properties, the Yb to Er energy transfer suggests that the potential is there. Materials that do have upconverting properties contain Er and Yb as dopants in an otherwise inert material. Since Lu is a similar size to Er and Yb, and its *f* orbitals are completely filled rendering it electronically silent, a Lu,Yb,Er-PVDC MOF should be facile to synthesize and worth exploring.

Using the same organic component, a zinc based MOF was developed and was successfully able to serve as a scaffold for the incorporation and sensitization of NIR emitting lanthanide cations. **Zn-PVDC-1** demonstrated its ability to effectively sensitize Er^{3+}, Yb^{3+}, and Nd^{3+} utilizing a post-synthetic modification method. Concentration studies showed that exchange procedures with 0.0025 M $YbCl_3$ gave the brightest emission amongst varying concentrations, suggesting that at some point self-quenching begins to limit ultimate lanthanide luminescent output. **Zn-PVDC-1** effectively sensitized several lanthanide cations simultaneously exhibiting great promise for use as a multimode sensor or multiplex assay. Using the same approach, another zinc based MOF, **BioMOF-1** was able to incorporate and sensitize lanthanide cations emitting in the visible and NIR ranges in water. These results are particularly exciting as water is a highly quenching solvent, but essential to biological compatibility. Future work may be targeted at developing nanosized lanthanide complexes containing **BioMOF-1** for use as bioimaging agents. Due to the ease of these experiments, frameworks can be chosen from the database and studied for their effectiveness at sensitizing lanthanides a high throughput, making this a revolutionary method for lanthanide sensitization.

Here we have demonstrated that lanthanide cations can be sensitized using a MOF approach through two different methods: 1) incorporating lanthanide cations in the MOF at the metal sites and using chromophoric organic linkers to sensitize the metals, and 2) forming MOFs

with organic chromophoric linkers and transition metals, then incorporating lanthanide cations as occupants of the MOF pores. Both these methods produce positive results and have their own benefits. One more potential way to sensitize lanthanide cations through a MOF approach would be to form MOFs with lanthanide cations at the metal sites, then incorporate sensitizing chromophores in the pores. This would allow for a greater range of potential chromophore choices, including nanocrystals, while still providing the controlled environment around lanthanide cations.

BIBLIOGRAPHY

(1) Shannon, R. D. *Acta Crystallographica Section A* **1976**, *32*, 751 - 767.

(2) Cotton, F. A.; Wilkinson, G.; Bochmann, M.; Murillo, C. *Advanced Inorganic Chemistry, 6th Edition*, 1998.

(3) Sabbatini, N.; Guardigli, M.; Lehn, J. M. *Coordination Chemistry Reviews* **1993**, *123*, 201-28.

(4) Faulkner, S.; Carrie, M.-C.; Pope, S. J. A.; Squire, J.; Beeby, A.; Sammes, P. G. *Dalton Trans.* **2004**, 1405-1409.

(5) *Handbook on the physics and chemistry of rare earths*; Gschneider, K. A.; Bunzli, J.-C. G.; Pecharski, V. K., Eds. North Holland, 2006; Vol. 36.

(6) Petoud, S.; Cohen, S. M.; Buenzli, J.-C. G.; Raymond, K. N. *Journal of the American Chemical Society* **2003**, *125*, 13324-13325.

(7) Zhang, J.; Badger, P. D.; Geib, S. J.; Petoud, S. *Angewandte Chemie, International Edition* **2005**, *44*, 2508-2512.

(8) Weissleder, R.; Tung, C.-H.; Mahmood, U.; Bogdanov, A., Jr. *Nat. Biotechnol.* **1999**, *17*, 375-378.

(9) Zaheer, A.; Lenkinski, R. E.; Mahmood, A.; Jones, A. G.; Cantley, L. C.; Frangioni, J. V. *Nat. Biotechnol.* **2001**, *19*, 1148-1154.

(10) Kim, S.; Lim, Y. T.; Soltesz, E. G.; De Grand, A. M.; Lee, J.; Nakayama, A.; Parker, J. A.; Mihaljevic, T.; Laurence, R. G.; Dor, D. M.; Cohn, L. H.; Bawendi, M. G.; Frangioni, J. V. *Nature Biotechnology* **2004**, *22*, 93-97.

(11) Muller, M. G.; Georgakoudi, I.; Zhang, Q.; Wu, J.; Feld, M. S. *Applied Optics* **2001**, *40*, 4633-4646.

(12) Hemmila, I.; Webb, S. *Drug Discovery Today* **1997**, *2*, 373-381.

(13) Mathis, G. *Journal of Biomolecular Screening* **1999**, *4*, 309-313.

(14) Buenzli, J. C. G.; Choppin, G. R.; Editors *Lanthanide Probes in Life, Chemical and Earth Sciences: Theory and Practice*, 1989.

(15) Weissman, S. I. *Journal of Chemical Physics* **1942**, *10*, 214-17.

(16) Beeby, A.; Clarkson, I. M.; Dickins, R. S.; Faulkner, S.; Parker, D.; Royle, L.; de Sousa, A. S.; Williams, J. A. G.; Woods, M. *Journal of the Chemical Society, Perkin Transactions 2: Physical Organic Chemistry* **1999**, 493-504.

(17) Forster, T. *Ann. Physik [6 Folge]* **1948**, *2*, 55-75.

(18) Dexter, D. L. *Journal of Chemical Physics* **1953**, *21*, 836-50.

(19) Horrocks, W. D., Jr.; Bolender, J. P.; Smith, W. D.; Supkowski, R. M. *Journal of the American Chemical Society* **1997**, *119*, 5972-5973.

(20) Faulkner, S.; Beeby, A.; Carrie, M. C.; Dadabhoy, A.; Kenwright, A. M.; Sammes, P. G. *Inorg. Chem. Commun.* **2001**, *4*, 187-190.

(21) Comby, S.; Imbert, D.; Chauvin, A.-S.; Buenzli, J.-C. G. *Inorganic Chemistry* **2006**, *45*, 732-743.
(22) Beeby, A.; Burton-Pye, B. P.; Faulkner, S.; Motson, G. R.; Jeffery, J. C.; McCleverty, J. A.; Ward, M. D. *J. Chem. Soc., Dalton Trans.* **2002**, 1923-1928.
(23) Coldwell, J. B.; Felton, C. E.; Harding, L. P.; Moon, R.; Pope, S. J. A.; Rice, C. R. *Chem. Commun. (Cambridge, U. K.)* **2006**, 5048-5050.
(24) Zhang, J.; Shade, C. M.; Chengelis, D. A.; Petoud, S. *Journal of the American Chemical Society* **2007**, *129*, 14834-14835.
(25) Chengelis, D. A.; Yingling, A. M.; Badger, P. D.; Shade, C. M.; Petoud, S. *Journal of the American Chemical Society* **2005**, *127*, 16752-16753.
(26) Souris, J. S. *Trends in Biotechnology* **2002**, *20*, 364-366.
(27) Weissleder, R.; Ntziachristos, V. *Nat. Med. (N. Y., NY, U. S.)* **2003**, *9*, 123-128.
(28) Flanagan, J. H., Jr.; Khan, S. H.; Menchen, S.; Soper, S. A.; Hammer, R. P. *Bioconjugate Chemistry* **1997**, *8*, 751-756.
(29) Lin, Y.; Weissleder, R.; Tung, C.-H. *Molecular Imaging* **2003**, *2*, 87-92.
(30) Zaheer, A.; Wheat, T. E.; Frangioni, J. V. *Molecular Imaging* **2002**, *1*, 354-364.
(31) Faulkner, S.; Matthews, J. L. In *Comprehensive Coordination Chemistry II*; McCleverty, J. A., Meyer, T. J., Eds.; Elsevier: Amsterdam, 2004; Vol. 9, p 913-944.
(32) Engelmann, M.; Cheng, I. F.; http://oxygen.chem.uidaho.edu/ifcheng/recent_seminars_and_presentation.htm: 2002; Vol. 2003.
(33) Brown, J. E.; Khodr, H.; Hider, R. C.; Rice-Evans, C. A. *Biochemistry Journal* **1998**, *330*, 1173-1178.
(34) Nagai, S.; Ohara, K.; Mukai, K. *J. Phys. Chem. B* **2005**, *109*, 4234-4240.
(35) Roshal, A. D.; Grigorovich, A. V.; Doroshenko, A. O.; Pivovarenko, V. G.; Demchenko, A. P. *Journal of Photochemistry and Photobiology A: Chemistry* **1999**, *127*, 89-100.
(36) Souza, R. F. V. d.; Giovani, W. F. D. *Spectrochimica Acta Part A* **2004**, *61*, 1985-1990.
(37) Porter, L. J.; Markham, K. R. *Journal of the Chemical Society Section C: Organic* **1970**, 344-9.
(38) Gutierrez Amanda, C.; Gehlen Marcelo, H. *Spectrochim Acta A Mol Biomol Spectrosc* **2002**, *58*, 83-9.
(39) Boudet, A. C.; Cornard, J. P.; Merlin, J. C. *Spectrochim. Acta, Part A* **2000**, *56A*, 829-839.
(40) Cornard, J. P.; Boudet, A. C.; Merlin, J. C. *Spectrochim. Acta, Part A* **2001**, *57A*, 591-602.
(41) Cornard, J. P.; Merlin, J. C. *J. Mol. Struct.* **2001**, *569*, 129-138.
(42) Cornard, J. P.; Merlin, J. C. *J. Inorg. Biochem.* **2002**, *92*, 19-27.
(43) Cornard, J. P.; Merlin, J. C. *J. Mol. Struct.* **2003**, *651-653*, 381-387.
(44) Cornard, J. P.; Vrielynck, L.; Merlin, J. C. *Spectrosc. Biol. Mol.: Mod. Trends, [Eur. Conf.], 7th* **1997**, 563-564.
(45) Sill, C. W.; Willis, C. P. *Analytical Chemistry* **1962**, *34*, 954-964.
(46) Sanz-Medel, A.; Alonso, J. I. G.; Gonzalez, E. B. *Analytical Chemistry* **1985**, *57*, 1681-1687.
(47) Woznicka, E.; Kopacz, M.; Umbreit, M.; Klos, J. *Journal of Inorganic Biochemistry* **2007**, *101*, 774-782.

(48) Nowak, D.; Woznicka, E.; Kuzniar, A.; Kopacz, M. *Journal of Alloys and Compounds* **2006**, *425*, 59-63.
(49) Anasari, A. A. *Journal of Coordination Chemistry* **2008**, *61*, 3869-3878.
(50) Barolli, M. G.; Werner, R. A.; Slep, L. D.; Pomilio, A. B. *Molecules* **2000**, *5*, 516-517.
(51) Offenhartz, P. O. D., Ph.D Thesis,1964.
(52) Apel, H. *CLB Chemie in Labor und Biotechnik* **1991**, *42*, 388, 391-3.
(53) Apel, H. *CLB Chemie in Labor und Biotechnik* **1992**, *43*, 549-52.
(54) Gampp, H.; Maeder, M.; Meyer, C. J.; Zuberbuhler, A. D. *Talanta* **1985**, *32*, 95-101.
(55) Bhaumik, M. L.; El-Sayed, M. A. *The Journal of Physical Chemistry* **1965**, *69*, 275-280.
(56) Turro, N. J. *Modern Molecular Photochemistry*; University Science Books: Sausalito, CA, 1991.
(57) Rohagti, S.; Sen Gupta, S. K. *Journal of Inorganic Nuclear Chemistry* **1972**, *34*, 3061.
(58) Klink, S. I.; Hebbink, G. A.; Grave, L.; Veggel, F. C. J. M. V.; Reinhoudt, D. N.; Slooff, L. H.; Polman, A.; Hofstraat, J. W. *Journal of Applied Physics* **1999**, *86*, 1181-1185.
(59) Hebbink, G. A.; Grave, L.; Woldering, L. A.; Reinhoudt, D. N.; van Veggel, F. C. J. M. *Journal of Physical Chemistry A* **2003**, *107*, 2483-2491.
(60) Davies, G. M.; Aarons, R. J.; Motson, G. R.; Jeffery, J. C.; Adams, H.; Faulkner, S.; Ward, M. D. *Dalton Transactions* **2004**, 1136-1144.
(61) Rusakova, N. V.; Korovin, V. Y.; Zhilina, Z. I.; Vodzinskii, S. V.; Ishkov, Y. V. *J. Appl. Spectrosc.* **2004**, *71*, 506-511.
(62) Corporation, Q. D.; http://www.qdots.com: 2004.
(63) Technologies, E.; http://www.evidenttech.com: 2004.
(64) Vossmeyer, T.; Katsikas, L.; Giersig, M.; Popovic, I. G.; Diesner, K.; Chemseddine, A.; Eychmueller, A.; Weller, H. *Journal of Physical Chemistry* **1994**, *98*, 7665-73.
(65) Brukowski, T. J.; Simmons, J. H. *Critical Reviews in Solid State and Materials Sciences* **2002**, *27*, 119-142.
(66) Qu, L.; Peng, X. *Journal of the Americal Chemical Society* **2002**, *124*, 2049-2055.
(67) Wu, X.; Liu, H.; Liu, J.; Haley, K. N.; Treadway, J. A.; Larson, J. P.; Ge, N.; Peale, F.; Bruchez, M. P. *Nature Biotechnology* **2002**, *21*, 41-46.
(68) Li, Y.; Rizzo, A.; Cingolani, R.; Gigli, G. *Microchimica Acta* **2007**, *159*, 207-215.
(69) Shim, M.; Guyot-Sionnest, P. *Nature* **2000**, *407*, 981.
(70) Erwin, S. C.; Zu, L. J.; Haftel, M. I.; Efros, A. L.; Kennedy, T. A.; Norris, D. J. *Nature* **2005**, *436*, 91-94.
(71) Zu, L. J.; Norris, D. J.; Kennedy, T. A.; Erwin, S. C.; Efros, A. L. *Nano Letters* **2006**, *6*, 334-340.
(72) Kwak, W.-C.; Kim, T. G.; Chae, W.-W.; Sung, Y.-M. *Nanotechnology* **2007**, *18*, 1 - 4.
(73) Qu, L.; Peng, X. *Journal of the American Chemical Society* **2002**, *124*, 2049-2055.
(74) Bhattacharyya, S.; Zitoun, D.; Gedanken, A. *Journal of Physical Chemistry C* **2008**, *112*, 7624 - 7630.

(75) Magana, D.; Perera Susanthri, C.; Harter Andrew, G.; Dalal Naresh, S.; Strouse Geoffrey, F. *Journal of the American Chemical Society* **2006**, *128*, 2931-9.

(76) Archer, P. I.; Santangelo, S. A.; Gamelin, D. R. *Journal of the American Chemical Society* **2007**, *129*, 9809 - 9818.

(77) Jose, G.; Jose, G.; Thomas, V.; Joseph, C.; Ittyachen, M. A.; Unnikrishnan, N. V. *Materials Letters* **2003**, *57*, 1051 - 1055.

(78) Kompe, K.; Lehmann, O.; Haase, M. *Chemistry of Materials* **2006**, *18*, 4442.

(79) Raola, O. E.; Strouse, G. F. *Nano Letters* **2002**, *2*, 1443-1447.

(80) Julian, B.; Planelles, J.; Cordoncillo, E.; Escribano, P.; Aschehoug, P.; Sanchez, C.; Viana, B.; Pelle, F. *Journal of Materials Chemistry* **2006**, *16*, 4612 - 4618.

(81) Tiseanu, C.; Mehra, R. K.; Kho, R.; Kumke, M. *Chemical Physics Letters* **2003**, *377*, 131 - 136.

(82) Okamoto, S.; Kobayashi, M.; Kanemitsu, Y.; Kushida, T. *Physica Status Solidi B: Basic Research* **2002**, *229*, 481 - 484.

(83) Chowdhury, P. S.; Patra, A. *Physical Chemistry Chemical Physics* **2005**, *8*, 1329 - 1334.

(84) Jose-Yacaman, M.; Ascencio, J. A. In *Handbook of Nanostructured Materials and Nanotechnology*; Nalwa, H. S., Ed.; Academic Press: 2000; Vol. 2, p 385-413.

(85) Raola, O. R.; Strouse, G. F. *Nano Letters* **2002**, *2*, 1443-1447.

(86) Skoog, D. A.; Leary, J. J. *Principles of Instrumental Analysis*; 4th ed.; Saunder College Publishing: Fort Worth, 1992.

(87) Peng, Z. A.; Peng, X. *Journal of the American Chemical Society* **2001**, *123*, 183-184.

(88) Peng, Z. A.; Peng, X. *Journal of the American Chemical Society* **2002**, *124*, 3343-3353.

(89) Fletcher, A. N. *Photochemistry and Photobiology* **1969**, *5*, 439-444.

(90) Werts, M. H. V.; Jukes, R. T. F.; Verhoeven, J. W. *Physical Chemistry Chemical Physics* **2002**, *4*, 1542-1548.

(91) Carnall, W. T.; Fields, P. R.; Rajnak, K. *Journal of Chemical Physics* **1968**, *49*, 4447-9.

(92) Beeby, A.; Clarkson, I. M.; Dickins, R. S.; Faulkner, S.; Parker, D.; Royle, L.; Sousa, A. S. d.; Williams, J. A. G.; Woods, M. *Journal of the Chemical Society, Perkin Transactions* **1999**, *2*, 493-503.

(93) Stein, G.; Wurzberg, E. *Journal of Chemical Physics* **1975**, *62*, 208-213.

(94) Bukowski, T. J.; Simmons, J. H. *Critical Reviews in Solid State and Materials Sciences* **2002**, *27*, 119-142.

(95) Yu, W. W.; Peng, X. *Angewandte Chemie, International Edition* **2002**, *41*, 2368-2371.

(96) Murray, C. B.; Nirmal, M.; Norris, D. J.; Bawendi, M. G. *Zeitschrift fuer Physik D: Atoms, Molecules and Clusters* **1993**, *26*, 231-3.

(97) Yu, W. W.; Qu, L.; Guo, W.; Peng, X. *Chemistry of Materials* **2003**, *15*, 2854-2860.

(98) Striolo, A.; Ward, J.; Prausnitz, J. M.; Parak, W. J.; Zanchet, D.; Gerion, D.; Milliron, D. J.; Alivisatos, A. P. *Journal of Physical Chemistry B* **2002**, *106*, 5500-5505.

(99) Yu, W. W.; Qu, L. H.; Guo, W. Z.; Peng, X. G. *Chemistry of Materials* **2003**, *15*, 2854-2860.

(100) Striolo, A.; Ward, J.; Prausnitz, J. M.; Parak, W. J.; Zanchet, D.; Gerion, D.; Milliron, D.; Alivisatos, A. P. *Journal of Physical Chemistry B* **2002**, *106*, 5500-5505.

(101) Fisher, B. R.; Eisler, H.-J.; Scott, N. E.; Bawendi, M. G. *Journal of Physical Chemistry B* **2004**, *108*, 143-148.

(102) Petoud, S.; Muller, G.; Moore, E. G.; Xu, J.; Sokolnicki, J.; Riehl, J. P.; Le, U. N.; cohen, S. M.; Raymond, K. N. *Journal of the American Chemical Society* **2006**, *129*, 77 - 83.

(103) Landes, C.; Braun, M.; Burda, C.; El-Sayed, M. A. *Nano Letters* **2001**, *1*, 667-670.

(104) Quaschning, V. *Renewable Energy Wold* **2003**, 90-93.

(105) Boyer, J. C.; Cuccia, L. A.; Capobianco, J. A. *Nano Letters* **2007**, *7*, 847-852.

(106) Mai, H.-X.; Zhang, Y.-W.; Si, R.; Yan, Z.-G.; Sun, L.-d.; You, L.-P.; Yan, C.-H. *Journal of the American Chemical Society* **2006**, *128*, 6426-6436.

(107) Sivakumar, S.; Diamente, P. R.; van Veggel, F. C. *Chemistry-a European Journal* **2006**, *12*, 5878-5884.

(108) Wang, F.; Chatterjee, D. K.; Li, Z. Q.; Zhang, Y.; Fan, X. P.; Wang, M. Q. *Nanotechnology* **2006**, *17*, 5786-5791.

(109) Boyer, J. C.; Vetrone, F.; Cuccia, L. A.; Capobianco, J. A. *Journal of the American Chemical Society* **2006**, *128*, 7444-7445.

(110) Page, R. H.; Schaffers, K. I.; Waide, P. A.; Tassano, J. B.; Payne, S. A.; Krupke, W. F.; Bischel, W. K. *Journal of the Optical Society of America B: Optical Physics* **1998**, *15*, 996-1008.

(111) Murray, C. B.; Norris, D. J.; Bawendi, M. G. *Journal of the American Chemical Society* **1993**, *115*, 8706-8715.

(112) Alivisatos, A. P. *Science* **1996**, *271*, 933-937.

(113) Dabbousi, B. O.; RodriguezViejo, J.; Mikulec, F. V.; Heine, J. R.; Mattoussi, H.; Ober, R.; Jensen, K. F.; Bawendi, M. G. *Journal of Physical Chemistry B* **1997**, *101*, 9463-9475.

(114) Peng, X. G.; Manna, L.; Yang, W. D.; Wickham, J.; Scher, E.; Kadavanich, A.; Alivisatos, A. P. *Nature* **2000**, *404*, 59-61.

(115) Peng, Z. A.; Peng, X. G. *Journal of the American Chemical Society* **2001**, *123*, 183-184.

(116) Qu, L. H.; Peng, X. G. *Journal of the American Chemical Society* **2002**, *124*, 2049-2055.

(117) Boyer, J.-C.; Vetrone, F.; Cuccia, L. A.; Capobianco, J. A. *Journal of the American Chemical Society* **2006**, *128*, 7444-7445.

(118) Yi, G.; Lu, H.; Zhao, S.; Ge, Y.; Yang, W.; Chen, D.; Guo, L.-H. *Nano Letters* **2004**, *4*, 2191-2196.

(119) Wintgens, V.; Valat, P.; Kossanyi, J.; Biczok, L.; Demeter, A.; Berces, T. *Journal of the Chemical Society-Faraday Transactions* **1994**, *90*, 411-421.

(120) Stouwdam, J. W.; van Veggel, F. C. J. M. *Nano Letters* **2002**, *2*, 733-737.

(121) Bazzi, R.; Flores, M. A.; Louis, C.; Lebbou, K.; Zhang, W.; Dujardin, C.; Roux, S.; Mercier, B.; Ledoux, G.; Bernstein, E.; Perriat, P.; Tillement, O. *Journal of Colloid and Interface Science* **2004**, *273*, 191-197.

(122) Riwotzki, K.; Meyssamy, H.; Schnablegger, H.; Kornowski, A.; Haase, M. *Angewandte Chemie, International Edition* **2001**, *40*, 573-576.

(123) Riwotzki, K.; Haase, M. *Journal of Physical Chemistry B* **2001**, *105*, 12709-12713.

(124) Frindell, K. L.; Bartl, M. H.; Popitsch, A.; Stucky, G. D. *Angewandte Chemie, International Edition* **2002**, *41*, 959-962.

(125) Wada, Y.; Okubo, T.; Ryo, M.; Nakazawa, T.; Hasegawa, Y.; Yanagida, S. *Journal of the American Chemical Society* **2000**, *122*, 8583-8584.

(126) Zhang, J.; Badger, P. D.; Geib, S. J.; Petoud, S. *Inorganic Chemistry* **2007**, *46*, 6473-6482.

(127) Ruessel, C. *Journal of Non-Crystalline Solids* **1993**, *152*, 161-6.

(128) Bao, H. B.; Gong, Y. J.; Li, Z.; Gao, M. Y. *Chemistry of Materials* **2004**, *16*, 3853-3859.

(129) Kim, S.; Fisher, B.; Eisler, H. J.; Bawendi, M. *Journal of the American Chemical Society* **2003**, *125*, 11466-11467.

(130) Peng, X. G.; Schlamp, M. C.; Kadavanich, A. V.; Alivisatos, A. P. *Journal of the American Chemical Society* **1997**, *119*, 7019-7029.

(131) Bruchez, M., Jr.; Moronne, M.; Gin, P.; Weiss, S.; Alivisatos, A. P. *Science* **1998**, *281*, 2013-2016.

(132) Karstens, T.; Kobs, K. *The Journal of Physical Chemistry* **1980**, *84*, 1871-1872.

(133) Magde, D.; Wong, R.; Seybold, P. G. *Photochemistry and Photobiology* **2002**, *75*, 327-334.

(134) Roy, D. M.; Roy, R. *Journal of the Electrochemical Society* **1964**, *111*, 421-9.

(135) Reinhard, C.; Guedel, H. U. *Inorganic Chemistry* **2002**, *41*, 1048-1055.

(136) Alivisatos, A. P.; Johnsson, K. P.; Peng, X. G.; Wilson, T. E.; Loweth, C. J.; Bruchez, M. P.; Schultz, P. G. **1996**, *382*, 609-611.

(137) Mitchell, G. P.; Mirkin, C. A.; Letsinger, R. L. **1999**, *121*, 8122-8123.

(138) Lee, J.; Govorov, A. O.; Kotov, N. A. **2005**, *5*, 2063-2069.

(139) Wolcott, A.; Gerion, D.; Visconte, M.; Sun, J.; Schwartzberg, A.; Chen, S. W.; Zhang, J. Z. **2006**, *110*, 5779-5789.

(140) White, K. A.; Chengelis, D. A.; Zeller, M.; Geib, S. J.; Szakos, J.; Petoud, S.; Rosi, N. L. *Chemical Communications* **2009**, *30*, 4506 - 4508.

(141) Kitagawa, S.; Kitaura, R.; Noro, S.-i. *Angew. Chem., Int. Ed.* **2004**, *43*, 2334-2375.

(142) Moulton, B.; Zaworotko, M. J. *Chem. Rev.* **2001**, *101*, 1629-1658.

(143) Rowsell, J. L. C.; Yaghi, O. M. *Microporous Mesoporous Mater.* **2004**, *73*, 3-14.

(144) Ferey, G. *Chem. Soc. Rev.* **2008**, *37*, 191-214.

(145) Maspoch, D.; Ruiz-Molina, D.; Veciana, J. *Chem. Soc. Rev.* **2007**, *36*, 770-818.

(146) Wong-Foy, A. G.; Matzger, A. J.; Yaghi, O. M. *J. Am. Chem. Soc.* **2006**, *128*, 3494-3495.

(147) Millward, A. R.; Yaghi, O. M. *J. Am. Chem. Soc.* **2005**, *127*, 17998-17999.

(148) Chen, B.; Ockwig, N. W.; Millward, A. R.; Contreras, D. S.; Yaghi, O. M. *Angew. Chem., Int. Ed.* **2005**, *44*, 4745-4749.

(149) Eddaoudi, M.; Kim, J.; Rosi, N.; Vodak, D.; Wachter, J.; O'Keeffe, M.; Yaghi, O. M. *Science* **2002**, *295*, 469-472.

(150) Dinca, M.; Yu, A. F.; Long, J. R. *J. Am. Chem. Soc.* **2006**, *128*, 8904-8913.

(151) Zhao, X.; Xiao, B.; Fletcher, A. J.; Thomas, K. M.; Bradshaw, D.; Rosseinsky, M. J. *Science* **2004**, *306*, 1012-1015.

(152) Ferey, G.; Latroche, M.; Serre, C.; Millange, F.; Loiseau, T.; Percheron-Guegan, A. *Chem. Commun.* **2003**, 2976-2977.

(153) Kubota, Y.; Takata, M.; Matsuda, R.; Kitaura, R.; Kitagawa, S.; Kato, K.; Sakata, M.; Kobayashi, T. C. *Angew. Chem., Int. Ed.* **2005**, *44*, 920-923, S920/1-S920/4.

(154) Liu, Y.; Eubank, J. F.; Cairns, A. J.; Eckert, J.; Kravtsov, V. C.; Luebke, R.; Eddaoudi, M. *Angew. Chem., Int. Ed.* **2007**, *46*, 3278-3283.

(155) Lin, X.; Jia, J.; Zhao, X.; Thomas, K. M.; Blake, A. J.; Walker, G. S.; Champness, N. R.; Hubberstey, P.; Schroeder, M. *Angew. Chem., Int. Ed.* **2006**, *45*, 7358-7364.

(156) Lee, J. Y.; Pan, L.; Kelly, S. P.; Jagiello, J.; Emge, T. J.; Li, J. *Adv. Mater.* **2005**, *17*, 2703-2706.

(157) Ma, S.; Sun, D.; Ambrogio, M.; Fillinger, J. A.; Parkin, S.; Zhou, H.-C. *J. Am. Chem. Soc.* **2007**, *129*, 1858-1859.

(158) Xiao, B.; Wheatley, P. S.; Zhao, X.; Fletcher, A. J.; Fox, S.; Rossi, A. G.; Megson, I. L.; Bordiga, S.; Regli, L.; Thomas, K. M.; Morris, R. E. *J. Am. Chem. Soc.* **2007**, *129*, 1203-1209.

(159) Hu, A.; Ngo Helen, L.; Lin, W. *J Am Chem Soc* **2003**, *125*, 11490-1.

(160) Seo, J. S.; Whang, D.; Lee, H.; Jun, S. I.; Oh, J.; Jeon, Y. J.; Kim, K. *Nature* **2000**, *404*, 982-986.

(161) Hasegawa, S.; Horike, S.; Matsuda, R.; Furukawa, S.; Mochizuki, K.; Kinoshita, Y.; Kitagawa, S. *J. Am. Chem. Soc.* **2007**, *129*, 2607-2614.

(162) Cho, S.-H.; Gadzikwa, T.; Afshari, M.; Nguyen, S. T.; Hupp, J. T. *Eur. J. Inorg. Chem.* **2007**, 4863-4867.

(163) Kosal, M. E.; Chou, J.-H.; Wilson, S. R.; Suslick, K. S. *Nat. Mater.* **2002**, *1*, 118-121.

(164) Chen, B.; Liang, C.; Yang, J.; Contreras Damacio, S.; Clancy Yvette, L.; Lobkovsky Emil, B.; Yaghi Omar, M.; Dai, S. *Angew Chem Int Ed Engl* **2006**, *45*, 1390-3.

(165) Vaidhyanathan, R.; Bradshaw, D.; Rebilly, J.-N.; Barrio, J. P.; Gould, J. A.; Berry, N. G.; Rosseinsky, M. J. *Angew. Chem., Int. Ed.* **2006**, *45*, 6495-6499.

(166) Cychosz, K. A.; Wong-Foy, A. G.; Matzger, A. J. *J. Am. Chem. Soc.* **2008**, *130*, 6938-6939.

(167) Reineke, T. M.; Eddaoudi, M.; O'Keeffe, M.; Yaghi, O. M. *Angew. Chem., Int. Ed.* **1999**, *38*, 2590-2594.

(168) Ma, L.; Evans, O. R.; Foxman, B. M.; Lin, W. *Inorg. Chem.* **1999**, *38*, 5837-5840.

(169) Pan, L.; Adams, K. M.; Hernandez, H. E.; Wang, X.; Zheng, C.; Hattori, Y.; Kaneko, K. *J. Am. Chem. Soc.* **2003**, *125*, 3062-3067.

(170) Devic, T.; Serre, C.; Audebrand, N.; Marrot, J.; Ferey, G. *J. Am. Chem. Soc.* **2005**, *127*, 12788-12789.

(171) Chen, B.; Yang, Y.; Zapata, F.; Lin, G.; Qian, G.; Lobkovsky, E. B. *Adv. Mater.* **2007**, *19*, 1693-1696.

(172) Rieter, W. J.; Taylor, K. M. L.; Lin, W. *J. Am. Chem. Soc.* **2007**, *129*, 9852-9853.

(173) Shi, F. N.; Cunha-Silva, L.; Sa Ferreira, R. A.; Mafra, L.; Trindade, T.; Carlos, L. D.; Almeida Paz, F. A.; Rocha, J. *J. Am. Chem. Soc.* **2008**, *130*, 150-167.

(174) Wong, K.-L.; Law, G.-L.; Yang, Y.-Y.; Wong, W.-T. *Adv. Mater.* **2006**, *18*, 1051-1054.

(175) De Lill, D. T.; De Bettencourt-Dias, A.; Cahill, C. L. *Inorg. Chem.* **2007**, *46*, 3960-3965.

(176) Reineke, T. M.; Eddaoudi, M.; Moler, D.; O'Keeffe, M.; Yaghi, O. M. *J. Am. Chem. Soc.* **2000**, *122*, 4843-4844.

(177) Chandler, B. D.; Cramb, D. T.; Shimizu, G. K. H. *J. Am. Chem. Soc.* **2006**, *128*, 10403-10412.

(178) Guo, X.; Zhu, G.; Li, Z.; Chen, Y.; Li, X.; Qiu, S. *Inorg. Chem.* **2006**, *45*, 4065-4070.

(179) Rieter, W. J.; Taylor, K. M. L.; An, H.; Lin, W.; Lin, W. *J. Am. Chem. Soc.* **2006**, *128*, 9024-9025.

(180) Mueller-Buschbaum, K.; Mokaddem, Y.; Schappacher, F. M.; Poettgen, R. *Angew. Chem., Int. Ed.* **2007**, *46*, 4385-4387.

(181) Deluzet, A.; Maudez, W.; Daiguebonne, C.; Guillou, O. *Cryst. Growth Des.* **2003**, *3*, 475-479.

(182) Reineke, T. M.; Eddaoudi, M.; Fehr, M.; Kelley, D.; Yaghi, O. M. *J. Am. Chem. Soc.* **1999**, *121*, 1651-1657.

(183) Chandler, B. D.; Yu, J. O.; Cramb, D. T.; Shimizu, G. K. H. *Chem. Mater.* **2007**, *19*, 4467-4473.

(184) Oh, M.; Mirkin, C. A. *Nature (London, U. K.)* **2005**, *438*, 651-654.

(185) Cross, J. P.; Lauz, M.; Badger, P. D.; Petoud, S. *J. Am. Chem. Soc.* **2004**, *126*, 16278-16279.

(186) Rosi, N. L.; Eddaoudi, M.; Kim, J.; O'Keeffe, M.; Yaghi, O. M. *Angew. Chem., Int. Ed.* **2002**, *41*, 284-287.

(187) Rosi, N. L.; Kim, J.; Eddaoudi, M.; Chen, B.; O'Keeffe, M.; Yaghi, O. M. *J. Am. Chem. Soc.* **2005**, *127*, 1504-1518.

(188) An, J.; Fiorella, R. P.; Geib, S. J.; Rosi, N. L. *Journal of the American Chemical Society* **2009**, *131*, 8401-8403.

(189) An, J.; Geib, S. J.; Rosi, N. L. *Journal of the American Chemical Society* **2009**, *131*, 8376-8377.

(190) Irngartinger, H.; Herpich, R. *Eur. J. Org. Chem.* **1998**, 595-604.

(191) Stammel, C.; Frohlich, R.; Wolff, C.; Wenck, H.; De Meijere, A.; Mattay, J. *Eur. J. Org. Chem.* **1999**, 1709-1718.

(192) Aebischer, A.; Gumy, F.; Buenzli, J.-C. G. *Phys. Chem. Chem. Phys.* **2009**, *11*, 1346-1353.

(193) Sun, D.; Ma, S.; Ke, Y.; Petersen, T. M.; Zhou, H.-C. *Chem. Commun. (Cambridge, U. K.)* **2005**, 2663-2665.

(194) Hunter, C. A.; Sanders, J. K. M. *J. Am. Chem. Soc.* **1990**, *112*, 5525-34.

(195) Foley, T. J.; Harrison, B. S.; Knefely, A. S.; Abboud, K. A.; Reynolds, J. R.; Schanze, K. S.; Boncella, J. M. *Inorg. Chem.* **2003**, *42*, 5023-5032.

(196) Goncalves e Silva, F. R.; Malta, O. L.; Reinhard, C.; Guedel, H.-U.; Piguet, C.; Moser, J. E.; Buenzli, J.-C. G. *J. Phys. Chem. A* **2002**, *106*, 1670-1677.

(197) Zhang, J.; Petoud, S. *Chem.--Eur. J.* **2008**, *14*, 1264-1272.

(198) Batten, S. R.; Robson, R. *Angew. Chem., Int. Ed.* **1998**, *37*, 1461-1494.

(199) Bauer, C. A.; Timofeeva, T. V.; Settersten, T. B.; Patterson, B. D.; Liu, V. H.; Simmons, B. A.; Allendorf, M. D. *Journal of the American Chemical Society* **2007**, *129*, 7136-7144.

(200) Gagliardo, M.; Rizzo, F.; Lutz, M.; Spek, A. L.; van Klink, G. P. M.; Merbach, A. E.; De Cola, L.; van Koten, G. *Eur. J. Inorg. Chem.* **2007**, 2853-2861.

(201) Giansante, C.; Ceroni, P.; Balzani, V.; Vogtle, F. *Angew. Chem., Int. Ed.* **2008**, *47*, 5422-5425.

(202) Guo, D.; Duan, C.-y.; Lu, F.; Hasegawa, Y.; Meng, Q.-j.; Yanagida, S. *Chem. Commun.* **2004**, 1486-1487.

(203) Klink, S. I.; Keizer, H.; Hofstraat, H. W.; van Veggel, F. C. J. M. *Synth. Met.* **2002**, *127*, 213-216.

(204) Lazarides, T.; Adams, H.; Sykes, D.; Faulkner, S.; Calogero, G.; Ward, M. D. *Dalton Trans.* **2008**, 691-698.

(205) Pope, S. J. A.; Coe, B. J.; Faulkner, S.; Laye, R. H. *Dalton Trans.* **2005**, 1482-1490.

APPENDIX A

Crystallographic data and structure refinement for metal-organic frameworks

Table AA 1. Crystal data and structure refinement for Yb-PVDC-1

Identification code	Yb-PVDC-1	
Empirical formula	C39 H30 O10 Yb	
Formula weight	831.67	
Temperature	253(2) K	
Wavelength	0.71073 Å	
Crystal system	Orthorhombic	
Space group	F d d d	
Unit cell dimensions	a = 16.247(6) Å	α= 90°.
	b = 48.939(19) Å	β= 90°.
	c = 80.84(3) Å	γ = 90°.
Volume	64280(43) $Å^3$	
Z	32	
Density (calculated)	0.688 Mg/m^3	
Absorption coefficient	1.189 mm^{-1}	
F(000)	13248	
Crystal size	0.32 x 0.23 x 0.21 mm^3	
Theta range for data collection	3.54 to 23.25°.	
Index ranges	-17<=h<=18, -54<=k<=54, -89<=l<=87	
Reflections collected	95076	
Independent reflections	11507 [R(int) = 0.1522]	
Completeness to theta = 23.25°	99.5 %	
Absorption correction	Semi-empirical from equivalents	
Max. and min. transmission	0.7883 and 0.7021	
Refinement method	Full-matrix least-squares on F^2	
Data / restraints / parameters	11507 / 33 / 399	
Goodness-of-fit on F^2	0.872	
Final R indices [I>2sigma(I)]	R1 = 0.0575, wR2 = 0.1229	
R indices (all data)	R1 = 0.1596, wR2 = 0.1464	
Largest diff. peak and hole	0.516 and -0.395 $e.Å^{-3}$	

Table AA 2. Atomic coordinates (x 10^4) and equivalent isotropic displacement parameters (Å^2 x 10^3) for Yb-PVDC-1. U(eq) is defined as one third of the trace of the orthogonalized U^{ij} tensor.

	x	y	z	U(eq)
Yb(1)	-1250	8750	6303(1)	88(1)
Yb(2)	1250	9097(1)	6250	110(1)
O(1)	1471(4)	8746(1)	6086(1)	120(2)
O(2)	2601(4)	8518(1)	6135(1)	105(2)
O(3)	-447(4)	6765(1)	3956(1)	139(2)
O(4)	708(4)	6525(1)	3986(1)	115(2)
O(5)	2397(9)	7265(3)	5261(1)	348(7)
O(6)	-113(14)	7738(4)	4906(2)	360(10)
O(7)	-1232(6)	9045(1)	6088(1)	149(3)
O(8)	40(5)	9059(2)	6117(1)	194(4)
O(9)	1170(9)	9550(3)	5036(2)	296(6)
O(10)	767(7)	9564(2)	6161(1)	315(6)
C(1)	1948(7)	8556(2)	6057(1)	101(3)
C(2)	1760(5)	8363(1)	5921(1)	111(3)
C(3)	1027(4)	8405(1)	5836(1)	149(4)
C(4)	839(4)	8246(2)	5698(1)	174(5)
C(5)	1385(5)	8046(1)	5645(1)	167(5)
C(6)	2119(4)	8004(1)	5730(1)	173(5)
C(7)	2306(4)	8162(2)	5868(1)	146(4)
C(8)	1199(7)	7898(3)	5484(2)	217(6)
C(9)	1722(9)	7735(3)	5410(2)	392(16)
C(10)	1340(6)	7619(2)	5242(1)	550(30)
C(11)	1702(6)	7396(2)	5164(1)	510(30)
C(12)	1392(6)	7302(2)	5015(1)	269(13)
C(13)	720(7)	7432(2)	4942(1)	255(10)
C(14)	358(7)	7655(3)	5020(1)	490(30)
C(15)	668(6)	7748(2)	5170(1)	590(40)
C(16)	445(11)	7345(3)	4759(2)	291(10)
C(17)	828(10)	7134(3)	4696(2)	258(8)
C(18)	600(5)	7020(2)	4521(1)	237(9)
C(19)	10(5)	7144(2)	4421(1)	267(9)
C(20)	-150(4)	7042(2)	4264(1)	210(6)
C(21)	279(5)	6816(2)	4206(1)	137(4)
C(22)	869(5)	6692(1)	4306(1)	166(5)
C(23)	1030(5)	6794(2)	4463(1)	220(7)
C(24)	184(7)	6690(2)	4035(1)	119(3)
C(25)	-551(9)	9112(2)	6035(1)	131(4)

C(26)	-484(5)	9251(1)	5879(1)	113(3)
C(27)	-1200(4)	9368(2)	5817(1)	156(4)
C(28)	-1186(4)	9503(2)	5665(1)	199(5)
C(29)	-457(4)	9521(2)	5576(1)	196(6)
C(30)	259(4)	9405(2)	5638(1)	233(7)
C(31)	246(4)	9270(2)	5790(1)	201(6)
C(32)	-471(7)	9679(3)	5410(2)	213(6)
C(33)	119(8)	9692(3)	5300(2)	254(8)
C(34)	18(8)	9844(3)	5142(1)	253(11)
C(35)	-517(7)	10064(2)	5132(1)	270(12)
C(36)	569(8)	9787(3)	5013(1)	235(7)
C(37)	2622(13)	7021(3)	5154(3)	470(20)
C(38)	1674(13)	9554(7)	4880(2)	450(20)
C(39)	-555(13)	7992(4)	4998(3)	369(12)

Table AA 3. Bond lengths (Å) and angles (°) for Yb-PVDC-1.

Yb(1)-O(4)#1	2.184(6)
Yb(1)-O(4)#2	2.184(6)
Yb(1)-O(2)#3	2.242(6)
Yb(1)-O(2)#4	2.242(6)
Yb(1)-O(7)#5	2.262(6)
Yb(1)-O(7)	2.262(6)
Yb(1)-O(8)#5	2.991(9)
Yb(1)-O(8)	2.991(9)
Yb(1)-C(25)#5	3.021(11)
Yb(1)-C(25)	3.021(11)
Yb(2)-O(1)#4	2.201(6)
Yb(2)-O(1)	2.201(6)
Yb(2)-O(8)	2.249(8)
Yb(2)-O(8)#4	2.250(8)
Yb(2)-O(3)#6	2.270(6)
Yb(2)-O(3)#1	2.270(6)
Yb(2)-O(10)#4	2.519(11)
Yb(2)-O(10)	2.519(11)
O(1)-C(1)	1.233(9)
O(2)-C(1)	1.248(9)
O(2)-Yb(1)#4	2.242(6)
O(3)-C(24)	1.264(9)
O(3)-Yb(2)#7	2.270(6)
O(4)-C(24)	1.237(10)

O(4)-Yb(1)#8	2.185(6)
O(5)-C(37)	1.523(14)
O(5)-C(11)	1.515(13)
O(6)-C(14)	1.27(2)
O(6)-C(39)	1.616(14)
O(7)-C(25)	1.230(12)
O(8)-C(25)	1.195(12)
O(9)-C(38)	1.505(17)
O(9)-C(36)	1.527(15)
C(1)-C(2)	1.480(9)
C(2)-C(3)	1.39
C(2)-C(7)	1.39
C(3)-C(4)	1.39
C(3)-H(3A)	0.93
C(4)-C(5)	1.39
C(4)-H(4A)	0.93
C(5)-C(6)	1.39
C(5)-C(8)	1.520(13)
C(6)-C(7)	1.39
C(6)-H(6A)	0.93
C(7)-H(7A)	0.93
C(8)-C(9)	1.3088(11)
C(8)-H(8A)	0.93
C(9)-C(10)	1.599(14)
C(9)-H(9A)	0.93
C(10)-C(11)	1.39
C(10)-C(15)	1.39
C(11)-C(12)	1.39
C(12)-C(13)	1.39
C(12)-H(12A)	0.93
C(13)-C(14)	1.39
C(13)-C(16)	1.608(15)
C(14)-C(15)	1.39
C(15)-H(15A)	0.93
C(16)-C(17)	1.3091(11)
C(16)-H(16A)	0.93
C(17)-C(18)	1.568(14)
C(17)-H(17A)	0.93
C(18)-C(19)	1.39
C(18)-C(23)	1.39
C(19)-C(20)	1.39
C(19)-H(19A)	0.93
C(20)-C(21)	1.39
C(20)-H(20A)	0.93
C(21)-C(22)	1.39

C(21)-C(24)	1.522(10)
C(22)-C(23)	1.39
C(22)-H(22A)	0.93
C(23)-H(23A)	0.93
C(25)-C(26)	1.440(10)
C(26)-C(27)	1.39
C(26)-C(31)	1.39
C(27)-C(28)	1.39
C(27)-H(27A)	0.93
C(28)-C(29)	1.39
C(28)-H(28A)	0.93
C(29)-C(30)	1.39
C(29)-C(32)	1.547(11)
C(30)-C(31)	1.39
C(30)-H(30A)	0.93
C(31)-H(31A)	0.93
C(32)-C(33)	1.3087(11)
C(32)-H(32A)	0.93
C(33)-C(34)	1.489(12)
C(33)-H(33A)	0.93
C(34)-C(35)	1.388(8)
C(34)-C(36)	1.402(8)
C(35)-C(36)#9	1.383(8)
C(35)-H(35A)	0.93
C(36)-C(35)#9	1.383(8)
C(37)-H(37A)	0.96
C(37)-H(37B)	0.96
C(37)-H(37C)	0.96
C(38)-H(38A)	0.96
C(38)-H(38B)	0.96
C(38)-H(38C)	0.96
C(39)-H(39A)	0.96
C(39)-H(39B)	0.96
C(39)-H(39C)	0.96
O(4)#1-Yb(1)-O(4)#2	95.0(3)
O(4)#1-Yb(1)-O(2)#3	82.6(2)
O(4)#2-Yb(1)-O(2)#3	80.0(2)
O(4)#1-Yb(1)-O(2)#4	80.0(2)
O(4)#2-Yb(1)-O(2)#4	82.6(2)
O(2)#3-Yb(1)-O(2)#4	154.1(3)
O(4)#1-Yb(1)-O(7)#5	156.8(3)
O(4)#2-Yb(1)-O(7)#5	97.0(2)
O(2)#3-Yb(1)-O(7)#5	119.0(3)
O(2)#4-Yb(1)-O(7)#5	81.9(3)
O(4)#1-Yb(1)-O(7)	97.0(2)

O(4)#2-Yb(1)-O(7)	156.8(3)
O(2)#3-Yb(1)-O(7)	82.0(3)
O(2)#4-Yb(1)-O(7)	119.0(3)
O(7)#5-Yb(1)-O(7)	79.3(3)
O(4)#1-Yb(1)-O(8)#5	159.2(2)
O(4)#2-Yb(1)-O(8)#5	75.3(2)
O(2)#3-Yb(1)-O(8)#5	77.6(2)
O(2)#4-Yb(1)-O(8)#5	116.1(2)
O(7)#5-Yb(1)-O(8)#5	44.0(2)
O(7)-Yb(1)-O(8)#5	86.7(3)
O(4)#1-Yb(1)-O(8)	75.3(2)
O(4)#2-Yb(1)-O(8)	159.2(2)
O(2)#3-Yb(1)-O(8)	116.1(2)
O(2)#4-Yb(1)-O(8)	77.6(2)
O(7)#5-Yb(1)-O(8)	86.8(3)
O(7)-Yb(1)-O(8)	44.0(2)
O(8)#5-Yb(1)-O(8)	119.5(3)
O(4)#1-Yb(1)-C(25)#5	176.6(3)
O(4)#2-Yb(1)-C(25)#5	88.4(3)
O(2)#3-Yb(1)-C(25)#5	98.3(3)
O(2)#4-Yb(1)-C(25)#5	100.2(3)
O(7)#5-Yb(1)-C(25)#5	21.3(3)
O(7)-Yb(1)-C(25)#5	80.0(3)
O(8)#5-Yb(1)-C(25)#5	22.9(2)
O(8)-Yb(1)-C(25)#5	101.4(3)
O(4)#1-Yb(1)-C(25)	88.4(3)
O(4)#2-Yb(1)-C(25)	176.6(3)
O(2)#3-Yb(1)-C(25)	100.2(3)
O(2)#4-Yb(1)-C(25)	98.3(3)
O(7)#5-Yb(1)-C(25)	80.0(3)
O(7)-Yb(1)-C(25)	21.3(3)
O(8)#5-Yb(1)-C(25)	101.4(3)
O(8)-Yb(1)-C(25)	22.9(2)
C(25)#5-Yb(1)-C(25)	88.3(5)
O(1)#4-Yb(2)-O(1)	77.3(3)
O(1)#4-Yb(2)-O(8)	94.6(3)
O(1)-Yb(2)-O(8)	77.8(3)
O(1)#4-Yb(2)-O(8)#4	77.8(3)
O(1)-Yb(2)-O(8)#4	94.6(3)
O(8)-Yb(2)-O(8)#4	170.4(5)
O(1)#4-Yb(2)-O(3)#6	145.0(2)
O(1)-Yb(2)-O(3)#6	75.3(2)
O(8)-Yb(2)-O(3)#6	100.4(3)
O(8)#4-Yb(2)-O(3)#6	83.1(2)
O(1)#4-Yb(2)-O(3)#1	75.3(2)

O(1)-Yb(2)-O(3)#1	145.0(2)
O(8)-Yb(2)-O(3)#1	83.1(2)
O(8)#4-Yb(2)-O(3)#1	100.4(3)
O(3)#6-Yb(2)-O(3)#1	137.5(3)
O(1)#4-Yb(2)-O(10)#4	126.0(3)
O(1)-Yb(2)-O(10)#4	146.0(3)
O(8)-Yb(2)-O(10)#4	119.0(3)
O(8)#4-Yb(2)-O(10)#4	70.6(3)
O(3)#6-Yb(2)-O(10)#4	72.6(3)
O(3)#1-Yb(2)-O(10)#4	69.0(3)
O(1)#4-Yb(2)-O(10)	146.0(3)
O(1)-Yb(2)-O(10)	126.0(3)
O(8)-Yb(2)-O(10)	70.6(3)
O(8)#4-Yb(2)-O(10)	119.0(4)
O(3)#6-Yb(2)-O(10)	69.0(3)
O(3)#1-Yb(2)-O(10)	72.6(3)
O(10)#4-Yb(2)-O(10)	49.9(5)
C(1)-O(1)-Yb(2)	143.9(6)
C(1)-O(2)-Yb(1)#4	138.3(6)
C(24)-O(3)-Yb(2)#7	137.1(6)
C(24)-O(4)-Yb(1)#8	153.7(6)
C(37)-O(5)-C(11)	102.5(9)
C(14)-O(6)-C(39)	100.4(14)
C(25)-O(7)-Yb(1)	116.7(8)
C(25)-O(8)-Yb(2)	161.7(10)
C(25)-O(8)-Yb(1)	79.9(8)
Yb(2)-O(8)-Yb(1)	114.4(2)
C(38)-O(9)-C(36)	103.6(15)
O(1)-C(1)-O(2)	123.2(9)
O(1)-C(1)-C(2)	119.6(9)
O(2)-C(1)-C(2)	117.2(10)
C(3)-C(2)-C(7)	120
C(3)-C(2)-C(1)	116.7(7)
C(7)-C(2)-C(1)	123.1(7)
C(2)-C(3)-C(4)	120
C(2)-C(3)-H(3A)	120
C(4)-C(3)-H(3A)	120
C(5)-C(4)-C(3)	120
C(5)-C(4)-H(4A)	120
C(3)-C(4)-H(4A)	120
C(4)-C(5)-C(6)	120
C(4)-C(5)-C(8)	118.2(4)
C(6)-C(5)-C(8)	121.5(4)
C(7)-C(6)-C(5)	120
C(7)-C(6)-H(6A)	120

C(5)-C(6)-H(6A)	120
C(6)-C(7)-C(2)	120
C(6)-C(7)-H(7A)	120
C(2)-C(7)-H(7A)	120
C(9)-C(8)-C(5)	123.5(11)
C(9)-C(8)-H(8A)	118.2
C(5)-C(8)-H(8A)	118.2
C(8)-C(9)-C(10)	110.6(10)
C(8)-C(9)-H(9A)	124.7
C(10)-C(9)-H(9A)	124.7
C(11)-C(10)-C(15)	120
C(11)-C(10)-C(9)	120
C(15)-C(10)-C(9)	120
C(10)-C(11)-C(12)	120
C(10)-C(11)-O(5)	114.4(7)
C(12)-C(11)-O(5)	125.5(7)
C(13)-C(12)-C(11)	120
C(13)-C(12)-H(12A)	120
C(11)-C(12)-H(12A)	120
C(14)-C(13)-C(12)	120
C(14)-C(13)-C(16)	120.5(4)
C(12)-C(13)-C(16)	119.1(4)
O(6)-C(14)-C(13)	100.2(8)
O(6)-C(14)-C(15)	138.5(9)
C(13)-C(14)-C(15)	120
C(14)-C(15)-C(10)	120
C(14)-C(15)-H(15A)	120
C(10)-C(15)-H(15A)	120
C(17)-C(16)-C(13)	115.6(12)
C(17)-C(16)-H(16A)	122.3
C(13)-C(16)-H(16A)	122.1
C(16)-C(17)-C(18)	121.1(13)
C(16)-C(17)-H(17A)	119.5
C(18)-C(17)-H(17A)	119.4
C(19)-C(18)-C(23)	120
C(19)-C(18)-C(17)	122.1(4)
C(23)-C(18)-C(17)	117.9(4)
C(18)-C(19)-C(20)	120
C(18)-C(19)-H(19A)	120
C(20)-C(19)-H(19A)	120
C(21)-C(20)-C(19)	120
C(21)-C(20)-H(20A)	120
C(19)-C(20)-H(20A)	120
C(20)-C(21)-C(22)	120
C(20)-C(21)-C(24)	125.2(7)

C(22)-C(21)-C(24)	114.7(7)
C(23)-C(22)-C(21)	120
C(23)-C(22)-H(22A)	120
C(21)-C(22)-H(22A)	120
C(22)-C(23)-C(18)	120
C(22)-C(23)-H(23A)	120
C(18)-C(23)-H(23A)	120
O(4)-C(24)-O(3)	125.8(9)
O(4)-C(24)-C(21)	119.1(9)
O(3)-C(24)-C(21)	115.1(9)
O(8)-C(25)-O(7)	118.2(10)
O(8)-C(25)-C(26)	121.9(12)
O(7)-C(25)-C(26)	119.9(12)
O(8)-C(25)-Yb(1)	77.1(7)
O(7)-C(25)-Yb(1)	42.0(5)
C(26)-C(25)-Yb(1)	159.4(9)
C(27)-C(26)-C(31)	120
C(27)-C(26)-C(25)	116.7(8)
C(31)-C(26)-C(25)	123.3(8)
C(26)-C(27)-C(28)	120
C(26)-C(27)-H(27A)	120
C(28)-C(27)-H(27A)	120
C(29)-C(28)-C(27)	120
C(29)-C(28)-H(28A)	120
C(27)-C(28)-H(28A)	120
C(28)-C(29)-C(30)	120
C(28)-C(29)-C(32)	117.9(4)
C(30)-C(29)-C(32)	122.1(4)
C(31)-C(30)-C(29)	120
C(31)-C(30)-H(30A)	120
C(29)-C(30)-H(30A)	120
C(30)-C(31)-C(26)	120
C(30)-C(31)-H(31A)	120
C(26)-C(31)-H(31A)	120
C(33)-C(32)-C(29)	127.0(10)
C(33)-C(32)-H(32A)	116.5
C(29)-C(32)-H(32A)	116.5
C(32)-C(33)-C(34)	121.9(11)
C(32)-C(33)-H(33A)	119.1
C(34)-C(33)-H(33A)	119.1
C(35)-C(34)-C(36)	120.8(7)
C(35)-C(34)-C(33)	120.4(7)
C(36)-C(34)-C(33)	118.1(7)
C(36)#9-C(35)-C(34)	119.8(8)
C(36)#9-C(35)-H(35A)	120.1

C(34)-C(35)-H(35A)	120.1
C(35)#9-C(36)-C(34)	119.1(8)
C(35)#9-C(36)-O(9)	122.9(10)
C(34)-C(36)-O(9)	117.9(10)
O(5)-C(37)-H(37A)	109.6
O(5)-C(37)-H(37B)	109.4
H(37A)-C(37)-H(37B)	109.5
O(5)-C(37)-H(37C)	109.5
H(37A)-C(37)-H(37C)	109.5
H(37B)-C(37)-H(37C)	109.5
O(9)-C(38)-H(38A)	109.6
O(9)-C(38)-H(38B)	109.4
H(38A)-C(38)-H(38B)	109.5
O(9)-C(38)-H(38C)	109.4
H(38A)-C(38)-H(38C)	109.5
H(38B)-C(38)-H(38C)	109.5
O(6)-C(39)-H(39A)	109.7
O(6)-C(39)-H(39B)	109.4
H(39A)-C(39)-H(39B)	109.5
O(6)-C(39)-H(39C)	109.4
H(39A)-C(39)-H(39C)	109.5
H(39B)-C(39)-H(39C)	109.5

Symmetry transformations used to generate equivalent atoms:

#1 -x,y+1/4,z+1/4; #2 x-1/4,-y+3/2,z+1/4; #3 x-1/2,-y+7/4,-z+5/4; #4 -x+1/4,y,-z+5/4; #5 -x-1/4,-y+7/4,z; #6 x+1/4,y+1/4,-z+1; #7 x-1/4,y-1/4,-z+1; #8 x+1/4,-y+3/2,z-1/4; #9 -x,-y+2,-z+1

Table AA 4. Anisotropic displacement parameters ($Å^2$ x 10^3) for Yb-PVDC-1. The anisotropic displacement factor exponent takes the form: $-2p^2[h^2 a^{*2}U^{11} + ... + 2hka^*b^*U^{12}]$.

	U^{11}	U^{22}	U^{33}	U^{23}	U^{13}	U^{12}
Yb(1)	120(1)	100(1)	45(1)	0	0	-2(1)
Yb(2)	151(1)	98(1)	81(1)	0	38(1)	0
O(1)	120(5)	147(6)	93(4)	-36(4)	-3(4)	18(5)
O(2)	121(5)	121(5)	72(3)	-28(3)	-5(3)	10(4)
O(3)	140(6)	143(5)	134(5)	-65(4)	-47(5)	42(4)
O(4)	132(5)	153(6)	59(3)	-26(3)	-6(3)	32(4)
O(5)	510(20)	391(19)	147(8)	-28(10)	-42(11)	-66(17)
O(6)	470(30)	370(30)	237(13)	-171(15)	52(15)	-51(19)
O(7)	243(9)	142(5)	62(4)	19(3)	38(5)	-8(6)
O(8)	216(8)	313(11)	55(4)	32(5)	-11(4)	143(8)

O(9)	340(16)	294(15)	255(13)	98(12)	-72(13)	-2(12)
O(10)	327(15)	281(12)	338(16)	3(10)	31(10)	22(9)
C(1)	89(8)	146(9)	67(6)	-29(6)	-16(5)	-2(7)
C(2)	123(8)	132(8)	77(6)	-34(6)	-7(6)	-8(7)
C(3)	163(10)	202(11)	81(6)	-58(7)	-20(6)	-7(8)
C(4)	154(10)	218(13)	151(10)	-97(9)	-25(8)	4(9)
C(5)	173(12)	214(13)	113(8)	-58(9)	-22(8)	-55(11)
C(6)	217(13)	155(10)	147(10)	-90(8)	32(9)	15(9)
C(7)	162(9)	158(10)	117(8)	-73(7)	-25(7)	35(8)
C(8)	241(14)	216(15)	195(14)	-74(11)	80(12)	-98(13)
C(9)	640(50)	320(30)	214(19)	-109(18)	-20(20)	-70(30)
C(11)	370(30)	700(60)	460(40)	470(50)	-240(30)	-300(40)
C(12)	340(30)	400(30)	73(8)	-70(12)	-4(10)	-240(20)
C(13)	310(20)	310(20)	143(12)	-36(13)	-136(13)	-94(18)
C(14)	360(40)	170(20)	950(100)	80(40)	180(50)	90(20)
C(15)	910(70)	740(60)	118(11)	-230(20)	220(20)	-720(60)
C(16)	310(20)	220(20)	340(30)	-46(18)	110(20)	-30(17)
C(17)	245(19)	320(30)	213(16)	19(17)	39(14)	-56(17)
C(18)	196(15)	410(20)	107(9)	-137(13)	1(9)	-130(15)
C(19)	197(14)	420(20)	188(13)	-236(15)	10(10)	-58(14)
C(20)	133(9)	271(15)	227(14)	-156(12)	-18(9)	39(10)
C(21)	117(8)	200(11)	94(7)	-65(7)	-27(6)	14(8)
C(22)	207(12)	216(12)	76(7)	-55(7)	-15(7)	-13(10)
C(23)	259(16)	285(18)	114(10)	-47(10)	-13(10)	-26(14)
C(24)	108(9)	163(10)	85(7)	-41(6)	-23(6)	21(8)
C(25)	184(13)	139(10)	70(7)	25(6)	28(8)	53(10)
C(26)	121(8)	149(8)	71(6)	49(5)	-2(6)	21(7)
C(27)	162(9)	212(11)	96(7)	74(7)	19(7)	6(9)
C(28)	190(12)	268(15)	139(10)	92(10)	22(9)	-4(11)
C(29)	246(15)	239(13)	102(8)	116(9)	-78(9)	-79(12)
C(30)	147(10)	460(20)	89(8)	100(11)	7(7)	-31(12)
C(31)	126(9)	386(19)	91(8)	68(10)	-4(7)	-23(11)
C(32)	225(15)	252(15)	161(13)	58(12)	-28(11)	-79(13)
C(33)	290(20)	310(20)	164(14)	32(14)	4(13)	-90(17)
C(34)	380(30)	229(19)	152(13)	158(13)	-114(14)	-129(18)
C(35)	450(30)	259(19)	107(9)	152(12)	-116(14)	-190(20)
C(36)	212(17)	300(20)	196(18)	33(18)	11(14)	-2(15)
C(37)	750(50)	145(15)	500(40)	-130(18)	320(40)	40(20)
C(38)	350(30)	810(60)	190(17)	-140(30)	144(18)	-60(30)
C(39)	390(30)	300(30)	420(30)	-50(20)	140(20)	10(20)

Table AA 5. Hydrogen coordinates (x 10^4) and isotropic displacement parameters (Å^2 x 10^3) for Yb-PVDC-1.

	x	y	z	U(eq)
H(3A)	662	8539	5871	178
H(4A)	349	8274	5641	209
H(6A)	2484	7870	5695	208
H(7A)	2797	8134	5924	175
H(8A)	686	7924	5436	261
H(9A)	2245	7693	5450	470
H(12A)	1634	7153	4962	323
H(15A)	425	7897	5222	708
H(16A)	41	7439	4700	349
H(17A)	1242	7049	4757	309
H(19A)	-277	7296	4460	320
H(20A)	-545	7125	4198	252
H(22A)	1157	6540	4267	200
H(23A)	1424	6711	4529	264
H(27A)	-1688	9356	5876	188
H(28A)	-1666	9581	5624	238
H(30A)	748	9417	5579	279
H(31A)	725	9192	5831	241
H(32A)	-950	9774	5386	255
H(33A)	616	9604	5322	305
H(35A)	-839	10112	5223	325
H(37A)	3076	6925	5203	699
H(37B)	2773	7083	5045	699
H(37C)	2157	6900	5146	699
H(38A)	2076	9410	4884	676
H(38B)	1948	9727	4870	676
H(38C)	1319	9527	4786	676
H(39A)	-957	8071	4925	553
H(39B)	-150	8127	5026	553
H(39C)	-821	7928	5096	553

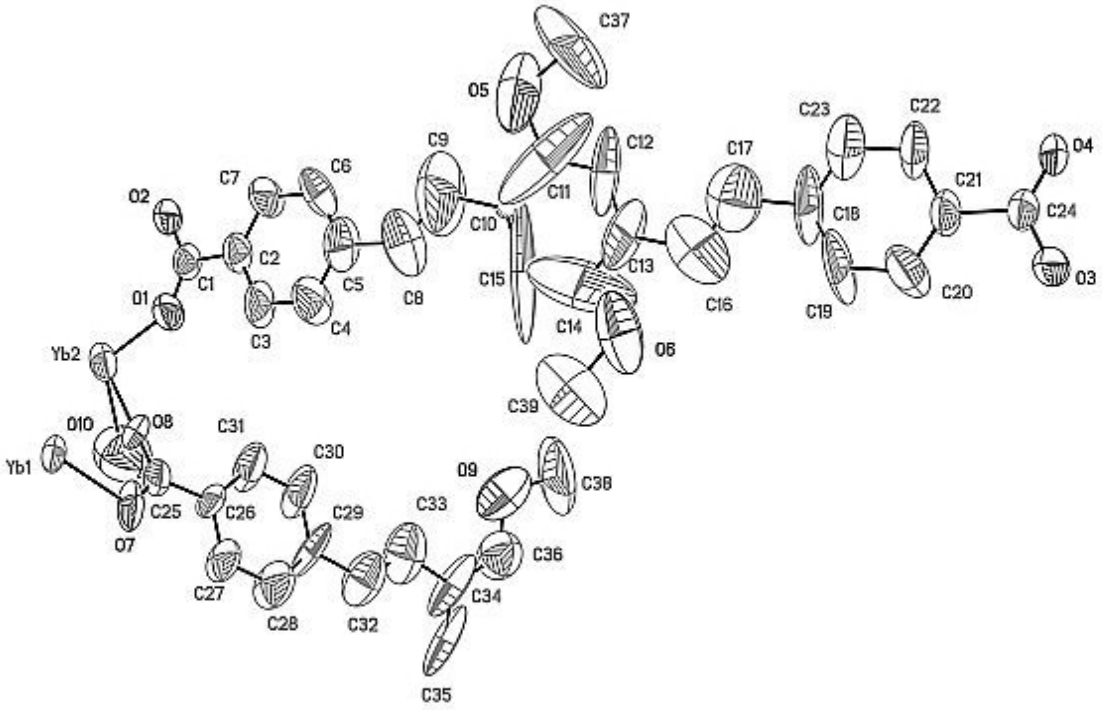

Figure AA 1. The asymmetric unit present in crystalline Yb-PVDC-1 with all atoms represented by thermal ellipsoids drawn at the 30% probability level. All hydrogen atoms were omitted for clarity.

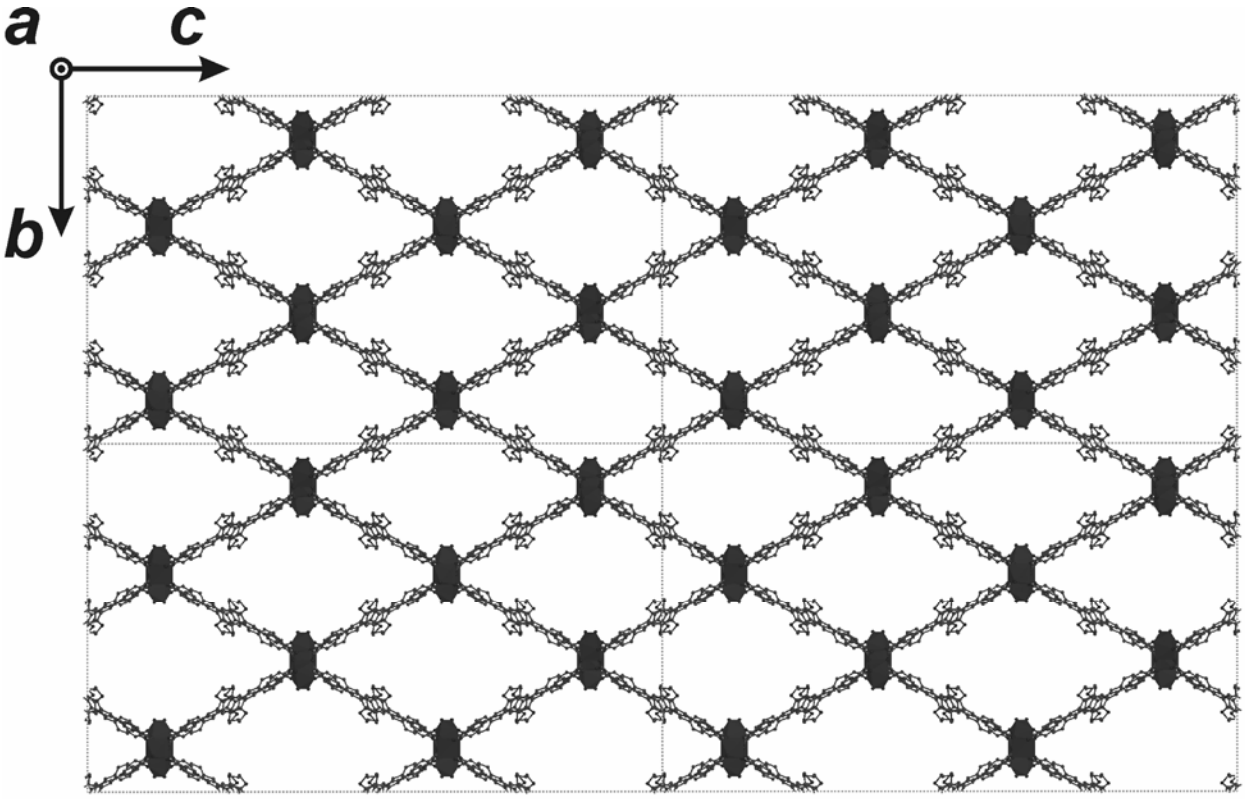

Figure AA 2. Unit cell packing for Yb-PVDC-1.

Table AA 6. Crystal data and structure refinement for Yb-PVDC-2.

Identification code	Yb-PVDC-2	
Empirical formula	$C_{78}H_{60}O_{18}Yb_2$	
Formula weight	1631.34 g/mol	
Temperature	298(2) K	
Wavelength	0.71073 Å	
Crystal system	Orthorhombic	
Space group	Pnna	
Unit cell dimensions	*a* = 16.0798(14) Å	a= 90º.
	b = 22.7096(19) Å	b= 90º.
	c = 38.484(3) Å	g = 90º.
Volume	14053(2) Å3	
Z	4	
Density (calculated)	0.771 Mg/m3	
Absorption coefficient	1.358 mm-1	
F(000)	3248	
Crystal size	0.5 x 0.45 x 0.45 mm3	
Theta range for data collection	3.44 to 28.29º.	

Index ranges	-21≤ *h* ≤21, -30≤ *k* ≤30, -51≤ *l* ≤51	
Reflections collected	123644	
Independent reflections	17435 [R(int) = 0.0580]	
Completeness to theta = 28.29∞	99.80%	
Absorption correction	Semi-empirical from equivalents	
Max. and min. transmission	0.543 and 0.468	
Refinement method	Full-matrix least-squares on F2	
Data / restraints / parameters	17435 / 1228 / 529	
Goodness-of-fit on F2	1.028	
Final R indices [I>2sigma(I)]	R1 = 0.0581, wR2 = 0.2103	
R indices (all data)	R1 = 0.1046, wR2 = 0.2528	
Largest diff. peak and hole	2.921 and -0.541 e.Å^{-3}	

Table AA 7. Atomic coordinates (x 10^4) and equivalent isotropic displacement parameters (Å^2 x 10^3) for Yb-PVDC-2. U(eq) is defined as one third of the trace of the orthogonalized U^{ij}.

	x	y	z	U(eq)
C(1)	1524(5)	756(3)	305(2)	48(2)
C(2A)	1830(20)	1165(11)	583(6)	55(2)
C(3A)	1305(16)	1298(10)	859(7)	68(4)
C(4A)	1581(19)	1660(11)	1127(6)	84(4)
C(5A)	2380(20)	1890(12)	1117(6)	89(3)
C(6A)	2906(17)	1757(13)	841(8)	82(3)
C(7A)	2630(20)	1395(13)	574(6)	66(3)
C(8A)	2877(19)	2251(18)	1377(8)	101(6)
C(9A)	2528(18)	2498(15)	1624(7)	98(6)
C(10A)	2935(15)	2808(13)	1915(5)	109(6)
C(11A)	3776(14)	2930(11)	1958(5)	115(6)
C(12A)	4054(14)	3205(13)	2259(6)	113(6)
C(13A)	3490(16)	3358(14)	2518(5)	107(6)
C(14A)	2649(15)	3236(12)	2475(5)	137(7)
C(15A)	2372(13)	2961(13)	2174(6)	120(7)
O(3A)	4492(18)	2796(16)	1722(7)	173(8)
O(4A)	1900(20)	3335(17)	2704(7)	193(9)
C(16A)	5240(30)	2970(20)	2010(13)	185(12)
C(17A)	1040(20)	3160(30)	2490(12)	212(16)
C(18A)	3810(20)	3670(20)	2835(8)	105(7)
C(19A)	4510(20)	3810(20)	2934(7)	107(7)
C(2B)	1776(12)	1185(6)	580(3)	55(2)
C(3B)	1194(9)	1469(6)	788(4)	68(4)
C(4B)	1455(11)	1847(6)	1050(3)	84(4)
C(5B)	2299(12)	1941(7)	1105(4)	89(3)
C(6B)	2882(10)	1657(8)	897(5)	82(3)

C(7B)	2620(11)	1279(7)	635(4)	66(3)
C(8B)	2506(11)	2298(10)	1426(5)	96(5)
C(9B)	3213(12)	2433(9)	1530(4)	106(5)
C(10B)	3429(11)	2760(7)	1853(3)	106(5)
C(11B)	4271(10)	2820(7)	1927(3)	134(5)
C(12B)	4523(8)	3120(8)	2224(4)	115(5)
C(13B)	3933(9)	3362(7)	2446(3)	102(5)
C(14B)	3091(8)	3302(7)	2372(3)	116(5)
C(15B)	2839(8)	3002(7)	2075(4)	119(5)
O(3B)	4927(14)	2550(10)	1720(5)	183(7)
O(4B)	2471(12)	3542(9)	2588(5)	160(6)
C(16B)	5873(19)	2802(16)	1755(9)	218(12)
C(17B)	1582(18)	3352(17)	2392(8)	234(12)
C(18B)	4155(14)	3567(12)	2803(5)	112(6)
C(19B)	4855(14)	3674(12)	2914(4)	112(6)
C(20)	4960(8)	3959(6)	3268(3)	111(4)
C(21)	5768(9)	4068(7)	3326(3)	132(5)
C(22)	6063(7)	4268(5)	3655(2)	98(3)
C(23)	5495(5)	4338(4)	3921(2)	59(2)
C(24)	4695(6)	4226(5)	3859(2)	81(3)
C(25)	4429(7)	4026(6)	3542(3)	108(4)
C(26)	5815(5)	4535(3)	4268(2)	46(2)
C(27)	6362(4)	5984(3)	4709(2)	44(2)
C(28)	6026(5)	6581(2)	4753(2)	72(2)
C(29)	5522(5)	6716(3)	5035(2)	91(3)
C(30)	5249(5)	7290(3)	5085(2)	122(4)
C(31)	5481(6)	7730(2)	4854(3)	136(5)
C(32)	5985(6)	7595(2)	4571(2)	150(5)
C(33)	6258(5)	7021(3)	4521(2)	124(4)
C(34)	5256(11)	8357(5)	4945(5)	181(6)
C(35)	5505(12)	8826(5)	4828(6)	192(7)
C(36)	5225(13)	9432(5)	4917(5)	195(7)
C(37)	4716(14)	9543(6)	5195(5)	234(10)
C(38)	5464(16)	9888(7)	4715(6)	260(10)
C(39)	6210(20)	10181(13)	4187(10)	393(19)
O(9)	5943(15)	9737(7)	4444(7)	327(10)
O(1)	2035(3)	583(2)	89(1)	53(1)
O(2)	765(3)	609(3)	303(1)	67(2)
O(5)	6560(3)	4672(2)	4301(1)	50(1)
O(6)	5284(3)	4545(2)	4513(1)	57(1)
O(7)	6114(3)	5554(2)	4898(1)	46(1)
O(8)	6940(3)	5901(2)	4495(1)	58(1)
Yb(1)	7500	5000	4674(1)	29(1)
Yb(2)	5000	5000	5000	32(1)

Table AA 8. Bond lengths (Å) and (º) for Yb-PVDC-2.

C(1)-O(1)	1.232(8)
C(1)-O(2)	1.264(9)
C(1)-C(2B)	1.497(9)
C(1)-C(2A)	1.501(13)
C(2A)-C(3A)	1.39
C(2A)-C(7A)	1.39
C(3A)-C(4A)	1.39
C(3A)-H(3AA)	0.93
C(4A)-C(5A)	1.39
C(4A)-H(4AA)	0.93
C(5A)-C(6A)	1.39
C(5A)-C(8A)	1.518(16)
C(6A)-C(7A)	1.39
C(6A)-H(6AA)	0.93
C(7A)-H(7AA)	0.93
C(8A)-C(9A)	1.238(18)
C(8A)-H(8A)	0.93
C(9A)-C(10A)	1.478(15)
C(9A)-H(9AA)	0.93
C(10A)-C(11A)	1.39
C(10A)-C(15A)	1.39
C(11A)-C(12A)	1.39
C(11A)-O(3A)	1.497(18)
C(12A)-C(13A)	1.39
C(12A)-H(12A)	0.93
C(13A)-C(14A)	1.39
C(13A)-C(18A)	1.498(15)
C(14A)-C(15A)	1.39
C(14A)-O(4A)	1.514(19)
C(15A)-H(15A)	0.93
O(3A)-C(16A)	1.69(2)
O(4A)-C(17A)	1.65(2)
C(16A)-H(16A)	0.96
C(16A)-H(16B)	0.96
C(16A)-H(16C)	0.96
C(17A)-H(17A)	0.96
C(17A)-H(17B)	0.96
C(17A)-H(17C)	0.96
C(18A)-C(19A)	1.231(18)
C(18A)-H(18A)	0.93
C(19A)-C(20)	1.514(15)
C(19A)-H(19A)	0.93
C(2B)-C(3B)	1.39
C(2B)-C(7B)	1.39

C(3B)-C(4B)	1.39
C(3B)-H(3BA)	0.93
C(4B)-C(5B)	1.39
C(4B)-H(4BA)	0.93
C(5B)-C(6B)	1.39
C(5B)-C(8B)	1.514(12)
C(6B)-C(7B)	1.39
C(6B)-H(6BA)	0.93
C(7B)-H(7BA)	0.93
C(8B)-C(9B)	1.244(15)
C(8B)-H(8BA)	0.93
C(9B)-C(10B)	1.490(12)
C(9B)-H(9BA)	0.93
C(10B)-C(11B)	1.39
C(10B)-C(15B)	1.39
C(11B)-C(12B)	1.39
C(11B)-O(3B)	1.457(15)
C(12B)-C(13B)	1.39
C(12B)-H(12B)	0.93
C(13B)-C(14B)	1.39
C(13B)-C(18B)	1.493(13)
C(14B)-C(15B)	1.39
C(14B)-O(4B)	1.410(14)
C(15B)-H(15B)	0.93
O(3B)-C(16B)	1.63(2)
O(4B)-C(17B)	1.67(2)
C(16B)-H(16D)	0.96
C(16B)-H(16E)	0.96
C(16B)-H(16F)	0.96
C(17B)-H(17D)	0.96
C(17B)-H(17E)	0.96
C(17B)-H(17F)	0.96
C(18B)-C(19B)	1.228(16)
C(18B)-H(18B)	0.93
C(19B)-C(20)	1.518(13)
C(19B)-H(19B)	0.93
C(20)-C(21)	1.341(16)
C(20)-C(25)	1.362(15)
C(21)-C(22)	1.426(12)
C(21)-H(21A)	0.93
C(22)-C(23)	1.383(11)
C(22)-H(22A)	0.93
C(23)-C(24)	1.332(11)
C(23)-C(26)	1.498(9)
C(24)-C(25)	1.373(12)

C(24)-H(24A)	0.93
C(25)-H(25A)	0.93
C(26)-O(5)	1.244(8)
C(26)-O(6)	1.273(8)
C(27)-O(8)	1.256(8)
C(27)-O(7)	1.280(8)
C(27)-C(28)	1.469(8)
C(27)-Yb(1)	2.891(7)
C(28)-C(29)	1.39
C(28)-C(33)	1.39
C(29)-C(30)	1.39
C(29)-H(29A)	0.93
C(30)-C(31)	1.39
C(30)-H(30A)	0.93
C(31)-C(32)	1.39
C(31)-C(34)	1.511(12)
C(32)-C(33)	1.39
C(32)-H(32A)	0.93
C(33)-H(33A)	0.93
C(34)-C(35)	1.222(15)
C(34)-H(34A)	0.93
C(35)-C(36)	1.488(13)
C(35)-H(35A)	0.93
C(36)-C(38)	1.353(14)
C(36)-C(37)	1.371(14)
C(37)-C(38)#1	1.370(14)
C(37)-H(37A)	0.93
C(38)-O(9)	1.34(2)
C(38)-C(37)#1	1.370(14)
C(39)-O(9)	1.48(3)
C(39)-H(39A)	0.96
C(39)-H(39B)	0.96
C(39)-H(39C)	0.96
O(1)-Yb(1)#2	2.206(5)
O(2)-Yb(2)#3	2.188(5)
O(5)-Yb(1)	2.215(4)
O(6)-Yb(2)	2.189(5)
O(7)-Yb(2)	2.224(5)
O(7)-Yb(1)	2.700(5)
O(8)-Yb(1)	2.339(5)
Yb(1)-O(1)#4	2.206(5)
Yb(1)-O(1)#5	2.206(5)
Yb(1)-O(5)#6	2.215(5)
Yb(1)-O(8)#6	2.339(5)
Yb(1)-O(7)#6	2.701(5)

Yb(1)-C(27)#6	2.891(7)
Yb(1)-Yb(2)	4.2110(3)
Yb(1)-Yb(2)#6	4.2110(3)
Yb(2)-O(2)#7	2.188(5)
Yb(2)-O(2)#5	2.188(5)
Yb(2)-O(6)#8	2.189(5)
Yb(2)-O(7)#8	2.224(5)
Yb(2)-Yb(1)#8	4.2110(4)
O(1)-C(1)-O(2)	123.8(6)
O(1)-C(1)-C(2B)	120.2(10)
O(2)-C(1)-C(2B)	116.0(9)
O(1)-C(1)-C(2A)	117.3(14)
O(2)-C(1)-C(2A)	118.9(14)
C(3A)-C(2A)-C(7A)	120
C(3A)-C(2A)-C(1)	119(2)
C(7A)-C(2A)-C(1)	121(2)
C(4A)-C(3A)-C(2A)	120
C(4A)-C(3A)-H(3AA)	120
C(2A)-C(3A)-H(3AA)	120
C(5A)-C(4A)-C(3A)	120
C(5A)-C(4A)-H(4AA)	120
C(3A)-C(4A)-H(4AA)	120
C(6A)-C(5A)-C(4A)	120
C(6A)-C(5A)-C(8A)	108(2)
C(4A)-C(5A)-C(8A)	132(2)
C(7A)-C(6A)-C(5A)	120
C(7A)-C(6A)-H(6AA)	120
C(5A)-C(6A)-H(6AA)	120
C(6A)-C(7A)-C(2A)	120
C(6A)-C(7A)-H(7AA)	120
C(2A)-C(7A)-H(7AA)	120
C(9A)-C(8A)-C(5A)	121(2)
C(9A)-C(8A)-H(8A)	119.6
C(5A)-C(8A)-H(8A)	119.6
C(8A)-C(9A)-C(10A)	127(2)
C(8A)-C(9A)-H(9AA)	116.7
C(10A)-C(9A)-H(9AA)	116.7
C(11A)-C(10A)-C(15A)	120
C(11A)-C(10A)-C(9A)	128.0(18)
C(15A)-C(10A)-C(9A)	112.0(18)
C(12A)-C(11A)-C(10A)	120
C(12A)-C(11A)-O(3A)	110.4(13)
C(10A)-C(11A)-O(3A)	129.6(13)
C(13A)-C(12A)-C(11A)	120
C(13A)-C(12A)-H(12A)	120

C(11A)-C(12A)-H(12A)	120
C(12A)-C(13A)-C(14A)	120
C(12A)-C(13A)-C(18A)	118(2)
C(14A)-C(13A)-C(18A)	122(2)
C(15A)-C(14A)-C(13A)	120
C(15A)-C(14A)-O(4A)	107.1(14)
C(13A)-C(14A)-O(4A)	132.9(14)
C(14A)-C(15A)-C(10A)	120
C(14A)-C(15A)-H(15A)	120
C(10A)-C(15A)-H(15A)	120
C(11A)-O(3A)-C(16A)	96(2)
C(14A)-O(4A)-C(17A)	110.0(16)
O(3A)-C(16A)-H(16A)	109.5
O(3A)-C(16A)-H(16B)	109.5
H(16A)-C(16A)-H(16B)	109.5
O(3A)-C(16A)-H(16C)	109.5
H(16A)-C(16A)-H(16C)	109.5
H(16B)-C(16A)-H(16C)	109.5
O(4A)-C(17A)-H(17A)	109.5
O(4A)-C(17A)-H(17B)	109.5
H(17A)-C(17A)-H(17B)	109.5
O(4A)-C(17A)-H(17C)	109.5
H(17A)-C(17A)-H(17C)	109.5
H(17B)-C(17A)-H(17C)	109.5
C(19A)-C(18A)-C(13A)	134(3)
C(19A)-C(18A)-H(18A)	113.1
C(13A)-C(18A)-H(18A)	113.1
C(18A)-C(19A)-C(20)	140(3)
C(18A)-C(19A)-H(19A)	110.2
C(20)-C(19A)-H(19A)	110.2
C(3B)-C(2B)-C(7B)	120
C(3B)-C(2B)-C(1)	121.8(12)
C(7B)-C(2B)-C(1)	118.2(12)
C(2B)-C(3B)-C(4B)	120
C(2B)-C(3B)-H(3BA)	120
C(4B)-C(3B)-H(3BA)	120
C(3B)-C(4B)-C(5B)	120
C(3B)-C(4B)-H(4BA)	120
C(5B)-C(4B)-H(4BA)	120
C(6B)-C(5B)-C(4B)	120
C(6B)-C(5B)-C(8B)	124.7(14)
C(4B)-C(5B)-C(8B)	114.8(14)
C(7B)-C(6B)-C(5B)	120
C(7B)-C(6B)-H(6BA)	120
C(5B)-C(6B)-H(6BA)	120

C(6B)-C(7B)-C(2B)	120
C(6B)-C(7B)-H(7BA)	120
C(2B)-C(7B)-H(7BA)	120
C(9B)-C(8B)-C(5B)	126.5(17)
C(9B)-C(8B)-H(8BA)	116.7
C(5B)-C(8B)-H(8BA)	116.7
C(8B)-C(9B)-C(10B)	127.2(17)
C(8B)-C(9B)-H(9BA)	116.4
C(10B)-C(9B)-H(9BA)	116.4
C(11B)-C(10B)-C(15B)	120
C(11B)-C(10B)-C(9B)	116.5(12)
C(15B)-C(10B)-C(9B)	123.5(12)
C(12B)-C(11B)-C(10B)	120
C(12B)-C(11B)-O(3B)	116.4(11)
C(10B)-C(11B)-O(3B)	123.5(11)
C(11B)-C(12B)-C(13B)	120
C(11B)-C(12B)-H(12B)	120
C(13B)-C(12B)-H(12B)	120
C(14B)-C(13B)-C(12B)	120
C(14B)-C(13B)-C(18B)	116.8(12)
C(12B)-C(13B)-C(18B)	121.8(12)
C(13B)-C(14B)-C(15B)	120
C(13B)-C(14B)-O(4B)	122.1(10)
C(15B)-C(14B)-O(4B)	117.9(10)
C(14B)-C(15B)-C(10B)	120
C(14B)-C(15B)-H(15B)	120
C(10B)-C(15B)-H(15B)	120
C(11B)-O(3B)-C(16B)	118.9(17)
C(14B)-O(4B)-C(17B)	103.8(14)
O(3B)-C(16B)-H(16D)	109.5
O(3B)-C(16B)-H(16E)	109.5
H(16D)-C(16B)-H(16E)	109.5
O(3B)-C(16B)-H(16F)	109.5
H(16D)-C(16B)-H(16F)	109.5
H(16E)-C(16B)-H(16F)	109.5
O(4B)-C(17B)-H(17D)	109.5
O(4B)-C(17B)-H(17E)	109.5
H(17D)-C(17B)-H(17E)	109.5
O(4B)-C(17B)-H(17F)	109.5
H(17D)-C(17B)-H(17F)	109.5
H(17E)-C(17B)-H(17F)	109.5
C(19B)-C(18B)-C(13B)	127.0(17)
C(19B)-C(18B)-H(18B)	116.5
C(13B)-C(18B)-H(18B)	116.5
C(18B)-C(19B)-C(20)	119.9(16)

C(18B)-C(19B)-H(19B)	120
C(20)-C(19B)-H(19B)	120
C(21)-C(20)-C(25)	117.4(9)
C(21)-C(20)-C(19A)	130.2(19)
C(25)-C(20)-C(19A)	112.3(18)
C(21)-C(20)-C(19B)	109.5(13)
C(25)-C(20)-C(19B)	132.1(13)
C(20)-C(21)-C(22)	121.8(10)
C(20)-C(21)-H(21A)	119.1
C(22)-C(21)-H(21A)	119.1
C(23)-C(22)-C(21)	118.4(10)
C(23)-C(22)-H(22A)	120.8
C(21)-C(22)-H(22A)	120.8
C(24)-C(23)-C(22)	118.9(7)
C(24)-C(23)-C(26)	123.2(7)
C(22)-C(23)-C(26)	117.9(7)
C(23)-C(24)-C(25)	121.6(9)
C(23)-C(24)-H(24A)	119.2
C(25)-C(24)-H(24A)	119.2
C(20)-C(25)-C(24)	121.9(10)
C(20)-C(25)-H(25A)	119.1
C(24)-C(25)-H(25A)	119.1
O(5)-C(26)-O(6)	124.5(6)
O(5)-C(26)-C(23)	119.7(6)
O(6)-C(26)-C(23)	115.7(7)
O(8)-C(27)-O(7)	119.2(6)
O(8)-C(27)-C(28)	119.0(6)
O(7)-C(27)-C(28)	121.6(6)
O(8)-C(27)-Yb(1)	52.1(3)
O(7)-C(27)-Yb(1)	68.6(4)
C(28)-C(27)-Yb(1)	162.0(5)
C(29)-C(28)-C(33)	120
C(29)-C(28)-C(27)	120.5(5)
C(33)-C(28)-C(27)	119.4(5)
C(30)-C(29)-C(28)	120
C(30)-C(29)-H(29A)	120
C(28)-C(29)-H(29A)	120
C(29)-C(30)-C(31)	120
C(29)-C(30)-H(30A)	120
C(31)-C(30)-H(30A)	120
C(32)-C(31)-C(30)	120
C(32)-C(31)-C(34)	122.0(9)
C(30)-C(31)-C(34)	117.6(9)
C(33)-C(32)-C(31)	120
C(33)-C(32)-H(32A)	120

C(31)-C(32)-H(32A)	120
C(32)-C(33)-C(28)	120
C(32)-C(33)-H(33A)	120
C(28)-C(33)-H(33A)	120
C(35)-C(34)-C(31)	131.0(16)
C(35)-C(34)-H(34A)	114.5
C(31)-C(34)-H(34A)	114.5
C(34)-C(35)-C(36)	128.4(17)
C(34)-C(35)-H(35A)	115.8
C(36)-C(35)-H(35A)	115.8
C(38)-C(36)-C(37)	118.7(9)
C(38)-C(36)-C(35)	119.3(16)
C(37)-C(36)-C(35)	122.0(16)
C(38)#1-C(37)-C(36)	119.8(11)
C(38)#1-C(37)-H(37A)	120.1
C(36)-C(37)-H(37A)	120.1
O(9)-C(38)-C(36)	114.6(17)
O(9)-C(38)-C(37)#1	124.0(18)
C(36)-C(38)-C(37)#1	121.1(12)
O(9)-C(39)-H(39A)	109.5
O(9)-C(39)-H(39B)	109.5
H(39A)-C(39)-H(39B)	109.5
O(9)-C(39)-H(39C)	109.5
H(39A)-C(39)-H(39C)	109.5
H(39B)-C(39)-H(39C)	109.5
C(38)-O(9)-C(39)	121(2)
C(1)-O(1)-Yb(1)#2	154.8(5)
C(1)-O(2)-Yb(2)#3	135.4(5)
C(26)-O(5)-Yb(1)	143.8(4)
C(26)-O(6)-Yb(2)	141.5(5)
C(27)-O(7)-Yb(2)	141.5(4)
C(27)-O(7)-Yb(1)	85.3(4)
Yb(2)-O(7)-Yb(1)	117.21(18)
C(27)-O(8)-Yb(1)	102.9(4)
O(1)#4-Yb(1)-O(1)#5	87.2(3)
O(1)#4-Yb(1)-O(5)#6	92.13(19)
O(1)#5-Yb(1)-O(5)#6	154.56(18)
O(1)#4-Yb(1)-O(5)	154.56(18)
O(1)#5-Yb(1)-O(5)	92.13(19)
O(5)#6-Yb(1)-O(5)	99.1(3)
O(1)#4-Yb(1)-O(8)	79.6(2)
O(1)#5-Yb(1)-O(8)	127.48(19)
O(5)#6-Yb(1)-O(8)	77.15(18)
O(5)-Yb(1)-O(8)	80.77(19)
O(1)#4-Yb(1)-O(8)#6	127.47(19)

O(1)#5-Yb(1)-O(8)#6	79.6(2)
O(5)#6-Yb(1)-O(8)#6	80.77(19)
O(5)-Yb(1)-O(8)#6	77.15(18)
O(8)-Yb(1)-O(8)#6	145.7(3)
O(1)#4-Yb(1)-O(7)	76.63(16)
O(1)#5-Yb(1)-O(7)	76.67(16)
O(5)#6-Yb(1)-O(7)	127.86(16)
O(5)-Yb(1)-O(7)	78.47(16)
O(8)-Yb(1)-O(7)	50.86(16)
O(8)#6-Yb(1)-O(7)	145.02(17)
O(1)#4-Yb(1)-O(7)#6	76.66(16)
O(1)#5-Yb(1)-O(7)#6	76.63(16)
O(5)#6-Yb(1)-O(7)#6	78.47(16)
O(5)-Yb(1)-O(7)#6	127.86(16)
O(8)-Yb(1)-O(7)#6	145.02(17)
O(8)#6-Yb(1)-O(7)#6	50.86(16)
O(7)-Yb(1)-O(7)#6	142.81(19)
O(1)#4-Yb(1)-C(27)	73.54(19)
O(1)#5-Yb(1)-C(27)	102.5(2)
O(5)#6-Yb(1)-C(27)	101.7(2)
O(5)-Yb(1)-C(27)	81.82(19)
O(8)-Yb(1)-C(27)	25.07(18)
O(8)#6-Yb(1)-C(27)	158.94(19)
O(7)-Yb(1)-C(27)	26.19(17)
O(7)#6-Yb(1)-C(27)	150.20(17)
O(1)#4-Yb(1)-C(27)#6	102.5(2)
O(1)#5-Yb(1)-C(27)#6	73.54(19)
O(5)#6-Yb(1)-C(27)#6	81.82(19)
O(5)-Yb(1)-C(27)#6	101.7(2)
O(8)-Yb(1)-C(27)#6	158.94(19)
O(8)#6-Yb(1)-C(27)#6	25.07(18)
O(7)-Yb(1)-C(27)#6	150.19(17)
O(7)#6-Yb(1)-C(27)#6	26.19(17)
C(27)-Yb(1)-C(27)#6	174.7(3)
O(1)#4-Yb(1)-Yb(2)	96.18(13)
O(1)#5-Yb(1)-Yb(2)	57.38(13)
O(5)#6-Yb(1)-Yb(2)	147.67(13)
O(5)-Yb(1)-Yb(2)	62.72(13)
O(8)-Yb(1)-Yb(2)	73.76(13)
O(8)#6-Yb(1)-Yb(2)	117.08(14)
O(7)-Yb(1)-Yb(2)	28.02(10)
O(7)#6-Yb(1)-Yb(2)	133.86(9)
C(27)-Yb(1)-Yb(2)	51.83(15)
C(27)#6-Yb(1)-Yb(2)	126.18(14)
O(1)#4-Yb(1)-Yb(2)#6	57.38(13)

O(1)#5-Yb(1)-Yb(2)#6	96.18(13)
O(5)#6-Yb(1)-Yb(2)#6	62.71(13)
O(5)-Yb(1)-Yb(2)#6	147.66(13)
O(8)-Yb(1)-Yb(2)#6	117.08(14)
O(8)#6-Yb(1)-Yb(2)#6	73.76(13)
O(7)-Yb(1)-Yb(2)#6	133.86(9)
O(7)#6-Yb(1)-Yb(2)#6	28.02(10)
C(27)-Yb(1)-Yb(2)#6	126.18(14)
C(27)#6-Yb(1)-Yb(2)#6	51.83(15)
Yb(2)-Yb(1)-Yb(2)#6	145.352(9)
O(2)#7-Yb(2)-O(2)#5	179.999(2)
O(2)#7-Yb(2)-O(6)#8	92.3(2)
O(2)#5-Yb(2)-O(6)#8	87.7(2)
O(2)#7-Yb(2)-O(6)	87.7(2)
O(2)#5-Yb(2)-O(6)	92.3(2)
O(6)#8-Yb(2)-O(6)	179.998(1)
O(2)#7-Yb(2)-O(7)	90.0(2)
O(2)#5-Yb(2)-O(7)	90.0(2)
O(6)#8-Yb(2)-O(7)	92.97(18)
O(6)-Yb(2)-O(7)	87.03(18)
O(2)#7-Yb(2)-O(7)#8	90.0(2)
O(2)#5-Yb(2)-O(7)#8	90.0(2)
O(6)#8-Yb(2)-O(7)#8	87.04(18)
O(6)-Yb(2)-O(7)#8	92.96(18)
O(7)-Yb(2)-O(7)#8	179.996(1)
O(2)#7-Yb(2)-Yb(1)#8	67.78(15)
O(2)#5-Yb(2)-Yb(1)#8	112.22(15)
O(6)#8-Yb(2)-Yb(1)#8	63.01(14)
O(6)-Yb(2)-Yb(1)#8	116.99(14)
O(7)-Yb(2)-Yb(1)#8	145.23(12)
O(7)#8-Yb(2)-Yb(1)#8	34.78(12)
O(2)#7-Yb(2)-Yb(1)	112.22(15)
O(2)#5-Yb(2)-Yb(1)	67.78(15)
O(6)#8-Yb(2)-Yb(1)	116.99(14)
O(6)-Yb(2)-Yb(1)	63.01(14)
O(7)-Yb(2)-Yb(1)	34.77(12)
O(7)#8-Yb(2)-Yb(1)	145.22(12)
Yb(1)#8-Yb(2)-Yb(1)	180

Symmetry transformations used to generate equivalent atoms:

#1 -x+1,-y+2,-z+1; #2 x-1/2,-y+1/2,z-1/2; #3 -x+1/2,y-1/2,-z+1/2; #4 -x+1,y+1/2,z+1/2;

#5 x+1/2,-y+1/2,z+1/2; #6 -x+3/2,-y+1,z; #7 -x+1/2,y+1/2,-z+1/2; #8 -x+1,-y+1,-z+1

Table AA 9. Anisotropic displacement parameters ($Å^2$ x 10^3) for Yb-PVDC-2. The anisotropic displacement factor exponent takes the form: $-2p^2[h^2a^{*2}U^{11} + ... + 2hka^*b^*U^{12}]$.

	U^{11}	U^{22}	U^{33}	U^{23}	U^{13}	U^{12}
C(1)	58(4)	52(4)	34(3)	-15(3)	-4(3)	-4(3)
C(2A)	60(4)	66(4)	38(3)	-23(3)	-8(3)	-9(4)
C(3A)	78(6)	76(7)	52(6)	-24(5)	-5(5)	3(6)
C(4A)	103(7)	84(8)	65(6)	-40(6)	-3(5)	5(6)
C(5A)	104(6)	95(6)	68(5)	-45(4)	-22(4)	-9(5)
C(6A)	85(5)	88(7)	71(6)	-29(5)	-23(5)	-20(5)
C(7A)	76(5)	73(7)	49(6)	-19(5)	-13(4)	-11(5)
C(8A)	108(12)	111(11)	84(10)	-41(9)	-19(10)	-8(10)
C(9A)	109(12)	103(11)	82(10)	-39(9)	-22(10)	-11(11)
C(10A)	126(11)	114(11)	88(10)	-38(9)	-37(10)	-8(11)
C(11A)	131(10)	127(10)	87(9)	-47(9)	-17(9)	-1(10)
C(12A)	135(11)	118(10)	87(10)	-44(9)	-23(9)	-7(10)
C(13A)	120(10)	114(10)	86(10)	-37(9)	-20(9)	-14(10)
C(14A)	147(10)	149(12)	116(11)	-35(10)	-11(10)	-12(11)
C(15A)	136(12)	125(12)	99(11)	-27(10)	-17(10)	-19(11)
O(3A)	199(15)	195(16)	125(13)	-71(14)	-8(13)	16(15)
O(4A)	201(16)	218(18)	159(16)	-43(16)	39(14)	-18(17)
C(16A)	164(15)	203(18)	188(18)	-11(15)	-21(14)	-13(15)
C(17A)	192(18)	230(20)	220(20)	-4(17)	15(16)	-26(17)
C(18A)	110(12)	117(12)	88(11)	-30(10)	-20(10)	-5(11)
C(19A)	114(12)	128(13)	78(10)	-41(10)	-33(10)	-4(11)
C(2B)	60(4)	66(4)	38(3)	-23(3)	-8(3)	-9(4)
C(3B)	78(6)	76(7)	52(6)	-24(5)	-5(5)	3(6)
C(4B)	103(7)	84(8)	65(6)	-40(6)	-3(5)	5(6)
C(5B)	104(6)	95(6)	68(5)	-45(4)	-22(4)	-9(5)
C(6B)	85(5)	88(7)	71(6)	-29(5)	-23(5)	-20(5)
C(7B)	76(5)	73(7)	49(6)	-19(5)	-13(4)	-11(5)
C(8B)	108(10)	104(9)	76(8)	-54(7)	-13(8)	-4(9)
C(9B)	114(10)	116(10)	86(9)	-42(8)	-21(8)	-23(9)
C(10B)	120(9)	115(9)	83(8)	-45(7)	-26(8)	-9(9)
C(11B)	155(10)	156(10)	89(9)	-59(8)	-6(9)	-2(9)
C(12B)	145(10)	127(10)	73(8)	-44(8)	-8(8)	1(10)
C(13B)	120(9)	114(9)	72(8)	-43(7)	-31(7)	-16(8)
C(14B)	133(9)	127(9)	88(8)	-46(7)	-29(8)	-19(9)
C(15B)	130(9)	128(10)	100(9)	-35(8)	-36(8)	-15(9)
O(3B)	199(13)	211(15)	140(11)	-87(11)	32(12)	37(12)
O(4B)	174(12)	179(13)	127(11)	-84(10)	-7(9)	-40(10)
C(16B)	200(15)	251(19)	203(18)	-33(15)	4(15)	20(15)
C(17B)	185(15)	261(19)	256(19)	23(16)	-31(15)	-26(15)
C(18B)	121(11)	129(10)	85(8)	-42(8)	-30(8)	-13(10)
C(19B)	122(12)	140(12)	72(8)	-42(8)	-33(8)	-6(10)
C(20)	116(8)	158(9)	60(6)	-45(6)	-23(6)	-23(7)

C(21)	134(9)	219(12)	44(5)	-59(7)	5(6)	-31(9)
C(22)	86(6)	164(10)	44(5)	-49(6)	3(4)	-20(7)
C(23)	65(5)	75(5)	38(4)	-27(4)	-8(3)	0(4)
C(24)	64(5)	120(8)	61(5)	-33(5)	-12(4)	-10(5)
C(25)	80(7)	163(10)	80(7)	-40(7)	-27(5)	-21(7)
C(26)	59(4)	50(4)	29(3)	-11(3)	-8(3)	7(3)
C(27)	47(4)	30(3)	55(4)	3(3)	-7(3)	6(3)
C(28)	87(6)	31(4)	96(6)	3(4)	14(5)	16(4)
C(29)	109(8)	46(5)	120(8)	-9(5)	37(6)	11(5)
C(30)	121(9)	66(7)	180(11)	-15(7)	46(8)	26(7)
C(31)	142(10)	52(6)	215(13)	2(7)	28(9)	35(7)
C(32)	187(12)	55(6)	208(13)	55(8)	55(10)	34(7)
C(33)	163(11)	46(5)	163(10)	28(6)	57(9)	7(6)
C(34)	177(13)	64(7)	302(17)	-20(9)	5(13)	39(9)
C(35)	203(15)	54(7)	321(17)	0(10)	28(14)	31(9)
C(36)	228(16)	49(7)	308(18)	-13(9)	50(14)	47(9)
C(37)	280(20)	66(9)	350(20)	-9(12)	77(18)	33(12)
C(38)	320(20)	76(9)	390(20)	-19(12)	135(18)	54(13)
C(39)	550(50)	160(20)	470(40)	50(20)	190(40)	-50(30)
O(9)	420(20)	107(10)	450(20)	14(13)	178(19)	50(13)
O(1)	54(3)	62(3)	44(3)	-23(2)	3(2)	-5(3)
O(2)	54(3)	86(4)	61(3)	-30(3)	2(3)	-19(3)
O(5)	52(3)	65(3)	34(2)	-12(2)	-13(2)	4(3)
O(6)	69(3)	67(3)	36(3)	-15(2)	0(2)	-4(3)
O(7)	55(3)	36(2)	47(3)	1(2)	-4(2)	-4(2)
O(8)	69(4)	46(3)	60(3)	10(2)	12(3)	10(3)
Yb(1)	36(1)	27(1)	24(1)	0	0	2(1)
Yb(2)	34(1)	33(1)	30(1)	-2(1)	-2(1)	4(1)

Table AA 10. Hydrogen coordinates (x 10^4) and isotropic displacement parameters (Å^2 x 10^3) for Yb-PVDC-1.

	x	y	z	U(eq)
H(3AA)	769	1144	866	82
H(4AA)	1230	1749	1311	100
H(6AA)	3442	1911	835	98
H(7AA)	2980	1306	389	79
H(8A)	3450	2288	1350	121
H(9AA)	1950	2488	1626	117
H(12A)	4616	3286	2287	136
H(15A)	1809	2880	2146	144
H(16A)	5779	2886	1911	277
H(16B)	5172	2744	2218	277

H(16C)	5211	3383	2065	277
H(17A)	564	3241	2633	318
H(17B)	1052	2754	2429	318
H(17C)	1005	3397	2282	318
H(18A)	3391	3766	2991	126
H(19A)	4866	3847	2746	128
H(3BA)	629	1407	751	82
H(4BA)	1065	2037	1189	100
H(6BA)	3447	1720	934	98
H(7BA)	3010	1089	496	79
H(8BA)	2059	2429	1558	115
H(9BA)	3656	2317	1390	127
H(12B)	5086	3160	2273	138
H(15B)	2276	2962	2026	143
H(16D)	6246	2554	1626	327
H(16E)	6034	2805	1995	327
H(16F)	5897	3195	1664	327
H(17D)	1120	3492	2527	351
H(17E)	1553	2931	2373	351
H(17F)	1564	3523	2164	351
H(18B)	3716	3619	2957	134
H(19B)	5320	3580	2782	134
H(21A)	6146	4011	3146	159
H(22A)	6624	4349	3689	118
H(24A)	4309	4285	4035	98
H(25A)	3870	3933	3512	129
H(29A)	5367	6422	5190	110
H(30A)	4912	7381	5274	147
H(32A)	6141	7889	4416	180
H(33A)	6595	6931	4332	149
H(34A)	4861	8393	5120	217
H(35A)	5923	8800	4662	231
H(37A)	4494	9232	5323	351
H(39A)	6577	9999	4020	589
H(39B)	6505	10493	4303	589
H(39C)	5737	10339	4069	589

Table AA 11. Torsion angles (°) for Yb-PVDC-2.

O(1)-C(1)-C(2A)-C(3A)	-170.4(12)
O(2)-C(1)-C(2A)-C(3A)	10(2)
C(2B)-C(1)-C(2A)-C(3A)	49(27)

O(1)-C(1)-C(2A)-C(7A)	7(2)
O(2)-C(1)-C(2A)-C(7A)	-172.3(13)
C(2B)-C(1)-C(2A)-C(7A)	-133(29)
C(7A)-C(2A)-C(3A)-C(4A)	0
C(1)-C(2A)-C(3A)-C(4A)	178(2)
C(2A)-C(3A)-C(4A)-C(5A)	0
C(3A)-C(4A)-C(5A)-C(6A)	0
C(3A)-C(4A)-C(5A)-C(8A)	-175(4)
C(4A)-C(5A)-C(6A)-C(7A)	0
C(8A)-C(5A)-C(6A)-C(7A)	176(3)
C(5A)-C(6A)-C(7A)-C(2A)	0
C(3A)-C(2A)-C(7A)-C(6A)	0
C(1)-C(2A)-C(7A)-C(6A)	-178(2)
C(6A)-C(5A)-C(8A)-C(9A)	170(4)
C(4A)-C(5A)-C(8A)-C(9A)	-15(6)
C(5A)-C(8A)-C(9A)-C(10A)	173(4)
C(8A)-C(9A)-C(10A)-C(11A)	6(6)
C(8A)-C(9A)-C(10A)-C(15A)	-171(4)
C(15A)-C(10A)-C(11A)-C(12A)	0
C(9[a])-C(10A)-C(11A)-C(12A)	-177(3)
C(15A)-C(10A)-C(11A)-O(3A)	178(2)
C(9A)-C(10A)-C(11A)-O(3A)	1(4)
C(10A)-C(11A)-C(12A)-C(13A)	0
O(3[a])-C(11A)-C(12A)-C(13A)	-178.7(18)
C(11A)-C(12A)-C(13A)-C(14A)	0
C(11A)-C(12A)-C(13A)-C(18A)	-179(3)
C(12A)-C(13A)-C(14A)-C(15A)	0
C(18A)-C(13A)-C(14A)-C(15A)	179(4)
C(12A)-C(13A)-C(14A)-O(4A)	179(2)
C(18A)-C(13A)-C(14A)-O(4A)	-2(4)
C(13A)-C(14A)-C(15A)-C(10A)	0
O(4[a])-C(14A)-C(15A)-C(10A)	-179.2(18)
C(11A)-C(10A)-C(15A)-C(14A)	0
C(9[a])-C(10A)-C(15A)-C(14A)	178(3)
C(12A)-C(11A)-O(3A)-C(16A)	9(3)
C(10A)-C(11A)-O(3A)-C(16A)	-170(3)
C(15A)-C(14A)-O(4A)-C(17A)	-7(3)
C(13A)-C(14A)-O(4A)-C(17A)	174(3)
C(12A)-C(13A)-C(18A)-C(19A)	-2(7)
C(14A)-C(13A)-C(18A)-C(19A)	179(5)
C(13A)-C(18A)-C(19A)-C(20)	-157(5)
O(1)-C(1)-C(2B)-C(3B)	168.4(8)
O(2)-C(1)-C(2B)-C(3B)	-8.9(14)
C(2A)-C(1)-C(2B)-C(3B)	-151(29)
O(1)-C(1)-C(2B)-C(7B)	-14.2(13)

O(2)-C(1)-C(2B)-C(7B)	168.5(8)
C(2A)-C(1)-C(2B)-C(7B)	26(28)
C(7B)-C(2B)-C(3B)-C(4B)	0
C(1)-C(2B)-C(3B)-C(4B)	177.4(14)
C(2B)-C(3B)-C(4B)-C(5B)	0
C(3B)-C(4B)-C(5B)-C(6B)	0
C(3B)-C(4B)-C(5B)-C(8B)	-172.5(18)
C(4B)-C(5B)-C(6B)-C(7B)	0
C(8B)-C(5B)-C(6B)-C(7B)	171.7(19)
C(5B)-C(6B)-C(7B)-C(2B)	0
C(3B)-C(2B)-C(7B)-C(6B)	0
C(1)-C(2B)-C(7B)-C(6B)	-177.5(14)
C(6B)-C(5B)-C(8B)-C(9B)	7(3)
C(4B)-C(5B)-C(8B)-C(9B)	179(2)
C(5B)-C(8B)-C(9B)-C(10B)	-177(2)
C(8B)-C(9B)-C(10B)-C(11B)	175(2)
C(8B)-C(9B)-C(10B)-C(15B)	-5(3)
C(15B)-C(10B)-C(11B)-C(12B)	0
C(9B)-C(10B)-C(11B)-C(12B)	179.9(17)
C(15B)-C(10B)-C(11B)-O(3B)	176.1(16)
C(9B)-C(10B)-C(11B)-O(3B)	-4.0(19)
C(10B)-C(11B)-C(12B)-C(13B)	0
O(3B)-C(11B)-C(12B)-C(13B)	-176.4(14)
C(11B)-C(12B)-C(13B)-C(14B)	0
C(11B)-C(12B)-C(13B)-C(18B)	166.0(19)
C(12B)-C(13B)-C(14B)-C(15B)	0
C(18B)-C(13B)-C(14B)-C(15B)	-166.7(18)
C(12B)-C(13B)-C(14B)-O(4B)	-179.6(16)
C(18B)-C(13B)-C(14B)-O(4B)	14(2)
C(13B)-C(14B)-C(15B)-C(10B)	0
O(4B)-C(14B)-C(15B)-C(10B)	179.6(15)
C(11B)-C(10B)-C(15B)-C(14B)	0
C(9B)-C(10B)-C(15B)-C(14B)	-179.9(18)
C(12B)-C(11B)-O(3B)-C(16B)	-22(3)
C(10B)-C(11B)-O(3B)-C(16B)	162(2)
C(13B)-C(14B)-O(4B)-C(17B)	-179.7(17)
C(15B)-C(14B)-O(4B)-C(17B)	1(2)
C(14B)-C(13B)-C(18B)-C(19B)	-176(3)
C(12B)-C(13B)-C(18B)-C(19B)	17(4)
C(13B)-C(18B)-C(19B)-C(20)	172(2)
C(18A)-C(19A)-C(20)-C(21)	174(5)
C(18A)-C(19A)-C(20)-C(25)	-12(7)
C(18A)-C(19A)-C(20)-C(19B)	136(11)
C(18B)-C(19B)-C(20)-C(21)	-176(2)
C(18B)-C(19B)-C(20)-C(25)	16(4)

C(18B)-C(19B)-C(20)-C(19A)	-26(5)
C(25)-C(20)-C(21)-C(22)	-2(2)
C(19A)-C(20)-C(21)-C(22)	172(3)
C(19B)-C(20)-C(21)-C(22)	-172.2(16)
C(20)-C(21)-C(22)-C(23)	1(2)
C(21)-C(22)-C(23)-C(24)	-1.1(17)
C(21)-C(22)-C(23)-C(26)	178.6(11)
C(22)-C(23)-C(24)-C(25)	2.0(17)
C(26)-C(23)-C(24)-C(25)	-177.5(10)
C(21)-C(20)-C(25)-C(24)	3(2)
C(19A)-C(20)-C(25)-C(24)	-172(2)
C(19B)-C(20)-C(25)-C(24)	170.4(18)
C(23)-C(24)-C(25)-C(20)	-3(2)
C(24)-C(23)-C(26)-O(5)	-174.8(9)
C(22)-C(23)-C(26)-O(5)	5.6(12)
C(24)-C(23)-C(26)-O(6)	5.5(12)
C(22)-C(23)-C(26)-O(6)	-174.1(9)
O(8)-C(27)-C(28)-C(29)	-166.0(6)
O(7)-C(27)-C(28)-C(29)	9.9(10)
Yb(1)-C(27)-C(28)-C(29)	-110.6(15)
O(8)-C(27)-C(28)-C(33)	10.0(9)
O(7)-C(27)-C(28)-C(33)	-174.1(6)
Yb(1)-C(27)-C(28)-C(33)	65.5(18)
C(33)-C(28)-C(29)-C(30)	0
C(27)-C(28)-C(29)-C(30)	176.0(8)
C(28)-C(29)-C(30)-C(31)	0
C(29)-C(30)-C(31)-C(32)	0
C(29)-C(30)-C(31)-C(34)	-172.6(11)
C(30)-C(31)-C(32)-C(33)	0
C(34)-C(31)-C(32)-C(33)	172.3(12)
C(31)-C(32)-C(33)-C(28)	0
C(29)-C(28)-C(33)-C(32)	0
C(27)-C(28)-C(33)-C(32)	-176.1(8)
C(32)-C(31)-C(34)-C(35)	-8(3)
C(30)-C(31)-C(34)-C(35)	165(2)
C(31)-C(34)-C(35)-C(36)	176.5(18)
C(34)-C(35)-C(36)-C(38)	-168(3)
C(34)-C(35)-C(36)-C(37)	11(4)
C(38)-C(36)-C(37)-C(38)#1	-7(5)
C(35)-C(36)-C(37)-C(38)#1	174(2)
C(37)-C(36)-C(38)-O(9)	-178.3(18)
C(35)-C(36)-C(38)-O(9)	0(4)
C(37)-C(36)-C(38)-C(37)#1	7(5)
C(35)-C(36)-C(38)-C(37)#1	-174(2)
C(36)-C(38)-O(9)-C(39)	176(2)

C(37)#1-C(38)-O(9)-C(39)	-9(5)
O(2)-C(1)-O(1)-Yb(1)#2	-16.8(18)
C(2B)-C(1)-O(1)-Yb(1)#2	166.2(11)
C(2A)-C(1)-O(1)-Yb(1)#2	163.5(15)
O(1)-C(1)-O(2)-Yb(2)#3	5.7(13)
C(2B)-C(1)-O(2)-Yb(2)#3	-177.1(8)
C(2A)-C(1)-O(2)-Yb(2)#3	-174.5(14)
O(6)-C(26)-O(5)-Yb(1)	-1.9(14)
C(23)-C(26)-O(5)-Yb(1)	178.4(6)
O(5)-C(26)-O(6)-Yb(2)	29.0(13)
C(23)-C(26)-O(6)-Yb(2)	-151.3(6)
O(8)-C(27)-O(7)-Yb(2)	-116.7(7)
C(28)-C(27)-O(7)-Yb(2)	67.4(10)
Yb(1)-C(27)-O(7)-Yb(2)	-129.2(7)
O(8)-C(27)-O(7)-Yb(1)	12.5(6)
C(28)-C(27)-O(7)-Yb(1)	-163.4(7)
O(7)-C(27)-O(8)-Yb(1)	-14.8(7)
C(28)-C(27)-O(8)-Yb(1)	161.2(6)
C(26)-O(5)-Yb(1)-O(1)#4	-45.2(11)
C(26)-O(5)-Yb(1)-O(1)#5	42.7(9)
C(26)-O(5)-Yb(1)-O(5)#6	-160.2(9)
C(26)-O(5)-Yb(1)-O(8)	-85.0(9)
C(26)-O(5)-Yb(1)-O(8)#6	121.5(9)
C(26)-O(5)-Yb(1)-O(7)	-33.2(8)
C(26)-O(5)-Yb(1)-O(7)#6	117.4(8)
C(26)-O(5)-Yb(1)-C(27)	-59.6(8)
C(26)-O(5)-Yb(1)-C(27)#6	116.3(8)
C(26)-O(5)-Yb(1)-Yb(2)	-8.5(8)
C(26)-O(5)-Yb(1)-Yb(2)#6	147.8(7)
C(27)-O(8)-Yb(1)-O(1)#4	-73.4(5)
C(27)-O(8)-Yb(1)-O(1)#5	4.8(5)
C(27)-O(8)-Yb(1)-O(5)#6	-168.0(5)
C(27)-O(8)-Yb(1)-O(5)	90.4(5)
C(27)-O(8)-Yb(1)-O(8)#6	140.8(5)
C(27)-O(8)-Yb(1)-O(7)	7.8(4)
C(27)-O(8)-Yb(1)-O(7)#6	-121.1(4)
C(27)-O(8)-Yb(1)-C(27)#6	-171.0(5)
C(27)-O(8)-Yb(1)-Yb(2)	26.3(4)
C(27)-O(8)-Yb(1)-Yb(2)#6	-118.1(4)
C(27)-O(7)-Yb(1)-O(1)#4	79.8(4)
Yb(2)-O(7)-Yb(1)-O(1)#4	-133.0(2)
C(27)-O(7)-Yb(1)-O(1)#5	170.1(4)
Yb(2)-O(7)-Yb(1)-O(1)#5	-42.8(2)
C(27)-O(7)-Yb(1)-O(5)#6	-2.3(4)
Yb(2)-O(7)-Yb(1)-O(5)#6	144.8(2)

C(27)-O(7)-Yb(1)-O(5)	-94.9(4)
Yb(2)-O(7)-Yb(1)-O(5)	52.2(2)
C(27)-O(7)-Yb(1)-O(8)	-7.5(4)
Yb(2)-O(7)-Yb(1)-O(8)	139.6(3)
C(27)-O(7)-Yb(1)-O(8)#6	-141.5(4)
Yb(2)-O(7)-Yb(1)-O(8)#6	5.7(4)
C(27)-O(7)-Yb(1)-O(7)#6	125.0(4)
Yb(2)-O(7)-Yb(1)-O(7)#6	-87.90(18)
Yb(2)-O(7)-Yb(1)-C(27)	147.1(5)
C(27)-O(7)-Yb(1)-C(27)#6	171.6(4)
Yb(2)-O(7)-Yb(1)-C(27)#6	-41.2(4)
C(27)-O(7)-Yb(1)-Yb(2)	-147.1(5)
C(27)-O(7)-Yb(1)-Yb(2)#6	84.3(4)
Yb(2)-O(7)-Yb(1)-Yb(2)#6	-128.52(14)
O(8)-C(27)-Yb(1)-O(1)#4	100.7(5)
O(7)-C(27)-Yb(1)-O(1)#4	-93.1(4)
C(28)-C(27)-Yb(1)-O(1)#4	34.8(16)
O(8)-C(27)-Yb(1)-O(1)#5	-176.1(4)
O(7)-C(27)-Yb(1)-O(1)#5	-9.9(4)
C(28)-C(27)-Yb(1)-O(1)#5	118.0(16)
O(8)-C(27)-Yb(1)-O(5)#6	11.9(5)
O(7)-C(27)-Yb(1)-O(5)#6	178.1(4)
C(28)-C(27)-Yb(1)-O(5)#6	-53.9(16)
O(8)-C(27)-Yb(1)-O(5)	-85.7(5)
O(7)-C(27)-Yb(1)-O(5)	80.5(4)
C(28)-C(27)-Yb(1)-O(5)	-151.6(16)
O(7)-C(27)-Yb(1)-O(8)	166.2(7)
C(28)-C(27)-Yb(1)-O(8)	-65.9(16)
O(8)-C(27)-Yb(1)-O(8)#6	-82.7(9)
O(7)-C(27)-Yb(1)-O(8)#6	83.5(7)
C(28)-C(27)-Yb(1)-O(8)#6	-148.6(14)
O(8)-C(27)-Yb(1)-O(7)	-166.2(7)
C(28)-C(27)-Yb(1)-O(7)	127.9(18)
O(8)-C(27)-Yb(1)-O(7)#6	99.1(5)
O(7)-C(27)-Yb(1)-O(7)#6	-94.7(6)
C(28)-C(27)-Yb(1)-O(7)#6	33.2(18)
O(8)-C(27)-Yb(1)-Yb(2)	-147.3(5)
O(7)-C(27)-Yb(1)-Yb(2)	18.9(3)
C(28)-C(27)-Yb(1)-Yb(2)	146.9(17)
O(8)-C(27)-Yb(1)-Yb(2)#6	76.6(5)
O(7)-C(27)-Yb(1)-Yb(2)#6	-117.3(3)
C(28)-C(27)-Yb(1)-Yb(2)#6	10.7(17)
C(26)-O(6)-Yb(2)-O(2)#7	92.4(8)
C(26)-O(6)-Yb(2)-O(2)#5	-87.6(8)
C(26)-O(6)-Yb(2)-O(7)	2.2(8)

C(26)-O(6)-Yb(2)-O(7)#8	-177.8(8)
C(26)-O(6)-Yb(2)-Yb(1)#8	155.9(7)
C(26)-O(6)-Yb(2)-Yb(1)	-24.1(7)
C(27)-O(7)-Yb(2)-O(2)#7	-11.7(7)
Yb(1)-O(7)-Yb(2)-O(2)#7	-131.5(2)
C(27)-O(7)-Yb(2)-O(2)#5	168.3(7)
Yb(1)-O(7)-Yb(2)-O(2)#5	48.5(2)
C(27)-O(7)-Yb(2)-O(6)#8	-104.0(7)
Yb(1)-O(7)-Yb(2)-O(6)#8	136.2(2)
C(27)-O(7)-Yb(2)-O(6)	76.0(7)
Yb(1)-O(7)-Yb(2)-O(6)	-43.8(2)
C(27)-O(7)-Yb(2)-Yb(1)#8	-60.2(8)
Yb(1)-O(7)-Yb(2)-Yb(1)#8	180
C(27)-O(7)-Yb(2)-Yb(1)	119.8(8)
O(1)#4-Yb(1)-Yb(2)-O(2)#7	99.7(2)
O(1)#5-Yb(1)-Yb(2)-O(2)#7	-177.6(2)
O(5)#6-Yb(1)-Yb(2)-O(2)#7	-4.2(3)
O(5)-Yb(1)-Yb(2)-O(2)#7	-65.3(2)
O(8)-Yb(1)-Yb(2)-O(2)#7	22.5(2)
O(8)#6-Yb(1)-Yb(2)-O(2)#7	-122.3(2)
O(7)-Yb(1)-Yb(2)-O(2)#7	54.1(3)
O(7)#6-Yb(1)-Yb(2)-O(2)#7	177.2(2)
C(27)-Yb(1)-Yb(2)-O(2)#7	36.3(3)
C(27)#6-Yb(1)-Yb(2)-O(2)#7	-149.9(3)
Yb(2)#6-Yb(1)-Yb(2)-O(2)#7	136.89(18)
O(1)#4-Yb(1)-Yb(2)-O(2)#5	-80.3(2)
O(1)#5-Yb(1)-Yb(2)-O(2)#5	2.4(2)
O(5)#6-Yb(1)-Yb(2)-O(2)#5	175.8(3)
O(5)-Yb(1)-Yb(2)-O(2)#5	114.7(2)
O(8)-Yb(1)-Yb(2)-O(2)#5	-157.5(2)
O(8)#6-Yb(1)-Yb(2)-O(2)#5	57.7(2)
O(7)-Yb(1)-Yb(2)-O(2)#5	-125.9(3)
O(7)#6-Yb(1)-Yb(2)-O(2)#5	-2.8(2)
C(27)-Yb(1)-Yb(2)-O(2)#5	-143.7(3)
C(27)#6-Yb(1)-Yb(2)-O(2)#5	30.1(3)
Yb(2)#6-Yb(1)-Yb(2)-O(2)#5	-43.11(18)
O(1)#4-Yb(1)-Yb(2)-O(6)#8	-5.1(2)
O(1)#5-Yb(1)-Yb(2)-O(6)#8	77.5(2)
O(5)#6-Yb(1)-Yb(2)-O(6)#8	-109.1(3)
O(5)-Yb(1)-Yb(2)-O(6)#8	-170.2(2)
O(8)-Yb(1)-Yb(2)-O(6)#8	-82.4(2)
O(8)#6-Yb(1)-Yb(2)-O(6)#8	132.8(2)
O(7)-Yb(1)-Yb(2)-O(6)#8	-50.8(3)
O(7)#6-Yb(1)-Yb(2)-O(6)#8	72.3(2)
C(27)-Yb(1)-Yb(2)-O(6)#8	-68.6(2)

C(27)#6-Yb(1)-Yb(2)-O(6)#8	105.2(2)
Yb(2)#6-Yb(1)-Yb(2)-O(6)#8	32.01(16)
O(1)#4-Yb(1)-Yb(2)-O(6)	174.9(2)
O(1)#5-Yb(1)-Yb(2)-O(6)	-102.5(2)
O(5)#6-Yb(1)-Yb(2)-O(6)	70.9(3)
O(5)-Yb(1)-Yb(2)-O(6)	9.8(2)
O(8)-Yb(1)-Yb(2)-O(6)	97.6(2)
O(8)#6-Yb(1)-Yb(2)-O(6)	-47.2(2)
O(7)-Yb(1)-Yb(2)-O(6)	129.2(3)
O(7)#6-Yb(1)-Yb(2)-O(6)	-107.7(2)
C(27)-Yb(1)-Yb(2)-O(6)	111.4(2)
C(27)#6-Yb(1)-Yb(2)-O(6)	-74.8(2)
Yb(2)#6-Yb(1)-Yb(2)-O(6)	-147.99(16)
O(1)#4-Yb(1)-Yb(2)-O(7)	45.7(2)
O(1)#5-Yb(1)-Yb(2)-O(7)	128.3(3)
O(5)#6-Yb(1)-Yb(2)-O(7)	-58.3(3)
O(5)-Yb(1)-Yb(2)-O(7)	-119.4(3)
O(8)-Yb(1)-Yb(2)-O(7)	-31.5(2)
O(8)#6-Yb(1)-Yb(2)-O(7)	-176.4(3)
O(7)#6-Yb(1)-Yb(2)-O(7)	123.1(3)
C(27)-Yb(1)-Yb(2)-O(7)	-17.7(3)
C(27)#6-Yb(1)-Yb(2)-O(7)	156.1(3)
Yb(2)#6-Yb(1)-Yb(2)-O(7)	82.8(2)
O(1)#4-Yb(1)-Yb(2)-O(7)#8	-134.3(2)
O(1)#5-Yb(1)-Yb(2)-O(7)#8	-51.7(3)
O(5)#6-Yb(1)-Yb(2)-O(7)#8	121.7(3)
O(5)-Yb(1)-Yb(2)-O(7)#8	60.6(3)
O(8)-Yb(1)-Yb(2)-O(7)#8	148.5(2)
O(8)#6-Yb(1)-Yb(2)-O(7)#8	3.6(3)
O(7)-Yb(1)-Yb(2)-O(7)#8	180
O(7)#6-Yb(1)-Yb(2)-O(7)#8	-56.9(3)
C(27)-Yb(1)-Yb(2)-O(7)#8	162.3(3)
C(27)#6-Yb(1)-Yb(2)-O(7)#8	-23.9(3)
Yb(2)#6-Yb(1)-Yb(2)-O(7)#8	-97.2(2)

Symmetry transformations used to generate equivalent atoms:

#1 -x+1,-y+2,-z+1; #2 x-1/2,-y+1/2,z-1/2; #3 -x+1/2,y-1/2,-z+1/2; #4 -x+1,y+1/2,z+1/2

#5 x+1/2,-y+1/2,z+1/2; #6 -x+3/2,-y+1,z; #7 -x+1/2,y+1/2,-z+1/2; #8 -x+1,-y+1,-z+1

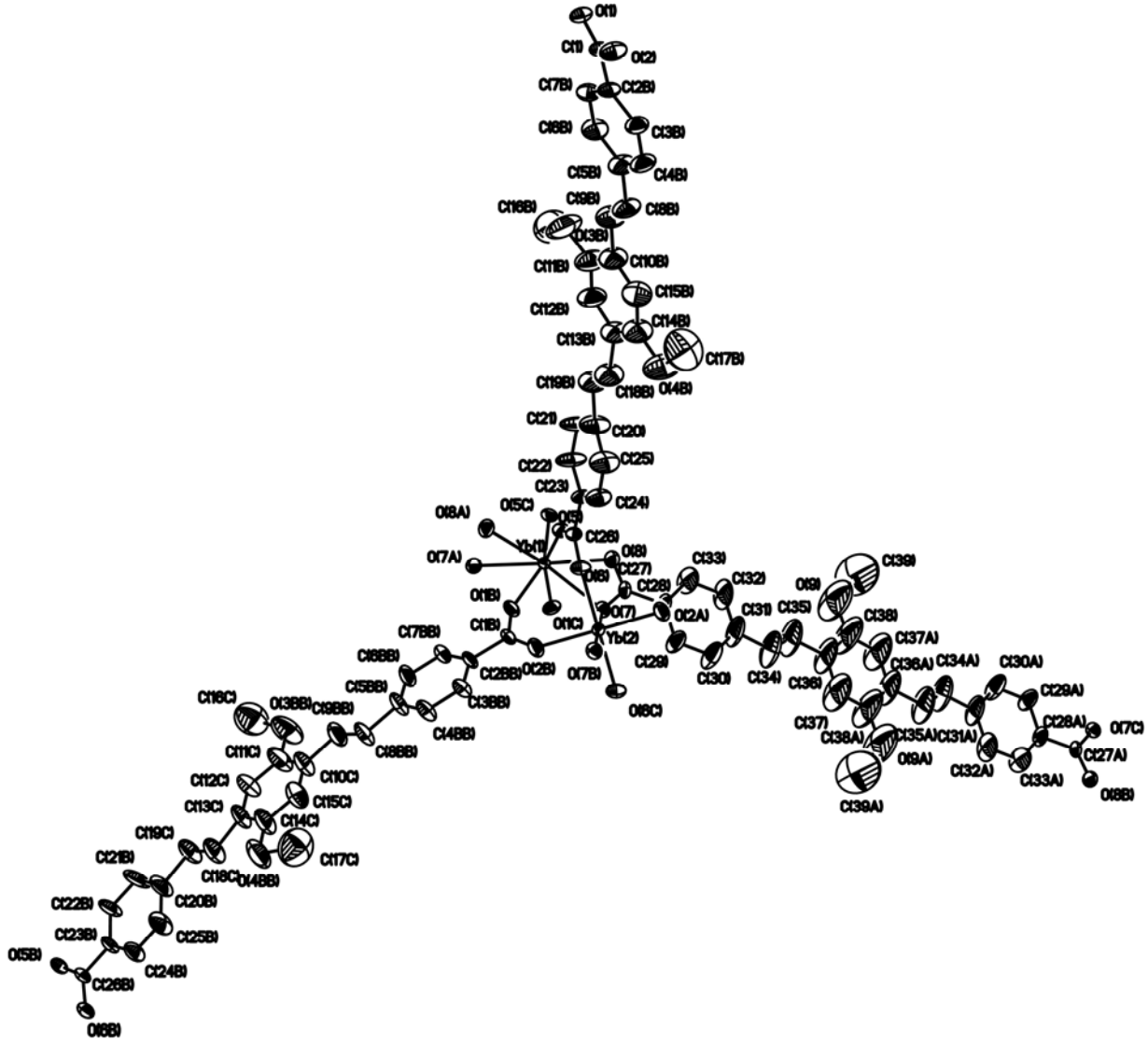

Figure AA 3. The building unit and asymmetric unit present in crystalline Yb-PVDC-2 with all atoms represented by thermal ellipsoids drawn at the 30% probability level. All hydrogen atoms were omitted for clarity.

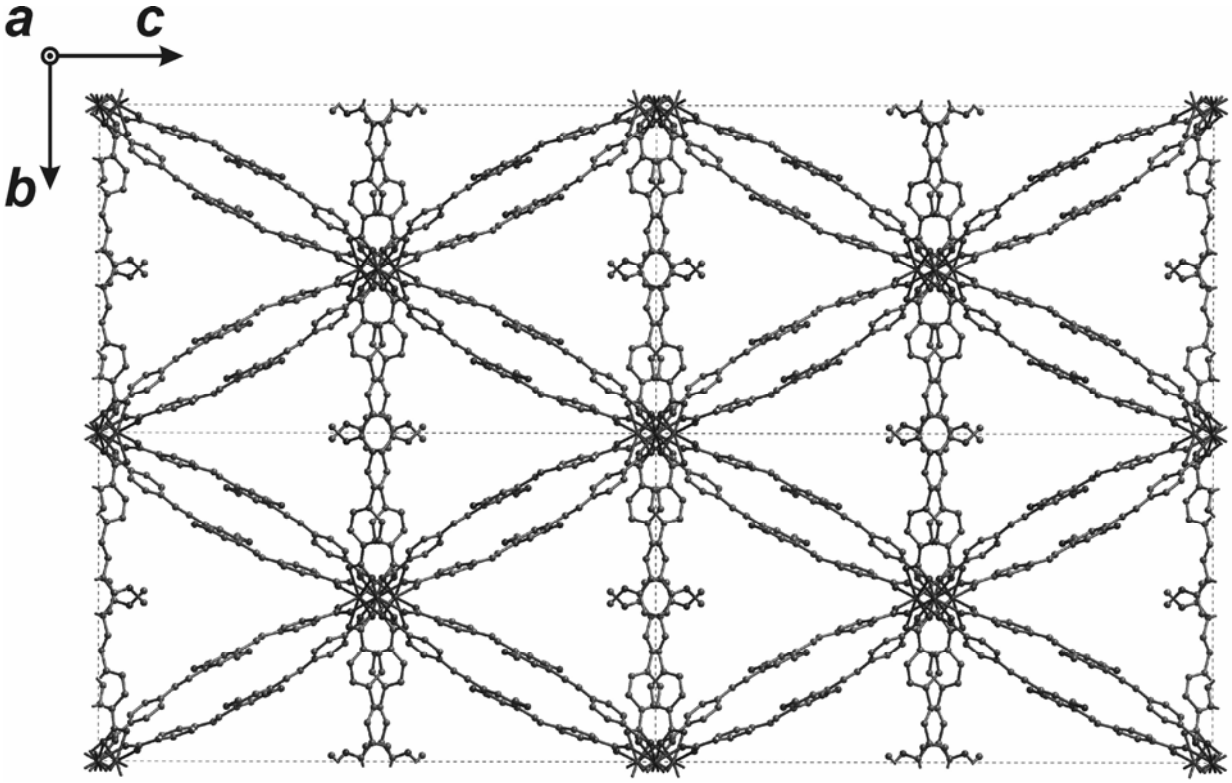

Figure AA 4. Unit cell packing for Yb-PVDC-2.

Table AA 12. Crystal data and structure refinement for Zn-PVDC-1.

Identification code	Zn-PVDC-1	
Empirical formula	$C_{156}H_{120}O_{38}Zn_8$	
Formula weight	3125.65	
Temperature	526(2) K	
Wavelength	0.71073 Å	
Crystal system, space group	Monoclinic, P2/c	
Unit cell dimensions	a = 25.954(8) Å	α = 90 º.
	b = 36.012(11) Å	β = 123.747(3) º
	c = 44.264(13) Å	γ = 90 º
Volume	34401(17) Å^3	
Z, Calculated density	4, 0.604 Mg/m^3	
Absorption coefficient	0.581 mm^-1	
F(000)	22360	
Crystal size	? x ? x ? mm	
Theta range for data collection	5.73 to 26.02 deg.	
Limiting indices	-31<=h<=32, -44<=k<=44, -53<=l<=54	

Reflections collected / unique	221229 / 66769 [R(int) = 0.2036]
Completeness to theta = 26.02	98.50%
Absorption correction	Semi-empirical from equivalents
Max. and min. transmission	0.8621 and 0.6904
Refinement method	Full-matrix least-squares on F^2
Data / restraints / parameters	66769 / 3162 / 1603
Goodness-of-fit on F^2	0.949
Final R indices [I>2sigma(I)]	R1 = 0.1169, wR2 = 0.2952
R indices (all data)	R1 = 0.3078, wR2 = 0.4035
Largest diff. peak and hole	1.816 and -0.466 e.A^-3

Table AA 13. Atomic coordinates (x 10^4) and equivalent isotropic displacement parameters (Å^2 x 10^3) for Zn-PVDC-1. U(eq) is defined as one third of the trace of the orthogonalized U^{ij} tensor.

	x	y	z	U(eq)
C(1)	10471(6)	7701(3)	8707(3)	87(3)
C(2)	10143(4)	7430(2)	8410(2)	109(4)
C(3)	10466(3)	7123(2)	8406(2)	135(5)
C(4)	10167(4)	6864(2)	8128(3)	136(5)
C(5)	9545(4)	6910(3)	7854(3)	161(6)
C(6)	9222(3)	7216(3)	7857(3)	215(9)
C(7)	9521(4)	7476(3)	8135(3)	198(8)
C(8)	9220(6)	6623(4)	7568(4)	171(7)
C(9)	8654(6)	6611(4)	7309(4)	155(6)
C(10)	8346(4)	6321(3)	7024(2)	141(5)
C(11)	8690(3)	6078(3)	6959(3)	182(7)
C(12)	8395(4)	5800(3)	6701(3)	180(7)
C(13)	7754(4)	5764(2)	6506(2)	128(4)
C(14)	7409(3)	6007(3)	6570(2)	120(4)
C(15)	7705(4)	6286(2)	6829(3)	130(5)
C(16)	6730(5)	6569(5)	6658(6)	241(11)
C(17)	9326(10)	5655(9)	6717(10)	350(18)
C(18)	7467(6)	5452(3)	6244(3)	127(5)
C(19)	6889(6)	5392(3)	6027(3)	114(4)
C(20)	6593(3)	5078(2)	5769(2)	109(4)
C(21)	5952(3)	5044(2)	5556(2)	107(4)
C(22)	5676(3)	4755(2)	5307(2)	104(4)
C(23)	6041(4)	4500(2)	5272(2)	104(4)
C(24)	6683(3)	4534(2)	5485(3)	175(7)
C(25)	6959(3)	4823(3)	5734(3)	185(8)
C(26)	5728(6)	4196(3)	5001(3)	93(3)
C(27)	12479(4)	8381(3)	9333(2)	67(2)

C(28)	13057(3)	8363(2)	9335(2)	76(3)
C(29)	13300(3)	8019(2)	9337(2)	102(4)
C(30)	13834(3)	7997(2)	9336(2)	116(4)
C(31)	14126(3)	8320(2)	9334(3)	100(4)
C(32)	13883(3)	8665(2)	9333(3)	145(5)
C(33)	13348(3)	8686(1)	9333(3)	129(5)
C(34)	14701(5)	8286(3)	9343(4)	116(4)
C(35)	15069(6)	8542(4)	9394(5)	160(6)
C(36)	15665(4)	8507(3)	9423(3)	152(6)
C(37)	15759(4)	8201(2)	9268(3)	137(5)
C(38)	16287(4)	8180(2)	9260(3)	138(5)
C(39)	16720(4)	8466(3)	9408(4)	152(6)
C(40)	16626(5)	8772(3)	9562(4)	226(10)
C(41)	16098(5)	8792(2)	9570(4)	242(10)
C(44)	17254(6)	8449(4)	9367(5)	158(6)
C(45)	17747(7)	8622(5)	9546(6)	218(9)
C(42)	16089(11)	7538(5)	9068(8)	284(13)
C(43)	16545(13)	9298(9)	10013(10)	374(19)
C(46)	18275(4)	8600(3)	9498(4)	158(6)
C(47)	18190(3)	8529(3)	9164(3)	171(7)
C(48)	18701(5)	8496(3)	9141(3)	174(7)
C(49)	19296(4)	8535(3)	9451(3)	121(5)
C(50)	19380(4)	8607(3)	9784(3)	183(7)
C(51)	18869(6)	8639(4)	9808(3)	202(8)
C(52)	19857(7)	8508(3)	9434(5)	102(4)
C(53)	11816(6)	9214(4)	9956(5)	139(6)
C(54)	12049(5)	9509(3)	10229(3)	151(6)
C(55)	12381(6)	9795(3)	10201(3)	189(7)
C(56)	12612(6)	10084(3)	10451(4)	220(9)
C(57)	12512(6)	10088(3)	10728(3)	167(7)
C(58)	12180(6)	9803(4)	10756(3)	210(9)
C(59)	11948(5)	9513(3)	10506(3)	185(7)
C(60)	12760(8)	10407(5)	10986(5)	209(9)
C(61)	12658(8)	10493(5)	11213(4)	192(8)
C(62)	12908(7)	10788(3)	11489(3)	191(7)
C(63)	13417(7)	10997(4)	11565(4)	205(8)
C(64)	13659(6)	11266(4)	11835(4)	211(9)
C(65)	13391(7)	11327(4)	12030(3)	205(8)
C(66)	12881(7)	11118(4)	11953(4)	232(10)
C(67)	12640(7)	10849(4)	11683(4)	212(8)
C(68)	14440(14)	11407(10)	11714(9)	341(18)
C(69)	11764(15)	10795(9)	11742(9)	337(17)
C(70)	13656(8)	11611(5)	12324(4)	209(9)
C(71)	13558(8)	11652(4)	12566(4)	184(7)
C(72)	13811(5)	11946(3)	12844(2)	136(5)

C(73)	14137(5)	12250(3)	12841(2)	150(5)
C(74)	14371(4)	12513(2)	13116(3)	133(5)
C(75)	14279(4)	12471(2)	13396(2)	89(3)
C(76)	13954(4)	12167(3)	13399(2)	130(5)
C(77)	13719(4)	11904(2)	13123(3)	154(6)
C(78)	14525(4)	12753(3)	13689(3)	71(3)
C(79)	5850(9)	2636(5)	4948(5)	143(6)
C(80)	6231(7)	2369(4)	5248(4)	185(7)
C(81)	5947(6)	2053(4)	5271(4)	198(8)
C(82)	6302(8)	1779(4)	5524(5)	270(13)
C(83)	6940(8)	1822(5)	5756(5)	341(17)
C(84)	7224(6)	2138(6)	5733(6)	450(20)
C(85)	6869(7)	2412(5)	5479(6)	386(19)
C(86)	7423(12)	1581(9)	6055(9)	349(19)
C(87)	7324(12)	1307(8)	6157(7)	298(14)
C(88)	7801(10)	1079(5)	6472(5)	290(13)
C(89)	7516(8)	804(6)	6550(6)	323(15)
C(90)	7874(11)	548(5)	6825(6)	341(16)
C(91)	8517(10)	569(5)	7022(5)	272(12)
C(92)	8802(8)	844(6)	6944(6)	306(14)
C(93)	8444(10)	1099(5)	6669(6)	333(16)
C(94)	9550(30)	1180(20)	6850(20)	640(50)
C(95)	6620(30)	494(19)	6527(18)	590(40)
C(96)	8807(14)	250(7)	7290(7)	283(13)
C(97)	9255(15)	240(6)	7572(7)	316(16)
C(98)	9475(7)	-106(4)	7801(3)	246(11)
C(99)	9165(5)	-402(5)	7834(4)	279(12)
C(100)	9488(6)	-653(4)	8118(4)	232(10)
C(101)	10121(6)	-609(3)	8369(3)	156(6)
C(102)	10431(5)	-313(4)	8336(3)	199(8)
C(103)	10108(7)	-62(3)	8052(4)	215(9)
C(104)	10442(9)	-862(5)	8673(5)	155(7)
C(105)	4491(5)	4142(3)	3721(3)	88(3)
C(106)	4254(5)	4459(3)	3455(3)	123(4)
C(107)	4313(6)	4432(3)	3162(3)	192(8)
C(108)	4102(8)	4719(4)	2909(3)	239(10)
C(109)	3833(7)	5032(3)	2950(3)	209(9)
C(110)	3774(6)	5059(3)	3243(4)	202(8)
C(111)	3985(6)	4772(3)	3495(3)	155(6)
C(112)	3609(14)	5357(6)	2692(7)	290(13)
C(113)	3643(16)	5385(6)	2430(7)	332(16)
C(114)	3457(13)	5729(6)	2205(6)	346(15)
C(115)	3145(13)	6036(7)	2218(5)	394(19)
C(116)	2912(10)	6303(5)	1947(6)	344(15)
C(117)	2990(11)	6264(5)	1662(5)	305(14)

C(118)	3301(13)	5957(6)	1649(5)	373(17)
C(119)	3535(12)	5689(5)	1920(7)	410(18)
C(120)	4491(19)	5350(20)	2140(30)	710(50)
C(121)	2500(30)	6594(16)	2259(15)	540(30)
C(122)	2736(17)	6588(7)	1406(8)	317(15)
C(123)	2777(15)	6634(7)	1153(7)	292(13)
C(124)	2494(7)	6930(4)	871(3)	222(9)
C(125)	2205(7)	7247(4)	887(3)	221(9)
C(126)	1977(6)	7512(3)	614(3)	192(8)
C(127)	2039(6)	7460(3)	324(3)	137(5)
C(128)	2328(6)	7143(3)	308(3)	176(7)
C(129)	2556(7)	6878(3)	582(4)	229(9)
Zn(1)	11526(1)	7992(1)	9351(1)	51(1)
C(130)	1764(5)	7731(3)	23(4)	93(3)
C(131)	3828(4)	3364(3)	4384(2)	60(2)
C(132)	3240(3)	3338(2)	4373(2)	71(3)
C(133)	2873(3)	3650(2)	4298(2)	119(4)
C(134)	2327(3)	3623(2)	4285(3)	135(5)
C(135)	2147(3)	3283(2)	4347(2)	93(3)
C(136)	2514(3)	2971(2)	4421(2)	113(4)
C(137)	3060(3)	2998(2)	4434(2)	103(4)
C(138)	1575(5)	3242(3)	4346(3)	110(4)
C(139)	1195(7)	3494(4)	4284(6)	184(8)
C(140)	595(5)	3458(4)	4249(5)	205(8)
C(141)	458(5)	3131(3)	4357(4)	180(7)
C(142)	-67(6)	3110(3)	4367(4)	209(8)
C(143)	-454(6)	3416(4)	4270(6)	236(10)
C(144)	-317(7)	3744(4)	4162(6)	337(15)
C(145)	208(7)	3765(3)	4152(6)	336(14)
C(147)	20(20)	4378(11)	4034(19)	570(30)
C(146)	101(17)	2481(8)	4538(13)	420(20)
C(148)	-978(9)	3401(6)	4323(8)	257(11)
C(149)	-1415(12)	3596(8)	4208(11)	354(15)
C(150)	-1909(6)	3530(5)	4271(6)	316(14)
C(151)	-1841(5)	3498(5)	4605(5)	292(13)
C(152)	-2361(7)	3476(5)	4619(4)	265(12)
C(153)	-2950(5)	3487(4)	4301(5)	179(7)
C(154)	-3018(6)	3519(5)	3967(4)	299(13)
C(155)	-2498(8)	3540(6)	3953(5)	359(16)
C(156)	-3492(10)	3453(5)	4340(9)	159(8)
Zn(2)	10279(1)	8436(1)	8944(1)	80(1)
O(1)	11132(2)	8445(1)	9349(1)	47(1)
O(2)	5201(2)	3435(1)	4394(1)	50(1)
O(3)	11029(3)	7659(2)	8943(2)	81(2)
O(4)	10140(3)	7963(3)	8706(2)	138(3)

O(5)	7400(4)	6561(3)	6888(3)	173(4)
O(6)	8691(6)	5578(4)	6602(4)	256(8)
O(7)	6079(4)	3977(3)	4982(3)	171(5)
O(8)	5164(3)	4196(2)	4799(2)	78(2)
O(9)	12263(3)	8702(2)	9314(2)	86(2)
O(10)	12256(3)	8080(2)	9343(2)	76(2)
O(11)	16039(8)	9042(4)	9786(6)	325(11)
O(12)	16443(5)	7881(3)	9147(4)	199(5)
O(13)	20369(4)	8521(2)	9718(3)	114(3)
O(14)	19723(3)	8450(2)	9106(3)	113(3)
O(15)	11893(4)	9212(2)	9710(2)	117(3)
O(16)	11491(5)	8962(3)	9997(3)	173(5)
O(17)	12070(8)	10680(5)	11558(5)	286(9)
O(18)	14130(7)	11497(4)	11897(4)	250(7)
O(19)	14781(4)	13034(2)	13655(2)	99(2)
O(20)	14487(3)	12696(2)	13948(2)	80(2)
O(21)	5301(4)	2611(2)	4758(2)	100(2)
O(22)	6151(5)	2890(3)	4910(4)	204(6)
O(23)	6869(14)	780(9)	6401(9)	434(16)
O(24)	9473(15)	876(11)	7045(10)	489(19)
O(27)	4412(3)	4176(2)	3977(2)	76(2)
O(28)	4745(4)	3877(2)	3671(2)	110(3)
O(29)	3821(17)	5405(8)	1911(10)	540(20)
O(30)	2623(15)	6589(7)	1971(7)	468(18)
O(31)	10115(6)	-1120(4)	8685(3)	205(6)
O(32)	11025(5)	-825(2)	8878(3)	133(3)
O(33)	-3415(4)	3479(3)	4649(4)	153(4)
O(34)	-4012(6)	3469(3)	4022(4)	156(4)
O(35)	3990(2)	3684(2)	4357(2)	69(2)
O(36)	4099(3)	3070(2)	4409(2)	76(2)
O(37)	334(10)	4043(7)	4013(9)	507(18)
O(38)	-266(7)	2824(4)	4442(6)	286(9)
O(39)	1815(3)	7677(2)	-233(2)	83(2)
O(40)	1520(4)	8019(3)	59(2)	126(3)
Zn(3)	11177(1)	8479(1)	9806(1)	78(1)
Zn(4)	11548(1)	8865(1)	9311(1)	56(1)
Zn(5)	6061(1)	3450(1)	4834(1)	83(1)
Zn(6)	4746(1)	3850(1)	4400(1)	49(1)
Zn(7)	5214(1)	3454(1)	3963(1)	69(1)
Zn(8)	4826(1)	2980(1)	4401(1)	52(1)

Table AA 14. Bond lengths (Å) and angles (º) for Zn-PVDC-1.

C(1)-O(3)	1.237(11)
C(1)-O(4)	1.275(11)
C(1)-C(2)	1.471(11)
C(2)-C(3)	1.39
C(2)-C(7)	1.39
C(3)-C(4)	1.39
C(3)-H(3A)	0.93
C(4)-C(5)	1.39
C(4)-H(4A)	0.93
C(5)-C(6)	1.39
C(5)-C(8)	1.482(10)
C(6)-C(7)	1.39
C(6)-H(6A)	0.93
C(7)-H(7A)	0.93
C(8)-C(9)	1.266(12)
C(8)-H(8A)	0.93
C(9)-C(10)	1.483(10)
C(9)-H(9A)	0.93
C(10)-C(11)	1.39
C(10)-C(15)	1.39
C(11)-C(12)	1.39
C(11)-H(11A)	0.93
C(12)-O(6)	1.338(12)
C(12)-C(13)	1.39
C(13)-C(14)	1.39
C(13)-C(18)	1.484(9)
C(14)-C(15)	1.39
C(14)-H(14A)	0.93
C(15)-O(5)	1.381(10)
C(16)-O(5)	1.447(11)
C(16)-H(16A)	0.96
C(16)-H(16B)	0.96
C(16)-H(16C)	0.96
C(17)-O(6)	1.457(13)
C(17)-H(17A)	0.96
C(17)-H(17B)	0.96
C(17)-H(17C)	0.96
C(18)-C(19)	1.271(11)
C(18)-H(18A)	0.93
C(19)-C(20)	1.483(9)
C(19)-H(19A)	0.93
C(20)-C(21)	1.39
C(20)-C(25)	1.39
C(21)-C(22)	1.39

C(21)-H(21A)	0.93
C(22)-C(23)	1.39
C(22)-H(22A)	0.93
C(23)-C(24)	1.39
C(23)-C(26)	1.489(11)
C(24)-C(25)	1.39
C(24)-H(24A)	0.93
C(25)-H(25A)	0.93
C(26)-O(8)	1.220(11)
C(26)-O(7)	1.241(11)
C(27)-O(10)	1.240(10)
C(27)-O(9)	1.266(10)
C(27)-C(28)	1.496(9)
C(28)-C(29)	1.39
C(28)-C(33)	1.39
C(29)-C(30)	1.39
C(29)-H(29A)	0.93
C(30)-C(31)	1.39
C(30)-H(30A)	0.93
C(31)-C(32)	1.39
C(31)-C(34)	1.477(9)
C(32)-C(33)	1.39
C(32)-H(32A)	0.93
C(33)-H(33A)	0.93
C(34)-C(35)	1.256(11)
C(34)-H(34A)	0.93
C(35)-C(36)	1.484(10)
C(35)-H(35A)	0.93
C(36)-C(37)	1.39
C(36)-C(41)	1.39
C(37)-C(38)	1.39
C(37)-H(37A)	0.93
C(38)-O(12)	1.343(11)
C(38)-C(39)	1.39
C(39)-C(40)	1.39
C(39)-C(44)	1.497(10)
C(40)-C(41)	1.39
C(40)-H(40A)	0.93
C(41)-O(11)	1.382(15)
C(44)-C(45)	1.235(13)
C(44)-H(44A)	0.93
C(45)-C(46)	1.500(11)
C(45)-H(45A)	0.93
C(42)-O(12)	1.463(12)
C(42)-H(42A)	0.96

C(42)-H(42B)	0.96
C(42)-H(42C)	0.96
C(43)-O(11)	1.453(14)
C(43)-H(43A)	0.96
C(43)-H(43B)	0.96
C(43)-H(43C)	0.96
C(46)-C(47)	1.39
C(46)-C(51)	1.39
C(47)-C(48)	1.39
C(47)-H(47A)	0.93
C(48)-C(49)	1.39
C(48)-H(48A)	0.93
C(49)-C(50)	1.39
C(49)-C(52)	1.504(13)
C(50)-C(51)	1.39
C(50)-H(50A)	0.93
C(51)-H(51A)	0.93
C(52)-O(13)	1.220(15)
C(52)-O(14)	1.310(15)
C(53)-O(15)	1.207(17)
C(53)-O(16)	1.321(17)
C(53)-C(54)	1.462(14)
C(54)-C(55)	1.39
C(54)-C(59)	1.39
C(55)-C(56)	1.39
C(55)-H(55A)	0.93
C(56)-C(57)	1.39
C(56)-H(56A)	0.93
C(57)-C(58)	1.39
C(57)-C(60)	1.491(11)
C(58)-C(59)	1.39
C(58)-H(58A)	0.93
C(59)-H(59A)	0.93
C(60)-C(61)	1.212(13)
C(60)-H(60A)	0.93
C(61)-C(62)	1.471(11)
C(61)-H(61A)	0.93
C(62)-C(63)	1.39
C(62)-C(67)	1.39
C(63)-C(64)	1.39
C(63)-H(63A)	0.93
C(64)-O(18)	1.375(18)
C(64)-C(65)	1.39
C(65)-C(66)	1.39
C(65)-C(70)	1.493(11)

C(66)-C(67)	1.39
C(66)-H(66A)	0.93
C(67)-O(17)	1.398(17)
C(68)-O(18)	1.461(14)
C(68)-H(68A)	0.96
C(68)-H(68B)	0.96
C(68)-H(68C)	0.96
C(69)-O(17)	1.479(14)
C(69)-H(69A)	0.96
C(69)-H(69B)	0.96
C(69)-H(69C)	0.96
C(70)-C(71)	1.238(13)
C(70)-H(70A)	0.93
C(71)-C(72)	1.471(11)
C(71)-H(71A)	0.93
C(72)-C(73)	1.39
C(72)-C(77)	1.39
C(73)-C(74)	1.39
C(73)-H(73A)	0.93
C(74)-C(75)	1.39
C(74)-H(74A)	0.93
C(75)-C(76)	1.39
C(75)-C(78)	1.483(11)
C(76)-C(77)	1.39
C(76)-H(76A)	0.93
C(77)-H(77A)	0.93
C(78)-O(20)	1.223(11)
C(78)-O(19)	1.264(11)
C(79)-O(21)	1.188(16)
C(79)-O(22)	1.272(16)
C(79)-C(80)	1.486(16)
C(80)-C(81)	1.39
C(80)-C(85)	1.39
C(81)-C(82)	1.39
C(81)-H(81A)	0.93
C(82)-C(83)	1.39
C(82)-H(82A)	0.93
C(83)-C(84)	1.39
C(83)-C(86)	1.493(14)
C(84)-C(85)	1.39
C(84)-H(84A)	0.93
C(85)-H(85A)	0.93
C(86)-C(87)	1.170(14)
C(86)-H(86A)	0.93
C(87)-C(88)	1.495(14)

C(87)-H(87A)	0.93
C(88)-C(89)	1.39
C(88)-C(93)	1.39
C(89)-C(90)	1.39
C(89)-O(23)	1.43(3)
C(90)-C(91)	1.39
C(90)-H(90A)	0.93
C(91)-C(92)	1.39
C(91)-C(96)	1.515(14)
C(92)-C(93)	1.39
C(92)-O(24)	1.54(4)
C(93)-H(93A)	0.93
C(94)-O(24)	1.480(16)
C(94)-H(94A)	0.96
C(94)-H(94B)	0.96
C(94)-H(94C)	0.96
C(95)-O(23)	1.478(16)
C(95)-H(95A)	0.96
C(95)-H(95B)	0.96
C(95)-H(95C)	0.96
C(96)-C(97)	1.142(14)
C(96)-H(96A)	0.93
C(97)-C(98)	1.502(14)
C(97)-H(97A)	0.93
C(98)-C(99)	1.39
C(98)-C(103)	1.39
C(99)-C(100)	1.39
C(99)-H(99A)	0.93
C(100)-C(101)	1.39
C(100)-H(10A)	0.93
C(101)-C(102)	1.39
C(101)-C(104)	1.444(17)
C(102)-C(103)	1.39
C(102)-H(10B)	0.93
C(103)-H(10C)	0.93
C(104)-O(32)	1.267(17)
C(104)-O(31)	1.282(17)
C(105)-O(28)	1.250(13)
C(105)-O(27)	1.262(13)
C(105)-C(106)	1.505(12)
C(106)-C(107)	1.39
C(106)-C(111)	1.39
C(107)-C(108)	1.39
C(107)-H(10D)	0.93
C(108)-C(109)	1.39

C(108)-H(10E)	0.93
C(109)-C(110)	1.39
C(109)-C(112)	1.509(13)
C(110)-C(111)	1.39
C(110)-H(11B)	0.93
C(111)-H(11C)	0.93
C(112)-C(113)	1.213(14)
C(112)-H(11D)	0.93
C(113)-C(114)	1.490(13)
C(113)-H(11E)	0.93
C(114)-C(115)	1.39
C(114)-C(119)	1.39
C(115)-C(116)	1.39
C(115)-H(11F)	0.93
C(116)-O(30)	1.31(3)
C(116)-C(117)	1.39
C(117)-C(118)	1.39
C(117)-C(122)	1.500(14)
C(118)-C(119)	1.39
C(118)-H(11G)	0.93
C(119)-O(29)	1.28(3)
C(120)-O(29)	1.461(16)
C(120)-H(12A)	0.96
C(120)-H(12B)	0.96
C(120)-H(12C)	0.96
C(121)-O(30)	1.483(15)
C(121)-H(12D)	0.96
C(121)-H(12E)	0.96
C(121)-H(12F)	0.96
C(122)-C(123)	1.192(14)
C(122)-H(12G)	0.93
C(123)-C(124)	1.488(13)
C(123)-H(12H)	0.93
C(124)-C(125)	1.39
C(124)-C(129)	1.39
C(125)-C(126)	1.39
C(125)-H(12I)	0.93
C(126)-C(127)	1.39
C(126)-H(12J)	0.93
C(127)-C(128)	1.39
C(127)-C(130)	1.476(13)
C(128)-C(129)	1.39
C(128)-H(12K)	0.93
C(129)-H(12L)	0.93
Zn(1)-O(1)	1.922(4)

Zn(1)-O(39)#1	1.924(6)
Zn(1)-O(10)	1.942(6)
Zn(1)-O(3)	1.944(6)
Zn(1)-Zn(2)	3.1283(15)
Zn(1)-Zn(4)	3.1516(16)
Zn(1)-Zn(3)	3.1547(15)
C(130)-O(39)	1.229(13)
C(130)-O(40)	1.269(12)
C(131)-O(36)	1.240(9)
C(131)-O(35)	1.253(9)
C(131)-C(132)	1.504(9)
C(132)-C(133)	1.39
C(132)-C(137)	1.39
C(133)-C(134)	1.39
C(133)-H(13A)	0.93
C(134)-C(135)	1.39
C(134)-H(13B)	0.93
C(135)-C(136)	1.39
C(135)-C(138)	1.489(9)
C(136)-C(137)	1.39
C(136)-H(13C)	0.93
C(137)-H(13D)	0.93
C(138)-C(139)	1.252(11)
C(138)-H(13E)	0.93
C(139)-C(140)	1.483(11)
C(139)-H(13F)	0.93
C(140)-C(141)	1.39
C(140)-C(145)	1.39
C(141)-C(142)	1.39
C(141)-H(14B)	0.93
C(142)-O(38)	1.276(15)
C(142)-C(143)	1.39
C(143)-C(144)	1.39
C(143)-C(148)	1.502(12)
C(144)-C(145)	1.39
C(144)-H(14C)	0.93
C(145)-O(37)	1.309(18)
C(147)-O(37)	1.493(16)
C(147)-H(14D)	0.96
C(147)-H(14E)	0.96
C(147)-H(14F)	0.96
C(146)-O(38)	1.470(14)
C(146)-H(14G)	0.96
C(146)-H(14H)	0.96
C(146)-H(14I)	0.96

C(148)-C(149)	1.184(14)
C(148)-H(14J)	0.93
C(149)-C(150)	1.476(13)
C(149)-H(14K)	0.93
C(150)-C(151)	1.39
C(150)-C(155)	1.39
C(151)-C(152)	1.39
C(151)-H(15A)	0.93
C(152)-C(153)	1.39
C(152)-H(15B)	0.93
C(153)-C(154)	1.39
C(153)-C(156)	1.518(18)
C(154)-C(155)	1.39
C(154)-H(15C)	0.93
C(155)-H(15D)	0.93
C(156)-O(33)	1.27(2)
C(156)-O(34)	1.30(2)
Zn(2)-O(31)#2	1.876(12)
Zn(2)-O(1)	1.925(5)
Zn(2)-O(4)	1.928(8)
Zn(2)-O(14)#3	1.935(8)
Zn(2)-Zn(4)	3.1534(16)
O(1)-Zn(4)	1.923(5)
O(1)-Zn(3)	1.961(5)
O(2)-Zn(6)	1.915(5)
O(2)-Zn(8)	1.916(5)
O(2)-Zn(7)	1.924(5)
O(2)-Zn(5)	1.989(5)
O(7)-Zn(5)	1.999(8)
O(8)-Zn(6)	1.930(6)
O(9)-Zn(4)	1.940(6)
O(13)-Zn(3)#4	1.914(8)
O(14)-Zn(2)#4	1.935(8)
O(15)-Zn(4)	1.932(7)
O(16)-Zn(3)	1.909(10)
O(19)-Zn(7)#5	1.928(7)
O(20)-Zn(8)#5	1.968(7)
O(21)-Zn(8)	1.903(7)
O(22)-Zn(5)	2.039(12)
O(27)-Zn(6)	1.957(6)
O(28)-Zn(7)	1.929(8)
O(31)-Zn(2)#6	1.876(11)
O(32)-Zn(4)#6	1.965(8)
O(33)-Zn(5)#3	1.941(12)
O(34)-Zn(7)#3	1.877(10)

O(35)-Zn(6)	1.957(5)
O(36)-Zn(8)	1.935(6)
O(39)-Zn(1)#7	1.924(6)
O(40)-Zn(3)#7	1.919(8)
Zn(3)-O(13)#3	1.914(8)
Zn(3)-O(40)#1	1.919(8)
Zn(4)-O(32)#2	1.966(8)
Zn(5)-O(33)#4	1.941(12)
Zn(6)-Zn(7)	3.1386(14)
Zn(6)-Zn(8)	3.1394(15)
Zn(7)-O(34)#4	1.877(10)
Zn(7)-O(19)#8	1.928(7)
Zn(7)-Zn(8)	3.1385(15)
Zn(8)-O(20)#8	1.968(7)
O(3)-C(1)-O(4)	124.3(10)
O(3)-C(1)-C(2)	119.9(10)
O(4)-C(1)-C(2)	115.7(10)
C(3)-C(2)-C(7)	120
C(3)-C(2)-C(1)	118.9(8)
C(7)-C(2)-C(1)	121.1(8)
C(4)-C(3)-C(2)	120
C(4)-C(3)-H(3A)	120
C(2)-C(3)-H(3A)	120
C(5)-C(4)-C(3)	120
C(5)-C(4)-H(4A)	120
C(3)-C(4)-H(4A)	120
C(6)-C(5)-C(4)	120
C(6)-C(5)-C(8)	120.2(8)
C(4)-C(5)-C(8)	119.8(8)
C(7)-C(6)-C(5)	120
C(7)-C(6)-H(6A)	120
C(5)-C(6)-H(6A)	120
C(6)-C(7)-C(2)	120
C(6)-C(7)-H(7A)	120
C(2)-C(7)-H(7A)	120
C(9)-C(8)-C(5)	128.3(12)
C(9)-C(8)-H(8A)	115.9
C(5)-C(8)-H(8A)	115.9
C(8)-C(9)-C(10)	126.8(11)
C(8)-C(9)-H(9A)	116.6
C(10)-C(9)-H(9A)	116.6
C(11)-C(10)-C(15)	120
C(11)-C(10)-C(9)	120.9(9)
C(15)-C(10)-C(9)	119.1(9)

C(12)-C(11)-C(10)	120
C(12)-C(11)-H(11A)	120
C(10)-C(11)-H(11A)	120
O(6)-C(12)-C(11)	123.0(8)
O(6)-C(12)-C(13)	116.7(8)
C(11)-C(12)-C(13)	120
C(14)-C(13)-C(12)	120
C(14)-C(13)-C(18)	122.4(8)
C(12)-C(13)-C(18)	117.5(8)
C(13)-C(14)-C(15)	120
C(13)-C(14)-H(14A)	120
C(15)-C(14)-H(14A)	120
O(5)-C(15)-C(14)	124.1(7)
O(5)-C(15)-C(10)	115.6(7)
C(14)-C(15)-C(10)	120
O(5)-C(16)-H(16A)	109.5
O(5)-C(16)-H(16B)	109.5
H(16A)-C(16)-H(16B)	109.5
O(5)-C(16)-H(16C)	109.5
H(16A)-C(16)-H(16C)	109.5
H(16B)-C(16)-H(16C)	109.5
O(6)-C(17)-H(17A)	109.5
O(6)-C(17)-H(17B)	109.5
H(17A)-C(17)-H(17B)	109.5
O(6)-C(17)-H(17C)	109.5
H(17A)-C(17)-H(17C)	109.5
H(17B)-C(17)-H(17C)	109.5
C(19)-C(18)-C(13)	126.0(11)
C(19)-C(18)-H(18A)	117
C(13)-C(18)-H(18A)	117
C(18)-C(19)-C(20)	126.8(10)
C(18)-C(19)-H(19A)	116.6
C(20)-C(19)-H(19A)	116.6
C(21)-C(20)-C(25)	120
C(21)-C(20)-C(19)	120.1(7)
C(25)-C(20)-C(19)	119.8(7)
C(20)-C(21)-C(22)	120
C(20)-C(21)-H(21A)	120
C(22)-C(21)-H(21A)	120
C(23)-C(22)-C(21)	120
C(23)-C(22)-H(22A)	120
C(21)-C(22)-H(22A)	120
C(24)-C(23)-C(22)	120
C(24)-C(23)-C(26)	121.6(7)
C(22)-C(23)-C(26)	118.4(7)

C(25)-C(24)-C(23)	120
C(25)-C(24)-H(24A)	120
C(23)-C(24)-H(24A)	120
C(24)-C(25)-C(20)	120
C(24)-C(25)-H(25A)	120
C(20)-C(25)-H(25A)	120
O(8)-C(26)-O(7)	125.3(10)
O(8)-C(26)-C(23)	119.0(9)
O(7)-C(26)-C(23)	115.4(10)
O(10)-C(27)-O(9)	127.0(8)
O(10)-C(27)-C(28)	116.6(8)
O(9)-C(27)-C(28)	116.4(8)
C(29)-C(28)-C(33)	120
C(29)-C(28)-C(27)	119.3(6)
C(33)-C(28)-C(27)	120.7(6)
C(28)-C(29)-C(30)	120
C(28)-C(29)-H(29A)	120
C(30)-C(29)-H(29A)	120
C(29)-C(30)-C(31)	120
C(29)-C(30)-H(30A)	120
C(31)-C(30)-H(30A)	120
C(32)-C(31)-C(30)	120
C(32)-C(31)-C(34)	121.6(7)
C(30)-C(31)-C(34)	118.4(7)
C(33)-C(32)-C(31)	120
C(33)-C(32)-H(32A)	120
C(31)-C(32)-H(32A)	120
C(32)-C(33)-C(28)	120
C(32)-C(33)-H(33A)	120
C(28)-C(33)-H(33A)	120
C(35)-C(34)-C(31)	126.9(10)
C(35)-C(34)-H(34A)	116.5
C(31)-C(34)-H(34A)	116.5
C(34)-C(35)-C(36)	127.3(11)
C(34)-C(35)-H(35A)	116.3
C(36)-C(35)-H(35A)	116.3
C(37)-C(36)-C(41)	120
C(37)-C(36)-C(35)	119.0(9)
C(41)-C(36)-C(35)	120.7(8)
C(36)-C(37)-C(38)	120
C(36)-C(37)-H(37A)	120
C(38)-C(37)-H(37A)	120
O(12)-C(38)-C(37)	124.0(7)
O(12)-C(38)-C(39)	115.7(7)
C(37)-C(38)-C(39)	120

C(40)-C(39)-C(38)	120
C(40)-C(39)-C(44)	121.3(8)
C(38)-C(39)-C(44)	118.5(8)
C(39)-C(40)-C(41)	120
C(39)-C(40)-H(40A)	120
C(41)-C(40)-H(40A)	120
O(11)-C(41)-C(40)	122.7(8)
O(11)-C(41)-C(36)	115.8(8)
C(40)-C(41)-C(36)	120
C(45)-C(44)-C(39)	127.0(13)
C(45)-C(44)-H(44A)	116.5
C(39)-C(44)-H(44A)	116.5
C(44)-C(45)-C(46)	125.7(14)
C(44)-C(45)-H(45A)	117.1
C(46)-C(45)-H(45A)	117.1
O(12)-C(42)-H(42A)	109.5
O(12)-C(42)-H(42B)	109.5
H(42A)-C(42)-H(42B)	109.5
O(12)-C(42)-H(42C)	109.5
H(42A)-C(42)-H(42C)	109.5
H(42B)-C(42)-H(42C)	109.5
O(11)-C(43)-H(43A)	109.5
O(11)-C(43)-H(43B)	109.5
H(43A)-C(43)-H(43B)	109.5
O(11)-C(43)-H(43C)	109.5
H(43A)-C(43)-H(43C)	109.5
H(43B)-C(43)-H(43C)	109.5
C(47)-C(46)-C(51)	120
C(47)-C(46)-C(45)	122.8(12)
C(51)-C(46)-C(45)	117.1(12)
C(46)-C(47)-C(48)	120
C(46)-C(47)-H(47A)	120
C(48)-C(47)-H(47A)	120
C(49)-C(48)-C(47)	120
C(49)-C(48)-H(48A)	120
C(47)-C(48)-H(48A)	120
C(48)-C(49)-C(50)	120
C(48)-C(49)-C(52)	121.3(10)
C(50)-C(49)-C(52)	118.6(11)
C(51)-C(50)-C(49)	120
C(51)-C(50)-H(50A)	120
C(49)-C(50)-H(50A)	120
C(50)-C(51)-C(46)	120
C(50)-C(51)-H(51A)	120
C(46)-C(51)-H(51A)	120

O(13)-C(52)-O(14)	127.8(11)
O(13)-C(52)-C(49)	118.6(14)
O(14)-C(52)-C(49)	113.4(14)
O(15)-C(53)-O(16)	123.9(12)
O(15)-C(53)-C(54)	123.3(15)
O(16)-C(53)-C(54)	112.8(16)
C(55)-C(54)-C(59)	120
C(55)-C(54)-C(53)	117.1(12)
C(59)-C(54)-C(53)	122.9(12)
C(54)-C(55)-C(56)	120
C(54)-C(55)-H(55A)	120
C(56)-C(55)-H(55A)	120
C(55)-C(56)-C(57)	120
C(55)-C(56)-H(56A)	120
C(57)-C(56)-H(56A)	120
C(58)-C(57)-C(56)	120
C(58)-C(57)-C(60)	121.9(12)
C(56)-C(57)-C(60)	118.1(13)
C(57)-C(58)-C(59)	120
C(57)-C(58)-H(58A)	120
C(59)-C(58)-H(58A)	120
C(58)-C(59)-C(54)	120
C(58)-C(59)-H(59A)	120
C(54)-C(59)-H(59A)	120
C(61)-C(60)-C(57)	129.1(16)
C(61)-C(60)-H(60A)	115.5
C(57)-C(60)-H(60A)	115.5
C(60)-C(61)-C(62)	132.4(16)
C(60)-C(61)-H(61A)	113.8
C(62)-C(61)-H(61A)	113.8
C(63)-C(62)-C(67)	120
C(63)-C(62)-C(61)	120.9(12)
C(67)-C(62)-C(61)	119.1(12)
C(64)-C(63)-C(62)	120
C(64)-C(63)-H(63A)	120
C(62)-C(63)-H(63A)	120
O(18)-C(64)-C(63)	121.3(11)
O(18)-C(64)-C(65)	118.5(11)
C(63)-C(64)-C(65)	120
C(66)-C(65)-C(64)	120
C(66)-C(65)-C(70)	119.8(12)
C(64)-C(65)-C(70)	120.2(12)
C(67)-C(66)-C(65)	120
C(67)-C(66)-H(66A)	120
C(65)-C(66)-H(66A)	120

C(66)-C(67)-C(62)	120
C(66)-C(67)-O(17)	121.1(11)
C(62)-C(67)-O(17)	118.0(11)
O(18)-C(68)-H(68A)	109.5
O(18)-C(68)-H(68B)	109.5
H(68A)-C(68)-H(68B)	109.5
O(18)-C(68)-H(68C)	109.5
H(68A)-C(68)-H(68C)	109.5
H(68B)-C(68)-H(68C)	109.5
O(17)-C(69)-H(69A)	109.5
O(17)-C(69)-H(69B)	109.5
H(69A)-C(69)-H(69B)	109.5
O(17)-C(69)-H(69C)	109.5
H(69A)-C(69)-H(69C)	109.5
H(69B)-C(69)-H(69C)	109.5
C(71)-C(70)-C(65)	128.3(15)
C(71)-C(70)-H(70A)	115.8
C(65)-C(70)-H(70A)	115.8
C(70)-C(71)-C(72)	126.6(14)
C(70)-C(71)-H(71A)	116.7
C(72)-C(71)-H(71A)	116.7
C(73)-C(72)-C(77)	120
C(73)-C(72)-C(71)	123.5(11)
C(77)-C(72)-C(71)	116.5(11)
C(72)-C(73)-C(74)	120
C(72)-C(73)-H(73A)	120
C(74)-C(73)-H(73A)	120
C(75)-C(74)-C(73)	120
C(75)-C(74)-H(74A)	120
C(73)-C(74)-H(74A)	120
C(74)-C(75)-C(76)	120
C(74)-C(75)-C(78)	120.1(8)
C(76)-C(75)-C(78)	119.9(8)
C(75)-C(76)-C(77)	120
C(75)-C(76)-H(76A)	120
C(77)-C(76)-H(76A)	120
C(76)-C(77)-C(72)	120
C(76)-C(77)-H(77A)	120
C(72)-C(77)-H(77A)	120
O(20)-C(78)-O(19)	124.6(9)
O(20)-C(78)-C(75)	119.2(11)
O(19)-C(78)-C(75)	116.1(10)
O(21)-C(79)-O(22)	123.0(13)
O(21)-C(79)-C(80)	121.6(17)
O(22)-C(79)-C(80)	115.5(16)

C(81)-C(80)-C(85)	120
C(81)-C(80)-C(79)	118.6(14)
C(85)-C(80)-C(79)	121.0(14)
C(82)-C(81)-C(80)	120
C(82)-C(81)-H(81A)	120
C(80)-C(81)-H(81A)	120
C(81)-C(82)-C(83)	120
C(81)-C(82)-H(82A)	120
C(83)-C(82)-H(82A)	120
C(84)-C(83)-C(82)	120
C(84)-C(83)-C(86)	108.8(17)
C(82)-C(83)-C(86)	131.1(17)
C(83)-C(84)-C(85)	120
C(83)-C(84)-H(84A)	120
C(85)-C(84)-H(84A)	120
C(84)-C(85)-C(80)	120
C(84)-C(85)-H(85A)	120
C(80)-C(85)-H(85A)	120
C(87)-C(86)-C(83)	125(2)
C(87)-C(86)-H(86A)	117.4
C(83)-C(86)-H(86A)	117.4
C(86)-C(87)-C(88)	125(2)
C(86)-C(87)-H(87A)	117.4
C(88)-C(87)-H(87A)	117.4
C(89)-C(88)-C(93)	120
C(89)-C(88)-C(87)	110.1(19)
C(93)-C(88)-C(87)	129.8(19)
C(90)-C(89)-C(88)	120
C(90)-C(89)-O(23)	114.1(19)
C(88)-C(89)-O(23)	125.5(18)
C(89)-C(90)-C(91)	120
C(89)-C(90)-H(90A)	120
C(91)-C(90)-H(90A)	120
C(92)-C(91)-C(90)	120
C(92)-C(91)-C(96)	129.2(19)
C(90)-C(91)-C(96)	110.7(19)
C(91)-C(92)-C(93)	120
C(91)-C(92)-O(24)	130.7(17)
C(93)-C(92)-O(24)	107.5(18)
C(92)-C(93)-C(88)	120
C(92)-C(93)-H(93A)	120
C(88)-C(93)-H(93A)	120
O(24)-C(94)-H(94A)	109.5
O(24)-C(94)-H(94B)	109.5
H(94A)-C(94)-H(94B)	109.5

O(24)-C(94)-H(94C)	109.5
H(94A)-C(94)-H(94C)	109.5
H(94B)-C(94)-H(94C)	109.5
O(23)-C(95)-H(95A)	109.5
O(23)-C(95)-H(95B)	109.5
H(95A)-C(95)-H(95B)	109.5
O(23)-C(95)-H(95C)	109.5
H(95A)-C(95)-H(95C)	109.5
H(95B)-C(95)-H(95C)	109.5
C(97)-C(96)-C(91)	130(2)
C(97)-C(96)-H(96A)	115
C(91)-C(96)-H(96A)	115
C(96)-C(97)-C(98)	123(2)
C(96)-C(97)-H(97A)	118.7
C(98)-C(97)-H(97A)	118.7
C(99)-C(98)-C(103)	120
C(99)-C(98)-C(97)	132.9(17)
C(103)-C(98)-C(97)	106.3(17)
C(100)-C(99)-C(98)	120
C(100)-C(99)-H(99A)	120
C(98)-C(99)-H(99A)	120
C(99)-C(100)-C(101)	120
C(99)-C(100)-H(10A)	120
C(101)-C(100)-H(10A)	120
C(102)-C(101)-C(100)	120
C(102)-C(101)-C(104)	120.9(13)
C(100)-C(101)-C(104)	119.1(13)
C(101)-C(102)-C(103)	120
C(101)-C(102)-H(10B)	120
C(103)-C(102)-H(10B)	120
C(102)-C(103)-C(98)	120
C(102)-C(103)-H(10C)	120
C(98)-C(103)-H(10C)	120
O(32)-C(104)-O(31)	126.9(15)
O(32)-C(104)-C(101)	116.3(16)
O(31)-C(104)-C(101)	116.4(17)
O(28)-C(105)-O(27)	126.5(10)
O(28)-C(105)-C(106)	117.8(12)
O(27)-C(105)-C(106)	115.6(12)
C(107)-C(106)-C(111)	120
C(107)-C(106)-C(105)	118.2(10)
C(111)-C(106)-C(105)	121.8(10)
C(106)-C(107)-C(108)	120
C(106)-C(107)-H(10D)	120
C(108)-C(107)-H(10D)	120

C(107)-C(108)-C(109)	120
C(107)-C(108)-H(10E)	120
C(109)-C(108)-H(10E)	120
C(110)-C(109)-C(108)	120
C(110)-C(109)-C(112)	117.3(14)
C(108)-C(109)-C(112)	122.6(14)
C(111)-C(110)-C(109)	120
C(111)-C(110)-H(11B)	120
C(109)-C(110)-H(11B)	120
C(110)-C(111)-C(106)	120
C(110)-C(111)-H(11C)	120
C(106)-C(111)-H(11C)	120
C(113)-C(112)-C(109)	126.1(18)
C(113)-C(112)-H(11D)	117
C(109)-C(112)-H(11D)	117
C(112)-C(113)-C(114)	123(2)
C(112)-C(113)-H(11E)	118.6
C(114)-C(113)-H(11E)	118.6
C(115)-C(114)-C(119)	120
C(115)-C(114)-C(113)	128(2)
C(119)-C(114)-C(113)	112(2)
C(116)-C(115)-C(114)	120
C(116)-C(115)-H(11F)	120
C(114)-C(115)-H(11F)	120
O(30)-C(116)-C(117)	122.1(18)
O(30)-C(116)-C(115)	117.9(18)
C(117)-C(116)-C(115)	120
C(116)-C(117)-C(118)	120
C(116)-C(117)-C(122)	112.5(19)
C(118)-C(117)-C(122)	127.5(19)
C(117)-C(118)-C(119)	120
C(117)-C(118)-H(11G)	120
C(119)-C(118)-H(11G)	120
O(29)-C(119)-C(118)	121(2)
O(29)-C(119)-C(114)	119(2)
C(118)-C(119)-C(114)	120
O(29)-C(120)-H(12A)	109.5
O(29)-C(120)-H(12B)	109.5
H(12A)-C(120)-H(12B)	109.5
O(29)-C(120)-H(12C)	109.5
H(12A)-C(120)-H(12C)	109.5
H(12B)-C(120)-H(12C)	109.5
O(30)-C(121)-H(12D)	109.5
O(30)-C(121)-H(12E)	109.5
H(12D)-C(121)-H(12E)	109.5

O(30)-C(121)-H(12F)	109.5
H(12D)-C(121)-H(12F)	109.5
H(12E)-C(121)-H(12F)	109.5
C(123)-C(122)-C(117)	126(2)
C(123)-C(122)-H(12G)	117.1
C(117)-C(122)-H(12G)	117.1
C(122)-C(123)-C(124)	129(2)
C(122)-C(123)-H(12H)	115.6
C(124)-C(123)-H(12H)	115.6
C(125)-C(124)-C(129)	120
C(125)-C(124)-C(123)	125.1(15)
C(129)-C(124)-C(123)	114.9(15)
C(124)-C(125)-C(126)	120
C(124)-C(125)-H(12I)	120
C(126)-C(125)-H(12I)	120
C(125)-C(126)-C(127)	120
C(125)-C(126)-H(12J)	120
C(127)-C(126)-H(12J)	120
C(128)-C(127)-C(126)	120
C(128)-C(127)-C(130)	120.1(10)
C(126)-C(127)-C(130)	119.8(10)
C(129)-C(128)-C(127)	120
C(129)-C(128)-H(12K)	120
C(127)-C(128)-H(12K)	120
C(128)-C(129)-C(124)	120
C(128)-C(129)-H(12L)	120
C(124)-C(129)-H(12L)	120
O(1)-Zn(1)-O(39)#1	115.4(3)
O(1)-Zn(1)-O(10)	112.6(2)
O(39)#1-Zn(1)-O(10)	104.3(3)
O(1)-Zn(1)-O(3)	116.3(2)
O(39)#1-Zn(1)-O(3)	103.4(3)
O(10)-Zn(1)-O(3)	103.5(3)
O(1)-Zn(1)-Zn(2)	35.62(14)
O(39)#1-Zn(1)-Zn(2)	125.5(2)
O(10)-Zn(1)-Zn(2)	127.87(19)
O(3)-Zn(1)-Zn(2)	80.8(2)
O(1)-Zn(1)-Zn(4)	34.95(13)
O(39)#1-Zn(1)-Zn(4)	129.3(2)
O(10)-Zn(1)-Zn(4)	77.68(18)
O(3)-Zn(1)-Zn(4)	125.9(2)
Zn(2)-Zn(1)-Zn(4)	60.28(3)
O(1)-Zn(1)-Zn(3)	36.08(14)
O(39)#1-Zn(1)-Zn(3)	79.4(2)
O(10)-Zn(1)-Zn(3)	123.36(19)

O(3)-Zn(1)-Zn(3)	131.2(2)
Zn(2)-Zn(1)-Zn(3)	60.85(4)
Zn(4)-Zn(1)-Zn(3)	60.24(3)
O(39)-C(130)-O(40)	124.2(10)
O(39)-C(130)-C(127)	118.8(12)
O(40)-C(130)-C(127)	116.9(12)
O(36)-C(131)-O(35)	126.2(8)
O(36)-C(131)-C(132)	117.6(8)
O(35)-C(131)-C(132)	116.2(8)
C(133)-C(132)-C(137)	120
C(133)-C(132)-C(131)	120.3(6)
C(137)-C(132)-C(131)	119.7(6)
C(132)-C(133)-C(134)	120
C(132)-C(133)-H(13A)	120
C(134)-C(133)-H(13A)	120
C(135)-C(134)-C(133)	120
C(135)-C(134)-H(13B)	120
C(133)-C(134)-H(13B)	120
C(134)-C(135)-C(136)	120
C(134)-C(135)-C(138)	122.0(7)
C(136)-C(135)-C(138)	118.0(7)
C(137)-C(136)-C(135)	120
C(137)-C(136)-H(13C)	120
C(135)-C(136)-H(13C)	120
C(136)-C(137)-C(132)	120
C(136)-C(137)-H(13D)	120
C(132)-C(137)-H(13D)	120
C(139)-C(138)-C(135)	126.3(10)
C(139)-C(138)-H(13E)	116.9
C(135)-C(138)-H(13E)	116.9
C(138)-C(139)-C(140)	127.9(12)
C(138)-C(139)-H(13F)	116
C(140)-C(139)-H(13F)	116
C(141)-C(140)-C(145)	120
C(141)-C(140)-C(139)	119.5(10)
C(145)-C(140)-C(139)	120.1(10)
C(140)-C(141)-C(142)	120
C(140)-C(141)-H(14B)	120
C(142)-C(141)-H(14B)	120
O(38)-C(142)-C(143)	113.2(11)
O(38)-C(142)-C(141)	126.7(11)
C(143)-C(142)-C(141)	120
C(142)-C(143)-C(144)	120
C(142)-C(143)-C(148)	118.9(12)
C(144)-C(143)-C(148)	120.8(12)

C(145)-C(144)-C(143)	120
C(145)-C(144)-H(14C)	120
C(143)-C(144)-H(14C)	120
O(37)-C(145)-C(144)	124.3(12)
O(37)-C(145)-C(140)	115.1(13)
C(144)-C(145)-C(140)	120
O(37)-C(147)-H(14D)	109.5
O(37)-C(147)-H(14E)	109.5
H(14D)-C(147)-H(14E)	109.5
O(37)-C(147)-H(14F)	109.5
H(14D)-C(147)-H(14F)	109.5
H(14E)-C(147)-H(14F)	109.5
O(38)-C(146)-H(14G)	109.5
O(38)-C(146)-H(14H)	109.5
H(14G)-C(146)-H(14H)	109.5
O(38)-C(146)-H(14I)	109.5
H(14G)-C(146)-H(14I)	109.5
H(14H)-C(146)-H(14I)	109.5
C(149)-C(148)-C(143)	130.2(17)
C(149)-C(148)-H(14J)	114.9
C(143)-C(148)-H(14J)	114.9
C(148)-C(149)-C(150)	123.3(18)
C(148)-C(149)-H(14K)	118.4
C(150)-C(149)-H(14K)	118.4
C(151)-C(150)-C(155)	120
C(151)-C(150)-C(149)	127.1(19)
C(155)-C(150)-C(149)	112.5(19)
C(150)-C(151)-C(152)	120
C(150)-C(151)-H(15A)	120
C(152)-C(151)-H(15A)	120
C(151)-C(152)-C(153)	120
C(151)-C(152)-H(15B)	120
C(153)-C(152)-H(15B)	120
C(154)-C(153)-C(152)	120
C(154)-C(153)-C(156)	123.4(16)
C(152)-C(153)-C(156)	116.6(16)
C(155)-C(154)-C(153)	120
C(155)-C(154)-H(15C)	120
C(153)-C(154)-H(15C)	120
C(154)-C(155)-C(150)	120
C(154)-C(155)-H(15D)	120
C(150)-C(155)-H(15D)	120
O(33)-C(156)-O(34)	127.6(14)
O(33)-C(156)-C(153)	121(2)
O(34)-C(156)-C(153)	110(2)

O(31)#2-Zn(2)-O(1)	107.9(5)
O(31)#2-Zn(2)-O(4)	120.5(6)
O(1)-Zn(2)-O(4)	107.1(3)
O(31)#2-Zn(2)-O(14)#3	104.0(4)
O(1)-Zn(2)-O(14)#3	111.3(3)
O(4)-Zn(2)-O(14)#3	106.0(4)
O(31)#2-Zn(2)-Zn(1)	126.8(4)
O(1)-Zn(2)-Zn(1)	35.55(13)
O(4)-Zn(2)-Zn(1)	71.6(2)
O(14)#3-Zn(2)-Zn(1)	123.1(3)
O(31)#2-Zn(2)-Zn(4)	73.3(4)
O(1)-Zn(2)-Zn(4)	34.93(14)
O(4)-Zn(2)-Zn(4)	122.6(3)
O(14)#3-Zn(2)-Zn(4)	125.3(3)
Zn(1)-Zn(2)-Zn(4)	60.22(4)
Zn(1)-O(1)-Zn(4)	110.1(2)
Zn(1)-O(1)-Zn(2)	108.8(2)
Zn(4)-O(1)-Zn(2)	110.1(2)
Zn(1)-O(1)-Zn(3)	108.7(2)
Zn(4)-O(1)-Zn(3)	109.1(2)
Zn(2)-O(1)-Zn(3)	109.9(2)
Zn(6)-O(2)-Zn(8)	110.0(2)
Zn(6)-O(2)-Zn(7)	109.7(2)
Zn(8)-O(2)-Zn(7)	109.6(2)
Zn(6)-O(2)-Zn(5)	109.2(2)
Zn(8)-O(2)-Zn(5)	108.1(2)
Zn(7)-O(2)-Zn(5)	110.1(2)
C(1)-O(3)-Zn(1)	124.8(7)
C(1)-O(4)-Zn(2)	136.9(7)
C(15)-O(5)-C(16)	118.2(8)
C(12)-O(6)-C(17)	121.2(12)
C(26)-O(7)-Zn(5)	137.7(8)
C(26)-O(8)-Zn(6)	120.4(6)
C(27)-O(9)-Zn(4)	131.5(6)
C(27)-O(10)-Zn(1)	128.6(6)
C(41)-O(11)-C(43)	119.1(13)
C(38)-O(12)-C(42)	119.0(10)
C(52)-O(13)-Zn(3)#4	130.6(8)
C(52)-O(14)-Zn(2)#4	128.4(8)
C(53)-O(15)-Zn(4)	127.2(9)
C(53)-O(16)-Zn(3)	135.5(9)
C(67)-O(17)-C(69)	115.7(15)
C(64)-O(18)-C(68)	117.3(14)
C(78)-O(19)-Zn(7)#5	132.9(7)
C(78)-O(20)-Zn(8)#5	130.3(7)

C(79)-O(21)-Zn(8)	120.2(10)
C(79)-O(22)-Zn(5)	135.4(11)
C(89)-O(23)-C(95)	121(3)
C(94)-O(24)-C(92)	113(3)
C(105)-O(27)-Zn(6)	126.4(7)
C(105)-O(28)-Zn(7)	133.2(7)
C(119)-O(29)-C(120)	125(3)
C(116)-O(30)-C(121)	119(2)
C(104)-O(31)-Zn(2)#6	135.7(11)
C(104)-O(32)-Zn(4)#6	122.9(10)
C(156)-O(33)-Zn(5)#3	136.2(13)
C(156)-O(34)-Zn(7)#3	122.3(11)
C(131)-O(35)-Zn(6)	130.0(5)
C(131)-O(36)-Zn(8)	130.6(6)
C(145)-O(37)-C(147)	107(2)
C(142)-O(38)-C(146)	117.6(17)
C(130)-O(39)-Zn(1)#7	127.2(7)
C(130)-O(40)-Zn(3)#7	137.1(8)
O(16)-Zn(3)-O(13)#3	99.6(4)
O(16)-Zn(3)-O(40)#1	125.6(5)
O(13)#3-Zn(3)-O(40)#1	106.7(4)
O(16)-Zn(3)-O(1)	106.3(4)
O(13)#3-Zn(3)-O(1)	111.2(3)
O(40)#1-Zn(3)-O(1)	107.0(3)
O(16)-Zn(3)-Zn(1)	125.9(3)
O(13)#3-Zn(3)-Zn(1)	125.7(3)
O(40)#1-Zn(3)-Zn(1)	71.9(2)
O(1)-Zn(3)-Zn(1)	35.25(13)
O(1)-Zn(4)-O(15)	115.1(3)
O(1)-Zn(4)-O(9)	110.1(2)
O(15)-Zn(4)-O(9)	103.6(3)
O(1)-Zn(4)-O(32)#2	114.5(4)
O(15)-Zn(4)-O(32)#2	104.1(4)
O(9)-Zn(4)-O(32)#2	108.6(4)
O(1)-Zn(4)-Zn(1)	34.93(13)
O(15)-Zn(4)-Zn(1)	127.3(3)
O(9)-Zn(4)-Zn(1)	75.22(19)
O(32)#2-Zn(4)-Zn(1)	126.6(3)
O(1)-Zn(4)-Zn(2)	34.98(14)
O(15)-Zn(4)-Zn(2)	127.5(3)
O(9)-Zn(4)-Zn(2)	125.21(19)
O(32)#2-Zn(4)-Zn(2)	79.5(3)
Zn(1)-Zn(4)-Zn(2)	59.49(3)
O(33)#4-Zn(5)-O(2)	104.7(4)
O(33)#4-Zn(5)-O(7)	101.1(5)

O(2)-Zn(5)-O(7)	99.0(3)
O(33)#4-Zn(5)-O(22)	94.6(5)
O(2)-Zn(5)-O(22)	95.6(4)
O(7)-Zn(5)-O(22)	155.0(6)
O(2)-Zn(6)-O(8)	118.6(2)
O(2)-Zn(6)-O(35)	110.7(2)
O(8)-Zn(6)-O(35)	108.1(3)
O(2)-Zn(6)-O(27)	113.7(3)
O(8)-Zn(6)-O(27)	102.3(3)
O(35)-Zn(6)-O(27)	101.8(3)
O(2)-Zn(6)-Zn(7)	35.24(15)
O(8)-Zn(6)-Zn(7)	130.1(2)
O(35)-Zn(6)-Zn(7)	120.79(18)
O(27)-Zn(6)-Zn(7)	78.5(2)
O(2)-Zn(6)-Zn(8)	34.99(14)
O(8)-Zn(6)-Zn(8)	129.77(19)
O(35)-Zn(6)-Zn(8)	75.92(17)
O(27)-Zn(6)-Zn(8)	126.4(2)
Zn(7)-Zn(6)-Zn(8)	59.99(3)
O(34)#4-Zn(7)-O(2)	118.0(4)
O(34)#4-Zn(7)-O(19)#8	106.2(4)
O(2)-Zn(7)-O(19)#8	110.5(3)
O(34)#4-Zn(7)-O(28)	107.4(5)
O(2)-Zn(7)-O(28)	109.9(3)
O(19)#8-Zn(7)-O(28)	104.0(3)
O(34)#4-Zn(7)-Zn(8)	128.0(4)
O(2)-Zn(7)-Zn(8)	35.10(14)
O(19)#8-Zn(7)-Zn(8)	75.5(2)
O(28)-Zn(7)-Zn(8)	122.9(2)
O(34)#4-Zn(7)-Zn(6)	130.7(4)
O(2)-Zn(7)-Zn(6)	35.07(14)
O(19)#8-Zn(7)-Zn(6)	121.4(2)
O(28)-Zn(7)-Zn(6)	74.8(2)
Zn(8)-Zn(7)-Zn(6)	60.02(3)
O(21)-Zn(8)-O(2)	120.7(3)
O(21)-Zn(8)-O(36)	107.0(3)
O(2)-Zn(8)-O(36)	111.5(2)
O(21)-Zn(8)-O(20)#8	101.5(3)
O(2)-Zn(8)-O(20)#8	111.7(2)
O(36)-Zn(8)-O(20)#8	102.6(3)
O(21)-Zn(8)-Zn(7)	127.6(3)
O(2)-Zn(8)-Zn(7)	35.26(14)
O(36)-Zn(8)-Zn(7)	124.80(19)
O(20)#8-Zn(8)-Zn(7)	76.6(2)
O(21)-Zn(8)-Zn(6)	135.3(2)

O(2)-Zn(8)-Zn(6)	34.97(13)
O(36)-Zn(8)-Zn(6)	76.57(18)
O(20)#8-Zn(8)-Zn(6)	121.6(2)
Zn(7)-Zn(8)-Zn(6)	59.99(3)

Symmetry transformations used to generate equivalent atoms:

#1 x+1,y,z+1; #2 x,y+1,z; #3 x-1,y,z; #4 x+1,y,z; #5 x+1,y+1,z+1; #6 x,y-1,z; #7 x-1,y,z-1;

#8 x-1,y-1,z-1

Table AA 15. Anisotropic displacement parameters ($Å^2$ x 10^3) for Zn-PVDC-1. The anisotropic displacement factor exponent takes the form: $-2pi^2[h^2a^{*2}U^{11} + ... + 2hka^*b^*U^{12}]$.

	U^{11}	U^{22}	U^{33}	U^{23}	U^{13}	U^{12}
C(1)	68(7)	81(8)	96(8)	-28(6)	36(7)	-11(6)
C(2)	80(8)	92(8)	111(9)	-59(7)	25(7)	-30(7)
C(3)	90(8)	105(9)	123(10)	-73(8)	4(7)	-7(7)
C(4)	99(9)	118(10)	143(11)	-67(9)	37(9)	9(8)
C(5)	74(9)	176(14)	175(13)	-108(11)	33(9)	12(9)
C(6)	83(10)	237(18)	198(15)	-145(14)	0(10)	0(11)
C(7)	92(10)	195(15)	196(15)	-142(13)	11(10)	-3(10)
C(8)	97(10)	157(12)	189(14)	-123(11)	36(10)	-27(9)
C(9)	109(11)	130(11)	155(12)	-94(10)	28(9)	-27(9)
C(10)	100(10)	149(12)	143(11)	-76(10)	48(9)	-21(9)
C(11)	114(11)	156(14)	213(16)	-115(12)	51(11)	-40(10)
C(12)	114(12)	177(15)	205(16)	-94(13)	62(12)	-21(11)
C(13)	93(9)	126(11)	126(10)	-35(9)	36(8)	-18(8)
C(14)	91(9)	111(9)	117(9)	-68(8)	33(7)	-7(7)
C(15)	97(10)	110(10)	117(10)	-52(8)	19(8)	-5(8)
C(16)	73(10)	270(20)	234(19)	-111(16)	-5(11)	29(12)
C(17)	190(20)	440(40)	460(40)	-210(30)	210(30)	-90(20)
C(18)	98(9)	103(9)	123(10)	-70(8)	27(8)	-20(7)
C(19)	110(10)	87(8)	111(9)	-46(7)	40(8)	-10(7)
C(20)	84(8)	93(8)	102(8)	-42(7)	21(7)	-7(7)
C(21)	77(8)	94(8)	104(8)	-36(7)	22(7)	15(6)
C(22)	87(8)	84(8)	82(7)	-40(6)	11(6)	-2(6)
C(23)	76(8)	93(8)	100(8)	-51(7)	22(6)	-1(6)
C(24)	67(8)	161(12)	207(14)	-132(11)	21(9)	2(8)
C(25)	87(9)	147(12)	230(16)	-109(12)	33(10)	6(9)
C(26)	78(8)	72(7)	109(9)	-36(6)	39(7)	9(6)
C(27)	49(5)	70(7)	88(7)	-1(6)	42(5)	1(5)
C(28)	58(6)	76(7)	112(7)	-7(6)	58(6)	-4(5)

C(29)	86(7)	59(6)	210(12)	2(7)	113(9)	-1(5)
C(30)	108(9)	56(6)	238(14)	20(7)	131(10)	18(6)
C(31)	76(7)	91(8)	173(11)	-7(7)	93(8)	2(6)
C(32)	124(10)	88(9)	295(17)	6(10)	161(12)	0(7)
C(33)	97(8)	83(8)	274(16)	-17(9)	144(10)	-11(6)
C(34)	87(8)	111(9)	192(12)	-9(8)	104(9)	2(7)
C(35)	118(10)	123(11)	320(20)	4(11)	173(13)	-9(8)
C(36)	121(11)	105(10)	307(19)	-18(11)	166(13)	-21(8)
C(37)	112(10)	123(11)	238(15)	-25(10)	136(11)	-25(8)
C(38)	121(10)	124(11)	244(15)	-62(10)	147(11)	-34(8)
C(39)	116(10)	133(12)	270(17)	-45(11)	147(12)	-37(9)
C(40)	173(14)	102(11)	510(30)	-83(15)	260(18)	-56(10)
C(41)	208(15)	111(12)	560(30)	-100(15)	307(19)	-54(11)
C(44)	105(10)	133(11)	300(19)	-56(11)	151(13)	-40(8)
C(45)	149(14)	207(17)	400(30)	-73(17)	219(17)	-48(12)
C(42)	280(20)	210(20)	490(40)	-160(20)	290(30)	-152(19)
C(43)	290(30)	400(40)	490(40)	-220(30)	250(30)	-100(30)
C(46)	116(11)	147(11)	290(20)	-56(13)	158(14)	-35(9)
C(47)	90(10)	192(15)	262(19)	-77(13)	118(12)	-17(9)
C(48)	97(10)	238(17)	233(17)	-59(13)	121(12)	-16(11)
C(49)	78(8)	122(9)	208(14)	-40(9)	107(10)	-26(7)
C(50)	130(12)	266(19)	220(17)	-56(14)	139(13)	-30(12)
C(51)	131(13)	290(20)	270(20)	-86(16)	165(15)	-52(14)
C(52)	97(10)	105(9)	131(12)	-9(9)	80(10)	11(8)
C(53)	87(9)	145(12)	201(15)	-120(12)	89(10)	-60(8)
C(54)	107(10)	162(13)	192(14)	-132(11)	89(10)	-62(9)
C(55)	224(17)	176(15)	216(16)	-136(13)	153(14)	-92(13)
C(56)	229(18)	187(16)	280(20)	-161(16)	166(17)	-116(14)
C(57)	144(13)	174(15)	173(14)	-118(12)	81(11)	-44(11)
C(58)	187(16)	250(20)	218(17)	-177(16)	129(14)	-79(14)
C(59)	197(15)	201(16)	214(16)	-142(13)	151(14)	-89(12)
C(60)	175(15)	217(17)	213(18)	-152(15)	94(14)	-38(13)
C(61)	188(16)	205(16)	176(15)	-135(13)	96(13)	-44(12)
C(62)	177(16)	188(16)	200(16)	-121(13)	100(14)	-62(13)
C(63)	171(16)	246(19)	202(16)	-155(15)	107(14)	-81(14)
C(64)	183(17)	224(19)	237(19)	-166(15)	123(15)	-78(14)
C(65)	182(16)	235(18)	206(16)	-160(15)	112(14)	-59(14)
C(66)	230(19)	239(19)	211(17)	-191(15)	113(15)	-137(15)
C(67)	230(20)	226(19)	229(19)	-119(15)	157(17)	-59(16)
C(68)	320(30)	450(40)	390(40)	-230(30)	270(30)	-160(30)
C(69)	370(30)	350(30)	470(40)	-200(30)	340(30)	-140(30)
C(70)	182(16)	194(16)	177(16)	-157(14)	54(13)	-55(12)
C(71)	205(16)	178(14)	148(13)	-125(12)	85(12)	-51(12)
C(72)	142(12)	128(12)	106(10)	-63(9)	50(9)	-24(9)
C(73)	195(15)	138(12)	111(10)	-61(9)	81(10)	-35(11)

C(74)	195(14)	112(10)	115(10)	-58(8)	99(10)	-51(9)
C(75)	98(8)	74(7)	82(7)	-30(6)	43(6)	-5(6)
C(76)	150(12)	120(10)	139(11)	-69(9)	92(10)	-43(9)
C(77)	191(15)	117(11)	123(11)	-51(9)	69(11)	-54(10)
C(78)	71(7)	66(7)	74(7)	-19(6)	38(6)	7(5)
C(79)	108(12)	148(13)	151(13)	90(11)	57(11)	45(11)
C(80)	118(12)	178(15)	192(16)	116(13)	44(12)	49(12)
C(81)	178(16)	155(15)	155(14)	63(12)	27(12)	34(13)
C(82)	290(30)	162(16)	179(18)	95(14)	22(17)	48(17)
C(83)	330(30)	260(20)	280(20)	230(20)	80(20)	120(20)
C(84)	280(30)	370(30)	410(40)	290(30)	10(30)	90(20)
C(85)	220(20)	320(30)	400(30)	270(30)	40(20)	60(20)
C(86)	260(30)	270(30)	370(30)	180(20)	80(20)	50(20)
C(87)	330(30)	280(30)	280(30)	140(20)	170(20)	90(20)
C(88)	290(30)	260(20)	260(20)	216(19)	120(20)	170(20)
C(89)	260(30)	280(30)	330(30)	200(20)	110(20)	130(20)
C(90)	290(30)	290(30)	300(30)	190(20)	80(20)	160(20)
C(91)	290(30)	250(20)	207(19)	166(17)	93(19)	150(20)
C(92)	260(30)	300(30)	300(30)	200(20)	110(20)	120(20)
C(93)	300(30)	280(20)	280(30)	170(20)	80(20)	180(20)
C(94)	570(60)	660(70)	750(80)	240(60)	400(50)	-210(50)
C(95)	490(60)	650(70)	670(70)	290(50)	340(50)	-100(50)
C(96)	280(30)	320(30)	170(20)	64(19)	85(19)	150(20)
C(97)	360(40)	320(30)	200(30)	80(20)	110(20)	120(30)
C(98)	330(30)	210(19)	167(15)	165(15)	122(17)	154(19)
C(99)	210(19)	320(30)	240(20)	220(20)	83(16)	127(18)
C(100)	178(17)	250(20)	260(20)	168(18)	118(16)	61(16)
C(101)	141(13)	168(14)	150(13)	92(11)	76(11)	35(11)
C(102)	233(19)	187(17)	197(16)	106(14)	132(15)	75(15)
C(103)	270(20)	199(17)	185(17)	140(14)	129(16)	104(16)
C(104)	120(13)	174(15)	202(16)	115(13)	108(13)	60(12)
C(105)	101(9)	80(8)	63(7)	15(6)	32(6)	-9(6)
C(106)	172(13)	106(10)	109(10)	34(8)	89(9)	10(9)
C(107)	340(20)	148(13)	165(13)	87(11)	188(16)	109(14)
C(108)	370(30)	230(20)	197(16)	118(16)	210(18)	115(19)
C(109)	310(20)	156(15)	166(15)	107(13)	138(15)	108(14)
C(110)	280(20)	154(14)	176(16)	97(13)	131(16)	78(13)
C(111)	211(16)	124(12)	152(12)	69(10)	114(12)	50(11)
C(112)	420(30)	230(20)	230(20)	159(18)	190(20)	110(20)
C(113)	490(40)	250(20)	220(20)	170(20)	170(20)	110(20)
C(114)	580(40)	260(30)	260(20)	190(20)	270(20)	130(20)
C(115)	590(40)	280(30)	300(30)	180(20)	240(30)	140(30)
C(116)	550(40)	260(30)	290(30)	200(20)	280(30)	200(20)
C(117)	520(30)	180(19)	230(20)	153(17)	210(20)	80(20)
C(118)	620(40)	240(30)	300(30)	170(20)	280(30)	140(30)

C(119)	700(40)	280(30)	350(30)	220(20)	350(30)	230(30)
C(120)	600(70)	880(90)	670(80)	20(70)	370(60)	70(60)
C(121)	690(70)	690(70)	440(50)	70(50)	430(50)	180(50)
C(122)	440(30)	310(30)	240(30)	150(20)	210(30)	100(20)
C(123)	390(30)	280(20)	230(20)	130(20)	190(20)	70(20)
C(124)	320(20)	191(18)	199(18)	127(15)	169(17)	92(16)
C(125)	290(20)	240(20)	180(16)	105(16)	159(16)	68(17)
C(126)	300(20)	177(15)	123(12)	87(11)	128(14)	81(14)
C(127)	199(14)	137(12)	107(10)	54(9)	105(10)	50(10)
C(128)	271(19)	133(12)	154(13)	74(11)	136(14)	82(12)
C(129)	300(20)	198(18)	177(17)	115(15)	128(17)	104(16)
Zn(1)	41(1)	50(1)	63(1)	-5(1)	30(1)	-2(1)
C(130)	105(9)	85(8)	97(9)	31(7)	62(8)	18(7)
C(131)	45(5)	73(7)	71(6)	2(5)	37(5)	-9(5)
C(132)	55(6)	72(6)	100(7)	-6(5)	50(5)	-2(5)
C(133)	100(9)	79(8)	227(14)	32(8)	121(10)	13(6)
C(134)	108(9)	94(9)	263(16)	40(9)	141(11)	30(7)
C(135)	79(7)	85(7)	139(9)	6(7)	75(7)	-1(6)
C(136)	105(9)	78(7)	217(13)	-7(8)	128(10)	-12(6)
C(137)	89(8)	70(7)	196(12)	2(7)	108(8)	-2(6)
C(138)	81(8)	95(8)	185(12)	-7(8)	94(9)	-5(6)
C(139)	159(13)	104(11)	380(20)	53(12)	208(16)	28(9)
C(140)	181(15)	114(12)	440(30)	69(14)	245(17)	55(10)
C(141)	139(13)	145(13)	310(20)	46(13)	154(14)	41(10)
C(142)	145(13)	159(14)	430(30)	24(16)	230(16)	-2(11)
C(143)	148(13)	208(18)	460(30)	104(18)	238(17)	50(12)
C(144)	210(19)	300(30)	640(40)	180(30)	330(20)	88(18)
C(145)	250(20)	240(20)	690(40)	210(20)	370(20)	100(17)
C(147)	440(40)	450(50)	1020(80)	200(50)	540(50)	220(40)
C(146)	420(40)	270(30)	760(60)	70(30)	460(40)	150(30)
C(148)	175(16)	214(19)	500(30)	114(19)	260(20)	88(13)
C(149)	270(20)	300(30)	690(40)	120(30)	390(30)	70(20)
C(150)	208(19)	300(20)	610(40)	70(30)	330(20)	55(18)
C(151)	125(14)	370(30)	460(30)	130(30)	212(19)	67(15)
C(152)	130(14)	350(30)	390(30)	120(20)	185(18)	53(16)
C(153)	113(11)	192(14)	300(20)	70(14)	159(14)	11(10)
C(154)	198(18)	420(30)	420(30)	-10(30)	270(20)	-48(18)
C(155)	230(20)	490(40)	540(40)	-60(30)	320(30)	-40(20)
C(156)	121(13)	128(12)	290(20)	22(15)	151(16)	59(11)
Zn(2)	48(1)	79(1)	102(1)	-17(1)	35(1)	1(1)
O(1)	29(3)	49(3)	65(3)	-3(3)	28(2)	2(2)
O(2)	36(3)	54(3)	57(3)	-7(3)	25(2)	1(2)
O(3)	70(4)	72(4)	75(4)	-33(3)	24(4)	-11(3)
O(4)	70(5)	146(7)	140(7)	-90(6)	23(5)	-15(5)
O(5)	105(7)	161(9)	164(8)	-99(7)	19(6)	2(6)

O(6)	143(10)	256(14)	351(17)	-202(13)	125(11)	-54(10)
O(7)	90(6)	145(8)	226(10)	-124(7)	54(7)	-22(5)
O(8)	62(4)	66(4)	81(4)	-24(3)	25(4)	-10(3)
O(9)	61(4)	69(4)	149(6)	-11(4)	70(4)	-1(3)
O(10)	61(4)	67(4)	124(5)	-5(4)	66(4)	-4(3)
O(11)	251(15)	235(15)	650(30)	-215(18)	350(20)	-105(12)
O(12)	164(9)	173(10)	354(15)	-75(10)	204(11)	-42(8)
O(13)	87(6)	166(8)	119(7)	-13(6)	75(6)	-1(6)
O(14)	65(5)	132(7)	155(8)	-15(6)	68(5)	-5(4)
O(15)	114(6)	118(6)	129(7)	-73(5)	74(6)	-30(5)
O(16)	154(8)	200(10)	219(10)	-147(9)	137(8)	-73(8)
O(17)	260(16)	309(17)	354(19)	-226(15)	211(15)	-178(14)
O(18)	224(14)	280(16)	261(14)	-194(12)	145(12)	-115(11)
O(19)	138(7)	84(5)	87(5)	-34(4)	71(5)	-31(5)
O(20)	85(5)	81(5)	81(5)	-23(4)	51(4)	-18(3)
O(21)	94(6)	100(5)	78(5)	24(4)	31(4)	33(5)
O(22)	101(7)	179(10)	293(14)	153(10)	86(8)	65(7)
O(23)	320(30)	440(30)	470(30)	230(30)	180(30)	150(20)
O(24)	310(20)	500(40)	490(30)	260(30)	120(30)	160(30)
O(27)	88(5)	71(4)	71(4)	23(3)	45(4)	12(3)
O(28)	177(8)	88(5)	98(5)	17(4)	98(6)	33(5)
O(29)	770(50)	370(30)	520(40)	220(30)	390(40)	320(30)
O(30)	770(50)	360(30)	360(30)	200(20)	370(30)	280(30)
O(31)	154(10)	262(14)	239(12)	177(11)	134(9)	120(10)
O(32)	144(8)	132(7)	142(8)	67(6)	91(7)	53(7)
O(33)	97(7)	182(10)	218(11)	-4(8)	110(8)	-1(6)
O(34)	126(8)	194(10)	228(12)	-16(9)	148(9)	-11(8)
O(35)	48(3)	68(4)	104(5)	9(3)	50(3)	2(3)
O(36)	70(4)	69(4)	115(5)	-3(4)	67(4)	1(3)
O(37)	390(20)	410(30)	1010(50)	410(30)	570(30)	210(20)
O(38)	232(13)	200(13)	590(30)	31(15)	327(17)	3(11)
O(39)	95(5)	86(5)	72(4)	22(4)	48(4)	8(4)
O(40)	173(8)	127(7)	120(6)	53(5)	108(6)	54(6)
Zn(3)	89(1)	80(1)	96(1)	3(1)	70(1)	9(1)
Zn(4)	52(1)	51(1)	74(1)	-4(1)	39(1)	0(1)
Zn(5)	43(1)	91(1)	89(1)	-24(1)	20(1)	5(1)
Zn(6)	40(1)	49(1)	57(1)	-6(1)	27(1)	-2(1)
Zn(7)	74(1)	71(1)	78(1)	-11(1)	52(1)	-8(1)
Zn(8)	47(1)	50(1)	61(1)	-2(1)	31(1)	2(1)

Table AA 16. Hydrogen coordinates (x 10^4) and isotropic displacement parameters ($Å^2$ x 10^3) for Zn-PVDC-1.

	x	y	z	U(eq)
H(3A)	10883	7093	8590	162
H(4A)	10383	6659	8126	163
H(6A)	8805	7246	7674	258
H(7A)	9305	7680	8138	238
H(8A)	9463	6426	7580	205
H(9A)	8405	6804	7296	187
H(11A)	9119	6102	7090	218
H(14A)	6980	5984	6440	144
H(16A)	6579	6772	6728	361
H(16B)	6569	6340	6685	361
H(16C)	6597	6599	6410	361
H(17A)	9462	5466	6622	525
H(17B)	9590	5655	6977	525
H(17C)	9344	5893	6626	525
H(18A)	7734	5285	6237	152
H(19A)	6624	5563	6031	137
H(21A)	5707	5214	5579	128
H(22A)	5247	4732	5165	124
H(24A)	6927	4363	5462	210
H(25A)	7388	4846	5877	222
H(29A)	13105	7802	9338	123
H(30A)	13997	7767	9338	139
H(32A)	14078	8881	9332	174
H(33A)	13186	8917	9332	155
H(34A)	14800	8049	9306	139
H(35A)	14956	8780	9416	191
H(37A)	15469	8010	9169	164
H(40A)	16915	8963	9661	271
H(44A)	17211	8292	9187	190
H(45A)	17794	8780	9726	262
H(42A)	16253	7351	8989	427
H(42B)	15662	7583	8880	427
H(42C)	16119	7455	9283	427
H(43A)	16439	9451	10148	560
H(43B)	16616	9452	9862	560
H(43C)	16914	9159	10178	560
H(47A)	17792	8503	8957	205
H(48A)	18644	8448	8918	208
H(50A)	19778	8633	9992	220
H(51A)	18926	8687	10031	242
H(55A)	12449	9792	10015	226
H(56A)	12834	10275	10432	265
H(58A)	12112	9805	10941	252

H(59A)	11726	9322	10524	221
H(60A)	13031	10562	10971	251
H(61A)	12367	10343	11213	231
H(63A)	13596	10956	11435	246
H(66A)	12702	11159	12083	278
H(68A)	14758	11587	11778	512
H(68B)	14143	11410	11456	512
H(68C)	14622	11164	11788	512
H(69A)	11380	10663	11640	505
H(69B)	11684	11057	11711	505
H(69C)	12030	10739	11997	505
H(70A)	13929	11780	12326	251
H(71A)	13299	11479	12574	221
H(73A)	14198	12278	12654	180
H(74A)	14589	12717	13114	160
H(76A)	13892	12139	13585	156
H(77A)	13501	11700	13125	184
H(81A)	5520	2024	5116	238
H(82A)	6112	1567	5539	324
H(84A)	7651	2167	5888	542
H(85A)	7059	2624	5464	463
H(86A)	7834	1655	6170	419
H(87A)	6916	1225	6032	358
H(90A)	7683	364	6877	409
H(93A)	8635	1283	6617	400
H(94A)	9973	1182	6915	966
H(94B)	9449	1411	6904	966
H(94C)	9281	1134	6589	966
H(95A)	6177	512	6389	887
H(95B)	6788	531	6780	887
H(95C)	6737	252	6492	887
H(96A)	8585	29	7212	339
H(97A)	9495	454	7665	380
H(99A)	8741	-432	7666	334
H(10A)	9281	-851	8140	278
H(10B)	10855	-283	8504	239
H(10C)	10315	136	8030	258
H(10D)	4493	4223	3134	231
H(10E)	4141	4701	2713	287
H(11B)	3594	5268	3270	243
H(11C)	3946	4790	3691	186
H(11D)	3428	5553	2737	347
H(11E)	3791	5185	2368	398
H(11F)	3093	6062	2409	473
H(11G)	3354	5931	1458	448

H(12A)	4587	5101	2104	1066
H(12B)	4634	5378	2391	1066
H(12C)	4693	5526	2078	1066
H(12D)	2282	6818	2241	814
H(12E)	2881	6582	2493	814
H(12F)	2245	6384	2230	814
H(12G)	2528	6770	1448	380
H(12H)	3019	6462	1130	350
H(12I)	2164	7282	1081	265
H(12J)	1784	7724	624	230
H(12K)	2370	7108	114	212
H(12L)	2749	6666	571	275
H(13A)	2994	3878	4257	143
H(13B)	2082	3832	4235	162
H(13C)	2393	2743	4463	136
H(13D)	3305	2788	4484	123
H(13E)	1493	3007	4396	131
H(13F)	1303	3732	4256	221
H(14B)	717	2926	4422	216
H(14C)	-576	3949	4097	404
H(14D)	100	4588	3934	848
H(14E)	169	4427	4284	848
H(14F)	-421	4334	3899	848
H(14G)	-97	2287	4588	624
H(14H)	509	2524	4750	624
H(14I)	130	2407	4339	624
H(14J)	-954	3207	4469	309
H(14K)	-1450	3802	4071	425
H(15A)	-1447	3490	4818	351
H(15B)	-2316	3455	4842	318
H(15C)	-3412	3526	3754	358
H(15D)	-2543	3562	3730	431

Table AA 17. Torsion angles (°) for Zn-PVDC-1.

O(3)-C(1)-C(2)-C(3)	1.8(14)
O(4)-C(1)-C(2)-C(3)	-176.0(9)
O(3)-C(1)-C(2)-C(7)	-178.1(9)
O(4)-C(1)-C(2)-C(7)	4.1(14)
C(7)-C(2)-C(3)-C(4)	0

C(1)-C(2)-C(3)-C(4)	-179.9(10)
C(2)-C(3)-C(4)-C(5)	0
C(3)-C(4)-C(5)-C(6)	0
C(3)-C(4)-C(5)-C(8)	-177.1(13)
C(4)-C(5)-C(6)-C(7)	0
C(8)-C(5)-C(6)-C(7)	177.1(13)
C(5)-C(6)-C(7)-C(2)	0
C(3)-C(2)-C(7)-C(6)	0
C(1)-C(2)-C(7)-C(6)	179.9(10)
C(6)-C(5)-C(8)-C(9)	0(3)
C(4)-C(5)-C(8)-C(9)	176.7(17)
C(5)-C(8)-C(9)-C(10)	179.1(16)
C(8)-C(9)-C(10)-C(11)	-17(2)
C(8)-C(9)-C(10)-C(15)	160.6(17)
C(15)-C(10)-C(11)-C(12)	0
C(9)-C(10)-C(11)-C(12)	177.5(12)
C(10)-C(11)-C(12)-O(6)	173.9(15)
C(10)-C(11)-C(12)-C(13)	0
O(6)-C(12)-C(13)-C(14)	-174.3(14)
C(11)-C(12)-C(13)-C(14)	0
O(6)-C(12)-C(13)-C(18)	8.1(14)
C(11)-C(12)-C(13)-C(18)	-177.6(10)
C(12)-C(13)-C(14)-C(15)	0
C(18)-C(13)-C(14)-C(15)	177.5(11)
C(13)-C(14)-C(15)-O(5)	173.6(12)
C(13)-C(14)-C(15)-C(10)	0
C(11)-C(10)-C(15)-O(5)	-174.1(11)
C(9)-C(10)-C(15)-O(5)	8.3(13)
C(11)-C(10)-C(15)-C(14)	0
C(9)-C(10)-C(15)-C(14)	-177.6(12)
C(14)-C(13)-C(18)-C(19)	7(2)
C(12)-C(13)-C(18)-C(19)	-175.1(13)
C(13)-C(18)-C(19)-C(20)	-178.6(11)
C(18)-C(19)-C(20)-C(21)	178.2(12)
C(18)-C(19)-C(20)-C(25)	-3.6(18)
C(25)-C(20)-C(21)-C(22)	0
C(19)-C(20)-C(21)-C(22)	178.3(9)
C(20)-C(21)-C(22)-C(23)	0
C(21)-C(22)-C(23)-C(24)	0
C(21)-C(22)-C(23)-C(26)	-179.5(9)
C(22)-C(23)-C(24)-C(25)	0
C(26)-C(23)-C(24)-C(25)	179.5(9)
C(23)-C(24)-C(25)-C(20)	0
C(21)-C(20)-C(25)-C(24)	0
C(19)-C(20)-C(25)-C(24)	-178.3(9)

C(24)-C(23)-C(26)-O(8)	-173.9(9)
C(22)-C(23)-C(26)-O(8)	5.6(14)
C(24)-C(23)-C(26)-O(7)	0.4(15)
C(22)-C(23)-C(26)-O(7)	179.9(10)
O(10)-C(27)-C(28)-C(29)	1.8(11)
O(9)-C(27)-C(28)-C(29)	-176.6(7)
O(10)-C(27)-C(28)-C(33)	-178.6(7)
O(9)-C(27)-C(28)-C(33)	3.1(11)
C(33)-C(28)-C(29)-C(30)	0
C(27)-C(28)-C(29)-C(30)	179.6(8)
C(28)-C(29)-C(30)-C(31)	0
C(29)-C(30)-C(31)-C(32)	0
C(29)-C(30)-C(31)-C(34)	178.6(9)
C(30)-C(31)-C(32)-C(33)	0
C(34)-C(31)-C(32)-C(33)	-178.5(10)
C(31)-C(32)-C(33)-C(28)	0
C(29)-C(28)-C(33)-C(32)	0
C(27)-C(28)-C(33)-C(32)	-179.6(8)
C(32)-C(31)-C(34)-C(35)	9.4(19)
C(30)-C(31)-C(34)-C(35)	-169.1(14)
C(31)-C(34)-C(35)-C(36)	176.4(13)
C(34)-C(35)-C(36)-C(37)	23(2)
C(34)-C(35)-C(36)-C(41)	-163.4(15)
C(41)-C(36)-C(37)-C(38)	0
C(35)-C(36)-C(37)-C(38)	173.7(12)
C(36)-C(37)-C(38)-O(12)	173.7(12)
C(36)-C(37)-C(38)-C(39)	0
O(12)-C(38)-C(39)-C(40)	-174.2(11)
C(37)-C(38)-C(39)-C(40)	0
O(12)-C(38)-C(39)-C(44)	10.8(14)
C(37)-C(38)-C(39)-C(44)	-174.9(12)
C(38)-C(39)-C(40)-C(41)	0
C(44)-C(39)-C(40)-C(41)	174.8(13)
C(39)-C(40)-C(41)-O(11)	165.3(15)
C(39)-C(40)-C(41)-C(36)	0
C(37)-C(36)-C(41)-O(11)	-166.3(14)
C(35)-C(36)-C(41)-O(11)	20.1(16)
C(37)-C(36)-C(41)-C(40)	0
C(35)-C(36)-C(41)-C(40)	-173.6(12)
C(40)-C(39)-C(44)-C(45)	23(2)
C(38)-C(39)-C(44)-C(45)	-161.7(18)
C(39)-C(44)-C(45)-C(46)	-180.0(15)
C(44)-C(45)-C(46)-C(47)	31(3)
C(44)-C(45)-C(46)-C(51)	-146.7(19)
C(51)-C(46)-C(47)-C(48)	0

C(45)-C(46)-C(47)-C(48)	-177.3(12)
C(46)-C(47)-C(48)-C(49)	0
C(47)-C(48)-C(49)-C(50)	0
C(47)-C(48)-C(49)-C(52)	-179.0(10)
C(48)-C(49)-C(50)-C(51)	0
C(52)-C(49)-C(50)-C(51)	179.1(9)
C(49)-C(50)-C(51)-C(46)	0
C(47)-C(46)-C(51)-C(50)	0
C(45)-C(46)-C(51)-C(50)	177.4(12)
C(48)-C(49)-C(52)-O(13)	-175.4(10)
C(50)-C(49)-C(52)-O(13)	5.5(15)
C(48)-C(49)-C(52)-O(14)	0.8(14)
C(50)-C(49)-C(52)-O(14)	-178.3(8)
O(15)-C(53)-C(54)-C(55)	-1.0(19)
O(16)-C(53)-C(54)-C(55)	-178.0(11)
O(15)-C(53)-C(54)-C(59)	178.7(12)
O(16)-C(53)-C(54)-C(59)	1.6(18)
C(59)-C(54)-C(55)-C(56)	0
C(53)-C(54)-C(55)-C(56)	179.7(11)
C(54)-C(55)-C(56)-C(57)	0
C(55)-C(56)-C(57)-C(58)	0
C(55)-C(56)-C(57)-C(60)	-179.1(13)
C(56)-C(57)-C(58)-C(59)	0
C(60)-C(57)-C(58)-C(59)	179.1(13)
C(57)-C(58)-C(59)-C(54)	0
C(55)-C(54)-C(59)-C(58)	0
C(53)-C(54)-C(59)-C(58)	-179.7(12)
C(58)-C(57)-C(60)-C(61)	-10(3)
C(56)-C(57)-C(60)-C(61)	169(2)
C(57)-C(60)-C(61)-C(62)	176.2(17)
C(60)-C(61)-C(62)-C(63)	-11(3)
C(60)-C(61)-C(62)-C(67)	172(2)
C(67)-C(62)-C(63)-C(64)	0
C(61)-C(62)-C(63)-C(64)	-177.8(15)
C(62)-C(63)-C(64)-O(18)	-174.7(17)
C(62)-C(63)-C(64)-C(65)	0
O(18)-C(64)-C(65)-C(66)	174.9(17)
C(63)-C(64)-C(65)-C(66)	0
O(18)-C(64)-C(65)-C(70)	-6.2(17)
C(63)-C(64)-C(65)-C(70)	179.0(16)
C(64)-C(65)-C(66)-C(67)	0
C(70)-C(65)-C(66)-C(67)	-179.0(15)
C(65)-C(66)-C(67)-C(62)	0
C(65)-C(66)-C(67)-O(17)	-168.9(18)
C(63)-C(62)-C(67)-C(66)	0

C(61)-C(62)-C(67)-C(66)	177.8(15)
C(63)-C(62)-C(67)-O(17)	169.3(17)
C(61)-C(62)-C(67)-O(17)	-12.9(18)
C(66)-C(65)-C(70)-C(71)	14(3)
C(64)-C(65)-C(70)-C(71)	-164.6(19)
C(65)-C(70)-C(71)-C(72)	-177.4(16)
C(70)-C(71)-C(72)-C(73)	9(3)
C(70)-C(71)-C(72)-C(77)	-170.2(18)
C(77)-C(72)-C(73)-C(74)	0
C(71)-C(72)-C(73)-C(74)	-178.8(12)
C(72)-C(73)-C(74)-C(75)	0
C(73)-C(74)-C(75)-C(76)	0
C(73)-C(74)-C(75)-C(78)	-179.5(8)
C(74)-C(75)-C(76)-C(77)	0
C(78)-C(75)-C(76)-C(77)	179.5(8)
C(75)-C(76)-C(77)-C(72)	0
C(73)-C(72)-C(77)-C(76)	0
C(71)-C(72)-C(77)-C(76)	178.9(11)
C(74)-C(75)-C(78)-O(20)	-173.7(7)
C(76)-C(75)-C(78)-O(20)	6.7(12)
C(74)-C(75)-C(78)-O(19)	3.9(11)
C(76)-C(75)-C(78)-O(19)	-175.7(7)
O(21)-C(79)-C(80)-C(81)	10(2)
O(22)-C(79)-C(80)-C(81)	-170.2(15)
O(21)-C(79)-C(80)-C(85)	-176.9(15)
O(22)-C(79)-C(80)-C(85)	3(2)
C(85)-C(80)-C(81)-C(82)	0
C(79)-C(80)-C(81)-C(82)	173.2(16)
C(80)-C(81)-C(82)-C(83)	0
C(81)-C(82)-C(83)-C(84)	0
C(81)-C(82)-C(83)-C(86)	178(3)
C(82)-C(83)-C(84)-C(85)	0
C(86)-C(83)-C(84)-C(85)	-178(2)
C(83)-C(84)-C(85)-C(80)	0
C(81)-C(80)-C(85)-C(84)	0
C(79)-C(80)-C(85)-C(84)	-173.0(17)
C(84)-C(83)-C(86)-C(87)	175(4)
C(82)-C(83)-C(86)-C(87)	-3(7)
C(83)-C(86)-C(87)-C(88)	-176(3)
C(86)-C(87)-C(88)-C(89)	171(4)
C(86)-C(87)-C(88)-C(93)	-11(6)
C(93)-C(88)-C(89)-C(90)	0
C(87)-C(88)-C(89)-C(90)	177(2)
C(93)-C(88)-C(89)-O(23)	172(3)
C(87)-C(88)-C(89)-O(23)	-11(3)

C(88)-C(89)-C(90)-C(91)	0
O(23)-C(89)-C(90)-C(91)	-172(3)
C(89)-C(90)-C(91)-C(92)	0
C(89)-C(90)-C(91)-C(96)	-176.6(19)
C(90)-C(91)-C(92)-C(93)	0
C(96)-C(91)-C(92)-C(93)	176(2)
C(90)-C(91)-C(92)-O(24)	-163(3)
C(96)-C(91)-C(92)-O(24)	13(3)
C(91)-C(92)-C(93)-C(88)	0
O(24)-C(92)-C(93)-C(88)	166(2)
C(89)-C(88)-C(93)-C(92)	0
C(87)-C(88)-C(93)-C(92)	-177(3)
C(92)-C(91)-C(96)-C(97)	37(5)
C(90)-C(91)-C(96)-C(97)	-146(4)
C(91)-C(96)-C(97)-C(98)	-180(2)
C(96)-C(97)-C(98)-C(99)	-32(5)
C(96)-C(97)-C(98)-C(103)	159(4)
C(103)-C(98)-C(99)-C(100)	0
C(97)-C(98)-C(99)-C(100)	-168(2)
C(98)-C(99)-C(100)-C(101)	0
C(99)-C(100)-C(101)-C(102)	0
C(99)-C(100)-C(101)-C(104)	176.8(14)
C(100)-C(101)-C(102)-C(103)	0
C(104)-C(101)-C(102)-C(103)	-176.7(14)
C(101)-C(102)-C(103)-C(98)	0
C(99)-C(98)-C(103)-C(102)	0
C(97)-C(98)-C(103)-C(102)	170.9(16)
C(102)-C(101)-C(104)-O(32)	-8(2)
C(100)-C(101)-C(104)-O(32)	175.0(13)
C(102)-C(101)-C(104)-O(31)	178.3(13)
C(100)-C(101)-C(104)-O(31)	2(2)
O(28)-C(105)-C(106)-C(107)	2.1(14)
O(27)-C(105)-C(106)-C(107)	-178.2(8)
O(28)-C(105)-C(106)-C(111)	-177.8(9)
O(27)-C(105)-C(106)-C(111)	2.0(14)
C(111)-C(106)-C(107)-C(108)	0
C(105)-C(106)-C(107)-C(108)	-179.8(10)
C(106)-C(107)-C(108)-C(109)	0
C(107)-C(108)-C(109)-C(110)	0
C(107)-C(108)-C(109)-C(112)	178.5(19)
C(108)-C(109)-C(110)-C(111)	0
C(112)-C(109)-C(110)-C(111)	-178.6(18)
C(109)-C(110)-C(111)-C(106)	0
C(107)-C(106)-C(111)-C(110)	0
C(105)-C(106)-C(111)-C(110)	179.8(11)

C(110)-C(109)-C(112)-C(113)	177(3)
C(108)-C(109)-C(112)-C(113)	-1(4)
C(109)-C(112)-C(113)-C(114)	-175(2)
C(112)-C(113)-C(114)-C(115)	-10(5)
C(112)-C(113)-C(114)-C(119)	-179(3)
C(119)-C(114)-C(115)-C(116)	0
C(113)-C(114)-C(115)-C(116)	-169(3)
C(114)-C(115)-C(116)-O(30)	-179.9(9)
C(114)-C(115)-C(116)-C(117)	0
O(30)-C(116)-C(117)-C(118)	179.9(9)
C(115)-C(116)-C(117)-C(118)	0
O(30)-C(116)-C(117)-C(122)	3(2)
C(115)-C(116)-C(117)-C(122)	-177(2)
C(116)-C(117)-C(118)-C(119)	0
C(122)-C(117)-C(118)-C(119)	177(3)
C(117)-C(118)-C(119)-O(29)	179.9(8)
C(117)-C(118)-C(119)-C(114)	0
C(115)-C(114)-C(119)-O(29)	-179.9(8)
C(113)-C(114)-C(119)-O(29)	-9(2)
C(115)-C(114)-C(119)-C(118)	0
C(113)-C(114)-C(119)-C(118)	170(2)
C(116)-C(117)-C(122)-C(123)	175(4)
C(118)-C(117)-C(122)-C(123)	-2(5)
C(117)-C(122)-C(123)-C(124)	174(3)
C(122)-C(123)-C(124)-C(125)	11(5)
C(122)-C(123)-C(124)-C(129)	-171(4)
C(129)-C(124)-C(125)-C(126)	0
C(123)-C(124)-C(125)-C(126)	178(2)
C(124)-C(125)-C(126)-C(127)	0
C(125)-C(126)-C(127)-C(128)	0
C(125)-C(126)-C(127)-C(130)	176.4(12)
C(126)-C(127)-C(128)-C(129)	0
C(130)-C(127)-C(128)-C(129)	-176.4(12)
C(127)-C(128)-C(129)-C(124)	0
C(125)-C(124)-C(129)-C(128)	0
C(123)-C(124)-C(129)-C(128)	-177.8(18)
C(128)-C(127)-C(130)-O(39)	-2.6(15)
C(126)-C(127)-C(130)-O(39)	-178.9(9)
C(128)-C(127)-C(130)-O(40)	-178.4(10)
C(126)-C(127)-C(130)-O(40)	5.2(15)
O(36)-C(131)-C(132)-C(133)	-171.8(7)
O(35)-C(131)-C(132)-C(133)	6.6(10)
O(36)-C(131)-C(132)-C(137)	7.7(10)
O(35)-C(131)-C(132)-C(137)	-174.0(6)
C(137)-C(132)-C(133)-C(134)	0

C(131)-C(132)-C(133)-C(134)	179.5(7)
C(132)-C(133)-C(134)-C(135)	0
C(133)-C(134)-C(135)-C(136)	0
C(133)-C(134)-C(135)-C(138)	178.3(9)
C(134)-C(135)-C(136)-C(137)	0
C(138)-C(135)-C(136)-C(137)	-178.4(8)
C(135)-C(136)-C(137)-C(132)	0
C(133)-C(132)-C(137)-C(136)	0
C(131)-C(132)-C(137)-C(136)	-179.5(7)
C(134)-C(135)-C(138)-C(139)	2(2)
C(136)-C(135)-C(138)-C(139)	-179.9(15)
C(135)-C(138)-C(139)-C(140)	174.3(16)
C(138)-C(139)-C(140)-C(141)	13(3)
C(138)-C(139)-C(140)-C(145)	-175.1(18)
C(145)-C(140)-C(141)-C(142)	0
C(139)-C(140)-C(141)-C(142)	172.2(17)
C(140)-C(141)-C(142)-O(38)	176.1(18)
C(140)-C(141)-C(142)-C(143)	0
O(38)-C(142)-C(143)-C(144)	-176.6(15)
C(141)-C(142)-C(143)-C(144)	0
O(38)-C(142)-C(143)-C(148)	10(2)
C(141)-C(142)-C(143)-C(148)	-173.3(19)
C(142)-C(143)-C(144)-C(145)	0
C(148)-C(143)-C(144)-C(145)	173(2)
C(143)-C(144)-C(145)-O(37)	171(2)
C(143)-C(144)-C(145)-C(140)	0
C(141)-C(140)-C(145)-O(37)	-172(2)
C(139)-C(140)-C(145)-O(37)	16(2)
C(141)-C(140)-C(145)-C(144)	0
C(139)-C(140)-C(145)-C(144)	-172.1(17)
C(142)-C(143)-C(148)-C(149)	-166(3)
C(144)-C(143)-C(148)-C(149)	21(4)
C(143)-C(148)-C(149)-C(150)	177(3)
C(148)-C(149)-C(150)-C(151)	57(5)
C(148)-C(149)-C(150)-C(155)	-130(4)
C(155)-C(150)-C(151)-C(152)	0
C(149)-C(150)-C(151)-C(152)	172.8(19)
C(150)-C(151)-C(152)-C(153)	0
C(151)-C(152)-C(153)-C(154)	0
C(151)-C(152)-C(153)-C(156)	178.6(13)
C(152)-C(153)-C(154)-C(155)	0
C(156)-C(153)-C(154)-C(155)	-178.5(14)
C(153)-C(154)-C(155)-C(150)	0
C(151)-C(150)-C(155)-C(154)	0
C(149)-C(150)-C(155)-C(154)	-173.8(17)

C(154)-C(153)-C(156)-O(33)	-169.5(14)
C(152)-C(153)-C(156)-O(33)	12(2)
C(154)-C(153)-C(156)-O(34)	-2(2)
C(152)-C(153)-C(156)-O(34)	179.7(12)
O(1)-Zn(1)-Zn(2)-O(31)#2	67.4(6)
O(39)#1-Zn(1)-Zn(2)-O(31)#2	152.1(7)
O(10)-Zn(1)-Zn(2)-O(31)#2	-8.1(7)
O(3)-Zn(1)-Zn(2)-O(31)#2	-108.0(6)
Zn(4)-Zn(1)-Zn(2)-O(31)#2	32.9(6)
Zn(3)-Zn(1)-Zn(2)-O(31)#2	103.3(6)
O(39)#1-Zn(1)-Zn(2)-O(1)	84.7(4)
O(10)-Zn(1)-Zn(2)-O(1)	-75.5(3)
O(3)-Zn(1)-Zn(2)-O(1)	-175.4(3)
Zn(4)-Zn(1)-Zn(2)-O(1)	-34.5(2)
Zn(3)-Zn(1)-Zn(2)-O(1)	35.8(2)
O(1)-Zn(1)-Zn(2)-O(4)	-177.8(4)
O(39)#1-Zn(1)-Zn(2)-O(4)	-93.1(4)
O(10)-Zn(1)-Zn(2)-O(4)	106.7(4)
O(3)-Zn(1)-Zn(2)-O(4)	6.8(4)
Zn(4)-Zn(1)-Zn(2)-O(4)	147.7(3)
Zn(3)-Zn(1)-Zn(2)-O(4)	-142.0(3)
O(1)-Zn(1)-Zn(2)-O(14)#3	-80.4(4)
O(39)#1-Zn(1)-Zn(2)-O(14)#3	4.3(4)
O(10)-Zn(1)-Zn(2)-O(14)#3	-155.9(4)
O(3)-Zn(1)-Zn(2)-O(14)#3	104.2(4)
Zn(4)-Zn(1)-Zn(2)-O(14)#3	-114.9(3)
Zn(3)-Zn(1)-Zn(2)-O(14)#3	-44.6(3)
O(1)-Zn(1)-Zn(2)-Zn(4)	34.5(2)
O(39)#1-Zn(1)-Zn(2)-Zn(4)	119.2(3)
O(10)-Zn(1)-Zn(2)-Zn(4)	-41.0(2)
O(3)-Zn(1)-Zn(2)-Zn(4)	-140.9(2)
Zn(3)-Zn(1)-Zn(2)-Zn(4)	70.36(4)
O(39)#1-Zn(1)-O(1)-Zn(4)	123.0(3)
O(10)-Zn(1)-O(1)-Zn(4)	3.4(3)
O(3)-Zn(1)-O(1)-Zn(4)	-115.7(3)
Zn(2)-Zn(1)-O(1)-Zn(4)	-120.8(4)
Zn(3)-Zn(1)-O(1)-Zn(4)	119.5(3)
O(39)#1-Zn(1)-O(1)-Zn(2)	-116.3(3)
O(10)-Zn(1)-O(1)-Zn(2)	124.1(3)
O(3)-Zn(1)-O(1)-Zn(2)	5.0(3)
Zn(4)-Zn(1)-O(1)-Zn(2)	120.8(4)
Zn(3)-Zn(1)-O(1)-Zn(2)	-119.7(3)
O(39)#1-Zn(1)-O(1)-Zn(3)	3.5(3)
O(10)-Zn(1)-O(1)-Zn(3)	-116.1(3)
O(3)-Zn(1)-O(1)-Zn(3)	124.8(3)

Zn(2)-Zn(1)-O(1)-Zn(3)	119.7(3)
Zn(4)-Zn(1)-O(1)-Zn(3)	-119.5(3)
O(31)#2-Zn(2)-O(1)-Zn(1)	-129.0(5)
O(4)-Zn(2)-O(1)-Zn(1)	2.2(4)
O(14)#3-Zn(2)-O(1)-Zn(1)	117.6(3)
Zn(4)-Zn(2)-O(1)-Zn(1)	-120.8(3)
O(31)#2-Zn(2)-O(1)-Zn(4)	-8.2(5)
O(4)-Zn(2)-O(1)-Zn(4)	122.9(4)
O(14)#3-Zn(2)-O(1)-Zn(4)	-121.6(3)
Zn(1)-Zn(2)-O(1)-Zn(4)	120.8(3)
O(31)#2-Zn(2)-O(1)-Zn(3)	112.1(4)
O(4)-Zn(2)-O(1)-Zn(3)	-116.8(4)
O(14)#3-Zn(2)-O(1)-Zn(3)	-1.4(4)
Zn(1)-Zn(2)-O(1)-Zn(3)	-118.9(3)
Zn(4)-Zn(2)-O(1)-Zn(3)	120.3(3)
O(4)-C(1)-O(3)-Zn(1)	-2.3(16)
C(2)-C(1)-O(3)-Zn(1)	-179.9(7)
O(1)-Zn(1)-O(3)-C(1)	-7.5(9)
O(39)#1-Zn(1)-O(3)-C(1)	120.0(9)
O(10)-Zn(1)-O(3)-C(1)	-131.4(8)
Zn(2)-Zn(1)-O(3)-C(1)	-4.5(8)
Zn(4)-Zn(1)-O(3)-C(1)	-47.0(9)
Zn(3)-Zn(1)-O(3)-C(1)	32.5(9)
O(3)-C(1)-O(4)-Zn(2)	16(2)
C(2)-C(1)-O(4)-Zn(2)	-166.5(9)
O(31)#2-Zn(2)-O(4)-C(1)	108.5(13)
O(1)-Zn(2)-O(4)-C(1)	-15.2(14)
O(14)#3-Zn(2)-O(4)-C(1)	-134.1(13)
Zn(1)-Zn(2)-O(4)-C(1)	-13.9(12)
Zn(4)-Zn(2)-O(4)-C(1)	19.6(15)
C(14)-C(15)-O(5)-C(16)	-2.1(19)
C(10)-C(15)-O(5)-C(16)	171.7(14)
C(11)-C(12)-O(6)-C(17)	-11(3)
C(13)-C(12)-O(6)-C(17)	164(2)
O(8)-C(26)-O(7)-Zn(5)	-32(2)
C(23)-C(26)-O(7)-Zn(5)	154.2(10)
O(7)-C(26)-O(8)-Zn(6)	-2.5(18)
C(23)-C(26)-O(8)-Zn(6)	171.2(7)
O(10)-C(27)-O(9)-Zn(4)	3.0(15)
C(28)-C(27)-O(9)-Zn(4)	-178.8(6)
O(9)-C(27)-O(10)-Zn(1)	-2.8(15)
C(28)-C(27)-O(10)-Zn(1)	179.0(5)
O(1)-Zn(1)-O(10)-C(27)	-0.7(9)
O(39)#1-Zn(1)-O(10)-C(27)	-126.6(8)
O(3)-Zn(1)-O(10)-C(27)	125.6(8)

Zn(2)-Zn(1)-O(10)-C(27)	36.9(9)
Zn(4)-Zn(1)-O(10)-C(27)	1.2(7)
Zn(3)-Zn(1)-O(10)-C(27)	-40.0(9)
C(40)-C(41)-O(11)-C(43)	1(3)
C(36)-C(41)-O(11)-C(43)	167(2)
C(37)-C(38)-O(12)-C(42)	-8(2)
C(39)-C(38)-O(12)-C(42)	165.9(16)
O(14)-C(52)-O(13)-Zn(3)#4	2(2)
C(49)-C(52)-O(13)-Zn(3)#4	177.6(7)
O(13)-C(52)-O(14)-Zn(2)#4	-10(2)
C(49)-C(52)-O(14)-Zn(2)#4	174.5(7)
O(16)-C(53)-O(15)-Zn(4)	3(2)
C(54)-C(53)-O(15)-Zn(4)	-174.0(9)
O(15)-C(53)-O(16)-Zn(3)	15(3)
C(54)-C(53)-O(16)-Zn(3)	-167.5(10)
C(66)-C(67)-O(17)-C(69)	-3(3)
C(62)-C(67)-O(17)-C(69)	-172(2)
C(63)-C(64)-O(18)-C(68)	-11(3)
C(65)-C(64)-O(18)-C(68)	175(2)
O(20)-C(78)-O(19)-Zn(7)#5	2.2(16)
C(75)-C(78)-O(19)-Zn(7)#5	-175.3(6)
O(19)-C(78)-O(20)-Zn(8)#5	-3.8(15)
C(75)-C(78)-O(20)-Zn(8)#5	173.6(6)
O(22)-C(79)-O(21)-Zn(8)	-5(2)
C(80)-C(79)-O(21)-Zn(8)	175.0(12)
O(21)-C(79)-O(22)-Zn(5)	46(3)
C(80)-C(79)-O(22)-Zn(5)	-133.9(14)
C(90)-C(89)-O(23)-C(95)	-3(5)
C(88)-C(89)-O(23)-C(95)	-175(4)
C(91)-C(92)-O(24)-C(94)	168(4)
C(93)-C(92)-O(24)-C(94)	4(5)
O(28)-C(105)-O(27)-Zn(6)	7.5(16)
C(106)-C(105)-O(27)-Zn(6)	-172.2(6)
O(27)-C(105)-O(28)-Zn(7)	-10.1(19)
C(106)-C(105)-O(28)-Zn(7)	169.6(8)
C(118)-C(119)-O(29)-C(120)	105(7)
C(114)-C(119)-O(29)-C(120)	-75(7)
C(117)-C(116)-O(30)-C(121)	173(4)
C(115)-C(116)-O(30)-C(121)	-7(4)
O(32)-C(104)-O(31)-Zn(2)#6	-7(3)
C(101)-C(104)-O(31)-Zn(2)#6	166.0(12)
O(31)-C(104)-O(32)-Zn(4)#6	-8(3)
C(101)-C(104)-O(32)-Zn(4)#6	178.9(10)
O(34)-C(156)-O(33)-Zn(5)#3	16(3)
C(153)-C(156)-O(33)-Zn(5)#3	-179.0(9)

O(33)-C(156)-O(34)-Zn(7)#3	-11(3)
C(153)-C(156)-O(34)-Zn(7)#3	-177.8(8)
O(36)-C(131)-O(35)-Zn(6)	-7.6(14)
C(132)-C(131)-O(35)-Zn(6)	174.2(5)
O(35)-C(131)-O(36)-Zn(8)	-2.6(14)
C(132)-C(131)-O(36)-Zn(8)	175.6(5)
C(144)-C(145)-O(37)-C(147)	26(3)
C(140)-C(145)-O(37)-C(147)	-163(3)
C(143)-C(142)-O(38)-C(146)	178(2)
C(141)-C(142)-O(38)-C(146)	2(3)
O(40)-C(130)-O(39)-Zn(1)#7	-2.3(18)
C(127)-C(130)-O(39)-Zn(1)#7	-177.9(7)
O(39)-C(130)-O(40)-Zn(3)#7	-3(2)
C(127)-C(130)-O(40)-Zn(3)#7	172.2(9)
C(53)-O(16)-Zn(3)-O(13)#3	-137.6(16)
C(53)-O(16)-Zn(3)-O(40)#1	103.7(16)
C(53)-O(16)-Zn(3)-O(1)	-22.0(17)
C(53)-O(16)-Zn(3)-Zn(1)	11.0(18)
Zn(1)-O(1)-Zn(3)-O(16)	130.2(4)
Zn(4)-O(1)-Zn(3)-O(16)	10.1(4)
Zn(2)-O(1)-Zn(3)-O(16)	-110.8(4)
Zn(1)-O(1)-Zn(3)-O(13)#3	-122.3(3)
Zn(4)-O(1)-Zn(3)-O(13)#3	117.5(3)
Zn(2)-O(1)-Zn(3)-O(13)#3	-3.3(4)
Zn(1)-O(1)-Zn(3)-O(40)#1	-6.2(4)
Zn(4)-O(1)-Zn(3)-O(40)#1	-126.3(3)
Zn(2)-O(1)-Zn(3)-O(40)#1	112.8(4)
Zn(4)-O(1)-Zn(3)-Zn(1)	-120.1(3)
Zn(2)-O(1)-Zn(3)-Zn(1)	119.0(3)
O(1)-Zn(1)-Zn(3)-O(16)	-64.9(5)
O(39)#1-Zn(1)-Zn(3)-O(16)	118.3(5)
O(10)-Zn(1)-Zn(3)-O(16)	18.1(5)
O(3)-Zn(1)-Zn(3)-O(16)	-143.2(5)
Zn(2)-Zn(1)-Zn(3)-O(16)	-100.3(5)
Zn(4)-Zn(1)-Zn(3)-O(16)	-29.8(5)
O(1)-Zn(1)-Zn(3)-O(13)#3	75.9(4)
O(39)#1-Zn(1)-Zn(3)-O(13)#3	-100.9(4)
O(10)-Zn(1)-Zn(3)-O(13)#3	158.8(4)
O(3)-Zn(1)-Zn(3)-O(13)#3	-2.4(4)
Zn(2)-Zn(1)-Zn(3)-O(13)#3	40.5(3)
Zn(4)-Zn(1)-Zn(3)-O(13)#3	110.9(3)
O(1)-Zn(1)-Zn(3)-O(40)#1	173.8(4)
O(39)#1-Zn(1)-Zn(3)-O(40)#1	-3.1(4)
O(10)-Zn(1)-Zn(3)-O(40)#1	-103.3(4)
O(3)-Zn(1)-Zn(3)-O(40)#1	95.5(4)

Zn(2)-Zn(1)-Zn(3)-O(40)#1	138.4(3)
Zn(4)-Zn(1)-Zn(3)-O(40)#1	-151.2(3)
O(39)#1-Zn(1)-Zn(3)-O(1)	-176.8(3)
O(10)-Zn(1)-Zn(3)-O(1)	82.9(3)
O(3)-Zn(1)-Zn(3)-O(1)	-78.3(3)
Zn(2)-Zn(1)-Zn(3)-O(1)	-35.4(2)
Zn(4)-Zn(1)-Zn(3)-O(1)	35.0(2)
Zn(1)-O(1)-Zn(4)-O(15)	-119.9(3)
Zn(2)-O(1)-Zn(4)-O(15)	120.1(3)
Zn(3)-O(1)-Zn(4)-O(15)	-0.7(4)
Zn(1)-O(1)-Zn(4)-O(9)	-3.2(3)
Zn(2)-O(1)-Zn(4)-O(9)	-123.2(3)
Zn(3)-O(1)-Zn(4)-O(9)	116.0(3)
Zn(1)-O(1)-Zn(4)-O(32)#2	119.4(3)
Zn(2)-O(1)-Zn(4)-O(32)#2	-0.6(4)
Zn(3)-O(1)-Zn(4)-O(32)#2	-121.3(3)
Zn(2)-O(1)-Zn(4)-Zn(1)	-120.0(3)
Zn(3)-O(1)-Zn(4)-Zn(1)	119.2(3)
Zn(1)-O(1)-Zn(4)-Zn(2)	120.0(3)
Zn(3)-O(1)-Zn(4)-Zn(2)	-120.8(3)
C(53)-O(15)-Zn(4)-O(1)	-8.8(14)
C(53)-O(15)-Zn(4)-O(9)	-129.1(13)
C(53)-O(15)-Zn(4)-O(32)#2	117.4(13)
C(53)-O(15)-Zn(4)-Zn(1)	-47.4(14)
C(53)-O(15)-Zn(4)-Zn(2)	29.9(14)
C(27)-O(9)-Zn(4)-O(1)	0.5(9)
C(27)-O(9)-Zn(4)-O(15)	124.1(9)
C(27)-O(9)-Zn(4)-O(32)#2	-125.6(9)
C(27)-O(9)-Zn(4)-Zn(1)	-1.4(8)
C(27)-O(9)-Zn(4)-Zn(2)	-35.4(9)
O(39)#1-Zn(1)-Zn(4)-O(1)	-78.2(4)
O(10)-Zn(1)-Zn(4)-O(1)	-176.8(3)
O(3)-Zn(1)-Zn(4)-O(1)	85.4(4)
Zn(2)-Zn(1)-Zn(4)-O(1)	35.2(2)
Zn(3)-Zn(1)-Zn(4)-O(1)	-36.2(2)
O(1)-Zn(1)-Zn(4)-O(15)	80.8(4)
O(39)#1-Zn(1)-Zn(4)-O(15)	2.6(4)
O(10)-Zn(1)-Zn(4)-O(15)	-96.0(4)
O(3)-Zn(1)-Zn(4)-O(15)	166.2(4)
Zn(2)-Zn(1)-Zn(4)-O(15)	116.0(3)
Zn(3)-Zn(1)-Zn(4)-O(15)	44.7(3)
O(1)-Zn(1)-Zn(4)-O(9)	176.9(3)
O(39)#1-Zn(1)-Zn(4)-O(9)	98.6(3)
O(10)-Zn(1)-Zn(4)-O(9)	0.1(3)
O(3)-Zn(1)-Zn(4)-O(9)	-97.8(3)

Zn(2)-Zn(1)-Zn(4)-O(9)	-147.9(2)
Zn(3)-Zn(1)-Zn(4)-O(9)	140.7(2)
O(1)-Zn(1)-Zn(4)-O(32)#2	-80.7(4)
O(39)#1-Zn(1)-Zn(4)-O(32)#2	-159.0(5)
O(10)-Zn(1)-Zn(4)-O(32)#2	102.4(4)
O(3)-Zn(1)-Zn(4)-O(32)#2	4.6(4)
Zn(2)-Zn(1)-Zn(4)-O(32)#2	-45.6(4)
Zn(3)-Zn(1)-Zn(4)-O(32)#2	-116.9(4)
O(1)-Zn(1)-Zn(4)-Zn(2)	-35.2(2)
O(39)#1-Zn(1)-Zn(4)-Zn(2)	-113.4(3)
O(10)-Zn(1)-Zn(4)-Zn(2)	148.0(2)
O(3)-Zn(1)-Zn(4)-Zn(2)	50.2(3)
Zn(3)-Zn(1)-Zn(4)-Zn(2)	-71.36(4)
O(31)#2-Zn(2)-Zn(4)-O(1)	171.9(5)
O(4)-Zn(2)-Zn(4)-O(1)	-72.2(4)
O(14)#3-Zn(2)-Zn(4)-O(1)	76.3(4)
Zn(1)-Zn(2)-Zn(4)-O(1)	-35.1(2)
O(31)#2-Zn(2)-Zn(4)-O(15)	91.2(6)
O(1)-Zn(2)-Zn(4)-O(15)	-80.7(4)
O(4)-Zn(2)-Zn(4)-O(15)	-152.9(5)
O(14)#3-Zn(2)-Zn(4)-O(15)	-4.3(5)
Zn(1)-Zn(2)-Zn(4)-O(15)	-115.8(3)
O(31)#2-Zn(2)-Zn(4)-O(9)	-114.1(5)
O(1)-Zn(2)-Zn(4)-O(9)	74.0(3)
O(4)-Zn(2)-Zn(4)-O(9)	1.8(5)
O(14)#3-Zn(2)-Zn(4)-O(9)	150.4(4)
Zn(1)-Zn(2)-Zn(4)-O(9)	38.9(3)
O(31)#2-Zn(2)-Zn(4)-O(32)#2	-8.6(5)
O(1)-Zn(2)-Zn(4)-O(32)#2	179.5(4)
O(4)-Zn(2)-Zn(4)-O(32)#2	107.3(5)
O(14)#3-Zn(2)-Zn(4)-O(32)#2	-104.2(4)
Zn(1)-Zn(2)-Zn(4)-O(32)#2	144.4(3)
O(31)#2-Zn(2)-Zn(4)-Zn(1)	-153.0(4)
O(1)-Zn(2)-Zn(4)-Zn(1)	35.1(2)
O(4)-Zn(2)-Zn(4)-Zn(1)	-37.1(4)
O(14)#3-Zn(2)-Zn(4)-Zn(1)	111.5(3)
Zn(6)-O(2)-Zn(5)-O(33)#4	-120.5(4)
Zn(8)-O(2)-Zn(5)-O(33)#4	119.8(4)
Zn(7)-O(2)-Zn(5)-O(33)#4	0.0(4)
Zn(6)-O(2)-Zn(5)-O(7)	-16.4(4)
Zn(8)-O(2)-Zn(5)-O(7)	-136.2(4)
Zn(7)-O(2)-Zn(5)-O(7)	104.1(4)
Zn(6)-O(2)-Zn(5)-O(22)	143.2(4)
Zn(8)-O(2)-Zn(5)-O(22)	23.5(5)
Zn(7)-O(2)-Zn(5)-O(22)	-96.3(4)

C(26)-O(7)-Zn(5)-O(33)#4	148.6(15)
C(26)-O(7)-Zn(5)-O(2)	41.6(16)
C(26)-O(7)-Zn(5)-O(22)	-83.4(17)
C(79)-O(22)-Zn(5)-O(33)#4	-160.7(18)
C(79)-O(22)-Zn(5)-O(2)	-55.4(18)
C(79)-O(22)-Zn(5)-O(7)	70(2)
Zn(8)-O(2)-Zn(6)-O(8)	119.4(3)
Zn(7)-O(2)-Zn(6)-O(8)	-119.9(3)
Zn(5)-O(2)-Zn(6)-O(8)	0.9(4)
Zn(8)-O(2)-Zn(6)-O(35)	-6.3(3)
Zn(7)-O(2)-Zn(6)-O(35)	114.4(3)
Zn(5)-O(2)-Zn(6)-O(35)	-124.9(3)
Zn(8)-O(2)-Zn(6)-O(27)	-120.2(3)
Zn(7)-O(2)-Zn(6)-O(27)	0.5(3)
Zn(5)-O(2)-Zn(6)-O(27)	121.2(3)
Zn(8)-O(2)-Zn(6)-Zn(7)	-120.7(3)
Zn(5)-O(2)-Zn(6)-Zn(7)	120.7(3)
Zn(7)-O(2)-Zn(6)-Zn(8)	120.7(3)
Zn(5)-O(2)-Zn(6)-Zn(8)	-118.6(3)
C(26)-O(8)-Zn(6)-O(2)	14.8(9)
C(26)-O(8)-Zn(6)-O(35)	141.8(8)
C(26)-O(8)-Zn(6)-O(27)	-111.2(8)
C(26)-O(8)-Zn(6)-Zn(7)	-26.0(9)
C(26)-O(8)-Zn(6)-Zn(8)	55.4(9)
C(131)-O(35)-Zn(6)-O(2)	12.2(8)
C(131)-O(35)-Zn(6)-O(8)	-119.3(7)
C(131)-O(35)-Zn(6)-O(27)	133.4(7)
C(131)-O(35)-Zn(6)-Zn(7)	49.9(8)
C(131)-O(35)-Zn(6)-Zn(8)	8.5(7)
C(105)-O(27)-Zn(6)-O(2)	-2.8(9)
C(105)-O(27)-Zn(6)-O(8)	126.4(8)
C(105)-O(27)-Zn(6)-O(35)	-121.9(8)
C(105)-O(27)-Zn(6)-Zn(7)	-2.5(8)
C(105)-O(27)-Zn(6)-Zn(8)	-40.8(9)
Zn(6)-O(2)-Zn(7)-O(34)#4	121.9(4)
Zn(8)-O(2)-Zn(7)-O(34)#4	-117.2(4)
Zn(5)-O(2)-Zn(7)-O(34)#4	1.6(5)
Zn(6)-O(2)-Zn(7)-O(19)#8	-115.8(3)
Zn(8)-O(2)-Zn(7)-O(19)#8	5.2(3)
Zn(5)-O(2)-Zn(7)-O(19)#8	124.0(3)
Zn(6)-O(2)-Zn(7)-O(28)	-1.6(4)
Zn(8)-O(2)-Zn(7)-O(28)	119.3(3)
Zn(5)-O(2)-Zn(7)-O(28)	-121.8(3)
Zn(6)-O(2)-Zn(7)-Zn(8)	-120.9(3)
Zn(5)-O(2)-Zn(7)-Zn(8)	118.8(3)

Zn(8)-O(2)-Zn(7)-Zn(6)	120.9(3)
Zn(5)-O(2)-Zn(7)-Zn(6)	-120.2(3)
C(105)-O(28)-Zn(7)-O(34)#4	-122.8(11)
C(105)-O(28)-Zn(7)-O(2)	6.6(12)
C(105)-O(28)-Zn(7)-O(19)#8	124.9(11)
C(105)-O(28)-Zn(7)-Zn(8)	43.3(12)
C(105)-O(28)-Zn(7)-Zn(6)	5.7(10)
O(2)-Zn(6)-Zn(7)-O(34)#4	-81.5(6)
O(8)-Zn(6)-Zn(7)-O(34)#4	2.4(6)
O(35)-Zn(6)-Zn(7)-O(34)#4	-164.1(6)
O(27)-Zn(6)-Zn(7)-O(34)#4	99.0(6)
Zn(8)-Zn(6)-Zn(7)-O(34)#4	-116.2(5)
O(8)-Zn(6)-Zn(7)-O(2)	83.9(3)
O(35)-Zn(6)-Zn(7)-O(2)	-82.6(3)
O(27)-Zn(6)-Zn(7)-O(2)	-179.5(3)
Zn(8)-Zn(6)-Zn(7)-O(2)	-34.7(2)
O(2)-Zn(6)-Zn(7)-O(19)#8	81.1(4)
O(8)-Zn(6)-Zn(7)-O(19)#8	165.0(4)
O(35)-Zn(6)-Zn(7)-O(19)#8	-1.5(3)
O(27)-Zn(6)-Zn(7)-O(19)#8	-98.4(3)
Zn(8)-Zn(6)-Zn(7)-O(19)#8	46.4(3)
O(2)-Zn(6)-Zn(7)-O(28)	178.4(4)
O(8)-Zn(6)-Zn(7)-O(28)	-97.6(4)
O(35)-Zn(6)-Zn(7)-O(28)	95.9(3)
O(27)-Zn(6)-Zn(7)-O(28)	-1.1(3)
Zn(8)-Zn(6)-Zn(7)-O(28)	143.7(3)
O(2)-Zn(6)-Zn(7)-Zn(8)	34.7(2)
O(8)-Zn(6)-Zn(7)-Zn(8)	118.7(3)
O(35)-Zn(6)-Zn(7)-Zn(8)	-47.8(2)
O(27)-Zn(6)-Zn(7)-Zn(8)	-144.83(19)
C(79)-O(21)-Zn(8)-O(2)	-10.2(13)
C(79)-O(21)-Zn(8)-O(36)	-139.1(12)
C(79)-O(21)-Zn(8)-O(20)#8	113.8(12)
C(79)-O(21)-Zn(8)-Zn(7)	31.9(13)
C(79)-O(21)-Zn(8)-Zn(6)	-51.2(13)
Zn(6)-O(2)-Zn(8)-O(21)	-126.4(3)
Zn(7)-O(2)-Zn(8)-O(21)	112.9(3)
Zn(5)-O(2)-Zn(8)-O(21)	-7.2(4)
Zn(6)-O(2)-Zn(8)-O(36)	0.4(3)
Zn(7)-O(2)-Zn(8)-O(36)	-120.3(3)
Zn(5)-O(2)-Zn(8)-O(36)	119.7(3)
Zn(6)-O(2)-Zn(8)-O(20)#8	114.6(3)
Zn(7)-O(2)-Zn(8)-O(20)#8	-6.2(3)
Zn(5)-O(2)-Zn(8)-O(20)#8	-126.2(3)
Zn(6)-O(2)-Zn(8)-Zn(7)	120.7(3)

Zn(5)-O(2)-Zn(8)-Zn(7)	-120.0(3)
Zn(7)-O(2)-Zn(8)-Zn(6)	-120.7(3)
Zn(5)-O(2)-Zn(8)-Zn(6)	119.3(3)
C(131)-O(36)-Zn(8)-O(21)	139.9(8)
C(131)-O(36)-Zn(8)-O(2)	5.9(9)
C(131)-O(36)-Zn(8)-O(20)#8	-113.7(8)
C(131)-O(36)-Zn(8)-Zn(7)	-31.4(9)
C(131)-O(36)-Zn(8)-Zn(6)	6.2(7)
O(34)#4-Zn(7)-Zn(8)-O(21)	-6.0(5)
O(2)-Zn(7)-Zn(8)-O(21)	-91.6(4)
O(19)#8-Zn(7)-Zn(8)-O(21)	93.4(4)
O(28)-Zn(7)-Zn(8)-O(21)	-169.1(4)
Zn(6)-Zn(7)-Zn(8)-O(21)	-126.3(3)
O(34)#4-Zn(7)-Zn(8)-O(2)	85.6(5)
O(19)#8-Zn(7)-Zn(8)-O(2)	-175.0(3)
O(28)-Zn(7)-Zn(8)-O(2)	-77.5(4)
Zn(6)-Zn(7)-Zn(8)-O(2)	-34.7(2)
O(34)#4-Zn(7)-Zn(8)-O(36)	163.5(5)
O(2)-Zn(7)-Zn(8)-O(36)	78.0(3)
O(19)#8-Zn(7)-Zn(8)-O(36)	-97.1(3)
O(28)-Zn(7)-Zn(8)-O(36)	0.5(4)
Zn(6)-Zn(7)-Zn(8)-O(36)	43.3(2)
O(34)#4-Zn(7)-Zn(8)-O(20)#8	-100.3(5)
O(2)-Zn(7)-Zn(8)-O(20)#8	174.1(3)
O(19)#8-Zn(7)-Zn(8)-O(20)#8	-0.9(3)
O(28)-Zn(7)-Zn(8)-O(20)#8	96.6(3)
Zn(6)-Zn(7)-Zn(8)-O(20)#8	139.4(2)
O(34)#4-Zn(7)-Zn(8)-Zn(6)	120.3(4)
O(2)-Zn(7)-Zn(8)-Zn(6)	34.7(2)
O(19)#8-Zn(7)-Zn(8)-Zn(6)	-140.3(2)
O(28)-Zn(7)-Zn(8)-Zn(6)	-42.8(3)
O(2)-Zn(6)-Zn(8)-O(21)	79.7(5)
O(8)-Zn(6)-Zn(8)-O(21)	-4.4(5)
O(35)-Zn(6)-Zn(8)-O(21)	-106.4(4)
O(27)-Zn(6)-Zn(8)-O(21)	159.2(4)
Zn(7)-Zn(6)-Zn(8)-O(21)	114.7(4)
O(8)-Zn(6)-Zn(8)-O(2)	-84.1(4)
O(35)-Zn(6)-Zn(8)-O(2)	173.9(3)
O(27)-Zn(6)-Zn(8)-O(2)	79.5(3)
Zn(7)-Zn(6)-Zn(8)-O(2)	35.0(2)
O(2)-Zn(6)-Zn(8)-O(36)	-179.6(3)
O(8)-Zn(6)-Zn(8)-O(36)	96.3(3)
O(35)-Zn(6)-Zn(8)-O(36)	-5.7(3)
O(27)-Zn(6)-Zn(8)-O(36)	-100.1(3)
Zn(7)-Zn(6)-Zn(8)-O(36)	-144.6(2)

O(2)-Zn(6)-Zn(8)-O(20)#8	-83.0(3)
O(8)-Zn(6)-Zn(8)-O(20)#8	-167.1(3)
O(35)-Zn(6)-Zn(8)-O(20)#8	91.0(3)
O(27)-Zn(6)-Zn(8)-O(20)#8	-3.4(3)
Zn(7)-Zn(6)-Zn(8)-O(20)#8	-48.0(2)
O(2)-Zn(6)-Zn(8)-Zn(7)	-35.0(2)
O(8)-Zn(6)-Zn(8)-Zn(7)	-119.1(3)
O(35)-Zn(6)-Zn(8)-Zn(7)	138.96(18)
O(27)-Zn(6)-Zn(8)-Zn(7)	44.6(2)

Symmetry transformations used to generate equivalent atoms:

#1 x+1,y,z+1; #2 x,y+1,z; #3 x-1,y,z; #4 x+1,y,z; #5 x+1,y+1,z+1; #6 x,y-1,z; #7 x-1,y,z-1

#8 x-1,y-1,z-1

Table AA 18. Crystal data and structural refinement for BIO-MOF-1

Identification code		
Empirical formula	C26 H16 N5 O6.25 Zn2	
Formula weight	629.18	
Temperature	298(2) K	
Wavelength	0.71073 Å	
Crystal system	Tetragonal	
Space group	I4(1)22	
Unit cell dimensions	a = 38.237(2) Å	α= 90°.
	b = 38.237(2) Å	β= 90°.
	c = 11.1753(12) Å	γ = 90°.
Volume	16339(2) $Å^3$	
Z	16	
Density (calculated)	1.023 Mg/m^3	
Absorption coefficient	1.207 mm^{-1}	
F(000)	5072	
Crystal size	0.20 x 0.16 x 0.16 mm^3	
Theta range for data collection	1.90 to 25.00°.	
Index ranges	-45<=h<=45, -45<=k<=45, -13<=l<=13	
Reflections collected	65848	
Independent reflections	7210 [R(int) = 0.1164]	
Completeness to theta = 23.25°	99.5 %	
Absorption correction	Multi-scan (Sadabs)	
Max. and min. transmission	0.8303 and 0.7943	

Refinement method	Full-matrix least-squares on F^2	
Data / restraints / parameters	7210 / 17 / 299	
Goodness-of-fit on F^2	1.528	
Final R indices [I>2sigma(I)]	R1 = 0.0940, wR2 = 0.2376	
R indices (all data)	R1 = 0.1267, wR2 = 0.2501	
Largest diff. peak and hole	0.966 and -0.640 e.$Å^{-3}$	

Table AA 19. Atomic coordinate (x 10^4) and equivalent displacement parameters ($Å^2$ x 10^3) for BIO-MOF-1. U(eq) is defined as one third of the trace of the orthogonalized Uij tensor.

	x	y	z	U(eq)
Zn(1)	4592(1)	5006(1)	3965(1)	44(1)
Zn(2)	5883(1)	5883(1)	0	40(1)
Zn(3)	4132(1)	5868(1)	0	40(1)
O(1)	5000	5000	5000	24(2)
O(2)	3919(2)	5016(4)	3267(8)	104(3)
O(3)	4183(2)	4881(3)	4944(8)	93(4)
O(4)	1298(2)	4299(3)	6789(8)	76(3)
O(5)	1516(2)	4016(2)	8269(7)	70(2)
O(6)	3710(2)	5687(3)	840(9)	84(4)
O(7)	3787(4)	6207(5)	1426(15)	190(7)
N(1)	5330(2)	5388(3)	2780(8)	51(3)
N(2)	4715(3)	5414(3)	2752(11)	80(4)
N(3)	4523(2)	5750(2)	1190(11)	64(3)
N(4)	5492(3)	5764(3)	1195(10)	64(3)
N(5)	4999(4)	6081(2)	-175(7)	80(3)
C(1)	5584(4)	5528(4)	2124(13)	75(5)
C(2)	5043(3)	5498(3)	2354(9)	62(3)
C(3)	4451(4)	5556(3)	2098(10)	74(4)
C(4)	4890(2)	5843(3)	777(11)	63(3)
C(5)	5131(3)	5720(3)	1425(10)	71(4)
C(6)	3918(3)	4935(5)	4297(12)	85(5)
C(7)	3267(2)	4906(3)	4228(8)	144(9)
C(8)	2944(2)	4808(3)	4690(9)	161(10)

C(9)	2924(1)	4648(3)	5805(8)	87(4)
C(10)	3228(2)	4586(3)	6457(7)	118(6)
C(11)	3551(2)	4684(3)	5995(8)	115(7)
C(12)	3571(1)	4844(3)	4881(8)	83(4)
C(13)	2286(2)	4725(3)	5933(13)	234(16)
C(14)	1956(2)	4616(3)	6290(13)	222(15)
C(15)	1919(1)	4323(3)	7013(9)	77(4)
C(16)	2214(2)	4138(2)	7379(9)	95(5)
C(17)	2545(2)	4247(3)	7022(9)	110(6)
C(18)	2581(1)	4541(3)	6299(10)	107(6)
C(19)	1559(3)	4195(3)	7399(13)	63(3)
C(20)	3617(4)	5922(5)	1442(16)	164(12)
C(21)	3236(4)	6172(4)	3100(20)	171(18)
C(22)	2923(5)	6158(5)	3729(17)	105(10)
C(23)	2675(4)	5905(5)	3450(20)	151(8)
C(24)	2740(5)	5665(5)	2550(20)	260(30)
C(25)	3053(5)	5678(5)	1915(17)	99(10)
C(26)	3301(3)	5931(4)	2191(15)	131(6)
C(21')	3104(5)	6235(3)	2346(18)	140
C(22')	2798(5)	6224(4)	3016(19)	136(14)
C(23')	2678(4)	5906(5)	3463(16)	151(8)
C(24')	2863(5)	5601(3)	3240(19)	119(11)
C(25')	3170(4)	5612(3)	2570(18)	92(9)
C(26')	3290(3)	5930(4)	2123(12)	131(6)

Table AA 20. Bond lengths [Å] and angles [°] for BIO-MOF-1.

Zn(1)-O(1)	1.9438(8)
Zn(1)-O(3)	1.965(7)
Zn(1)-N(1)#1	2.028(9)
Zn(1)-N(2)	2.119(12)
Zn(1)-Zn(1)#1	3.1246(16)

Zn(2)-O(4)#2	1.906(7)
Zn(2)-O(4)#3	1.906(7)
Zn(2)-N(4)#4	2.056(11)
Zn(2)-N(4)	2.056(11)
Zn(3)-O(6)	1.992(9)
Zn(3)-O(6)#5	1.992(9)
Zn(3)-N(3)#5	2.048(9)
Zn(3)-N(3)	2.049(9)
Zn(3)-O(7)	2.443(15)
Zn(3)-O(7)#5	2.443(15)
Zn(3)-C(20)#5	2.553(17)
Zn(3)-C(20)	2.553(17)
O(1)-Zn(1)#6	1.9437(8)
O(1)-Zn(1)#7	1.9437(8)
O(1)-Zn(1)#1	1.9439(8)
O(2)-C(6)	1.193(14)
O(3)-C(6)	1.263(14)
O(4)-C(19)	1.271(13)
O(4)-Zn(2)#8	1.906(7)
O(5)-C(19)	1.201(13)
O(6)-C(20)	1.18(2)
O(7)-C(20)	1.265(19)
N(1)-C(2)	1.268(14)
N(1)-C(1)	1.328(14)
N(1)-Zn(1)#1	2.028(9)
N(2)-C(3)	1.361(14)
N(2)-C(2)	1.371(15)
N(3)-C(3)	1.286(15)
N(3)-C(4)	1.521(14)
N(4)-C(5)	1.414(14)
N(4)-C(1)	1.421(16)
N(5)-C(4)	1.459(15)
N(5)-H(5A)	0.8600
N(5)-H(5B)	0.8600
C(1)-H(1A)	0.9300
C(2)-C(5)	1.382(15)
C(3)-H(3A)	0.9300
C(4)-C(5)	1.262(13)
C(6)-C(12)	1.520(12)

C(7)-C(8)	1.3900
C(7)-C(12)	1.3900
C(7)-H(7A)	0.9300
C(8)-C(9)	1.3900
C(8)-H(8A)	0.9300
C(9)-C(10)	1.3900
C(9)-C(18)	1.484(7)
C(10)-C(11)	1.3900
C(10)-H(10A)	0.9300
C(11)-C(12)	1.3900
C(11)-H(11A)	0.9300
C(13)-C(14)	1.3900
C(13)-C(18)	1.3900
C(13)-H(13A)	0.9300
C(14)-C(15)	1.3900
C(14)-H(14A)	0.9300
C(15)-C(16)	1.3900
C(15)-C(19)	1.524(12)
C(16)-C(17)	1.3900
C(16)-H(16A)	0.9300
C(17)-C(18)	1.3900
C(17)-H(17A)	0.9300
C(20)-C(26')	1.47(2)
C(20)-C(26)	1.47(2)
C(21)-C(22)	1.3900
C(21)-C(26)	1.3900
C(21)-H(21A)	0.9300
C(22)-C(23)	1.3900
C(22)-H(22A)	0.9300
C(23)-C(24)	1.3900
C(23)-C(23)#9	1.50(2)
C(24)-C(25)	1.3900
C(24)-H(24A)	0.9300
C(25)-C(26)	1.3900
C(25)-H(25A)	0.9300
C(21')-C(22')	1.3900
C(21')-C(26')	1.3900
C(21')-H(21B)	0.9300
C(22')-C(23')	1.3900

C(22')-H(22B)	0.9300
C(23')-C(24')	1.3900
C(23')-C(23')#9	1.50(2)
C(24')-C(25')	1.3900
C(24')-H(24B)	0.9300
C(25')-C(26')	1.3900
C(25')-H(25B)	0.9300
O(1)-Zn(1)-O(3)	107.7(2)
O(1)-Zn(1)-N(1)#1	105.1(3)
O(3)-Zn(1)-N(1)#1	107.5(4)
O(1)-Zn(1)-N(2)	102.1(3)
O(3)-Zn(1)-N(2)	135.4(4)
N(1)#1-Zn(1)-N(2)	95.5(3)
O(1)-Zn(1)-Zn(1)#1	36.51(3)
O(3)-Zn(1)-Zn(1)#1	142.3(2)
N(1)#1-Zn(1)-Zn(1)#1	80.9(2)
N(2)-Zn(1)-Zn(1)#1	77.7(3)
O(4)#2-Zn(2)-O(4)#3	141.6(6)
O(4)#2-Zn(2)-N(4)#4	100.9(4)
O(4)#3-Zn(2)-N(4)#4	104.7(4)
O(4)#2-Zn(2)-N(4)	104.7(4)
O(4)#3-Zn(2)-N(4)	100.9(4)
N(4)#4-Zn(2)-N(4)	95.7(5)
O(6)-Zn(3)-O(6)#5	141.5(5)
O(6)-Zn(3)-N(3)#5	103.4(4)
O(6)#5-Zn(3)-N(3)#5	102.1(4)
O(6)-Zn(3)-N(3)	102.1(4)
O(6)#5-Zn(3)-N(3)	103.4(4)
N(3)#5-Zn(3)-N(3)	95.9(6)
O(6)-Zn(3)-O(7)	55.7(4)
O(6)#5-Zn(3)-O(7)	93.6(5)
N(3)#5-Zn(3)-O(7)	158.2(4)
N(3)-Zn(3)-O(7)	95.0(5)
O(6)-Zn(3)-O(7)#5	93.6(5)
O(6)#5-Zn(3)-O(7)#5	55.7(4)
N(3)#5-Zn(3)-O(7)#5	95.0(5)
N(3)-Zn(3)-O(7)#5	158.2(4)
O(7)-Zn(3)-O(7)#5	81.4(9)
O(6)-Zn(3)-C(20)#5	119.8(5)

O(6)#5-Zn(3)-C(20)#5	26.5(5)
N(3)#5-Zn(3)-C(20)#5	99.8(5)
N(3)-Zn(3)-C(20)#5	129.7(5)
O(7)-Zn(3)-C(20)#5	87.6(5)
O(7)#5-Zn(3)-C(20)#5	29.2(5)
O(6)-Zn(3)-C(20)	26.5(5)
O(6)#5-Zn(3)-C(20)	119.8(5)
N(3)#5-Zn(3)-C(20)	129.7(5)
N(3)-Zn(3)-C(20)	99.8(5)
O(7)-Zn(3)-C(20)	29.2(5)
O(7)#5-Zn(3)-C(20)	87.6(5)
C(20)#5-Zn(3)-C(20)	105.8(8)
Zn(1)#6-O(1)-Zn(1)#7	106.97(5)
Zn(1)#6-O(1)-Zn(1)	109.58(9)
Zn(1)#7-O(1)-Zn(1)	111.90(9)
Zn(1)#6-O(1)-Zn(1)#1	111.90(9)
Zn(1)#7-O(1)-Zn(1)#1	109.58(9)
Zn(1)-O(1)-Zn(1)#1	106.97(5)
C(6)-O(3)-Zn(1)	106.3(7)
C(19)-O(4)-Zn(2)#8	108.3(8)
C(20)-O(6)-Zn(3)	104.4(12)
C(20)-O(7)-Zn(3)	80.2(12)
C(2)-N(1)-C(1)	106.8(11)
C(2)-N(1)-Zn(1)#1	128.4(7)
C(1)-N(1)-Zn(1)#1	123.4(10)
C(3)-N(2)-C(2)	114.2(12)
C(3)-N(2)-Zn(1)	118.2(11)
C(2)-N(2)-Zn(1)	125.9(8)
C(3)-N(3)-C(4)	124.8(11)
C(3)-N(3)-Zn(3)	118.9(9)
C(4)-N(3)-Zn(3)	115.1(8)
C(5)-N(4)-C(1)	91.9(10)
C(5)-N(4)-Zn(2)	148.7(9)
C(1)-N(4)-Zn(2)	115.9(9)
C(4)-N(5)-H(5A)	120.0
C(4)-N(5)-H(5B)	120.0
H(5A)-N(5)-H(5B)	120.0
N(1)-C(1)-N(4)	118.6(13)
N(1)-C(1)-H(1A)	120.7

N(4)-C(1)-H(1A)	120.7
N(1)-C(2)-N(2)	126.2(10)
N(1)-C(2)-C(5)	106.1(8)
N(2)-C(2)-C(5)	127.7(10)
N(3)-C(3)-N(2)	119.8(14)
N(3)-C(3)-H(3A)	120.1
N(2)-C(3)-H(3A)	120.1
C(5)-C(4)-N(5)	116.3(11)
C(5)-C(4)-N(3)	114.4(11)
N(5)-C(4)-N(3)	129.0(11)
C(4)-C(5)-C(2)	118.9(11)
C(4)-C(5)-N(4)	124.3(11)
C(2)-C(5)-N(4)	116.5(8)
O(2)-C(6)-O(3)	126.3(10)
O(2)-C(6)-C(12)	118.4(11)
O(3)-C(6)-C(12)	114.8(12)
C(8)-C(7)-C(12)	120.0
C(8)-C(7)-H(7A)	120.0
C(12)-C(7)-H(7A)	120.0
C(9)-C(8)-C(7)	120.0
C(9)-C(8)-H(8A)	120.0
C(7)-C(8)-H(8A)	120.0
C(8)-C(9)-C(10)	120.0
C(8)-C(9)-C(18)	120.3(6)
C(10)-C(9)-C(18)	119.7(6)
C(11)-C(10)-C(9)	120.0
C(11)-C(10)-H(10A)	120.0
C(9)-C(10)-H(10A)	120.0
C(10)-C(11)-C(12)	120.0
C(10)-C(11)-H(11A)	120.0
C(12)-C(11)-H(11A)	120.0
C(11)-C(12)-C(7)	120.0
C(11)-C(12)-C(6)	122.2(8)
C(7)-C(12)-C(6)	117.7(8)
C(14)-C(13)-C(18)	120.0
C(14)-C(13)-H(13A)	120.0
C(18)-C(13)-H(13A)	120.0
C(15)-C(14)-C(13)	120.0
C(15)-C(14)-H(14A)	120.0

C(13)-C(14)-H(14A)	120.0
C(14)-C(15)-C(16)	120.0
C(14)-C(15)-C(19)	120.8(7)
C(16)-C(15)-C(19)	119.2(7)
C(15)-C(16)-C(17)	120.0
C(15)-C(16)-H(16A)	120.0
C(17)-C(16)-H(16A)	120.0
C(16)-C(17)-C(18)	120.0
C(16)-C(17)-H(17A)	120.0
C(18)-C(17)-H(17A)	120.0
C(17)-C(18)-C(13)	120.0
C(17)-C(18)-C(9)	121.9(7)
C(13)-C(18)-C(9)	117.9(6)
O(5)-C(19)-O(4)	120.3(10)
O(5)-C(19)-C(15)	122.3(10)
O(4)-C(19)-C(15)	117.3(11)
O(6)-C(20)-O(7)	119.6(17)
O(6)-C(20)-C(26')	124.5(17)
O(7)-C(20)-C(26')	115.4(17)
O(6)-C(20)-C(26)	126.1(18)
O(7)-C(20)-C(26)	114.1(18)
C(26')-C(20)-C(26)	3.4(9)
O(6)-C(20)-Zn(3)	49.1(9)
O(7)-C(20)-Zn(3)	70.5(10)
C(26')-C(20)-Zn(3)	171.2(11)
C(26)-C(20)-Zn(3)	174.3(15)
C(22)-C(21)-C(26)	120.0
C(22)-C(21)-H(21A)	120.0
C(26)-C(21)-H(21A)	120.0
C(21)-C(22)-C(23)	120.0
C(21)-C(22)-H(22A)	120.0
C(23)-C(22)-H(22A)	120.0
C(24)-C(23)-C(22)	120.0
C(24)-C(23)-C(23)#9	119.0(19)
C(22)-C(23)-C(23)#9	120.8(17)
C(23)-C(24)-C(25)	120.0
C(23)-C(24)-H(24A)	120.0
C(25)-C(24)-H(24A)	120.0
C(26)-C(25)-C(24)	120.0

C(26)-C(25)-H(25A)	120.0
C(24)-C(25)-H(25A)	120.0
C(25)-C(26)-C(21)	120.0
C(25)-C(26)-C(20)	114.7(16)
C(21)-C(26)-C(20)	125.3(16)
C(22')-C(21')-C(26')	120.0
C(22')-C(21')-H(21B)	120.0
C(26')-C(21')-H(21B)	120.0
C(23')-C(22')-C(21')	120.0
C(23')-C(22')-H(22B)	120.0
C(21')-C(22')-H(22B)	120.0
C(22')-C(23')-C(24')	120.0
C(22')-C(23')-C(23')#9	116.9(5)
C(24')-C(23')-C(23')#9	122.60(16)
C(25')-C(24')-C(23')	120.0
C(25')-C(24')-H(24B)	120.0
C(23')-C(24')-H(24B)	120.0
C(26')-C(25')-C(24')	120.0
C(26')-C(25')-H(25B)	120.0
C(24')-C(25')-H(25B)	120.0
C(25')-C(26')-C(21')	120.0
C(25')-C(26')-C(20)	116.9(12)
C(21')-C(26')-C(20)	123.1(12)

Symmetry transformations used to generate equivalent atoms:

#1 -x+1,-y+1,z+0; #2 x+1/2,-y+1,-z+3/4; #3 -y+1,x+1/2,z-3/4; #4 y+0,x+0,-z+0;

#5 -y+1,-x+1,-z; #6 -y+1,-x+1,-z+1; #7 y+0,x+0,-z+1; #8 y-1/2,-x+1,z+3/4 #9 -x+1/2,y,-z+3/4

Table AA 21. Anistropic displacement parameters ($Å^2x10^3$) for BIO-MOF-1. The anisotropic displacement factor exponent takes the form: $-2p^2[h^2a^{*2}U^{11} + ... + 2hka^*b^*U^{12}]$.

	U^{11}	U^{22}	U^{33}	U^{23}	U^{13}	U^{12}
Zn(1)	28(1)	64(1)	40(1)	17(1)	-5(1)	4(1)
Zn(2)	36(1)	36(1)	49(1)	2(1)	-2(1)	10(1)
Zn(3)	37(1)	37(1)	47(1)	15(1)	15(1)	22(1)
O(2)	53(4)	167(9)	92(6)	70(9)	18(4)	-22(7)
O(3)	36(4)	164(11)	78(5)	26(6)	-1(4)	-25(5)

O(4)	34(4)	116(8)	79(6)	31(6)	-13(5)	-33(4)
O(5)	58(5)	93(6)	59(5)	18(5)	3(4)	-14(4)
O(6)	65(6)	102(7)	86(7)	55(6)	54(5)	59(5)
O(7)	133(12)	242(18)	196(15)	-37(13)	96(11)	-75(11)
N(1)	28(5)	64(6)	61(7)	13(6)	11(4)	5(4)
N(2)	113(11)	49(6)	79(9)	3(6)	-52(8)	37(6)
N(3)	14(4)	53(6)	124(10)	23(7)	-23(5)	11(4)
N(4)	77(8)	60(7)	55(7)	-18(6)	17(6)	-8(5)
N(5)	117(7)	55(5)	70(5)	40(4)	36(10)	8(7)
C(1)	60(9)	60(9)	105(13)	-19(9)	28(9)	-16(7)
C(2)	81(10)	61(6)	46(6)	-5(5)	34(8)	-25(7)
C(3)	116(12)	57(9)	48(8)	27(7)	-49(8)	-11(7)
C(4)	30(6)	77(8)	82(9)	-30(7)	-19(5)	15(5)
C(5)	87(10)	88(9)	39(6)	2(6)	2(6)	6(7)
C(6)	46(7)	137(15)	73(8)	-19(9)	13(6)	-35(8)
C(7)	49(7)	250(20)	131(13)	133(16)	-13(7)	-20(10)
C(8)	21(6)	320(30)	141(13)	156(16)	-9(7)	-22(9)
C(9)	32(6)	135(13)	95(10)	29(9)	-9(6)	4(7)
C(10)	46(8)	250(20)	63(8)	50(11)	-8(7)	-27(10)
C(11)	49(8)	230(20)	70(9)	19(11)	-3(7)	-54(10)
C(12)	30(6)	115(11)	104(10)	17(8)	-19(6)	-17(5)
C(13)	12(6)	320(30)	370(30)	280(30)	-11(11)	-16(10)
C(14)	29(7)	320(30)	320(30)	260(30)	7(12)	1(12)
C(15)	39(7)	119(11)	74(8)	16(8)	7(6)	-8(6)
C(16)	34(6)	137(13)	114(11)	65(10)	6(7)	8(6)
C(17)	41(7)	211(17)	79(10)	64(11)	3(7)	14(9)
C(18)	47(8)	173(15)	101(12)	71(12)	10(7)	-14(8)
C(19)	29(6)	63(7)	98(10)	6(7)	-4(6)	-10(5)
C(20)	62(11)	280(30)	150(20)	140(20)	33(12)	36(16)

Table AA 22. Hydrogen coordinates (x10^4) and isotropic displacement parameters (Å^2 x 10^3) for BIO-MOF-1

	x	**y**	**z**	**U(eq)**
H(5A)	5217	6130	-268	96
H(5B)	4845	6172	-642	96
H(1A)	5817	5472	2271	90
H(3A)	4219	5514	2306	88
H(7A)	3281	5013	3482	173
H(8A)	2741	4850	4254	193

H(10A)	3214	4479	7203	142
H(11A)	3753	4642	6432	138
H(13A)	2310	4922	5449	281
H(14A)	1759	4739	6045	266
H(16A)	2190	3942	7863	114
H(17A)	2741	4124	7267	132
H(21A)	3402	6341	3282	205
H(22A)	2880	6319	4335	126
H(24A)	2574	5495	2362	309
H(25A)	3097	5517	1308	118
H(21B)	3185	6447	2047	168
H(22B)	2674	6428	3166	163
H(24B)	2783	5388	3539	143
H(25B)	3294	5408	2421	111